Proceedings of the

Helmholtz International Summer School Quantum Field Theory at the Limits: from Strong Fields to Heavy Quarks (HQ 2016)

July 18-30, 2016

BLTP, JINR, Dubna, Russia

Editors: Ahmed Ali, David Blaschke, Aidos Issadykov, Mikhail Ivanov

Verlag Deutsches Elektronen-Synchrotron

Impressum

Proceedings of the Helmholtz International Summer School 2016 (HQ 2016)

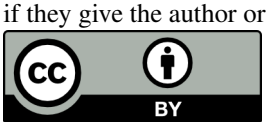
July 18-30, 2016 BLTP, JINR, Dubna, Russia

Conference homepage
http://indico-new.jinr.ru/event/hq2016/

Slides at
http://indico.jinr.ru/conferenceDisplay.py?confId=99

Online proceedings at
http://dx.doi.org/10.3204/DESY-PROC-2016-04

The copyright is governed by the Creative Commons agreement under CC BY 4.0, which allows to copy, distribute, display and perform the work and make derivative works and remixes based on it only if they give the author or licensor the credits (attribution) in the manner specified by these.



Editors:
Ahmed Ali, David Blaschke, Aidos Issadykov, Mikhail Ivanov
April 2017
DESY-PROC-2016-04
ISBN 978-3-945931-07-3
ISSN 1435-8077

Published by
Verlag Deutsches Elektronen-Synchrotron
Notkestraße 85
22607 Hamburg
Germany

Printed by
Kopierzentrale Deutsches Elektronen-Synchrotron

Organizing Committee

Ahmed Ali (DESY)
David Blaschke (JINR, Uni Wroclaw, NRNU Moscow)
Holger Giess (HI, Jena)
Mikhail A. Ivanov (JINR)

Local Organizers

Yu. Bystritskiy (JINR)
A. Issadykov (JINR)
A. Khvorostukhin (JINR)
V. Novikova (JINR)
I. Pirozhenko (JINR)
J. Schmelzer (Rostock Univ. & JINR)
V. Zhuravlev (JINR)

Preface

The Helmholtz International Summer School (HISS) entitled "Quantum Field Theory at the Limits: from Strong Fields to Heavy Quarks (SF→ HQ)", was held in the period July 18-30, 2016 at the Bogoliubov Laboratory of Theoretical Physics (BLTP) of the Joint Institute for Nuclear Research (JINR) in Dubna, Russia, as part of the activities of the Dubna International Advanced School of Theoretical Physics (DIAS-TH). It was co-organized by Ahmed Ali (DESY Hamburg), David Blaschke (JINR Dubna, MEPhI & Univ. Wroclaw), Holger Gies (HI Jena), and Mikhail Ivanov (JINR Dubna), and was attended by 82 participants (faculty + students), not counting the JINR physicists who attended some lectures as non-registered participants. The school (SF→ HQ) continued the workshops and schools of the HISS series held earlier in Dubna (1993, 1996, 2000, 2005, 2008, 2013), Bad Honnef (1994) and Rostock (1997). The scientific program of the school consisted of five regular (one-hour long) lectures in the morning and afternoon sessions, with typically two contributed talks given by younger participants (students and postdocs), each half-hour long, in the late afternoons. Altogether, we had sixty lectures by the faculty and participants. In addition, black-board exercises were held in the post-lunch periods on selected aspects of strong fields and field theory.

The HISS series of schools has played an important role in bringing together an international faculty and young physicists (Ph.D. and postdocs), mostly from Russia and Germany, but increasingly also from other countries, including those affiliated to JINR Dubna. They participate in two-week long intense scientific discourse, mainly dedicated lectures on selected topics covering the foundation and the frontiers of high energy physics and cosmology. The novelty of this year's school was its bifocal interest, which brought together two different physical science communities - particle and laser physicists. There were two broad areas of research covered at this school: heavy quark physics and physics of high field intensities. The focus of the former was on the latest results on heavy quark physics from all four large experimental collaborations at the LHC (ALICE, ATLAS, CMS, LHCb), at the B-factory experiments (BaBar and Belle), and from BESIII. This was accompanied with lectures on the theoretical aspects of heavy quark physics, Quarkonia and Quarkonia-like multiquarks states (tetra- and pentaquarks), including various state-of-the-art calculational techniques, such as perturbative QCD, lattice-QCD, and effective field theories. The focus on the later topic was on the high intensity frontier and extreme states of matter as probed by current and upcoming high power laser and high-Z ion facilities all around the world. An afternoon tour at the heavy ion collider facility NICA, the superconducting accelerator complex under construction at the Veksler-Baldin Laboratory for High-Energy Physics, was also organized.

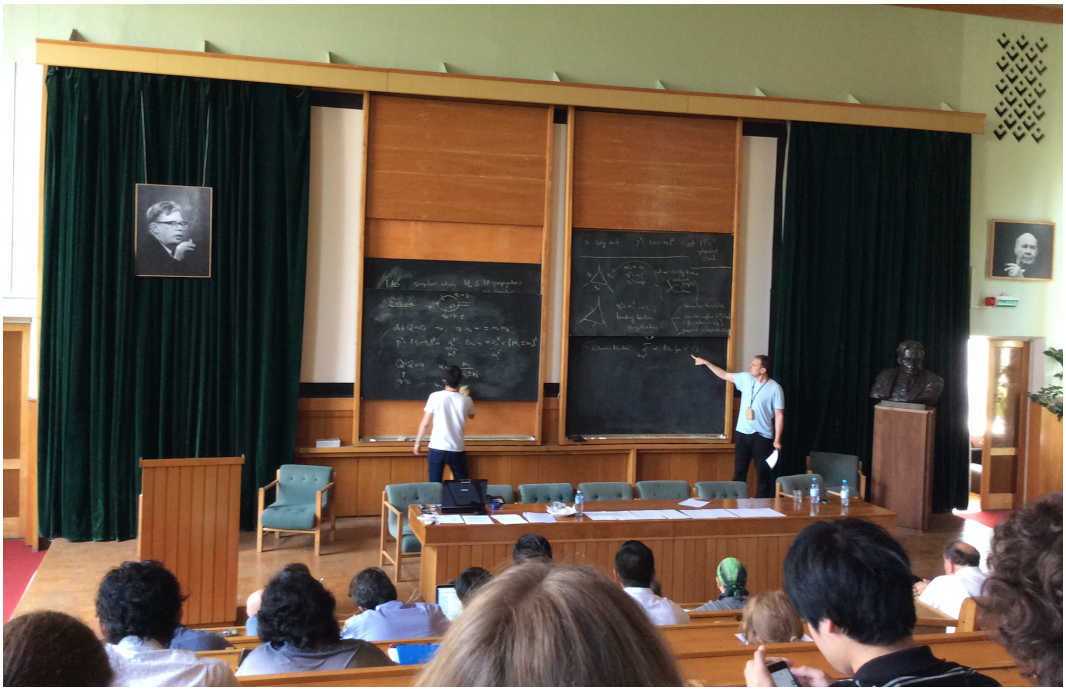
A number of experimental facilities are now operating effectively, foremost among them the LHC, providing extremely precise measurements on a wide variety of phenomena, in particular, the top quark - Higgs boson complex. A new force - the Higgs force - has been discovered at the LHC, which in all likelihood will act as a portal to physics at very high energy scales, deepening our understanding also of the early stages of the cosmic evolution. Apart from the emphasis on the high energy frontier, which is probing new phenomena and forces in nature, also the so-called rare processes in the charm and bottom quark physics are of great interest. They test the standard theory of particle physics at the quantum level, and hence also probe physics beyond-the-standard model. Experimental precision achieved on a number of observables is impressive and has to be matched by theory to have meaningful and quantitative tests of the standard model. Consequently, the focus of the talks was on theoretical tools and their applications, enabling the required high precision. At the same time, a second layer of

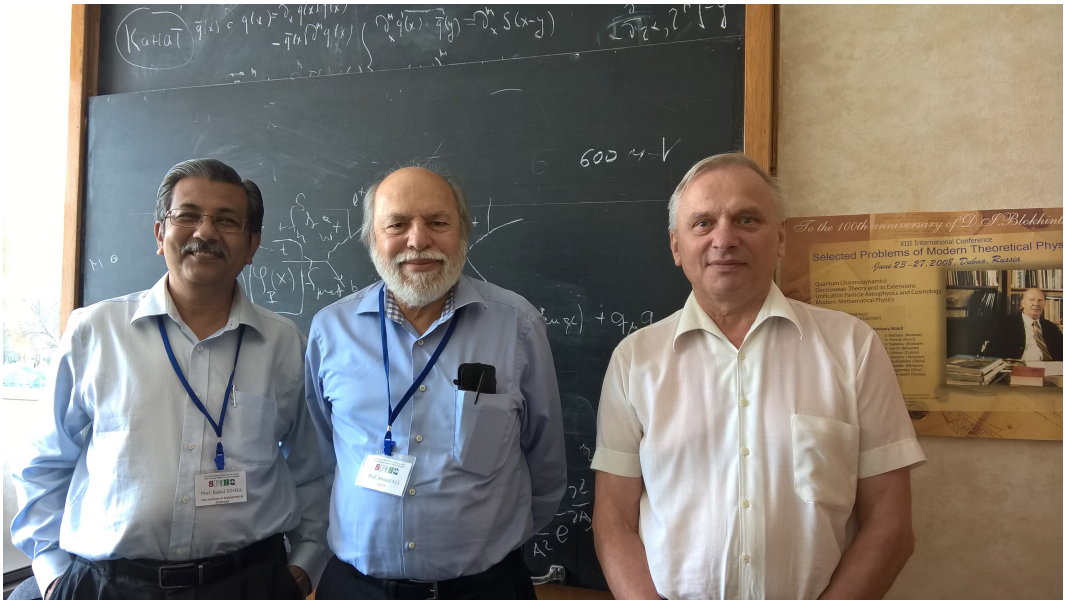
hadrons seem to exist in nature, consisting of multiquark states, and also this emergent field was one of the topics at this school.

The school was supported financially on the basis of the HISS Dubna collaboration agreement concluded between a group of Helmholz Centres (DESY, Juelich, GSI, KIT, HZDR), Helmholtz Institutes (Jena, Mainz, FAIR-Russia Research Centre) and JINR Dubna (with its Bogoliubov-Infeld and Heisenberg-Landau Programs), as well as by the Russian Foundation for Basic Research (RFBR). The proceedings of the 2016 HISS Dubna School on "Quantum Field Theory at the Limits: from Strong Fields to Heavy Quarks" are being published with the help of DESY. We thank all the funding agencies and supporting institutes for their financial support, and the local organizing committee of the school, for its help in running the scientific program and in taking care of the administrative aspects. We also thank the spokespersons of all the experimental collaborations, who nominated their speakers and their respective institutes for partially contributing to the travel costs. Finally, we thank Frau Maren Stein and Frau Kirsten Sachs of the DESY Library and Scientific Documentation group for their help in preparing these proceedings.

Co-editors:
Ahmed Ali, David Blaschke, Aidos Issadykov, Mikhail Ivanov






To the 100th anniversary of D.I.Blokhint
XIII International Conference
Selected Problems of Modern Theoretical Phys
June 23 - 27, 2008, Dubna, Russia



Contents

Particle Production in Strong Time-dependent Fields **1**
D. B. Blaschke, S. A. Smolyansky, A. Panferov, L. Juchnowski

Volkov States and Non-linear Compton Scattering in Short and Intense Laser Pulses **24**
Daniel Seipt

The quantum vacuum in electromagnetic fields: From the Heisenberg-Euler effective action to vacuum birefringence **44**
Felix Karbstein

Non-linear quantum dynamics in strong and short electromagnetic fields **58**
Alexander I. Titov, Burkhard Kämpfer, A Hosaka and H. Takabe

Quantum regime of laser-matter interactions at extreme intensities **68**
Alexander Fedotov

Time scales of thermalization of a strongly interacting non-Abelian plasma **79**
L. Bellantuono, P. Colangelo, F. De Fazio, F. Giannuzzi and S. Nicotri

A brief Introduction to Dispersion Relations and Analyticity **93**
Roman Zwicky

Lectures on Soft-Collinear Effective Theory **121**
Andrey Grozin

Distribution Amplitudes of Heavy Hadrons: Theory and Applications **150**
Alexander Parkhomenko

Search for light dark vector boson. NA64 experiment **167**
S. N. Gninenko and N. V. Krasnikov

Recent results on B-physics and multiquark states from LHCb **177**
Bernardo Adeva

Search for Resonances and New Physics **187**
Nuno T. Leonardo

New results on the XYZ states and B-decays from Belle **198**
Makoto Takizawa

Multiquark Hadrons - Current Status and Issues **208**
Ahmed Ali

Heavy Quark Symmetry and Hidden Charm Pentaquarks **239**
Ahmed Ali, Ishtiaq Ahmed, M. Jamil Aslam and Abdur Rehman

XYZ mesons and Glueballs: effects of the quark-gluon mixing **246**
Nikolai Kochelev

Hadrons and Multiquark States in Holographic QCD **256**
Valery E. Lyubovitskij, Thomas Gutsche, Ivan Schmidt

Heavy quark production at the LHC in the Parton Reggeization Approach **266**
Anton Karpishkov, Maxim Nefedov, Vladimir Saleev, Alexandra Shipilova

The physics of Heavy Quark Distributions in Hadrons: Collider Tests **276**
G. I. Lykasov, A. V. Lipatov, Yu. Yu. Stepanenko

The interference effects of multi-channel pion-pion scattering in final states of charmonia and bottomonia decays **286**
Yu. S. Surovtsev, P. Bydžovský, T. Gutsche, R. Kamiński, V. E. Lyubovitskij, M. Nagy

Relativistic Description of Baryon Properties **297**
D. Ebert, R. N. Faustov, V. O. Galkin

Spectroscopy and Regge Trajectories of Light Mesons **307**
D. Ebert, R. N. Faustov, V. O. Galkin

Non-Leptonic Two-Body Decays of Charmed Mesons and CP Violation **317**
Pietro Santorelli

Analyzing New Physics in $\bar{B}^0 \to D^{(*)}\tau^-\bar{\nu}_\tau$ **326**
C. T. Tran, M. A. Ivanov, J. G. Körner

Implications from $B \to K^*\ell^+\ell^-$ observables using LHCb data. **339**
Abinash Kumar Nayak, Rusa Mandal, Rahul Sinha

Probing New Physics through FCNC Transition **353**
Ishtiaq Ahmed

The study of b-s anomaly decays in covariant quark model **358**
Aidos Issadykov, Mikhail A. Ivanov

LKF Transformations in QCD and Quark Propagator **371**
M. Jamil Aslam, L. X. Gutiérrez-Guerrero

Critical behaviour of (2+1)-dimensional QED: $1/N$**-corrections** **377**
Anatoly V. Kotikov, Sofian Teber

QCD Vacuum as Domain Wall Network **387**
Sergei N. Nedelko, Vladimir E. Voronin

Particle Production in Strong Time-dependent Fields

D. B. Blaschke[1,2,3], *S. A. Smolyansky*[4], *A. Panferov*[4], *L. Juchnowski*[1]

[1]Institute of Theoretical Physics, University of Wroclaw, 50-204 Wroclaw, Poland
[2]Bogoliubov Laboratory for Theoretical Physics, JINR, RU - 141980 Dubna, Russia
[3]National Research Nuclear University (MEPhI), RU - 115409 Moscow, Russia
[4]Saratov State University, RU - 410026 Saratov, Russia

DOI: http://dx.doi.org/10.3204/DESY-PROC-2016-04/Blaschke

In these lecture notes we give an introduction to the kinetic equation approach to pair production form the vacuum in strong, time-dependent external fields (dynamical Schwinger process). We first give a derivation of the kinetic equation with the source term for the case of fermions starting from the Dirac equation and for bosons from the Klein-Gordon equation. In a second part we discuss the application of the approach to the situation of external field pulses as single-sheeted functions of time (like the Sauter-pulse) and as multi-sheeted functions approximating the situation in the focal point of counter-propagating laser beams. Special emphasis is on the discussion of the time evolution of the system that exhibits the characteristics of a field-induced phase transition for which we discuss the behaviour of the entropy and particle density of the system. We give an outlook to applications of the approach in describing particle production in strong fields formed in particle and nuclear collisions.

1 Introduction

Vacuum e^+e^- pair creation by a classical electric field is a longstanding prediction in QED [1, 2, 3]. A complete theoretical description of the effect exists [4, 5, 6, 7, 8], but there is still no experimental verification. The main obstacle is the high value of the critical electric field strength for pair creation; viz., $E_c = m^2/e = 1.3 \times 10^{16}$ V/cm for the electron-positron case.According to the so-called Schwinger formula [3], the pair creation rate in a constant electric field,

$$S^{\rm cl} = \frac{e^2\ E^2}{4\pi^3} \exp\left(-\frac{\pi m^2}{|eE|}\right)\ , \tag{1}$$

is suppressed exponentially when $E \ll E_c$. However, a very different situation occurs when the field acts only in a finite time interval (dynamical Schwinger effect) [4, 9, 10, 12]. In this case, the Schwinger formula, as well as its analog for a monochromatic field (Brezin - Itzykson formula [13]), become inapplicable in the weak field regime.

A few examples have been discussed of physical situations where the Schwinger effect could occur despite the high critical field strength; e.g., relativistic heavy ion collisions [14, 15, 17] and focused laser pulses [18]. Since the Schwinger effect is non-perturbative and it requires

an exact solution of the dynamical equations it is customary to approximate the complicated structure of a real laser field by a spatially uniform time-dependent electric field. According to different estimates [12, 13, 14, 18, 19, 20, 21] the effect of vacuum pair creation is unlikely to be observable with presently available laser parameters. However, recent developments in laser technology, in particular the invention of the chirped pulse amplification method, have resulted in a huge increase in the light intensity at the laser focal spot [22, 23]. On this basis the European Extreme Light Infrastructure (ELI) project will be developed in order to provide radiation beams of femto- to atto-second duration in the deeply relativistic regime, exceeding intensities of 10^{25} W/cm^2 [24, 25]. On the other hand, construction of X-ray free electron lasers XFEL [26] based on the SASE principle is underway at DESY Hamburg. Thus an experimental verification of the Schwinger effect is coming within reach.

Under conditions of short duration pulses time-dependent effects become important. Therefore in our works [9, 27, 28, 29, 10, 30] we have developed a kinetic equation approach, which allows us to consider the dynamics of the vacuum pair creation process while accounting properly for the initial conditions [9, 31]. Compared to alternative treatments, this approach is essentially nonperturbative and contains new dynamical aspects, such as longitudinal momentum dependence in the distribution functions and non-Markovian character of the time evolution [32]. It also takes into account the effects of field switching and particle statistics [32, 33, 34]. This approach has been applied already to the periodical field case [11] with near-critical values of the field strength and X-ray frequencies. In particular, it was shown that there is an accumulation effect when the intensity of the field is about half critical: the average density of pairs grows steadily with increasing number of field periods. The method [9] also found application in describing the pre-equilibrium evolution of a quark-gluon plasma produced in ultrarelativistic heavy ion collisions at RHIC and LHC [32, 33, 34].

A characteristic feature of the kinetic approach is the possibility to describe the evolution of the particle distribution functions during all stages of the external field evolution. In the second main part of these lectures we will investigate this aspect more in detail and elucidate that the process of pair creation in a strong, time-dependent external field can be viewed as a field induced phase transition (FIPT) [35, 36]. We introduce the concept of an order parameter and describe its evolution through three stages, the initial quasiparticle (QEPP) stage, the transient stage and the final residual (REPP) stage of the electron-positron plasma (EPP) created in the external field. We suggest that these features are rather universal and appear qualitatively similar in physical systems of different nature. In concluding these lectures we discuss the question related with the observation that the spectra of hadrons in ultrarelativistic heavy-ion collisions appear thermal despite the fact that the production mechanism by the Schwinger process would entail non-thermal spectra and time scales between creation and freeze-out are too short for equilibration by multiple collisions.

2 Dynamics of pair creation

2.1 Creation of fermion pairs

This section contains the derivation of a kinetic equation for the fermion-antifermion pair production. For the description of e^+e^- production in an electric field we start from the QED

Lagrangian

$$\mathcal{L} = \bar{\psi} i\gamma^\mu(\partial_\mu + ieA_\mu)\psi - m\bar{\psi}\psi - \frac{1}{4}F_{\mu\nu}F^{\mu\nu}\,, \tag{2}$$

where $F^{\mu\nu}$ is the field strength, the metric is taken as $g^{\mu\nu} = \mathrm{diag}(1,-1,-1,-1)$ and for the γ– matrices we use the conventional definition. The equation of motion for the case of e^+e^- production in an external classical electric field is given by the Dirac equation

$$(i\gamma^\mu\partial_\mu - e\gamma^\mu A_\mu - m)\psi(x) = 0\,. \tag{3}$$

where A_μ denote the vector potential in Hamiltonian gauge

$$A_\mu = (0,0,0,A(t)) \tag{4}$$

The resulting electric field

$$E(t) = -\dot{A}(t) = -dA(t)/dt \tag{5}$$

is homogeneous in space and time-dependent. There is no magnetic component because

$$B = \nabla \times A = 0 \tag{6}$$

The scenario with purely electrical field described by (5) and (6) can be realized in laboratory by two counter-propagating laser beams forming a standing wave. It is worth noticing that particle production occurs only if one of two Lorentz invariants

$$\frac{1}{4}F_{\mu\nu}F^{\mu\nu} = \frac{1}{2}(E^2 + B^2), \tag{7}$$

$$\frac{1}{4}F_{\mu\nu}\tilde{F}^{\mu\nu} = E\dot{B} \tag{8}$$

is non-zero. For the present calculations (7) has a non-zero value.

Since the Schwinger mechanism is not perturbative one needs to find an exact solution. The first step is the introduction of an ansatz for the spinor field

$$\psi^{(\pm)}_{\bar{p}r}(x) \quad = \quad \left[i\gamma^0\partial_0 + \gamma^k p_k - e\gamma^3 A(t) + m\right]\, \chi^{(\pm)}(\bar{p},t)\; R_r\; \mathrm{e}^{i\bar{p}\bar{x}}, \tag{9}$$

where $k = 1,2,3$ and $(\pm)$ denotes eigenstates with positiv/negative frequencies.

$$R_1 = \begin{pmatrix} 0 \\ 1 \\ 0 \\ -1 \end{pmatrix}\,, \qquad\qquad R_2 = \begin{pmatrix} 1 \\ 0 \\ -1 \\ 0 \end{pmatrix}\,, \tag{10}$$

are eigenvectors of the matrix $\gamma^0\gamma^3$ so that $R_r^+ R_s = 2\delta_{rs}$. Substitution of (9) to (3) gives the parametric oscillator-type equation

$$\ddot{\chi}^{(\pm)}(\bar{p},t) \quad = \quad -\Big(\omega^2(\bar{p},t) + ie\dot{A}(t)\Big)\; \chi^{(\pm)}(\bar{p},t)\;. \tag{11}$$

The quasi-particle energy $\omega(\bar{p},t)$, the transverse energy $\varepsilon_\perp$ and the longitudinal quasi-particle momentum are defined as

$$\omega(\bar{p},t) = \sqrt{\varepsilon_\perp^2(\bar{p}_\perp) + P^2(\bar{p}_\parallel,t)}, \tag{12}$$

$$\varepsilon_\perp(\bar{p}_\perp) = \sqrt{m^2+\bar{p}_\perp^2}, \tag{13}$$

$$P(\bar{p}_\parallel,t) = \bar{p}_\parallel - eA(t), \tag{14}$$

The system of the spinor functions (9) is complete and orthonormalized so the field operators $\psi(x)$, $\bar{\psi}(x)$ can be decomposed in the spinor functions (9) as follows:

$$\psi(x) = \sum_{r,\bar{p}} \left[\psi^{(-)}_{\bar{p}r}(x)\ b_{\bar{p}r}(t_0) + \psi^{(+)}_{\bar{p}r}(x)\ d^+_{-\bar{p}r}(t_0) \right], \tag{15}$$

where $b_{\bar{p}r}(t_0), b^+_{\bar{p}r}(t_0)$, $d_{\bar{p}r}(t_0), d^+_{\bar{p}r}(t_0)$ are creation and annihilation operators of electrons and positrons. They act on the vacuum in-state $|0_{\rm in}\rangle$ at the initial time $t = t_0$, and obey the anti-commutation relations

$$\{b_{\bar{p}r}(t_0), b^+_{\bar{p}'r'}(t_0)\} = \{d_{\bar{p}r}(t_0), d^+_{\bar{p}'r'}(t_0)\} = \delta_{rr'}\ \delta_{\bar{p}\bar{p}'}\,. \tag{16}$$

In general the evolution of a relativistic system affects the vacuum state and mixes states with negative $\psi^{(-)}_{\bar{p}r}(x)$ and positive $\psi^{(+)}_{\bar{p}r}(x)$ energies. As a result in the Hamiltonian appear non-diagonal terms that are responsible for pair creation. For the Hamiltonian corresponding to the Dirac equation (3) in a homogeneous electric field the diagonalization is achieved by a time-dependent Bogoliubov transformation

$$b_{\bar{p}r}(t) = \alpha_{\bar{p}}(t)\ b_{\bar{p}r}(t_0) + \beta_{\bar{p}}(t)\ d^+_{-\bar{p}r}(t_0)\ , \tag{17}$$

$$d_{\bar{p}r}(t) = \alpha_{-\bar{p}}(t) d_{\bar{p}r}(t_0) - \beta_{-\bar{p}}(t) b^+_{-\bar{p}r}(t_0) \tag{18}$$

with the normalization condition

$$|\alpha_{\bar{p}}(t)|^2 + |\beta_{\bar{p}}(t)|^2 = 1\ . \tag{19}$$

Thus the new operators $b_{\bar{p}r}(t)$ and $d_{\bar{p}r}(t)$ describe quasiparticles at the time t with the instantaneous vacuum $|0_t\rangle$. Clearly, the operator system $b(t_0), b^+(t_0); d(t_0), d^+(t_0)$ is unitary non-equivalent to the system $b(t), b^+(t); d(t), d^+(t)$. The application of the Bogoliubov transformation to Eq. (70) gives the new representation of the field operators

$$\psi(x) = \sum_{r,\bar{p}} \left[\Psi^{(-)}_{\bar{p}r}(x)\ b_{\bar{p}r}(t) + \Psi^{(+)}_{\bar{p}r}(x)\ d^+_{-\bar{p}r}(t) \right]. \tag{20}$$

The correspondence between the new $\Psi^{(\pm)}_{\bar{p}r}(x)$ and the former $\psi^{(\pm)}_{\bar{p}r}(x)$ spinor functions is defined by a canonical transformation

$$\psi^{(-)}_{\bar{p}r}(x) = \alpha_{\bar{p}}(t)\ \Psi^{(-)}_{\bar{p}r}(x) - \beta^*_{\bar{p}}(t)\ \Psi^{(+)}_{\bar{p}r}(x)\ , \tag{21}$$

$$\psi^{(+)}_{\bar{p}r}(x) = \alpha^*_{\bar{p}}(t)\ \Psi^{(+)}_{\bar{p}r}(x) + \beta_{\bar{p}}(t)\ \Psi^{(-)}_{\bar{p}r}(x)\ . \tag{22}$$

Therefore it is justified to assume that the functions $\Psi^{(\pm)}_{\bar{p}r}$ have a spin structure similar to that of $\psi^{(+)}_{\bar{p}r}$ in Eq. (9),

$$\Psi^{(\pm)}_{\bar{p}r}(x) = \Big[i\gamma^0\partial_0 + \gamma^k p_k - e\gamma^3 A(t) + m \Big] \phi^{(\pm)}_{\bar{p}}(x)\ R_r\ \mathrm{e}^{\pm i\Theta(t)} \mathrm{e}^{i\bar{p}\bar{x}}, \tag{23}$$

where the dynamical phase is defined as

$$\Theta(\bar{p},t) = \int_{t_0}^{t} dt' \omega(\bar{p},t')\ . \tag{24}$$

and $\phi^{(\pm)}_{\bar{p}}$ are yet unknown functions. The substitution of Eq. (23) into Eqs. (21) and (22) leads to the relations

$$\chi^{(-)}(\bar{p},t) = \alpha_{\bar{p}}(t)\ \phi^{(-)}_{\bar{p}}(t)\ \mathrm{e}^{-i\Theta(\bar{p},t)} - \beta^*_{\bar{p}}(t)\ \phi^{(+)}_{\bar{p}}(t)\ \mathrm{e}^{i\Theta(\bar{p},t)}\ , \tag{25}$$

$$\chi^{(+)}(\bar{p},t) = \alpha^*_{\bar{p}}(t)\ \phi^{(+)}_{\bar{p}}(t)\ \mathrm{e}^{i\Theta(\bar{p},t)} + \beta_{\bar{p}}(t)\ \phi^{(-)}_{\bar{p}}(t)\ \mathrm{e}^{-i\Theta(\bar{p},t)}\ . \tag{26}$$

On the other hand $\chi^{(\pm)}$ are solutions of Eq. (64). Their behavior is directly related to the asymptotics of the vector potential. At $t_0 = t \to -\infty$ we have $A(t_0) = 0$ so that

$$\chi^{(\pm)}(\bar{p},t) \sim \exp\big(\pm i\omega_0(\bar{p})\, t \big)\ . \tag{27}$$

Now, according to the Lagrange method, we can use Eqs. (64) and (68) to introduce additional constraints on $\chi^{(\pm)}$

$$\dot{\chi}^{(-)}(\bar{p},t) = -i\omega(\bar{p},t) \left[\alpha_{\bar{p}}(t)\ \phi^{(-)}_{\bar{p}}(t)\ \mathrm{e}^{-i\Theta(\bar{p},t)} + \beta^*_{\bar{p}}(t)\ \phi^{(+)}_{\bar{p}}(t)\ \mathrm{e}^{i\Theta(\bar{p},t)} \right], \tag{28}$$

$$\dot{\chi}^{(+)}(\bar{p},t) = i\omega(\bar{p},t) \left[\alpha^*_{\bar{p}}(t)\ \phi^{(+)}_{\bar{p}}(t)\ \mathrm{e}^{i\Theta(\bar{p},t)} - \beta_{\bar{p}}(t)\ \phi^{(-)}_{\bar{p}}(t)\ \mathrm{e}^{-i\Theta(\bar{p},t)} \right]. \tag{29}$$

These new conditions together with the ansatz

$$\phi^{(\pm)}_{\bar{p}}(t) = \sqrt{\frac{\omega(\bar{p},t) \pm P_\parallel(t)}{\omega(\bar{p},t)}}\ , \tag{30}$$

enable us to extract the differential equation for the Bogoliubov coefficients

$$\dot{\alpha}_{\bar{p}}(t) = \frac{eE(t)\varepsilon_\perp}{2\omega^2(\bar{p},t)}\ \beta^*_{\bar{p}}(t)\ \mathrm{e}^{2i\Theta(\bar{p},t)}\ , \tag{31}$$

$$\dot{\beta}^*_{\bar{p}}(t) = -\frac{eE(t)\varepsilon_\perp}{2\omega^2(\bar{p},t)}\ \alpha_{\bar{p}}(t)\ \mathrm{e}^{-2i\Theta(\bar{p},t)}\ . \tag{32}$$

by differentiating (28) and using (64) and (25).

After integration of above equations we get the new coefficients describing the instantaneous state at the time t.

$$\alpha_{\bar{p}}(t) = \frac{1}{2\sqrt{\omega(\bar{p},t)\ (\omega(\bar{p},t) - P_\parallel(t))}} \Big(\omega(\bar{p},t)\ \chi^{(-)}(\bar{p},t) + i\ \dot{\chi}^{(-)}(\bar{p},t) \Big)\ \mathrm{e}^{i\Theta(\bar{p},t)}\ , \tag{33}$$

$$\beta^*_{\bar{p}}(t) = -\frac{1}{2\sqrt{\omega(\bar{p},t)\ (\omega(\bar{p},t) - P_\parallel(t))}} \Big(\omega(\bar{p},t)\ \chi^{(-)}(\bar{p},t) - i\ \dot{\chi}^{(-)}(\bar{p},t) \Big)\ \mathrm{e}^{-i\Theta(\bar{p},t)}\ . \tag{34}$$

It is convenient to redefine operators in order to absorb the dynamical phase

$$B_{\bar{p}r}(t) = b_{\bar{p}r}(t)\ e^{-i\Theta(\bar{p},t)}\,, \tag{35}$$

$$D_{\bar{p}r}(t) = d_{\bar{p}r}(t)\ e^{-i\Theta(\bar{p},t)} \tag{36}$$

while preserving the anti-commutation relations:

$$\{B_{\bar{p}r}(t), B^+_{\bar{p}'r'}(t)\} = \{D_{\bar{p}r}(t), D^+_{\bar{p}'r'}(t)\} = \delta_{rr'}\ \delta_{\bar{p}\bar{p}'}\,. \tag{37}$$

It is straightforward to show that these redefined operators satisfy the Heisenberg-like equations of motion

$$\frac{dB_{\bar{p}r}(t)}{dt} = -\frac{eE(t)\varepsilon_\perp}{2\omega^2(\bar{p},t)}\ D^+_{-\bar{p}r}(t) + i\ [H(t),\ B_{\bar{p}r}(t)]\ , \tag{38}$$

$$\frac{dD_{\bar{p}r}(t)}{dt} = \frac{eE(t)\varepsilon_\perp}{2\omega^2(\bar{p},t)}\ B^+_{-\bar{p}r}(t) + i\ [H(t),\ D_{\bar{p}r}(t)]\ , \tag{39}$$

where $H(t)$ is the hamiltonian of the quasiparticle system

$$H(t) = \sum_{r,\bar{p}} \omega(\bar{p},t)\Big(B^+_{\bar{p}r}(t)\ B_{\bar{p}r}(t) - D_{-\bar{p}r}(t)\ D^+_{-\bar{p}r}(t)\Big)\ . \tag{40}$$

The first term on the r.h.s. of Eqs. (38) and (39) is caused by the unitary non-equivalence of the in-representation and the quasiparticle one.

On this stage of the calculations we can construct the distribution function of electrons (with the momentum $\bar{p}$ and spin r)

$$f_r(\bar{p},t) = \langle 0_{\rm in}|b^+_{\bar{p}r}(t)\ b_{\bar{p}r}(t)|0_{\rm in}\rangle = \langle 0_{\rm in}|B^+_{\bar{p}r}(t)\ B_{\bar{p}r}(t)|0_{\rm in}\rangle \tag{41}$$

and positrons

$$\bar{f}_r(\bar{p},t) = \langle 0_{\rm in}|d^+_{-\bar{p}r}(t)\ d_{-\bar{p}r}(t)|0_{\rm in}\rangle = \langle 0_{\rm in}|D^+_{-\bar{p}r}(t)\ D_{-\bar{p}r}(t)|0_{\rm in}\rangle\ . \tag{42}$$

Charge conservation implies $f_r(\bar{p},t) = \bar{f}_r(\bar{p},t)$, so that summation over momentum and spin gives the normalization to the total number of pairs at a given time t

$$\sum_{r,\bar{p}} f_r(\bar{p},t) = \sum_{r,\bar{p}} \bar{f}_r(\bar{p},t) = N(t)\ . \tag{43}$$

Now the differentiation of Eq. (41) w.r.t. time and the use of the equation of motion (38) results in

$$\frac{df_r(\bar{p},t)}{dt} = -\frac{eE(t)\varepsilon_\perp}{\omega^2(\bar{p},t)}\ {\rm Re}\{\Phi_r(\bar{p},t)\}\ , \tag{44}$$

where the function

$$\Phi_r(\bar{p},t) = \langle 0_{\rm in}|D_{-\bar{p}r}(t)\ B_{\bar{p}r}(t)|0_{\rm in}\rangle \tag{45}$$

governs the reaction of the QED vacuum in the presence of an external electric field.
Differentiation of (45) requires again the use of the equation of motion (38) and together with $f_r(\bar{p},t) = \bar{f}_r(\bar{p},t)$ leads to

$$\frac{d\Phi_r(\bar{p},t)}{dt} = \frac{eE(t)\varepsilon_\perp}{2\omega^2(\bar{p},t)}\Big[2f_r(\bar{p},t)-1\Big] - 2i\omega(\bar{p},t)\ \Phi_r(\bar{p},t)\ . \tag{46}$$

The solution of Eq. (46) has the integral form

$$\Phi_r(\bar{p},t) = \frac{\varepsilon_\perp}{2}\int_{t_0}^{t} dt' \frac{eE(t')}{\omega^2(\bar{p},t')}\Big[2f_r(\bar{p},t')-1\Big] \mathrm{e}^{2i[\Theta(\bar{p},t')-\Theta(\bar{p},t)]}\ . \tag{47}$$

It is straightforward to see that $\Phi_r(\bar{p},t)\big|_{t=t_0}$ vanishes when $A(t_0)=0$.

Now we are ready to write the expression (44) in the full form

$$\frac{df_r(\bar{p},t)}{dt} = \frac{eE(t)\varepsilon_\perp}{2\omega^2(\bar{p},t)}\int_{t_0}^{t} dt' \frac{eE(t')\varepsilon_\perp}{\omega^2(\bar{p},t')}\Big[1-2f_r(\bar{p},t')\Big]\cos\Big(2[\Theta(\bar{p},t)-\Theta(\bar{p},t')]\Big)\ , \tag{48}$$

which is the wanted kinetic equation for particle production. Since the distribution function does not depend on spin (48), we can skip the index r.

2.2 Creation of boson pairs

The derivation procedure of the kinetic equation for bosons is similar to that of fermions. The starting point is the Klein-Gordon equation

$$\Big((\partial^\mu + ieA^\mu)(\partial_\mu + ieA_\mu) + m^2\Big)\phi(x) = 0 \tag{49}$$

with the external vector potential $A_\mu = (0,0,0,A(t))$. In this case the ansatz for the solution is given in the form [37]

$$\phi^{(\pm)}_{\bar{p}}(x) = [2\omega(p)]^{-1/2}\ e^{i\bar{x}\bar{p}} g^{(\pm)}(\bar{p},t)\ , \tag{50}$$

where the functions $g^{(\pm)}(\bar{p},t)$ are analogues of $\chi^{(\pm)}(\bar{p},t)$ from (64) and satisfy the oscillator-type equation

$$\ddot{g}^{(\pm)}(\bar{p},t) + \omega^2(\bar{p},t)\ g^{(\pm)}(\bar{p},t) = 0\ . \tag{51}$$

The field operator in the in-state is defined as

$$\phi(x) = \int d^3p\ [\ \phi^{(-)}_{\bar{p}}(x)\ a_{\bar{p}}(t_0) + \phi^{(+)}_{\bar{p}}(x)\ b^+_{vp}(t_0)\ ]\,. \tag{52}$$

The diagonalization of the Hamiltonian with respect to the instantaneous states is achieved by the transition to the quasiparticle representation. The Bogoliubov transformation for creation and annihilation operators of quasiparticles has the form

$$a_{\bar{p}}(t) = \alpha_{\bar{p}}(t)\ a_{\bar{p}}(t_0) + \beta_{\bar{p}}(t)\ b^+_{-\bar{p}}(t_0)\ , \tag{53}$$

$$b_{-\bar{p}}(t) = \alpha_{-\bar{p}}(t)\ b_{\bar{p}}(t_0) + \beta_{-\bar{p}}(t)\ a^+_{-\bar{p}}(t_0) \tag{54}$$

with the condition

$$|\alpha_{\bar{p}}(t)|^2 - |\beta_{\bar{p}}(t)|^2 = 1\ . \tag{55}$$

The calculation of the coefficients α and β requires similar steps like in the fermion case. We obtain the equations of motion for the coefficients of the canonical transformation (53) as follows

$$\dot{\alpha}_{\bar{p}}(t) = \frac{\dot{\omega}(\bar{p},t)}{2\omega(\bar{p},t)}\,\beta^*_{\bar{p}}(t)\,e^{2i\Theta(\bar{p},t)}\,, \tag{56}$$

$$\dot{\beta}_{\bar{p}}(t) = \frac{\dot{\omega}(\bar{p},t)}{2\omega(\bar{p},t)}\,\alpha^*_{\bar{p}}(t)\,e^{2i\Theta(\bar{p},t)}\,. \tag{57}$$

Following the derivation procedure for the case of fermion production, we get

$$\frac{df_r(\bar{p},t)}{dt} = \frac{eE(t)p_\parallel}{2\omega^2(\bar{p},t)}\int_{-\infty}^{t} dt' \frac{eE(t')p_\parallel}{\omega^2(\bar{p},t')}\Big[1+2f_r(\bar{p},t')\Big]\cos\Big(2[\Theta(\bar{p},t)-\Theta(\bar{p},t')]\Big)\,. \tag{58}$$

3 Discussion of the source term

3.1 Properties of the source term

In the previous section the derivation of the kinetic equation has been given. We can give a combined result for the Schwinger source term for bosons(+) and fermions(-) on the right hand side of the kinetic equation

$$S_\pm = \frac{1}{2}\lambda_\pm(\bar{p},t)\int_{t_0}^{t} dt'\lambda_\pm(\bar{p},t')\Big[1\pm 2f(\bar{p},t')\Big]\cos\Big(2[\Theta(\bar{p},t)-\Theta(\bar{p},t')]\Big)\,, \tag{59}$$

where

$$\lambda_-(\bar{p},t) = eE(t)\varepsilon_\perp/\omega^2(\bar{p},t)\,, \qquad \lambda_+(\bar{p},t) = eE(t)\mathrm{p}_\parallel/\omega^2(\bar{p},t). \tag{60}$$

This source term does not include the effects of back reaction of created pairs on the electric field and e^+e^- collisions. Nevertheless it possesses interesting properties which we enumerate in the following.

1. The source term is of non-Markovian type. This means that memory effects are present in the pair creation process. In our case the non-Markovianity comes in via the statistical factor $1\pm 2f(\bar{p},t)$ under time integral in (59), which makes the term dependent on the whole pre-history of $f(\bar{p},t)$. Studies done by Rau [38] also have shown the non-Markovian character of the particle production process. They have used a projection method so one can conclude that the memory effects in $S_\pm$ are not artefacts.

2. The source term is characterized by three time scales: the time scale of the external field, the memory time
$$\tau_{\rm mem} \sim \frac{\varepsilon_\perp}{eE} \tag{61}$$
and the production interval
$$\tau_{\rm prod} = 1/ < S_\pm >\,, \tag{62}$$
where $\langle S_\pm\rangle$ denotes the time averaged production rate. The Markovian limit (approximate absent of statistical factor) is reached when $\tau_{\rm mem} \ll \tau_{\rm prod}$. This condition translates to $E \ll m^2/e < \varepsilon_\perp^2/e$. For the low density limit and constant field the equation (58) resemble results of Rau [38].

3. The difference of the dynamical phases, $\Theta(\bar{p},t)-\Theta(\bar{p},t')$, under the integral in $S_\pm$ is the source of the high frequency oscillations related to Zitterbewegung.

4. The source term of the form (59) causes entropy production (see also [38]) and thus is the reason of time irreversibility. However, the increase is non-monotonic due to lack of collision [39, 40].

5. Particles are produced with non-zero momentum in contrast to previous studies, e.g. Ref. [41].

6. In the case of the low-density limit and a constant electric field one can reproduce Schwinger's formula and Rau's results [38])

$$\mathcal{S}^{\rm cl}=\lim_{t\to+\infty}(2\pi)^{-3}g\int d^3P\ \mathcal{S}(\bar{P},t)=\frac{e^2E^2}{4\pi^3}\exp\left(-\frac{\pi m^2}{|eE|}\right). \tag{63}$$

In the next subsection we discuss the Markovian and the low-density limits more in detail.

3.2 Low-density and Markovian limit

In this section we discuss in short two related approximations which are applicable when the external electric field is considerably smaller than the critical field $E\ll E_c$. These are the Markovian approximation and the low-density limit.

The Markovian limit of the non-Markovian source term (59) is defined by the neglect of memory effects, i.e. by replacing the argument of the distribution function in the source term $f(\bar{p},t')\to f(\bar{p},t)$ so that it becomes independent of the prehistory of the distribution function and the KE takes the form

$$\frac{d\,f^M_\pm(t)}{dt}=[1\pm 2f^M_\pm(t)]S^0_\pm(t)=S^M_\pm(t), \tag{64}$$

where

$$S^0_\pm(t)=\frac{1}{2}\lambda_\pm(\bar{p},t)\int_{t_0}^{t}dt'\lambda_\pm(\bar{p},t')\cos\left(2[\Theta(\bar{p},t)-\Theta(\bar{p},t')]\right). \tag{65}$$

is the source term in the low-density limit when $f(\bar{p},t)\ll 1$ for every time t so that the statistical factor becomes trivial $1\pm 2f(\bar{p},t)\approx 1$.

Together with the initial condition $f(t_0)=0$ the Markovian KE (64) has the solution

$$f^M_\pm(t)=\mp\frac{1}{2}\left(1-\exp\left[\pm 2\int_{t_0}^{t}d\,t'S^0_\pm(t')\right]\right). \tag{66}$$

The lowest order expansion of Eq. (66) w.r.t. the source term results in the low density solution

$$f^0_\pm(t)=\int_{t_0}^{t}d\,t'S^0_\pm(t'). \tag{67}$$

Both low density approximation and Markovian limit hold only when $E\ll E_c$.

The low density limit gives us a tool to prove the positive definiteness of the distribution function. Using the trigonometric identity $\cos(\alpha-\beta)=\cos\alpha\cdot\cos\beta+\sin\alpha\cdot\sin\beta$ we rewrite (67) as

$$f^0_\pm(t)=\frac{1}{2}\int\limits_{t_0}^{t}d\,t'g^1_\pm(t')\int\limits_{t_0}^{t'}d\,t''g^1_\pm(t'')+\frac{1}{2}\int\limits_{t_0}^{t}d\,t'g^2_\pm(t')\int\limits_{t_0}^{t'}d\,t''g^2_\pm(t'')\,, \tag{68}$$

$$g^{1,2}_\pm(\tau)=\lambda_\pm(\tau)\left\{\begin{array}{c}\cos[2\Theta(\tau)]\\ \sin[2\Theta(\tau)]\end{array}\right\}.$$

The next step is done with the standard trick

$$\int\limits_{t_0}^{t}d\,t'A(t')\int\limits_{t_0}^{t'}d\,t''B(t'')=\frac{1}{2}\int\limits_{t_0}^{t}d\,t'A(t')\int\limits_{t_0}^{t}d\,t''B(t'') \tag{69}$$

used in the derivation of the Dyson series. The application of (69) to (68) leads to the quadratic form

$$f^0_\pm(t)=\frac{1}{4}\Big(\int\limits_{-\infty}^{t}d\,t'g^1_\pm(t')\Big)^2+\frac{1}{4}\Big(\int\limits_{-\infty}^{t}d\,t'g^2_\pm(t')\Big)^2\,. \tag{70}$$

Now it straightforward to see that the distribution function is positive definit as it is required by the kinetic theory

$$f^0_\pm(t)\geq 0\,. \tag{71}$$

More detailed studies of the kinetic equation and its limiting cases have been presented in [32].

3.3 Entirely differential form of the kinetic equation

The numerical solution of the integro-differential equation

$$\frac{df_r(\bar p,t)}{dt}=\frac{1}{2}\lambda_\pm(\bar p,t)\int_{t_0}^{t}dt'\lambda_\pm(\bar p,t')\Big[1\pm 2f(\bar p,t')\Big]\cos\Big(2[\Theta(\bar p,t)-\Theta(\bar p,t')]\Big) \tag{72}$$

although being straightforward is highly ineffective due to the double time integration. First of all one need to deal with the fastly oscillating term $\cos(2[\Theta(\bar p,t)-\Theta(\bar p,t')])$. To address this problem we can make the integration step small enough. However, due to the non-Markovian character of the equation the storage of entire prehistory of $f(t)$ in the computer memory is required. Luckily one can avoid these complications by transforming (72) to the equivalent system of time local ordinary differential equations [33]. In order to perform the transformation we introduce two auxiliary functions

$$v(t) = \int_{t_0}^{t}dt'\lambda_\pm(\bar p,t')\Big[1\pm 2f(\bar p,t')\Big]\sin\Big(2[\Theta(\bar p,t)-\Theta(\bar p,t')]\Big)\,, \tag{73}$$

$$u(t) = \int_{t_0}^{t}dt'\lambda_\pm(\bar p,t')\Big[1\pm 2f(\bar p,t')\Big]\cos\Big(2[\Theta(\bar p,t)-\Theta(\bar p,t')]\Big)\,. \tag{74}$$

The differentiation of these functions with respect to t together with

$$\partial_t \Big(2[\Theta(\bar{p},t) - \Theta(\bar{p},t')] \Big) = \partial_t \int_{t'}^{t} \omega(\bar{p},t'')dt'' = \omega(\bar{p},t) \tag{75}$$

yields

$$\dot{v} = \lambda_{\pm}(\bar{p},t)\Big[1 \pm 2f(\bar{p},t)\Big] - 2\omega(\bar{p},t)u(t), \tag{76}$$

$$\dot{u} = 2\omega(\bar{p},t)v(t)\ . \tag{77}$$

Taking into account (72) results in the system of first order coupled differential equations

$$\dot{f} = \lambda_{\pm}(\bar{p},t)v(t), \tag{78}$$

$$\dot{v} = \lambda_{\pm}(\bar{p},t)\Big[1 \pm 2f(\bar{p},t)\Big] - 2\omega(\bar{p},t)u(t), \tag{79}$$

$$\dot{u} = 2\omega(\bar{p},t)v(t) \tag{80}$$

with the initial condition

$$f(t_0) = u(t_0) = v(t_0) = 0\ . \tag{81}$$

The above system is much simpler to solve numerically.

4 Vacuum particle-antiparticle creation in strong fields as a field induced phase transition

The functions $u(\mathbf{p},t)$ and $v(\mathbf{p},t)$ are defined by the anomalous averages

$$f^{(+)}(\mathbf{p},t) = \langle \mathrm{in}|B^{+}(\mathbf{p},t)D^{+}(-\mathbf{p},t)|\mathrm{in}\rangle, \tag{82}$$

$$f^{(-)}(\mathbf{p},t) = \langle \mathrm{in}|D(-\mathbf{p},t)B(\mathbf{p},t)|\mathrm{in}\rangle \tag{83}$$

by means of the relations [9, 31]

$$u(\mathbf{p},t) = 2\mathrm{Re}f^{(+)}(\mathbf{p},t) = 2\mathrm{Re}f^{(-)}(\mathbf{p},t) \tag{84}$$

$$v(\mathbf{p},t) = 2\mathrm{Im}f^{(+)}(\mathbf{p},t) = -2\mathrm{Im}f^{(-)}(\mathbf{p},t)\,. \tag{85}$$

Hence their combination $\Phi(\mathbf{p},t) = u(\mathbf{p},t) + iv(\mathbf{p},t)$ fulfills the role of the order parameter for the phase transition from the vacuum where $\Phi(\mathbf{p},t) = 0$ is set as initial condition, to $\Phi(\mathbf{p},t) \neq 0$ for the REPP. The appearance of a nonvanishing value for this order parameter is stipulated by the violation of the time inversion symmetry of the Hamiltonian as induced by the time dependent external field. The creation and annihilation operators $a^{(\pm)}(\mathbf{p},t)$ and $b^{(\pm)}(\mathbf{p},t)$ of the electrons and positrons are used in Eqs. (82) and (83) in the quasiparticle representation, in which the Hamiltonian of the system is diagonal.

The order parameter $\Phi(\mathbf{p},t)$ obeys to the equation of motion

$$\dot{\Phi} = \lambda(1-2f) + 2i\omega\Phi, \tag{86}$$

which follows from the system of equations (78). For any finite field with $E(t) \to 0$ and $A(t) \to A_{\rm out}$ at $t \to \infty$ we have $\lambda(t) \to 0$ and

$$\omega(t) \to \omega_{\rm out} = \sqrt{\varepsilon_\perp^2 + (p_\parallel - eA_{\rm out})^2}. \tag{87}$$

The order parameter in this asymptotics oscillates with the frequency $2\varepsilon_{\rm out}$:

$$\Phi(t) \to \Phi_{\rm out}(t) \sim \exp(2i\omega_{\rm out}t). \tag{88}$$

Thus, $|\Phi_{\rm out}(t)|^2 = {\rm const}$ after switching off the external field, i.e. the long-range order is formed. Such situation is typical for a phase transitions in systems with broken symmetry.

In the low density approximation $2f \ll 1$, the KE (48) has a closed formal solution in the form of a useful quadrature formula [32]

$$f(\mathbf{p},t) = \frac{1}{2}\int\limits_{t_0}^{t} dt' \lambda(\mathbf{p},t') \int\limits_{t_0}^{t'} dt'' \lambda(\mathbf{p},t'') \cos\theta(t',t'') \ . \tag{89}$$

The total number density of pairs is defined as

$$n(t) = 2\int \frac{d\mathbf{p}}{(2\pi)^3} f(\mathbf{p},t) \ , \tag{90}$$

where the factor 2 corresponds to the spin degree of freedom.

In these lectures we discuss the numerical solution of the KE (48) for two relevant models of the electric field

(i) the Eckart-Sauter field with characteristic duration of action T (single-sheeted field)

$$E(t) = E_0 \cosh^{-2}(t/T),\ A(t) = -TE_0 \tanh(t/T),\ \text{and} \tag{91}$$

(ii) the Gaussian envelope model of the laser pulse (multi-sheeted field) [48]

$$\begin{aligned} E(t) &= E_0 \cos(\omega t)\ e^{-t^2/2\tau^2}, \\ A(t) &= -\sqrt{\frac{\pi}{8}} E_0 \tau \exp(-\sigma^2/2)\ {\rm erf}\left(\frac{t}{\sqrt{2}\tau} - i\frac{\sigma}{\sqrt{2}}\right) + c.c., \end{aligned} \tag{92}$$

where $\sigma = \omega\tau$ is a dimensionless measure for the characteristic duration of the pulse τ connected with the number of periods of the carrier field.

The Eckart-Sauter field (91) admits an exact solution [4, 5, 46] and is thus a benchmark case.

In order to introduce the Keldysh parameter $\gamma = E_c\omega/E_0 m$ for the discussion of the field model (91) one can use the substitution $\omega \to 1/T$ and the definition of the critical value of the electric field $E_c = m^2/e$. In the limiting case $\gamma \ll 1$ the tunneling mechanism (with participation of an infinite number of photons) dominates, whereas for $\gamma \gg 1$ pair creation is driven by the absorption of few photons.

The vacuum oscillations (Zitterbewegung) play a crucial role in the mechanism of vacuum EPP creation. The usual energy of vacuum oscillations $\varepsilon_0 = \sqrt{m^2 + \mathbf{p}^2}$ is transformed here to the quasienergy (12) in the presence of the time dependent electric field. The memory effect

(non-Markovian character of the KE), the fastly oscillating factor with the phase (24) and the frequency 2ε (the dynamical energy gap) are the essential elements in the KE (48). This equation contains two characteristic time scales: a slow one associated with the time scale of the external field period, $2\pi/\omega$, and a fast one given by the Compton time $\tau_c = 2\pi/m$. These scales are usually vastly different, $\omega \ll m$. The coupling of the dynamics related to these two scales leads to a very complicated structure of the distribution function, both in the first stage (generation of the quasiparticle EPP (QEPP)) and in the final stage (formation of the residual EPP (REPP)) [10].

5 Field induced phase transition

In the considered situation, the FIPT appears as rearrangement of the vacuum state under the action of a classical electromagnetic field. It leads to the $t-$ noninvariant quasiparticle vacuum which corresponds to a non-stationary Hamiltonian of the system (the Coleman theorem [4, 49]). In this connection, the quasiparticle electron-positron pairs are the massive analog of the Goldstone bosons [4, 50]. Let us consider features of the FIPT.

5.1 Transient stage

5.1.1 One-sheeted field model

The typical picture of the EPP evolution under the action of the one-sheeted pulse (91) is presented in Fig. 1. The left panel shows that the transient process of the fast EPP oscillations divides the evolution of the EPP into two domains, the QEPP and the REPP. After momentum integration the fast oscillations of the transient process are smoothed out, see the right panel of Fig. 1. The inset of that panel shows the local production rate. The results of the numerical solutions of the KE (48) (or (78)) coincide with the exact solution [4, 5, 47]. On all figures the time and frequency are scaled with the electron mass.

For qualitative orientation one can introduce here the time interval of the strong oscillations limited by point t_1 of the begin (that can be identified with the moment when the oscillations of the distribution function reach for the first time the level of the REPP) and the end t_2 (corresponding to the moment when the mean level of oscillations approaches that of the REPP and the elongation of the oscillations is significantly reduced). This transient period of the Zitterbewegung separates the smoothed QEPP stage from the REPP stage.

Under similar conditions strong oscillations are observed also in other physical models with massive constituents. For example, they appeared in the domain of the relativistic phase transition with dynamical mass generation (the inertial mechanism of particle creation) including the Higgs mechanism [51]. Their existence can be found also in the strong field dynamical models of strongly correlated systems (see, e.g., Ref. [52]). Let us underline that the appearance of the transient region with strong oscillations takes place in the considered case of a smooth impulse (91) without a carrier wave that would possess a high frequency component.

For a better understanding of this phenomenon let us consider the mechanisms of particle creation acting in the KE (48) or in its approximate solution (89). We will trace the evolution of the system in the smooth field (91) for $t > 0$ which is accompanied by a field strength depletion. If the electric field is rather strong, for $t < t_1$ the acceleration mechanism represented by the force factor $eE(t)$ in the numerator of the amplitude (60) is dominant whereas the fastly oscillating factor $\cos\theta(t, t')$ on the r.h.s. of the KE (48) smoothes out. The vicinity

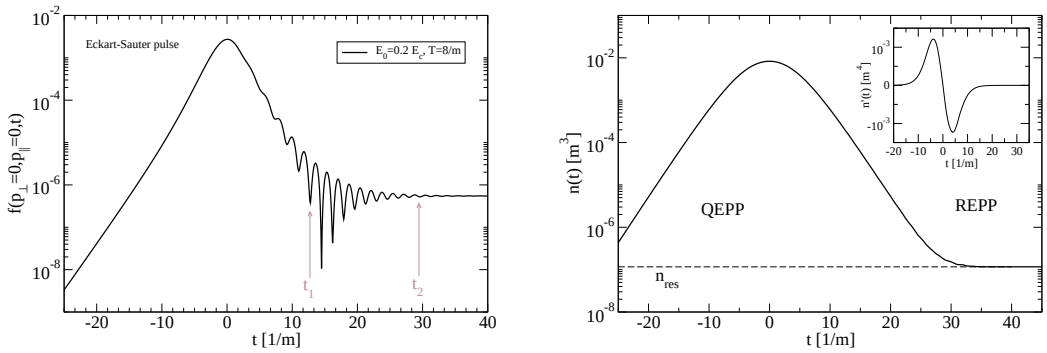


Figure 1: The transition from the QEPP plasma to the final state for the Eckart-Sauter pulse type (91) with $E_0 = 0.2E_c$ and $T = 8$. The labels t_1 and t_2 denote approximately the begin and the end of the transient stage. **Left panel:** Evolution of the distribution function for the point $p_\perp = p_\parallel = 0$. **Right panel:** Evolution of the pair number density (90) and the local pair production rate $w(t) = \dot{n}(t)$ (inset).

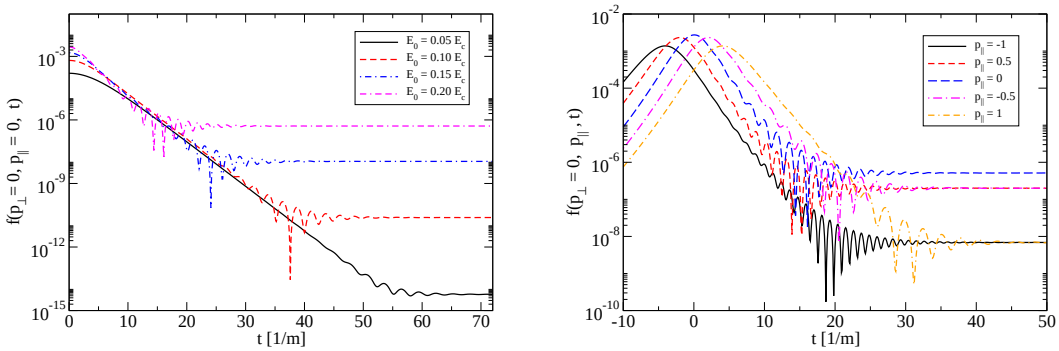


Figure 2: Time evolution of the distribution function for the Eckart-Sauter pulse (91) with $T = 8.24$. **Left panel:** At $p_\perp = p_\parallel = 0$ for subcritical fields $E_0/E_c = 0.05, 0.10, 0.15$ and 0.20. **Right panel:** The details of phase transition at $E_0/E_c = 0.2$ and $p_\perp = 0$ for different values $p_\parallel = -1.0, -0.5, 0.0, 0.5, 1.0$.

of the moment t_1 of the begin of the transient stage is characterized by a weakening of the accelerating field action and by the growth of the role of the fast oscillations with the frequency $2\varepsilon(\mathbf{p}, t) \geq 2m$, in which one can neglect now the influence of a weak field so that the oscillation "beard" in the transient stage appears Fig. 1. The subsequent field depletion accompanied by the growth of the vector potential (and the quasi-momentum $P(t)$ (14)) in the denominator of the amplitude (60) leads to the asymptotic extinction of the oscillations and the approach of

the final REPP state.

Fig. 2 demonstrates the fine structure of the distribution function in the transient period for varying field strength at fixed momentum (left panel) and for varying $p_\parallel = p_3$ at $p_\perp = 0$ and fixed field strength (right panel). One can see from here that the behavior of the distribution function depends on the selection of a point $\mathbf{p}$ in momentum space. The maximum of the distribution function is realised for $p_\perp = 0$ in different points $p_\parallel = p_3$ at different time moments because the component $p_\parallel$ is contained in the amplitude (60) together with the vector potential in the quasi-momentum $P(t)$ (14).

The features of these oscillations are defined by the double quasienergy $2\varepsilon(\mathbf{p}, t)$ and are reproduced well also by the numerical solution of the KE.

Transient area arises also in the case of an other exact solution with the infinite field model $A(t) = -E_0 t$ [47].

5.1.2 Multi-sheeted field model

These features of the transient process are complicated in the case of a high frequency periodic field with a Gaussian envelope (92), $\omega \gg 1/\tau$ (multi-sheeted field model). Typical patterns are presented in Figs. 3 and 4. In this case the neighboring intermediate smooth domains (peaks) separate the high-frequency transient stages. They are defined by the sub-pulses with a half-period π/ω of the external field (92). The red dashed lines in Figs. 3 and 4 show the modulus of the external field (92) with the appropriately chosen normalization. The evolution is finished by the final intensive transient bubble, after which the EPP goes over to the out-state REPP. The final transient bubble is traced also on the density curve of the EPP (the right panel of Fig. 3. Apparently, this illustrates the effect of mutual amplification of EPP production as a result of the nonlinear interaction of the fast and slow components [53, 30, 54] of the field (92).

Fig. 4 demonstrates the evolution of the QEPP under the action of a periodical field with Gaussian envelope (19) for another wavelength of the carrier signal, five times larger than the one in Fig. 3. This allows to show some details of the evolution more clearly. Some features of this type of field appear in presence of repeated passages through the zero points of the field $E(t)$. If such transitions occur sufficiently smoothly, then each of them has enough time to form a transition region, similar to the single "beard" in the left panel of Fig. 1. The reduction of the carrier frequency allows to demonstrate in quite clear detail the repeated transient areas (see the upper right panel of Fig. 4). With the decrease in the pulse amplitude they cease to form a stable QEPP (see the lower right panel of Fig. 4). As a result, we are seeing a stretched area of the transition to the REPP. In this transition region vacuum fluctuations modulated acting field. When turning off the field by the Gaussian envelope the modulation disappears and the transition to the REPP state is completed.

The presence of a transient region of fast oscillations in the distribution function is characteristic for every field model. In this regard the discussed phase transition under the action of a strong electric field is a universal effect for quantum field systems with an energy gap. We remark that in the case of massless 2+1 dimensional QED (e.g., for graphene), the high-frequency transient region is absent and the evolution of the particle-antiparticle plasma distribution function is smooth [55].

The left panel of Fig. 5 demonstrates the dependence of the EPP pair density (90) on the pulse duration at fixed frequency ω in the field model (92). It exhibits a nonlinear accumulation effect for which the slope is approximately constant for weak fields whereas for strong fields we observe a saturation effect. Finally, the right panel of Fig. 5 shows the dependence of the EPP

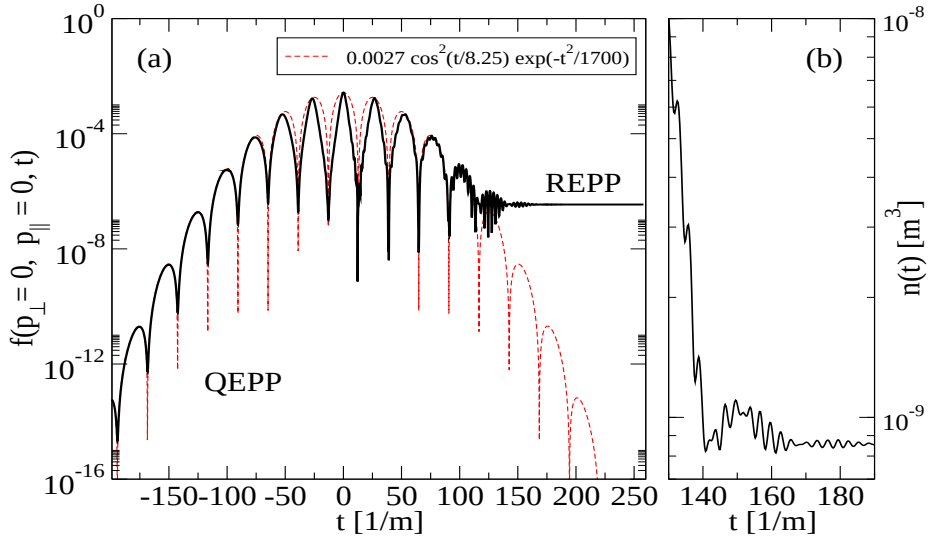


Figure 3: Transition from QEPP to REPP in the case of a harmonic field with Gaussian envelope (92) with $E_0 = 0.2E_c$, $\sigma = 5.0$ and wavelength 0.02 nm. **Left panel:** The distribution function for the point $p_\perp = p_\parallel = 0$. The red dashed line shows the squared external electric field (92) for orientation. **Right panel:** The density $n(t)$ (90) in the region of the final transient bubble.

pair density in the out-state in comparison to the maximal value attained within the entire period of the EPP evolution (see, e.g., Fig. 1, right).

5.2 Strong nonequilibrium

The entire process of vacuum EPP creation is a strong nonequilibrium one, including the final out-state. In the first place, this conclusion follows from the exactly solvable models. The distribution functions of the out-state turn out to be the same for both, the constant field model $E(t) = E_0$ [47, 56] and the Eckart-Sauter model (91) for $T \to \infty$ [42, 4]

$$f_{\rm out}(\mathbf{p}) = \exp\left[-\pi \frac{E_c}{E_0}\left(\frac{\varepsilon_\perp}{m}\right)^2\right]. \tag{93}$$

This function is degenerate with respect to $p^3 = p_\parallel$ and therefore non-normalizable. This leads to the necessity to extend the definition of macroscopic observables of the type (90). As a rule, the substitution

$$\int dp_\parallel \to eTE_0 \tag{94}$$

is introduced which results in the well known Schwinger formula [3] for the EPP production rate. The constant field model has been analyzed in detail in the recent work [57].

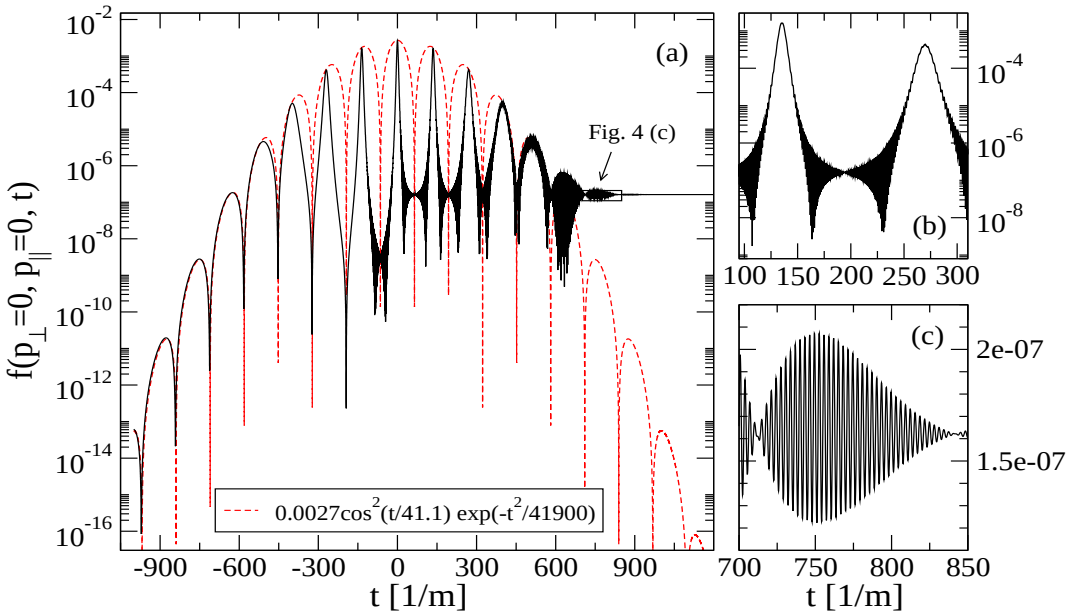


Figure 4: Details of the evolution of the distribution function in the case of a harmonic field with the Gaussian envelope (92) with $E_0 = 0.2E_c$, $\sigma = 5.0$ and wavelength 0.1 nm. **Left panel:** Evolution of the EPP over a large interval of 3000 Compton times. The red dashed line shows the squared external electric field (92) for orientation. **Upper right panel:** Evolution of the EPP under the action of a single subpulse with a half-period duration. **Lower right panel:** The fine structure of the final transient bubble.

The strongly anisotropic nonequilibrium distribution (93) is defined by the symmetry of the external field and leads to strong longitudinal flow. A detailed consideration of the nonequilibrium feature of this distribution can found in the work [58].

The asymptotic distribution (93) in the constant field model is a smooth function of the transversal energy $\varepsilon_\perp(p_\perp)$. In more realistic field models the structure of the distribution function becomes very complicated. As an example, see the right panel of Fig. 6.

5.3 Non-monotonic entropy growth

The transition from the in-state to the out-state is accompanied by an non-monotonic entropy growth. This phenomenon was marked and discussed long ego (e.g., [59, 56, 39]). For example, the function (93) leads to the following entropy production rate:

$$\frac{S_{\text{out}}}{T} = \frac{m^4}{8\pi^2}\frac{E_0}{E_c}\left(1+\frac{E_0}{\pi E_c}\right)\exp\left(-\pi\frac{E_c}{E_0}\right), \tag{95}$$

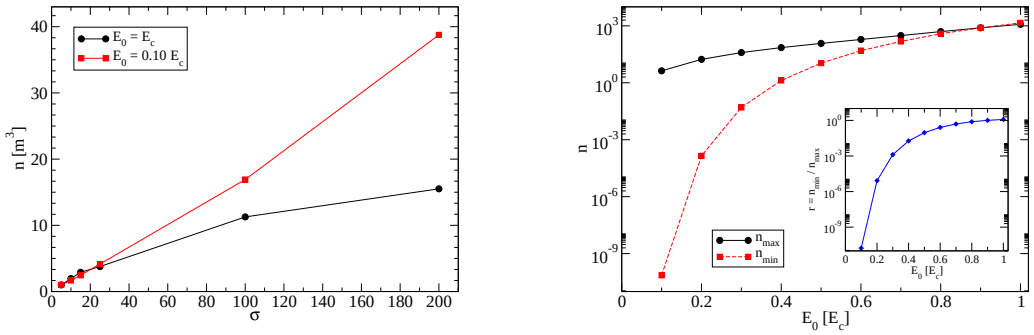


Figure 5: Influence of the parameters the field pulse on REPP production. **Left panel:** Influence of the laser pulse (92) duration σ on the REPP density for the medium ($E_0/E_c = 0.1$) and high ($E_0/E_c = 1.0$) amplitude of the electric field. For both values of the field the unit value of density is determined as the density of the REPP produced by a pulse with a duration $\sigma = 5$. **Right panel:** Comparison of the maximum density of QEPP and density of the REPP in the range of values $0.1E_c \leq E_0 \leq 1.0E_c$ for the laser pulse (92) with a wavelength 0.02426 nm ($\omega = 0.1$) and $\sigma = 5$. The insertion shows the transformation coefficient $r(E_0/E_c) = n_{\rm res}/n_{\rm max}$ for the shown values of the densities.

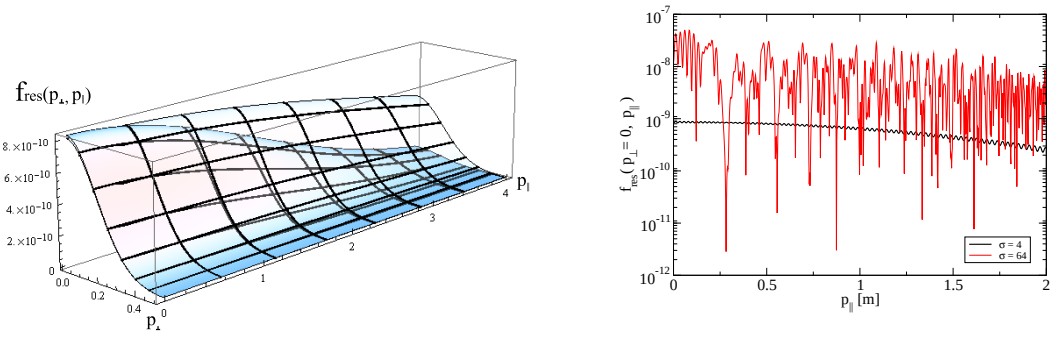


Figure 6: **Left panel:** REPP distribution function $f(p_\perp, p_\parallel)$ for the Eckart-Sauter pulse (91) with $T = 82.4$ (bottom surface) and with $T = 164.8$ (top surface) at $E_0/E_c = 0.15$ in momentum space for $0.0 \leq p_\perp \leq 0.5, 0.0 \leq p_\parallel \leq 4.0$. **Right panel:** REPP distribution functions $f(p_\perp = 0, p_\parallel)$ for a short pulse $\sigma = 4$ and a long pulse $\sigma = 64$ with the same amplitude of the field $E_0 = 0.15E_c$. The cyclic frequency ω of the oscillating field satisfies the condition $1/\omega = 82.4$ that corresponds to the wavelength $0.1nm$.

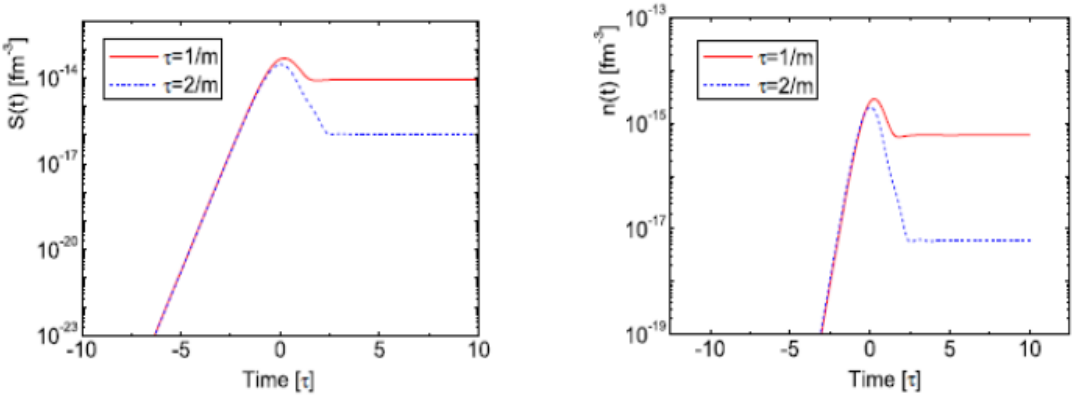


Figure 7: Non-monotonous growth of the entropy (left panel) and of the density (right panel) for two values of the parameter τ.

where the pulse duration is defined by the relation (94). In Eq. (95) the definition of the information entropy with the density

$$S(t) = -\int \frac{d\mathbf{p}}{(2\pi)^3} f(\mathbf{p},t) \ln f(\mathbf{p},t) \tag{96}$$

was used. The most complete investigation was implemented in the work [40] on the basis of the KE (48). Results from that work are shown in Fig. 7.

Let us notice that the KE (48) or the system of ODE (78) is not invariant with respect to time inversion. Indeed, if $E(t) = E(-t)$ and $A(t) = -A(-t)$, one can see that replacement $f(\mathbf{p},t) \to f(-\mathbf{p},-t)$ is not change KE, but $f(\mathbf{p},t) \neq f(\mathbf{p},-t)$. Thus, the entropy growth observed here is a result of transforming of the primordial vacuum fluctuations under the action of a strong external field to the statistical ensemble of the EPP with well defined entropy.

6 Schwinger process and thermalization

As an application of the Schwinger process the particle production in heavy-ion collisions has been considered which may proceed by the decay of color electric flux tubes [14, 16, 60]. The flux tubes are characterized by a linear, stringlike potential between color charges, analogous to the case of a homogeneous electric field considered by Schwinger. Using this analogy that $|eE| = \sigma$ with $\sigma \sim 0.19$ GeV^2 being the string tension, the transverse energy spectrum of produced particles according to the Schwinger mechanism would be (1)

$$\frac{dN_{\rm Schwinger}}{d^2p_\perp} \sim \exp\left(-\frac{\pi\varepsilon_\perp^2}{\sigma}\right) , \tag{97}$$

with $\varepsilon_\perp = \sqrt{m^2+p_\perp^2}$ being the transverse energy (13), often also denoted as "transverse mass" $m_\perp$. This spectrum of produced particles is nonthermal and thus would contradict the observation of thermal particle spectra in heavy-ion collision experiments

$$\frac{dN_{\rm exp}}{d^2p_\perp} \sim \exp\left(-\frac{\varepsilon_\perp}{T_{\rm eff}}\right) , \tag{98}$$

with an effective temperature $T_{\rm eff} \sim 180$ MeV (inverse slope parameter; see, e.g., [69]). Thus the question for the thermalization arises. It has been suggested that it proceeds via collisions described by a kinetic equation [15, 61]. For a most recent discussion of the issue, see [17, 62, 63, 64]. It has been questioned whether in high-energy nuclear collisions there is enough time for the thermal equilibration of the system by collisions, after the particle production in a Schwinger process.

As an alternative picture for the emergence of a thermal particle spectrum in ultrarelativistic particle collisions the analogue of the Hawking-Unruh radiation has been discussed [65, 66, 67]. This reasoning predicts thermal spectra of hadrons with the Hawking-Unruh temperature

$$T_H = \sqrt{\frac{\sigma}{2\pi}} \sim 173 \text{ MeV}, \tag{99}$$

where for the string tension $\sigma = 0.19$ GeV^2 has been used.

In this context it is interesting to note a possible synthesis of both pictures as provided by the argument elucidated by Bialas [68]. If the string tension in the Schwinger process for flux tube decay would fluctuate and follow, e.g., a Poissonian distribution

$$P(\sigma) = \exp(-\sigma/\sigma_0)/\sqrt{\pi\sigma\sigma_0}\ , \tag{100}$$

which is normalized $\int d\sigma P(\sigma) = 1$ and has a mean value $\langle\sigma\rangle = \int d\sigma\sigma P(\sigma) = \sigma_0/2$, then the initial Gaussian transverse energy spectrum (97) after averaging with the string tension fluctuations becomes exponential, i.e. thermal with the temperature parameter $T = \sqrt{\langle\sigma\rangle/(2\pi)}$,

$$\int d\sigma P(\sigma) \exp\left(-\frac{\pi\varepsilon_\perp^2}{\sigma}\right) = \exp\left(-\frac{\varepsilon_\perp}{T}\right)\ . \tag{101}$$

Here the integral $\int_0^\infty dt \exp[-t - k^2/(4t)]/\sqrt{\pi t} = \exp(-k)$ has been used [70].

This coincides with the Hawking-Unruh picture of thermal hadron production, where in the case of fluctuating strings the string tension of Eq. (99) is now replaced by its mean value. We would like to note at this point that a largely thermal spectrum would arise also from the solution of a kinetic equation with the Schwinger source term, as has been demonstrated by Florkowski in Ref. [71] for the case of parton creation (a more detailed calculation has recently been done in [17]). This demonstrates the dynamical origin of thermal spectra.

In order to draw the link to the observed hadron spectra in heavy-ion collision experiments, it remains to consider also the hadronization process when starting from the parton level of description. For this purpose one could employ, e.g., kinetic theory approaches built on the basis of the Nambu–Jona-Lasinio model Lagrangian, see [72, 73, 74, 75]. In this context the dynamical chiral symmetry breaking in the quark sector plays an essential role as it triggers the binding of quarks into hadrons (inverse Mott effect). The increase in the sigma meson mass that accompanies the dynamical chiral symmetry breaking gives rise to additional sigma meson production by the inertial mechanism (see [76] and references therein). By the dominant decay $\sigma \to \pi\pi$ this leads to an additional population of low-momentum pion states and can contribute to the observed effect that s also discussed as a precursor of pion Bose condensation and may simultaneously resolve the LHC proton puzzle [77] within a non-equilibrium model.

7 Summary

In these lectures, we have given the derivation of the kinetic equation for pair production in a homogeneous, time-dependent external field (dynamical Schwinger mechanism) and discussed the Markovian as well as the low-density limiting cases. Further, we have investigated numerical solutions of the full kinetic equation for one-sheeted and multi-sheeted external field models. We have demonstrated that the dynamical Schwinger mechanism can be considered as a field induced phase transition from the primordial in-state with latent vacuum fluctuations to the final massive quantum field system of particle-antiparticle pairs under the action of a strong external field. Thus, in the simplest situation, this process starts from the vacuum in-state (in the considered statement of the problem the electrons and positrons are absent in the initial state) and possesses the following characteristic features:

(i) presence of three different stages in the time evolution: smooth quasiparticle, fastly oscillating transient and asymptotic final stage;

(ii) strong nonequilibrium character of FIPT, including the out-state;

(iii) non-monotonic entropy growth.

The nonperturbative kinetic description is a reliable basis for the investigation of secondary physical phenomena such as, for example, the electromagnetic radiation from the region of the action of an external field [10]. Here one can expect that the considered stages of the FIPT will be reflected in the time-based sweeps of these phenomena.

On the other hand, these features are rather universal and are characteristic on the qualitative level for physical systems of different nature.

On the formal level this universality appears because the corresponding KE's belong to the united class of integro-differential equations of non-Markovian type with fastly oscillating kernel. Examples of this kind are, e.g., KE's for description of the vacuum creation of scalar bosons and of fermions in the FRW space-time [4], the noncontradictory KE for massive vector bosons in the same metric space [4] and the nonperturbative KE for description of the carrier excitations in graphene [55].

In these lectures we have restricted ourselves to the consideration of the domain of the tunneling mechanism of particle creation, $\gamma \ll 1$. The first step in investigation of the few-photon domain of EPP creation ($\gamma \gg 1$) has been made in the work [36].

We have discussed the application of the Schwinger process in the description of particle production in heavy-ion collisions, mentioning the initial ideas as well as recent developments devoted to the understanding of the apparent thermal spectra of produced hadrons as well as the recent pion and proton puzzles observed at CERN in LHC experiments. The kinetic approach to particle production in strong, time-dependent fields is indispensable for a microphysical elucidation of the mechanisms at work under these extreme conditions.

Acknowledgements

We thank A. Fedotov, T. Fischer, W. Florkowski, D.M. Gitman, B. Kämpfer, A. Otto, R. Ryblewski, D. Seipt and A. Titov for discussions and collaboration. We acknowledge support by the HISS Dubna program for our participation at this Summer School, by NCN grant No. UMO-2014/15/B/ST2/03752 (D.B., J.L., A.S.), by COST Action CA15213 "THOR" (D.B., L.J.) and by IFT internal grant No. 1441/M/IFT/15 (L.J.).

References

[1] F. Sauter, Z. Phys. **69**, 742 (1931).

[2] W. Heisenberg and H. Euler, Z. Phys. **98**, 714 (1936).

[3] J. S. Schwinger, Phys. Rev. **82**, 664 (1951).

[4] A. A. Grib, S. G. Mamaev and V. M. Mostepanenko, "Vacuum Quantum Effects in Strong External Fields", Friedmann Laboratory Publishing, St. Petersburg, 1994.

[5] A. I. Nikishov, Zh. Eksp. Teor. Fiz. **57**, 1210 (1969).

[6] N. B. Narozhnyi and A. I. Nikishov, Yad. Fiz. **11**, 1072 (1970) [Sov. J. Nucl. Phys. **11**, 596 (1970)].

[7] W. Greiner, B. Müller and J. Rafelski, "Quantum Electrodynamics Of Strong Fields," Berlin, Germany: Springer (1985) 594 P. (Texts and Monographs In Physics)

[8] E. S. Fradkin, D. M. Gitman and S. M. Shvartsman, "Quantum electrodynamics with unstable vacuum," Berlin, Germany: Springer (1991) 288 p. (Springer series in nuclear and particle physics)

[9] S. M. Schmidt, D. Blaschke, G. Röpke, S. A. Smolyansky, A. V. Prozorkevich and V. D. Toneev, Int. J. Mod. Phys. E **7**, 709 (1998).

[10] D. B. Blaschke, B. Kämpfer, S. M. Schmidt, A. D. Panferov, A. V. Prozorkevich and S. A. Smolyansky, Phys. Rev. D **88**, 045017 (2013).

[11] C. D. Roberts, S. M. Schmidt and D. V. Vinnik, Phys. Rev. Lett. **89**, 153901 (2002).

[12] V. S. Popov, Phys. Lett. A **298**, 83 (2002).

[13] E. Brezin and C. Itzykson, Phys. Rev. D **2**, 1191 (1970).

[14] A. Casher, H. Neuberger and S. Nussinov, Phys. Rev. D **20**, 179 (1979); Phys. Rev. D **21**, 1966 (1980).

[15] A. Bialas and W. Czyz, Phys. Rev. D **30**, 2371 (1984);

[16] A. Bialas and W. Czyz, Phys. Rev. D **31**, 198 (1985).

[17] R. Ryblewski and W. Florkowski, Phys. Rev. D **88**, 034028 (2013).

[18] B. Richards and E. Wolf, Proc. Roy. Soc. A (London) **253**, 358 (1959).

[19] F. V. Bunkin and I. I. Tugov, Dokl. Akad. Nauk Ser. Fiz. **187**, 541 (1969).

[20] S. S. Bulanov, Phys. Rev. E **69**, 036408 (2004).

[21] S. S. Bulanov, N. B. Narozhny, V. D. Mur and V. S. Popov, Phys. Lett. A **330**, 1 (2004).

[22] G. A. Mourou, C. P. J. Barty, M. D. Perry, Phys. Today **51**, 22 (1998).

[23] G. A. Mourou, T. Tajima and S. V. Bulanov, Rev. Mod. Phys. **78**, 309 (2006).

[24] G. V. Dunne, Eur. Phys. J. D **55**, 327 (2009).

[25] T. Heinzl and A. Ilderton, Eur. Phys. J. D **55**, 359 (2009).

[26] A. Ringwald, Phys. Lett. B **510**, 107 (2001).

[27] D. B. Blaschke, A. V. Prozorkevich, C. D. Roberts, S. M. Schmidt and S. A. Smolyansky, Phys. Rev. Lett. **96**, 140402 (2006).

[28] D. B. Blaschke, A. V. Prozorkevich, G. Röpke, C. D. Roberts, S. M. Schmidt, D. S. Shkirmanov and S. A. Smolyansky, Eur. Phys. J. D **55**, 341 (2009).

[29] D. B. Blaschke, V. V. Dmitriev, G. Röpke and S. A. Smolyansky, Phys. Rev. D **84**, 085028 (2011).

[30] A. Otto, D. Seipt, D. Blaschke, S. A. Smolyansky and B. Kämpfer, Phys. Rev. D **91**, 105018 (2015).

[31] V. N. Pervushin, V. V. Skokov, A. V. Reichel, S. A. Smolyansky and A. V. Prozorkevich, Int. J. Mod. Phys. A **20**, 5689 (2005).

[32] S. M. Schmidt, D. Blaschke, G. Röpke, A. V. Prozorkevich, S. A. Smolyansky and V. D. Toneev, Phys. Rev. D **59**, 094005 (1999).

[33] J. C. R. Bloch, V. A. Mizerny, A. V. Prozorkevich, C. D. Roberts, S. M. Schmidt, S. A. Smolyansky and D. V. Vinnik, Phys. Rev. D **60**, 116011 (1999).

[34] A. V. Prozorkevich, S. A. Smolyansky, V. V. Skokov and E. E. Zabrodin, Phys. Lett. B **583**, 103 (2004).

[35] S. A. Smolyansky, A. D. Panferov, D. B. Blaschke, L. Juchnowski, B. Kämpfer and A. Otto, arXiv:1607.08775 [hep-ph].

[36] A. D. Panferov, S. A. Smolyansky, A. I. Titov, B. Kämpfer, A. Otto, D. B. Blaschke and L. Juchnowski, arXiv:1611.06992 [physics.plasm-ph].

[37] J. D. Bjorken and S. D. Drell, "Relativistic quantum fields," McGraw-Hill, New York (1965).

[38] J. Rau, Phys. Rev. D **50**, 6911 (1994).

[39] S. Habib, Y. Kluger, E. Mottola and J. P. Paz, Phys. Rev. Lett. **76**, 4660 (1996).

[40] S. A. Smolyansky, A. D. Panferov, A. V. Prozorkevich and M. Bonitz, P-Adic Numbers, Ultrametric Analysis, and Applications **4**, 319 (2012).

[41] Y. Kluger, J. M. Eisenberg and B. Svetitsky, Int. J. Mod. Phys. E **2**, 333 (1993).

[42] S. P. Gavrilov and D. M. Gitman, Phys. Rev. D **53**, 7162 (1996).

[43] I. Bialynicki-Birula, P. Gornicki and J. Rafelski, Phys. Rev. D **44**, 1825 (1991).

[44] H. T. Elze and U. W. Heinz, Phys. Rept. **183**, 81 (1989).

[45] F. Hebenstreit, R. Alkofer and H. Gies, Phys. Rev. D **82**, 105026 (2010).

[46] A. M. Fedotov, E. G. Gelfer, K. Y. Korolev and S. A. Smolyansky, Phys. Rev. D **83**, 025011 (2011).

[47] F. Hebenstreit, "Schwinger effect in inhomogeneous electric fields," arXiv:1106.5965 [hep-ph].

[48] F. Hebenstreit, R. Alkofer, G. V. Dunne and H. Gies, Phys. Rev. Lett. **102**, 150404 (2009).

[49] S. Coleman. J. Math. Phys. **7**, 787 (1966).

[50] S. L. Glashow and S. Weinberg, Phys. Rev. Lett. **20**, 224 (1968).

[51] A. V. Filatov, A. V. Prozorkevich, S. A. Smolyansky and V. D. Toneev, Phys. Part. Nucl. **39**, 886 (2008).

[52] T. Oka, Phys. Rev. B **86**, 075148 (2012).

[53] G. V. Dunne, H. Gies and R. Schützhold, Phys. Rev. D **80**, 111301 (2009).

[54] A. D. Panferov, S. A. Smolyansky, A. Otto, B. Kämpfer, D. B. Blaschke and L. Juchnowski, Eur. Phys. J. D **70**, 56 (2016).

[55] A. D. Panferov, S. A. Smolyansky, D. Blaschke, N. Gevorgyan and D. V. Churochkin, in preparation (2017).

[56] F. Cooper, J. M. Eisenberg, Y. Kluger, E. Mottola and B. Svetitsky, Phys. Rev. D **48**, 190 (1993).

[57] N. Tanji, Annals Phys. **324**, 1691 (2009).

[58] B. L. Spokoiny, Yad. Fiz. **36**, 474 (1982).

[59] J. Rau and B. Müller, Phys. Rept. **272**, 1 (1996).

[60] G. Gatoff, A. K. Kerman and T. Matsui, Phys. Rev. D **36**, 114 (1987).

[61] K. Kajantie and T. Matsui, Phys. Lett. **164B**, 373 (1985).

[62] F. Gelis and N. Tanji, Prog. Part. Nucl. Phys. **87**, 1 (2016).

[63] F. Gelis, "Initial State and Thermalization in the Color Glass Condensate Framework," doi:10.1142/9789814663717_0002

[64] J. P. Blaizot, J. Liao and Y. Mehtar-Tani, arXiv:1609.02580 [hep-ph].

[65] P. Castorina, D. Kharzeev and H. Satz, Eur. Phys. J. C **52**, 187 (2007).

[66] P. Castorina and H. Satz, Adv. High Energy Phys. **2014**, 376982 (2014).

[67] P. Castorina, A. Iorio and H. Satz, Int. J. Mod. Phys. E **24**, no. 07, 1550056 (2015).

[68] A. Bialas, Phys. Lett. B **466**, 301 (1999).

[69] W. Broniowski and W. Florkowski, Phys. Rev. Lett. **87**, 272302 (2001).

[70] M. Abramowicz and I. Stegun, Handbook of Mathematical Functions, Dover (N.Y.), Eq. (29.3.82), p. 1026.

[71] W. Florkowski, Acta Phys. Polon. B **35**, 799 (2004).

[72] P. Rehberg, S. P. Klevansky and J. Hufner, Phys. Rev. C **53**, 410 (1996).

[73] P. Rehberg, L. Bot and J. Aichelin, Nucl. Phys. A **653**, 415 (1999).

[74] A. V. Friesen, Y. V. Kalinovsky and V. D. Toneev, Nucl. Phys. A **923**, 1 (2014).

[75] R. Marty, J. M. Torres-Rincon, E. Bratkovskaya and J. Aichelin, J. Phys. Conf. Ser. **668**, 012001 (2016).

[76] L. Juchnowski, D. Blaschke, T. Fischer and S. A. Smolyansky, J. Phys. Conf. Ser. **673**, 012009 (2016).

[77] V. Begun, W. Florkowski and M. Rybczynski, Phys. Rev. C **90**, 014906 (2014).

Volkov States and Non-linear Compton Scattering in Short and Intense Laser Pulses

Daniel Seipt

Lancaster University, Physics Department, Lancaster LA1 4YB, United Kingdom &
The Cockcroft Institute Daresbury Laboratory, Warrington WA4 4AD, United Kingdom

DOI: http://dx.doi.org/10.3204/DESY-PROC-2016-04/Seipt

The collision of ultra-relativistic electron beams with intense short laser pulses makes possible to study QED in the high-intensity regime. Present day high-intensity lasers mostly operate with short pulse durations of several tens of femtoseconds, i.e. only a few optical cycles. A profound theoretical understanding of short pulse effects is important not only for studying fundamental aspects of high-intensity laser matter interaction, but also for applications as novel X- and gamma-ray radiation sources. In this article we give a brief overview of the theory of high-intensity QED with focus on effects due to the short pulse duration. The non-linear spectral broadening in non-linear Compton scattering due to the short pulse duration and its compensation is discussed.

1 Introduction & High-Intensity Parameters

Rapid advances in tera- and petawatt-class laser technology allow to explore light-matter interactions in the experimentally uncharted high-intensity regime. Theoretical predictions include, for instance, intensity dependent non-linearities in high-energy photon emission and pair production processes [1], or non-linear quantum vacuum optics effects such as vacuum birefringence and photon splitting [2–5]. Eventually one expects the spontaneous creation of particle antiparticle pairs from the vacuum (so-called Sauter-Schwinger effect) for field strengths on the order of[1] $E_s \sim m^2/e \sim 1.3 \times 10^{18}\,\mathrm{V/m}$ [6–9].

When an electron interacts with a high-intensity laser, the laser pulse can be described as a plane wave. Plane waves are null-fields, i.e. both field invariants vanish: $E^2 - B^2 = \mathbf{E}\cdot\mathbf{B} = 0$, which means no pairs can be produced from vacuum via the Sauter-Schwinger mechanism). The majority of modern high-intensity laser systems produces laser pulses with wavelengths on the order of 1 μm, and with pulse durations on the order of tens of femtoseconds, i.e. only a few optical cycles. We therefore shall investigate in this article the important effects of the short pulse duration in high-intensity laser matter interactions.

Let us first recall some of the properties of (transverse) plane waves, which we assume to propagate along the negative z axis, and with frequency $\omega = \mathcal{O}(1\,\mathrm{eV})$. Their wave vector is a light-like four-vector, $k^2 = \omega^2 - \mathbf{k}^2 = 0$, and the field strength is a univariate function, $F^{\mu\nu} = F^{\mu\nu}(k\cdot x)$. In this case, $\phi = k\cdot x = \omega x^+$, which tells us that the field depends solely on the light-front variable $x^+ = t + z$ (cf. Appendix A). In addition, Maxwells equations

[1] We use natural Heaviside-Lorentz units with $\hbar = c = 1$ and fine structure constant $\alpha = e^2/4\pi \simeq 1/137$. Scalar products between four-vectors are denoted as $(kp) = k\cdot p = k^\mu p_\mu = k^0p^0 - \mathbf{k}\cdot\mathbf{p}$.

in vacuum require that $F^{\mu\nu}$ is transverse, $k_\mu F^{\mu\nu} = 0$. The field can be represented by a transverse vector potential, $A^\mu = (0, \mathbf{A}_\perp(k\cdot x), 0)$, with $k\cdot A = 0$, and parametrized as $\mathbf{A}_\perp = A_0 g(\phi/\Delta\phi)\mathrm{Re}[\boldsymbol{\epsilon} e^{-i\phi}]$ with a complex polarization vector $\boldsymbol{\varepsilon}$, and an envelope function g with pulse duration $\Delta\phi$. The interaction of a probe electron with four-momentum p^μ with the plane wave field can be characterized by the following dimensionless gauge and Lorentz invariant parameters: (i) the classical nonlinearity parameter $a_0 = eA_0/m$ [10], (ii) the quantum energy parameter $b_0 = (kp)/m^2$, and (iii) the quantum efficiency parameter $\chi_e = e\sqrt{(F\cdot p)^2}/m^3 = a_0\, b_0$. For a pulsed laser field one has in addition the dephasing parameter $a_0^2\Delta\phi$ [11], which represents the ratio of the laser peak intensity and the laser bandwidth $a_0^2\Delta\phi \propto I/(\Delta\omega/\omega)$.

The classical nonlinearity parameter a_0 represents the laser energy density seen by the probe electron and can be related to the laser intensity via $a_0^2 = 7.309\times 10^{-19} I[\mathrm{W/cm^2}]\lambda^2[\mu\mathrm{m}]$. With present laser technology one is able to reach light intensities on the order of $I = 2\times 10^{22}$ W/cm^2, which corresponds to $a_0 \sim 100$ at $\lambda = 800$ nm typical for Ti:Sa laser systems [12,13]. With the upcoming generation of multi-petawatt lasers one expects to reach intensities up to $10^{23}\ldots 10^{25}$ W/cm^2 and even beyond [2]. The parameter also a_0 represents the work done by the field in one wavelength λ of the wave in units of the electron mass $a_0 = \frac{eE_0\lambda}{m}$. The limit $a_0 \to \infty$, refers to both the limit of infinite intensity at fixed frequency and the static limit $\omega \to 0$ ($\lambda \to \infty$) at fixed intensity. For $a_0 \gg 1$ the probabilities of processes happening in the laser field approach those in a constant crossed field [1] and are described by the quantum efficiency parameter χ_e alone. The regime $a_0 \gg 1$ is also referred to as "quasi-static" or "tunnelling" regime, i.e. $1/a_0$ serves as the Keldysh parameter of the electron laser interaction.

The quantum efficiency parameter χ_e is the value of the electric field experienced by the particle in its rest frame in units of the Sauter-Schwinger field strength, $\chi_e = 2\gamma E/E_s$, with $E_s = m^2/e$. This means that χ_e can be large for ultra-relativistic particles with $\gamma \gg 1$ colliding with a laser pulse, although the electric field in the laboratory frame is much weaker than E_s due to the Lorentz transformation of the transverse electric field.

2 Classical Dynamics of an Electron in a Laser Pulse

Before we dive into the quantum theory of the laser matter interaction let us start with a classical description. The classical picture is valid whenever both the quantum energy parameter $b_0 \ll 1$ and the quantum efficiency parameter $\chi_e \ll 1$. According to the classical theory of electrodynamics, the dynamics of point-like charged particles in a given external field configuration, described by the field strength tensor $F_{\mu\nu} = \partial_\mu A_\nu - \partial_\nu A_\mu$, is governed by the Lorentz force equation [14]

$$m\,\frac{du^\mu}{d\tau} = F^{\mu\nu}(x)u_\nu\,, \tag{1}$$

where m is the electron mass and we have conveniently absorbed the electron charge into the background field vector potential $eA \to A$. The electron's four-velocity $u^\mu = dx^\mu/d\tau$ is the tangent vector to the particle's world line $x^\mu(\tau)$, parametrized by proper time τ. Due to the anti-symmetry of the field strength tensor the four-acceleration $du^\mu/d\tau$ is always orthogonal to the four-velocity, and the four-velocity is normalized as $u\cdot u = 1$.

[2] For instance, the Vulcan laser at RAL-CLF (UK) (`http://www.clf.stfc.ac.uk/CLF/`), the ELI project (Czech Republic, Hungary, Romania) `http://www.eli-beams.eu`, or the OMEGA EP-OPAL project (Rochester, USA).

In general this is a non-linear differential equation as the field strength has to be taken along the world line of the particle to be solved for $F^{\mu\nu} = F^{\mu\nu}(x(\tau))$. The solution of (1) can be quite a difficult task. For instance, the motion of an electron in standing waves can show chaotic behaviour [15]. Luckily, the dynamics of an electron in a plane wave laser field is one of the few exactly solvable cases.

2.1 Solution of the Lorentz Force Equation in Plane Waves

The solution of the Lorenz force equation in a plane wave field becomes particularly simple when employing light-front coordinates (cf. Appendix A), as one can find a very simple relation between the laser phase $\phi = \omega x^+$ and the particle's proper time τ. By dotting the laser wave-vector into the equation of motion (1) we immediately find $\frac{d}{d\tau}(k \cdot u) = 0$. That means $k \cdot u = const.$ is a constant of motion, i.e. the u^+ component of the electron's four-velocity is conserved $u^+ = u_0^+$. From this we find that the relation between the laser phase ϕ, light-front time x^+ and proper time τ can be expressed as

$$\frac{d\phi}{d\tau} = k \cdot u = \omega u^+ \quad \Rightarrow \quad x^+ = u^+ \tau \,. \tag{2}$$

That means one can replace the proper time derivative by a light-front time derivative in the equations of motion. Since the normalized laser vector potential has only transverse components, $a^\mu = eA^\mu/m = (0, 0, \mathbf{a}_\perp(x^+))$, the transverse components of the Lorentz force equation can be written as

$$\frac{d\mathbf{u}_\perp}{d\tau} = -(k \cdot u)\, \frac{d\mathbf{a}_\perp}{d\phi} \,,$$

which gives $\mathbf{u}_\perp + \mathbf{a}_\perp = const = \mathbf{u}_{\perp,0}$ because of (2). Because the four-velocity is normalized, $u^2 = 1$, the fourth component u^- of the velocity can be obtained simply via

$$u^-(\phi) = \frac{1 + \mathbf{u}_\perp^2(\phi)}{u^+} = \frac{1 + [\mathbf{u}_{\perp,0} - \mathbf{a}_\perp(\phi)]^2}{u^+}$$

The particle world line x^μ is obtain by integrating the four-velocity again

$$x^\mu = \int d\tau\, u^\mu = \int \frac{dx^+}{u^+}\, u^\mu \,. \tag{3}$$

For later use we here also define the *kinetic four momentum* of the electron as $\pi^\mu = mu^\mu$. The solution for the kinetic momentum can also be represented in a covariant way as

$$\pi^\mu(x^+) = \Lambda^\mu{}_\nu(x^+)\, p^\nu \,, \tag{4}$$

where p^ν is the initial value of the momentum, and $\Lambda^\mu{}_\nu(\phi) = (e^X)^\mu{}_\nu$ with

$$X^{\mu\nu} = \int^{x^+} \frac{dz^+}{p^+}\, F^{\mu\nu}(z^+) = \frac{k^\mu A^\nu - k^\nu A^\mu}{k \cdot p}$$

has the form of a Lorentz transformation [16, 17]. In particular, the minus-component of the kinetic electron momentum can be written as

$$\pi^- = p^- + \frac{2\, p \cdot A - A^2}{p^+} \,. \tag{5}$$

2.2 Radiation Back-Reaction

When the electron interacts with a high-intensity laser pulse the back-reaction of the emission of radiation on the electron motion, the so-called radiation reaction (RR), can become significant. The radiation power is given by the Larmor formula, $P = -\frac{2\alpha}{3}\dot{u}^2$. Whenever the emitted radiation energy $\sim \alpha\gamma^2\omega a_0^2\Delta\phi$ becomes comparable to the electron's initial energy γm, the equations of motion (1) have to be amended by a radiation force term F_R^μ:

$$m\dot{u}^\mu = F^{\mu\nu}u_\nu + F_R^\mu\,. \tag{6}$$

In the radiation dominated regime, characterized by the parameter $R_C = \alpha\chi_e a_0 \gtrsim 1$, the electron loses a large fraction of it's kinetic energy in one cycle of the background laser field, and the RR force F_R^μ becomes comparable to the Lorentz force. This regime could be reached, for instance by colliding a 500 MeV electron beam with a laser pulse with $a_0 = 200$, which corresponds to a peak intensity of $10^{23}\mathrm{W/cm}^2$.

Many different forms for the RR force F_R^μ have been suggested since the seminal works of Lorenz and Abraham more than a century ago [18–21]. A particularly popular form of the RR force (which is often used in numerical simulations of laser-matter interaction at high intensity [22–24]) is the so-called Landau-Lifshitz force [25]. It reads

$$F_{R,LL}^\mu = \frac{2\alpha}{3m}\left[(u^\alpha\partial_\alpha F^{\mu\nu})u_\nu + \frac{1}{m}F^{\mu\nu}F_{\nu\alpha}u^\alpha + \frac{1}{m}(F^{\alpha\nu}u_\nu)^2 u^\mu\right]. \tag{7}$$

The equations of motion (6) with the LL radiation force (7) also possess closed form analytic solutions in the presence of plane wave backgrounds [26]. By dotting again the laser wave-vector k into the equations of motion we find

$$\frac{d(k\cdot u)}{d\tau} = \frac{2\alpha}{3m}(a'\cdot a')\,(k\cdot u)^3$$

which can be integrated to find a (non-linear) relation between the laser phase ϕ and proper time τ [cf. (2)] allowing to integrate (6) [26].

Finally, we note that the classical RR is a continuous process, in contrast to quantum RR which is stochastic. Quantum RR effects are important whenever already the emission of a single photon can alter the electron trajectory significantly due to the momentum recoil [27–29]. The transition from the classical to the quantum RR regime is characterized by $\chi_e \gtrsim 1$ and $R_Q = \alpha a_0 \gtrsim 1$ [27].

3 High-intensity QED in the Furry Picture

In high-intensity QED the laser field is usually described as a background field[3]. This background field has to be treated to all orders, which can be achieved by going to the Furry interaction picture in which the background field is treated as part of the unperturbed system [34]. For this we need to know the solutions of the Dirac equation

$$[i\partial\!\!\!/ - A\!\!\!/(\phi) - m]\Psi(x) = 0 \tag{8}$$

[3]However, the development of avalanche type QED cascades at extreme intensities could cause a depletion of the laser, turning an initially strong field weak, and rendering the background field approximation invalid [30–33]. See also A. M. Fedotov's contribution in this volume.

in a given background A describing the laser field. The solutions $\Psi(x)$ of (8) in a univariate null-field background $A = A(\phi)$ are called Volkov wave functions [35]. We use here the Dirac slash notation $\not{p} = p^\mu \gamma_\mu$ to denote scalar products between four-vectors and the Dirac matrices γ_μ.

3.1 Derivation of Volkov States

Let us now explicitly calculate the Volkov wave functions. Although the derivation can be found in textbooks (e.g. in [36]) will be present it here in some detail to work out why a null-field background is required in order to solve Eq. (8) and indicate possible extensions to more general backgrounds. In the first step on transforms (8) into a second order differential equation by multiplying with the adjoint Dirac operator $i\not{\partial} - \not{A} + m$ from the left [36], yielding

$$\left[(i\partial - A)^2 - m^2 - \frac{1}{2}\sigma^{\mu\nu}F_{\mu\nu}(x)\right]\Psi(x) = 0\,, \tag{9}$$

with $\sigma^{\mu\nu} = \frac{i}{2}[\gamma^\mu, \gamma^\nu]$ as the commutator of gamma matrices. The so-called Pauli interaction term $\frac{1}{2}\sigma^{\mu\nu}F_{\mu\nu}(x)$ describes the interaction of the half-integer electron spin with the background field. The general idea is to seek a solution of (9) in the form $\Psi(x) = e^{-i(px)}\Omega(\phi)u$ with a constant four-vector p^μ, and where Ω is a (4×4) Dirac matrix depending only on the laser phase $\phi = k \cdot x$ and u denotes a Dirac bi-spinor.

When switching off the background field, the quantum numbers p^μ represent the four-momentum of a free particle. With the background field present, they represent the asymptotic electron momentum outside the laser pulse. Because three momentum operators $p^1 = -i\partial/\partial x^1$, $p^2 = -i\partial/\partial x^2$ and $p^+ = 2i\partial/\partial x^-$ commute with the Dirac-operator, the corresponding quantum numbers are conserved. In addition, $p^- = (\mathbf{p}_\perp^2 + m^2)/p^+$ is determined by the mass shell condition $p^2 = m^2$. Similarly, the Dirac bi-spinors are the the free Dirac spinors $u_{p,r}$ for (on-shell) momentum p, fulfilling $(\not{p} - m)u_{p,r} = 0$, and where $r = 1, 2$ is the spin quantum number. We choose here and in the following the normalization $\bar{u}_{p,r}u_{p,r'} = 2m\,\delta_{rr'}$.

By plugging the above ansatz for the wave function into (9) one obtains an equation for the unknown matrix function Ω. Because Eq. (9) is a second order differential equation, in general the equation for Ω can be expected to be a second order as well. However, the coefficient of the second order term turns out to be k^2. That means for a light-like univariate background field with wave vector $k^2 = 0$ the equation for Ω is of first order. Note that this is not true for space-like ($k^2 < 0$) or time-like ($k^2 > 0$) wave vectors. The first case, for instance, corresponds to magnetic undulators or the wave propagation in a medium with refractive index $n_r > 1$. The latter case may refer to time dependent electric fields, or the propagation of waves in a medium with refractive index $n_r < 1$, e.g. a plasma. No general solutions of relativistic wave equations exist in background fields with $k^2 \neq 0$. Recent attempts to find (approximate) solutions can be found in Refs. [37–40]. The situation becomes even more complicated for *bi-variate* backgrounds, for instance for the electron dynamics in two counter-propagating laser beams [41].

For the Volkov problem, with $k^2 = 0$, we eventually find the following *first order* ordinary differential equation for the hitherto unknown matrix function Ω:

$$2i(kp)\,\frac{d\Omega}{d\phi} = \left(2(pA) - A^2 - i\not{k}\not{A}'\right)\Omega\,. \tag{10}$$

This equation can be easily integrated yielding

$$\Omega_p(\phi) = \left(1 + \frac{\not{k}\not{A}}{2(kp)}\right) e^{-if_p(\phi)}\,, \tag{11}$$

$$f_p(\phi) = \int \frac{d\phi}{2k\cdot p}\left[2p\cdot A(\phi) - A^2(\phi)\right] = -\frac{p^- x^+}{2} + \frac{1}{2}\int dx^+\,\pi^-(x^+) \tag{12}$$

where we used that $\not{k}\not{A}$ is a nilpotent operator of grade 2, i.e. $(\not{k}\not{A})^{n\geq 2} = 0$, which again holds because the background field has a light-like wave vector with $\not{k}\not{k} = k^2 = 0$ and $(kA) = 0$. The non-linear phase f_p can be written as an integrals of the minus component of the classical kinetic four-momentum (5) by using that $\phi = \omega x^+$. Note that the Volkov wave functions (14) are normalized using a covariant light-front normalization,[4]

$$(\bar{\Psi}_{p',r'}|\Psi_{p,r}) = \frac{1}{2}\int dx^- d\mathbf{x}^\perp\, \bar{\Psi}_{p',r'}(x)\gamma^+\Psi_{p,r}(x) = 2p^+(2\pi)^3\delta(\mathsf{p}'-\mathsf{p})\delta_{r'r} \tag{13}$$

and where p stands for $(p^+, \mathbf{p}^\perp)$, i.e. $\delta(\mathsf{p}) = \delta(p^+)\delta(p^1)\delta(p^2)$.

It is also convenient to define the so-called Ritus matrices $E_p(x) = e^{-i(px)}\Omega_p(\phi)$, such that the Volkov states can be written as

$$\Psi_{p,r}(x) = E_p(x)u_{p,r}\,. \tag{14}$$

The Ritus matrices can decomposed as $E_p = V(\phi)\, e^{-iS_{\rm HJ}}$, where $S_{\rm HJ}$ denotes the classical Hamilton-Jacobi action of a classical particle in the background field. That means Volkov wave function is an exact semiclassical wavefunction, i.e. while being an exact solution of the wave equation (8) the action does not contain quantum corrections (in powers of $\hbar$). The matrix $V(\phi)$ is the bi-spinorial representation of the Lorentz transformation $\Lambda^\mu{}_\nu(\phi)$ that generates the classical orbits (4), and which is defined by

$$V^{-1}\,\gamma^\mu V = \Lambda^\mu{}_\nu\gamma^\nu\,.$$

The Lorentz transformation $V(\phi)$ transports the spinor $u_{p,r}$ along the classical trajectory [16, 17]. The Ritus matrices, analytically continued to off-shell momenta $p^2 \neq m^2$, have the following orthogonality and completeness properties:

$$\int d^4x\,\bar{E}_{p'}(x)E_p(x) = (2\pi)^4\,\delta(p'-p)\,, \qquad \int d^4p\,E_p(x')\bar{E}_p(x) = (2\pi)^4\,\delta(x-x')\,.$$

The wave functions (14) represent the positive energy solutions $\Psi_{p,r} \equiv \Psi^{(+)}_{p,r}$ of (8), i.e. they describe the propagation of electrons in a background field. In order to describe positrons as well (for instance to calculate the probabilities for pair production in a laser field) we need the negative energy solutions of (8). They can be obtained from (14) via the transformation $p \to -p$, i.e. $\Psi^{(-)}_p(x) \equiv \Psi_{-p}(x)$, where the notation for negative energy spinors is as usual $u_{-p} \equiv v_p$ [43, 44].

[4] The scalar product between any two spinor wave functions is defined in a Lorentz invariant way as [42] $(\bar{\Psi}_1|\Psi_2) = \int_\sigma d\sigma_\mu\bar{\Psi}_1(x)\gamma^\mu\Psi_2(x)$, with σ being a hypersurface in Minkowski space and $d\sigma_\mu$ the infinitesimal normal vector thereupon. The hypersurface can be expressed in general curvilinear coordinates $\xi^\mu(x)$, where $\xi^0 = const.$ defines the hypersurface and $\xi^1, \xi^2\xi^3$ parametrize σ, such that $d\sigma_\mu = \frac{d\xi^0(x)}{\partial x^\mu}\sqrt{-g}d\xi^1 d\xi^2 d\xi^3$ with the determinant g of the metric tensor in the coordinates ξ^μ. Choosing a light-front surface $x^+ = const.$ yields (13).

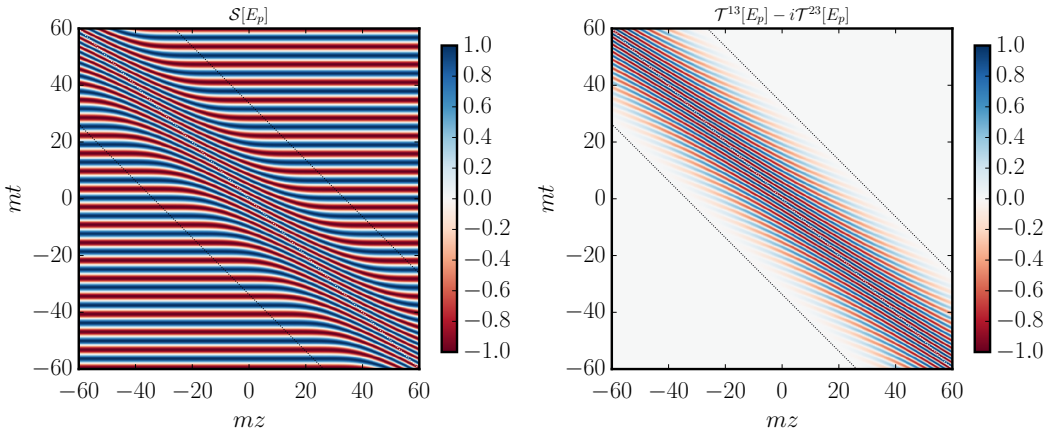


Figure 1: Contour plot of (the real part of) the scalar and tensor projections of the Ritus matrices $E_p(x)$ in the (z-t) plane for a circularly polarized laser pulse with $a_0 = 2$ and pulse duration $\Delta\phi = 20$.

3.2 Properties of Volkov States

The properties of the Volkov states can be studied by investigating the Ritus matrix function $E_p(x)$ as they contain all the information on the interaction with the laser field. Since the $E_p(x)$ are 4×4 matrices it is reasonable to study the different projections onto the basis elements of the Clifford algebra [45]. It turns out that only the scalar and anti-symmetric tensor projections yield non-zero results:

$$\mathcal{S}[E_p] = \frac{1}{4}\mathrm{tr}\, E_p(x) = \exp\{iS_p(x)\}\,, \tag{15}$$

$$\mathcal{T}^{\mu\nu}[E_p] = \frac{1}{4}\mathrm{tr}\,\sigma^{\mu\nu}E_p(x) = \frac{i}{2k\cdot p}(A^\mu k^\nu - A^\nu k^\mu)\exp\{iS_p(x)\}\,, \tag{16}$$

where $\sigma^{\mu\nu} = \frac{i}{2}[\gamma^\mu, \gamma^\nu]$, and tr denotes the trace over the Dirac matrix indices.

The real parts of the scalar projection $\mathcal{S}[E_p]$ and the combination of tensor projections $\mathcal{T}^{13} - i\mathcal{T}^{23}$ are exhibited in Figure 1 for an electron with an energy of 50 GeV propagating head-on through a strong laser pulse with $a_0 = 2$ and a pulse duration $\Delta\phi = 20$. The two projections are shown in the frame where the electron is initially at rest. In that frame, the free electron wave function outside the laser pulse behaves as $\propto \exp\{-ip\cdot x\} = \exp\{-imt\}$. In the case of the scalar projection of the Ritus matrices the effect of the laser pulse is a local tilt of the electron wave fronts, see left panel of Fig. 1. This behaviour corresponds to the build-up of an intensity dependent ponderomotive quasi-momentum inside the laser pulse [46]. The tensor projection of the Ritus matrices shown in the right panel of Fig. 1 are non-zero only in regions where the laser pulse is present. They correspond to the $\not{k}\not{A}$ term in the Volkov states, i.e. the Pauli interaction term.

In the following we construct wave packets from the Volkov wave functions and show that the motion of the centroid of the packet follows is closely related to the classical trajectory [47, 48].

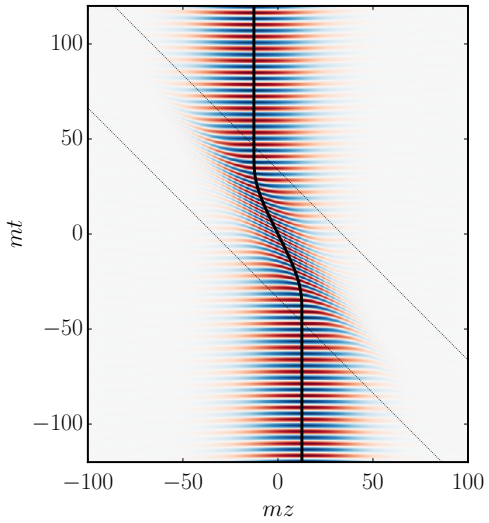


Figure 2: Contour plot of a normalized scalar Volkov wave packet in the (t-z) plane. For comparison, the classical trajectory is depicted as solid black curve. The laser pulse propagates between the two black dotted lines.

We will restrict the discussion to the scalar part of the Volkov wave function which describes charged spin-0 bosons. As a simple example it suffices to construct a one-dimensional wave packet as a superposition of Volkov waves with a light-front momentum distribution $h_+(p^+)$ but all having the same transverse momenta $\mathbf{p}_\perp = 0$,

$$\chi(x) = \int \frac{dp^+}{2p^+}\, h_+(p^+)\, \mathcal{S}[E_p(x)]\,. \tag{17}$$

Such a wave packet has a finite temporal duration, but remains infinitely extended in the transverse coordinates. In the following we choose a Gaussian distribution $h_+ = \mathcal{N} e^{-(p^+ - p_0^+)^2/2\Delta^2}$ with Gaussian width $\Delta = 0.05\, m$ and with $p_0^+ = m$. The laser pulse parameters are the same as for Figures 1. This construction provides a localized wave packet in the (t-z) plane with a minimum Gaussian size at $t = z = 0$. This wavepacket is shown in Figure 2 in the (t-z) plane. The centroid of the wave packet follows the classical trajectory $z(t)$ (black curve), which shows the close correspondence between the classical trajectory solutions and the Volkov wave functions. In addition, the Dirac-Volkov current

$$j^\mu = \frac{\bar\Psi_{p,r}\, \gamma^\mu\, \Psi_{p,r}}{\bar\Psi_{p,r} \Psi_{p,r}} = \frac{\pi^\mu(\phi)}{m} = u^\mu(\phi)\,, \tag{18}$$

coincides with the classical four-velocity u^μ.

Let us now investigate the momentum space spectrum of the Volkov states and find relations to the classical motion. The Ritus matrices $E_p(x)$ have a spectral representation as a

superposition of plane waves

$$E_p(x) = \int \frac{d\ell}{2\pi}\, e^{-i(p+\ell k)\cdot x}\, \mathcal{E}_p(\ell) \tag{19}$$

with the spectral components

$$\mathcal{E}_p(\ell) = \mathscr{K}_0(\ell) + \frac{ma_0 \not{k}}{2(kp)} \left[\not{\epsilon}\, \mathscr{K}_+(\ell) + \not{\epsilon}^*\, \mathscr{K}_-(\ell) \right]. \tag{20}$$

which are be represented by the three scalar functions

$$\begin{Bmatrix} \mathscr{K}_0(\ell) \\ \mathscr{K}_\pm(\ell) \end{Bmatrix} = \int d\phi \begin{Bmatrix} 1 \\ g(\phi) e^{\mp i(\phi+\hat{\phi})} \end{Bmatrix} \exp\{i\ell\phi - i f_p(\phi)\}\,. \tag{21}$$

The variable ℓ parametrizes the amount of light-front laser momentum k^- which is exchanged between the electron and the background field. It can be interpreted as some continuous analogue to the number of exchanged laser photons.

Let us now investigate the limit of infinitely long monochromatic plane wave background fields (IPW), formally achieved by setting $g \to 1$. In that case the background is a periodic function such that the Floquet theorem applies [49]: The solution of the Dirac equation (8) in a periodic background takes the form

$$\Psi_p(\phi) = e^{-iq\cdot x}\, \Phi(\phi)\,, \tag{22}$$

where $\Phi(\phi + 2\pi) = \Phi(\phi)$ has the same periodicity as the background, and $q^\mu = p^\mu + \frac{m^2 a_0^2}{4k\cdot p} k^\mu$ is called the quasi-momentum. The Fourier-zero mode, i.e. the non-periodic part of the non-linear phase f_p in (12), has been absorbed into the definition of the quasi-momentum.

In the limit of an IPW background the momentum distribution functions (21) degenerate to a delta comb

$$\mathscr{K}_j(\ell) \xrightarrow{g\to 1} \sum_{n=-\infty}^{\infty} \delta(\ell - n - \frac{m^2 a_0^2}{4k\cdot p}) K_j(n) \tag{23}$$

with support at discrete momentum values $q^\mu + nk^\mu$. For arbitrary polarization of the background field the coefficients $K_j(n)$ are related to generalized Bessel functions (see e.g. [50, 51]), and they turn into ordinary Bessel functions of the first kind in the case of circular polarization. The Volkov wave function in an IPW background appears as an infinite sum over discrete momentum states

$$E_p(x) = \sum_{n=-\infty}^{\infty} e^{-i(q+nk)\cdot x}\, \mathcal{E}_p^{\mathrm{IPW}}(n)\,, \tag{24}$$

which are also called Zel'dovich levels [52]. The level structure furnishes an easy interpretation of strong-field phenomena. For instance, the appearance of harmonics in the non-linear Compton spectra or the resonant singularities in second-order strong-field scattering processes can be seen as transitions between different Zel'dovich of the incident and final state Volkov electrons. Modifications of this level structure due to radiative corrections, i.e. the electron self-energy have been calculated as well [53].

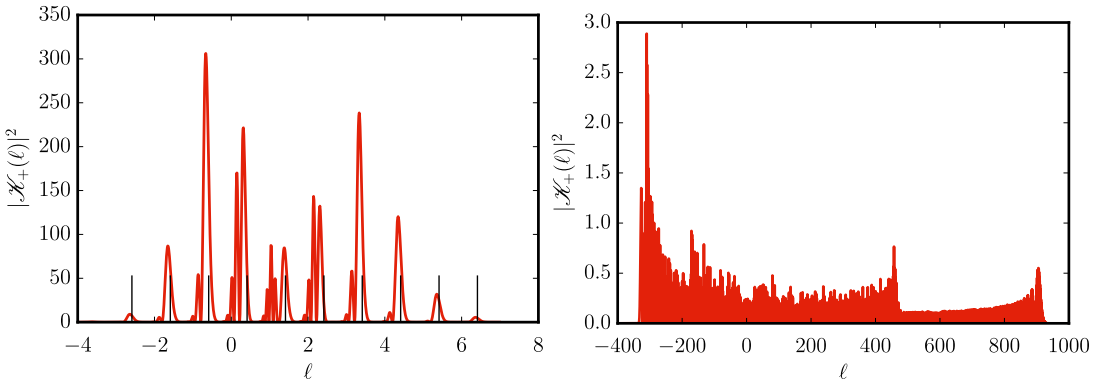


Figure 3: Spectral components of the Volkov state with a small (large) range of spectral components ℓ contributing in the left (right) panels. In the left panel the black vertical lines indicate the positions of the Zel'dovich levels at $\ell = n + \frac{ma_0^2}{8\omega\gamma}$ in the case of an infinite monochromatic plane wave. One can make a clear connection between these Zel'dovich levels and the peaks in the Volkov spectrum for a pulsed field. In the right panel a large number of spectral components contribute the width of each level is larger than their separation which makes a clear identification of individual Zel'dovich levels difficult.

If one now starts from the well known case of infinite monochromatic plane waves (with the discrete level structure) and looks at modifications due to *finite* pulse duration one finds a broadening of the Zel'dovich levels. There are two different contributions to the level broadening: (i) a bandwidth broadening $\Delta\phi^{-1}$ due to the finite laser bandwidth (ii) a non-linear, intensity dependent broadening $\sim \frac{ma_0^2}{\omega\gamma}$ due to the gradual change in the laser intensity in a pulsed field. This second mechanism is related to the ponderomotive, i.e. slowly varying, part of the non-linear phase f_p, and can be seen as a gradual build-up of an intensity-dependent quasi-momentum as the laser intensity increases [46]. Depending on the bandwidth and the peak intensity either of the two mechanisms can be dominating the broadening of the Zel'dovich levels. The broadened Zel'dovich levels are shown in Fig. 3.

The scalar spectral components $\mathscr{K}_j(\ell)$ of a Volkov state also have a close relation to the classical electron motion in a laser pulse. The effective range of values of ℓ is determined by the classical dynamics [51]. To be specific, the maximum and minimum values of the minus component of the kinetic four-momentum determine the cut-off values of ℓ via $\ell_{\mathrm{max/min}} = (\pi^-_{\mathrm{max/min}} - p^-)/k^-$. Beyond those cut-off values the functions $\mathscr{K}_j(\ell)$ drop to zero exponentially fast. The reason is that only for $\ell_{\mathrm{min}} < \ell < \ell_{\mathrm{max}}$ the phase integrals in (21) posses real stationary phase points. Also the local minima and maxima of π^-, which appear during the course of the laser pulse, lead to pronounced structures in the Volkov state spectral component $\mathscr{K}_+(\ell)$. This is caused by a sudden change in the number of stationary phase points related to fold-type caustics. All the local extremal points of π^- are indicated by red lines in Figure 1, connecting them to pronounced structures in the spectral components $\mathscr{K}_j(\ell)$. One could possibly observe those spectral features of the Volkov states by using laser-assisted Compton scattering of X-rays [54].

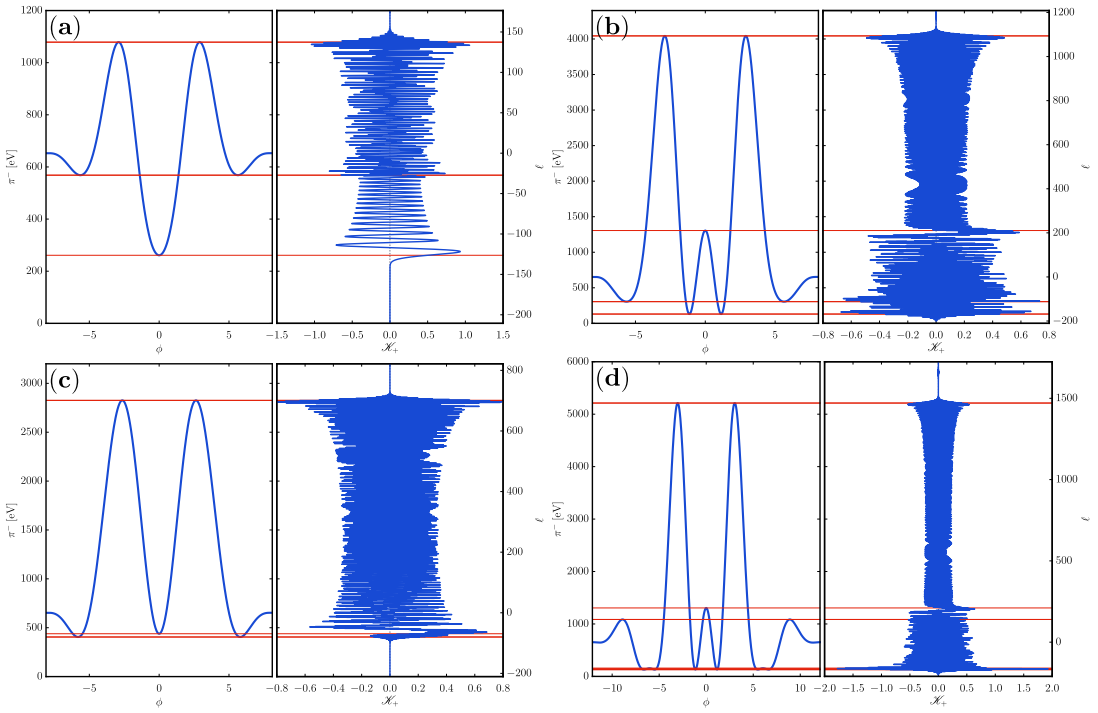


Figure 4: The light-front momentum component π^- along the classical trajectory of an electron in a short laser pulse as a function of the laser phase $\phi = \omega x^+$ (left panel) is compared to the spectral component $\mathscr{K}_+(\ell)$ of the Volkov state in the same pulse (right panel). The electron counterpropagates the laser pulse with initial energy of 1 GeV at an angle of $\theta = 2/\gamma$. Other parameters are as follows: (a) $a_0 = 1$, $\Delta\phi = 8$, linear polarization; (b) $a_0 = 5$, $\Delta\phi = 8$, linear polarization; (c) $a_0 = 5$, $\Delta\phi = 8$, circular polarization; (d) $a_0 = 5$, $\Delta\phi = 12$, linear polarization.

3.3 The Dirac-Volkov Propagator

The laser-dressed Green's function (Dirac-Volkov propagator) is the solution of an inhomogeneous Dirac equation in the background field with delta inhomogeneity, $[i\partial\!\!\!/ - A\!\!\!/ - m]\,\mathcal{G}(x,y) = \delta(x-y)$. Many different representations of this Dirac-Volkov propagator $\mathcal{G}(x,y)$ are known, see e.g. [1, 55–60]. A particularly useful representation is given in terms of the Ritus matrix functions E_p as [1]

$$\mathcal{G}(x,y) = \int \frac{d^4p}{(2\pi)^4}\, E_p(x) G_0(p) \bar{E}_p(y)\,, \tag{25}$$

where the free propagator in momentum space is given by $G_0(p) = (p\!\!\!/ + m)/(p^2 - m^2 + i0^+)$. The Dirac-Volkov propagator is needed for the calculation of higher-order processes in laser fields such as nonlinear Double Compton scattering [61–63], laser assisted Bremsstrahlung [64] or laser assisted pair production in the field of a nucleus [65], as well as the calculation of radiative corrections such as the electron mass operator [66]. It is worth noting that the background field determines the pole structure of the propagator, with an infinite series of

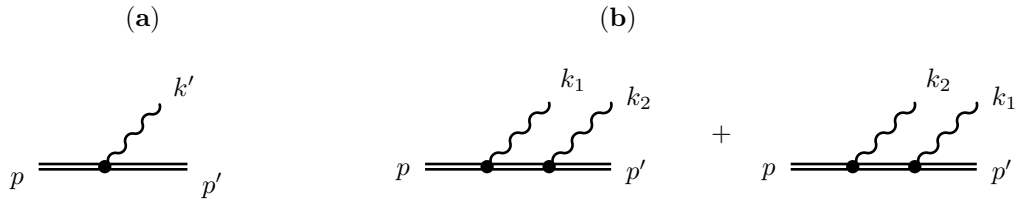


Figure 5: Strong-field Feynman diagrams in the Furry picture for Non-linear Compton scattering (a) and Non-linear Double Compton scattering (b). Double lines represent laser dressed electron wave functions and propagators for external and internal lines, respectively.

poles for infinite monochromatic plane waves and just a single pole plus finite resonances for short pulses [62, 67–69].

3.4 Strong-Field Feynman Rules

In order to calculate the S matrix elements of high-intensity QED processes one may employ the Feynman diagram technique in coordinate space. The Feynman rules for high-intensity QED in the Furry picture can be summarized as follows [60]:

1. External incoming or outgoing electrons with momentum p are represented by laser dressed Volkov wave function $\Psi_p(x)$ or $\bar{\Psi}_p(x)$, respectively. For incoming and outgoing positrons one uses the corresponding negative energy Volkov wave function $\bar{\Psi}_{-p}(x)$ and $\Psi_{-p}(x)$.

2. An internal fermion line corresponds to the Dirac-Volkov propagator $\mathcal{G}(x, y)$.

3. Internal and external photon lines are translated into the free photon propagator and the free photon wave functions, respectively, see e.g. Ref. [45].

4. Each interaction vertex corresponds to a factor $-ie\gamma^\mu$ and an integral over d^4x.

5. Symmetry factors for identical particles etc. are the same as in usual QED.

Let us look at few examples. Firstly, the S matrix for non-linear Compton scattering, i.e. the emission of a high-energy photon by an electron moving in an intense laser field, given in Fig. 5 (a). This diagram is are forbidden in ordinary QED without the background field because it is impossible to fulfil four-momentum conservation. The background field provides the missing four-momentum to make this process possible. Diagram (a) translates into the formula

$$S = \int d^4x \, \bar{\Psi}_{p'}(x)[-ie\gamma^\mu \varepsilon^*_\mu e^{ik' \cdot x}]\Psi_p(x) \,, \tag{26}$$

where the wave function of the emitted photon with momentum k' and polarization vector ε' is given by $\varepsilon^*_\mu e^{ik' \cdot x}$. The non-linear Compton scattering is discussed in some more detail in Section 4.

The second example is the non-linear Double Compton scattering in (b), where two photons are emitted coherently by the same electron. Because the two emitted photons are indistinguishable the S matrix is represented by two diagrams with the outgoing photon lines interchanged.

The S matrix for this process reads

$$S = -e^2 \int d^4x d^4y \, \bar{\Psi}_{p'}(x) \, \not{\epsilon}_2^* e^{ik_2 \cdot y} \, \mathcal{G}(y,x|A) \, \not{\epsilon}_1^* e^{ik_1 \cdot x} \, \Psi_p(x)$$
$$- e^2 \int d^4x d^4y \, \bar{\Psi}_{p'}(x) \, \not{\epsilon}_1^* e^{ik_1 \cdot y} \, \mathcal{G}(y,x|A) \, \not{\epsilon}_2^* e^{ik_2 \cdot x} \, \Psi_p(x) \, .$$

The pole structure of the Dirac-Volkov propagator strongly affects the spectrum of the emitted photons [61, 62, 70].

4 Non-linear Compton Scattering

The process of non-linear Compton scattering in high-intensity lasers has been investigated theoretically since the early 1960's [71–74], but in most studies infinite monochromatic plane wave laser fields or constant crossed fields have been assumed. But as mentioned above, modern laser systems produce very short high-intensity pulses with only a few cycles oscillations of the laser's electric field. The influence of the short laser pulse duration on the non-linear Compton process has been investigated in the recent years, see for instance Refs. [46, 75–81]. We shall here discuss some of the short pulse effects on the non-linear Compton spectra. Similar effects can be seen also for other processes occuring in strong and short laser pulses, for instance in the non-linear Breit-Wheeler pair production [43, 82–86].

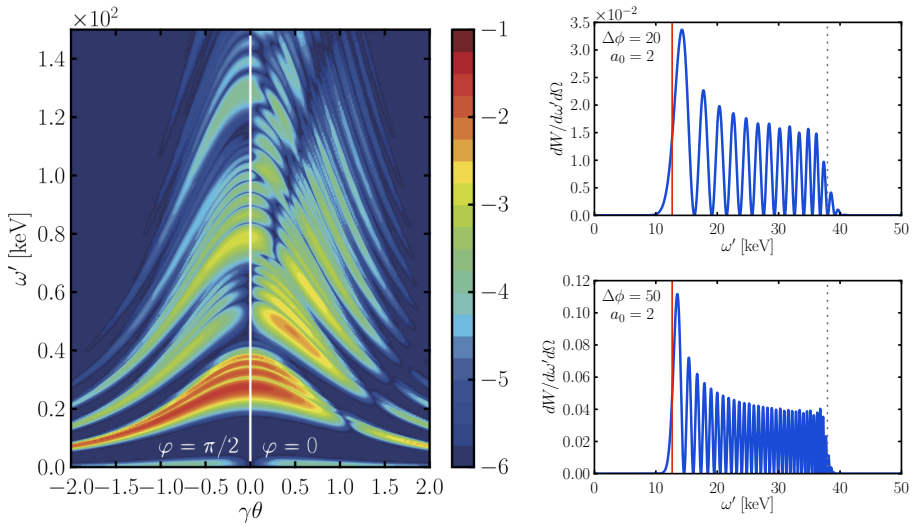


Figure 6: Spectra for non-linear Compton scattering in a short laser pulse. Left panel: angular and energy differential spectra for linearly polarized laser light in the plane of the laser polarization ($\varphi = 0$) and perpendicular to it ($\varphi = \pi/2$). Right panels: Line-outs of the on-axis spectrum for circularly polarized laser light show the broadening of the spectral lines in short pulses. In the case of an infinitely long laser wave the spectrum would be located just at the red vertical line.

The differential photon emission probability is given by $dW = |S|^2\, d\Pi/2p^+$, with the S matrix element from (26), and where the Lorentz invariant phase space of the final particles is conveniently parametrized by $d\Pi = \frac{dp'^+ d^2\mathbf{p}^\perp}{2(2\pi)^3 p'^+} \frac{\omega' d\omega' d\Omega}{2(2\pi)^3}$, yielding

$$\frac{dW}{d\omega' d\Omega} = \frac{\alpha\,\omega'\,\langle|\mathcal{M}|^2\rangle}{16\pi^2\,(kp)(kp')}\,, \qquad\qquad \mathcal{M} = \int d\phi\;\bar{u}_{p'}\Gamma(\phi)u_p\; e^{i\int d\phi \frac{k'\cdot\pi}{k\cdot p'}} \tag{27}$$

where $\langle ...\rangle$ refers to the average and summation over all initial and final particle polarization states, respectively. In the exponent of the amplitude $\mathcal{M}$ we rediscover the classical kinetic momentum π, which is now projected onto the four-momentum of the emitted photon.

When the probability (27) is analysed for an infinite monochromatic plane wave one finds a discrete spectrum of emitted harmonics, which can be understood in terms of *quasi-momentum* conservation $q + nk = q' + k'$. The emitted photons are dominantly emitted into a narrow cone with opening angle $\theta \sim \gamma^{-1}$ for $a_0 \lesssim 1$ and $\sim a_0\gamma^{-1}$ for $a_0 > 1$, and with harmonic frequencies $\omega'_n \simeq 4n\gamma^2\omega/(1 + \gamma^2\theta^2 + 2nb_0 + a_0^2/2)$. For $a_0 \gg 1$ on the order of $n \sim a_0^3$ harmonics contribute to the spectrum. In non-linear Compton scattering with a *short laser pulse* one observes a broadening of the spectral lines (see Fig. 6), similar to the broadening to the Zel'dovich level structure of the Volkov states discussed in Section 3. First of all, in a short laser pulse the harmonics acquire a bandwidth $\Delta\omega'/\omega' \sim \Delta\omega/\omega \sim \Delta\phi^{-1}$ due to the bandwidth of the laser. But there is also a intensity dependent ponderomotive broadening effect related to the gradual build-up of quasi-momentum as the electron enters the laser pulse. The ponderomotively broadened spectral lines have a (relative) bandwidth $\sim (a_0^2/2)/(1 + a_0^2/2)$. One sees in Fig. 6 that the broadened spectral lines consist of a large number of $\mathcal{O}(a_0^2\,\Delta\phi)$ subsidiary peaks. This can be explained as the interference of radiation emitted at the leading and trailing slopes of the pulse envelope [80]. It turns out that this ponderomotive broadening effect always occurs whenever the dephasing parameter $a_0^2\,\Delta\phi \gtrsim 1$. This is true also for quite weak laser pulses $a_0 \ll 1$ as long as the spectral bandwidth of the laser $\Delta\phi^{-1}$ is sufficiently small [11].

This broadening effect, while being an interesting phenomenon in the interplay between bandwidth and intensity effects will be a severe limitation for the spectral brightness of inverse Compton backscattering x- and gamma-ray sources. One way of dealing with the broadening is to limit the laser intensity to an acceptable level of broadening for a specific application [87], which limits the brightness of the source, of course. A more advanced possibility is to use *chirped* laser pulses, i.e. with a time-dependent frequency. It has been shown theoretically that with properly chirped laser pulses (which are spectrally blue-shifted at the pulse centre where the intensity is highest) the spectral broadening can be compensated [79, 88–90], see Fig. 7. This opens an avenue towards bright narrowband hard-gamma radiation sources operated at large laser intensities $a_0 \gtrsim 1$.

5 Summary

In this article an overview of the theory of high-intensity QED was given with focus on effects due to the short pulse duration. Both the solutions of the classical equations of motion, as well as the Volkov wave functions and the Dirac-Volkov propagator in the case of high-field QED were presented. The spectrum of non-linear Compton scattering in short intense pulses was discussed. The intensity dependent spectral broadening can be compensated by chirping the laser pulse.

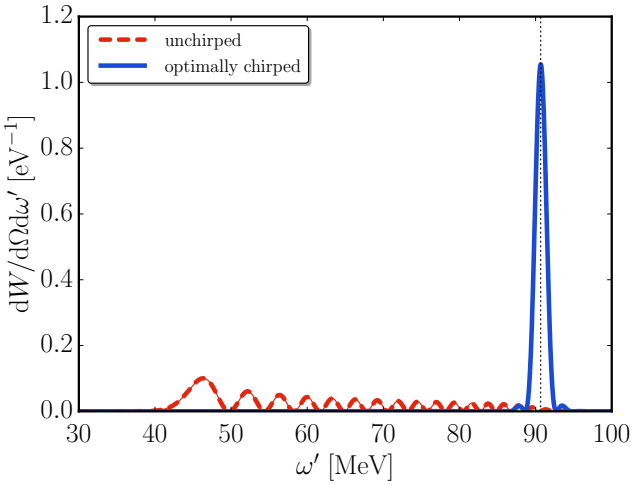


Figure 7: By using a chirped laser pulse with, the spectral broadening of the backscattered light (red curve) can be compensated (blue curve) allowing to operate inverse Compton sources at high laser intensity ($a_0 = 1.5$) for increased brightness.

Appendix A: Light-Front Coordinates

Because the laser's wave-vector (four-momentum vector) k^μ is a light like vector with $k^2 = 0$ it is very convenient to use so-called light-front co-ordinates to describe the dynamics of charged particles in laser background fields. Let us assume that the laser pulse propagates along the negative z-axis, $k = (\omega, 0, 0, -\omega)$, such that it's phase argument $k \cdot x = \omega(t + z) = \omega x^+$. That means the background field depends only on the single light-front variable $x^+ = t + z$. All particles will enter (leave) the laser pulse at the same value of the the light-front time coordinate x^+, see Fig. 8. The light-front components of a generic four-vector with Cartesian coordinates $(b^\mu) = (b^0, b^1, b^2, b^3)$ are defined as

$$b^- = b^0 - b^3\,, \qquad b^+ = b^0 + b^3\,, \qquad \mathbf{b}^\perp = (b^1, b^2)\,. \tag{28}$$

The inverse coordinate transformation is given by $b^0 = \frac{1}{2}(b^+ + b^-)$ and $b^3 = \frac{1}{2}(b^+ - b^-)$. We immediately find that the laser four-momentum has only a single non-vanishing component in light-front coordinates: $k^- = 2\omega$ The metric tensor in light-front coordinates, using the arrangement of components $(b^\mu) = (b^+, b^-, \mathbf{b}^\perp)$, has non-diagonal components

$$(g_{\mu\nu}) = \begin{pmatrix} 0 & \frac{1}{2} & 0 & 0 \\ \frac{1}{2} & 0 & 0 & 0 \\ 0 & 0 & -1 & 0 \\ 0 & 0 & 0 & -1 \end{pmatrix}, \qquad (g^{\mu\nu}) = \begin{pmatrix} 0 & 2 & 0 & 0 \\ 2 & 0 & 0 & 0 \\ 0 & 0 & -1 & 0 \\ 0 & 0 & 0 & -1 \end{pmatrix}. \tag{29}$$

The covariant components of a four-vector are related to the contravariant components as

$$b_- = \frac{1}{2}\, b^+\,, \qquad b_+ = \frac{1}{2}\, b^-\,, \qquad \mathbf{b}_\perp = -\mathbf{b}^\perp\,,$$

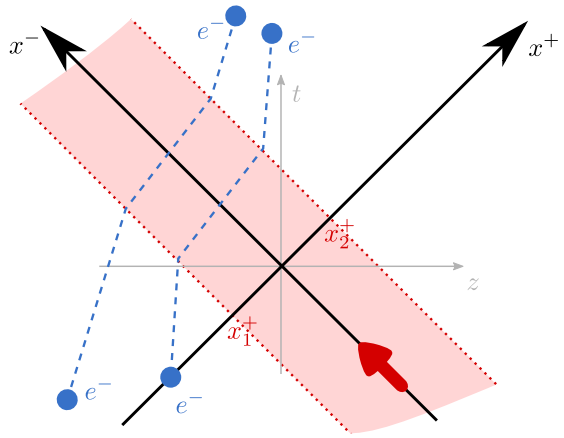


Figure 8: The laser pulse (red) propagates along the negative z axis. All electrons enter (leave) the laser at the same value of the light-front variable $x^+ = x_1^+$ (x_2^+).

and scalar products between two four-vectors read

$$x \cdot y = x^+ y_+ + x^- y_- + \mathbf{x}^\perp \cdot \mathbf{y}_\perp = \frac{1}{2} x^+ y^- + \frac{1}{2} x^- y^+ - \mathbf{x}_\perp \cdot \mathbf{y}_\perp \,.$$

The Lorentz invariant integration measure in light-front coordinates is given by

$$\sqrt{-g}\, d^4x = \frac{1}{2}\, dx^+ dx^- d^2\mathbf{x}_\perp \,,$$

with $\sqrt{-g} = \sqrt{-\det g_{\mu\nu}} = 1/2$ as the determinant of the metric tensor. For a four-dimensional delta distribution one writes in light-front form

$$\delta^4(p) = \frac{1}{\sqrt{-g}} \delta(p^+)\delta(p^-)\delta(p^1)\delta(p^2) = 2\,\delta^3(\mathsf{p})\delta(p^-) \,,$$

where we introduced the short-hand notation $\mathsf{p} \equiv (p^+, \mathbf{p}^\perp)$. The free particle dispersion relations (mass shell conditions) read in light-front coordinates

$$p^- = \frac{\mathbf{p}_\perp^2 + m^2}{p^+} \,, \qquad k^- = \frac{\mathbf{k}_\perp^2}{k^+}$$

for massive and massless particles, respectively. The Lorentz invariant on-shell phase space element is

$$\int \frac{d^4p}{(2\pi)^4}\, (2\pi)\delta(p^2 - m^2) = \frac{d^3\mathsf{p}}{(2\pi)^3 2p^+} \,,$$

with $d^3\mathsf{p} \equiv dp^+ dp^1 dp^2$. Thus the Lorentz invariant on-shell delta distributions are given by $(2\pi)^3 2p^+ \delta^3(\mathsf{p} - \mathsf{p}')$.

The light-front components of the Dirac matrices γ^μ obey the anti-commutation relations $\{\gamma^\mu, \gamma^\nu\} = 2g^{\mu\nu}$ with the metric tensor (29). In particular it follows that $(\gamma^+)^2 = (\gamma^-)^2 = 0$.

References

[1] V. I. Ritus, "Quantum effects of the interaction of elementary particles with an intense electromagnetic field," J. Sov. Laser Res. **6**, 497 (1985).

[2] G. V. Dunne, "The HeisenbergEuler Effective Action: 75 Years On," Int. J. Mod. Phys. A **27**, 1260004 (2012).

[3] T. Heinzl, B. Liesfeld, K.-U. Amthor, H. Schwoerer, R. Sauerbrey, and A. Wipf, "On the observation of vacuum birefringence," Opt. Commun. **267**, 318 (2006).

[4] F. Karbstein and R. Shaisultanov, "Stimulated photon emission from the vacuum," Phys. Rev. D **91**, 113002 (2015).

[5] H. Gies, F. Karbstein, and N. Seegert, "Photon merging and splitting in electromagnetic field inhomogeneities," Phys. Rev. D **93**, 085034 (2016).

[6] J. Schwinger, "On Gauge Invariance and Vacuum Polarization," Phys. Rev. **82**, 664 (1951).

[7] V. S. Popov, "On Schwinger mechanism of e^+e^- pair production from vacuum by the field of optical and X-ray lasers," Phys. Lett. A **298**, 83 (2002).

[8] D. B. Blaschke, A. V. Prozorkevich, C. D. Roberts, S. M. Schmidt, and S. A. Smolyansky, "Pair production and optical lasers," Phys. Rev. Lett. **96**, 140402 (2006).

[9] F. Hebenstreit, R. Alkofer, and H. Gies, "Pair production beyond the Schwinger formula in time-dependent electric fields," Phys. Rev. D **78**, 61701 (2008).

[10] T. Heinzl and A. Ilderton, "A Lorentz and gauge invariant measure of laser intensity," Opt. Commun. **282**, 1879 (2009).

[11] F. V. Hartemann, F. Albert, C. W. Siders, and C. P. J. Barty, "Low-Intensity Nonlinear Spectral Effects in Compton Scattering," Phys. Rev. Lett. **105**, 130801 (2010).

[12] C. Danson, D. Hillier, N. Hopps, and D. Neely, "Petawatt class lasers worldwide," High Power Laser Sci. Eng. **3**, 1 (2015).

[13] V. Yanovsky, V. Chvykov, G. Kalinchenko, P. Rousseau, T. Planchon, T. Matsuoka, A. Maksimchuk, J. Nees, G. Cheriaux, G. Mourou, et al., "Ultra-high intensity- 300-TW laser at 0.1 Hz repetition rate," Opt. Express **16**, 2109 (2008).

[14] J. D. Jackson, *Klassische Elektrodynamik*, Walter de Gruyter, Berlin, New York, 2nd edition (1983).

[15] D. Bauer, P. Mulser, and W. Steeb, "Relativistic ponderomotive force, Uphill acceleration, and transition to chaos." Phys. Rev. Lett. **75**, 4622 (1995).

[16] R. W. Brown and K. L. Kowalski, "Volkov Solutions, Gauge-Poincaré Transformations, and Plane-Wave Decoupling," Phys. Rev. Lett. **51**, 2355 (1983).

[17] R. W. Brown and K. L. Kowalski, "Gauge couplings as local gauge and Poincaré transformations: Generalized Taub-Volkov solutions," Phys. Rev. D **30**, 2602 (1984).

[18] M. Abraham, "Prinzipien der Dynamik des Elektrons," Ann. Phys. **315**, 105 (1902).

[19] P. Dirac, "Classical theory of radiating electrons," Proc. R. Soc. Lond. Ser. A **167**, 148 (1938).

[20] I. V. Sokolov, N. M. Naumova, J. A. Nees, G. A. Mourou, and V. P. Yanovsky, "Dynamics of emitting electrons in strong laser fields," Phys. Plasmas **16** (2009).

[21] A. Ilderton and G. Torgrimsson, "Radiation reaction in strong field QED," Phys. Lett. B **725**, 481 (2013).

[22] R. Capdessus, E. D'Humières, and V. T. Tikhonchuk, "Modeling of radiation losses in ultrahigh power laser-matter interaction." Phys. Rev. E **86**, 036401 (2012).

[23] M. Vranic, J. Martins, R. Fonseca, and L. Silva, "Classical radiation reaction in particle-in-cell simulations," Comput. Phys. Commun. **204**, 141 (2016), 1502.02432.

[24] S. Tang, N. Kumar, and C. H. Keitel, "Optimized plasma high harmonics generation from ultra-intense laser pulses," arXiv:1608.02513 (2016).

[25] L. D. Landau and E. M. Lifschitz, *Klassische Feldtheorie*, volume 2 of *Lehrbuch der Theoretischen Physik*, Akademie Verlag, 12th editi edition (1992).

[26] A. Di Piazza, "Exact solution of the Landau-Lifshitz equation in a plane wave," Lett. Math. Phys. **83**, 305 (2008).

[27] A. Di Piazza, K. Z. Hatsagortsyan, and C. H. Keitel, "Quantum Radiation Reaction Effects in Multiphoton Compton Scattering," Phys. Rev. Lett. **105**, 220403 (2010).

[28] N. Neitz and A. Di Piazza, "Stochasticity Effects in Quantum Radiation Reaction," Phys. Rev. Lett. **111**, 054802 (2013).

[29] T. G. Blackburn, C. P. Ridgers, J. G. Kirk, and A. R. Bell, "Quantum Radiation Reaction in Laser–Electron-Beam Collisions," Phys. Rev. Lett. **112**, 015001 (2014).

[30] A. M. Fedotov, N. B. Narozhny, G. Mourou, and G. Korn, "Limitations on the Attainable Intensity of High Power Lasers," Phys. Rev. Lett. **105**, 080402 (2010).

[31] S. S. Bulanov, T. Z. Esirkepov, A. G. R. Thomas, J. K. Koga, and S. V. Bulanov, "Schwinger Limit Attainability with Extreme Power Lasers," Phys. Rev. Lett. **105**, 220407 (2010).

[32] P. Zhang, C. P. Ridgers, and A. G. R. Thomas, "The effect of nonlinear quantum electrodynamics on relativistic transparency and laser absorption in ultra-relativistic plasmas," New J. Phys. **17**, 043051 (2015), `arXiv:1403.5034`.

[33] D. Seipt, T. Heinzl, M. Marklund, and S. S. Bulanov, "Depletion of intense fields," arXiv:1605.00633 (2016).

[34] W. H. Furry, "On Bound States and Scattering in Positron Theory," Phys. Rev. **81**, 115 (1951).

[35] D. M. Volkov, "Über eine Klasse von Lösungen der Diracschen Gleichung," Z. Phys. **94**, 250 (1935).

[36] W. B. Berestetzki, E. M. Lifschitz, and L. P. Pitajewski, *Relativistische Quantentheorie*, volume IV of *Lehrbuch der Theoretischen Physik*, Akademie Verlag, Berlin (1980).

[37] T. Heinzl, A. Ilderton, and B. King, "Classical and quantum particle dynamics in univariate background fields," Phys. Rev. D **94**, 065039 (2016).

[38] E. Raicher and S. Eliezer, "Analytical solutions of the Dirac and the Klein-Gordon equations in plasma induced by high-intensity laser," Phys. Rev. A **88**, 022113 (2013).

[39] E. Raicher, S. Eliezer, and A. Zigler, "A novel solution to the KleinGordon equation in the presence of a strong rotating electric field," Phys. Lett. B **750**, 76 (2015), `1502.03558`.

[40] J. T. Mendonça and A. Serbeto, "Volkov solutions for relativistic quantum plasmas," Phys. Rev. E **83**, 026406 (2011).

[41] B. King and H. Hu, "Classical and quantum dynamics of a charged scalar particle in a background of two counterpropagating plane waves," arXiv:1609.08105 (2016).

[42] V. G. Bagrov and D. M. Gitman, *Exact Solutions of Relativistic Wave Equations*, Kluwer Academic Publishers, Dordrecht (1990).

[43] T. Nousch, D. Seipt, B. Kämpfer, and A. Titov, "Pair production in short laser pulses near threshold," Phys. Lett. Sect. B Nucl. Elem. Part. High-Energy Phys. **715**, 246 (2012).

[44] C. Itzykson and J.-B. Zuber, *Quantum Field Theory*, McGraw-Hill (1980).

[45] M. E. Peskin and D. V. Schroeder, *An Introduction to Quantum Field Theory*, Addison-Wesley Publishing Company (1995).

[46] N. B. Narozhnyi and M. S. Fofanov, "Photon emission by an electron in a collision with a short focused laser pulse," J. Exp. Theor. Phys. **83**, 14 (1996).

[47] R. A. Neville and F. Rohrlich, "Quantum Electrodynamics on Null Planes and Applications to Lasers," Phys. Rev. D **3**, 1692 (1971).

[48] S. Zakowicz, "Square-integrable wave packets from the Volkov solutions," J. Math. Phys. **46**, 032304 (2005).

[49] G. Floquet, "Sur les équations différentielles linéaires à coefficients périodiques," Ann. l'École Norm. Supérieure **12**, 47 (1883).

[50] H. J. Korsch, A. Klumpp, and D. Witthaut, "On two-dimensional Bessel functions," J. Phys. A **39**, 14947 (2006).

[51] E. Loetstedt and U. D. Jentschura, "Recursive algorithm for arrays of generalized Bessel functions: Numerical access to Dirac-Volkov solutions," Phys. Rev. E **79**, 026707 (2009).

[52] Y. B. Zel'dovich, "The Quasienergy of a Quantum-Mechanical System Subjected to a Periodic Action," Sov. Phys. J. Exp. Theor. Phys. **24**, 1006 (1967).

[53] W. Becker and H. Mitter, "Modification of the quasi-levels of an electron in a laser field due to radiative corrections," J. Phys. A **9**, 2171 (1976).

[54] D. Seipt, A. Surzhykov, S. Fritzsche, and B. Kämpfer, "Caustic structures in x-ray Compton scattering off electrons driven by a short intense laser pulse," New J. Phys. **18**, 023044 (2016).

[55] J. H. Eberly and H. R. Reiss, "Electron Self-Energy in Intense Plane-Wave Field," Phys. Rev. **145**, 1035 (1966).

[56] L. S. Brown and T. W. B. Kibble, "Interaction of intense laser beams with electrons," Phys. Rev. **133**, A705 (1964).

[57] T. W. B. Kibble, A. Salam, and J. Strathdee, "Intensity-dependent mass shift and symmetry breaking," Nucl. Phys. B **96**, 255 (1975).

[58] V. N. Baĭer, V. M. Katkov, and V. M. Strakhovenko, "Operator approach to quantum electrodynamics in an external field. Electron loops," Sov. Phys. J. Exp. Theor. Phys. **41**, 198 (1975).

[59] V. N. Baĭer, A. I. Mil'shteĭn, and V. M. Strakhovenko, "Interaction between a photon and an intense electromagnetic wave," Sov. Phys. J. Exp. Theor. Phys. **42**, 961 (1976).

[60] H. Mitter, "Quantum Electrodynamics in Laser Fields," Acta Phys. Austriaca, Suppl. XIV pages 397–468 (1975).

[61] E. Lötstedt and U. D. Jentschura, "Nonperturbative Treatment of Double Compton Backscattering in Intense Laser Fields," Phys. Rev. Lett. **103**, 110404 (2009).

[62] D. Seipt and B. Kämpfer, "Two-photon Compton process in pulsed intense laser fields," Phys. Rev. D **85**, 101701 (2012).

[63] F. Mackenroth and A. Di Piazza, "Nonlinear double Compton scattering in the full quantum regime," Phys. Rev. Lett. **110**, 070402 (2013).

[64] E. Lötstedt, U. D. Jentschura, and C. H. Keitel, "Evaluation of Laser-Assisted Bremsstrahlung with Dirac-Volkov Propagators," Phys. Rev. Lett. **98**, 043002 (2007).

[65] E. Lötstedt, U. D. Jentschura, and C. H. Keitel, "Laser Channeling of Bethe-Heitler Pairs," Phys. Rev. Lett. **101**, 203001 (2008).

[66] V. Ritus, "Radiative corrections in quantum electrodynamics with intense field and their analytical properties," Ann. Phys. (N. Y). **69**, 555 (1972).

[67] D. Seipt, *Strong Field QED Processes in Short Laser Pulses*, Ph.D. thesis, Technische Universität Dresden (2012).

[68] A. Ilderton and G. Torgrimsson, "Scattering in plane-wave backgrounds: Infrared effects and pole structure," Phys. Rev. D **87**, 085040 (2013).

[69] M. Lavelle, D. McMullan, and M. Raddadi, "Propagation in an intense background," Phys. Rev. D **87**, 085024 (2013), `1301.3072`.

[70] V. P. Oleĭnik, "Resonance effects in the field of an intense laser beam," Sov. Phys. J. Exp. Theor. Phys. **25**, 697 (1967).

[71] A. I. Nikishov and V. I. Ritus, "Quantum processes in the field of a plane electromagnetic wave and in a constant field. I," Sov. Phys. J. Exp. Theor. Phys. **19**, 529 (1964).

[72] A. I. Nikishov and V. I. Ritus, "Quantum processes in the field of a plane electromagnetic wave and in a constant field," Sov. Phys. J. Exp. Theor. Phys. **19**, 1191 (1964).

[73] A. I. Nikishov and V. I. Ritus, "Nonlinear effects in Compton scattering and pair production owing to absorption of several photons," Sov. Phys. J. Exp. Theor. Phys. **20**, 757 (1965).

[74] N. B. Narozhnyi, A. I. Nikishov, and V. I. Ritus, "Quantum processes in the field of a circularly polarized electromagnetic wave," Sov. Phys. J. Exp. Theor. Phys. **20**, 622 (1965).

[75] M. Boca and V. Florescu, "Nonlinear Compton scattering with a laser pulse," Phys. Rev. A **80**, 053403 (2009).

[76] D. Seipt and B. Kämpfer, "Non-Linear Compton Scattering of Ultrashort and Intense Laser Pulses," Phys. Rev. A **83**, 022101 (2011).

[77] F. Mackenroth and A. Di Piazza, "Nonlinear Compton scattering in ultra-short laser pulses," Phys. Rev. A **83**, 032106 (2011).

[78] K. Krajewska and J. Z. Kamiński, "Compton Process in Intense Short Laser Pulses," Phys. Rev. A **85**, 062102 (2012).

[79] D. Seipt, S. G. Rykovanov, A. Surzhykov, and S. Fritzsche, "Narrowband inverse Compton scattering x-ray sources at high laser intensities," Phys. Rev. A **91**, 033402 (2015).

[80] V. Y. Kharin, D. Seipt, and S. G. Rykovanov, "Temporal laser-pulse-shape effects in nonlinear Thomson scattering," Phys. Rev. A **93**, 063801 (2016), 1602.03062.

[81] D. Seipt, V. Kharin, S. Rykovanov, A. Surzhykov, and S. Fritzsche, "Analytical results for nonlinear Compton scattering in short intense laser pulses," J. Plasma Phys. **82**, 655820203 (2016).

[82] K. Krajewska and J. Z. Kamiński, "Breit-Wheeler process in intense short laser pulses," Phys. Rev. A **86**, 052104 (2012).

[83] A. I. Titov, H. Takabe, B. Kämpfer, and A. Hosaka, "Enhanced Subthreshold e^+e^- Production in Short Laser Pulses," Phys. Rev. Lett. **108**, 240406 (2012).

[84] A. I. Titov, B. Kämpfer, A. Hosaka, T. Nousch, and D. Seipt, "Determination of the carrier envelope phase for short, circularly polarized laser pulses," Phys. Rev. D **93**, 045010 (2016).

[85] S. Meuren, C. H. Keitel, and A. Di Piazza, "Semiclassical picture for electron-positron photoproduction in strong laser fields," Phys. Rev. D **93**, 085028 (2016).

[86] M. J. A. Jansen, J. Z. Kamiński, K. Krajewska, and C. Müller, "Strong-field Breit-Wheeler pair production in short laser pulses: Relevance of spin effects," Phys. Rev. D **94**, 013010 (2016).

[87] F. V. Hartemann and S. S. Q. Wu, "Nonlinear Brightness Optimization in Compton Scattering," Phys. Rev. Lett. **111**, 044801 (2013).

[88] I. Ghebregziabher, B. A. Shadwick, and D. Umstadter, "Spectral Bandwidth Reduction of Thomson Scattered Light by Pulse Chirping," Phys. Rev. ST Accel. Beams **16**, 030705 (2013).

[89] B. Terzić, K. Deitrick, A. S. Hofler, and G. A. Krafft, "Narrow-Band Emission in Thomson Sources Operating in the High-Field Regime," Phys. Rev. Lett. **112**, 074801 (2014).

[90] S. G. Rykovanov, C. G. R. Geddes, C. B. Schroeder, E. Esarey, and W. P. Leemans, "Controlling the spectral shape of nonlinear Thomson scattering with proper laser chirping," Phys. Rev. Accel. Beams **19**, 030701 (2016).

The quantum vacuum in electromagnetic fields: From the Heisenberg-Euler effective action to vacuum birefringence

Felix Karbstein[1,2]

[1]Theoretisch-Physikalisches Institut, Abbe Center of Photonics, Friedrich-Schiller-Universität Jena, Max-Wien-Platz 1, D-07743 Jena, Germany
[2]Helmholtz Institut Jena, Fröbelstieg 3, D-07743 Jena, Germany

DOI: http://dx.doi.org/10.3204/DESY-PROC-2016-04/Karbstein

The focus of these lectures is on the quantum vacuum subjected to classical electromagnetic fields. To this end we explicitly derive the renowned Heisenberg-Euler effective action in constant electromagnetic fields in a rather pedagogical and easy to conceive way. As an application, we use it to study vacuum birefringence constituting one of the most promising optical signatures of quantum vacuum nonlinearity.

1 Introduction

These lecture notes are about the quantum vacuum in strong electromagnetic fields. They are intended to provide interested students having basic knowledge in quantum field theory with an introduction to this topic. To this end it is instructive to first recall the classical understanding of the vacuum: In a classical field theory context, the vacuum can be defined as "the absence of anything," and can be considered as a kind of absolute ground state, not featuring any excitations, etc.

When adding classical electromagnetic fields to this vacuum, we arrive at the classical field theory of electrodynamics, which can be defined by the following Lagrangian density,

$$\mathcal{L}_{\rm ED} = -\frac{1}{4}F_{\rm cl.\mu\nu}F^{\mu\nu}_{\rm cl.} - j_\mu A^\mu_{\rm cl.}\,, \tag{1}$$

where $F^{\mu\nu}_{\rm cl.} = \partial^\mu A^\nu_{\rm cl.} - \partial^\nu A^\mu_{\rm cl.}$ is the field strength tensor, and j^μ a current sourcing the electromagnetic four-potential $A^\mu_{\rm cl.}$. In these lectures, we are only interested in the vacuum subjected to electromagnetic fields far away from any classical sources. Correspondingly, we set $j_\mu = 0$.

The equations of motion for a Lagrangian $\mathcal{L}(A^\mu, F^{\mu\nu})$ are given by the following Euler-Lagrange equations,

$$\frac{\partial\mathcal{L}}{\partial A_\nu} - 2\partial_\mu\frac{\partial\mathcal{L}}{\partial F_{\mu\nu}} = 0\,, \tag{2}$$

such that for $\mathcal{L}(A^\mu, F^{\mu\nu}) \to \mathcal{L}_{\rm ED}(A^\mu_{\rm cl.}, F^{\mu\nu}_{\rm cl.})|_{j=0}$ we obtain the free Maxwell equations, $\partial_\mu F^{\mu\nu}_{\rm cl.} = 0$. Obviously, these homogeneous linear differential equations have the feature that any combination $F^{\mu\nu}_{\rm cl.} = \sum_i F^{\mu\nu}_{{\rm cl.}i}$ of solutions $F^{\mu\nu}_{{\rm cl.}i} = (\partial^\mu g^\nu{}_\alpha - \partial^\nu g^\mu{}_\alpha)A^\alpha_{{\rm cl.}i}$ is also a solution, which

implies the superposition principle to hold for electromagnetic fields in the *vacuum of classical electrodynamics*.

In a next step we turn to the notion of the vacuum in a quantum field theory (QFT) context, also referred to as the quantum vacuum. The quantum vacuum is not empty, but rather permeated by fluctuations of the particle degrees of freedom of the theory under consideration (in quantum electrodynamics: electrons, positrons and photons) in so-called virtual processes. In contrast to real particles, virtual particles are typically not on the mass shell, i.e., do not fulfill the relativistic energy-momentum relation. These virtual processes can be excited by external influences, e.g., electromagnetic fields [1], or by imposing physical boundary conditions [2]. Aiming at unveiling the quantum nature of the vacuum in an experiment (Gedankenexperiment or actual experiment), the basic idea is to look for potential imprints of the fluctuating fields in the measured response.

In these lectures we limit ourselves to the vacuum of quantum electrodynamics (QED), defined by the following Lagrangian,

$$\mathcal{L}_{\mathrm{QED}} = -\frac{1}{4} F_{\mu\nu} F^{\mu\nu} + \bar{\psi}(\mathrm{i}\not{D} - m)\psi \,, \tag{3}$$

with $\bar{\psi} = \psi^\dagger \gamma^0$, $\not{D} = \gamma^\mu D_\mu$, $D_\mu = \partial_\mu - \mathrm{i}eA_\mu$ and $F^{\mu\nu} = \frac{\mathrm{i}}{e}[D^\mu, D^\nu]$, where e is the electron charge. The latter term mediates the coupling of the four-component Dirac spinors ψ, describing spin-$\frac{1}{2}$ fermions of mass m to the photon field A^μ. Note that ψ accounts for both electron and positrons degrees of freedom. The defining property of the Dirac gamma matrices γ^μ is $\{\gamma^\mu, \gamma^\nu\} = -2g^{\mu\nu}\mathbb{1}$, and our metric convention is $g_{\mu\nu} = \mathrm{diag}(-1, 1, 1, 1)$. We use the Heaviside-Lorentz System with $c = \hbar = 1$. A slightly different representation of Eq. (3) is

$$\mathcal{L}_{\mathrm{QED}} = -\frac{1}{4} F_{\mu\nu} F^{\mu\nu} + \bar{\psi}(\mathrm{i}\not{\partial} - m)\psi + eA^\mu \bar{\psi}\gamma_\mu \psi \,, \tag{4}$$



where we split $\mathcal{L}_{\mathrm{QED}}$ into three terms: The first one is the Maxwell term, describing the dynamics of free electromagnetic fields quantized in terms of photons. The second one represents freely propagating electrons and positrons. Finally, the third one accounts for the interaction between the fermions and the photons, whose coupling is parameterized by e.

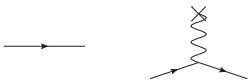
In addition, we provide the graphical representation of these terms in the diagrammatic language of Feynman diagrams. From these building blocks all possible QED processes can be constructed, following the simple recipe that *every diagram that can be constructed by assembling the above elementary building blocks can happen* (if it is not vanishing due to symmetries, kinematic restrictions, etc.). Generically, this gives rise to loop diagrams. In fact, for any given physical process specified by fixing the external legs, characterizing the incident and outgoing real particles, there are infinitely many loop diagrams. As they do not involve any real particles (in QED: in- and outgoing photons, electrons and positrons) pure vacuum-type diagrams correspond to Feynman diagrams without external lines. Favorably for us, in the regime of validity of perturbative QED, loop diagrams are more and more suppressed with increasing loop order, as each additional loop results in a parametric suppression by a factor of $\alpha = \frac{e^2}{4\pi}$.

2 Towards the Heisenberg-Euler effective Lagrangian

Let us now turn to QED in an external classical background field $A^\mu_{\text{cl.}}$ and for the moment completely ignore quantized dynamical photons. This ad hoc assumption can actually be justified by the fact that for the effect we are interested in here, the leading order contribution is insensitive to dynamical photons. Their presence only becomes important at higher loop order; cf. also below.

Hence, from now on we focus on the Lagrangian (3) with the replacement $A_\mu \to A_{\text{cl.}\mu}$. The Lagrangian and Feynman rules for this theory are given by

$$\mathcal{L} = -\frac{1}{4} F_{\text{cl.}\mu\nu} F^{\mu\nu}_{\text{cl.}} + \bar{\psi}(\mathrm{i}\partial\!\!\!/ - m)\psi + e A_{\text{cl.}\mu} \bar{\psi}\gamma^\mu \psi \,, \tag{5}$$

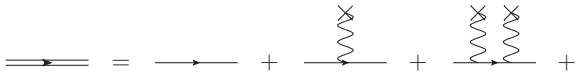


i.e., the only quantum degrees of freedom of this theory are electrons and positrons. In the Feynman rules, the external character of $A_{\text{cl.}\mu}$ is symbolized by the wiggly line ending at a cross.

Aiming at pure vacuum phenomena, we are only interested in effective interactions among electromagnetic fields, and do not consider situations with *real* electrons or positrons in the initial and final states. However, let us emphasize once more that within a quantum field theory we can never prevent the quantum fields constituting the theory under consideration to occur as internal, *virtual* states. In turn, it is immediately clear that all possible connected Feynman diagrams without external electron/positron lines which can be drawn for the theory defined by the Lagrangian (5) can be represented in terms of a single one-loop diagram,



with "dressed" fermion propagator



In order to evaluate this diagram explicitly, we turn to the partition function Z associated with Eq. (5),

$$Z[A^\mu_{\text{cl.}}] = \mathcal{N} \int \mathcal{D}\bar{\psi} \int \mathcal{D}\psi \, \mathrm{e}^{\mathrm{i}S} \,, \tag{6}$$

where $S = \int \mathrm{d}^4x \, \mathcal{L}$ is the corresponding action, and $\mathcal{N}$ denotes an overall normalization factor to be fixed below. As the action is bilinear in the Dirac field ψ, the functional integrations can be performed explicitly, providing us with an *effective action* $S_{\text{eff.}}[A^\mu_{\text{cl.}}]$, which only depends on $A^\mu_{\text{cl.}}$. To this end, recall that $\int \mathcal{D}\bar{\psi} \int \mathcal{D}\psi \exp\{\mathrm{i} \int \mathrm{d}^4x \, \bar{\psi} M \psi\} = \det M$. Introducing the classical Maxwell action $S_{\text{MW}} = \int \mathrm{d}^4x \big(-\frac{1}{4} F_{\text{cl.}\mu\nu} F^{\mu\nu}_{\text{cl.}}\big)$ and the definition $D_{\text{cl.}\mu} = \partial_\mu - \mathrm{i}e A_{\text{cl.}\mu}$, we obtain

$$\begin{aligned} Z[A^\mu_{\text{cl.}}] &= \mathcal{N} \mathrm{e}^{\mathrm{i}S_{\text{MW}}} \det(\mathrm{i}D\!\!\!/_{\text{cl.}} - m) \\ &= \mathcal{N} \mathrm{e}^{\mathrm{i}[S_{\text{MW}} - \mathrm{i} \ln\det(\mathrm{i}D\!\!\!/_{\text{cl.}} - m)]} \\ &=: \mathrm{e}^{\mathrm{i}S_{\text{eff.}}[A^\mu_{\text{cl.}}]} \,. \end{aligned} \tag{7}$$

It is convenient to demand that $Z[A^\mu_{\text{cl.}}=0]=1$, or equivalently $S_{\text{eff.}}[A^\mu_{\text{cl.}}=0]=0$, so that the effective action vanishes at zero field. In turn, we have $\mathcal{N}=\det{}^{-1}(\mathrm{i}\partial\!\!\!/-m)$, and the effective action can be expressed as

$$S_{\text{eff.}}[A^\mu_{\text{cl.}}]=S_{\text{MW}}[A^\mu_{\text{cl.}}]+S^1[A^\mu_{\text{cl.}}]\,, \tag{8}$$

where

$$S^1[A^\mu_{\text{cl.}}]=-\mathrm{i}\ln\det(\mathrm{i}\not{D}_{\text{cl.}}-m)+\mathrm{i}\ln\det(\mathrm{i}\partial\!\!\!/-m) \tag{9}$$



is the so-called one-loop effective action. For completeness, note that this definition of $S_{\text{eff.}}$ agrees with the standard definition of the effective action as a Legendre transform of the Schwinger functional. Accounting for the fluctuations of dynamical photons, of course also additional diagrams mediating effective interactions among classical electromagnetic fields arise. As these diagrams have at least one internal photon line, they are of higher-loop order and thus suppressed by additional powers of α as compared to the one-loop result.

In even space-time dimensions we can define a matrix γ_5 ($\gamma_5=\mathrm{i}\gamma^0\gamma^1\gamma^2\gamma^3$) which fulfills $\{\gamma^\mu,\gamma_5\}=0$ and $(\gamma_5)^2=\mathbb{1}$. Therewith, $\det(\mathrm{i}\not{D}_{\text{cl.}}-m)=\det[(\mathrm{i}\not{D}_{\text{cl.}}-m)\gamma_5^2]=\det[\gamma_5(-\mathrm{i}\not{D}_{\text{cl.}}-m)\gamma_5]=\det(-\mathrm{i}\not{D}_{\text{cl.}}-m)$, such that we can write

$$S^1[A^\mu_{\text{cl.}}]=-\frac{\mathrm{i}}{2}\ln\det(\not{D}^2_{\text{cl.}}+m^2)+\frac{\mathrm{i}}{2}\ln\det(\partial\!\!\!/^2+m^2)\,. \tag{10}$$

Moreover, note that

$$\begin{aligned}\not{D}^2_{\text{cl.}}&=D_{\text{cl.}\mu}D_{\text{cl.}\nu}\gamma^\mu\gamma^\nu=D_{\text{cl.}\mu}D_{\text{cl.}\nu}\tfrac{1}{2}\big(\{\gamma^\mu,\gamma^\nu\}+[\gamma^\mu,\gamma^\nu]\big)\\&=-D^2_{\text{cl.}}-\tfrac{e}{2}\sigma^{\mu\nu}F_{\text{cl.}\mu\nu}\,,\end{aligned} \tag{11}$$

where we employed $\{\gamma^\mu,\gamma^\nu\}=-2g^{\mu\nu}\mathbb{1}$, $F^{\mu\nu}_{\text{cl.}}=\frac{\mathrm{i}}{e}[D^\mu_{\text{cl.}},D^\nu_{\text{cl.}}]$ (cf. above) and the definition $\sigma^{\mu\nu}\equiv\frac{\mathrm{i}}{2}[\gamma^\mu,\gamma^\nu]$, fulfilling $\frac{1}{2}\{\sigma^{\mu\nu},\sigma^{\alpha\beta}\}=g^{\mu\alpha}g^{\nu\beta}-g^{\mu\beta}g^{\nu\alpha}+\mathrm{i}\gamma_5\epsilon^{\mu\nu\alpha\beta}$ [3, 4]. Hence, with $\ln\det M=\operatorname{Tr}\ln M$, we have

$$S^1[A^\mu_{\text{cl.}}]=-\frac{\mathrm{i}}{2}\operatorname{Tr}\ln(-D^2_{\text{cl.}}+m^2-\tfrac{e}{2}\sigma^{\mu\nu}F_{\text{cl.}\mu\nu})+\frac{\mathrm{i}}{2}\operatorname{Tr}\ln(-\partial^2+m^2)\,. \tag{12}$$

The trace $\operatorname{Tr}\{\ldots\}=\operatorname{tr}_\gamma\operatorname{tr}_x\{\ldots\}$ is over both spinor indices and coordinate space; we denote the trace over spinor indices by $\operatorname{tr}_\gamma\{\ldots\}$ and the trace over coordinate space by $\operatorname{tr}_x\{\ldots\}$. In the next step we employ the *proper time representation* of the logarithm [3],

$$-\ln M+\ln M_0=\lim_{\Lambda\to\infty}\int_{-\mathrm{i}/\Lambda^2}^{\infty}\frac{\mathrm{d}T}{T}\big(\mathrm{e}^{-\mathrm{i}MT}-\mathrm{e}^{-\mathrm{i}M_0T}\big)\,, \tag{13}$$

valid for $\Im\{M,M_0\}<0$. Here, Λ (of dimension mass) is a regulator for potentially occurring ultraviolet (UV) divergences. The precise form of the integral's lower bound is chosen such that if in addition $\Re\{M,M_0\}>0$ we can use a contour rotation $\mathrm{i}T\to T$ to write $-\ln M+\ln M_0=\lim_{\Lambda\to\infty}\int_{1/\Lambda^2}^{\infty}\frac{\mathrm{d}T}{T}\big(\mathrm{e}^{-MT}-\mathrm{e}^{-M_0T}\big)$. In turn, we obtain the following proper time representation of the one-loop effective action,

$$S^1[A^\mu_{\text{cl.}}]=\frac{\mathrm{i}}{2}\int_{-\mathrm{i}/\Lambda^2}^{\infty}\frac{\mathrm{d}T}{T}\,\mathrm{e}^{-\mathrm{i}m^2T}\Big\{\operatorname{Tr}\mathrm{e}^{\mathrm{i}(D^2_{\text{cl.}}+\frac{e}{2}\sigma^{\mu\nu}F_{\text{cl.}\mu\nu})T}-\operatorname{Tr}\mathrm{e}^{\mathrm{i}\partial^2T}\Big\}\,, \tag{14}$$

where $\lim_{\Lambda\to\infty}$ is implicitly understood, and to be taken at the very end of the calculation. Let us emphasize that this expression is still valid for arbitrary fields $A^\mu_{\text{cl.}}(x)$. It, or at least the integrand of the proper time integral, i.e., $\text{Tr}\{\ldots\}$, can be evaluated analytically for several special cases:

- A parameter integral representation of S^1 is known for *constant electromagnetic fields*, $F^{\mu\nu}_{\text{cl.}} = \text{const.}$, of arbitrary relative orientation of $\vec{E}$ and $\vec{B}$ [1, 3]; cf. also the explicit derivation presented below. For completeness, note that for this case also the two-loop effective action is known explicitly in terms of a parameter integral representation [5].

- For plane wave *null fields* $A^\mu_{\text{cl.}}(x) \sim \cos(\kappa^\mu x_\mu)$, with $\kappa^2 = 0$, $\vec{E} \perp \vec{B}$ and $|\vec{E}| = |\vec{B}|$, the effective action vanishes identically, i.e., $S^1 = 0$ [3].

- Parameter integral representations of S^1 are also known for specific one-dimensional field inhomogeneities, namely $E(t) \sim \cosh^{-2}(t/\tau)$ and $B(\text{x}) \sim \cosh^{-2}(\text{x}/\lambda)$, with reference scales τ and λ, respectively [6].

To perform the traces in Eq. (14) for a given field configuration $A^\mu_{\text{cl.}}(x)$, we need the eigenvalues of the exponentiated differential operators $D^2_{\text{cl.}} + \frac{e}{2}\sigma^{\mu\nu}F_{\text{cl.}\mu\nu}$ and ∂^2.

Subsequently, we stick to a *constant electromagnetic fields* and evaluate S^1 explicitly for this case. For $F^{\mu\nu}_{\text{cl.}} = \text{const.}$, the expressions $D^2_{\text{cl.}}$ and $\frac{e}{2}\sigma^{\mu\nu}F_{\text{cl.}\mu\nu}$ in the argument of the first exponential in Eq. (14) of course commute, such that $\text{Tr}\,\text{e}^{\text{i}(D^2_{\text{cl.}}+\frac{e}{2}\sigma^{\mu\nu}F_{\text{cl.}\mu\nu})T} = \text{Tr}\,\text{e}^{\text{i}\frac{e}{2}\sigma^{\mu\nu}F_{\text{cl.}\mu\nu}T}\,\text{e}^{\text{i}D^2_{\text{cl.}}T}$. It can moreover be shown that in this case the entire background field dependence can be expressed in terms of the Lorentz and gauge invariant quantities $\mathcal{F} = \frac{1}{4}F_{\text{cl.}\mu\nu}F^{\mu\nu}_{\text{cl.}} = \frac{1}{2}(\vec{B}^2 - \vec{E}^2)$ and $\mathcal{G} = \frac{1}{4}F_{\text{cl.}\mu\nu}{}^*F^{\mu\nu}_{\text{cl.}} = -\vec{B}\cdot\vec{E}$, with dual field strength tensor ${}^*F^{\mu\nu} = \frac{1}{2}\epsilon^{\mu\nu\alpha\beta}F_{\alpha\beta}$; note that in our metric convention we have $F_{\text{cl.}0i} = -E_i$ and $F_{\text{cl.}ij} = \epsilon_{ijk}B_k$. The reason for this is as follows: Due to translational invariance in constant fields the effective action as well as the corresponding Lagrangian cannot explicitly depend on any space-time coordinate x^μ and derivative ∂_μ. Gauge invariance demands the field dependence to be entirely via $F^{\mu\nu}_{\text{cl.}}$. The fact that the effective Lagrangian is a scalar quantity and Lorentz invariance demand all Minkowski indices to be fully contracted. Finally, all Lorentz-contracted monomials of the field strength tensor are reducible to $\mathcal{F}$ and $\mathcal{G}$ by means of the following identities [4]

$$\begin{aligned} F^{\mu\alpha}_{\text{cl.}}F^{\nu}_{\text{cl.}\alpha} - {}^*F^{\mu\alpha}_{\text{cl.}}{}^*F^{\nu}_{\text{cl.}\alpha} &= 2\mathcal{F}g^{\mu\nu}, \\ F^{\mu\alpha}_{\text{cl.}}{}^*F^{\nu}_{\text{cl.}\alpha} = {}^*F^{\mu\alpha}_{\text{cl.}}F^{\nu}_{\text{cl.}\alpha} &= \mathcal{G}g^{\mu\nu}. \end{aligned} \tag{15}$$

More precisely, as $S_{\text{eff.}}$ is a scalar quantity and $\mathcal{G}$ transforms as a pseudoscalar under Lorentz transformations, we actually have $S_{\text{eff.}}(\mathcal{F}, \mathcal{G}^2)$.

The trace over spinor indices is most conveniently performed by noting that $(\frac{1}{2}\sigma^{\mu\nu}F_{\text{cl.}\mu\nu})^2 = \frac{1}{8}\{\sigma^{\mu\nu}, \sigma^{\alpha\beta}\}F_{\text{cl.}\mu\nu}F_{\text{cl.}\alpha\beta} = 2(\mathcal{F} + \text{i}\gamma_5\mathcal{G})$ and the fact that the eigenvalues of γ_5 are doubly degenerate and given by ± 1 [3]. The latter property follows straightforwardly from $(\gamma_5)^2 = \mathbb{1}$ and $\text{tr}_\gamma\gamma_5 = 0$. In turn, the eigenvalues of $(\frac{1}{2}\sigma^{\mu\nu}F_{\text{cl.}\mu\nu})^2$ are also doubly degenerate and read $2(\mathcal{F} \pm \text{i}\mathcal{G})$. Taking into account that $\sigma^{\mu\nu}$ is traceless, it is then obvious that the four eigenvalues of $\frac{1}{2}\sigma^{\mu\nu}F_{\text{cl.}\mu\nu}$ are given by $\pm\sqrt{2(\mathcal{F} \pm \text{i}\mathcal{G})}$, and correspondingly

$$\text{tr}_\gamma\,\text{e}^{\text{i}\frac{e}{2}\sigma^{\mu\nu}F_{\text{cl.}\mu\nu}T} = 2\,\text{Re}\sum_{s=\pm 1}\text{e}^{-\text{i}se\sqrt{2(\mathcal{F}+\text{i}\mathcal{G})}\,T}\,. \tag{16}$$

Therewith, S^1 can be expressed as

$$S^1(\mathcal{F},\mathcal{G}^2) = \frac{\mathrm{i}}{2}\int_{-\mathrm{i}/\Lambda^2}^{\infty}\frac{\mathrm{d}T}{T}\,\mathrm{e}^{-\mathrm{i}m^2T}\left\{\mathrm{tr}_x\,\mathrm{e}^{\mathrm{i}D^2_{\mathrm{cl.}}T}\,2\,\mathrm{Re}\sum_{s=\pm1}\mathrm{e}^{-\mathrm{i}se\sqrt{2(\mathcal{F}+\mathrm{i}\mathcal{G})}\,T} - 4\,\mathrm{tr}_x\,\mathrm{e}^{\mathrm{i}\partial^2T}\right\}. \quad (17)$$

To determine S^1 for generic constant electromagnetic fields explicitly, we make use of the following "trick": We perform the calculation for the special case of $\vec{E}\parallel\vec{B}$, for which both $\mathcal{F}$ and $\mathcal{G}$ are nonzero and later express the result in terms of $\mathcal{F}$ and $\mathcal{G}$. For the sake of definiteness we moreover assume $B>E$, such that there is a one-to-one correspondence between the quantities E, B and $\mathcal{F}$, $\mathcal{G}$. More specifically, we have

$$E\leftrightarrow a := \left(\sqrt{\mathcal{F}^2+\mathcal{G}^2}-\mathcal{F}\right)^{1/2} \quad\text{and}\quad B\leftrightarrow b := \left(\sqrt{\mathcal{F}^2+\mathcal{G}^2}+\mathcal{F}\right)^{1/2}. \quad (18)$$

By means of Eq. (18), our result for S^1 written in terms of E and B can then be straightforwardly generalized to arbitrary oriented constant electric and magnetic fields of arbitrary strength.

Let us now turn to the explicit calculation. Without loss of generality we choose $A^\mu_{\mathrm{cl.}}(x) = (0,0,B\mathrm{x},-Et)$, so that we have $\vec{B}=B\vec{e}_{\mathrm{z}}$, $\vec{E}=E\vec{e}_{\mathrm{z}}$ and $D^2_{\mathrm{cl.}} = \partial^2_{\mathrm{x}} + (\partial_{\mathrm{y}} - \mathrm{i}eB\mathrm{x})^2 - \partial_t^2 + (\partial_{\mathrm{z}} + \mathrm{i}eEt)^2$. The second trace in Eq. (17) can be evaluated straightforwardly in momentum space as $\partial_\mu = \mathrm{i}\hat{p}_\mu$, with momentum operator $\hat{p}_\mu$ fulfilling $\hat{p}_\mu|p_\mu\rangle = p_\mu|p_\mu\rangle$ (no summation over repeated indices). Note that $\langle p'|p\rangle = (2\pi)^4\delta^{(4)}(p'-p)$ and $\langle x'|x\rangle = \delta^{(4)}(x'-x)$. With $|p\rangle\equiv|p_0\rangle|p_1\rangle|p_2\rangle|p_3\rangle$ we obtain

$$\mathrm{tr}_x\,\mathrm{e}^{\mathrm{i}\partial^2T} = \int\frac{\mathrm{d}^4p}{(2\pi)^4}\langle p|\mathrm{e}^{\mathrm{i}\partial^2T}|p\rangle = L^4\int\frac{\mathrm{d}^4p}{(2\pi)^4}\mathrm{e}^{-\mathrm{i}p^2T} = -\mathrm{i}\,\frac{L^4}{16\pi^2}\frac{1}{T^2}, \quad (19)$$

where we employed the identity $\langle p_\mu|p_\mu\rangle = L$ (no summation over repeated indices), with space-time extension L. To perform the first trace in Eq. (17), we employ a mixed momentum and position space representation, i.e., $\mathrm{tr}_x\{\ldots\} = \int\mathrm{d}t\int\mathrm{d}\mathrm{x}\int\frac{\mathrm{d}p_{\mathrm{y}}}{2\pi}\int\frac{\mathrm{d}p_{\mathrm{z}}}{2\pi}\langle t|\langle\mathrm{x}|\langle p_{\mathrm{y}}|\langle p_{\mathrm{z}}|\ldots|p_{\mathrm{z}}\rangle|p_{\mathrm{y}}\rangle|\mathrm{x}\rangle|t\rangle$. In turn, we have

$$\begin{aligned}\mathrm{tr}_x\,\mathrm{e}^{\mathrm{i}D^2_{\mathrm{cl.}}T} = L\int\frac{\mathrm{d}p_{\mathrm{z}}}{2\pi}\int\mathrm{d}t\,\langle t|\mathrm{e}^{\mathrm{i}eE[\frac{1}{eE}(-\mathrm{i}\partial_t)^2 - eE(t+\frac{p_{\mathrm{z}}}{eE})^2]T}|t\rangle \\ \times L\int\frac{\mathrm{d}p_{\mathrm{y}}}{2\pi}\int\mathrm{d}\mathrm{x}\,\langle\mathrm{x}|\,\mathrm{e}^{-\mathrm{i}eB[\frac{1}{eB}(-\mathrm{i}\partial_{\mathrm{x}})^2 + eB(\mathrm{x}-\frac{p_{\mathrm{y}}}{eB})^2]T}|\mathrm{x}\rangle,\end{aligned} \quad (20)$$

and after shifting and rescaling $t\to\tilde{t}=\sqrt{eE}(t+\frac{p_{\mathrm{z}}}{eE})$ and $\mathrm{x}\to\tilde{\mathrm{x}}=\sqrt{eB}(\mathrm{x}-\frac{p_{\mathrm{y}}}{eB})$,

$$\begin{aligned}\mathrm{tr}_x\,\mathrm{e}^{\mathrm{i}D^2_{\mathrm{cl.}}T} = \frac{LP_{\mathrm{z}}}{2\pi}\int\mathrm{d}\tilde{t}\,\langle\tilde{t}|\mathrm{e}^{\mathrm{i}2eE[\frac{1}{2}(-\mathrm{i}\partial_{\tilde{t}})^2 + \frac{1}{2}\mathrm{i}^2\tilde{t}^2]T}|\tilde{t}\rangle \\ \times\frac{LP_{\mathrm{y}}}{2\pi}\int\mathrm{d}\tilde{\mathrm{x}}\,\langle\tilde{\mathrm{x}}|\,\mathrm{e}^{-\mathrm{i}2eB[\frac{1}{2}(-\mathrm{i}\partial_{\tilde{\mathrm{x}}})^2 + \frac{1}{2}\tilde{\mathrm{x}}^2]T}|\tilde{\mathrm{x}}\rangle,\end{aligned} \quad (21)$$

where we employed $\int\mathrm{d}p_i = \lim_{P_i\to\infty}P_i$, and the limit $\lim_{P_i\to\infty}$ is implicitly understood.

It is now helpful to note that the expressions in the squared brackets in Eq. (21) amount to the (position space) Hamilton operator of a quantum harmonic oscillator in one dimensions, $\hat{H} = \frac{1}{2m}\hat{p}^2_{\mathrm{x}} + \frac{1}{2}m\omega^2\hat{\mathrm{x}}^2$, whose eigenvalues are given by $E_n = \omega(n+\frac{1}{2})$, with $n\in\mathbb{N}_0$. For the expression in the lower line of Eq. (21) we have $\omega=1$. The expression in the upper line of Eq. (21) is to be understood as harmonic oscillator with its frequency analytically continued to

$\omega = \mathrm{i}$. This becomes obvious from the fact that as a direct consequence of $S^1 = S^1(\mathcal{F}, \mathcal{G}^2)$, the results for the effective action in a purely magnetic field and a purely electric field are related by an analytical continuation from $B \leftrightarrow -\mathrm{i}E$ [7] (cf. also below). Note that seemingly the choice of $\omega = -\mathrm{i}$ would be equally justified. However, only $\omega = \mathrm{i}$ results in a convergent result, and thus is compatible with the limit of $eE \to 0$ in the first line of Eq. (23) below. Correspondingly, we have

$$\mathrm{tr}_x \, \mathrm{e}^{\mathrm{i}D^2_{\mathrm{cl.}}T} = \frac{LP_\mathrm{z}}{2\pi} \sum_{n'=0}^{\infty} \rho'(n') \, \mathrm{e}^{-eE(2n'+1)T} \, \frac{LP_\mathrm{y}}{2\pi} \sum_{n=0}^{\infty} \rho(n) \, \mathrm{e}^{-\mathrm{i}eB(2n+1)T}, \tag{22}$$

where $\rho'(n')$ and $\rho(n)$ denote the densities of states of the discrete eigenvalues. They can be determined by considering the limits of $eE \to 0$ and $eB \to 0$, respectively,

$$\begin{aligned} \lim_{eE\to 0} \frac{LP_\mathrm{z}}{2\pi} \sum_{n'=0}^{\infty} \rho'(n') \, \mathrm{e}^{-eE(2n'+1)T} &= L^2 \int \frac{\mathrm{d}p_\mathrm{z}}{2\pi} \int \frac{\mathrm{d}p_t}{2\pi} \, \mathrm{e}^{-(p_\mathrm{z}^2+p_t^2)T} \,, \\ \lim_{eB\to 0} \frac{LP_\mathrm{y}}{2\pi} \sum_{n=0}^{\infty} \rho(n) \, \mathrm{e}^{-\mathrm{i}eB(2n+1)T} &= L^2 \int \frac{\mathrm{d}p_\mathrm{x}}{2\pi} \int \frac{\mathrm{d}p_\mathrm{y}}{2\pi} \, \mathrm{e}^{-\mathrm{i}(p_\mathrm{x}^2+p_\mathrm{y}^2)T} \,. \end{aligned} \tag{23}$$

where we made use of the identity $\int \frac{\mathrm{d}p_\mathrm{z}}{2\pi} \int \frac{\mathrm{d}p_t}{2\pi} \, \mathrm{e}^{-\mathrm{i}(p_\mathrm{z}^2-p_t^2)T} = \int \frac{\mathrm{d}p_\mathrm{z}}{2\pi} \int \frac{\mathrm{d}p_t}{2\pi} \, \mathrm{e}^{-(p_\mathrm{z}^2+p_t^2)T}$. The latter line can be expressed as

$$\lim_{eB\to 0} \sum_{n=0}^{\infty} \Delta p_\perp^2 \frac{\rho(n)}{2eB} \, \mathrm{e}^{-\mathrm{i}n\Delta p_\perp^2 T} = \frac{L}{P_\mathrm{y}} \frac{1}{2} \int_0^\infty \mathrm{d}p_\perp^2 \mathrm{e}^{-\mathrm{i}p_\perp^2 T}, \tag{24}$$

where we defined $p_\perp^2 \equiv p_\mathrm{x}^2 + p_\mathrm{y}^2$ and $\Delta p_\perp^2 = 2eB$. Herefrom we infer $\rho(n) = eB\frac{L}{P_\mathrm{y}}$. An analogous manipulation of the expression in the first line yields $\rho'(n') = eE\frac{L}{P_\mathrm{z}}$. In turn, Eq. (22) becomes

$$\begin{aligned} \mathrm{tr}_x \, \mathrm{e}^{\mathrm{i}D^2_{\mathrm{cl.}}T} &= \frac{L^4}{4\pi^2} \sum_{n'=0}^{\infty} eE \, \mathrm{e}^{-eE(2n'+1)T} \sum_{n=0}^{\infty} eB \, \mathrm{e}^{-\mathrm{i}eB(2n+1)T} \\ &= -\mathrm{i} \, \frac{L^4}{16\pi^2} \frac{1}{T^2} \frac{(eET)(eBT)}{\sinh(eET)\sin(eBT)} \,. \end{aligned} \tag{25}$$

This expression is clearly invariant under the transformation $B \leftrightarrow -\mathrm{i}E$. Noting that $2(\mathcal{F}+\mathrm{i}\mathcal{G}) = (B - \mathrm{i}E)^2$, it is moreover obvious that Eq. (16) can be written as

$$\mathrm{tr}_\gamma \, \mathrm{e}^{\mathrm{i}\frac{e}{2}\sigma^{\mu\nu}F_{\mathrm{cl.}\mu\nu}T} = 2 \, \mathrm{Re} \sum_{s=\pm 1} \mathrm{e}^{-\mathrm{i}se(B-\mathrm{i}E)T} = 4\cosh(eET)\cos(eBT) \,. \tag{26}$$

Putting everything together, we finally obtain

$$\begin{aligned} S^1(\mathcal{F}, \mathcal{G}^2) &= \frac{L^4}{8\pi^2} \int_{-\mathrm{i}/\Lambda^2}^{\infty} \frac{\mathrm{d}T}{T^3} \, \mathrm{e}^{-\mathrm{i}m^2T} \left\{ \frac{(eaT)(ebT)}{\tanh(eaT)\tan(ebT)} - 1 \right\} \\ &= -\frac{L^4}{8\pi^2} \int_{1/\Lambda^2}^{\infty} \frac{\mathrm{d}T}{T^3} \, \mathrm{e}^{-m^2T} \left\{ \frac{(eaT)(ebT)}{\tan(eaT)\tanh(ebT)} - 1 \right\} . \end{aligned} \tag{27}$$

where we employed a contour rotation $\mathrm{i}T \to T$ in the last step. Equation (27) provides us with a compact expression of the unrenormalized on-loop effective action in constant electromagnetic

fields. The corresponding Lagrangian density is $\mathcal{L}^1(\mathcal{F},\mathcal{G}^2) = S^1(\mathcal{F},\mathcal{G}^2)/L^4$. Note that

$$\frac{(eaT)(ebT)}{\tan(eaT)\tanh(ebT)} - 1 = \frac{2}{3}\mathcal{F}(eT)^2 - \Big(\frac{4}{45}\mathcal{F}^2 + \frac{7}{45}\mathcal{G}^2\Big)(eT)^4 + \mathcal{O}(T^6)\,, \tag{28}$$

which implies that Eq. (27) contains a log-type divergence for $\Lambda \to \infty$ in the term $\sim \mathcal{F}$. All other contributions are finite in this limit. However, let us emphasize once again that so far we worked with unrenomalized fields and not at all bothered about renormalization.

In a next step we want go over to *renormalized quantities*. To this end we isolate this term. Upon its subtraction, the expression in Eq. (27) is finite for $\Lambda \to \infty$ and we can explicitly take the limit and set the lower integration bound to zero. This results in

$$\begin{aligned}\mathcal{L}^1(\mathcal{F},\mathcal{G}^2) = &-\mathcal{F}\frac{\alpha}{3\pi}\int_{1/\Lambda^2}^{\infty}\frac{\mathrm{d}T}{T}\,\mathrm{e}^{-m^2T} \\ &-\frac{1}{8\pi^2}\int_{1/\Lambda^2}^{\infty}\frac{\mathrm{d}T}{T^3}\,\mathrm{e}^{-m^2T}\bigg\{\frac{(eaT)(ebT)}{\tan(eaT)\tanh(ebT)} - \frac{2}{3}(eT)^2\mathcal{F} - 1\bigg\}\,,\end{aligned} \tag{29}$$

with $\alpha = \frac{e^2}{4\pi}$ and $\int_{1/\Lambda^2}^{\infty}\frac{\mathrm{d}T}{T}\,\mathrm{e}^{-m^2T} = \ln(\frac{\Lambda^2}{m^2}) - \gamma_E + \mathcal{O}(\frac{m^2}{\Lambda^2})$, where γ_E denotes the Euler-Mascheroni constant. Together with the Maxwell term $\mathcal{L}_{\mathrm{MW}} = -\mathcal{F}$ the effective Lagrangian can be expressed as

$$\begin{aligned}\mathcal{L}_{\mathrm{eff.}}(\mathcal{F},\mathcal{G}^2) = &-\mathcal{F}\bigg\{1 + \frac{\alpha}{3\pi}\Big[\ln\Big(\frac{\Lambda^2}{m^2}\Big) - \gamma_E\Big]\bigg\} \\ &-\frac{1}{8\pi^2}\int_{0}^{\infty}\frac{\mathrm{d}T}{T^3}\,\mathrm{e}^{-m^2T}\bigg\{\frac{(eaT)(ebT)}{\tan(eaT)\tanh(ebT)} - \frac{2}{3}(eT)^2\mathcal{F} - 1\bigg\}\,.\end{aligned} \tag{30}$$

Let us now impose the renormalization condition that the term $\sim \mathcal{F}$ in Eq. (30) matches the physical (measured) Maxwell term. For this purpose we introduce a wave function renormalization factor

$$Z^{-1} \equiv 1 + \frac{\alpha}{3\pi}\Big[\ln\Big(\frac{\Lambda^2}{m^2}\Big) - \gamma_E\Big]\,, \tag{31}$$

and define the renormalized field strength tensor by $F^{\mu\nu}_{\mathrm{cl.,R}} = Z^{-1/2}F^{\mu\nu}_{\mathrm{cl.}}$, such that the renormalized four-potential is given by $A^{\mu}_{\mathrm{cl.,R}} = Z^{-1/2}A^{\mu}_{\mathrm{cl.}}$. For the interaction vertex in the Lagrangian (5) this rescaling implies $eA^{\mu}_{\mathrm{cl.}}\bar{\psi}\gamma_\mu\psi \to Z^{1/2}eA^{\mu}_{\mathrm{cl.,R}}\bar{\psi}\gamma_\mu\psi$. Demanding it to be given by $e_{\mathrm{R}}A^{\mu}_{\mathrm{cl.,R}}\bar{\psi}\gamma_\mu\psi$, i.e., to match the physical interaction, we infer $e_{\mathrm{R}} = Z^{1/2}e$. Correspondingly, we have

$$\begin{aligned}F^{\mu\nu}_{\mathrm{R}} &= Z^{-1/2}F^{\mu\nu} = F^{\mu\nu}_{\mathrm{R}}(m)\,, \\ e_{\mathrm{R}} &= Z^{1/2}e = e_{\mathrm{R}}(m)\,,\end{aligned} \tag{32}$$

but $e_{\mathrm{R}}F^{\mu\nu}_{\mathrm{R}} = eF^{\mu\nu}$ independent of the renormalization scale $\mu = m$. Note that the choice of $\mu = m$ is conventionally referred to as "on-shell" renormalization. For this choice we have $\frac{e^2_{\mathrm{R}}(m)}{4\pi} = \alpha_{\mathrm{R}}(m) \simeq \frac{1}{137}$. In turn, the (on-shell) renormalized effective Lagrangian reads

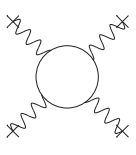
$$\begin{aligned}\mathcal{L}^{\mathrm{R}}_{\mathrm{eff.}}(\mathcal{F}_{\mathrm{R}},\mathcal{G}^2_{\mathrm{R}}) = &-\mathcal{F}_R \\ &-\frac{1}{8\pi^2}\int_{0}^{\infty}\frac{\mathrm{d}T}{T^3}\,\mathrm{e}^{-m^2T}\bigg\{\frac{(e_{\mathrm{R}}a_{\mathrm{R}}T)(e_{\mathrm{R}}b_{\mathrm{R}}T)}{\tan(e_{\mathrm{R}}a_{\mathrm{R}}T)\tanh(e_{\mathrm{R}}b_{\mathrm{R}}T)} - \frac{2}{3}(e_{\mathrm{R}}T)^2\mathcal{F}_{\mathrm{R}} - 1\bigg\}\,.\end{aligned} \tag{33}$$

The expression in Eq. (33) amounts to the renowned *Heisenberg-Euler effective Lagrangian* [1, 3] first derived by Werner Heisenberg and Hans Euler and published eighty years ago in 1936 [1]. The analogous result for scalar QED can be obtained along the same lines and was first derived by Victor Weisskopf [8] and also published in 1936; see [9] for a review. All our subsequent considerations will be based upon Eq. (33), i.e., we will exclusively work with renormalized quantities. However, in order to keep notations compact we will suppress the label "R" in the following.

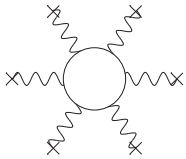
Let us emphasize once again that the one-loop effective Lagrangian (33) accounts for all orders in $\mathcal{F}$ and $\mathcal{G}^2$, and thus is fully nonperturbative in the combined parameter $eF^{\mu\nu}_{\text{cl.}}$. Due to "Furry's theorem" [10] (charge conjugation invariance of QED), the effective Lagrangian is moreover even in the elementary charge e, and in turn even in $eF^{\mu\nu}_{\text{cl.}}$. To lowest order in a perturbative expansion of Eq. (33) – counting $\mathcal{O}(\mathcal{F}) = \mathcal{O}(\mathcal{G}) = \mathcal{O}(F^2)$ – we obtain [cf. Eq. (28)]

$$\begin{aligned}\mathcal{L}_{\text{eff.}}(\mathcal{F},\mathcal{G}^2) &= -\mathcal{F} + \frac{1}{8\pi^2}\int_0^\infty \frac{\mathrm{d}T}{T^3}\,\mathrm{e}^{-m^2T}\left[\frac{4}{45}\mathcal{F}(eT)^4 + \frac{7}{45}\mathcal{G}^2(eT)^4 + \mathcal{O}\big((eFT)^6\big)\right] \\ &= -\mathcal{F} + \underbrace{\frac{8}{45}\frac{\alpha^2}{m^4}}_{=:c_1}\mathcal{F}^2 + \underbrace{\frac{14}{45}\frac{\alpha^2}{m^4}}_{=:c_2}\mathcal{G}^2 + m^4\mathcal{O}\Big(\big(\tfrac{\alpha F^2}{m^4}\big)^3\Big)\,. \end{aligned} \tag{34}$$

$$= \quad -\mathcal{F} \quad +$$



$$+$$



$$+ \quad \cdots$$

The expression $c_1\mathcal{F}^2 + c_2\mathcal{G}^2 \sim F^4$ obviously corresponds to the first loop diagram exhibiting four couplings to the electromagnetic field. For completeness, note that by means of an expansion of the integrand of the proper time integral the explicit expression of any perturbative one-loop interaction among constant electromagnetic fields can be obtained; cf. also [9].

Even though the above results are strictly speaking only valid for constant electromagnetic fields, they can also be adopted for *slowly varying fields*: Vacuum fluctuations of virtual electrons and positrons typically probe distances of the order of the (reduced) Compton wavelength of the electron $\lambda\!\!\!^{-}_c = \frac{1}{m} \approx 3.9\cdot 10^{-13}\text{m}$; the associated time scale is the Compton time $\tau_c \approx 1.3\cdot 10^{-21}\text{s}$. In turn, $\lambda\!\!\!^{-}_c$ provides us with a natural reference scale to classify spatial variations. Consider now a derivative expansion around the constant field result. As the derivatives are rendered dimensionless by $\lambda\!\!\!^{-}_c$, terms involving $n \in \mathbb{N}_0$ derivatives scale as $(\lambda\!\!\!^{-}_c\partial_{\text{x}})^n \sim (\frac{\omega}{m})^n$, where ω is the typical momentum scale of variation of the field configuration under consideration. Hence, for *slowly varying fields*, characterized by $\frac{\omega}{m} \ll 1$, all derivative terms can be neglected and we can employ the substitution $F^{\mu\nu} \to F^{\mu\nu}(x)$ in the constant field result for $\mathcal{L}_{\text{eff.}}$ in Eqs. (33) and (34). This substitution amounts to a *locally constant field approximation* (LCFA).

Let us emphasize that in fact most of the field configurations attainable in the laboratory vary on scales much larger than $\lambda\!\!\!^{-}_c$ and thus fall into this category. Correspondingly, the LCFA allows for reliable analytical insights into a variety of experimental relevant field configurations, without having to determine the effective action in the dedicated inhomogeneous electromagnetic field profile.

3 Vacuum birefringence as an optical signature of quantum vacuum nonlinearity

In the following, we adopt the LCFA and study *light propagation* in the quantum vacuum subjected to classical electromagnetic fields. As $\mathcal{L}_{\text{eff.}} = \mathcal{L}_{\text{eff.}}(F^{\mu\nu}_{\text{cl.}}) = -\mathcal{F} + \mathcal{L}^1(\mathcal{F},\mathcal{G}^2)$, the equations of motion (2) for the electromagnetic field in the quantum vacuum are given by

$$\partial_\mu \frac{\mathcal{L}_{\text{eff.}}}{\partial F_{\text{cl.}\mu\nu}} = 0 \quad \leftrightarrow \quad \partial_\mu \left(F^{\mu\nu}_{\text{cl.}} - \frac{\partial \mathcal{L}^1}{\partial \mathcal{F}} F^{\mu\nu}_{\text{cl.}} - \frac{\partial \mathcal{L}^1}{\partial \mathcal{G}} {}^*F^{\mu\nu}_{\text{cl.}} \right) = 0 \,. \tag{35}$$

Equation (35) constitutes the "true" *quantum Maxwell equations* (at one-loop order) amounting to the *true* equations of motion governing the dynamics of classical electromagnetic field in the quantum vacuum far away from any classical sources. Note that these equations are no longer linear in $F^{\mu\nu}_{\text{cl.}}$ and thus – at least in principle – violate the superposition principle of classical electrodynamics; cf. below Eq. (2) above. Due to the fact that these nonlinearities are suppressed parametrically by powers of $\frac{eE}{m^2} = \frac{E[\text{V/m}]}{1.3\cdot 10^{18}}$ and $\frac{eB}{m^2} = \frac{B[\text{T}]}{4\cdot 10^9}$, and all the macroscopic electromagnetic fields available in the laboratory clearly fulfill $\{\frac{eE}{m^2}, \frac{eB}{m^2}\} \ll 1$, these nonlinearities are typically extremely tiny, preserving the applicability of the Maxwell's classical equations for essentially all practical purposes. As will be shown explicitly below they can give rise to striking consequences for photon propagation in electromagnetic fields. From Eq. (34) we infer $\frac{\partial \mathcal{L}^1}{\partial \mathcal{F}} = 2c_1\mathcal{F}\big[1 + \mathcal{O}\big((\frac{eF}{m^2})^2\big)\big]$ and $\frac{\partial \mathcal{L}^1}{\partial \mathcal{G}} = 2c_2\mathcal{G}\big[1 + \mathcal{O}\big((\frac{eF}{m^2})^2\big)\big]$, such that to cubic order in the field strength we have

$$\partial_\mu \big[(1 - 2c_1\mathcal{F})F^{\mu\nu}_{\text{cl.}} - 2c_2\mathcal{G}{}^*F^{\mu\nu}_{\text{cl.}}\big] = 0 \,. \tag{36}$$

A generic field strength tensor $F^{\mu\nu}$ fulfills the Bianchi identity $\partial^\alpha F^{\beta\gamma} + \partial^\beta F^{\gamma\alpha} + \partial^\gamma F^{\alpha\beta} = 0 \leftrightarrow \partial_\mu {}^*F^{\mu\nu} = 0$. With its help Eq. (36) can be written as

$$\partial_\mu \big[(1 - 2c_1\mathcal{F})F^{\mu\nu}_{\text{cl.}}\big] - 2c_2\big(\partial_\mu \mathcal{G}\big)^*F^{\mu\nu}_{\text{cl.}} = 0 \,. \tag{37}$$

In a next step we decompose the field strength tensor as $F^{\mu\nu}_{\text{cl.}} \to F^{\mu\nu}_{\text{cl.}} + f^{\mu\nu}(x)$ into a constant background field $F^{\mu\nu}_{\text{cl.}}$ and a probe photon field $f^{\mu\nu}(x)$, and linearize the equations of motion (36) in $f^{\mu\nu}$ [4, 11], i.e., neglect self-interactions of the probe photon field. Note that under the above decomposition we have

$$\begin{aligned} \mathcal{F} &\to \mathcal{F} + \frac{1}{2} F_{\text{cl.}\mu\nu} f^{\mu\nu}(x) + \mathcal{O}(f^2) \,, \\ \mathcal{G} &\to \mathcal{G} + \frac{1}{2} {}^*F_{\text{cl.}\mu\nu} f^{\mu\nu}(x) + \mathcal{O}(f^2) \,. \end{aligned} \tag{38}$$

Correspondingly, we obtain the following linearized equations of motion

$$\big(1 - 2c_1\mathcal{F}\big)\partial_\mu f^{\mu\nu}(x) - c_1 F_{\text{cl.}\alpha\beta} F^{\mu\nu}_{\text{cl.}} \partial_\mu f^{\alpha\beta}(x) - c_2 {}^*F_{\text{cl.}\alpha\beta} {}^*F^{\mu\nu}_{\text{cl.}} \partial_\mu f^{\alpha\beta}(x) = 0 \,. \tag{39}$$

In order to solve them, we first go to momentum space, i.e., $a^\mu(x) = \int \frac{\mathrm{d}^4k}{(2\pi)^4} \mathrm{e}^{\mathrm{i}kx} a^\mu(k) \leftrightarrow f^{\mu\nu}(x) = \mathrm{i}\int \frac{\mathrm{d}^4k}{(2\pi)^4} \mathrm{e}^{\mathrm{i}kx}[k^\mu a^\nu(k) - k^\nu a^\mu(k)]$, and work in Lorenz gauge, $\partial_\mu a^\mu(x) = 0 \leftrightarrow k_\mu a^\mu(k) = 0$. In momentum space the equations of motion can be cast into the following form,

$$\big(1 - 2c_1\mathcal{F}\big)k^2 a^\nu(k) - 2c_1 F_{\text{cl.}\alpha\beta} F^{\mu\nu}_{\text{cl.}} k_\mu k^\alpha a^\beta(k) - 2c_2 {}^*F_{\text{cl.}\alpha\beta} {}^*F^{\mu\nu}_{\text{cl.}} k_\mu k^\alpha a^\beta(k) = 0 \,. \tag{40}$$

Let us now search for nontrivial solutions of this equation. Our strategy is to use the following ansätze

$$\begin{aligned} a_1^\mu(k) &\sim F_{\text{cl.}}^{\mu\nu}k_\nu \equiv (F_{\text{cl.}}k)^\mu = (\vec{k}\cdot\vec{E}, \vec{k}\times\vec{B} + \omega\vec{E})\,, \\ a_2^\mu(k) &\sim {}^*F_{\text{cl.}}^{\mu\nu}k_\nu \equiv ({}^*F_{\text{cl.}}k)^\mu = (\vec{k}\cdot\vec{B}, -\vec{k}\times\vec{E} + \omega\vec{B})\,, \end{aligned} \tag{41}$$

with $k^\mu = (\omega, \vec{k})$ and the contraction identities (15). These ansätze obviously fulfill $k_\mu a_i^\mu(k) = 0$, i.e., are compatible with the Lorenz gauge condition. Also note that $(F_{\text{cl.}}k)^2 = \omega^2\vec{E}^2 + \vec{k}^2\vec{B}^2 - (\vec{k}\cdot\vec{E})^2 - (\vec{k}\cdot\vec{B})^2 + 2\omega(\vec{k}\times\vec{B})\cdot\vec{E}$. From Eq. (40) it is obvious that the dispersion relations for the $a_i^\mu(k)$ are of the form $k^2 = 0 + \alpha\,\mathcal{O}\big((\frac{eF}{m^2})^2\big)$.

Let us have a closer look on the physical meaning of the above ansätze. Our main focus is on their polarizations, defined by the directions of the associated electric field vectors. With the classical free Maxwell equations in the vacuum, $\partial_\mu F_{\text{cl.}}^{\mu\nu} = 0$, we obtain

$$\begin{aligned} &\text{position space:} \quad \begin{cases} \vec{e}_i(x) = -\vec{\nabla}a_i^0(x) - \partial_t\vec{a}_i(x) \\ \vec{b}_i(x) = \vec{\nabla}\times\vec{a}_i(x) \end{cases}, \\ \rightarrow \quad &\text{momentum space:} \quad \begin{cases} \vec{e}_i(k) \sim -\vec{k}a_i^0(k) + \omega\vec{a}_i(k) \\ \vec{b}_i(k) \sim \vec{k}\times\vec{a}_i(k) \end{cases}. \end{aligned} \tag{42}$$

The use of the classical Maxwell equations neglecting quantum corrections is justified here, as the quantum corrections only give rise to subleading corrections. The electric $\vec{e}_i$ and magnetic $\vec{b}_i$ fields associated with the $a_i^\mu(k)$ in Eq. (41) read

$$a_1^\mu(k): \quad \begin{cases} \vec{e}_1 & \sim -\vec{k}(\vec{k}\cdot\vec{E}) + \omega(\vec{k}\times\vec{B}) + \omega^2\vec{E} \\ \vec{b}_1 & \sim \omega(\vec{k}\times\vec{E}) - \vec{k}^2\vec{B} + \vec{k}(\vec{k}\cdot\vec{B}) \end{cases}, \tag{43}$$

$$a_2^\mu(k): \quad \begin{cases} \vec{e}_2 & \sim -\vec{k}(\vec{k}\cdot\vec{B}) - \omega(\vec{k}\times\vec{E}) + \omega^2\vec{B} \\ \vec{b}_2 & \sim \omega(\vec{k}\times\vec{B}) + \vec{k}^2\vec{E} - \vec{k}(\vec{k}\cdot\vec{E}) \end{cases}. \tag{44}$$

Note that $\vec{k}\cdot\vec{e}_1 \sim \vec{k}\cdot\vec{e}_2 \sim \mathcal{G}k^2$ and $\vec{e}_1\cdot\vec{e}_2 \sim k^2\big[(\vec{k}\cdot\vec{E})(\vec{k}\cdot\vec{B}) + \omega^2\mathcal{G}\big]$. This implies that for probe photons propagating on the light cone, i.e., fulfilling $k^2 = 0$, the $a_i^\mu(k)$ span the two transverse photon polarization modes. More specifically, they correspond to the two orthogonal linear polarization modes $\sim \vec{e}_i$ in a particular basis set by the background field configuration and the photons' wave vector. Of course, for the case of $k^2 = 0 + \alpha\,\mathcal{O}\big((\frac{eF}{m^2})^2\big)$ this is still well-justified.

With the shorthand notations introduced in Eq. (41), we can express Eq. (40) as

$$\big(1 - 2c_1\mathcal{F}\big)k^2a^\nu(k) + 2c_1(F_{\text{cl.}}k)^\nu k^\alpha F_{\text{cl.}\alpha\beta}a^\beta(k) + 2c_2({}^*F_{\text{cl.}}k)^\nu k^\alpha {}^*F_{\text{cl.}\alpha\beta}a^\beta(k) = 0\,. \tag{45}$$

In a next step we plug the above ansätze into this equation. After some rearrangements and using the contraction identities (15), the respective equations become

$$\begin{aligned} a_1^\mu(k): &\quad \big[\big(1 - 2c_1\mathcal{F}\big)k^2 - 2c_1(F_{\text{cl.}}k)^2\big](F_{\text{cl.}}k)^\nu + 2c_2\mathcal{G}k^2({}^*F_{\text{cl.}}k)^\nu = 0\,, \\ a_2^\mu(k): &\quad \big[\big(1 - 2c_1\mathcal{F} + 2c_2\mathcal{F}\big)k^2 - 2c_2(F_{\text{cl.}}k)^2\big]({}^*F_{\text{cl.}}k)^\nu - 2c_1\mathcal{G}k^2(F_{\text{cl.}}k)^\nu = 0\,. \end{aligned} \tag{46}$$

These equations can be solved with the ansatz $k^2 = 0 + \Delta$, where $\Delta = \alpha\,\mathcal{O}\big((\frac{eF}{m^2})^2\big)$ (cf. also above). Note that this solution procedure can systematically (recursively) be extended to higher

orders. We denote the solution of the equation for $a_i^\mu(k)$ by Δ_i. In fact, it is very easy to see that

$$\Delta_i = 2c_i(F_{\text{cl.}}k)^2 + \alpha\,\mathcal{O}\big((\tfrac{eF}{m^2})^4\big)\,. \tag{47}$$

Hence, the dispersion relations for the modes $a_i^\mu(k)$ are given by

$$k^2 = 2c_i(F_{\text{cl.}}k)^2 + \alpha\,\mathcal{O}\big((\tfrac{eF}{m^2})^4\big) \quad \leftrightarrow \quad \omega\big(|\vec{k}|\big) = |\vec{k}|\big[1 - c_i(F_{\text{cl.}}k)^2/\vec{k}^2\big] + \alpha\,\mathcal{O}\big((\tfrac{eF}{m^2})^4\big)\,. \tag{48}$$

Taking into account $(F_{\text{cl.}}k)^2 = (F_{\text{cl.}}k)^2\big|_{k^2=0} + (eF)^2\,\mathcal{O}\big((\tfrac{eF}{m^2})^4\big)$, with $(F_{\text{cl.}}k)^2\big|_{k^2=0} = (\vec{k}\times\vec{E})^2 + (\vec{k}\times\vec{B})^2 - 2|\vec{k}|\,\vec{k}\cdot(\vec{E}\times\vec{B})$ (cf. above), the dispersion relations (48) can finally be written as

$$\omega\big(|\vec{k}|\big) = |\vec{k}|\Big\{1 - c_i\Big[E^2\sin^2\sphericalangle(\vec{k},\vec{E}) + B^2\sin^2\sphericalangle(\vec{k},\vec{B}) - 2EB\,\hat{\vec{k}}\cdot\hat{\vec{s}}\Big]\Big\} + \alpha\,\mathcal{O}\big((\tfrac{eF}{m^2})^4\big)\,, \tag{49}$$

with $\hat{\vec{k}} = \vec{k}/|\vec{k}|$, $E = |\vec{E}|$, $B = |\vec{B}|$, and unit Poynting vector $\hat{\vec{s}} = \frac{\vec{E}\times\vec{B}}{EB}$.

In turn, the probe photons' group and phase velocities derived from Eq. (49) agree with each other, i.e., $v_{\text{gr},i} = \frac{\mathrm{d}\omega}{\mathrm{d}|\vec{k}|} = v_{\text{ph},i} = \frac{\omega}{|\vec{k}|} =: v_i$, and are given by

$$\left\{\begin{matrix} v_1 \\ v_2 \end{matrix}\right\} = 1 - \frac{\alpha}{\pi}\frac{1}{90}\left\{\begin{matrix} 7 \\ 4 \end{matrix}\right\}\left[\Big(\frac{eE}{m^2}\Big)^2\sin^2\sphericalangle(\vec{k},\vec{E}) + \Big(\frac{eB}{m^2}\Big)^2\sin^2\sphericalangle(\vec{k},\vec{B}) - 2\frac{eE}{m^2}\frac{eB}{m^2}\,\hat{\vec{k}}\cdot\hat{\vec{s}}\right], \tag{50}$$

where the neglected higher order corrections are $\sim \alpha\,\mathcal{O}\big((\tfrac{eF}{m^2})^4\big)$. The first (second) line is the result for probe photons polarized in mode a_1^μ (a_2^μ). The associated indices of refraction are given by $n_i = 1/v_i$. Up to corrections $\sim \alpha\,\mathcal{O}\big((\tfrac{eF}{m^2})^4\big)$, their explicit expressions are

$$\left\{\begin{matrix} n_1 \\ n_2 \end{matrix}\right\} = 1 + \frac{\alpha}{\pi}\frac{1}{90}\left\{\begin{matrix} 7 \\ 4 \end{matrix}\right\}\left[\Big(\frac{eE}{m^2}\Big)^2\sin^2\sphericalangle(\vec{k},\vec{E}) + \Big(\frac{eB}{m^2}\Big)^2\sin^2\sphericalangle(\vec{k},\vec{B}) - 2\frac{eE}{m^2}\frac{eB}{m^2}\,\hat{\vec{k}}\cdot\hat{\vec{s}}\right]. \tag{51}$$

Correspondingly, in generic electromagnetic background fields (for which the expression in the square brackets does not vanish) the two orthogonal probe photon polarization modes a_1^μ and a_2^μ propagate with different velocities $v_i \leq 1$, or equivalently, experience different indices of refraction, implying that the quantum vacuum subjected to electromagnetic fields acts like a *birefringent* medium [12,13].

Shining linearly polarized light with overlap to both polarization modes through an electromagnetic field, due to the birefringence effect an ellipticity signal is induced. The ellipticity signal is typically specified by an angle $\Delta\Phi = 2\pi\frac{L}{\lambda}\Delta n$ characterizing the phase shift between the two polarization components, with $\Delta n = n_1 - n_2$. Here λ is wavelength of the probe photons and L denotes their optical path length in the electromagnetic field.

As essentially all electromagnetic fields available in the laboratory fulfill $\{\frac{eE}{m^2}, \frac{eB}{m^2}\} \ll 1$ (cf. above), the vacuum birefringence signal is extremely tiny, making its experimental detection very challenging. It is so far searched for in experiments using macroscopic magnetic fields of several Tesla and high-finesse cavities to increase the optical path length of the probe photons in the magnetic field [14–16].

An alternative proposal to verify vacuum birefringence with the aid of high-intensity lasers in an all-optical experimental setup has been put forward by [17,18], envisioning the combination of an optical high-intensity laser as pump and a linearly polarized x-ray pulse as probe; cf. also [19,20]. Resorting to the locally constant field approximation on the level of the effective Lagrangian (33), recently we have reanalyzed this vacuum birefringence scenario [21,22], rephrasing the phenomenon in terms of a vacuum emission process [23].

4 Conclusions

In these lectures we focused on the quantum vacuum subjected to classical electromagnetic fields. To this end we explicitly derived the renowned Heisenberg-Euler effective action in constant electromagnetic fields. As an application, we demonstrated how the experimental signature of vacuum birefringence can be obtained from this effective action. Let us finally emphasize that the Heisenberg-Euler effective action of course also gives rise to many other signatures of quantum vacuum nonlinearity; for reviews, see [4, 24–31].

Acknowledgements: I would like to thank the organizers of the Helmholtz International Summer School (HISS) - Dubna International Advanced School of Theoretical Physics (DIAS-TH) "Quantum Field Theory at the Limits: from Strong Fields to Heavy Quarks" for organizing a very nice and pleasant summer school in Dubna. Moreover, I am indebted to Елена Мосман for various stimulating discussions ☹☹ and to Holger Gies for many stimulating discussions as well as helpful comments on this manuscript.

References

[1] W. Heisenberg and H. Euler, Z. Phys. **98**, 714 (1936), an English translation is available at [physics/0605038].

[2] H.B.G. Casimir, Kon. Ned. Akad. Wetensch. Proc. **51**, 793 (1948).

[3] J. S. Schwinger, Phys. Rev. **82**, 664 (1951).

[4] W. Dittrich and H. Gies, Springer Tracts Mod. Phys. **166**, 1 (2000).

[5] V. I. Ritus, Zh. Eksp. Teor. Fiz. **69**, 1517 (1975) [Sov. Phys. JETP **42**, 774 (1975)]; Zh. Eksp. Teor. Fiz. **73**, 807 (1977) [Sov. Phys. JETP **46**, 423 (1977)].

[6] D. Cangemi, E. D'Hoker and G. V. Dunne, Phys. Rev. D **52**, 3163 (1995) [hep-th/9506085]; G. V. Dunne and T. M. Hall, Phys. Lett. B **419**, 322 (1998) [hep-th/9710062]; G. V. Dunne and T. Hall, Phys. Rev. D **58**, 105022 (1998) [hep-th/9807031].

[7] U. D. Jentschura, H. Gies, S. R. Valluri, D. R. Lamm and E. J. Weniger, Can. J. Phys. **80**, 267 (2002) [hep-th/0107135].

[8] V. Weisskopf, Kong. Dans. Vid. Selsk., Mat.-fys. Medd. **XIV**, 6 (1936).

[9] G. V. Dunne, In *Shifman, M. (ed.) et al.: From fields to strings, vol. 1* 445-522 [hep-th/0406216].

[10] W. H. Furry, Phys. Rev. **52**, 569 (1937).

[11] Z. Bialynicka-Birula and I. Bialynicki-Birula, Phys. Rev. D **2**, 2341 (1970).

[12] J. S. Toll, Ph.D. thesis, Princeton Univ., 1952 (unpublished).

[13] R. Baier and P. Breitenlohner, Act. Phys. Austriaca **25**, 212 (1967); Nuov. Cim. B **47** 117 (1967).

[14] G. Cantatore [PVLAS Collaboration], Lect. Notes Phys. **741**, 157 (2008); E. Zavattini *et al.* [PVLAS Collaboration], Phys. Rev. D **77**, 032006 (2008); F. Della Valle *et al.*, New J. Phys. **15** 053026 (2013).

[15] P. Berceau, R. Battesti, M. Fouche and C. Rizzo, Can. J. Phys. **89**, 153 (2011); P. Berceau, M. Fouche, R. Battesti and C. Rizzo, Phys. Rev. A, **85**, 013837 (2012); A. Cadene, P. Berceau, M. Fouche, R. Battesti and C. Rizzo, Eur. Phys. J. D **68**, 16 (2014).

[16] F. Karbstein, arXiv:1510.03178 [hep-ph].

[17] T. Heinzl, B. Liesfeld, K. U. Amthor, H. Schwoerer, R. Sauerbrey and A. Wipf, Opt. Commun. **267**, 318 (2006).

[18] H. -P. Schlenvoigt, T. Heinzl, U. Schramm, T. Cowan and R. Sauerbrey, Physica Scripta **91**, 023010 (2016).

[19] A. Di Piazza, K. Z. Hatsagortsyan and C. H. Keitel, Phys. Rev. Lett. **97**, 083603 (2006) [hep-ph/0602039].

[20] V. Dinu, T. Heinzl, A. Ilderton, M. Marklund and G. Torgrimsson, Phys. Rev. D **89**, 125003 (2014) [arXiv:1312.6419 [hep-ph]]; Phys. Rev. D **90**, 045025 (2014) [arXiv:1405.7291 [hep-ph]].

[21] F. Karbstein, H. Gies, M. Reuter and M. Zepf, Phys. Rev. D **92**, 071301 (2015) [arXiv:1507.01084 [hep-ph]].

[22] F. Karbstein and C. Sundqvist, Phys. Rev. D **94**, 013004 (2016) doi:10.1103/PhysRevD.94.013004 [arXiv:1605.09294 [hep-ph]].

[23] F. Karbstein and R. Shaisultanov, Phys. Rev. D **91**, 113002 (2015) [arXiv:1412.6050 [hep-ph]].

[24] W. Dittrich and M. Reuter, Lect. Notes Phys. **220**, 1 (1985).

[25] M. Marklund and J. Lundin, Eur. Phys. J. D **55**, 319 (2009) [arXiv:0812.3087 [hep-th]].

[26] G. V. Dunne, Eur. Phys. J. D **55**, 327 (2009) [arXiv:0812.3163 [hep-th]].

[27] T. Heinzl and A. Ilderton, Eur. Phys. J. D **55**, 359 (2009) [arXiv:0811.1960 [hep-ph]].

[28] A. Di Piazza, C. Muller, K. Z. Hatsagortsyan and C. H. Keitel, Rev. Mod. Phys. **84**, 1177 (2012) [arXiv:1111.3886 [hep-ph]].

[29] G. V. Dunne, Int. J. Mod. Phys. A **27**, 1260004 (2012) [Int. J. Mod. Phys. Conf. Ser. **14**, 42 (2012)] [arXiv:1202.1557 [hep-th]].

[30] R. Battesti and C. Rizzo, Rept. Prog. Phys. **76**, 016401 (2013) [arXiv:1211.1933 [physics.optics]].

[31] B. King and T. Heinzl, High Power Laser Science and Engineering, 4, e5 (2016) [arXiv:1510.08456 [hep-ph]].

Non-linear quantum dynamics in strong and short electromagnetic fields

Alexander I. Titov[1], *Burkhard Kämpfer*[2,3], *A Hosaka*[4] *and H. Takabe*[2]

[1]Bogoliubov Laboratory of Theoretical Physics, JINR, Dubna 141980, Russia
[2]Helmholtz-Zentrum Dresden-Rossendorf, 01314 Dresden, Germany
[3]Institut für Theoretische Physik, TU Dresden, 01062 Dresden, Germany
[4]RCNP, 10-1 Mihogaoka Ibaraki, 567-0047 Osaka, Japan

DOI: http://dx.doi.org/10.3204/DESY-PROC-2016-04/Titov

In our contribution we give a brief overview of two widely discussed quantum processes: electron-positron pairs production off a probe photon propagating through a polarized short-pulsed electromagnetic (e.m.) (e.g. laser) wave field or generalized Breit-Wheeler process and a single a photon emission off an electron interacting with the laser pules, so-called non-linear Compton scattering. We show that at small and moderate laser field intensities the shape and duration of the pulse are very important for the probability of considered processes. However, at high intensities the multi-photon interactions of the fermions with laser field are decisive and completely determined all aspects of subthreshold e^+e^- pairs and photon production.

1 Introduction

The rapidly progressing laser technology [1] offers unprecedented opportunities for investigations of quantum systems with intense laser beams [2]. A laser intensity I_L of $\sim 2\times 10^{22}$ W/cm^2 has been already achieved [3]. Intensities of the order of $I_L \sim 10^{23}...10^{25}$ W/cm^2 are envisaged in near future, e.g. at the CLF [4], ELI [5], HiPER [6]. Further facilities are in planning on construction stage, e.g. PEARL laser facility [7] at Sarov/Nizhny Novgorod, Russia. The high intensities are provided in short pulses on a femtosecond pulse duration level [2, 8, 9], with only a few oscillations of the electromagnetic (e.m.) field or even sub-cycle pulses. (The tight connection of high intensity and short pulse duration is further emphasized in [10]. The attosecond regime will become accessible at shorter wavelengths [11, 12]).

Quantum processes occurring in the interactions of charge fermions in very (infinitely) long e.m. pulse were investigated in detail in the pioneering works of Reiss [13] as well as Narozhny, Nikishov and Ritus [14, 15, 16]. We call the such approaches as an infinite pulse approximation (IPA) since it refers to a stationary scattering process. Many simple and clear expressions for the production probabilities and cross sections have been obtain within IPA. It was shown that the charged fermion (electron, for instance) can interact with $n \geq 1$ photon simultaneously (n is an integer number),

However, recently it has become clear that for the photon production off an electron interacting with short laser pulse (Compton scattering) and for e^+e^- pair production off a probe

photon interacting with short e.m. pulses (Breit-Wheeler process) the finite pulse shape and the pulse duration become important (see, for example [17] and reference their in). That means the treatment of the intense and short laser field as an infinitely long wave train is no longer adequate. The theory must operate with essentially finite pulse. We call such approaches as a finite pulse approximation (FPA).

In this contribution we consider some particularities of generalized Breit-Wheeler and Compton processes in a short and strong laser pulses. For this purpose we use the widely employed the four electromagnetic (e.m.) potential for a circularly polarized laser field in the axial gauge $A^\mu = (0,\, \mathbf{A}(\phi))$ with

$$\mathbf{A}(\phi) = f(\phi)\left(\mathbf{a}_1 \cos(\phi + \tilde{\phi}) + \mathbf{a}_2 \sin(\phi + \tilde{\phi})\right) \,, \tag{1}$$

where $\phi = k \cdot x$ is invariant phase with four-wave vector $k = (\omega, \mathbf{k})$, obeying the null field property $k^2 = k \cdot k = 0$ (a dot between four-vectors indicates the Lorentz scalar product) implying $\omega = |\mathbf{k}|$, $\mathbf{a}_{(1,2)} \equiv \mathbf{a}_{(x,y)}$; $|\mathbf{a}_x|^2 = |\mathbf{a}_y|^2 = a^2$, $\mathbf{a}_x\mathbf{a}_y = 0$; transversality means $\mathbf{k}\mathbf{a}_{x,y} = 0$ in the present gauge. The envelope function $f(\phi)$ with $\lim\limits_{\phi\to\pm\infty} f(\phi) = 0$ accounts for the finite pulse length. We are going to analyze dependence of observables on the shape of $f(\phi)$ in Eq. (1) for two types of envelopes: the one-parameter hyperbolic secant (hs) shape and the two-parameter symmetrized Fermi (sF) shape widely used for parametrization of the nuclear density [**?**]: $f_{\rm hs}(\phi) = (\cosh\phi/\Delta)^{-1}$ and $f_{\rm sF}(\phi) = (\cosh\Delta/b + 1)(\cosh\Delta/b + \cosh\phi/b)^{-1}$. The parameter Δ characterizes the pulse duration 2Δ with $\Delta = \pi N$, where N has a meaning of a "number of oscillations" in the pulse. The parameter b in the sF shape describes the ramping time in the neighborhood of $\phi \sim \Delta$. Small values of ratio b/Δ cause a flat-top shaping. At $b/\Delta \to 0$, the sF shape becomes a rectangular pulse. In the following, we choose the ratio b/Δ as the second independent parameter for the sF envelope function. These two shapes cover a variety of relevant envelopes discussed in literature (for details see [18]). The carrier envelope phase $\tilde{\phi}$ is particularly important for the short the pulse duration with $N \leq 1$. Therefore we start our presentation with case of $\tilde{\phi} = 0$ and discuss impact of finite carrier phase at the end. Finally we note that, the interaction of the background field is determined by dimensionless reduced e.m. intensity $\xi^2 = \sqrt{-A^2}/M_e^2$, where M_e is the electron mass (we use natural units with $c = \hbar = 1$, $e^2/4\pi = \alpha \approx 1/137.036$). (for more detail see [17]).

Some important difference between IPA and FPA is that in the first case the variable $n = 1, 2, \cdots$ is integer, it refers to the contribution of the individual harmonics. The value $n\omega$ is related to the energy of the background field involved into considered quantum process. Obviously, this value is a multiple of ω. In FPA, the basic subprocess operate with l *background photons*, where l is a continuous variable. The quantity $l\omega$ can be considered as the energy partition of the laser beam involved into considered process, and it is not a multiple ω. Mindful of this fact, without loss of generality, we denote the processes with $l > 1$ as a generalized multi-photon processes, remembering that l is a continuous quantity.

This lecture is based on the review paper [17] and is organized as follows. Sect. 2 is devoted to the non-linear Breit-Wheeler process. In Sect. 3 we discuss several aspects of non-linear Compton scattering for short and sub-cycle pulses. Our conclusions are presented in Sect. 5.

2 The e^+e^- pair production in a finite pulse

We consider e^+e^- pair production in the interaction of a probe photon with a circularly polarized e.m.field (1 within the Furry picture, which diagrammatically is represented by a one-vertex graph, describing the decay of the probe photon with the four-momentum k' into a laser dressed e^+e^- pair. The presence of the background e.m. field is included in the Volkov solution of the outgoing e^+ and e^-. (In the weak-field approximation this graph turns into the known two two-vertex graphs for the perturbative Breit-Wheeler process). Contrary to the IPA, utilization of (1) the Volkov solutions in FPA assume all fermion momenta and masses take their vacuum values p and m, respectively, whereas the corresponding wave functions are modified in accordance with the Volkov solution [19, 20] (with more complicated compare to IPA, phase factor). The finite (in space-time) e.m. potential (1) for FPA requires the use of Fourier integrals for invariant amplitudes, instead of Fourier series which are employed in IPA. The partial harmonics become thus continuously in FPA. The S matrix element is expressed generically as

$$S_{fi} = \frac{-ie}{\sqrt{2p_0 2p_0' 2\omega'}} \int\limits_{\zeta}^{\infty} dl\, M_{fi}(l)(2\pi)^4\delta^4(k' + lk - p - p'), \tag{2}$$

where k, k', p and p' refer to the four-momenta of the background (laser) field (1), incoming probe photon, outgoing positron and electron, respectively, the low limit ζ is defined in Eq. (**??**). The transition matrix $M_{fi}(l)$ consists of four terms

$$M_{fi}(l) = \sum_{i=0}^{3} M^{(i)}\, C^{(i)}(l)\ , \tag{3}$$

where transition matrices M^i are determined by the Dirac structure in the amplitude (2) (cf. [17]), whereas the non-linear dynamics of pair production is determined by the functions $C^i(l)$ expressed trough the basic functions Y_l, X_l which are an analog of the Bessel functions

$$C^{(0)}(l) = \widetilde{Y}_l(z)\mathrm{e}^{il\phi_0},\ \widetilde{Y}_l(z) = \frac{z}{2l}\left(Y_{l+1}(z) + Y_{l-1}(z)\right) - \xi^2\frac{u}{u_l}\,X_l(z)'\ C^{(1)}(l) = X_l(z)\,\mathrm{e}^{il\phi_0},$$
$$C^{(2)}(l) = \frac{1}{2}\left(Y_{l+1}\mathrm{e}^{i(l+1)\phi_0} + Y_{l-1}\mathrm{e}^{i(l-1)\phi_0}\right),\ C^{(3)}(l) = \frac{1}{2i}\left(Y_{l+1}\mathrm{e}^{i(l+1)\phi_0} - Y_{l-1}\mathrm{e}^{i(l-1)\phi_0}\right) \tag{4}$$

with

$$Y_l(z) = \frac{1}{2\pi}\mathrm{e}^{-il\phi_0}\int\limits_{-\infty}^{\infty} d\phi\, f(\phi)\,\mathrm{e}^{il\phi - i\mathcal{P}(\phi)}\ ,\ X_l(z) = \frac{1}{2\pi}\mathrm{e}^{-il\phi_0}\int\limits_{-\infty}^{\infty} d\phi\, f^2(\phi)\,\mathrm{e}^{il\phi - i\mathcal{P}(\phi)}\ , \tag{5}$$

$$\mathcal{P}(\phi) = z\int\limits_{-\infty}^{\phi} d\phi'\,\cos(\phi' - \phi_0 + \tilde{\phi})f(\phi') - \xi^2\zeta u\int\limits_{-\infty}^{\phi} d\phi'\, f^2(\phi')\ . \tag{6}$$

The quantity z is related to ξ, l, and $u \equiv (k'\cdot k)^2/\left(4(k\cdot p)(k\cdot p')\right)$ via $z = 2l\xi\sqrt{\frac{u}{u_l}\left(1 - \frac{u}{u_l}\right)}$; with $u_l \equiv l/\zeta$. The phase ϕ_0 is equal to the azimuthal angle of the direction of flight of the outgoing electron in the e^+e^- pair rest frame $\phi_0 = \phi_{p'} \equiv \phi_e$. The quantity

$$\zeta = \frac{4M_e^2}{s} \tag{7}$$

is important variable for the generalized Breit-Wheeler process: $\zeta > 1$ or $\zeta < 1$ correspond to the above- and subthreshold- pair production, respectively. The later one is mainly described by by the multi-photon interactions.

The production probability is presented as the integral over the variables ϕ_e, u and l

$$W = \frac{\alpha m \zeta^{1/2}}{16\pi N_0} \int\limits_0^{2\pi_e} d\phi_e \int\limits_1^{\frac{l}{\zeta}} \frac{du}{u^{3/2}\sqrt{u-1}} \int\limits_\zeta^\infty dl \; w(l) \tag{8}$$

with $N_0 \simeq N$ and the partial probability

$$w(l) = 2\widetilde{Y}_l^2(z) + \xi^2(2u-1)\left(Y_{l-1}^2(z) + Y_{l+1}^2(z) - 2\widetilde{Y}_l(z)X_l^*(z)\right) \; . \tag{9}$$

2.1 Pair production at small field intensities ($\xi^2 \ll 1$)

In case of small $\xi^2 \ll 1$, implying $z < 1$, we decompose $l = n + \epsilon$, where n is the integer part of l, yielding

$$\begin{aligned} Y_l &\simeq \frac{1}{2\pi} \int\limits_{-\infty}^{\infty} d\psi \, \mathrm{e}^{il\psi - iz\sin\psi \, f(\psi+\phi_0)} f(\psi+\phi_0) \\ &= \frac{1}{2\pi} \int\limits_{-\infty}^{\infty} d\psi \sum_{m=0}^{\infty} \frac{(iz)^m}{m!} \sin^m\psi \, \mathrm{e}^{i(n+\epsilon)\psi} f^{m+1}(\psi+\phi_0) \; . \end{aligned} \tag{10}$$

Similarly, for the function $X_l(z)$ the substitution $f^{m+1} \to f^{m+2}$ applies. The dominant contribution to the integral in (10) with rapidly oscillating integrand comes from the term with $m = n$, which results in

$$Y_{n+\epsilon} \simeq \frac{z^n}{2^n n!} \, \mathrm{e}^{-i\epsilon\phi_0} F^{(n+1)}(\epsilon) \; , \qquad X_{n+\epsilon} \simeq \frac{z^n}{2^n n!} \, \mathrm{e}^{-i\epsilon\phi_0} F^{(n+2)}(\epsilon) \; , \tag{11}$$

where the function $F^{(n)}(\epsilon)$ is the Fourier transform of the function $f^n(\psi)$.

As an example, let us analyze the e^+e^- production near the threshold, i.e. $\zeta \sim 1$. In this case, the contribution with $n = 1$ is dominant and, therefore, the functions $Y_{0+\epsilon}$ are crucial, including the first term in (9). The functions $X_{0+\epsilon}$ are not important because they are multiplied by the small ξ^2 and may be omitted. Negative $\epsilon = \zeta - 1$ and positive ϵ correspond to the above- and sub-threshold pair production, respectively. The function $Y_{0+\epsilon}$ reads $Y_{0+\epsilon} = F^{(1)}(\epsilon)\exp[-i\phi_0\epsilon]$, where the Fourier transforms $F^{(1)}(x)$ for the hs and sF envelope decrease as a function of l in a different way $F_{\rm hs}(l) \sim \exp[-\frac{1}{2}\Delta l]$ and $F_{\rm sF}(l) \sim [-\pi b l]$ which is manifested in the spectra of e^+e^- pair production. The ϕ_0 dependence of the production probability disappears in this case because the latter one is determined by the quadratic terms of the Y functions. As we have seen the Fourier transform of the envelope function plays important role in shape and absolute value of the production probability. As an example, in Fig. 1 we show the total probability W of e^+e^- emission as a function of the sub-threshold parameter ζ in the vicinity $\zeta \sim 1$. The dashed and solid curves correspond to the hyperbolic secant and symmetrized Fermi envelope shapes, respectively. The left and right panels correspond to the short pulses with $\Delta = \pi N$ for $N = 2$, and 10, respectively, at $\xi^2 = 10^{-4}$. For comparison, we

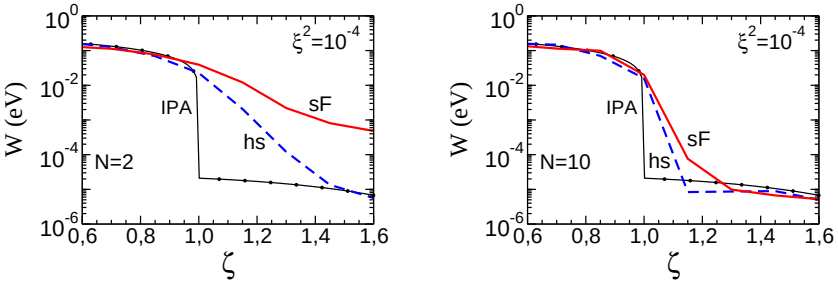


Figure 1: The total probability W of the e^+e^- pair production as a function of ζ for short pulses with $\Delta = \pi N$ for $N = 2$, and 10 shown in the left and right panels, respectively; $\xi^2 = 10^{-4}$. The dashed and solid curves correspond to the hyperbolic secant and symmetrized Fermi envelope shapes with $b/Delta = 0.1$, respectively. The thin solid curves marked by dots depict the IPA result.

present also the IPA results. Naturally, that in the above-threshold region, results of IPA and FPA are equal to each other. However, in the sub-threshold region, where ζ is close to integer numbers, the probability of FPA considerably exceeds (by more than two orders of magnitude) the corresponding IPA result. In the case of the hyperbolic secant envelope function, the probability increases with decreasing pulse duration. The results of FPA and IPA become comparable at $N \geq 10$. Qualitatively, this result is also valid for the case of the symmetrized Fermi distribution. However, in this case the enhancement of the probability in FPA is much greater. Other important details may be found in [18].

2.2 Effect of the finite carrier phase

It is naturally to expect that the effect of the finite carrier phase and appears in the azimuthal angle distribution of the outgoing electron (positron) in case of finite $\xi \sim 1$ and smooth envelope function with $N < 1$, because at this conditions the functions C^i are greatly enhanced [21]. As an example, in Fig. 2 (left panels) we show the differential cross section $d\sigma/d\phi_e$ of e^+e^- pair production as a function of the azimuthal angle ϕ_e for different values of the carrier envelope phase $\tilde{\phi}$ and for pulse durations $\Delta = N\pi$ with $N = 1$, and for $\xi^2 = 0.5$. The calculation is done for the essentially multi-photon region with $\zeta = 4$. The corresponding anisotropy of the electron (positron) emission defined as

$$\mathcal{A} = \frac{d\sigma(\phi_e) - d\sigma(\phi_e + \pi)}{d\sigma(\phi_e) + d\sigma(\phi_e + \pi)} , \tag{12}$$

are exhibited in Fig. 2 (right panels). One can see a strong dependence of the anisotropy as a function of CEP. The increase of the pulse duration leads to a decrease of the bump structure inn the differential cross sections and in absolute value of $\mathcal{A}$ and leads to the disappearance of the carrier phase effect.

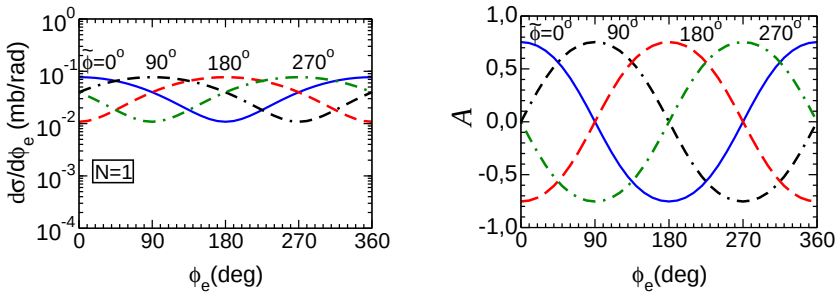


Figure 2: (Color online) Left column: The differential cross section as a function of the azimuthal angle of the direction of flight of the outgoing electron ϕ_e, for different values of the carrier phase $\tilde{\phi}$ and for $N = 1$. The solid, dash-dash-dotted, dashed and dash-dotted curves are for the CEP equal to 0, 90, 180 and 270 degrees, respectively. Right column: The anisotropy (12) for different values of $\tilde{\phi}$ as in left column. For $\xi^2 = 0.5$ and $\zeta = 4$.

2.3 Pair production at large field intensity ($\xi^2 \gg 1$)

At large values of $\xi^2 \gg 1$, the basic functions Y_l and X_l in Eq. (5) can be expressed as follows

$$Y_l = \int_{-\infty}^{\infty} dq\, F^{(1)}(q)\, G(l-q)\ , \qquad X_l = \int_{-\infty}^{\infty} dq\, F^{(2)}(q)\, G(l-q)\ , \tag{13}$$

where $F^{(1)}(q)$ and $F^{(2)}(q)$ are Fourier transforms of the functions $f(\phi)$ and $f^2(\phi)$, respectively, and $G(l)$ may be written as

$$G(l) = \frac{1}{2\pi} \int_{-\infty}^{\infty} d\phi\, \mathrm{e}^{i\left(l\phi - z\sin\phi + \xi^2\zeta u\phi\right)}\ . \tag{14}$$

In deriving this equation we have considered the following facts: (i) at large ξ^2 the probability is isotropic, therefore we put $\phi_0 = 0$, (ii) the dominant contribution to the rapidly oscillating exponent comes from the region $\phi \simeq 0$, where the difference of two large values $l\phi$ and $z\sin\phi$ is minimal, and therefore, one can decompose the last term in the function $\mathcal{P}(\phi)$ in (**??**) around $\phi = 0$, and (iii) replace in exponent $f(\phi)$ by $f(0) = 1$.

Equation (14) represent an asymptotic form of the Bessel functions $J_{\tilde{l}}(z)$ [22] with $\tilde{l} = l + \xi^2\zeta u$ at $\tilde{l} \gg 1$, $z \gg 1$, and therefore the following identities are valid

$$G(\tilde{l}-1) - G(\tilde{l}+1) = 2G'_z(\tilde{l}), \qquad G(\tilde{l}-1) + G(\tilde{l}+1) = 2\frac{\tilde{l}}{z}G(\tilde{l})\ , \tag{15}$$

which allow to express the partial probability $w(\tilde{l})$ in (9) as a sum of the diagonal (relative to $\tilde{l}$) terms: $Y^2_{\tilde{l}}$, $Y_{\tilde{l}}X_{\tilde{l}}$, $X^2_{\tilde{l}}$ and $Y'^2_{\tilde{l}}$. The integral over $\tilde{l}$ from the diagonal term can be expressed as

$$I_{YY} = \int_{\tilde{l}_0}^{\infty} d\tilde{l}\, Y_l^2 = \int dq\, dq'\, F^{(1)}(q)\, F^{(1)}(q') \int_{\tilde{l}_0}^{\infty} d\tilde{l} G(\tilde{l}-q)G(\tilde{l}-q')\ , \tag{16}$$

where $\tilde{l}_0 = \zeta(1+\xi^2 u$. Taking into account that for the rapidly oscillating G functions $G(l-q)G(l-q') \simeq \delta(q-q')G^2(l-q)$ and $\langle q\rangle \ll \langle l\rangle \ \sim \xi^2$ one gets

$$I_{YY} = \frac{1}{2\pi}\int\limits_{-\infty}^{\infty} d\phi f^2(\phi) \int\limits_{\tilde{l}_0}^{\infty} d\tilde{l} G^2(\tilde{l}) = N_{YY} \int\limits_{\tilde{l}_0}^{\infty} d\tilde{l} G^2(\tilde{l}) \ . \tag{17}$$

Similar expressions are valid for the other diagonal terms with own normalization factors. For the $X_{\tilde{l}}^2$ term it is $N_{XX} = \frac{1}{2\pi}\int\limits_{-\infty}^{\infty} d\phi f^4(\phi)$, and for $Y_{\tilde{l}}X_{\tilde{l}}$, $N_{YX} = \frac{1}{2\pi}\int\limits_{-\infty}^{\infty} d\phi f^3(\phi)$. At large ξ^2, the probability does not depend on the envelope shape, because only the central part of the envelope is important. Therefore, for simplicity, we choose the flat-top shape with $N_{YY} = N_{YX} = N_{XX} = N_0 = \Delta/\pi$ which is valid for any smooth (at $\phi \simeq 0$) envelopes.

Making a change of the variable $l \to \tilde{l} = l + \xi^2\zeta u$ the variable z takes the following form

$$z^2 = 4\xi^2\zeta^2\left(uu_l - u^2\right) = \frac{4\xi^2 l_0^2}{1+\xi^2}\left(uu_{\tilde{l}} - u^2\right) \tag{18}$$

with $l_0 = \zeta(1+\xi^2)$ and $u_{\tilde{l}} \equiv \tilde{l}/l_0$, that is exactly the same as the variable z in IPA with the substitution $l \to \tilde{l}$. All these transformations allow to express the total probability in a form similar to the probability in IPA for large values of ξ^2 and a large number of partial harmonics n, replacing the sum over n by an integral over n [16]

$$\begin{aligned} W &= \frac{1}{2}\alpha M_e \zeta^{1/2} \int\limits_{l_0}^{\infty} d\tilde{l} \int\limits_{1}^{u_{\tilde{l}}} \frac{du}{u^{3/2}\sqrt{u-1}} \{J_{\tilde{l}}^2(z) \\ &+ \xi^2(2u-1)[(\frac{\tilde{l}^2}{z^2}-1)J_{\tilde{l}}^2(z) + J'^2_{\tilde{l}}(z)]\} \ . \end{aligned} \tag{19}$$

Utilizing Watson's representation [22] for the Bessel functions at $\tilde{l}, z \gg 1$ and $\tilde{l} > z$, $J_{\tilde{l}}(z) = (2\pi\tilde{l}\tanh\alpha)^{-1/2}\exp[-\tilde{l}(\alpha - \tanh\alpha)]$ with $\cosh\alpha = \tilde{l}/z$, and employing a saddle point approximation in the integration in (19) we find the total probability of e^+e^- production as (for details see Appendix A of [17])

$$W = \frac{3}{8}\sqrt{\frac{3}{2}}\frac{\alpha M_e \xi}{\zeta^{1/2}}\, d\, \exp\left[-\frac{4\zeta}{3\xi}(1-\frac{1}{15\xi^2})\right], \ d = 1 + \frac{\xi}{6\zeta}\left(1+\frac{\xi}{8\zeta}\right) \ . \tag{20}$$

This expression resembles the production probability in IPA which is the consequence of the fact that, at $\xi^2 \gg 1$ in a short pulse, only the central part of the envelope at $\phi \simeq 0$ is important. In case of $\xi/\zeta << 1$, approximating $d = 1 + \mathcal{O}(\xi/\zeta)$, the leading order term recovers the Ritus result [16].

For completeness, in Fig. 3 (left panel) we present FPA results of a full numerical calculation for finite values of $\xi^2 \leq 10$ for the hyperbolic secant envelope shape with $N = 2$ (curves are marked by "stars") and the asymptotic probability calculated by Eq. (20) at $\zeta = 2$, 4 and 6, shown by solid, dashed and dot-dashed curves, respectively. The transition region between the two regimes is in the neighborhood of $\xi^2 \simeq 10$. In the right panel, we show the production probability at asymptotically large values of ξ^2 for $5 \leq \zeta \leq 20$. The exponential factor in (20) is most important at relatively low values of $\xi^2 \sim 10$ (large ζ/ξ). At extremely large values of ξ^2 (small ζ/ξ), the pre-exponential factor is dominant.

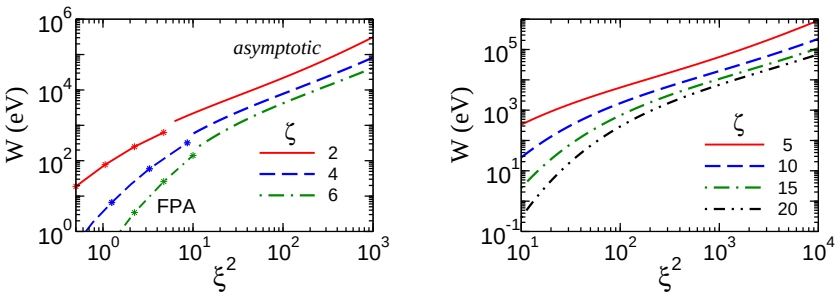


Figure 3: The total probability W of the e^+e^- pair production as a function of ξ^2 for various values of ζ. Left panel: Results of full numerical calculation in FPA for finite values of $\xi^2 \leq 10$ (curves marked by "stars" in "FPA" sections) and the asymptotic probability (20) for large values of ξ^2 (sections labeled by "asymptotic") at $\zeta = 2$, 4 and 6. Right panel: The asymptotic probability (20) for various values of ζ as indicated in the legend.

3 Compton scattering in short laser pulse

The Compton scattering process, symbolically $e^- + L \to e^{-\prime} + \gamma'$ is considered here as the spontaneous emission of one photon off an electron in an external e.m. field (1). Some important aspects of generalized Compton scattering were discussed elsewhere (for references see [17]). Being crossing to the Breit-Wheeler e^+e^- pair production the structure of the matrix elements and cross sections (production rates) of the both processes are the the same. The principle difference between them is absent the threshold behaviour of both processes. Thus, in Breit-Wheeler $\gamma' + \gamma \to e^+ + e^-$ one has a minimum value of the energy $\omega_{\min}(\gamma')$ of the probe photon γ' responsible for two electron mass production (at fixed "target" photon energy $\omega(\gamma)$). The processes with subthreshold energy $\omega' < \omega_{\min}$ or sub-threshold invariant variables $\zeta > 1$ are determined by the multi-photon dynamics. The Compton process $e^- + \gamma \to e^{-\prime} + \gamma'$ is always above threshold at any energy of incoming photon γ. Therefore extracting multi-photon interactions in such process is an incredibly difficult problem.

In [23] we suggested to use so-called partially integrated cross sections determined at fixed and large angle of outgoing photon $\theta' = 170^0$

$$\tilde{\sigma}(\omega') = \int\limits_{\omega'}^{\infty} d\bar{\omega}' \frac{d\sigma(\bar{\omega}')}{d\bar{\omega}'} = \int\limits_{l'}^{\infty} dl \frac{d\sigma(l)}{dl} \ , \tag{21}$$

where $d\sigma(\omega)/\omega$ is the Compton scattering involving l photons, while the lower limit of integration $l'(\omega_{\min})$ ir related to the four momentum of incoming electron $p(E, \mathbf{p})$ and laser frequency ω

$$l' = \frac{\omega'}{\omega} \frac{E + |\mathbf{p}| \cos\theta'}{E + |\mathbf{p}| - \omega'(1 - \cos\theta')} \ . \tag{22}$$

Experimentally, this can be realized by an absorptive medium which is transparent for frequencies above a certain threshold ω'. Otherwise, such a partially integrated spectrum can be synthesized from a completely measured spectrum. Admittedly, the considered range of energies with a spectral distribution uncovering many decades is experimentally challenging. Thus

the ratio $\omega'(l)/omega'(1)$ may be considered as a threshold parameter for the partly integrated Compron scattering. The partially integrated cross sections of Eq. (21) are presented in Fig. 4.

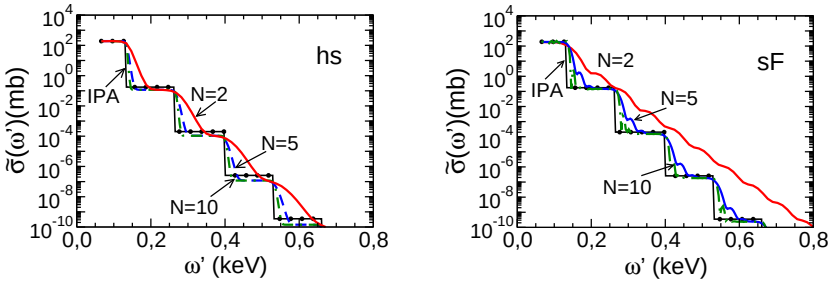


Figure 4: The partially integrated cross section (21) for $\xi^2 = 10^{-3}$. The thin solid curve marked by dots depicts the IPA result. The solid, dashed, and dot-dashed curves correspond to $N = 2$, 5 and 10, respectively. Left and right panels are for hyperbolic secant (hs) and symmetrized Fermi (sF) envelopes.

The thin solid curve (marked by dots) depicts results the photon emission in the infinite pulse (IPA) (cf. [23]). In this case the partially integrated cross section becomes a step-like function, where each new step corresponds to the contribution of a new (higher) harmonic n, which can be interpreted as n-laser photon process. Results for the finite pulse exhibited by solid, dashed, and dot-dashed curves correspond to $N = 2$, 5 and 10, respectively. In the above-threshold region with $\omega' \leq \omega'_1$, the cross sections do not depend on the widths and shapes of the envelopes, and the results of IPA and FPA coincide. The situation changes significantly in the deep sub-threshold region, where $\omega' > \omega'_1$ ($l \gg 1$), $n \gg 1$. For short pulses with $N \simeq 2$, the FPA results exceed that of IPA considerably, and the excess may reach several orders of magnitude, especially for the flat-top envelope shown by the solid curve in Fig. 4 (right panel). However, when the number of oscillation in a pulse increases ($N \gtrsim 10$) there is a qualitative convergence of FPA and IPA results, independently of the pulse shape. Thus, at $N = 10$ and $\omega' = 0.6$ keV the difference between predictions for hs and sF shapes is a factor of two, as compared with the difference of the few orders of magnitude at $N = 2$ for the same value of ω'.

4 Summary

In summary, we briefly discussed main aspects of multi-photon dynamics in two important OCD processes in intensive laser field: Breit-Wheeler e^+e^- pair production and single photon radiation in propagation of an electron thought the laser beam. More detailed description of these and related topics may be found in our review paper [17].

References

[1] G. A, Mourou, T Tajima, and S. V. Bulanov.// Rev. Mod. Phys. **78**, 309 (2006).

[2] A¿ Di Piazza, C. Müller, K. Z. Hatsagortsyan, and C. H. Keitel// Rev. Mod. Phys. **84**, 1177 (2012).

[3] V. Yanovsky, P. Rousseau, T. Planchon, T ,Matsuoka, A. Maksimchuk, J. Nees, G. Cheriaux, G. Mourou, K. Krushelnick.// Optics Express. **16**, 2109 (2008).

[4] `http://www.clf.stfc.ac.uk/CLF/.`

[5] `http://www.eli-beams.eu.`

[6] `http://www.hiper-laser.org.`

[7] `https://www.ipfran.ru/english/science/las_phys.html.`

[8] A. L. Cavalieri A, E. Goulielmakis, B. Horvath, W. Helml, M. Schultze, M. Fiess, V. Pervak, L. Veisz, V. S. Yakovlev, M. Uiberacker, A. Apolonski, F. Krausz, and R. Kienberger.// New J. Phys. **9**, 242 (2007).

[9] Z. Major, S. Klingebiel, C. Krobol, I. Ahmad, C. Wandt, S. A. Trushin, F. Krausz, and S. Karsch. Status of the Petawatt Field Synthesizer pump-seed synchronization measurements // AIP Conference Proceedings. **1228**, 117 (2010).

[10] F. Mackenroth, and A. Di Piazza Phys. Rev. A**83**, 032106 (2011).

[11] F. Feng, S. Gilbertson, H. Mashiko, Wang He, S. D. Khan, M. Chini, Wu Yi, K. Zhao, and Z. Chang. Phys. Rev. Lett. **103**, 183901 (2009).

[12] F. Krausz, and M. Ivanov. Rev. Mod. Phys. **81**, 163 2009.

[13] H. R. Reiss. J. Math. Phys. **3**, 59 (1962); Phys. Rev. Lett. **26**, 1072 (1971).

[14] A. I. Nikishov and V.‘I. Ritus. Sov. Phys. JETP. **16**, 529 (1964).

[15] N. V. Narozhny, A. I. Nikishov, and V. I. Ritus. Sov. Phys. JETP. **20**, 622 (1965).

[16] V. I. Ritus. J. Sov. Laser Res. (United States). **6:5**, 497 (1985).

[17] A. I. Titov, B. Kämpfer, A. Hosaka and H. Takabe. Phys. Part. Nucl. **47**, no. 3, 456 (2016).

[18] A. I. Titov, B. Kämpfer, H. Takabe, and A. Hosaka. Phys. Rev. Abf87, 042106 (2013).

[19] D. M. Volkov. // Z. Phys. **94**, 250 (1935).

[20] V. B. Berestetskii, E. M. Lifshitz , and L. P. Pitaevskii. *Quantum Electrodynamics*. 2nd ed., (Course of theoretical physics; vol. 4.) 1982. Oxford, New York, Pergamon Press Ltd.

[21] A. I. Titov, B. Kampfer, A. Hosaka, T. Nousch and D. Seipt.
Phys. Rev.D**93**, no. 4, 045010 (2016).

[22] G. N. Watson. *A Treatise of the Theory of Bessel Functions* (The University Press, Cambridge, 1944), 2nd ed.

[23] . A. I. Titov, B. Kmpfer, T. Shibata, A. Hosaka and H. Takabe. Eur. Phys. J. D**68**, 299 (2014).

Quantum regime of laser-matter interactions at extreme intensities

Alexander Fedotov

National Research Nuclear University MEPhI (Moscow Engineering Physics Institute), 115409 Kashirskoe sh. 31, Moscow, Russia

DOI: http://dx.doi.org/10.3204/DESY-PROC-2016-04/Fedetov

A survey of physical parameters and of a ladder of various regimes of laser-matter interactions at extreme intensities is given. Special emphases is made on three selected topics: (i) qualitative derivation of the scalings for probability rates of the basic processes; (ii) self-sustained cascades (which may dominate at the intensity levels attainable with next generation laser facilities); and (iii) possibility of breaking down the Intense Field QED approach for ultrarelativistic electrons and high-energy photons at certain intensity level.

1 Introduction

One of the notable trends of the last decades was unprecedented growth of laser power and intensity accessible for experimental research. As of now, the most striking progress was achieved in the (near-)optical range, which corresponds to a typical wavelength $\lambda \simeq 1\mu$m, frequency $\nu = c/\lambda \simeq 10^{15}$Hz and photon energy $\hbar\omega \simeq 1$eV. For the state-of-the-art facilities, pulse energy is typically $W_{\rm L} \simeq 0.1$kJ and pulse duration $\tau_{\rm L} \simeq 100$fs [1]. As a consequence, the *peak* laser power is huge,

$$P_{\rm L} = \frac{W_{\rm L}}{\tau_{\rm L}} \simeq \frac{10^2{\rm J}}{10^{-13}{\rm s}} = 10^{15}{\rm W} \equiv 1{\rm PW},$$

comparable to the net power produced by a large country. The *average* power, though, of course remains low due to a small repetition rate $\nu_{\rm R} \simeq 10^{-4} \div 10$ Hz. Assuming that the pulses are focused to diffraction limit, the expected peak intensity is estimated by (cf. [2]):

$$I_{\rm L} = \frac{P_{\rm L}}{R^2} \simeq \frac{P_{\rm L}}{\lambda^2} \simeq \frac{10^{15}{\rm W}}{(10^{-4}{\rm cm})^2} \simeq 10^{23}{\rm W/cm}^2.$$

Furthermore, the ongoing construction or upgrade at such facilities as CLF (UK), Apollon (France), PEARL (Russia), ELI Beamlines (Czech Republic), ELI-NP (Romania), EP-OPAL (USA), QiangGuang (China) and alike is very promising in attaining laser intensities of the order of 10^{24}W/cm^2 or even higher in the nearest future. Moreover, far-reaching exawatt-class facilities such as ELI [3] and XCELS [4] aiming at achieving the intensity $\gtrsim 10^{26}$ W/cm^2 are being also planned already. All this brings reasonable prospects on further advance of experimental studies of a variety of yet unexplored phenomena of laser-matter interactions at such extreme intensities.

[1] $1{\rm fs} \equiv 10^{-15}$s – such small durations became attainable after invention of Chirped Pulse Amplification [1].

2 Basic parameters and physical regimes

Let us discuss the key parameters of the theory, and the characteristic intensity levels corresponding to the various non-perturbative regimes of high-intensity laser-matter interaction to be compared to the experimentally accessed or expected values from the Introduction.

Perhaps the main element of the strong field approach is a concept of external (classical) background field $\mathcal{A}_\mu$. Obviously, this implies that the number of photons in relevant field modes is not changed essentially by absorption or scattering events, in particular is huge enough. Assuming ω is characteristic frequency and estimating laser pulse energy as $W_\mathrm{L} \simeq \frac{E^2+H^2}{8\pi} V \simeq \frac{E^2}{4\pi} V$, we arrive at $\bar{N}_\gamma \simeq W_\mathrm{L}/\hbar\omega \gg 1$, or $E \gg \sqrt{\hbar\omega/V} \gg 1$. This criterion is always satisfied in cases of either $\omega = 0$ (static field) or $V = \infty$ (infinitely extended field), but both are formally unphysical. For a tightly focused laser pulse we may assume $V \simeq \lambda^3$ which results in $E \gg \omega^2\sqrt{\hbar/c^2}$. Then the limitation on corresponding intensity reads $I_L = \frac{c}{4\pi}E^2 \gtrsim 10^5 \mathrm{W/cm}^2$ and is almost ever satisfied with huge margins (it is perhaps enough to mention that typically $\bar{N}_\gamma \simeq 10^{30}\mathrm{cm}^{-3}$), hence we adopt it wherever possible.

Another important and instructive example is a strong field concept in atomic physics. The atomic length (Bohr radius) and energy (Rydberg) are $l_\mathrm{at} = \hbar^2/Zme^2 = 5.3 \times 10^{-9}\mathrm{cm}$ and $\mathcal{E}_\mathrm{at} \simeq Ze^2/l_\mathrm{at} = mZ^2e^4/\hbar^4 \simeq 10\mathrm{eV}$, respectively (where the particular numbers are given for hydrogen with $Z = 1$). In this context the field can be considered 'strong' if the work it produces across the size of an atom $eEl_\mathrm{at} \gtrsim \mathcal{E}_\mathrm{at}$, resulting in $E \gtrsim E_\mathrm{at} \equiv Ze/l_\mathrm{at}^2 = m^2Z^3e^5/\hbar^4 = 5 \times 10^9 \mathrm{V/cm}$ and $I_\mathrm{L} \gtrsim \frac{c}{4\pi}E_\mathrm{at}^2 = 3 \times 10^{16}\mathrm{W/cm}^2$. For such laser intensities material targets are rapidly ionized, thus turning into plasma. Laser-plasma interactions are usually simulated with Particle-In-Cell (PIC) codes.

One of the most important parameters arises in a criterion of whether free electron motion driven by laser field is relativistic or not. Consider the classical equation of electron motion

$$\frac{d\vec{p}}{dt} = e\left(\vec{E} + \frac{\vec{v}}{c} \times \vec{H}\right). \tag{1}$$

From Eq. (1) the momentum of laser driven electron quiver oscillation can be estimated as $p_\perp \simeq eE/\omega$, hence the motion is relativistic if $a_0 \equiv p_\perp/mc \simeq eE/m\omega c \gtrsim 1$ (as in this case $\gamma \simeq a_0 \gtrsim 1$). This corresponds to $E \gtrsim E_\mathrm{rel} \equiv m\omega c/e$, or $I_\mathrm{L} \gtrsim \frac{c}{4\pi}E_\mathrm{rel}^2 \simeq 3 \times 10^{18}\mathrm{W/cm}^2$. The resulting dimensionless parameter a_0 admits a Lorentz- and gauge-invariant[2] definition for a plane wave field, $a_0 = \frac{e}{mc}\sqrt{-\mathcal{A}_\mu\mathcal{A}^\mu}$, and a number of alternative interpretations. For example, one point is that for $a_0 \gtrsim 1$ the equation of motion (1) also becomes essentially non-linear, thus leading e.g. to harmonic generation. Hence a_0 is often called the (dimensionless) classical nonlinearity parameter. Due to its importance, it is also often used in laser physics community to quantify the field strength and intensity (the latter via $a_0 \approx 6 \times 10^{-10}\lambda\,[\mu\mathrm{m}]\sqrt{I_\mathrm{L}[\mathrm{W/cm}^2]}$). In these terms the currently attained intensity level corresponds to $a_0 \simeq 10^2$.

Yet another interpretation arises in the framework of QED, where motion of an electron in a given external field $\mathcal{A}_\mu$ is described by a sum of diagrams shown in Fig. 1a. Here each vertex corresponds to the factor $-ie\gamma^\mu\mathcal{A}_\mu$, while each thin electron line (free propagator) to $iS_0 = \frac{1}{\gamma p - m} \simeq 1/m$. Hence, the expansion parameter of the QED perturbation theory is given by $e\mathcal{A}/m$, i.e. by the same parameter a_0 as above. In this context, $a_0 \gtrsim 1$ corresponds to non-perturbative (also often called multiphoton) with respect to $\mathcal{A}_\mu$ interaction regime. This can

[2] This is indeed invariant under gauge transformations $\delta A^\mu \propto k^\mu$ of a plane wave.

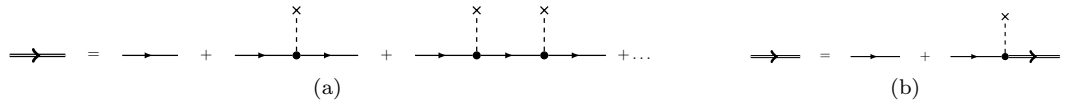


Figure 1: Exact propagator in external field (a) and a closed-form equation it obeys (b).

be understood in a pictorial way by noticing that in presence of a large number of background photons in the relevant field mode the interaction vertex weight ($\sim \sqrt{\alpha}$ in vacuum) should acquire an additional Bose factor $\sqrt{\bar{N}_\gamma(-1)} \approx \sqrt{\bar{N}_\gamma}$,

$$\sqrt{\alpha} \to \sqrt{\alpha} \times \sqrt{\bar{N}_\gamma} \simeq \sqrt{\alpha} \times \sqrt{l_C^2 \times \lambda \times \bar{n}_\gamma} \simeq \frac{e}{\sqrt{\hbar c}} \times \sqrt{\left(\frac{\hbar}{mc}\right)^2 \times \frac{2\pi c}{\omega} \times \frac{E^2}{4\pi\hbar\omega}} \simeq a_0, \qquad (2)$$

and hence is effectively replaced by a_0. Here we assumed that the electron probes the photons contained in an effective tubular interaction volume of Compton width $\simeq l_C = \hbar/mc$ around the classical electron trajectory of length λ. Note that $\hbar$ totally cancels, thus assuring that a_0, even though being an expansion parameter of QED perturbation theory, is nevertheless still of purely classical origin.

Since the focus of the rest of the paper is on laser-matter interactions at the high-power laser facilities, we always assume below that $a_0 \gg 1$. Under such condition all-orders summation with respect to interaction with external field should be done (see Fig. 1a). This is naturally done within the approach which I call the Intense Field QED (IFQED). Namely, it is easy to see that the 'exact' (with respect to interaction with external field), or 'dressed', electron propagator obeys the equation shown schematically in Fig. 1b. The rules for computation of the QED amplitudes are then formulated as in ordinary QED, but with free fermion lines and propagators replaced with the dressed ones. This approach was tested experimentally many times indirectly in atomic physics as well as directly in the late 90's famous E144 SLAC experiment [5, 6].

When laser intensity is further increasing, novel physical regimes should show up. For example, under the condition $a_{0i} = (Ze)E/M\omega c \gtrsim 1$, or $a_0 = eE/m\omega c \gtrsim M/Zm \simeq 2M_p/m \sim 4 \times 10^3$, the ions should also become relativistic. The corresponding intensity is $I_{\rm L} \gtrsim 5 \times 10^{25}{\rm W/cm}^2$ and is far beyond the currently attainable level. Another complication should show up at even lower intensities. Assuming $\gamma \simeq a_0$ and $E_\perp$, $H \simeq E$, the radiation reaction force

$$\vec{F}_{\rm rad} \simeq -\frac{2e^4 \left(\vec{E} + \frac{\vec{v}}{c} \times \vec{H}\right)_\perp^2 \gamma^2}{3m^2c^5}\vec{v}, \qquad (3)$$

acting on electron, becomes $\gtrsim eE$ for $E \gtrsim \left(m^4\omega^2c^6/e^5\right)^{1/3}$, or $a_0 \gtrsim \left(mc^3/e^2\omega\right)^{1/3} \simeq 400$, which corresponds to $I_{\rm L} \gtrsim 5 \times 10^{23}{\rm W/cm}^2$. In this regime one should account for classical radiation reaction in simulations of laser-matter interactions. Accounting for both effects requires just adequate correction of the developed PIC codes, and this is now indeed a hot topic in the laser physics community.

Self-action of an electron was at the focus of classical theory for decades and, as well known, was one of original motivations for invention of quantum theory. Besides radiation reaction force, it also implies existence of electromagnetic contribution into electron mass, classically of the order of $\mathcal{E}_{\rm em}(r_0) \simeq e^2/r_0$, where r_0 is the electron radius. In the limit of a pointlike electron

($r_0 \to 0$) this contribution diverges, but paradoxes appear in classical theory already when the mass correction $\mathcal{E}_{\rm em}(r_0) \gtrsim mc^2$, i.e. for $r_0 \lesssim r_e \equiv e^2/mc^2$ (r_e is called the 'classical electron radius'). The radiation reaction force (3) may produce across the distance r_e the work $\gtrsim mc^2$ if the field strength in a proper reference frame exceeds $E_{\rm P} \gtrsim E_{\rm cr} \equiv m^2c^4/e^3$. These conditions are considered as limits of applicability of Classical Electrodynamics.

Regime	$a_0 \ll 1$	$a_0 \gtrsim 1$
$\chi \ll 1$	classical non-relativistic	classical relativistic
$\chi \gtrsim 1$	perturbative QED	IFQED

(a)

$I_{\rm L}$[W/cm^2]	PHYSICAL REGIME
5×10^{29}(?)	Sauter-Schwinger QED critical field
5×10^{25}	Relativistic ions
2.5×10^{25}	Massive self-sustained QED cascades
10^{24}	Quantum radiation reaction, pair photoproduction ($\chi \gtrsim 1$)
5×10^{23}	Classical radiation reaction
5×10^{22}	*Mid'2010s state-of-the-art*
3×10^{18}	Relativistic electrons ($a_0 \gtrsim 1$)
3×10^{16}	Strong field of atomic physics (rapid ionization and plasma formation)
10^5	External (given classical background) field concept
$< 10^5$	Week field quantum regime

(b)

Table 1: Classification of physical regimes of laser-matter interactions according to the values of the key parameters a_0 and χ (a) and the ladder of various regimes successively attainable upon increasing laser intensity (b). Domain corresponding to quantum regime at extreme intensity is colored in gray.

However, things are quite different in quantum theory (QED), which introduces a novel Compton scale $l_{\rm C} = \hbar/mc \approx 137 r_e$. Even though electron still formally remains pointlike (as required by relativity), it turns out it cannot be localized at size smaller that $l_{\rm C}$ because of uncontrollable disturbance of vacuum (pair creation). For example, the average of the charge density operator in one-electron state is delocalized to a size $\simeq l_{\rm C}$. As a consequence, the divergency of electron self energy is partially canceled by contribution of vacuum virtual pairs and becomes much weaker, $\mathcal{E}_{\rm em}(r_0) \simeq (e^2/l_{\rm C}) \log(l_{\rm C}/r_0)$. In this sense, a pointlike charge is effectively replaced by a cloud of virtual pairs of size $\simeq l_{\rm C} = 1/m \simeq 4 \times 10^{-11}$cm. That is why we adopted the Compton length as the effective width of electron 'trajectory' in our above estimation (2). Unlike in Classical Electrodynamics, radiation reaction in QED can never outreach the Lorentz force (thus the known paradoxes of the former are avoided), however the work produced by the field across the distance $l_{\rm C}$ can still exceed the rest energy, $eE_{\rm S} l_{\rm C} \simeq mc^2$. The required field strength $E_{\rm S} \equiv m^2c^3/e\hbar = 1.3 \times 10^{16}$V/cm (note that $E_{\rm S} \simeq \frac{1}{137} E_{\rm cr}$) is called the Sauter-Schwinger, or QED critical field, and corresponds to laser intensity $I_{\rm L} = \frac{c}{4\pi} E_{\rm S}^2 \simeq 5 \times 10^{29}$W/cm^2, which is far beyond the capabilities of the existing or prospective laser facilities. Besides laser physics, the electric and magnetic[3] fields $\gtrsim E_{\rm S}$ may arise in heavy ion collisions, magnetic fields $H \simeq m^2c^3/e\hbar \simeq 4 \times 10^{13}$G are also anticipated around compact astrophysical objects (magnetars).

Since the electromagnetic field strengths are not Lorentz invariant, it may seem not obvious for which reference frame the condition E, $H \gtrsim E_{\rm S}$ should be formulated. In fact this criterion should be formulated in terms of Lorentz

[3]Since magnetic fields do not produce work, for them the criticality condition is formulated e.g. by demanding the principle Landau level to be relativistic.

invariants. For example, in absence of particles (i.e. in vacuum) the only field invariants are $E^2 - H^2 = -\frac{1}{2}F_{\mu\nu}F^{\mu\nu}$ and $\vec{E}\cdot\vec{H} = \frac{1}{8}\epsilon_{\mu\nu\lambda\varkappa}F^{\mu\nu}F^{\lambda\varkappa}$. In such a case the field strengths should actually exceed E_S in a reference frame, for which either electric or magnetic fields vanishes or they are parallel. However, in presence of a particle with 4-momentum p^μ one extra Lorentz invariant, usually called the dynamical quantum parameter, can be defined:

$$\chi = \frac{e\hbar}{m^3c^4}\sqrt{-(F_{\mu\nu}p^\nu)^2} = \frac{\gamma\sqrt{\left(\vec{E}+\frac{\vec{v}\times\vec{H}}{c}\right)^2 - \frac{(\vec{v}\cdot\vec{E})^2}{c^2}}}{E_\mathrm{S}}. \tag{4}$$

It actually acquires several equivalent native physical meanings, e.g. in case of electron a ratio of the electric field strength to E_S in its proper (rest) frame, or proper acceleration in Compton units. Typically, in the lab frame $E_\parallel \sim E_\perp$, where the components are denoted according to direction of particle momentum. Hence for ultrarelativistic particle $E_{\mathrm{P}\parallel} \sim E_\parallel$, $E_{\mathrm{P}\perp} \sim \gamma E_\perp \gg E_{\mathrm{P}\parallel}$ and $\chi = E_\mathrm{P}/E_\mathrm{S} \simeq \gamma E_\perp/E_\mathrm{S}$. Yet another interpretation stems from the fact that for radiating electron with $\chi \lesssim 1$ it is also the average emitted photon energy-to-electron energy ratio, hence the condition $\chi \gtrsim 1$ also indicates the significance of quantum recoil. The quantum regime of laser-matter interaction is naturally discriminated by[4] $\chi \gtrsim 1$.

Generally speaking, the introduced parameters $a_0 = eE/m\omega c$ (classical nonlinearity parameter) and $\chi \simeq \gamma E_\perp/E_\mathrm{S}$ (dynamical quantum parameter) are independent and allow for classification of various regimes of laser-matter interactions, see Table 1a. For instance, in SLAC experiment both $a_0, \chi \sim 1$. However, if the electrons are not accelerated by external sources but driven by the field then, assuming $E_\perp \sim E$ and $\gamma \sim a_0 \gg 1$, we arrive at $\chi \simeq (\hbar\omega/mc^2)a_0^2 \gtrsim 1$ for $a_0 \gtrsim \sqrt{mc^2/\hbar\omega} \simeq 700$. The required laser intensity in such case would be $I_\mathrm{L} \gtrsim 10^{24}\mathrm{W/cm}^2$. The list of various laser-matter interaction regimes discussed above, along with the required laser intensities, given relative to the present day state-of-the-art level, is summarized in Table 1b. Further details can be found in the reviews [7–9].

3 Qualitative analysis of basic IFQED processes

Within the framework of IFQED approach, calculation of probabilities of a process is reduced to calculation of diagrams with 'exact', or 'dressed' electron external lines and propagators (see Fig. 1a), determined by equation in Fig. 1b. The latter equation can be solved exactly for just a few particular external field backgrounds (e.g. constant field, plane wave, Coulomb field), but even when it admits exact solution, application of the method usually results in extremely bulky intermediate calculations [10]. But as a rule, qualitative considerations may result in a deeper insight into the problem. Here I am going to demonstrate how at least some of the known asymptotic expressions for probability rates of basic QED processes in strong external field could receive a simple-man derivation, based exclusively on kinematical and dimensional arguments together with the uncertainty principle (see [11] for a more detailed presentation).

In presence of external field the QED processes can be subdivided into field-modified (i.e. those which occur even in absence of the field) and field-induced. Let us focus below on the field-induced processes only. The diagrams for the basic processes of this kind, single photon emission

[4] It should be stressed that the quantum regime of interaction with *strong external classical background* under discussion arises due to recoil in essentially multiphoton radiation processes (e.g. hard photon emission), as opposed to the (completely different!) *week field quantum regime* on bottom of Table 1b, where quantum effects arise due to absorption or emission of individual laser photons.



Figure 2: Basic IFQED processes: photon emission (a) and pair photoproduction (b).

and pair photoproduction, are shown in Fig. 2. For such sort of processes we can introduce the energy lack $\Delta\varepsilon = \sum \varepsilon_f - \sum \varepsilon_i > 0$ (where the indices refer to final and initial particles) and a couple of characteristic time scales, the first one (t_e) is the time it takes for the field to provide the amount of work required for a process to occur (symbolically, $e\int_0^{t_e} \vec{E}\cdot d\vec{s} \simeq \Delta\varepsilon$), and the second one ($t_q \simeq 1/\Delta\varepsilon$) is the time for which according to the uncertainty principle the final state can endure as a virtual one. As we will shortly observe, it turns out that in a relativistically strong laser field of our interest ($a_0 \gg 1$) both these timescales are much smaller than the laser period $\sim 1/\omega$, hence the laser field can be considered as *locally constant*. In addition, we also assume whenever possible that the particles are ultrarelativistic and moving transversely with respect to the field, in such a case the field can be also considered *crossed* ($\vec{E} \perp \vec{H}$ and $E = H$), and the total probabilities depend exclusively on the quantum dynamical parameter(s) χ_i. Furthermore, since *any* field is all the same equivalent to a constant crossed field, we can replace it e.g. with the constant purely electric field directed orthogonally to the momentum of the initial particle. Then, by picking up the time gauge $\vec{A}(t) = -\vec{E}t$, the energies of the charged particles can be written as $\varepsilon_{\vec{p}}(t) = [(\vec{p} - e\vec{A}(t))^2 + m^2]^{1/2}$.

Obviously, if $t_e \gg t_q$ then the process is (quasi-)classical, in particular its probability should be exponentially suppressed. The probability of the process under such conditions can be estimated by the quasiclassical 'imaginary time' technique,

$$W_{i\to f} \propto \left|\exp\left\{-\int_0^{t_*} \Delta\varepsilon(it')\,dt'\right\}\right|^2, \tag{5}$$

where t_* is determined by the conditions of energy-momentum conservation $\Delta\varepsilon(it_*) = 0$, $\Delta\vec{p} = 0$. It turns out that typically $t_* \simeq t_e$, so that $W_{i\to f} = \mathcal{O}(e^{-t_e/t_q})$. If, on the contrary, $t_e \ll t_q$, then the process is essentially quantum and unsuppressed.

Let us first demonstrate how the scheme works using a popular example of electron-positron pair creation from vacuum. For this case $\Delta\varepsilon = 2m$, $t_e \simeq m/eE$ and $t_q \simeq 1/m$. Note that for $a_0 \gg 1$ we have $t_e = 1/\omega a_0 \ll 1/\omega$, thus the locally constant field approximation should work. For $E \ll E_S = m^2/e$ we have $t_e \gg t_q$, so that the process should be suppressed. The expected suppression factor is $e^{-t_e/t_q} \simeq e^{-E_S/E}$. More precisely, assuming[5] (for the sake of simplicity only) $\vec{p}_\perp = 0$ we obtain: $\Delta\varepsilon(t) = 2\sqrt{m^2 + e^2E^2t^2}$, $\Delta\varepsilon(it_*) = 0$, $t_* = m/eE = t_e$ (as announced above), and

$$W_{e^-e^+} = \left|\exp\left\{-2\int_0^{m/eE} \sqrt{m^2 - e^2E^2t'^2}\,dt'\right\}\right|^2 = e^{-\pi m^2/eE}, \tag{6}$$

[5]Here $\vec{p}_\perp$ denotes the component of the momentum which is orthogonal to the field.

in perfect agreement with the exact result of Sauter, Heisenberg-Euler, Schwinger and others.

As a second illustration, consider pair photoproduction by a hard photon (see Fig. 2b). For this case, the energy lack can be written as

$$\Delta\varepsilon(t) = \varepsilon_{\vec{p}'}(t) + \varepsilon_{\vec{p}}(t) - k \approx \sqrt{(k-p)^2 + e^2E^2t^2 + m^2} + \sqrt{p^2 + e^2E^2t^2 + m^2} - k \approx$$
$$\approx k - p + \frac{e^2E^2t^2 + m^2}{2(k-p)} + p + \frac{e^2E^2t^2 + m^2}{2p} - k = \frac{k\left(e^2E^2t^2 + m^2\right)}{2p(k-p)} \gtrsim \frac{2\left(e^2E^2t^2 + m^2\right)}{k}, \tag{7}$$

where the minimum is attained for $p = p' = k/2$. In the weak field limit the second term in the numerator (m^2) should dominate over the first term ($e^2E^2t^2$) so that $\Delta\varepsilon \simeq m^2/k$. It is well known that for ultrarelativistic kinematics $\theta, \vartheta \simeq m/k \ll 1$. Hence the characteristic scales

$$t_q \simeq 1/\Delta\varepsilon \simeq k/m^2 \ll t_e \simeq \Delta\varepsilon/eE\vartheta \simeq m/eE,$$

if the dynamical quantum parameter of the initial hard photon $\varkappa = \frac{eEk}{m^3} \lesssim 1$. According to the above in such a regime we expect that $W_{e^-e^+} = \mathcal{O}(e^{-1/\varkappa})$. Indeed, looking for a stationary point we obtain $\Delta\varepsilon(it_*) = 2\left(-e^2E^2t_*^2 + m^2\right)/k = 0$, $t_* = m/eE = t_e$, and

$$W_{e^-e^+} = \left|\exp\left(-\int_0^{m/eE} \frac{2\left(-e^2E^2t^2 + m^2\right)}{k}\, dt\right)\right|^2 = \left|e^{-4m^3/3eEk}\right|^2 = e^{-8/3\varkappa}. \tag{8}$$

This is again in accordance with exact computations, but [unlike Eq. (6)] we are unaware of other simple-man derivations of this result in previous literature.

In the opposite (quantum, $\varkappa \gg 1$) strong field limit, according to Eq. (7), $\Delta\varepsilon(t) \simeq e^2E^2t^2/k$ and angular spread arises mostly due to contortion of electron and positron trajectories by the field, $\theta(t), \vartheta(t) \simeq eEt/k \ll 1$. Hence $eE\vartheta(t)t \simeq \Delta\varepsilon(t)$ identically, i.e. t_e is not fixed but arbitrary. At the same time, from its definition $t_q \simeq 1/\Delta\varepsilon(t_q) \simeq k/e^2E^2t_q^2$ we obtain

$$t_q \simeq \left(\frac{k}{e^2E^2}\right)^{1/3} \equiv \frac{m}{eE}\varkappa^{1/3} \equiv \frac{k}{m^2\varkappa^{2/3}}. \tag{9}$$

Hence, for $\varkappa \gg 1$ having just a single time scale parameter t_q, on dimensional grounds we have

$$W_{e^-e^+}(\varkappa \gg 1) \simeq \frac{e^2}{t_q} \sim \frac{e^2m^2}{k}\varkappa^{2/3}, \quad W_\gamma(\chi \gg 1) \simeq \frac{e^2m^2}{p}\chi^{2/3}, \tag{10}$$

where the second formula gives the probability W_γ of hard photon emission by electron (see Fig. 2a) for $\chi \gg 1$, as ultrarelativistic kinematics for both processes is exactly the same as soon as electron mass is neglected. These results are (up to numerical factor ~ 1) also in perfect agreement with exact calculations.

4 Self-sustained QED cascades

In case seed particle in a strong field has $\chi \gtrsim 1$, it can emit photons with $\varkappa \sim 1$, which are in turn capable for pair photoproduction. In such a case these events may follow one by one, thus forming a chain called a QED cascade. In principle, this is very similar to the

Property	QED cascades in external field	
	S(hower)-type	A(valanche)-type
Energy source	energy ε_0 of seed particle	external field (donates energy by particles acceleration)
Multiplicity $N_{e^-e^+}$	limited by ε_0	exponentially increases ($\propto e^{\Gamma t}$), potentially up to macroscopic value
Proceeds until...	...secondary particles lose energy and χ	• ...particles escape (?); • ...field depletion (?); • ...thermolization (?);
Similar to:	Extensive Air Showers	gas or dielectric discharge

Table 2: S(hower)-type *vs.* A(valanche)-type QED cascades in external field.

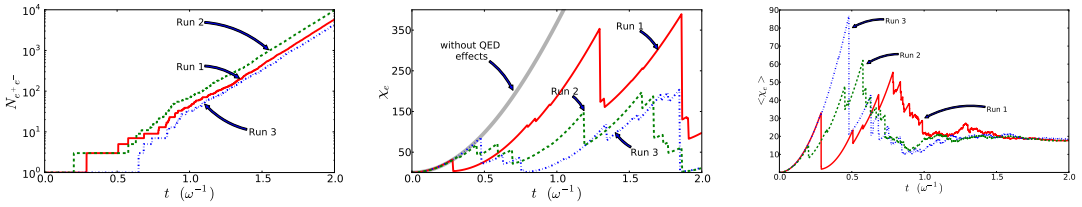
familiar cascades generated by high energy particles in matter due to Bremsstrahlung and pair photoproduction on nuclei (e.g., as in Extensive Air Showers). However, a novel distinctive feature for cascades in a strong laser field is that such a field may not serve only a target, but in general is also capable for acceleration of charged particles, thus donating them energy and making the cascade self-sustained. The principle differences between these two types of cascades (which we abbreviate S- and A-type [12]) are summarized in Table 2. Here our point is that production of A-type cascades starting from a certain intensity level may dominate in laser-matter interactions resulting in creation of macroscopic amount of pairs and hard photons, as shown in Table 1b, thus totally changing the landscape of laser-matter interactions [13]. Moreover, since this process (at least in most probable scenarios) leads to depletion of external field, it can also prevent practical attainability of the Sauter-Schwinger critical field with optical lasers [14] (this point is indicated in Table 1b by a question mark).

During the process of hard photon emission or pair photoproduction the values of energy ε and dynamical quantum parameter χ of a parental particle are partitioned among the secondary ones. As stressed above, the main distinctive feature of a self-sustained (A-type) cascade against the ordinary S-type cascade is the 'acceleration stage' where these ε and even more importantly χ are then restored back by the field before the next QED event takes place. In contrast to consideration of a QED process itself, at this stage the difference between the actual field and a constant crossed one should be necessarily taken into account (that is why we call our constant and crossed field approximation *local*), as otherwise χ would be conserved exactly. At the same time, motion of ultrarelativistic particles in between the QED events may be still considered classically[6]. Concerning a problem of ε and χ evolution along a particle trajectory in a generic field configuration, a non-trivial result is that (apart from a few artificial particular cases, e.g. linearly polarized purely electric field or a running plane wave field) for an initially slow particle at time scales $m/eE \ll t \ll 1/\omega$ we always have

$$\varepsilon(t) = m\gamma(t) \simeq eEt, \quad E_\perp(t) \simeq E\omega t, \quad \chi(t) \simeq \frac{E_\perp(t)}{E_\mathrm{S}}\gamma(t) \simeq \frac{mc^2}{\hbar\omega}\left(\frac{E}{E_\mathrm{S}}\right)^2 (\omega t)^2. \tag{11}$$

Hence it takes for such a particle $t_\mathrm{acc} \simeq \alpha E_\mathrm{S}/\omega E$ to gain $\chi \sim 1$, where for illustration purpose

[6] It turns out that motion in a constant crossed field is classical exactly. In a general setting, for a subcritical ($E \ll E_\mathrm{S}$) electric field quasiclassical approximation breaks down only near the turning points, where particles are slow. Ultrarelativistic motion in a subcritical magnetic field is also classical since particle occupies high Landau levels.



(a) (b) (c)

Figure 3: Simulation campaign of QED cascade generation: evolution of cascade multiplicity (a); parameter χ of the seed electron (b); and parameter χ averaged over the cascade (c) for three independent Monte Carlo runs @$a_0 = 2 \times 10^3$ (from [16]).

we have skipped the accidental dimensionless factor $\sqrt{\alpha^2 mc^2/\hbar\omega} \simeq 4.5$ (square root of Rydberg in eV's).

On the other hand, by combining Eq. (10) with Eq. (11) and the definition $t_e \simeq 1/W_\gamma(\chi(t_e))$ for a free path time (i.e. typical time between the QED events), in the same manner we obtain

$$t_e \simeq \frac{1}{\omega}\left(\frac{\alpha E_S}{E}\right)^{1/4}, \quad \chi(t_e) \simeq \left(\frac{E}{\alpha E_S}\right)^{3/2}. \tag{12}$$

Obviously, for $E \gtrsim \alpha E_S$ (or $I \gtrsim \alpha^2 I_S \sim 2.5 \times 10^{25}\mathrm{W/cm}^2$) the time scales hierarchy $t_{acc} \ll t_e \ll 1/\omega$ is established, meaning that (i) photons are mostly emitted when $\chi \sim 1$ and hence are capable for subsequent photoproduction; and (ii) a plenty of QED events should happen on a time scale $1/\omega$ of the laser field. These are exactly the conditions singling out a QED cascade. Since due to acceleration the parameters of the particles in each generation remain the same on average, the cascade multiplicity should grow exponentially $N_{e^-e^+} \simeq e^{\Gamma t}$. This qualitative picture is fully supported by Monte Carlo simulations [15–17], see Fig. 3. In particular, one can observe in Fig. 3c how the average parameter χ tends to a definitive value, which is in fact in fairly good agreement with the estimate (12). The same agreement was observed for other relevant quantities, including the increment $\Gamma \simeq 1/t_e$.

The final stage of a self-sustained (A-type) cascade still remains poorly understood. For laser power 10PW (i.e. intensities $\sim 10^{24}\mathrm{W/cm}^2$ and tight focusing) the duration of exponential growth of cascade multiplicity is restricted either by driving laser pulse duration or by particles escape from the focal region. However, for higher power (either higher intensity or weaker focusing) it was demonstrated that cascade multiplicity may rapidly become macroscopic [17,18]. When the density of created pairs exceeds the relativistic critical plasma density, the arising electron-positron plasma starts depleting the driving laser field. However, in an alternative scenario at high density the electron-positron-photon plasma may come to (quasi-)equilibrium due to various relaxation processes. Such processes, however, as of now remain almost unexplored.

5 Radiation corrections and IFQED approach breakdown

In ordinary QED, the running coupling constant $\alpha(\varepsilon \gg m) \simeq \mathcal{E}_{em}(\varepsilon)/m \simeq \alpha \log(\varepsilon/m)$ remains small within the whole reasonable region of energy (in particular, up to the Electroweak Theory energy scale), hence perturbation theory always works pretty well. However, as was noticed

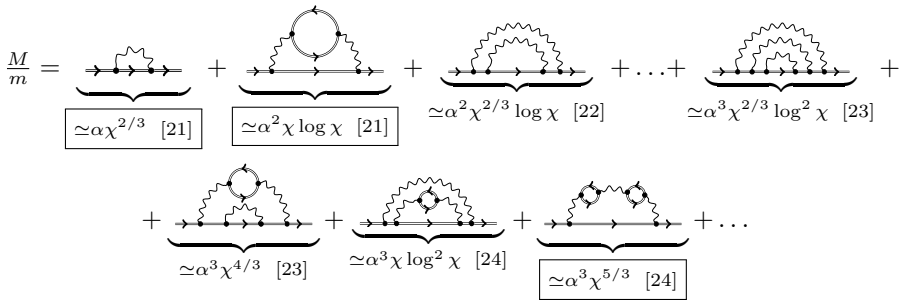


Figure 4: Some 2nd and 4th order radiation corrections to electron mass operator M computed or estimated by the Ritus group in 1972-1980. The key results are enclosed in boxes.

already soon after the very birth of IFQED approach [19, 20], the leading order contributions to the mass and polarization operators within IFQED are growing surprisingly fast with χ or $\varkappa$ (i.e. with both energy and field strength):

$$M^{(2)}(\chi \gg 1) \simeq \alpha m \chi^{2/3}, \quad \mathcal{P}^{(2)}(\varkappa \gg 1) \simeq \alpha m^2 \varkappa^{2/3}. \tag{13}$$

This can be easily traced back to Eqs. (10) via the optical theorem, and implies that for χ, $\varkappa \gtrsim \alpha^{-3/2} \simeq 1.6 \times 10^3$ the radiation corrections cease to be small, $M^{(2)} \simeq m$, $\mathcal{P}^{(2)} \simeq m^2$. In addition, in a proper reference frame

$$t_\mathrm{e} \sim W_\gamma^{-1} \simeq t_\mathrm{C}, \quad t_\gamma \sim W_{e^+e^-}^{-1} \simeq t_\mathrm{C}, \tag{14}$$

meaning that the concept of radiation-free motion, obviously underlying the IFQED approach, could show up only at Compton scale, where localization is all the same impossible. If so, this should blow up the approach, thus making IFQED a truly non-perturbative theory like QCD.

Systematic analysis of the actual expansion parameter of IFQED perturbation theory was undertaken by the Ritus group [21, 22], and especially by Narozhny [23, 24], see Fig. 4. By comparing 2-nd and 4-th order contributions to the mass operator it was initially conjectured that the expansion parameter is $M^{(4)}/M^{(2)} \simeq \alpha\chi^{1/3}$. However, further estimation of the 6-th order contributions identified $M^{(6)}/M^{(4)} \simeq \alpha\chi^{2/3}$ as the true expansion parameter. This conclusion is consistent with the also known data for polarization and vertex operators (not shown here for brevity). Origination of both parameters can be easily understood in terms of the qualitative approach of Sec. 3 [25]. Indeed, the estimations (9), (10) were based exclusively on the uncertainty principle and thus are valid for virtual processes as well. In a proper reference frame the characteristic longitudinal and transverse sizes of a vacuum polarization[7] loop are estimated by $l_{\parallel,\mathrm{P}} \simeq (m/k)t_q \simeq l_\mathrm{C}\varkappa^{-2/3}$, $l_{\perp,\mathrm{P}} \simeq \vartheta t_q \simeq eEt_q^2/k \simeq l_\mathrm{C}\varkappa^{-1/3}$. Interestingly, for $\varkappa \gg 1$ both sizes turn out to be smaller than l_C and moreover that $l_{\parallel,\mathrm{P}} \sim r_e$ (classical electron radius!) for $\alpha\varkappa^{2/3} \sim 1$. Now the aforementioned expansion parameters can be revealed exactly as in ordinary QED as Coulomb to rest energy ratios $(e^2/l)/m$ for transverse ($l = l_{\perp,\mathrm{P}}$) and longitudinal ($l = l_{\parallel,\mathrm{P}}$) loop sizes, respectively. On the grounds of the optical theorem there might be also a tight relation between the higher-order radiation corrections and cascades (since

[7] Estimations for self energy are exactly the same because ultrarelativistic kinematics is similar for both cases.

cutting the former diagrams leads to the latter ones). However, for self-sustained cascades due to the scaling (12) we have always $\alpha\chi^{2/3} \simeq E/E_S \lesssim 1$ in a view of critical field unattainability due to field depletion via cascades seeded by spontaneous pair production [14]. Still, as pointed out above, one can attain $\alpha\chi^{2/3} \gtrsim 1$ by using an external accelerator. In fact this condition is not as exotic as one could imagine but rather is almost realizable e.g. by colliding a bunch of TeV electrons with the presently available laser pulses.

Unfortunately, in spite of obvious urgency and importance of further development of these considerations, I am not aware of any progress since the beginning of 80's.

Acknowledgments

I am grateful to the organizers of the Helmholtz International Summer School "QFT at the Limits: from Strong Fields to Heavy Quarks" (JINR, Dubna, 2016) for inviting me to give this lecture, and to D. Blaschke, S.A. Smolyansky, A.I. Titov, A. Ilderton, T. Heinzl and A.A. Mironov for fruitful comments and inspiring discussions. The work was supported by RFBR grant 16-02-00963a.

References

[1] D. Strickland and G. Mourou, Opt. comm. **56** 219 (1985).
[2] V. Yanovsky *et al*, Optics Express **16** 2109 (2008).
[3] `www.eli-laser.eu`.
[4] `www.xcels.iapras.ru`.
[5] D.L. Burke *et al*, Phys. Rev. Lett. **79** 1626 (1997).
[6] C. Bamber *et al*, Phys. Rev. **D60** 092004 (1999).
[7] G.A. Mourou, T. Tajima, S.V. Bulanov, Rev. Mod. Phys. **78** 309 (2006).
[8] A. Di Piazza, C. Müller, K.Z. Hatsagortsyan, and C.H. Keitel, Rev. Mod. Phys. **84** 1177 (2012).
[9] N.B. Narozhny, A.M. Fedotov, Contemp. Phys. **56** 249 (2015).
[10] V.I. Ritus, Journ. Soviet Laser Research **6** 497 (1985).
[11] A.M. Fedotov, arXiv:1507.08512 (2015).
[12] A.A. Mironov, N.B. Narozhny, A.M. Fedotov, Phys. Lett. **A378** 3254 (2014)
[13] N.B. Narozhny, A.M. Fedotov, Eur. Phys. Journ. ST **223**, 1083 (2014).
[14] A.M. Fedotov, N.B. Narozhny, G. Mourou, G. Korn, Phys. Rev. Lett. **105** 080402 (2010).
[15] M.V. Legkov, A.M. Fedotov, N. Elkina, H. Ruhl, Proc. SPIE **7994** 799423 (2010).
[16] N.V. Elkina *et al*, Phys. Rev. STAB **14** 054401 (2011).
[17] T. Grismayer *et al*, Phys. Plasmas **23**, 056706 (2016).
[18] E.N. Nerush *et al*, Phys. Rev. Lett. **106** 035001 (2011).
[19] N.B. Narozhny, Sov. Phys. JETP **28** 371 (1969).
[20] V.I. Ritus, Sov. Phys. JETP **30** 1181 (1970).
[21] V.I. Ritus, Ann. Phys. **69** 555 (1972).
[22] D.A. Morozov, V.I. Ritus, Nucl. Phys. **B 86** 309 (1975).
[23] N.B. Narozhny, Phys. Rev. **D20** 1313 (1979).
[24] N.B. Narozhny, Phys. Rev. **D21** 1176 (1980).
[25] A.M. Fedotov, arXiv:1608.02261 (2016).

Time scales of thermalization of a strongly interacting non-Abelian plasma

L. Bellantuono[a,b], *P. Colangelo*[a], *F. De Fazio*[a], *F. Giannuzzi*[a] *and S. Nicotri*[a]

[a]Istituto Nazionale di Fisica Nucleare, Sezione di Bari, Italy
[b]Dipartimento di Fisica, Universitá degli Studi di Bari, Italy

DOI: http://dx.doi.org/10.3204/DESY-PROC-2016-04/Colangelo

We use gauge/gravity duality to investigate the thermalization of a strongly interacting plasma, taken out-of-equilibrium by boundary quenching. In particular, we show how information can be obtained from local and nonlocal observables, in particular concerning the time scales of thermalization.

1 Introduction

There are experimental evidences that the plasma produced in ultrarelativistic heavy ion collisions at RHIC and LHC is a realization of a strongly coupled deconfined phase of QCD. It behaves as a perfect fluid, with a small viscosity to entropy density ratio $\eta/s \sim \mathcal{O}(0.1)$, at odds with perturbative QCD which predicts larger values for η/s. The out-of-equilibrium configuration lasts for a short time, $\mathcal{O}(1$ fm/c), followed by a hydrodynamic evolution [1]. The description of the early-time out-of-equilibrium dynamics is a challenging task, which can be faced by holographic methods. Indeed, using gauge/gravity duality [2], the equilibration problem of the $4d$ strongly interacting non-Abelian system can be mapped into a gravity problem in a $5d$ space-time [3]. [1]

In the gauge/gravity duality framework, thermalization in the boundary gauge theory occurs in correspondence to the formation of a black brane in the higher dimensional space. The equilibration can be monitored through the boundary stress-energy tensor T^μ_ν. For a plasma behaving like a perfect fluid the T^μ_ν components obey the Bjorken relations [5]. Within the AdS/CFT correspondence, the dual of the boundary stress-energy tensor is the bulk metric. In particular, the dual of $T_{\mu\nu}$ fulfilling Bjorken hydrodynamics is identified as a black brane metric with time-dependent horizon [6]. In general cases, to determine $T_{\mu\nu}$ one has to solve the bulk Einstein equation, subject to appropriate initial and boundary conditions, and the components of the boundary stress-energy tensor are obtained from of the coefficients of the near-boundary expansion of the gravity metric, by the holographic renormalization procedure [7]. This approach has been applied within different contexts [8].

In Refs. [9] it has been proposed to study thermalization of a strongly coupled plasma after a distortion of the boundary metric (a "quench"), to mimic a perturbation driving the system out-of-equilibrium. The response depends on the profile of the quench, which is expected also considering the nonlinear nature of the dual gravity problem: this motivated a dedicated

[1] Ref. [4] contains a review of applications of holographic methods to the heavy ion collision phenomenology.

investigation of different quenches [10], to assess universal features in the time dependence of the components of $T_{\mu\nu}$. Moreover, it was possible to establish a hierarchy of the thermalization times at different length scales in the system [11], studying nonlocal observables and their time evolution, as proposed in [12]. We shall describe the results from two-point correlation function of operators defined in the boundary theory, and from the expectation values of Wilson loops defined on the boundary. Nonlocal probes have also been scrutinized in other contexts [13].

2 Thermalization by boundary sourcing: results from local probes

To study the thermalization of a boost-invariant non-Abelian plasma one can make use of boundary sourcing, to mimic the way the system is driven out-of-equilibrium [9]. In [10] different kinds of quenches in the boundary metric where scrutinized, monitoring the stress-energy tensor of the boundary theory. The tensor is written as $T^\mu_\nu = \frac{N_c^2}{2\pi^2}\, diag(-\epsilon, p_\perp, p_\perp, p_\parallel)$, with components the system energy density ϵ, the pressure $p_\perp$ along one of the two transverse directions (with respect, e.g., to the heavy ion collision axis) and the pressure $p_\parallel$ in the longitudinal direction.[2] The $4d$ boundary coordinates are denoted as $x^\mu = (x^0, x^1, x^2, x^3)$, and the $x^3 = x_\parallel$ direction is identified with the collision axis along which the plasma is supposed to expand. Boost-invariance along this axis, as well as translational and $O(2)$ rotational invariances in the transverse plane $x_\perp = \{x^1, x^2\}$ are assumed. In terms of the proper time τ and the spacetime rapidity y, defined through the relations $x^0 = \tau \cosh y$ and $x_\parallel = \tau \sinh y$, the $4d$ boundary line element reads: $ds_4^2 = -d\tau^2 + dx_\perp^2 + \tau^2 dy^2$.

This line element is modified if a quench described by the profile $\gamma(\tau)$ is introduced in the boundary metric, to describe the process driving the system out-of-equilibrium:

$$ds_4^2 = -d\tau^2 + e^{\gamma(\tau)} dx_\perp^2 + \tau^2 e^{-2\gamma(\tau)} dy^2 \ ; \tag{1}$$

this leaves the spatial three-volume unchanged, and respects the translational and $O(2)$ symmetries in the transverse plane.

The gravity dual is defined on a $5d$ spacetime, described adopting the Eddington-Finkelstein coordinates with a fifth radial coordinate r and having the metric (1) as a boundary. The $5d$ line element can be written as

$$ds^2 = -A(r,\tau) d\tau^2 + \Sigma(r,\tau)^2 e^{B(r,\tau)} dx_\perp^2 + \Sigma(r,\tau)^2 e^{-2B(r,\tau)} dy^2 + 2 d\tau dr \ , \tag{2}$$

with the boundary obtained for $r \to \infty$, and the metric functions A, Σ and B depending only on r and τ, due to the symmetries imposed to the system. Such metric function are determined

[2] Along the paper, energy density and pressures are referred to without considering the factor $\frac{N_c^2}{2\pi^2}$.

solving $5d$ Einstein equations with negative cosmological constant, written in the form [9]:

$$\begin{aligned}
&\Sigma(\dot{\Sigma})' + 2\Sigma'\dot{\Sigma} - 2\Sigma^2 = 0 \\
&\Sigma(\dot{B})' + \frac{3}{2}\left(\Sigma'\dot{B} + B'\dot{\Sigma}\right) = 0 \\
&A'' + 3B'\dot{B} - 12\frac{\Sigma'\dot{\Sigma}}{\Sigma^2} + 4 = 0 \\
&\ddot{\Sigma} + \frac{1}{2}\left(\dot{B}^2\Sigma - A'\dot{\Sigma}\right) = 0 \\
&\Sigma'' + \frac{1}{2}B'^2\Sigma = 0\,.
\end{aligned} \tag{3}$$

In (3), for a generic function $\xi(r,\tau)$, the directional derivatives along the infalling radial null geodesics and the outgoing radial null geodesics are denoted by $\xi' = \partial_r\xi$ and $\dot{\xi} = \partial_\tau\xi + \frac{1}{2}A\partial_r\xi$, respectively.

Two boundary conditions need to be imposed. The first one consists in the requirement that the metric (2) reproduces the $4d$ metric Eq. (1) for $r \to \infty$. The second condition is that, at the initial time slice $\tau = \tau_i$ when the quench is switched on, one has the AdS_5 bulk metric:

$$ds^2 = r^2\left[-d\tau^2 + dx_\perp^2 + \left(\tau + \frac{1}{r}\right)^2 dy^2\right] + 2drd\tau \ . \tag{4}$$

In [10] several quench profiles were considered, to understand whether and how thermalization depends on the specific choice of sourcing. Each profile is characterized by a function $\gamma(\tau)$, representing quenches with different number, structures and intensities, parametrized as

$$\gamma(\tau) = w\left[\tanh\left(\frac{\tau-\tau_0}{\eta}\right)\right]^7 + \sum_{j=1}^{N}\gamma_j(\tau,\tau_{0,j}) \tag{5}$$

with

$$\gamma_j(\tau,\tau_{0,j}) = c_j f_j(\tau,\tau_{0,j})^6 e^{-1/f_j(\tau,\tau_{0,j})}\Theta\left(1 - \frac{(\tau-\tau_{0,j})^2}{\Delta_j^2}\right) \tag{6}$$

and

$$f_j(\tau,\tau_{0,j}) = 1 - \frac{(\tau-\tau_{0,j})^2}{\Delta_j^2} \ . \tag{7}$$

The set of parameters $w, \eta, \tau_0, \tau_{0,j}, c_j$ and Δ_j defines the various quench models: among these, we focus on two models, denoted by $\mathcal{A}(2)$ and $\mathcal{B}$ in Ref.[10]. Model $\mathcal{A}(2)$ has two short pulses in the boundary metric, obtained using the parameters $w = 0$, $N = 2$, $c_1 = 1$, $\Delta_{1,2} = 1$, $\tau_{0,1} = \frac{5}{4}\Delta_1$, $c_2 = 2$, $\tau_{0,2} = \frac{9}{4}\Delta_2$. The quench ends at $\tau_f^{\mathcal{A}} = 3.25$. Model $\mathcal{B}$ represents the superimposition of a short pulse to a slow deformation, and is obtained when the parameters are set to $w = \frac{2}{5}$, $\eta = 1.2$, $\tau_0 = 0.25$, $N = 1$, $c_1 = 1$, $\Delta_1 = 1$, $\tau_{0,1} = 4\Delta_1$. The pulse ends at $\tau_f^{\mathcal{B}} = 5$, even if the slow distortion continues with τ and approaches a constant value. In both cases, the quench is switched on at $\tau_i = 0.25$. The two profiles $\gamma(\tau)$ are depicted in Fig. 6.

The metric functions $A(r,\tau)$, $\Sigma(r,\tau)$ and $B(r,\tau)$ in Eq. (2) are calculated by solving the Einstein equations (3) with the boundary conditions at the initial time slice and at $r \to \infty$

[10]. Using the solutions, several quantities of interest are determined, in particular the thermalization time, comparing the boundary stress-energy tensor to the same quantity computed in the viscous hydrodynamic regime. Notice that, due to homogeneity, boost-invariance and invariance under rotations in the transverse plane, the various components of T_μ^ν depend only on the proper time τ [5]. Moreover, imposing that T_μ^ν is conserved and traceless, its components depend on a single function $f(\tau)$, so that

$$T_\mu^\nu = diag\left(-f(\tau),\, f(\tau)+\frac{1}{2}\tau f'(\tau),\, f(\tau)+\frac{1}{2}\tau f'(\tau),\, -f(\tau)-\tau f'(\tau)\right) \quad . \tag{8}$$

For a perfect fluid one has $\epsilon = 3p$ and the relation $p = p_\parallel = p_\perp$: the τ dependence is hence fixed, $\epsilon(\tau) = \dfrac{const}{\tau^{4/3}}$. This dependence includes subleading terms in $1/\tau$ when viscous effects are taken into account [6]. An effective temperature $T_{eff}(\tau)$ can be defined through the relation $\epsilon(\tau) = \dfrac{3}{4}\pi^4 T_{eff}(\tau)^4$, and for $T_{eff}(\tau)$ the subleading terms in the large-τ expansion can be computed in $\mathcal{N}=4$ SYM [14]:

$$\begin{aligned} T_{eff}(\tau) &= \frac{\Lambda}{(\Lambda\tau)^{1/3}}\left[1-\frac{1}{6\pi(\Lambda\tau)^{2/3}}+\frac{-1+\log 2}{36\pi^2(\Lambda\tau)^{4/3}}+\frac{-21+2\pi^2+51\log 2-24(\log 2)^2}{1944\pi^3(\Lambda\tau)^2}\right. \\ &+ \left.\mathcal{O}\left(\frac{1}{(\Lambda\tau)^{8/3}}\right)\right] , \end{aligned} \tag{9}$$

with Λ a parameter. This expression corresponds to the large τ dependence for the energy density ϵ, the longitudinal $p_\parallel$ and transverse $p_\perp$ pressures:

$$\epsilon = \frac{3\pi^4\Lambda^4}{4(\Lambda\tau)^{4/3}}\left[1-\frac{2c_1}{(\Lambda\tau)^{2/3}}+\frac{c_2}{(\Lambda\tau)^{4/3}}+\mathcal{O}\left(\frac{1}{(\Lambda\tau)^2}\right)\right] , \tag{10}$$

$$p_\parallel(\tau) = \frac{\pi^4\Lambda^4}{4(\Lambda\tau)^{4/3}}\left[1-\frac{6c_1}{(\Lambda\tau)^{2/3}}+\frac{5c_2}{(\Lambda\tau)^{4/3}}+\mathcal{O}\left(\frac{1}{(\Lambda\tau)^2}\right)\right] , \tag{11}$$

$$p_\perp(\tau) = \frac{\pi^4\Lambda^4}{4(\Lambda\tau)^{4/3}}\left[1-\frac{c_2}{(\Lambda\tau)^{4/3}}+\mathcal{O}\left(\frac{1}{(\Lambda\tau)^2}\right)\right] , \tag{12}$$

with $c_1 = \dfrac{1}{3\pi}$ and $c_2 = \dfrac{1+2\log 2}{18\pi^2}$. The large τ dependence of the pressure ratio $\dfrac{p_\parallel}{p_\perp}$ and anisotropy $\dfrac{\Delta p}{\epsilon} = \dfrac{p_\perp - p_\parallel}{\epsilon}$ can also be worked out. The differences among different quech models are encoded in Λ. Hence, the components of T_μ^ν, computed from the bulk geometry, can be compared with the asymptotic expressions (10), (11) and (12).

We summarize the results for the quench models $\mathcal{A}(2)$ and $\mathcal{B}$, although all models scrutinized in [10] share common features concerning the horizon formation in the bulk and the evolution towards the hydrodynamic regime of temperature and pressures. However, the equilibration occurs with different features, depending on the observable. The effective temperature and the energy density start to follow their hydrodynamic expressions immediately after the quench is switched off. On other contrary, the two pressures take longer to reach the hydrodynamic forms. This effect can be described introducing a "thermalization time" τ_p, by the condition $\left|\dfrac{p_{||}(\tau_p)/p_\perp(\tau_p) - (p_{||}(\tau_p)/p_\perp(\tau_p))_H}{p_{||}(\tau_p)/p_\perp(\tau_p)}\right| = 0.05$, with $(p_{||}(\tau_p)/p_\perp(\tau_p))_H$ obtained from (11),(12).

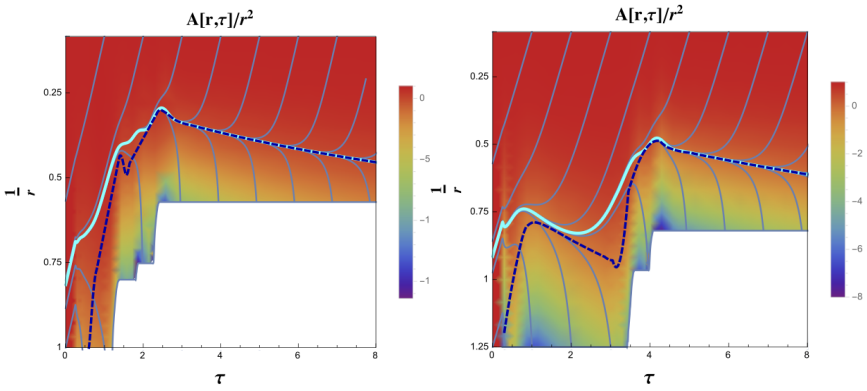


Figure 1: Metric function $A(r,\tau)/r^2$ vs τ and $1/r$, obtained solving the Einstein equations in the case of the model $\mathcal{A}(2)$ (left panel) and of the model $\mathcal{B}$ (right panel). The color bars indicate the values of the function. The gray lines are radial null outgoing geodesics, the dashed dark blue line is the apparent horizon, the continuous cyan line is the event horizon. The excision in the low-r region used in the calculation is shown.

In Fig. 1 the metric function $A(r,\tau)/r^2$ is displayed for the two models; the apparent and event horizons are depicted. Fig. 2 shows the time dependence of the temperature, the area of the apparent horizon per unit of rapidity, $\Sigma(r_h,\tau)^3$, and the components of T^μ_ν. Considering the temperature, the relaxation of the system, right after the end of the perturbation follows the hydrodynamic expression. The same conclusion can be inferred looking at the area of the apparent horizon per unit of rapidity, $\Sigma(r_h,\tau)^3$, that reaches a constant value soon after the pulses. As for the components of T^μ_ν, their behaviour after the end of the quench is displayed in Fig. 3, which shows that the time τ^*, at which $\epsilon(\tau^*)$ differs from the corresponding hydrodynamic value $\epsilon_H(\tau^*)$ in (10) by less than 5%, essentially coincides with the end of the perturbation. On the other hand, the thermalization time τ_p is larger. The difference $\tau_p - \tau^*$ is the time elapsed after the end of the quench to restore the hydrodynamic regime. It can be expressed in physical units introducing a scale in the system, namely imposing $T_{eff}(\tau^*) = 500$ MeV, with the results collected in Table 1 for various models [10]. The difference $\tau_p - \tau^*$ is always found to be order (or less than) 1 fm/c, a result comparable to the values inferred from the analyses of heavy ion collision phenomenology.

model	τ^*	τ_p	Λ	$\Delta\tau = \tau_p - \tau^*$ (fm/c)
$\mathcal{A}$ (1)	5.25	6.8	2.25	0.60
$\mathcal{A}$ (2)	3.25	6.0	1.73	1.03
$\mathcal{B}$	5	6.74	1.12	0.42
$\mathcal{C}$	9.45	10.24	1.59	0.20

Table 1: Results from different quench models [10].

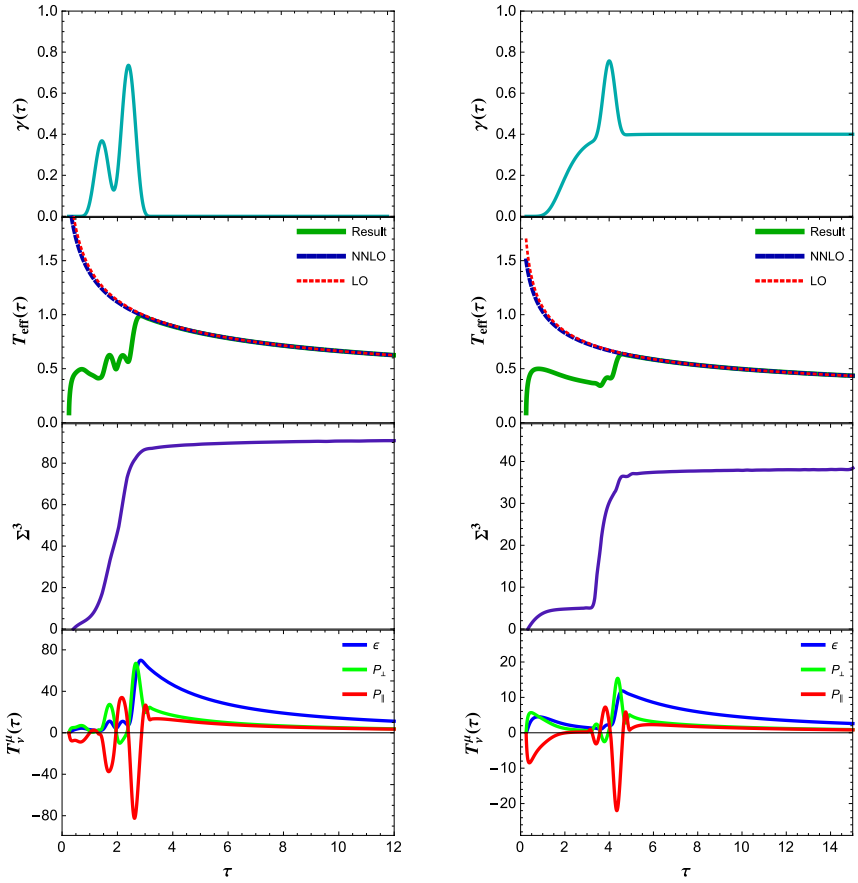


Figure 2: For two different quench profiles, models $\mathcal{A}(2)$ and $\mathcal{B}$, the panels show (from top to bottom) the profile $\gamma(\tau)$, the temperature $T_{eff}(\tau)$, the horizon area $\Sigma^3(r_h, \tau)$ per unit of rapidity, and the three components $\epsilon(\tau)$, $p_\perp(\tau)$ and $p_\parallel(\tau)$ of the stress-energy tensor T^μ_ν.

3 Nonlocal probes of thermalization

Several nonlocal probes can be computed using the calculated metric functions $A(r,\tau)$, $\Sigma(r,\tau)$ and $B(r,\tau)$ in the geometry (2). The properties of the same observables in the hydrodynamic setup are useful for the comparison. The $5d$ metric reproducing, through holographic renormalization, the results in (10)-(12) was derived for the Fefferman-Graham [6, 14, 15] and Eddington-Finkelstein coordinates [16]. To connect it with the stress-energy tensor components, the $5d$ metric dual to viscous hydrodynamics can be written as [11]

$$ds^2 = -A^H(r,\tau)d\tau^2 + [\Sigma^H(r,\tau)]^2 e^{B^H(r,\tau)} dx_\perp^2 + [\Sigma^H(r,\tau)]^2 e^{-2B^H(r,\tau)} dy^2 + 2dr d\tau \ , \qquad (13)$$

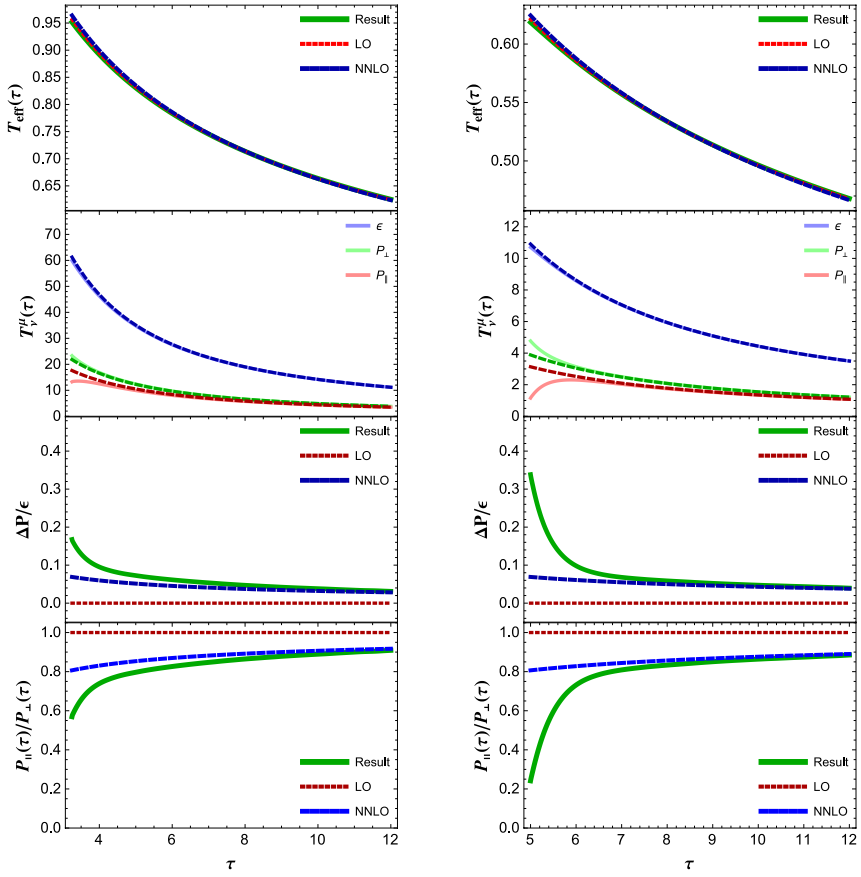


Figure 3: For models $\mathcal{A}(2)$ and $\mathcal{B}$ the panels show (from top to bottom) the temperature $T_{eff}(\tau)$, the components $\epsilon(\tau)$, $p_\perp(\tau)$ and $p_\parallel(\tau)$ of the stress-energy tensor, pressure anisotropy $\Delta p/\epsilon = (p_\perp - p_\parallel)/\epsilon$ and ratio $p_\parallel/p_\perp$, computed for $\tau > \tau_f^{\mathcal{A}(2),\mathcal{B}}$. The short and long dashed lines correspond to the hydrodynamic result and to the NNLO result in the $1/\tau$ expansion.

with the metric functions given in terms of the energy density and the pressures:

$$\begin{aligned} A^H(r,\tau) &= r^2\left(1-\frac{4}{3r^4}\epsilon(\tau)\right), \qquad \Sigma^H(r,\tau) = r\left(\tau+\frac{1}{r}\right)^{1/3}, \\ B^H(r,\tau) &= \frac{1}{3r^4}\left(p_\perp(\tau)-p_\parallel(\tau)\right) - \frac{2}{3}\log\left(\tau+\frac{1}{r}\right) . \end{aligned} \tag{14}$$

Among various nonlocal observable, we first consider the equal-time two-point correlation functions, computed in geodesic approximation. The AdS/CFT correspondence etsblishes a connection between a boundary scalar operator $\mathcal{O}(t, \boldsymbol{x})$ of conformal dimension Δ in d dimensions and its dual bulk field $\phi(t, \boldsymbol{x}, r)$ with mass m in $(d+1)$ dimensions, with $\Delta = \frac{1}{2}(d + \sqrt{d^2 + 4m^2})$. In the strong coupling regime of the boundary theory, the equal-time two-point function $\langle \mathcal{O}(t, \boldsymbol{x}) \mathcal{O}(t, \boldsymbol{x}') \rangle$ can be computed starting from the on-shell $5d$ supergravity action. In the geometric optic limit, such two-point correlation function is given in terms of the length $\mathcal{L}$ of the space-like geodesics that connect the two points on the boundary,

$$\langle \mathcal{O}(t, \boldsymbol{x}) \mathcal{O}(t, \boldsymbol{x}') \rangle \simeq \sum_{\text{geodesics}} e^{-\Delta \mathcal{L}} \ , \tag{15}$$

an approximation holding for large Δ. $\mathcal{L}$ is computed by extremizing the length of the curves connecting the two points, given by

$$\mathcal{L} = \int_P^Q d\lambda \sqrt{\pm g_{MN} \dot{x}^M \dot{x}^N}, \tag{16}$$

where g_{MN} is the metric, P and Q are boundary points and the coordinates $x^M(\lambda)$ ($M = 1, \ldots, d+1$) are functions of a parameter λ, and the derivative $\dot{x}^M \equiv dx^M/d\lambda$ is defined. The integrand in (16) can be treated as a Lagrangian, from which Euler-Lagrange equations stem. The solutions of such equations provide the geodesic that extremizes $\mathcal{L}$.

Wilson loops can be treated analogusly. In the boundary theory, the loop is defined as

$$W_{\mathcal{C}}[A] = \frac{1}{N_c} Tr \left(P e^{-ig \oint_{\mathcal{C}} dx^\mu A_\mu^a T^a} \right), \tag{17}$$

with $\mathcal{C}$ a closed contour. In the strong coupling limit, the holographic expression for the expectation value of (17) is [17]:

$$\langle W_{\mathcal{C}} \rangle \sim e^{-S_{NG}}, \tag{18}$$

where S_{NG} is the Nambu-Goto action, giving the area of the string worldsheet bounded by $\mathcal{C}$:

$$S_{NG} = \frac{1}{2\pi\alpha'} \int d^2\xi \sqrt{det\left[g_{MN} \partial_\alpha X^M \partial_\beta X^N \right]}. \tag{19}$$

ξ^α ($\alpha, \beta = 1, 2$) are the worldsheet coordinates, and $X^M(\xi^\alpha)$ the embedding functions. The details of the calculation of the two-point correlation function and of the vacuum expectation values of different Wilson loops can be found in [11]. Here we only mention that the space-like paths connecting the boundary points $P = (t_0, -\ell/2, x_2, y)$ and $Q = (t_0, \ell/2, x_2, y)$, and extending in the bulk at fixed (x_2, y) are described by two functions $\tau(x)$ and $r(x)$ which depend on the coordinate $x_1 \equiv x$. In the middle point $x = 0$ they assume the values $\tau(0) = \tau_*$, $r(0) = r_*$, and have a minimum: $\tau'(0) = r'(0) = 0$, with the prime standing for the derivative with respect to x. The conditions $\tau(-\ell/2) = \tau(\ell/2) = t_0$, $r(-\ell/2) = r(\ell/2) = r_0$ are satisfied, with r_0 the maximum radial coordinate used in the calculation. The geodesic length

$$\mathcal{L} = \int_{-\ell/2}^{\ell/2} dx \frac{\tilde{\Sigma}(r, \tau)}{\sqrt{\tilde{\Sigma}(r_*, \tau_*)}} \tag{20}$$

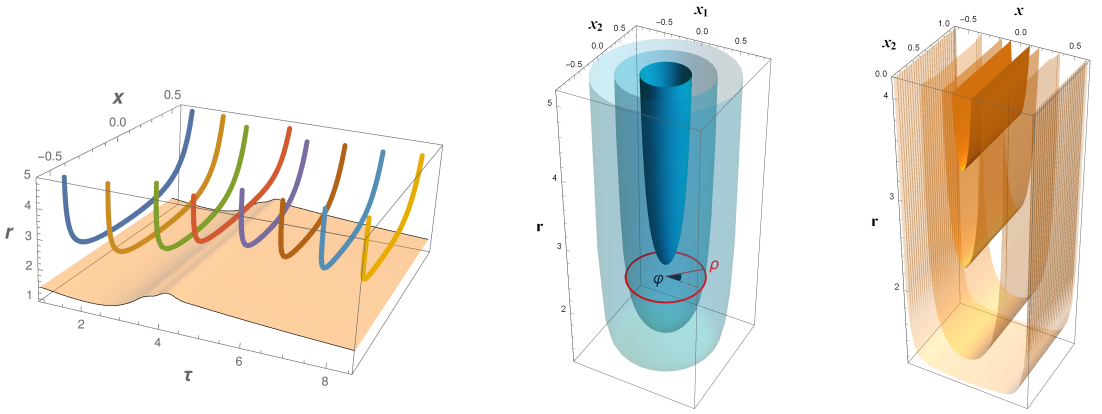


Figure 4: Left panel: geodesics obtained in the case of the quench model $\mathcal{B}$ for various (r_*, τ_*). The shaded area represents the event horizon. Middle and right panel: extremal surfaces of circular and rectangular Wilson loops, computed for quench model $\mathcal{B}$. The value of τ_* is set to $\tau_* = 3$.

is given in terms of the metric functions, with $\tilde{\Sigma}(r,\tau) = \Sigma(r,\tau)^2 e^{B(r,\tau)}$. Its expression requires a regularization, which we implement subtracting from the lenght (20) the same quantity computed in pure AdS_5. The distance ℓ is provided by the relation $r\,(\ell/2) = r_0$. Typically resulting geodesics are depicted in Fig. 4, and the thermalization of the boundary theory is studied computing their lengths as time proceeds. The hydrodynamic expression of the geodesic lengths $\mathcal{L}_H$ are determined in the geometry (13)-(14) with the same regularization prescription. This allows to identify the difference $\Delta\mathcal{L} = \mathcal{L} - \mathcal{L}_H$ as an observable.

In the case of Wilson loops as nonlocal probes of the boundary theory thermalization, we consider two shapes, circles and strips. For a Wilson loop along a circumference of radius $R = \ell/2$ on the plane $\boldsymbol{x}_\perp \equiv (x_1, x_2)$ at the boundary, the space-like worldsheet of minimal area based on the circular path and extending in the bulk at fixed y must be computed. Such a surface has an azimuthal symmetry and a tip at $(\tau, \boldsymbol{x}_\perp, r) = (\tau_*, \mathbf{0}, r_*)$ with (r_*, τ_*) input values in the calculation. The transverse section at fixed τ and r is a circumference. For each section the worldsheet can be parameterized in polar coordinates $\xi^\alpha = (\rho, \varphi)$, so that $\tau = \tau(\rho)$, $x_1 = \rho\cos\varphi$, $x_2 = \rho\sin\varphi$, $r = r(\rho)$, with y fixed. The area of the worldsheet is obtained from the Nambu-Goto action

$$\mathcal{A}_C = \frac{1}{\alpha'}\int_0^{\ell/2} d\rho\,\rho\left(\tilde{\Sigma}(r,\tau)\left[-A(r,\tau)\tau'(\rho)^2 + \tilde{\Sigma}(r,\tau) + 2\tau'(\rho)r'(\rho)\right]\right)^{1/2}, \tag{21}$$

with the prime in the functions τ and r denoting a derivative with respect to ρ, and the angle φ integrated out. The area of the extremal surface is regularized using the same scheme adopted for the geodesic lengths. The corresponding quantity in the hydrodynamic geometry is obtained using the metric functions (14), and thermalization is probed using the difference $\Delta\mathcal{A}_C = \mathcal{A}_C - \mathcal{A}_{C,H}$. Examples of extremal surfaces of circular Wilson loops computed using the bulk geometry (2) are shown in Fig. 4.

A less symmetric Wilson loop is an infinite rectangular strip, with one side length q is taken

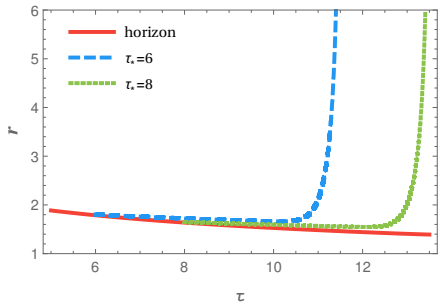


Figure 5: Two geodesics in the (τ, r) plane, in quench model $\mathcal{B}$. Increasing τ_* (after the pulse in the quench) and for large ℓ, the radial coordinate closely follows the event horizon.

to infinity on the other one set to ℓ. The extremal area has the expression

$$\mathcal{A}_R = \frac{q}{2\pi\alpha'} \int_{-\ell/2}^{\ell/2} dx \frac{\tilde{\Sigma}(r,\tau)^2}{\tilde{\Sigma}\left(r_*,\tau_*\right)} \ , \tag{22}$$

to be regularized. This is done computing $\mathcal{A}_{RH}$ in the geometry (14), and considering the difference $\Delta\mathcal{A}_R = (\mathcal{A}_R - \mathcal{A}_{RH})/q$ at various τ_0 and for different ℓ defines an observable to study thermalization of the boundary theory. An example of rectangular Wilson loops computed in the geometry (2) is shown in Fig. 4.

Let us now describe the results for geodesics in the quench model $\mathcal{B}$. Depending on r_* and τ_*, two sets of geodesics $r(x)$ are found: those reaching the AdS boundary, the class we are interested in, and those falling into the bulk. After the quench, at a fixed τ_*, a critical value r_{*c} separates the two classes of solutions, and corresponds to the position of the black brane event horizon. The solutions at large ℓ approach and follow the horizon, as shown in Fig. 5. On the other hand, during the quench, when large time gradients are present, solutions starting from the boundary and crossing the apparent horizon are also found, a remarkable phenomenon observed for nonlocal observables in rapidly changing time-dependent setups.

The regularized geodesic length $\mathcal{L}(t_0,\ell)$, the regularized area of extremal surfaces for the rectangular Wilson loop $\mathcal{A}_{\mathcal{R}}(t_0,\ell)$ (divided by q) and the circular Wilson loop $\mathcal{A}_{\mathcal{C}}(t_0,\ell)$ in model $\mathcal{B}$ are shown in Fig. 6 for several values of the distance ℓ in the correlation function, of the side (again denoted by ℓ) of the rectangular Wilson loop, and of the diameter ℓ of the circular Wilson loop (α' is set to 1). The curves start at different values of the initial time t_0, all corresponding to $\tau_* = 0.25$. Fig. 6 shows that the observables follow the quench profile, with a delay that increases for increasing sizes of the probes.

Let us focus on the time region that follows the end of the spike in the quench, when the profile $\gamma(\tau)$ is nearly constant. We are interested in understanding if the nonlocal observables follow the hydrodynamic behavior and, in that case, how fast such a regime is reached after the end of the quench, in comparison with the thermalization time determined through local observables (in particular the pressures). In Fig. 7 we display the differences $\Delta\mathcal{L}$, $\Delta\mathcal{A}_R$ (divided by q) and $\Delta\mathcal{A}_C$. Each observable thermalizes at different times, where all differences vanish. The thermalization times are different for different sizes of the probes. This result indicates how nonlocal observables recover the hydrodynamic regime after the end of the quench in comparison

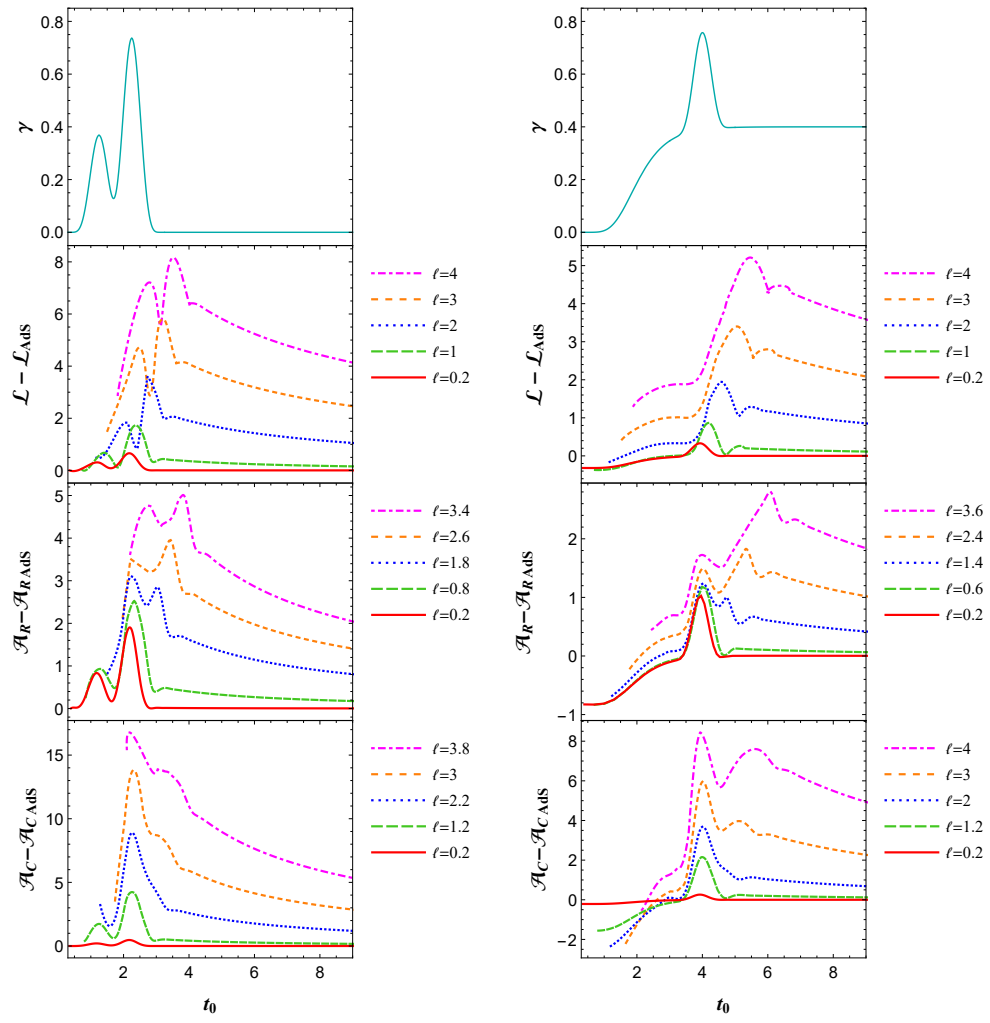


Figure 6: Quench models $\mathcal{A}(2)$ (left) and $\mathcal{B}$ (right). From top down: profile of the quench γ, geodesics regularized lengths, regularized areas of the extremal surfaces for rectangular (divided by q) and circular Wilson loops versus t_0, for the sizes of the probes specified in the legendae. The regularization scheme consists in subtracting from each observable the corresponding quantity computed in pure AdS_5.

with the local observables: $\Delta\mathcal{L}$, $\Delta\mathcal{A}_R$ and $\Delta\mathcal{A}_C$ are smaller for low values of ℓ: the system is seen to thermalize faster using observables remaining as local as possible.

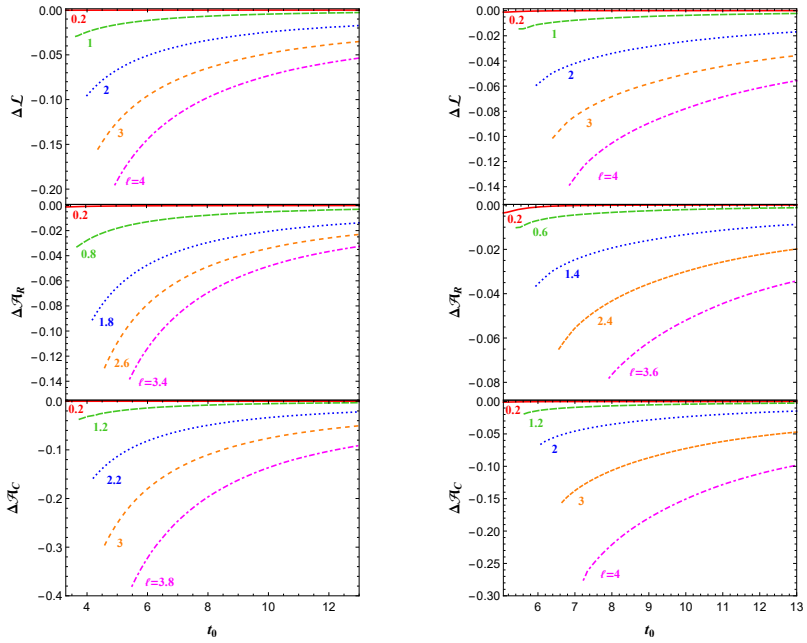


Figure 7: Quench models $\mathcal{A}(2)$ (left) and $\mathcal{B}$ (right). From top down: Difference between the regularized geodesic length $\Delta\mathcal{L}$ (top), the regularized area (divided by q) of the extremal surface for the rectangular Wilson loop $\Delta\mathcal{A}_R$ (middle), and the regularized area of the extremal surface for the circular Wilson loop $\Delta\mathcal{A}_C$ (bottom) in the models with quench and using the hydrodynamic metric. The time t_0 starts after the end of the pulse in the quench.

To provide a quantitative measure of thermalization for the nonlocal probes, several criteria can be used to determine the value of the size ℓ above which the observables are not thermalized, at a fixed value t_0 which corresponds to the restoration of pressure isotropy. For example, we define $t_{1/2}(\ell)$ as the value of t_0 at which $|\Delta\mathcal{L}|$ is reduced by a half with respect to the end of the quench at fixed ℓ, and similarly for $|\Delta\mathcal{A}_R|$ and $|\Delta\mathcal{A}_C|$. The results in Fig. 8 show that $t_{1/2}(\ell)$ exceeds the thermalization time obtained using local observables for size $\ell \simeq 1$. The rectangular Wilson loop takes more time to thermalize. Another feature emerging for $t_{1/2}$ is the linear increase against the size ℓ. The hierarchy found between the thermalization times of the energy density, the pressures and the large size probes indicates that the onset of thermalization starts at short distances.

As for the quench model $\mathcal{A}(2)$, the results in Fig. 6 show how the nonlocal observables follow the quench in the boundary, and how thermalization is reached with the curves approaching the hydrodynamic behavior, as understood inspecting Fig. 7. The half thermalization time $t_{1/2}(\ell)$ is depicted in Fig. 8, and its behavior is linear for large sizes. As in model $\mathcal{B}$, the rectangular Wilson loop thermalizes more slowly than the other two observables.

The conclusion, for both the quench models, is the emergence of time scales related to the onset of hydrodynamics, depending on the size of the probes. The observation of a hierarchy in thermalization among the different sizes and distances is connected to the use of space-like

probes. Analyses based on time correlators, or on horizon-to-boundary propagators in the same dynamical framework, are useful to show a hierarchy in thermalization among different frequencies and modes of the boundary field theory [18].

4 Conclusions

Equilibration of a strongly interacting non-Abelian plasma can be studied in a fully dynamical holographic $5d$ setup with boundary sourcing, using local and nonlocal observables that provide indications on the hierarchy of thermalization times. The energy density follows the hydrodynamic viscous behavior immediately after the end of the quenches that drive the system out-of-equilibrium, while there is a time delay for the pressures to reach the viscous time dependence and the isotropy condition $p_\perp = p_\parallel$. For nonlocal observables, the thermalization time changes with the size of the observable. For larger sizes, the thermalization time increases linearly with the size of the probe. The hierarchy among the thermalization times of the energy density, pressures and large probes indicates that short distances thermalize first.

Acknowledgments. One of us, PC, is grateful to Prof. A. Ali and Prof. M. Ivanov for the invitation at the 2016 School "Quantum Field Theory at the Limits" in Dubna. This lecture is based on works carried out within the INFN project (Iniziativa Specifica) QFT-HEP.

References

[1] U. W. Heinz, AIP Conf. Proc. **739** (2005) 163; E. Shuryak, arXiv:1412.8393 [hep-ph].

[2] J. M. Maldacena, Int. J. Theor. Phys. **38** (1999) 1113 [Adv. Theor. Math. Phys. **2** (1998) 231]; E. Witten, Adv. Theor. Math. Phys. **2** (1998) 253; S. S. Gubser, I. R. Klebanov and A. M. Polyakov, Phys. Lett. B **428** (1998) 105.

[3] S. Bhattacharyya, V. E. Hubeny, S. Minwalla and M. Rangamani, JHEP **0802** (2008) 045; V. E. Hubeny, S. Minwalla and M. Rangamani, arXiv:1107.5780 [hep-th].

[4] J. Casalderrey-Solana, H. Liu, D. Mateos, K. Rajagopal and U. A. Wiedemann, arXiv:1101.0618 [hep-th].

[5] J. D. Bjorken, Phys. Rev. D **27** (1983) 140.

[6] R. A. Janik and R. B. Peschanski, Phys. Rev. D **73** (2006) 045013.

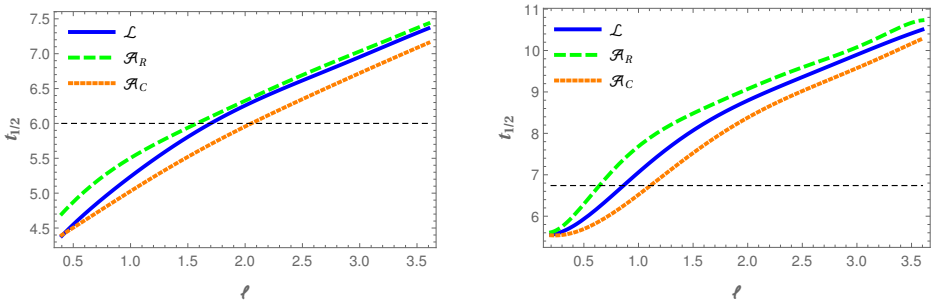


Figure 8: Quench model $\mathcal{A}(2)$ (left) and $\mathcal{B}$ (right): time $t_{1/2}$ versus the size ℓ for the three nonlocal observables. The horizontal dashed line indicates the thermalization time obtained from the pressure anisotropy.

[7] S. de Haro, S. N. Solodukhin and K. Skenderis, Commun. Math. Phys. **217** (2001) 595.

[8] Y. V. Kovchegov and A. Taliotis, Phys. Rev. C **76** (2007) 014905; J. Abajo-Arrastia, J. Aparicio and E. Lopez, JHEP **1011** (2010) 149; S. Bhattacharyya and S. Minwalla, JHEP **0909** (2009) 034; T. Albash and C. V. Johnson, New J. Phys. **13** (2011) 045017; J. Aparicio and E. Lopez, JHEP **1112** (2011) 082; V. Keranen, E. Keski-Vakkuri and L. Thorlacius, Phys. Rev. D **85** (2012) 026005; D. Galante and M. Schvellinger, JHEP **1207** (2012) 096; W. Baron, D. Galante and M. Schvellinger, JHEP **1303** (2013) 070; E. Caceres and A. Kundu, JHEP **1209** (2012) 055; P. Basu and S. R. Das, JHEP **1201** (2012) 103; R. Auzzi, S. Elitzur, S. B. Gudnason and E. Rabinovici, JHEP **1311** (2013) 016; E. Caceres, A. Kundu, J. F. Pedraza and W. Tangarife, JHEP **1401** (2014) 084; H. Liu and S. J. Suh, Phys. Rev. Lett. **112** (2014) 011601; P. Basu, D. Das, S. R. Das and K. Sengupta, JHEP **1312** (2013) 070; X. X. Zeng, X. M. Liu and W. B. Liu, JHEP **1403** (2014) 031; E. Caceres, A. Kundu, J. F. Pedraza and D. L. Yang, JHEP **1506** (2015) 111; H. Liu and S. J. Suh, Phys. Rev. D **89** (2014) no.6, 066012; T. Andrade, J. Casalderrey-Solana and A. Ficnar, arXiv:1610.08987 [hep-th].

[9] P. M. Chesler and L. G. Yaffe, Phys. Rev. Lett. **102** (2009) 211601; P. M. Chesler and L. G. Yaffe, Phys. Rev. D **82** (2010) 026006.

[10] L. Bellantuono, P. Colangelo, F. De Fazio and F. Giannuzzi, JHEP **1507** (2015) 053.

[11] L. Bellantuono, P. Colangelo, F. De Fazio, F. Giannuzzi and S. Nicotri, Phys. Rev. D **94** (2016) 025005.

[12] V. Balasubramanian *et al.*, Phys. Rev. Lett. **106** (2011) 191601; V. Balasubramanian *et al.*, Phys. Rev. D **84** (2011) 026010.

[13] D. Galante and M. Schvellinger, JHEP **1207** (2012) 096; J. F. Pedraza, Phys. Rev. D **90** (2014) no.4, 046010; C. Ecker, D. Grumiller and S. A. Stricker, JHEP **1507** (2015) 146; A. Buchel, R. C. Myers and A. van Niekerk, JHEP **1502** (2015) 017 Erratum: [JHEP **1507** (2015) 137]; C. Ecker, D. Grumiller, P. Stanzer, S. A. Stricker and W. van der Schee, JHEP **1611** (2016) 054.

[14] M. P. Heller and R. A. Janik, Phys. Rev. D **76** (2007) 025027; M. P. Heller, R. A. Janik and P. Witaszczyk, Phys. Rev. D **85** (2012) 126002.

[15] R. A. Janik, Phys. Rev. Lett. **98** (2007) 022302.

[16] W. van der Schee, Phys. Rev. D **87** (2013) 061901.

[17] J. M. Maldacena, Phys. Rev. Lett. **80** (1998) 4859.

[18] S. Caron-Huot, P. M. Chesler and D. Teaney, Phys. Rev. D **84** (2011) 026012.

A brief Introduction to Dispersion Relations and Analyticity

Roman Zwicky

Higgs Centre for Theoretical Physics, School of Physics and Astronomy,
University of Edinburgh, Edinburgh EH9 3JZ, Scotland

DOI: http://dx.doi.org/10.3204/DESY-PROC-2016-04/Zwicky

In these lectures we provide a basic introduction into the topic of dispersion relation and analyticity. The properties of 2-point functions are discussed in some detail from the viewpoint of the Källén-Lehmann and general dispersion relations. The Weinberg sum rules figure as an application. The analytic structure of higher point functions in perturbation theory are analysed through the Landau equations and the Cutkosky rules.

1 Prologue

Dispersion relations are a powerful non-perturbative tool which have originated in classical electrodynamics in the theory of Kramers-Kronig dispersion relations. Analytic properties follow from causality and the use of Cauchy's theorem allows to obtain the real part of an amplitude from the knowledge of the imaginary part which is often better accessible. This is the idea of the S-matrix program from the fifties and sixties. Dispersion relations are sparsely discussed in modern textbooks as the focus is on other aspects of Quantum Field Theory (QFT). There are some excellent older textbooks on analyticity e.g. [1, 2, 3], some modern textbooks devote some chapters to the topic e.g.[4, 5], as well as some lecture notes [6]. I would hope that a student who has followed an introductory course on QFT or has read some chapters of a QFT textbook would be able to largely follow the presentation below.

1.1 Introduction

In the fifties and sixties QFT has found a big success in describing quantum electrodynamics (QED) thanks to the successful renormalisation program carried out by Dyson, Feynman, Schwinger, Tomonaga and others [7]. The description of the strong force with QFT proved to be difficult and there was some prejudice that a solution outside field theory had to be found. Two such approaches are dispersion theory using analytic properties [1] (Heisenberg, Chew, ...) and Wilson's operator product expansion [8]. As Weinberg remarks in his book [5] both of these approaches later became a part of QFT! By analytic properties we mean analyticity in the external momenta. In QFT analytic continuation is inherent in the field description (second quantisation). Let us remind ourselves how this is related to scattering matrix elements of particles.

A primary goal of particle physics is to describe scattering of n-particles via the so-called

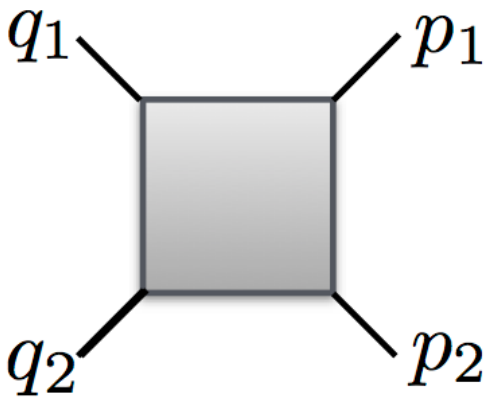


Figure 1: Schematic diagram for $2 \to 2$ scattering corresponding to the matrix element in Eq. (1). Time goes from left to right.

S-matrix. For the scattering of $2 \to 2$ particles this reads (cf. Fig.1)

$$ {}_{\rm out}\langle p_1, p_2 | q_1 q_2 \rangle_{\rm in} = {}_{\rm out}\langle p_1, p_2 | S | q_1 q_2 \rangle_{\rm out} \ , \tag{1}$$

where we have assumed the particles to be of spin 0. In the case where they are all of equal mass this implies the following on-shell conditions: $p_1^2 = p_2^2 = q_1^2 = q_2^2 = m^2$. Hence one might wonder how analytic properties come into play. The answer is through the celebrated *Lehman-Symmanzik-Zimmermann (LSZ) formula* whose derivation can be found in most textbooks e.g. [4]. For our case it reads

$$\begin{aligned} {}_{\rm out}\langle p_1, p_2 | q_1 q_2 \rangle_{\rm in} \quad = \quad & -(iZ^{-1/2})^4 \int_{x_1,x_2,y_1,y_2} e^{-i(q_1\cdot x_1 + q_2 \cdot x_2 - p_1 \cdot y_1 - p_2 \cdot y_2)} K_{x_1} K_{x_2} K_{y_1} K_{y_2} \times \\ & \langle T\phi(x_1)\phi(x_2)\phi^\dagger(y_1)\phi^\dagger(y_1)\rangle + \text{disconnected terms} \ , \end{aligned} \tag{2}$$

where $\int_x = \int d^4x$ hereafter, T is the time ordering, $\langle \ldots \rangle$ is the vacuum expectation value (VEV), the quanta are assumed to carry a charge (complex conjugation for outgoing particle), K is the Klein-Gordon operator $K_{x_1} = \Box + m^2 \to -(q_1^2 - m^2)$ and the Z factor results from the *asymptotic condition*,

$$\langle 0 | \phi(x) | q_1 \rangle \overset{x_0 \to \mp\infty}{\to} Z^{1/2} \langle 0 | \phi_{\rm in(out)}(x) | q_1 \rangle \ , \tag{3}$$

The asymptotic condition is the key idea of the LSZ-approach. Namely that when the particles are well separated from each other all that remains is the self-interaction which is parameterised by the renormalisation factor Z. The field ϕ is what is known as an interacting field whereas $\phi_{\rm in(out)}$ are free fields in which case the right-hand side of the equation above equals $\sqrt{Z/(2\pi)^3} e^{-iq_1\cdot x}$.[1][2] The disconnected part corresponds, for example, to the case where

[1] The LSZ formalism, in its elegancy and efficiency, also allows for the description of composite particles. For example a pion of $SU(2)$-isospin quantum number a may be described by $\phi \to \varphi^a = \phi \bar{q} T^a \gamma_5 q$ in the sense that $\langle 0 | \varphi^a | \pi^b \rangle = g_\pi \delta^{ab}$. In such a case φ^a is referred to as an interpolating field.

[2] It is crucial that this condition is only imposed on the matrix element (weak topology) as otherwise one

particle $q_1 \to p_1$ and $q_2 \to p_2$ without any interaction which is of no interest to us. From (2) we conclude that

a) The scattering of n-particles ($n = n_{\text{in}} + n_{\text{out}}$) is described by n-point functions (or n-point correlators). The study of the latter is therefore of primary importance.

b) The n-point correlators are functions of the external momenta e.g. $p_{1,2}^2, q_{1,2}^2, p_1 \cdot p_2, \ldots$. First and foremost they are defined for real values or more precisely for real values with a small imaginary part e.g. $p_1^2 = \text{Re}[p_1^2] + i0$.[3] From there they can be analytically continued into the complex plane. Hence it is the second quantisation, describing particles with fields, that allows us to go off-shell for correlation functions.[4]

The course consists of three parts. Analytic properties of 2-point functions (section 2), which comes with definite answer in terms of the non-perturbative Källén-Lehmann spectral representation. Applications of 2-point function in section 3. Last a short discussion of the analytic properties of higher point function in perturbation theory (PT) e.g. Landau equations and Cutkosky rules in section 4.

2 2-point Function

2.1 Dispersion Relation from 1st-principles: Källén-Lehmann Representation

Let us define the Fourier transform of the 2-point correlator as follows

$$\Gamma(p^2) = i \int_x e^{ip\cdot x} \langle T\phi(x)\phi^\dagger(0)\rangle \ . \tag{4}$$

What determines the analytic structure of $\Gamma(p^2)$? By analytic structure we mean the singularities e.g. poles, branch points and the associated branch cuts. The Källén-Lehmann representation [10, 11] gives a very definite answer to this question. The presentation is straightforward and can be found in most textbooks e.g. [5].

The 2-point function in the free and interacting case can be written as

$$\Gamma(p^2) = \begin{cases} \frac{1}{m^2 - p^2 - i0} = -\Delta_F(p^2, m^2) & \text{free} \\ \frac{Z(\lambda)}{m^2 - p^2 - i0} + f(\lambda, p^2) & \text{interacting} \end{cases} \ . \tag{5}$$

The function $Z(\lambda)$ and $f(\lambda, p^2)$, where λ is the coupling constant e.g. $\mathcal{L}_{\text{int}} = \lambda\phi^3 + \text{h.c.}$, obey

$$Z(\lambda) \overset{\lambda\to 0}{\to} 1 \ , \quad f(\lambda, p^2) \overset{\lambda\to 0}{\to} 0 \ , \tag{6}$$

runs into Haag's theorem [9] which states that any field which is unitarity equivalent to a free field is itself a free field.

[3] In perturbation theory (PT) the reality of the momenta is implicitly used when shifting momenta (e.g. completing squares for example).

[4] In it's most standard formulation string theory is first quantised and does not allow this analytic continuation. String field theory does exist but is less developed than first quantised string theory for technical reasons.

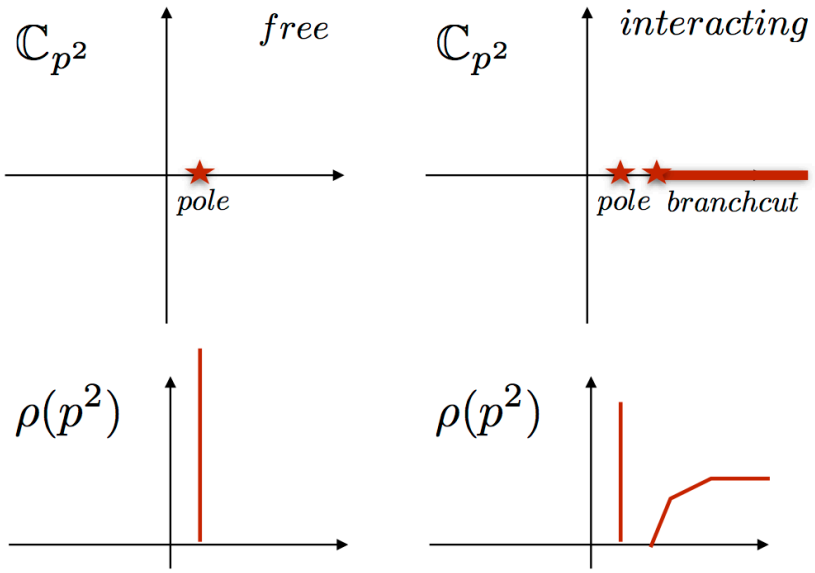


Figure 2: (left) analytic structure for free field theory propagator with spectral function underneath (right) idem for an interacting theory with a stable 1-particle state and a multiparticle-threshold

in order to reproduce the free field theory limit. In what follows it is our goal to determine the properties of $f(\lambda, p^2)$ in more detail. At the end of this section we are going to make remarks about the possible ranges of the $Z(\lambda)$-function. The first lesson to be learnt from the free field theory case is that it is the mass (i.e. the spectrum) which determines the analytic properties cf. Fig. 2(left). As we shall see this generalises to the interacting case.

For technical reason it is advantageous to first study the positive frequency distribution

$$\langle \phi(x)\phi^\dagger(0)\rangle = \begin{cases} \Delta_+(x^2, m^2) = \int \frac{d^4p}{(2\pi)^3} e^{-ip\cdot x}\delta^+(p^2-m^2) & \text{free} \\ (*) & \text{interacting} \end{cases} \tag{7}$$

where $\delta^+(p^2-m^2) \equiv \delta(p^2-m^2)\theta(p_0)$ assures that energies are positive and that the momenta are on the mass-shell. It is the quantity $(*)$ that we intend to study. First we use the formal decomposition of the identity into a complete set of states $\mathbb{1} = \sum_n |n\rangle\langle n|$ which follow from unitarity. Inserting this relation and using translation invariance one gets

$$(*) = \sum_n e^{-ip_n\cdot x} |\underbrace{\langle 0|\phi(0)|n(p_n)\rangle}_{\equiv f_n}|^2 \,. \tag{8}$$

Further using $1 = \frac{1}{(2\pi)^4}\int_p e^{-ip\cdot x}\int_x e^{ip\cdot x}$ and interchanging the $\sum_n$ and the $\int_x$ [5] leads to

$$(*) = \int d^4p e^{-ip\cdot x} \underbrace{\equiv \sum_n \delta(p-p_n)|f_n|^2}_{(2\pi)^{-3}\rho(p^2)\theta(p_0)} , \tag{9}$$

where $\rho(p^2)$ is known as the *spectral function*, $(2\pi)^{-3}$ a convenient normalisation factor and $\theta(p_0)$ assures positive energies which come from the positive energy condition on the external momentum. Upon using $\int_p F(p) = \int_p \int ds\delta(s-p^2)F(s)$ and exchanging the ds and d^4p integration one finally gets

$$(*) = \int_0^\infty ds\rho(s)\Delta_+(x^2,s) , \tag{10}$$

a spectral representation.

From (5) and (7) it seems plausible that this spectral representation generalises to the time ordered 2-point function as follows

---

$$\Gamma(p^2) = \int_0^\infty ds\rho(s)(-\Delta_F(s,p^2)) = \int_0^\infty ds\frac{\rho(s)}{s-p^2-i0} . \tag{11}$$

Eq. (11) is referred to as the *Källén-Lehmann (spectral) representation.*

At this stage we can make many relevant comments.

1. The Källén-Lehmann representation is a special case of dispersion relation. It shows that dispersion representation follow from first principles in QFT.

2. The analytic properties of $\Gamma(p^2)$ are in one-to-one correspondence with the spectrum of the theory which is the answer to the question what determines the analytic properties of the 2-point function. Hence for the 2-point function there are no other singularities on the first sheet (known as the physical sheet)[6] other than on the positive real axis determined by the spectrum. The analytic structure is depicted in Fig. 2(right). An example of an unphysical singularity (not on the physical sheet) is given in section 4.2.3.

3. The spectral function $\rho(s) \geq 0$ is positive definite as a direct consequence of unitarity. [As a homework question you could try to show that for a non-unitary theory with negative normed states (i.e. $\langle gh|gh\rangle = -1$ where "gh" stands for ghost) $\rho(s)$ loses positive definiteness.]

[5] We will come back to these interchanges which are ill-defined when there are UV-divergences.

[6] More precisely the 2-point function is at first defined for real $p^2 + i0$ with $p^2 \in \mathbb{R}$. Analytic continuation which is unique from an interval proceeds through the upper half-plane to the left and passes below zero for real p^2 below the singlarities on the positive real line.

4. Often the spectral function is decomposed into a pole part[7]

$$\rho(s) = Z\delta(s - m^2) + \theta(s - s_0)\sigma(s) \tag{12}$$

and continuum part $\sigma(s)$. The latter is the concrete realisation of the function $f(\lambda, s)$ in (5). In many applications f_0, the residue of the lowest state,

$$\Gamma(p^2) = \frac{|f_0|^2}{m^2 - p^2 - i0} + \int_{s_0}^{\infty} \frac{\sigma(s)}{m^2 - p^2 - i0} \, , \tag{13}$$

is the non-perturbative quantity that is to be extracted. The left-hand side is computed and the σ-part is then either estimated or suppressed by applying an operation to the equation. This technique is the basis of QCD sum rules [12] and lattice QCD [13] extraction of low-lying hadronic parameters. In the former case the σ-part is suppressed by a Borel-transformation and in lattice QCD σ-part is exponentially suppressed in euclidian time.

5. The Källén-Lehmann representation straightforwardly applies to the case of a non-diagonal correlation function e.g. $\langle \phi_A(x)\phi_B^\dagger(0)\rangle$ but clearly positive definiteness is, in general, lost since $|f_n|^2 \to f_n^A(f_n^B)^*$.

6. As promised we return to the issue of interchanging various sums and integrals. This is of no consequence as long as there are no UV-divergences. As is well-known most field theories show UV-divergences so care has to be taken. UV-divergences demand regularisations and a prescription to renormalise the ambiguities which arise from removing the infinities. There are two ways to formally handle this problem. First, assuming a logarithmic divergence, we may amend (11) as

$$\Gamma(p^2) = \int_0^{\Lambda_{\rm UV}} ds \frac{\rho(s)}{s - p^2 - i0} + A \, , \tag{14}$$

where the so-called subtraction constant is adjusted to cancel the logarithmic divergence coming form the integral: $A = A_0 \ln(\Lambda_{\rm UV}^2/\mu_0^2) + A_1$ with μ_0 being some arbitrary reference scale. The constant A_1 has either to be taken from experiment in the case where $\Gamma(p^2)$ is physical (which implies scheme-independence) or is dependent on the scheme. The dependence in the latter case has to disappear when physical information is extracted from $\Gamma(p^2)$. A more elegant way, in my opinion, is to handle the problem with a once subtracted dispersion

$$\Gamma(p^2) = \Gamma(p_0^2) + (p^2 - p_0^2) \int_0^{\infty} ds \frac{\rho(s)}{(s - p^2 - i0)(s - p_0^2)} \, . \tag{15}$$

It is observed that the integral is now convergent due to the extra $1/(s - p_0^2)$ factor. The same remarks apply to $\Gamma(p_0^2)$ as for the previously discussed A_1. To derive the above expression one writes an unsubtracted dispersion relation for $\Gamma(p^2)$ and $\Gamma(p_0^2)$ separately takes the difference and combines the fraction. They key point is that the divergent parts are the same and cancel each other.

[7] When the particle becomes unstable and acquires a width then the pole wanders on the second sheet since the principle that there are no singularities on the physical sheet holds up e.g. [1]. This would have been an interesting additional topic which we can unfortunately not cover in these short lectures.

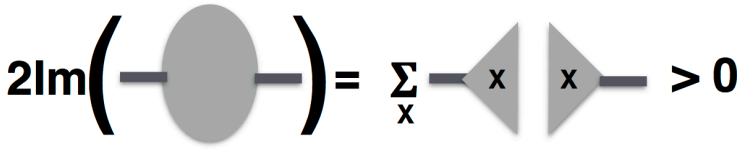


Figure 3: Standard sketch of optical theorem. The right-hand side is the sum over all intermediate states. It is a particular case of the cutting rules to be discussed in section 4.3.

7. Following the presentation in Weinberg's book [5]: imposing the canonical commutation relation $[\partial_t \phi^\dagger(x), \phi(0)]_{x_0=0} = -i\delta(\vec{x})$ (in $\hbar = 1$ units) leads to the sum rule

$$\int_0^\infty ds\rho(s) = 1 \,, \tag{16}$$

from where one deduces that:

- $Z = 1$ for a free theory
- $0 \leq Z \leq 1$ for an interacting theory
- $Z = 0$ if ϕ is a confined field

The last case does not follow directly from (16) but is an important result due to Weinberg. An example is given by the quark propagator for which we do not expect a residue since it is a confined (coloured) particle. The fact that $Z_{\text{quark}} \neq 0$ in each order in PT is a sign that the latter is not suited to describe the phenomenon of confinement.

8. By using causality, i.e. $\langle[\phi(x), \phi^\dagger(0)]\rangle = 0$ for $x^2 < 0$ spacelike, it follows that $\bar{\rho}(s) = \rho(s)$ where $\bar{\rho}(s)$ is the antiparticle spectral function associated with $\Delta_-(x^2, m^2) = \langle\phi^\dagger(x)\phi(0)\rangle$. This is a special case of the CPT theorem. Related to this matter it was Gell-Mann, Goldberger and Thirring [14] in 1954 who derived analyticity properties from causality, for $\gamma + N \to \gamma + N$, justifying dispersion relations from a non-perturbative viewpoint.

2.2 Dispersion Relations and Cauchy's Theorem

It is our goal to characterise the spectral function $\rho(s)$ in other ways than through the spectrum. In preparation to the general case we are going to recite the optical theorem for the S-matrix. The S-matrix (1) is conveniently parameterised as

$$S = \mathbb{1} + iT \,, \tag{17}$$

where T is the non trivial part of the scattering operator. From the unitarity of the S-matrix it follows that

$$\mathbb{1} = SS^\dagger = \mathbb{1} + \underbrace{i(T - T^\dagger)}_{-2\text{Im}[T]} + |T|^2 \,, \tag{18}$$

if and only if

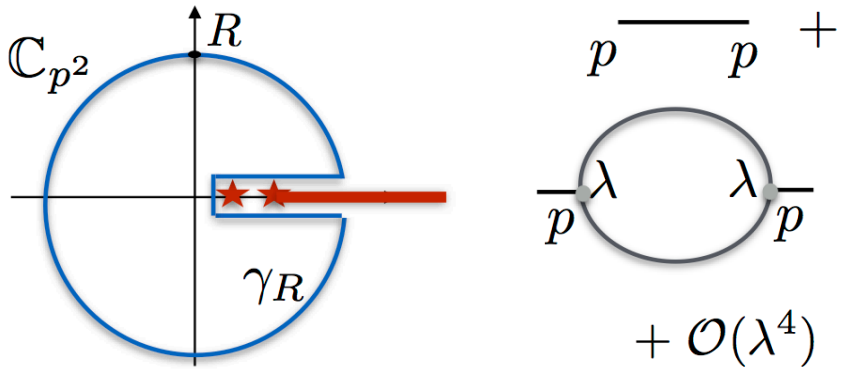


Figure 4: (left) Integration contour for 2-point function dispersion representation. (right) 2-point function in ϕ^3 theory in perturbation theory.

$$2\text{Im}[T] = |T|^2 = T^\dagger \sum_n |n\rangle\langle n|T \; . \tag{19}$$

Eq. (19) is the celebrated *the optical theorem* depicted in Fig. 3.

The right-hand side of the equation above is reminiscent of the spectral function in the case where T is associated with ϕ. Hence the expectation that $\rho(s)$ is related to an imaginary part is not unexpected from the viewpoint of the optical theorem. Below we are going to see that this is the case on very general grounds.

To do so we first take a little detour to discuss integral representations of arbitrary analytic functions by the use of Cauchy's theorem. Let $f(p^2)$ be an analytic function then by Cauchy's theorem the following integral representation holds

$$f(p^2) = \frac{1}{2\pi i} \int_\gamma \frac{ds\, f(s)}{s - p^2} \; , \tag{20}$$

provided that i) p^2 is inside the contour of γ , ii) the contour of γ does not cross any singularities.

Applying this techniques to the 2-point function in QFT one makes use of the knowledge of the analytic structure and chooses a contour γ_R as in Fig. 4 which does not cross any singularities. The radius is then taken to infinity, $R \to \infty$, which in the case where there are UV divergences results in subtraction which we generically parameterised $P(p^2)$ by a polynomial

function (the $P = A$ in (14) is a constant polynomial). The integral is then written as

$$\begin{aligned}\Gamma(p^2) &= \frac{1}{2\pi i}\int_{\gamma_R}\frac{ds\,\Gamma(s)}{s-p^2}\overset{R\to\infty}{\to}\frac{1}{2\pi i}\int_{s_1}^{\infty}\frac{ds\,(\Gamma(s+i0)-\Gamma(s-i0))}{s-p^2}+P(p^2)\\ &= \frac{1}{2\pi i}\int_{s_1}^{\infty}\frac{ds\,\mathrm{disc}[\Gamma(s)]}{s-p^2-i0}+P(p^2)=\frac{1}{\pi}\int_{s_1}^{\infty}\frac{ds\,\mathrm{Im}[\Gamma(s)]}{s-p^2-i0}+P(p^2)\,,\end{aligned}\tag{21}$$

where $s_1 <$ singularities (to the left of red part in Fig. 4(left)) and the second line is the definition of what is called the discontinuity along the branch cut. The last equality follows from $2i\mathrm{Im}[\Gamma(s)] = \mathrm{disc}[\Gamma(s)]$. This formula can be verified in each order in PT but is also justified on general grounds by the Schwartz reflection principle (cf. appendix A). In summary we then have that the spectral function is related to the the imaginary part and the discontinuity by

$$\rho(s) = \frac{1}{\pi}\mathrm{Im}[\Gamma(s)] = \frac{1}{2\pi i}\mathrm{disc}[\Gamma(s)]\,.\tag{22}$$

This equation follows from equating (11) and (21) and the knowledge that the subtraction constant are the same in both cases since they originate from UV divergences. Hence eliminating the contributions from the arc may result in UV-divergences and subtraction constants.

2.3 Dispersion Relations in Perturbation Theory

This section aims to illustrate (22) from the viewpoint of PT. In order to do PT one needs to specify a theory for which we choose $\mathcal{L}_{\mathrm{int}} = \lambda\phi^3 + \mathrm{h.c.}$. The pole contribution is then just the propagator and the first non-trivial interaction is generated by the diagram in Fig. 4(right). The 1-loop graph is UV divergent and requires regularisation. Using dimensional regularisation $d = 4 - 2\epsilon$ the result reads

$$\Gamma(p^2) = \frac{Z(\lambda)}{m^2-p^2-i0} - \lambda^2|A|\left(\frac{1}{\epsilon}+2-\beta\ln\left(\frac{\beta+1}{\beta-1}\right)\right)+\mathcal{O}(\lambda^4)\,,\tag{23}$$

with $\beta = \sqrt{1-(4m^2-i0)/p^2}$. The corresponding imaginary part divided by π must be the spectral function

$$\rho(p^2)\overset{(22)}{=}\frac{1}{\pi}\mathrm{Im}[\Gamma(p^2)]\overset{(23)}{=}Z(\lambda)\delta(p^2-m^2)+\lambda^2|A|\beta\theta(p^2-4m^2)+\mathcal{O}(\lambda^4)\,.\tag{24}$$

The UV divergence is not important for our purposes since it does not affect the imaginary part. Of course the UV-divergence means that the dispersion relation does not converge in the UV. This problem can be handled either by a subtracted dispersion relation or a polynomial counterterm and regularisation as discussed under point 6 in section 2.1.

Having resolved this technical issue we focus on the interpretation of the imaginary part. The propagator term is a pole singularity with a delta function in the spectral function and the

logarithm corresponds to a branch cut singularity resulting in a θ-function part. By the spectral representation (33) this branch cut must correspond to some physical intermediate state. This state is a 2-particle state starting at the minimum centre of mass energy $4m^2$ ranging all the way up to infinity. The precise value depends on the corresponding momentum configuration. Let the two particle momenta be parameterised by

$$p_{1,2} = (\sqrt{m^2+x^2}, 0, 0, \pm x) \ , \quad x > 0 \ , \quad p_{1,2}^2 = m^2 \ , \quad p^2 = (p_1+p_2)^2 = 4m^2 + 4x^2 \tag{25}$$

and therefore $4x^2 = p^2 - 4m^2$ which can be satisfied for any (arbitrarily large) $p^2 \geq 4m^2$.

3 Application of 2-point Functions

There are numerous applications of 2-point functions and dispersion relations. For example deep-inelastic scattering, QCD sum rules which we have alluded to in and below (13), $e^+e^- \to$ hadrons and inclusive $b \to X_{u,c}\ell\nu$ decays with the additional assumption of analytic continuation to Minkowski-space.[8] We choose to present the Weinberg sum rules (WSR).

3.1 Weinberg Sum Rules

The Weinberg sum rules are an ingenious construction involving a variety of conceptual ideas. They were proposed in 1967 by Weinberg [15] in the pre-QCD era but we are going to present them from the viewpoint of QCD e.g. [6, 16]. One considers the correlation function of left and right-handed current with two massless quark flavours

$$i\int d^4x e^{iq\cdot x}\langle T J_\mu^{a,L}(x) J_\nu^{b,R}(x)\rangle = (q_\mu q_\nu - q^2 g_{\mu\nu})\Pi_{\rm LR}^{a,b}(q^2) \ , \tag{26}$$

where

$$J_\mu^{a,(L,R)} = \bar{q} T^a \gamma_\mu q_{L,R} \ , \tag{27}$$

with $q_{L,R} = P_{L,R} q$, $P_{L,R} = 1/2(1 \mp \gamma_5)$, T^a being an $SU(2)$-generator (Pauli-matrix). The Lorentz-decomposition in (26) is valid in the limit of massless quarks. According to the previous sections the function $\Pi_{\rm LR}^{a,b}(-Q^2)$, with $-q^2 = Q^2 > 0$ satisfies a dispersion relation of the form

$$\Pi_{\rm LR}^{a,b}(-Q^2) = \frac{1}{\pi}\int_{s_0}^{\infty} \frac{ds\, {\rm Im}[\Pi_{\rm LR}^{a,b}(s)]}{s+Q^2} + A \tag{28}$$

where A is a subtraction constant due to the potential logarithmic divergence which may arise since $\Pi_{\rm LR}^{a,b}$ is of mass dimension zero.

The peculiarity of the WSR relies on the absence of lower dimension corrections in the OPE. This can be seen in an elegant manner using $SU(2)$ representation theory. We denote by $1, F$ and A the trivial, fundamental and adjoint representation of $SU(2)$ which are of dimension $1, 2$ and 3. The correlation function is in the (A,A)-representation of the $(SU(2)_L, SU(2)_R)$ global flavour symmetry. The individual OPE-contribution must be in the same global flavour symmetry representation or vanish otherwise.

[8] Without going into any details let us mention that it is in particular the inclusive decay rate and amplitudes of exclusive decays that are amenable to a dispersive treatment. It is the amplitude and not the rate that has the simple analytic properties. The inclusive case is special in that the rate can be written as an amplitude!

One considers Wilson's OPE in momentum space, valid for $Q^2 = -q^2 \gg \Lambda^2_{\rm QCD}$

$$\Pi^{a,b}_{\rm LR}(-Q^2) = C_{\not 1\!\!1}(Q^2)\langle \not 1\!\!1\rangle + C_{\bar q q}(Q^2)\frac{(\langle \bar q^a_L q^b_R\rangle + \text{h.c.})}{Q^3} + C_{JJ}(Q^2)\frac{\langle J^{L,a}_\mu J^{R,b}_\mu\rangle}{Q^6} + \mathcal{O}\left(\frac{\Lambda^8_{\rm QCD}}{Q^8}\right) . \quad (29)$$

The functions $C(Q^2)$ are known as Wilson coefficients and carry logarithmic correction in QCD. As can be seen from the formula above the condensate terms of dimension d are suppressed by $1/Q^d$ relative to the identity term. The $\langle \not 1\!\!1\rangle$-term corresponds to PT and the condensates, i.e. VEVs of operators, are of non-perturbative nature. The former is in $(1,1)$-representation and therefore absent.[9] A quark bilinear $\langle \bar q^a_L q^b_R\rangle$ is in the (F,F)-representation and absent for the same reason. The dimension six operator is, somewhat trivially, in the (A,A)-representation and therefore the leading term appears at $\mathcal{O}(1/Q^6)$. The vanishing of the $1/Q^2$- and $1/Q^4$-terms lead to constraints. The latter can be obtained by expanding the denominator in inverse powers of Q^2,

$$\frac{1}{s+Q^2} = \frac{1}{Q^2}\frac{1}{1+s/Q^2} = \frac{1}{Q^2} - \frac{s}{Q^4} + \frac{s^2}{Q^6} + \dots . \quad (30)$$

The exact sum rules on the spectral function

$$\int_{s_0}^\infty ds\, \Pi^{a,b}_{\rm LR}(s) = 0 , \qquad \int_{s_0}^\infty ds\, \Pi^{a,b}_{\rm LR}(s) s = 0 \quad (31)$$

known as the *first and second Weinberg sum rule* follow.

Note the absence of the perturbative term means in particular that there is no UV-divergence and hence $A = 0$. Since the convergence is two powers in s higher (1st and 2nd WSR) the dispersion relation is referred to a as superconvergent.

The WSR (31) are a powerful non-perturbative constraint. We present the original application pursued by Weinberg. First we notice that the left-right correlator can be written as a difference of the vector and axial correlator

$$\Pi^{a,b}_{\rm LR}(s) = \frac{1}{4}\left(\Pi^{a,b}_{\rm VV}(s) - \Pi^{a,b}_{\rm AA}(s)\right) , \quad (32)$$

where $J^{V(A),a}_\mu \equiv \bar q T^a \gamma_\mu(\gamma_5) q$. Taking into account the lowest lying particles π, ρ and a_1 in the narrow width approximation and assuming isospin symmetry (i.e. global $SU(2)_V$ -flavour symmetry) one arrives at[10]

$$\rho^{a,b}_V(s) = \frac{1}{\pi}\text{Im}[\Pi^{a,b}_{\rm VV}](s) = \delta^{ab}(f^2_\rho \delta(s-m^2_\rho) + \theta(s-s_0)\sigma_V) ,$$
$$\rho^{a,b}_A(s) = \frac{1}{\pi}\text{Im}[\Pi^{a,b}_{\rm AA}](s) = \delta^{ab}(f^2_\pi \delta(s) + f^2_{a_1}\delta(s-m^2_{a_1}) + \theta(s-s_0)\sigma_A) . \quad (33)$$

[9] The practitioner will notice the absence of from the orthogonality of the projectors $P_L P_R = 0$ which necessarily arises in the a perturbative computation in the limit of massless quark.

[10] Note since we work in the massless limit the pion is massless as it is the goldstone boson of broken chiral symmetry $SU(2)_L \otimes SU(2)_R \to SU(2)_V$. The spin parity quantum numbers J^P of the π, ρ and a_1 are $0^-, 1^+, 1^-$ respectively.

The functions $\sigma_{V,A}$ contain any higher states and multiparticle states. If one assumes that around s_0 perturbation theory is valid then $\rho_{\rm LR}(s) = 0$ for $s > s_0$ which in turn implies $\sigma_V = \sigma_A$.

Hence using (33) the two WSR (31) read

$$f_\rho^2 = f_\pi^2 + f_{a_1}^2 \ , \qquad m_\rho^2 f_\rho^2 = m_{a_1}^2 f_{a_1}^2 \ , \tag{34}$$

where the decay constants are defined as

$$\langle \rho[a_1]^b(p)|J_\mu^{V[A],a}|0\rangle = \delta^{ab}\eta_\mu(p) m_{\rho[a_1]} f_{\rho[a_1]} \ , \quad \langle \pi^b(p)|J_\mu^{A,a}|0\rangle = \delta^{ab} p_\mu f_\pi \ , \tag{35}$$

with η being the polarisation vector.

In his original paper Weinberg used the experimentally motivated KSFR relation $f_\rho^2 = 2f_\pi^2$ which then leads to $m_{a_1} = \sqrt{2} m_\rho$. This relation is reasonably satisfied by experiment: $m_{a_1}/m_\rho \simeq 1.63 \simeq 1.15\sqrt{2}$. Let us end this section with mentioning two further applications of this reasoning.

- Being related to chirality the WSR, or the Π_{LR} function, is a measure of contributions to electroweak precision measurement in the case of physics beyond the Standard Model coupling to new fermions. The WSR serve to estimate the contribution of strongly coupled extensions of the standard model such as technicolor and the composite Higgs model.

- The inverse moments of the spectral function, with pion pole subtracted, are related to the low energy constant L_{10} of chiral perturbation theory. Note, chiral perturbation theory is an expansion in Q^2, and not $1/Q^2$ as the OPE, and thus leads to inverse moments rather than moments themselves. It is not the WSR per se which are important in this respect but the onset of the duality threshold of PT-QCD which allows to estimate L_{10} in terms of f_{π,ρ,a_1}. The estimate of L_{10} obtained is in reasonable agreement with experiment.

At this point the students were given the choice of continuing with applications (e.g. infrared interpretation of the chiral anomaly, positivity of low energy constants ...) or a the more conceptual topic of higher point functions properties. Their choice was the latter.

4 Analyticity Properties of higher point Functions

There are many motivations to study higher point functions and their analytic structure amongst which we quote the following:

a) As seen in the introduction they describe the scattering of n-particles.

b) From the discussion in section 2.2 it is clear that to write down dispersion relations one needs to know first and foremost the analytic structure of the amplitude in question.

b) 3-point functions are relevant for the study of form factors. Consider for example the $B \to \pi$ form factor, relevant for the determination of the CKM-element $|V_{\rm ub}|$, defined by

$$\langle \pi(p)|V_\mu|B(p_B)\rangle = (p_B)_\mu f_+^{B\to\pi}(q^2) + \dots \ , \tag{36}$$

where the dots stand for the other Lorentz structure and $V_\mu = \bar{b}\gamma_\mu u$ is the weak current (the axial part does not contribute in QCD by parity conservation). Then the form factor

can be extracted from the following 3-point function, by using a double dispersion relation (dispersion relation in the p_B^2 and p^2-variable)

$$\begin{aligned}\Gamma(p^2,p_B^2,q^2) &= i^2\int_{x,y} e^{-i(p_B\cdot x-p\cdot y)}\langle TJ_B(x)J_\pi(y)V_\mu(0)\rangle\ ,\\ &= (p_B)_\mu\left(\frac{g_\pi\, f_B\, f_+^{B\to\pi}(q^2)}{(p_B^2-m_B^2)(p^2-m_\pi^2)}+\text{higher}\right)+\dots\ ,\end{aligned}\tag{37}$$

where "higher" stands for higher contributions in the spectrum (the analogue of $\sigma(s)$ in (24)) and

$$\begin{aligned}J_B &= \bar{q}i\gamma_5 b\ ,\quad \langle B|J_B|0\rangle = f_B\ ,\\ J_\pi &= \bar{q}i\gamma_5 q\ ,\quad \langle 0|J_\pi|\pi\rangle\ = g_\pi\ ,\end{aligned}\tag{38}$$

play the role of the interpolating operators of the LSZ-formalism cf. footnote 1. As previously mentioned the key idea is then to compute $\Gamma(p^2,p_B^2,q^2)$ in some formalism and to find ways to either estimate or suppress the higher states in order to extract the form factor where g_π and f_B are assumed to be known quantities.

In fact if we were able to compute $\Gamma(p^2,p_B^2,q^2)$ with arbitrary precision then the function would assume the form in (37) and we could simply extract the form factor from the limiting expression

$$f_+^{B\to\pi}(q^2)=\frac{1}{g_\pi f_B}\lim_{p_B^2\to m_B^2,p^2\to m_\pi^2}(p_B^2-m_B^2)(p^2-m_\pi^2)\Gamma(p^2,p_B^2,q^2)\ ,\tag{39}$$

which makes the connection to the LSZ-formalism (2) apparent. Unfortunately at present we cannot hope to do so and therefore we have to resort to the approximate techniques as alluded to above.

We have seen that for the 2-point function the analytic structure of the first sheet (physical sheet) is fully understood through the Källén-Lehmann representation. Moreover the singularities on the physical sheet are in one-to-one correspondence with the physical spectrum. For higher point function less is known in all generality. We refer the reader to the works of Källén-Wightman [17] and Källén [18] for some general studies of 3- and 4-point functions using first principles and the summary by Andrè Martin [19] for a comparatively recent survey of rigorous results.[11]

Hence one has to become immediately more modest! We are going to restrain ourselves to analysing singularities in PT for *physical momenta* (i.e. real momenta). This is done by the use of two major tools:

i) *Landau equations*: which answer the question about the location of the singularities cf. section 4.2. The question on which sheet the singularities are is a difficult question which we comment on.

[11] Am important topic was the conjecture by Mandelstam of a double dispersion relation for $2\to 2$ scattering (i.e. 4-point function) which was consistent with known results but never proven in all generality even in perturbation theory. From this the Froissart bound was derived which states that the cross section for the scattering of two particles cannot grow faster than $\ln^2 s$ (where s is the centre of mass energy).

ii) *Cutkosky rules*: are rules for computing the discontinuity of an amplitude cf. section 4.3.

Before analysing these matters in more details let us first consider the normal-thresholds for higher point functions.

4.1 Normal Thresholds: cutting Diagrams into two Pieces

The so-called normal thresholds are directly associated with unitarity. They originate from cutting (to be made more precise when discussing the Cutkosky rules) the diagram into two pieces and generalise the equal size optical theorems cuts. Cutting a diagram into two pieces is equivalent to the combinatorial problem of grouping the external momenta into two sets. Tab. 1 provides the overview of the number of cuts versus number of independent kinematic variables. For the two lowest functions there are no constraints whereas for all higher point functions there are constraints due to momentum conservation. For the 4-point functions this constraint is known as the famous *Mandelstam constraint*

$$\sum_{i=1}^{4} p_i^2 = s + t + u \;, \quad s = (p_1 + p_2)^2 \;, \quad t = (p_1 + p_3)^2 \;, \quad u = (p_1 + p_4)^2 \;, \tag{40}$$

where we choose conventions such that all momenta are incoming (momentum conservation reads $\sum_{i=1}^{4} (p_i)_\mu = 0$). The fact that the amplitudes become functions of several complex

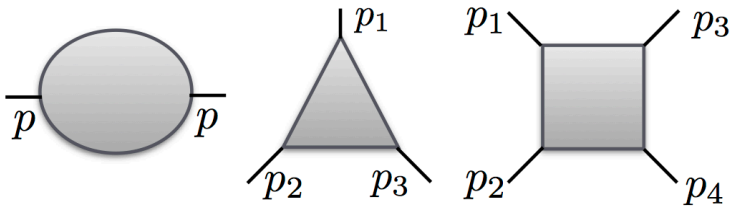


Figure 5: Sketch of generic $2, 3, 4$-point function. The number of unitarity cuts and independent kinematic variables are listed in Tab. 1.

variables makes matters more difficult. For example:

- From the Mandelstam constraint it can be seen that the unitarity cuts from one channel do appear on the negative real axis in the complex plane of another channel. Say the u-channel cuts, with forward kinematics $t = 0$, do appear on the negative real axis in the complex plane of $s = \sum_i m_i^2 - u$ ($p_i^2 = m_i^2$ on shell). These u-channel cuts in the s-plane are sometimes referred to as left-hand cuts as opposed to the proper s-channel unitarity cuts on the right-hand side of the complex plane (cf. Fig. 4).
- Several complex variables allow for dispersion relations in multiple channels. An example of which is the conjectured Mandelstam representation, cf. [4, 1], which is a double dispersion relation.
- There are cuts which are not directly related to unitarity, so-called anomalous thresholds, cutting the diagram into more than 2 pieces. We will return to the latter briefly when discussing the Landau equations and Cutkosky rules.

n-point function	#cuts	#variables	#constraints
2	1	1	0
3	3	3	0
4	7	6	1
5	15	10	5

Table 1: The number (=#) of unitarity cuts equals the number of independent variables plus the number of constraints. Cf. Fig. 5 some diagrams. For the 2- and 3-point functions there are no constraints whereas for the 4-point function there is the famous Mandelstam constraint (40). Generally for $n \geq 4$ the number of invariants is $4n - 10$ where $4n$ corresponds to all the components of the four momenta and 10 subtracts the Lorentz-symmetries. (For $n \leq 4$ the formula reads $n(n-1)/2$ which gives a larger number since not all the Lorentz symmetries can be used for reduction of parameters). For the 5-point function the reduction from 15 cuts to 10 independent variables follows from multiple use of the Mandelstam relation (40) on subtopologies of the kinematic diagram e.g.[20].

4.2 Landau Equations

Before stating the Landau equations it is useful to look at singularities of a one-variable integral representation where the integrand has pole singularities as a function of external parameters. The Landau equations originate from analysing this problem for the integrals of several variables appearing in PT. The presentation in this section closely follows the original paper [21] and the textbook[1].

4.2.1 Singularities of one-variable Integral Representations

Consider the following integral representation of a analytic function $f(z)$

$$f(z) = \int_{\gamma_{ab}} g(z, w) dw \ , \tag{41}$$

where the integrand $g(z, w)$ contains pole singularities $w_i(z)$ which depend on z. The path γ_{ab} ranges from a point a to b and does not cross any singularities for some $z = z_0$ as shown in Fig. 6(left). The analytic properties of $f(z)$ depend on whether or not the path γ_{ab} can be smoothly deformed away from approaching pole singularities $\omega(z_i)$.

For example, if we start from $z = z_0$ and go to $z = z_1$ with $\omega(z_1)$ crossing the γ_{ab} (cf. Fig. 6(middle)) then the path γ_{ab} can be smoothly deformed as in Fig. 6(right) and this constitutes an analytic continuation of the function $f(z)$. There are though instances when this is not possible:

a) When a singularity $w_i(z)$ approaches one of the endpoints a or b; e.g. $w_i(z_1) = a$ Fig. 7(left). This case is known as an *endpoint singularity.*

b) When two singularities approach each other, $w_1(z_1) = w_2(z_1)$ from different direction of the integration path as depicted in Fig. 7(right). This case is known as a *pinch singularity.*

c) When the path needs to be deformed to infinity (can be reduced to case b).

In PT it is the pinch singularity type that gives rise to the singularities.

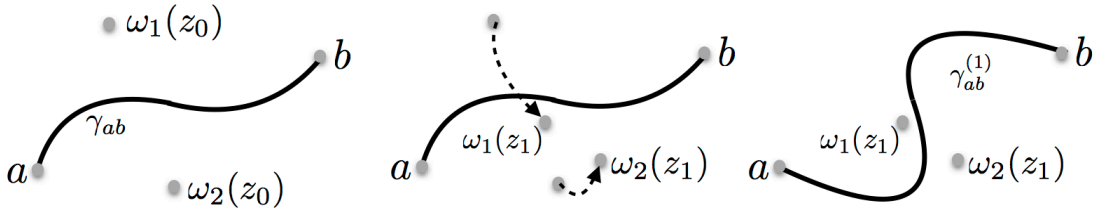


Figure 6: Path γ_{ab} between endpoints a and b. (left) Poles $\omega_{1,2}(z_0)$ of the integrand $g(z,\omega)$ in (41) for $z = z_0$ (middle) Deformation of poles $\omega_{1,2}$ by the parameter z_0 to z_1. This is not provide an analytic continuation of the function $f(z)$ around z_0 to z_1. (right) deformation of path γ_{ab} to $\gamma_{ab}^{(1)}$ serves as a (legitimate) analytic continuation of the function $f(z)$ in (41) around z_0 to z_1.

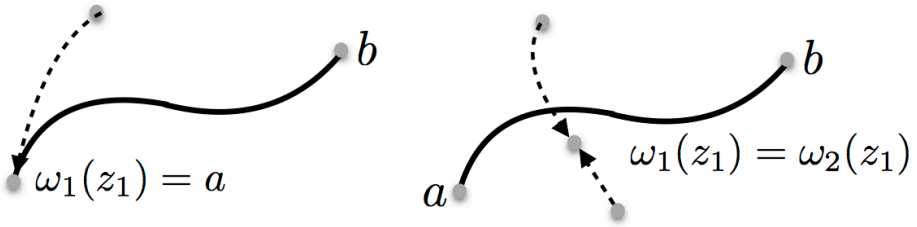


Figure 7: (left) endpoint singularity (right) pinch singularity

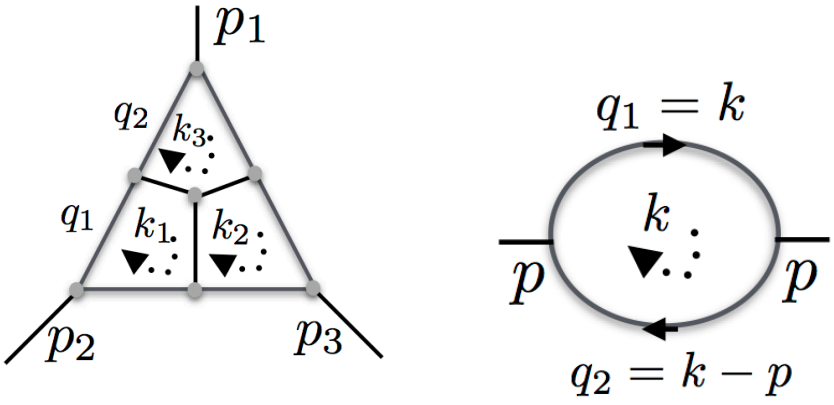


Figure 8: (left) Generic Feynman diagram aimed to clarify notation used in text (right) bubble graph discussed in the text

4.2.2 Landau Equations = several-variable Case

Landau [21] and others (cf. [1] for further references) have analysed the problem of singularities, discussed for a single integral above, for the case of several variables in the context of Feynman graphs. A generic Feynman graph of L-loop of momenta k_i $(i = 1 \dots L)$, N-propagators, external momenta p_i (cf. Fig. 8(left) for a representative graph) can be written as follows

$$I = \int Dk \frac{1}{\prod_{i=1}^{N}(q_i^2 - m_i^2 + i0)} , \qquad Dk = \prod_{i=1}^{L} d^4k_i , \tag{42}$$

where $q_i = q_i(p_j, k_l)$ are the momenta of the propagators. By the technique of Feynman parameters (generalisation of $(AB)^{-1} = \int_0^1 d\alpha(\alpha A + (1-\alpha)B)^{-2}$) one may rewrite I as follows

$$I = \int Dk \int_0^1 D\alpha \frac{1}{(F + i0)^N} , \qquad D\alpha = \prod_{i=1}^{N} d\alpha_i \delta(1 - \sum_{i=1}^{N} \alpha_i) , \tag{43}$$

where the crucial denominator F reads

$$F = \sum_{i=1}^{N} \alpha_i (q_i^2 - m_i^2) . \tag{44}$$

Is seems worthwhile to emphasise that even though these formulae look rather involved they are completely straightforward.

The key idea is that there are different types of singularities depending on how many of the N propagators are on shell, i.e. $q_i^2 - m_i^2$. It is the number of on-shell propagators which serves as a classification of the singularities. The Landau equations in condensed form are:[12]

[12]The Landau equations enjoy an interpretation in terms of electric circuits since the equations are analoguous to Kirchoff's equations cf. [1] and references therein.

Landau equations/conditions There are singularities if and only if

$$\text{[i] either } q_i^2 = m_i^2 \text{ or } \alpha_i = 0 \,, \tag{45}$$

$$\text{[ii]} \sum_{i \in \text{loop}(l)} \alpha_i (q_i)^\mu = 0 \text{ for } l = 1 \dots L. \tag{46}$$

We have assumed $q_i = k + \dots$ with k being the loop momentum as otherwise one needs to introduce spurious minus signs into the sum above.

We are not going to show a proof of the Landau equations but state the result and argue for its plausibility below. Let us emphasise that the Landau equations neither tell us on which sheet the singularities are (cf. section 4.2.3 for the refinement in this direction) nor how to compute the discontinuity relevant for the dispersion relations (cf. Cutkosky rules section 4.3). The first condition assures that $F = 0$ by demanding that each summand is zero in (44). The interpretation of $q_i^2 = m_i^2$ is of course that the corresponding propagator is on-shell and contributes to the singularity. Correspondingly $\alpha_i = 0$ means that the corresponding line does not enter the singularity. In Fig. 11 we give an example of a 3-point function cut. The second condition (46) has a geometric interpretation. It means that the corresponding singularity surfaces are parallel to each other and that the hypercontour can therefore not be deformed away from the approaching singularity surfaces. This is the analogy of the pinch singularity discussed in section 4.2.1. Eq. (46) can be cast into a more convenient form by contracting the equation by a vector $(q_j)_\mu$ which leads to the matrix equatons

$$\text{[ii']} \quad Q\vec{\alpha} = 0 \,, \qquad (Q)_{ij} = q_i \cdot q_j \,, \quad (\vec{\alpha})_i = \alpha_i \,. \tag{47}$$

For non-trivial $\vec{\alpha}$ the second Landau equation is then solved by demanding that the so-called Cayley-determinant detQ $= 0$ vanishes.

4.2.3 Landau Equation exemplified: 1-loop 2-point Function (bubble graph)

Consider the bubble graph depicted in Fig. 8(right) with external momenta p, loop momenta k and momenta $q_1 = k$ and $q_2 = k - p$. The first Landau equation (45) tells us that [As a homework you could ask yourself why the case $\alpha_1 = 0$ and $q_2^2 = m_2^2$ is not an option for a singularity] $q_1^2 = m_1^2$ and $q_2^2 = m_2^2$. The second Landau equation (47) can be cast into the form $\det Q = 0$

$$\det Q = \det \begin{pmatrix} m_1^2 & q_1 \cdot q_2 \\ q_1 \cdot q_2 & m_2^2 \end{pmatrix} = 0 \quad \Leftrightarrow q_1 \cdot q_2 = \pm m_1 m_2 \tag{48}$$

which we may reinsert back into $p = q_1 + q_2$ which yields the two singularities $p_{(+)}^2 = (m_1 + m_2)^2$ *and* $p_{(-)}^2 = (m_1 - m_2)^2$,

$$p^2 = (q_1 - q_2)^2 = q_1^2 - 2q_1 \cdot q_2 + q_2^2 = (m_1 \mp m_2)^2 \,. \tag{49}$$

This might surprise us at first since from unitarity we expect there to be a branch point at $p^2_{(+)}$ but the point $p^2_{(-)} < p^2_{(+)}$ has no place in this picture. The resolution comes upon recalling that the Landau equations inform us about the singularities but do not tell us on which sheet they are! In order to learn more we may solve $Q\vec{\alpha} = 0$ with $\vec{\alpha} = (\alpha, (1-\alpha))^T$ which gives

$$\alpha_\pm = \frac{m_2}{m_2 \pm m_1} \Rightarrow \quad 0 < \alpha_+ < 1 \,, \quad \alpha_- > 1 \text{ or } \alpha_- < 0 \,, \tag{50}$$

for $m_{1,2} > 0$. From this we learn that α_+ is within the integration region (recall $\int_0^1 D\alpha$ (43)) and $p^2_{(+)}$ is therefore on the physical sheet, wheras α_- is outside the integration region necessitating the deformation of the α-contour. This indicates that α_- may not be on the physical sheet as the contour may crosses singularities in the course of deformation. The singularity $p^2_{(-)} = (m_1 - m_2)^2$ is sometimes referred to as a pseudo threshold. These findings suggest an important refinement of the Landau conditions.

Refinement of Landau equations For physical configuration, by which we mean the real external momenta, the Landau singularities are

- on the first (physical) sheet when $\alpha_i \in [0, 1]$
- may or may not be on the first (physicial) sheet when $\alpha_i \notin [0, 1]$

For non physical configuration, complex momenta, the situation is far from straightforward to say the least. The method of choice is often deformation to a case of a physical configuration and then deform to complex momenta checking whether or not singularities are crossed in that process. Crossing a singularity correspond to changing the Riemann sheet. Alternatively one can deform the masses to complex values keeping the $\alpha_i \in [0, 1]$ and then deform back.

Geometric interpretation and the forgotten second type singularity We take a detour and give a geometrical interpretation of the singularities of the bubble graph. The first and second Landau equations (45,46) read

$$(k-p)^2 = m_1^2 \,, \quad k^2 = m_2^2 \,, \quad \alpha k_\mu + (1-\alpha)(k-p)_\mu = 0 \,. \tag{51}$$

The first Landau equation defines two hyperboloids with centres displaced by p with respect to each other. The second Landau equation assures that p and k are parallel. First we discuss the previously found solutions and then uncover the forgotten second type singularity.

- *Normal and pseudo threshold*
  Equations (51) are satisfied when the two hyperboloids touch each other at the symmetric point with displacement in the k_0-direction. The displacement is given by $p^2_{(\pm)} = (m_1 \pm m_2, 0, 0, 0)^2 = (m_1 \pm m_2)^2$ in the case where the hyperboloids open up in opposite and the same direction respectively. We refer the reader to Fig. 9 (left) and (middle) for an illustration and the relevant equations in the caption.

- *Second type singularity*
  Fig. 9 (right) shows yet another type of singularity. For any light-like displacement p, the two hyperboloids meet at infinity. These type of singularities were first noted by Cutkosky [22] who named them non-Landauian singularities whereas nowadays they are known as *second type singularities* [1]. The Cayley-determinant is zero since q_1 and q_2 are parallel with k and p being light-like. If we parameterise $p/k = \epsilon$ then the second Landau equation is satisfied when $\alpha = (1+\epsilon)/\epsilon$ which diverges when $\epsilon \to 0$ and in particular outside the $[0,1]$-interval. Hence the singularity may therefore not be on the physical sheet. More directly the singularity $p^2_{(0)} = 0$ has no interpretation in terms of the spectrum. By the one-to-one relation of the spectrum and the 2-point function singularities (cf. Källén-Lehmann representation in section 2) it is to be concluded that this singularity is not on the physical sheet.

More generally second type singularities are determined by the vanishing of the Gram-determinant $\det p_i \cdot p_j = 0$ (where the p_i are the external momenta) [1]. The singularity $p^2_{(0)} = 0$ for the bubble-graph is then just the solution of the one-dimensional Gram-determinant. In summary second-type singularities are therefore independent of the masses and not on the physical sheet.[13]

Discussion upon using explicit 1-loop result: After these abstract considerations we consider it advantageous to illustrate these type of singularities explicitly. The bubble graph

$$B_0(p^2, m_1^2, m_2^2) = \frac{4\pi^2}{i} \int \frac{d^4k}{(2\pi)^4} \frac{1}{(k-p)^2 - m_1^2 + i0)(k^2 - m_2^2 + i0)} \,, \tag{52}$$

is UV-divergent. In order to avoid regularisation we may use the same trick as for the subtracted dispersion relation and take the difference with a fixed value. The results, valid on the physical sheet, reads (e.g. [4])

$$B_0(p^2, m_1^2, m_2^2) - B_0(\bar{p}^2, m_1^2, m_2^2) = \frac{1}{2p^2} \left[X(p^2, m_1, m_2) - X(0, m_1, m_2) \right] - [p^2 \leftrightarrow \bar{p}^2] \,, \tag{53}$$

where $\bar{p}^2$ is the arbitrary subtraction point,

$$X(p^2, m_1, m_2) = \sqrt{\lambda} \ln \left(\frac{\sqrt{(m_1+m_2)^2 - p^2} + \sqrt{(m_1-m_2)^2 - p^2}}{\sqrt{(m_1+m_2)^2 - p^2} - \sqrt{(m_1-m_2)^2 - p^2}} \right)^2 \tag{54}$$

and $\lambda = (p^2 - (m_1+m_2)^2)(p^2 - (m_1-m_2)^2)$ the Källén-function and not to be confused with a coupling constant.[14] It is noted that the expression above is consistent with (23) in the limit $m = m_1 = m_2$. We can learn three things from the representation (53). On the physical sheet: (i) there is a branch cut starting at $p^2 \geq (m_1+m_2)^2$ (normal threshold) (ii) there is no branch cut at $p^2 = (m_1-m_2)^2$ (pseudo threshold) and (iii) there is no singularity for $p^2 \to 0$

[13] There also exist mixed type singularities where some loop momenta are pinched at infinity and others not. The reader is referred to the book [1] for examples and discussion.

[14] From the viewpoint of the optical theorem the Källén-function arises from the phase space integration. In the rest-frame of the particle associated with the four momentum squared p^2, the absolute velocity of one of the decaying particles $|v_1| = |v_2|$ is related to the Källén-function as follows $|v_{1,2}| = \sqrt{\lambda}/2p^2$. Hence at this singularity the velocity is infinite consistent with the hyperboloids meeting at infinity.

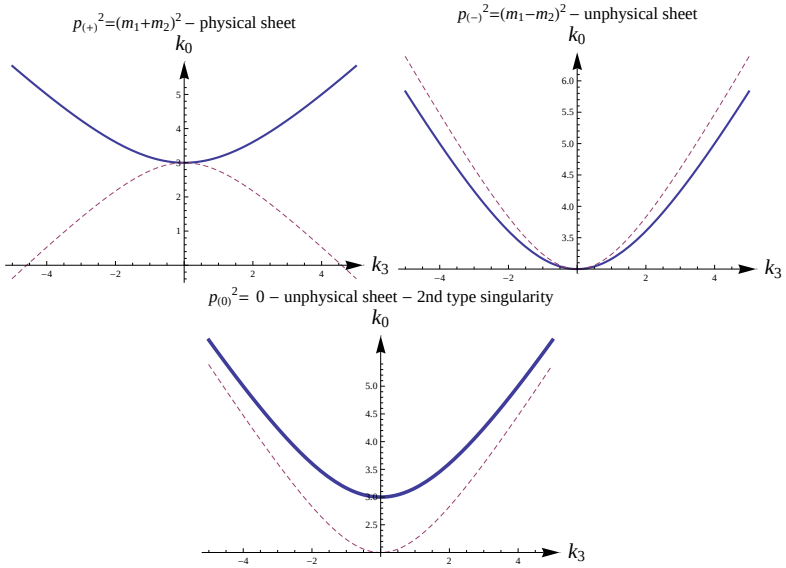


Figure 9: Choosen $m_1 = 3$ and $m_2 = 2$ in arbitrary units. (left) *Normal threshold:* $k_0 = \sqrt{k_3^2 + m_1^2}$ and $k_0 = (m_1 + m_2) - \sqrt{k_3^2 + m_2^2}$ and $p_+ = (m_1 + m_2, 0, 0, 0)$. (middle) *Pseudo threshold:* $k_0 = \sqrt{k_3^2 + m_1^2}$ and $k_0 = (m_1 - m_2) + \sqrt{k_3^2 + m_2^2}$ and $p_- = (m_1 - m_2, 0, 0, 0)$. (right) *Second type singularity:* $k_0 = \sqrt{k_3^2 + m_1^2}$ and $k_0 = \sqrt{k_3^2 + m_2^2}$ and $p_{(0)} = (0, 0, 0, 0)$ the two curves meet at infinity and are independent of the masses. It is obvious that any light-like p, e.g. $p_{(0)} = (x, 0, 0, x)$ for x real, is also a valid parametrisation.

(second type singularity). To see the correctness of (ii) one has to note that $\sqrt{\lambda}$ is imaginary for $(m_1-m_2)^2 < p^2 < (m_1+m_2)^2$. In summary it is confirmed from the explicit representation (53) that the pseudo threshold and the second type singularity are, indeed, not present on the physical sheet.

4.3 Cutkosky rules

The question of how to compute the actual singularities for physical configurations is answered by the cutting rules stated by Cutkosky [22] shortly after the Landau equations were formulated. This is by no means accidental as they are closely related. The Landau equations tell us that there is a singularity if either $q_i^2 = m_i^2$ or $\alpha_i = 0$ (45) and the Cutkosky rules state that the corresponding singularity can be computed by replacing each on-shell (or cut propagator)

$$\frac{1}{q_i^2 - m_i^2 - i0} \to -2\pi i \delta^{(+)}(q_i^2 - m_i^2) \, , \tag{55}$$

with the $\delta^{(+)}(p^2 - m^2) \equiv \delta(p^2 - m^2)\theta(p_0)$-distribution. Before we motivate this rather elegant and surprisingly simple prescription let us state the result more explicitly.

The discontinuity of I (42), for real momenta, with propagators $i = 1 \dots r \leq N$ cut is given by

$$\text{disc}[I] = (-2\pi i)^r \int Dk \frac{\prod_{i=1}^{r} \delta^{(+)}(q_i^2 - m_i^2)}{\prod_{j=1}^{N-r}(q_{r+j}^2 - m_{r+j}^2)} \, , \tag{56}$$

and is known as the Cutkosky or cutting rule!

Before trying to make plausible the formula (56) let us state the obvious. The rule (55) certainly gives the discontinuity of the propagator. The somewhat surprising fact is that this seems to be the recipe in any diagram. In the book of Peskin and Schröder [23] one can find the bubble graph evaluated in this way.

In order to motivate the Cutkosky rules we are going to sketch an argument given in the original paper [22] which is also reproduced in [1]. One considers an integral representation of the form

$$I(z) = \int dk_1^2 \frac{F(k_1^2, z)}{k_1^2 - m_1^2 - i0} \, , \tag{57}$$

where the variable z is a function of the other momenta external and internal. Let the integrand F contain a pole $w_1(z)$ which approaches m_1^2 for some z such that there is going to be a pinch singularity as shown in Fig.10(left). One then switches to the equivalent configuration where the contour is deformed below the mass m_1^2 at the cost of encircling the singularity m_1^2. In the next step the integral is performed using Cauchy's theorem which is equivalent to replacing the denominator by $\delta(k_1^2 - m_1^2)$. This argument falls short in justifying the additional physical condition $\theta((k_1)_0)$. Repeated use of the argument above, for each propagator gives the celebrated Cutkosky rules. The Cutkosky rules have recently been proven more rigorously [24] using ideas and methods by Pham. For the case of normal thresholds (unitarity cuts only) the method of the largest time equation [25] provides an elegant derivation of the cutting rules.

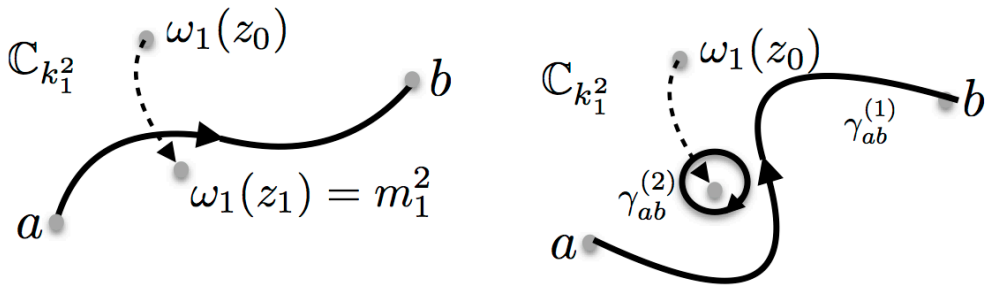


Figure 10: (left) pinch singularity (right) equivalent path $\gamma_{ab} \sim \gamma_{ab}^1 + \gamma_{ab}^2$ with isolated pinch singularity

4.4 Anomalous Thresholds & physical Interpretation of Landau Equations

4.4.1 Brief remarks on anomalous Thresholds

By studying the 1-loop bubble graph, in section 4.1, we have encountered singularities of the normal & pseudo and 2nd type; cf. Tab. 2. The most important singularities for practical purposes (e.g. dispersion relation, experiments) are the singularities which are on the physical sheet of which the normal one is the only type so far. This poses the questions whether there are any singularities on the physical sheet. By the work of Källén-Lehmann (11) we know that this is not the case for 2-point function and we must therefore look at higher point functions.

There are indeed new classes of singularities for 3- and higher point functions. A 3-point function Fig. 11(right), for example, can be cut into more than two pieces which is going beyond the singularities discussed so far. Putting all three propagators on shell corresponds to $\alpha_i \neq 0$ at the level of the Landau equations. The corresponding singularities are known as *anomalous thresholds*.[15] It is obvious that the singularities in say p_1^2 depend on the values of p_2^2 and p_3^2 (provided the line between the two is not contracted $\alpha_1 \neq 0$ as otherwise one encounters the singularities discussed so far).

Whether or not anomalous thresholds appear on the physical sheet, returning to our original questions, depends on the external momenta $p_{1,2}^2$. Below we mention examples where the anomalous thresholds appear on the physical sheet.

(a) Consider the 1-loop version of the 3-point function with $p^2 \equiv p_2^2 = p_3^2$, $m \equiv m_2 = m_3$ with masses as indicated in Fig. 11(left). For this configuration there is an anomalous threshold in $p_1^2 \geq X$ with $X = 4m^2 - (p^2 - (m^2 + m_1^2))^2/m_1^2$ provided the condition $p^2 > m^2 + m_1^2$ holds [4]. X is a branch point and the higher values are branch cuts. This anomalous threshold is below the two particle threshold at $4m^2$ and might be regarded as the very reason for calling these thresholds anomalous![16]

[15] Their existence can be deduced from hermitian analyticity [1] which in our case corresponds to the property that the imaginary part is proportional to the discontinuity.

[16] This is of relevance for form factors which, as we have seen, can be related to 3-point functions. The anomalous threshold does appear for the electromagnetic form factors of the hyperons whereas for for the pion

(b) For an example of a momentum configuration where the anomalous threshold is complex and on the physical sheet we refer the reader to the appendix in [26]. This anomalous threshold has to be taken into account in the dispersion relations by choosing the contour accordingly.

The corresponding 3-point function serves as an example where the Schwartz reflection principle (60) does not apply since the amplitude is imaginary on the entire real axis. In some more detail: the 1-loop 3-point function evaluated in PT does obey Schwartz's reflection principle (60) with no anomalous threshold on the first sheet. It is though not the correct analytic continuation into the lower half-plane. Crucially, after elimination of an unphysical branch cut on the real line Schwartz's reflection principle is not obeyed anymore allowing for the anomalous threshold to appear on the physical sheet in the lower half plane.

singularity	normal	pseudo	2nd type	anomalous
physical sheet	yes	no	no	$p^2_{2,3}$-dependent
remark	unitarity		mass-indep.	Leading Landau

Table 2: Different type of singularities described in the text: normal-, pseudo- & anomalous thresholds and 2nd type singularities. Whether or not the anomalous threshold is on the physical sheet depends on the momentum configuration of the other channels. E.g. in the example the triangle graph (cf. Fig. 11(right)) in the text the p_1^2-channels singularities are $p^2_{2,3}$-dependent. In addition to the singularities mentioned above there are also, the previously mentioned, mixed type singularities; mixed between 2nd type and others for different loop momenta. Not much is known about the Riemann sheet properties of mixed type singularities [1].

We end this section with a miscellaneous remarks on terminology and practicalities.

- Anomalous thresholds go beyond the concept of unitarity cuts in that they allow for cutting the diagram into more than two pieces. Cutkosky [22] was well aware of this and introduced the term *generalised unitarity* in the context of his equations.
- The number of propagators that are put on-shell (in a loop) give rise to a natural classification. The singularity with the maximal number of on-shell propagators (all $\alpha_i \neq 0 \Rightarrow \det Q = 0$) is usually referred to as the *leading Landau singularity*. In the case of the triangle diagram the anomalous threshold is the leading Landau singularity.
- When all but one external momenta are kept below the thresholds there are only normal thresholds on the physical sheet in the corresponding four momentum squared. For analytic computations this constitutes a method for obtaining correlation functions in a certain kinematic range. The remaining domain is then obtained by analytic continuation.[17]

and kaons they do not since global quantum numbers do not allow the condition to be satisfied [4]. Appearing and not appearing stands for being on the physical sheet or not.

[17] This makes use of the analyticity postulate of the S-matrix theory in the that the domain of analyticity is the maximal one consistent with unitarity (normal thresholds) and crossing symmetry. Crossing symmetry means that if scattering $A+B \to C+D$ and the decay $A \to \bar{B}+C+D$ are both possible then they are described by the same amplitude through analytic continuation. These postulates are seen to be correct in concrete QFT computations and believed to be true in general. Some results are known for 3- and 4-point function through the work of Källén [17, 18] and even more generally from tools like the Edge of the Wedge theorem [4, 27].

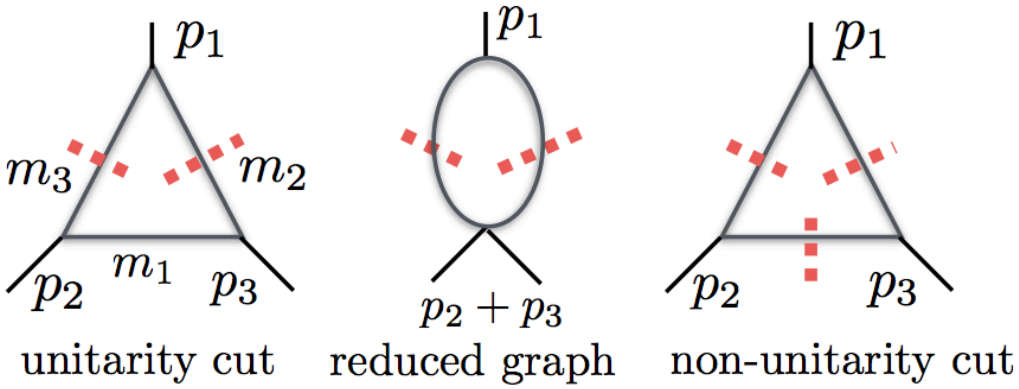


Figure 11: (left) normal threshold cut (non-leading singularity) (middle) the corresponding reduced graph for which $\alpha_1 = 0$ in the Landau equations. From the reduced graphs all lower singularities can be found. (right) the leading Landau singularity corresponding to a so called anomalous threshold (non-normal threshold)

For the assessment of dispersion relation, outside the range of concrete computations, this is not a practical method since one needs to know the location of all singularities on the physical sheet in order to choose a path γ which does not cross any singularity.

4.4.2 Physical Interpretation of the second Landau Equations (46,47)

For physical momenta Coleman and Norton have given an interpretation of the second Landau equation [28]. It is found that (46,47) ensures that the corresponding diagram can occur as a real process where the Feynman-parameter $\alpha_i \sim \tau_i/m_i$ has the interpretation of being the proper time τ_i divided by the mass of the propagating particle.

This means that $\alpha_i = 0$ corresponds to the case where the i^{th} particle does not propagate at all and gives the reduced graphs (e.g. Fig. 11(middle)) a more direct meaning. At last we note that the Coleman-Norton interpretation is a very reassuring result in view of the optical theorem's (19) statemant that the discontinuity (related to singularities), of the forward scattering amplitude, originates from physical intermediate states.

5 Outlook

Even though dispersion relations are an old subject and a pure dispersive approach to particle physics has proven to be too complicated in practice, dispersion theory is and will remain a powerful tool in QFT as it follows from first principles and is intrinsically non-perturbative. This makes it particularly useful for hadronic physics which is not directly accessible by a perturbation expansion in the strong coupling constant. Dispersion relations are the most solid approach to quark hadron duality. Any approach to quark hadron duality should either start from or connect to dispersion relations.

In recent years dispersion relations and unitarity methods have also seen a major revival in evaluating perturbative diagrams (e.g. [29, 30, 31, 32] for reviews and applications). The bootstrapping programme has witnessed new exciting developments by limiting/fixing the target space functions of amplitudes. Old tools such as the Steinman relations, which are physical conditions on double discontinuities, have led to promising simplifications valid beyond perturbation theory [33].

Furthermore dispersion relations can serve to prove positivity, for example, when a physical quantity can be expressed as an unsubtracted dispersion integral with positive integrand (discontinuity). Examples are the so-called c- and a-theorems, which characterise the irreversibility of the renormalisation group flows in 2D and 4D. The dispersive proofs are given in [34, 35] in two and four dimensions by looking at two and four-point functions respectively. On another note, positivity of the Källén-Lehmann representation seemed to exclude the possibility of asymptotically free gauge theories in 1970 [36]. The Faddeev-Popov ghosts (negative metric) proved to be the loophole in this argument as they give rise to the negative sign of the β-function [37, 38].

I am grateful to James Gratrex for proofreading and to Einan Gardi for discussions on second type singularities. Apologies for all relevant references that were omitted. Last but not least I would like to thank the organisers of the "Strong Fields and Heavy Quarks" as well as the participants for a stimulating and pleasant atmosphere. I really did enjoy my trip to and around Dubna!

A The Schwartz Reflection Principle

Consider an analytic function $f(z)$ with $f(z) \in \mathbb{R}$ for $z \in I_R$ where I_R is an interval on the real line. Then the following relation holds

$$f(z) = f(z^*)^* \,, \tag{58}$$

which can be analytically continued to the entire plane. Note that analytic continuation is unique from any set with an accumulation point for which an interval is a special case. Hence Eq. (58) implies that

$$\mathrm{Re}[f(z)] = \mathrm{Re}[f(z^*)] \,, \quad \mathrm{Im}[f(z)] = -\mathrm{Im}[f(z^*)] \,. \tag{59}$$

Choosing $z = s + i0$ with $s \in \mathbb{R}$ it then follows that

$$\mathrm{disc}[\Gamma(s)] = 2i\mathrm{Im}[\Gamma(s)] \,, \tag{60}$$

which is a result known from experience with 2-point functions and intuitively in accordance with the optical theorem.

B Conventions

Here we summarise a few conventions. We are using the Minkowski metric of the form

$$g_{\mu\nu} = \mathrm{diag}(1, -1, -1, -1) \,, \tag{61}$$

the following abbreviations for integrals over space and momentum space

$$\int_x = \int d^4x \ , \quad \int_k = \int d^4k \ , \tag{62}$$

and the relativistic state normalisation

$$\langle p|p'\rangle = 2E_p(2\pi)^3\delta^{(3)}(\vec{p}-\vec{p'}) \ , \tag{63}$$

where $E_p = \sqrt{\vec{p}^2 + m^2}$ with $p = (E_p, \vec{p})$.

References

[1] R. Eden, D. Landshoff, P. Olive, and J. Polkinhorne, *The analytic S-matrix*. International Series In Pure and Applied Physics. McGraw-Hill, New York, 1966.

[2] I. Todorov, *Analytic Properties of Feynman Diagrams in Quantum Field Theory*. Volume 38 in International Series of Monographs in Natural Philosophy. Elsevier, 1970.

[3] G. Barton, *Dispersion Techniques in Field Theory*. 1965.

[4] C. Itzykson and J. B. Zuber, *Quantum Field Theory*. International Series In Pure and Applied Physics. McGraw-Hill, New York, 1980. http://dx.doi.org/10.1063/1.2916419.

[5] S. Weinberg, *The Quantum theory of fields. Vol. 1: Foundations*. Cambridge University Press, 2005.

[6] E. de Rafael, "An Introduction to sum rules in QCD: Course," in *Probing the standard model of particle interactions. Proceedings, Summer School in Theoretical Physics, NATO Advanced Study Institute, 68th session, Les Houches, France, July 28-September 5, 1997. Pt. 1, 2*, pp. 1171–1218. 1997. arXiv:hep-ph/9802448 [hep-ph].

[7] S. S. Schweber, *QED and the men who made it: Dyson, Feynman, Schwinger, and Tomonaga*. 1994.

[8] K. G. Wilson, "Nonlagrangian models of current algebra," *Phys. Rev.* **179** (1969) 1499–1512.

[9] R. Haag, "On quantum field theories," *Kong. Dan. Vid. Sel. Mat. Fys. Med.* **29N12** (1955) 1–37. [Phil. Mag.46,376(1955)].

[10] G. Kallen, "On the definition of the Renormalization Constants in Quantum Electrodynamics," *Helv. Phys. Acta* **25** no. 4, (1952) 417. [,509(1952)].

[11] H. Lehmann, "On the Properties of propagation functions and renormalization contants of quantized fields," *Nuovo Cim.* **11** (1954) 342–357.

[12] M. A. Shifman, A. I. Vainshtein, and V. I. Zakharov, "QCD and Resonance Physics. Theoretical Foundations," *Nucl. Phys.* **B147** (1979) 385–447.

[13] T. DeGrand and C. E. Detar, *Lattice methods for quantum chromodynamics*. 2006.

[14] M. Gell-Mann, M. L. Goldberger, and W. E. Thirring, "Use of causality conditions in quantum theory," *Phys. Rev.* **95** (1954) 1612–1627.

[15] S. Weinberg, "Precise relations between the spectra of vector and axial vector mesons," *Phys. Rev. Lett.* **18** (1967) 507–509.

[16] S. Weinberg, *The quantum theory of fields. Vol. 2: Modern applications*. Cambridge University Press, 2013.

[17] G. Kallen and A. S. Wightman, *The Analytic Properties of the Vacuum Expectation Value of a Product of Three Scalar Local Fields*, vol. 1. 1958.

[18] G. Kallen, "The analyticity domain of the four point function," *Nucl. Phys.* **25** (1961) 568–603.

[19] A. Martin, "The Rigorous analyticity unitarity program and its successes," *Lect. Notes Phys.* **558** (2000) 127–135, arXiv:hep-ph/9906393 [hep-ph]. [,127(1999)].

[20] E. Byckling and K. Kajantie, *Particle Kinematics*. University of Jyvaskyla, Jyvaskyla, Finland, 1971. http://www-spires.fnal.gov/spires/find/books/www?cl=QC794.6.K5B99.

[21] L. D. Landau, "On analytic properties of vertex parts in quantum field theory," *Nucl. Phys.* **13** (1959) 181–192.

[22] R. E. Cutkosky, "Singularities and discontinuities of Feynman amplitudes," *J. Math. Phys.* **1** (1960) 429–433.

[23] M. E. Peskin and D. V. Schroeder, *An Introduction to quantum field theory*. 1995. http://www.slac.stanford.edu/spires/find/books/www?cl=QC174.45%3AP4.

[24] S. Bloch and D. Kreimer, "Cutkosky Rules and Outer Space," arXiv:1512.01705 [hep-th].

[25] G. 't Hooft and M. J. G. Veltman, "DIAGRAMMAR," *NATO Sci. Ser. B* **4** (1974) 177–322.

[26] M. Dimou, J. Lyon, and R. Zwicky, "Exclusive Chromomagnetism in heavy-to-light FCNCs," *Phys. Rev.* **D87** no. 7, (2013) 074008, arXiv:1212.2242 [hep-ph].

[27] R. F. Streater and A. S. Wightman, *PCT, spin and statistics, and all that*. 1989.

[28] S. Coleman and R. E. Norton, "Singularities in the physical region," *Nuovo Cim.* **38** (1965) 438–442.

[29] L. J. Dixon, "A brief introduction to modern amplitude methods," in *Proceedings, 2012 European School of High-Energy Physics (ESHEP 2012): La Pommeraye, Anjou, France, June 06-19, 2012*, pp. 31–67. 2014. arXiv:1310.5353 [hep-ph]. https://inspirehep.net/record/1261436/files/arXiv:1310.5353.pdf.

[30] H. Elvang and Y.-t. Huang, "Scattering Amplitudes," arXiv:1308.1697 [hep-th].

[31] J. M. Henn, "Lectures on differential equations for Feynman integrals," *J. Phys.* **A48** (2015) 153001, arXiv:1412.2296 [hep-ph].

[32] E. Remiddi and L. Tancredi, "Differential equations and dispersion relations for Feynman amplitudes. The two-loop massive sunrise and the kite integral," *Nucl. Phys.* **B907** (2016) 400–444, arXiv:1602.01481 [hep-ph].

[33] S. Caron-Huot, L. J. Dixon, A. McLeod, and M. von Hippel, "Bootstrapping a Five-Loop Amplitude from Steinmann Relations," arXiv:1609.00669 [hep-th].

[34] A. Cappelli, D. Friedan, and J. I. Latorre, "C theorem and spectral representation," *Nucl. Phys.* **B352** (1991) 616–670.

[35] Z. Komargodski and A. Schwimmer, "On Renormalization Group Flows in Four Dimensions," *JHEP* **12** (2011) 099, arXiv:1107.3987 [hep-th].

[36] K. G. Wilson, "The Renormalization Group and Strong Interactions," *Phys. Rev.* **D3** (1971) 1818.

[37] D. J. Gross and F. Wilczek, "Ultraviolet Behavior of Nonabelian Gauge Theories," *Phys. Rev. Lett.* **30** (1973) 1343–1346.

[38] H. D. Politzer, "Reliable Perturbative Results for Strong Interactions?," *Phys. Rev. Lett.* **30** (1973) 1346–1349.

Lectures on Soft-Collinear Effective Theory

Andrey Grozin

Budker Institute of Nuclear Physics, Lavrentiev St. 11, Novosibirsk 630090, Russia

DOI: http://dx.doi.org/10.3204/DESY-PROC-2016-04/Grozin

Introductory lectures on SCET mainly following the first chapters of [1].

1 Introduction

Soft-Collinear Effective Theory (SCET) has been first proposed as an effective field theory describing inclusive B meson decays with an energetic light quark in the final state and exclusive B decays with an energetic light hadron in the final state. Physics at short distances ($\sim 1/M_b$) is encapsulated in matching coefficients; soft dynamics of the b quark is described by Heavy Quark Effective Theory (HQET); soft and collinear degrees of freedom of light quarks and gluons are described by SCET. Speaking more precisely, there are two closely related effective theories, SCET-I and SCET-II. Later SCET was successfully applied to numerous problems in hadron collider physics. In this area there are at least two large nearly light-like momenta, and hence several collinear regions (jets, initial hadrons). Additional effective field theories were proposed for various classes of such problems.

These lectures are an elementary introduction to SCET. A very nice textbook on SCET has recently appeared [1], I follow the first chapters of this book. There are also lecture notes [2]. I don't cite original papers here, citations can be found in [1, 2]. SCET can be formulated in two different languages: the coordinate space Lagrangian or the label formalism. The book [1] mostly follows the first approach, while the lectures [2] – the second one. I shall not describe the label formalism here.

Let's first discuss what are effective field theories. Many problems in quantum field theory contain several widely separated energy scales. Suppose there is a high momentum scale Q (and a short distance scale $1/Q$), and we are interested in interactions of light particles ($m_i \ll Q$) having small momenta ($p_i \ll Q$), or in other words, physics at large distances $\gg 1/Q$. The ratio of the characteristic soft scale to Q is the small expansion parameter λ. One of approaches to such problems is the method of regions for loop diagrams. A brief introduction to this method is given in Sect. 2, see [3] for more details.

Another approach is low energy (or large distance) effective field theories. One can construct an effective Lagrangian containing only light fields. Physics at small distances $\lesssim 1/Q$ produces local interactions of these fields. The Lagrangian contains all possible operators (allowed by symmetries of the full theory). In order to find coefficients of these operators matching is performed. We calculate some scattering amplitudes in the full theory and expands them in λ up to some order; then we calculate the same amplitudes in the effective theory, equate the results and find the coefficients in the effective Lagrangian. In other words, hard degrees of freedom are integrated out from the path integral producing the soft effective action.

Similarly, operators of the full theory can be represented as $1/Q$ expansions in terms of operators of the effective theory with appropriate quantum numbers. Coefficients in such expansions are also obtained by matching: calculate some on-shell matrix elements in the full theory, expand in λ, calculate them in the effective theory, equate the results and find matching coefficients.

There is a close correspondence between effective theories and the method of regions. Hard regions produce matching coefficients, while soft ones are Feynman diagrams of the effective theory. If one wants to consider just a single process described by a small number of diagrams, it is rather easy to find many terms of its λ expansion by the method of regions. The effective field theory framework quickly becomes very complicated with the growth of order of this expansion; usually, only a few first terms can be considered. On the other hand, an effective field theory is applicable to all processes at once. It often allows one to derive various properties which are valid to all orders of perturbation theory, such as factorization theorems and renormalization group (RG) equations. The leading terms of an effective Lagrangian can have some symmetry which is not obvious in the full theory.

SCET is more complicated than simple effective theories because it is anisotropic[1]. Characteristic momentum scales (and distance scales) are different in different directions. We discuss SCET for the scalar φ^3 field theory in Sect. 3. This simple example shows most typical features of SCET; however, the coupling constant g is dimensionful, and the situation with resummation of all orders of perturbation theory radically differs fro that in QCD (φ^3 in $d = 6$ dimensional space–time has dimensionless g, and is more like QCD). QCD is a gauge theory, and additional complications related to gauge invariance and Wilson lines appear; these topics are discussed in Sect. 4.

2 Method of regions

Let's consider the vacuum integral

$$I = \int \frac{d^d k}{i\pi^{d/2}} \frac{1}{(M^2 - k^2 - i0)(m^2 - k^2 - i0)}$$

with two masses M and m (Fig. 1) at $M \gg m$ and $d = 2$. It contains neither ultraviolet (UV) nor infrared (IR) divergences. After Wick rotation to Euclidean momentum space it becomes

$$I = \int \frac{d^d k_E}{\pi^{d/2}} \frac{1}{(k_E^2 + M^2)(k_E^2 + m^2)} \,. \tag{2.1}$$

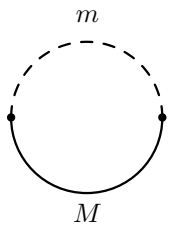
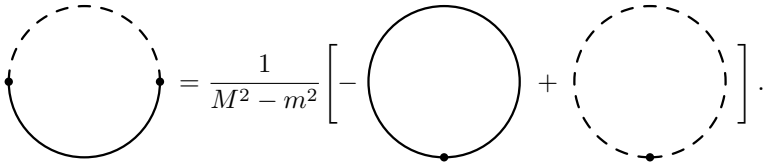


Figure 1: Vacuum diagram with two masses.

Of course, in this simple example it is easy to obtain the exact solution. We use partial fraction decomposition

$$I = \frac{1}{M^2 - m^2} \int \frac{d^d k_E}{\pi^{d/2}} \left[-\frac{1}{k_E^2 + M^2} + \frac{1}{k_E^2 + m^2} \right] ,$$

[1] This is also true for NRQCD and pNRQCD.



These two integrals, taken separately, diverge; therefore, we use dimensional regularization ($d = 2 - 2\varepsilon$) and obtain

$$I = -\Gamma(\varepsilon)\frac{M^{-2\varepsilon} - m^{-2\varepsilon}}{M^2 - m^2}\,.$$

This result is finite at $\varepsilon \to 0$:

$$I = \frac{\log(M^2/m^2)}{M^2 - m^2} = \frac{1}{M^2}\log\frac{M^2}{m^2}\left[1 + \frac{m^2}{M^2} + \frac{m^4}{M^4} + \cdots\right]. \tag{2.2}$$

It is easier to obtain this result using the prescription known as the method of regions [3]. The integral (2.1) is written at the sum of contributions of two regions, the hard one and the soft one:

$$I = I_h + I_s\,.$$

In the hard region $k_E \sim M$; in the soft one $k_E \sim m$. The integrand is expanded to Taylor series in accordance to these power counting rules in each region. After that, the integral is taken over the full (d-dimensional) space.

In the hard region ($k_E \sim M$) we have

$$I_h = \int \frac{d^d k_E}{\pi^{d/2}} T_h \frac{1}{(k_E^2 + M^2)(k_E^2 + m^2)}\,,$$

where the operator T_h expands the integrand in small parameter(s) counting k_E as a quantity of order M:

$$T_h \frac{1}{(k_E^2 + M^2)(k_E^2 + m^2)} = \frac{1}{k_E^2 + M^2}\frac{1}{k_E^2}\left[1 - \frac{m^2}{k_E^2} + \frac{m^4}{k_E^4} - \cdots\right].$$

Calculating the loop integrals, we arrive at

$$I_h = -\frac{M^{-2\varepsilon}}{M^2}\Gamma(\varepsilon)\left[1 + \frac{m^2}{M^2} + \frac{m^4}{M^4} + \cdots\right]. \tag{2.3}$$

The result is a Taylor series in m. Each loop integral is IR divergent; it contains a single scale M, and hence, by dimensions counting, is proportional to $M^{-2\varepsilon}$.

In the soft region ($k_E \sim m$) we have

$$I_s = \int \frac{d^d k_E}{\pi^{d/2}} T_s \frac{1}{(k_E^2 + M^2)(k_E^2 + m^2)}$$

where T_s counts k_E as a quantity of order m:

$$T_s \frac{1}{(k_E^2 + M^2)(k_E^2 + m^2)} = \frac{1}{M^2}\frac{1}{k_E^2 + m^2}\left[1 - \frac{k_E^2}{M^2} + \frac{k_E^4}{M^4} - \cdots\right],$$

and we obtain

$$I_s = \frac{m^{-2\varepsilon}}{M^2}\Gamma(\varepsilon)\left[1 + \frac{m^2}{M^2} + \frac{m^4}{M^4} + \cdots\right]. \tag{2.4}$$

The result is a Taylor series in $1/M$. Each loop integral is UV divergent; it contains a single scale m, and hence, by dimensions counting, is proportional to $m^{-2\varepsilon}$.

The sum of the hard contribution (2.3) and the soft one (2.4) produces the complete result (2.2). IR divergences in the hard region cancel UV divergences in the soft one.

In this simple case it is easy to prove this prescription [4]. Let's introduce some boundary Λ such that $m \ll \Lambda \ll M$, and write

$$I = \int_{k_E>\Lambda} \frac{d^d k_E}{\pi^{d/2}} \frac{1}{(k_E^2 + M^2)(k_E^2 + m^2)} + \int_{k_E<\Lambda} \frac{d^d k_E}{\pi^{d/2}} \frac{1}{(k_E^2 + M^2)(k_E^2 + m^2)}.$$

We may apply T_h to the first integrand and T_s to the second one:

$$I = \int_{k_E>\Lambda} \frac{d^d k_E}{\pi^{d/2}} T_h \frac{1}{(k_E^2 + M^2)(k_E^2 + m^2)} + \int_{k_E<\Lambda} \frac{d^d k_E}{\pi^{d/2}} T_s \frac{1}{(k_E^2 + M^2)(k_E^2 + m^2)}.$$

For each of these two integrals, we add and subtract the integral over the remaining part of the k_E space:

$$I = I_h + I_s - \Delta I\,,$$

where

$$\Delta I = \int_{k_E<\Lambda} \frac{d^d k_E}{\pi^{d/2}} T_h \frac{1}{(k_E^2 + M^2)(k_E^2 + m^2)} + \int_{k_E>\Lambda} \frac{d^d k_E}{\pi^{d/2}} T_s \frac{1}{(k_E^2 + M^2)(k_E^2 + m^2)}$$

are the integrals of the two expansions over the "wrong" parts of the k_E space. In these wrong regions, we may apply the other expansion in addition to the existing one:

$$\Delta I = \int_{k_E<\Lambda} \frac{d^d k_E}{\pi^{d/2}} T_s T_h \frac{1}{(k_E^2 + M^2)(k_E^2 + m^2)} + \int_{k_E>\Lambda} \frac{d^d k_E}{\pi^{d/2}} T_h T_s \frac{1}{(k_E^2 + M^2)(k_E^2 + m^2)}.$$

But this is the integral over the full k_E space:

$$\Delta I = \int \frac{d^d k_E}{\pi^{d/2}} T_s T_h \frac{1}{(k_E^2 + M^2)(k_E^2 + m^2)}\,,$$

because the Taylor expansion operators commute:

$$T_s T_h \frac{1}{(k_E^2 + M^2)(k_E^2 + m^2)} = T_h T_s \frac{1}{(k_E^2 + M^2)(k_E^2 + m^2)}$$
$$= \frac{1}{M^2 k_E^2}\left[1 - \frac{m^2}{k_E^2} + \frac{m^4}{k_E^4} - \cdots\right]\left[1 - \frac{k_E^2}{M^2} + \frac{k_E^4}{M^4} - \cdots\right].$$

And hence

$$\Delta I = 0\,,$$

because each integral has no scale.

Let's stress that the method of regions works thanks to dimensional regularization. Taylor expansions in each region (i.e., for each set of power counting rules) must be performed completely, up to the end; otherwise, integrals in the defect ΔI can contain some scale(s), and hence not vanish.

3 Scalar φ^3 theory

3.1 Form factor

Let's consider massless φ^3 theory (at $d = 4$):

$$L = \frac{1}{2}\,(\partial_\mu\varphi)\,(\partial^\mu\varphi) - \frac{g}{3!}\varphi^3\,. \tag{3.1}$$

The dimensionality of the Lagrangian is $[L] = d$, and hence $[\varphi] = (d-2)/2$, $[g] = (6-d)/2$. We want to calculate the slightly off-shell form factor

$$I = \int \frac{d^dk}{i\pi^{d/2}} \frac{1}{[-k^2 - i0][-(k+p)^2 - i0][-(k+p')^2 - i0]} \tag{3.2}$$

at $-p^2, -p'^2 \ll -q^2$.

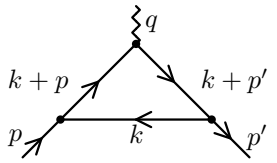


Figure 2: Form factor in the scalar φ^3 theory.

It is convenient to use light-front components of vectors. Instead of the ordinary basis vectors e_0, e_1 we shall use

$$e_\pm = e_0 \pm e_1 \quad (e_\pm^2 = 0\,, \quad e_+ \cdot e_- = 2)\,.$$

The light-front components of a vector x are

$$x_\pm = x \cdot e_\pm = x^0 \mp x^1\,; \tag{3.3}$$

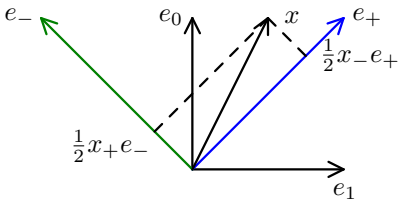


Figure 3: Light-front components.

the vector can be written via them as

$$x = \frac{1}{2}\,(x_-e_+ + x_+e_-) + x_\perp \equiv (x_+, x_-, \vec{x}_\perp)\,.$$

The scalar product of two vectors is

$$x \cdot y = \frac{1}{2}\,(x_+y_- + x_-y_+) - \vec{x}_\perp \cdot \vec{y}_\perp\,;$$

in particular, the square of a vector is

$$x^2 = x_+x_- - \vec{x}_\perp^{\,2}\,.$$

A boost along the e_1 direction (a Minkowski rotation in the e_0, e_1 plane) transforms light-front components in a simple way:

$$x'_\pm = x_\pm e^{\pm\varphi}\,.$$

The d-dimensional volume element is

$$d^dx = \frac{1}{2}dx_+\,dx_-\,d^{d-2}\vec{x}_\perp\,.$$

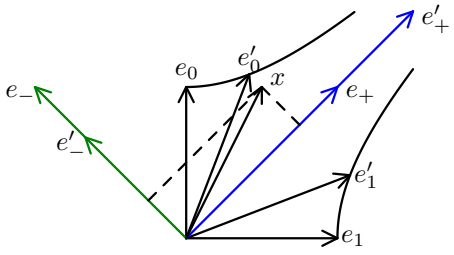


Figure 4: A boost.

The full differential of a function $f(x)$ is

$$\begin{aligned} df(x) &= \frac{\partial f}{\partial x^0} dx^0 + \frac{\partial f}{\partial x^1} dx^1 + \frac{\partial f}{\partial \vec{x}_\perp} \cdot d\vec{x}_\perp \\ &= \partial^0 f \, dx^0 - \partial^1 f \, dx^1 - \vec{\partial}_\perp f \cdot d\vec{x}_\perp \,, \end{aligned}$$

and hence

$$\partial^0 = \frac{\partial}{\partial x^0} \,, \quad \partial^1 = -\frac{\partial}{\partial x^1} \,, \quad \vec{\partial}_\perp = -\frac{\partial}{\partial \vec{x}_\perp} \,.$$

In light-front components,

$$df(x) = \frac{\partial f}{\partial x_+} dx_+ + \frac{\partial f}{\partial x_-} dx_- + \frac{\partial f}{\partial \vec{x}_\perp} \cdot d\vec{x}_\perp = \frac{1}{2} \partial_+ f \, dx_- + \frac{1}{2} \partial_- f \, dx_+ - \vec{\partial}_\perp \cdot d\vec{x}_\perp \,,$$

and hence

$$\partial_+ = 2 \frac{\partial}{\partial x_-} \,, \quad \partial_- = 2 \frac{\partial}{\partial x_+} \,;$$

taking into account

$$dx_+ = dx^0 - dx^1 \,, \quad dx_- = dx^0 + dx^1 \,,$$

we obtain

$$\partial_+ = \partial^0 - \partial^1 \,, \quad \partial_- = \partial^0 + \partial^1 \,,$$

in agreement with (3.3).

We choose e_0, e_1 (and hence e_+, e_-) in the p, p' plane, then

$$\begin{aligned} p &= \frac{1}{2} \left(p_- e_+ - \frac{-p^2}{p_-} e_- \right) \,, \quad p' = \frac{1}{2} \left(-\frac{-p'^2}{p'_+} e_+ + p'_+ e_- \right) \,, \\ -q^2 &= p_- p'_+ - p^2 - p'^2 + \frac{(-p^2)(-p'^2)}{p_- p'_+} \,; \end{aligned}$$

our small parameter is

$$\lambda^2 \sim \frac{-p^2}{-q^2} \sim \frac{-p'^2}{-q^2} \ll 1 \,.$$

In the Breit frame $q^0 = 0$ (or in any frame related to it by a moderate boost) light-front components of the external momenta are

$$p \sim (\lambda^2, 1, 0) Q \,, \quad p' \sim (1, \lambda^2, 0) Q \,, \tag{3.4}$$

where $Q^2 = -q^2 \approx p_- p'_+$.

3.2 Method of regions

The form factor (3.2) is given by the sum of 4 regions (Table 1):

$$I = I_h + I_{c_+} + I_{c_-} + I_s \,.$$

hard	h	$k \sim (1, 1, 1) Q$	$k^2 \sim Q^2$
collinear	c_+	$k \sim (1, \lambda^2, \lambda) Q$	$k^2 \sim Q^2 \lambda^2$
collinear	c_-	$k \sim (\lambda^2, 1, \lambda) Q$	$k^2 \sim Q^2 \lambda^2$
soft	s	$k \sim (\lambda^2, \lambda^2, \lambda^2) Q$	$k^2 \sim Q^2 \lambda^4$

Table 1: Regions.

Hyperbolas in Fig. 5 show lines of constant virtuality $k_+ k_-$ (at $\vec{k}_\perp = \vec{0}$).

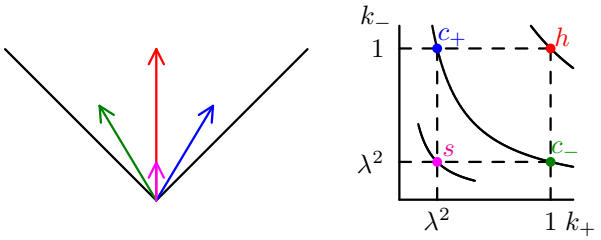


Figure 5: Regions in the k space.

In the hard region $k \sim (1,1,1)Q$; recalling $p \sim (\lambda^2,1,0)Q$, $p' \sim (1,\lambda^2,0)Q$, we found that the three denominators are

$$\begin{aligned}
-k^2 &= \underbrace{-k_+k_- + \vec{k}_\perp^{\,2}}_{\mathcal{O}(1)}, \\
-(k+p)^2 &= -(k_++p_+)(k_-+p_-) + \vec{k}_\perp^{\,2} = \underbrace{-k^2 - p_-k_+}_{\mathcal{O}(1)} - \underbrace{p_+(k_-+p_-)}_{\mathcal{O}(\lambda^2)}, \\
-(k+p')^2 &= -(k_++p'_+)(k_-+p'_-) + \vec{k}_\perp^{\,2} = \underbrace{-k^2 - p'_+k_-}_{\mathcal{O}(1)} - \underbrace{p'_-(k_++p'_+)}_{\mathcal{O}(\lambda^2)},
\end{aligned}$$

and $d^dk \sim \mathcal{O}(1)$. At the leading order in λ^2, the hard contribution

$$I_h = \int \frac{d^dk}{i\pi^{d/2}} \frac{1}{(-k^2-i0)(-k^2-p_-k_+-i0)(-k^2-p'_+k_--i0)}$$

is the form factor with on-shell external legs. This integral contains a single scale $-q^2 = p_-p'_+$: if we make the substitution

$$k_- = p_-\tilde{k}_-\,, \quad k_+ = p'_+\tilde{k}_+\,, \quad \vec{k}_\perp = \sqrt{p_-p'_+}\,\vec{\tilde{k}}_\perp\,,$$

where $\tilde{k}$ is a dimensionless integration momentum, then

$$I_h = (-q^2)^{d/2-3} \int \frac{d^d\tilde{k}}{i\pi^{d/2}} \frac{1}{(-\tilde{k}^2-i0)(-\tilde{k}^2-\tilde{k}_+-i0)(-\tilde{k}^2-\tilde{k}_--i0)}\,.$$

We shall use Feynman parametrization. First, we use α parametrization 3 times:

$$\frac{1}{D_1D_2D_3} = \int d\alpha_1 d\alpha_2 d\alpha_3 e^{-\alpha_1D_1-\alpha_2D_2-\alpha_3D_3}\,;$$

then we insert $d\eta\,\delta(\alpha_1+\alpha_2+\alpha_3-\eta)$ under the integral sign, substitute $\alpha_i = \eta x_i$:

$$\frac{1}{D_1D_2D_3} = \int dx_1dx_2dx_3\delta(x_1+x_2+x_3-1) \int d\eta\,\eta^2 e^{-\eta(x_1D_1+x_2D_2+x_3D_3)}\,,$$

and integrate in η:

$$\frac{1}{D_1 D_2 D_3} = \Gamma(3) \int \frac{dx_1 dx_2 dx_3 \delta(x_1 + x_2 + x_3 - 1)}{(x_1 D_1 + x_2 D_2 + x_3 D_3)^3} \,. \tag{3.5}$$

We set $-q^2 = 1$ (its power can be reproduced from dimensions counting), and use Feynman parametrization:

$$I_h = \Gamma(3) \int dx_1 \, dx_2 \, dx_3 \, \delta(x_1 + x_2 + x_3 - 1) \frac{d^d k}{i\pi^{d/2}} \frac{1}{D^3} \,,$$

where the denominator is

$$D = -x_1 k^2 - x_2 (k^2 + k_+) - x_3 (k^2 + k_-) - i0 = -k^2 - (x_2 e_+ + x_3 e_-) \cdot k - i0 \,.$$

Shifting the integration momentum

$$k' = k + \frac{1}{2}(x_2 e_+ + x_3 e_-) \,,$$

we obtain

$$D = -k'^2 + x_2 x_3 - i0 \,.$$

Now it is easy to calculate the integral in $d^d k'$:

$$I_h = \Gamma\left(3 - \frac{d}{2}\right) \int_{x_2 + x_3 < 1} dx_2 dx_3 (x_2 x_3)^{d/2 - 3} \,.$$

Substituting $x_2 = zx$, $x_3 = z(1 - x)$, we have

$$I_h = \Gamma\left(3 - \frac{d}{2}\right) \int_0^1 dz \, z^{d-5} \cdot \int_0^1 dx \, [x(1-x)]^{d/2 - 3} = \frac{\Gamma\left(3 - \frac{d}{2}\right) \Gamma^2\left(\frac{d}{2} - 2\right)}{\Gamma(d - 3)} \,.$$

Finally, restoring the power of $-q^2$, we obtain

$$I_h = \frac{\Gamma(1 + \varepsilon)}{\Gamma(1 - 2\varepsilon)} \Gamma^2(-\varepsilon)(-q^2)^{-1-\varepsilon} \,. \tag{3.6}$$

This integral contains both IR divergence ($k \to 0$) and collinear ones (k non-zero but parallel to e_+ or e_-); thus it is $1/\varepsilon^2$. It contains the single scale $-q^2$.

In the c_+ collinear region, $k \sim (\lambda^2, 1, \lambda) Q$; recalling $p \sim (\lambda^2, 1, 0) Q$, $p' \sim (1, \lambda^2, 0) Q$, we found that the three denominators are

$$-k^2 = \underbrace{-k_+ k_- + \vec{k}_\perp^2}_{\mathcal{O}(\lambda^2)} \,,$$

$$-(k+p)^2 = \underbrace{-(k_+ + p_+)(k_- + p_-) + \vec{k}_\perp^2}_{\mathcal{O}(\lambda^2)} \,,$$

$$-(k+p')^2 = -(k_+ + p'_+)(k_- + p'_-) + \vec{k}_\perp^2 = \underbrace{-p'_+ k_-}_{\mathcal{O}(1)} \underbrace{- (k^2 + p'_+ p'_-)}_{\mathcal{O}(\lambda^2)} \underbrace{- p'_- k_+}_{\mathcal{O}(\lambda^4)} \,,$$

and $d^dk \sim \mathcal{O}(\lambda^d)$. At the leading order in λ^2, the c_+ collinear contribution is

$$I_{c_+} = \frac{1}{p'_+}\int \frac{d^dk}{i\pi^{d/2}} \frac{1}{(-k^2-i0)(-(k+p)^2-i0)(-k_- - i0)}\,.$$

This integral contains a single scale $-p^2 = -p_+p_-$: if we make the substitution

$$k_+ = (-p_+)\tilde{k}_+\,, \quad k_- = p_-\tilde{k}_-\,, \quad \vec{k}_\perp = \sqrt{-p_+p_-}\,\vec{\tilde{k}}_\perp\,,$$

where $\tilde{k}$ is a dimensionless integration momentum and $\tilde{p} = (-1, 1, \vec{0})$, then

$$I_{c_+} = \frac{(-p_+p_-)^{d/2-2}}{p_-p'_+}\int \frac{d^d\tilde{k}}{i\pi^{d/2}} \frac{1}{(-\tilde{k}^2-i0)(-(\tilde{k}+\tilde{p})^2-i0)(-\tilde{k}_- - i0)}\,.$$

We shall use a variant of Feynman parametrization in which $d\eta\,\delta(\alpha_1+\alpha_2-\eta)$ is inserted under the integral sign (the substitutions $\alpha_i = \eta x_i$ are used for all 3 variables α_i); the result is similar to (3.5), but the δ function is now $\delta(x_1+x_2-1)$. The Feynman parameters $x_{1,2}$ correspond to the quadratic denominators; x_3 (which varies from 0 to ∞) – to the linear one. Setting the pre-integral factor $(-p^2)^{-\varepsilon}/(-q^2)$ to 1, we obtain

$$I_{c_+} = \Gamma(3)\int dx_1dx_2\delta(x_1+x_2-1)dx_3\frac{d^dk}{i\pi^{d/2}}\frac{1}{D^3}\,,$$

where

$$D = -x_1k^2 - x_2(k+p)^2 - x_3k_- - i0 = -k^2 - (2x_2p + x_3e_-)\cdot k + x_2 - i0$$
$$= -k'^2 + x_2(1-x_2+x_3) - i0\,, \qquad k' = k + x_2p + \frac{1}{2}x_3e_-\,,$$

and hence

$$I_{c_+} = \Gamma\left(3-\frac{d}{2}\right)\int dx_1dx_3[x_1(1-x_1+x_3)]^{d/2-3}\,.$$

Substituting $x_3 = (1-x_1)z$ we have

$$I_{c_+} = \Gamma\left(3-\frac{d}{2}\right)\int_0^\infty dz\,(1+z)^{d/2-3}\cdot\int_0^1 dx_1\,x_1^{d/2-3}(1-x_1)^{d/2-2}$$
$$= \frac{\Gamma\left(2-\frac{d}{2}\right)\Gamma\left(\frac{d}{2}-2\right)\Gamma\left(\frac{d}{2}-1\right)}{\Gamma(d-3)}\,.$$

Finally, restoring the pre-integral factor, we arrive at

$$I_{c_+} = \frac{\Gamma(1-\varepsilon)}{\Gamma(1-2\varepsilon)}\Gamma(\varepsilon)\Gamma(-\varepsilon)\frac{(-p^2)^{-\varepsilon}}{-q^2}\,. \tag{3.7}$$

Of course,

$$I_{c_-} = \frac{\Gamma(1-\varepsilon)}{\Gamma(1-2\varepsilon)}\Gamma(\varepsilon)\Gamma(-\varepsilon)\frac{(-p'^2)^{-\varepsilon}}{-q^2}\,.$$

In the soft region $k \sim (\lambda^2, \lambda^2, \lambda^2)Q$; recalling $p \sim (\lambda^2, 1, 0)Q$, $p' \sim (1, \lambda^2, 0)Q$, we found that the three denominators are

$$-k^2 = \underbrace{-k_+k_- + \vec{k}_\perp^2}_{\mathcal{O}(\lambda^4)},$$

$$-(k+p)^2 = -(k_+ + p_+)(k_- + p_-) + \vec{k}_\perp^2 = \underbrace{-p_-(k_+ + p_+)}_{\mathcal{O}(\lambda^2)} - \underbrace{(k^2 + p_+k_-)}_{\mathcal{O}(\lambda^4)},$$

$$-(k+p')^2 = -(k_+ + p'_+)(k_- + p'_-) + \vec{k}_\perp^2 = \underbrace{-p'_+(k_- + p'_-)}_{\mathcal{O}(\lambda^2)} - \underbrace{(k^2 + p'_-k_+)}_{\mathcal{O}(\lambda^4)},$$

and $d^dk \sim \mathcal{O}(\lambda^{2d})$. At the leading order in λ^2, the soft contribution is

$$I_s = \frac{1}{p_-p'_+} \int \frac{d^dk}{i\pi^{d/2}} \frac{1}{(-k^2 - i0)(-k_+ - p_+ - i0)(-k_- - p'_- - i0)}.$$

This integral contains a single scale

$$\frac{(-p^2)(-p'^2)}{-q^2} = \underbrace{p_+p'_-}_{\mathcal{O}(\lambda^4)} + \mathcal{O}(\lambda^6) :$$

if we make the substitution

$$k_+ = (-p_+)\tilde{k}_+, \quad k_- = (-p'_-)\tilde{k}_-, \quad \vec{k}_\perp = \sqrt{(-p_+)(-p'_-)}\,\vec{\tilde{k}}_\perp,$$

where $\tilde{k}$ is a dimensionless integration momentum, then

$$I_s = \frac{(p_+p'_-)^{d/2-2}}{p_-p'_+} \int \frac{d^d\tilde{k}}{i\pi^{d/2}} \frac{1}{(-\tilde{k}^2 - i0)(-\tilde{k}_+ + 1 - i0)(-\tilde{k}_- + 1 - i0)}.$$

This integral is similar to off-shell HQET ones (but with light-like directions e_+, e_-); it is UV divergent.

We shall use a variant of Feynman parametrization (3.5) with $\delta(x_1 - 1)$ where x_1 corresponds to the quadratic denominator. Setting the scale factor $[(-p^2)(-p'^2)]^{-\varepsilon}/(-q^2)^{1-\varepsilon}$ to 1, we obtain

$$I_s = \Gamma(3) \int dx_2 dx_3 \frac{d^dk}{i\pi^{d/2}} \frac{1}{D^3},$$

where

$$D = -k^2 + x_2(-k_+ + 1) + x_3(-k_- + 1) - i0 = -k^2 - (x_2e_+ + x_3e_-) \cdot k + x_2 + x_3 - i0$$
$$= -k'^2 + x_2 + x_3 + x_2x_3 - i0, \qquad k' = k + \frac{1}{2}(x_2e_+ + x_3e_-),$$

and hence

$$I_s = \Gamma\left(3 - \frac{d}{2}\right) \int dx_2 dx_3 (x_2 + x_3 + x_2x_3)^{d/2-3}.$$

Substituting $x_2 = yx$, $x_3 = y(1-x)$, we have

$$I_s = \Gamma\left(3-\frac{d}{2}\right)\int_0^\infty dy\, y^{d/2-2}\int_0^1 dx\,[1+yx(1-x)]^{d/2-3}\,.$$

Substituting $yx(1-x)=z$, we have

$$I_s = \Gamma\left(3-\frac{d}{2}\right)\int_0^\infty dz\, z^{d/2-2}(1+z)^{d/2-3}\cdot\int_0^1 dx\,[x(1-x)]^{1-d/2}\,.$$

Substituting $1+z=1/u$, we obtain

$$I_s = \Gamma\left(3-\frac{d}{2}\right)\int_0^1 du\, u^{3-d}(1-u)^{d/2-2}\cdot\int_0^1 dx\,[x(1-x)]^{1-d/2} = \Gamma\left(\frac{d}{2}-1\right)\Gamma^2\left(2-\frac{d}{2}\right).$$

Finally, restoring the pre-integral factor, we arrive at

$$I_s = \Gamma(1-\varepsilon)\Gamma^2(\varepsilon)\frac{\left[(-p^2)(-p'^2)\right]^{-\varepsilon}}{(-q^2)^{1-\varepsilon}}\,. \tag{3.8}$$

Now we can combine I_h (3.6), I_{c_+} (3.7), I_{c_-}, and I_s (3.8):

$$I = \frac{\Gamma(1+\varepsilon)}{\Gamma(1-2\varepsilon)}\Gamma^2(-\varepsilon)(-q^2)^{-1-\varepsilon} \times\left[1-\left(\frac{-p^2}{-q^2}\right)^{-\varepsilon}-\left(\frac{-p'^2}{-q^2}\right)^{-\varepsilon}+\frac{\Gamma(1+\varepsilon)\Gamma(1-2\varepsilon)}{\Gamma(1-\varepsilon)}\left(\frac{-p^2}{-q^2}\right)^{-\varepsilon}\left(\frac{-p'^2}{-q^2}\right)^{-\varepsilon}\right].$$

The diagram (3.2) we are calculating is finite at $\varepsilon\to 0$; and indeed, all divergences cancel, and we obtain

$$I = \frac{1}{-q^2}\left(\log\frac{-p^2}{-q^2}\log\frac{-p'^2}{-q^2}+\frac{\pi^2}{3}\right)+\mathcal{O}(\lambda^2)\,. \tag{3.9}$$

This cancellation of $1/\varepsilon^2$ and $1/\varepsilon$ divergences is a good check that we have not forgotten some region.

What does happen if we invent some other region and calculate its contribution? For example, consider a region $k\sim(\lambda,\lambda,\lambda)Q$ (let's call it semihard). The denominators are

$$\begin{aligned}
-k^2 &= \underbrace{-k_+k_- + \vec{k}_\perp^{\,2}}_{\mathcal{O}(\lambda^2)}\,,\\
-(k+p)^2 &= -(k_++p_+)(k_-+p_-)+\vec{k}_\perp^{\,2} = \underbrace{-p_-k_+}_{\mathcal{O}(\lambda)}+\mathcal{O}(\lambda^2)\,,\\
-(k+p')^2 &= -(k_++p'_+)(k_-+p'_-)+\vec{k}_\perp^{\,2} = \underbrace{-p'_+k_-}_{\mathcal{O}(\lambda)}+\mathcal{O}(\lambda^2)\,.
\end{aligned}$$

The contribution of this region is

$$I_{sh} = \frac{1}{p_-p'_+}\int\frac{d^dk}{i\pi^{d/2}}\frac{1}{(-k^2-i0)(-k_+-i0)(-k_--i0)} = 0$$

because the integral contains no scale. Similarly, with some work, one can check that there exist no regions of the form $k \sim (\lambda^a, \lambda^b, \lambda^c)Q$ producing non-zero contributions to I except the ones we have considered in this section. This is not a complete proof that there are no extra regions if they don't have such a form in terms of the light-front components, but their existence is highly unlikely.

3.3 SCET Lagrangian

Instead of using the method of regions for diagrams in the full theory, we can formulate a low-energy effective field theory. Hard contributions are integrated out; they only appear in matching coefficients which accumulate information about physics at small distances. Processes at larger distances, namely, collinear and soft contributions (Table 1, Fig. 5), are explicitly considered in the effective theory. Instead of a single field φ in the full theory, we now have 3 fields:

$$\varphi \to \varphi_{c_+} + \varphi_{c_-} + \varphi_s \,.$$

Substituting this field decomposition into the full theory Lagrangian (3.1), we obtain

$$L = L_{c_+} + L_{c_-} + L_s + L_{cs} \,,$$

where

$$\begin{aligned} L_{c_+} &= \frac{1}{2}(\partial_\mu \varphi_{c_+})(\partial^\mu \varphi_{c_+}) - \frac{g}{3!}\varphi_{c_+}^3 \,, \\ L_{c_-} &= \frac{1}{2}(\partial_\mu \varphi_{c_-})(\partial^\mu \varphi_{c_-}) - \frac{g}{3!}\varphi_{c_-}^3 \,, \\ L_s &= \frac{1}{2}(\partial_\mu \varphi_s)(\partial^\mu \varphi_s) - \frac{g}{3!}\varphi_s^3 \end{aligned}$$

are 3 copies of the Lagrangian (3.1), and L_{cs} describes interactions of collinear and soft fields.

Our small parameter is λ; each quantity in the effective theory scales as some power of λ. Soft field momenta scale as $k_s \sim \lambda^2$; this means $\partial_s \sim \lambda^2$ where ∂_s acts on soft fields, and $x_s \sim \lambda^{-2}$ where x_s is a distance at which soft fields substantially change. In order to find power counting for the soft field φ_s, we consider the correlator

$$<T\varphi_s(x_s)\varphi_s(0)> = \int \frac{d^d k_s}{(2\pi)^d} e^{-ik_s \cdot x_s} \frac{i}{k_s^2 + i0} \sim \lambda^{2d-4} \,,$$

and hence

$$\varphi_s \sim \lambda^{d-2} \,.$$

Therefore, the Lagrangian is

$$L_s \sim (\partial_\mu \varphi_s)(\partial^\mu \varphi_s) \sim \lambda^{2d} \,,$$

and the action for a region of size $\sim x_s$ is

$$S_s = \int d^d x \, L_s \sim 1 \,.$$

This is natural: the characteristic action is ~ 1, not a small correction, and we cannot expand in it when calculating the path integral.

For c_+ collinear fields $k_{c_+} \sim (\lambda^2, 1, \lambda)$ and $\partial_{c_+} \sim (\lambda^2, 1, \lambda)$; from $k_+ x_- \sim 1$, $k_- x_+ \sim 1$, $k_\perp x_\perp \sim 1$ we find $x_{c_+} \sim (1, \lambda^{-2}, \lambda^{-1})$. The correlator of collinear fields is

$$<T\varphi_{c_+}(x)\varphi_{c_+}(0)> = \int \frac{d^d k_{c_+}}{(2\pi)^d} e^{-ik_{c_+}\cdot x_{c_+}} \frac{i}{k_{c_+}^2 + i0} \sim \lambda^{d-2}\,,$$

and hence

$$\varphi_{c_+} \sim \lambda^{d/2-1}\,.$$

Therefore, the Lagrangian is

$$L_{c_+} \sim (\partial_+ \varphi_{c_+})(\partial_- \varphi_{c_+}) \sim \lambda^d\,,$$

and the action for a characteristic region $\sim x_{c_+}$ is

$$S_{c_+} = \int d^d x\, L_{c_+} \sim 1\,.$$

Similar estimates can be made for φ_{c_-}.

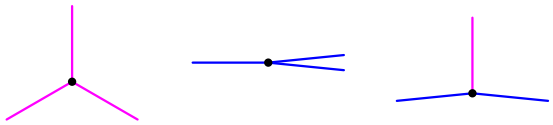


Figure 6: Interactions: 3 soft fields (a); 3 c_+ collinear fields (b); 2 c_+ collinear fields and soft field (c).

There is interaction of 3 soft fields (Fig. 6a) from the term $-\frac{g}{3!}\varphi_s^3$ in L_s; momentum conservation is consistent with power counting: $(\lambda^2, \lambda^2, \lambda^2) + (\lambda^2, \lambda^2, \lambda^2) = (\lambda^2, \lambda^2, \lambda^2)$. There is interaction of 3 c_+ collinear fields (Fig. 6b) from the term $-\frac{g}{3!}\varphi_{c_+}^3$ in L_{c_+}; momentum conservation is consistent: $(\lambda^2, 1, \lambda) + (\lambda^2, 1, \lambda) = (\lambda^2, 1, \lambda)$ (of course, there is also interaction of 3 c_- collinear fields). There is also interaction of 2 c_+ collinear fields and soft one (Fig. 6c) from the collinear–soft Lagrangian

$$L_{cs} = -\frac{g}{2}\varphi_{c_+}^2 \varphi_s - \frac{g}{2}\varphi_{c_-}^2 \varphi_s \tag{3.10}$$

momentum conservation is consistent: $(\lambda^2, 1, \lambda) + (\lambda^2, \lambda^2, \lambda^2) = (\lambda^2, 1, \lambda)$ (of course, there is also interaction of 2 c_- collinear fields and soft one). Other possible interactions ($\varphi_{c_+}{}^2\varphi_{c_-}$, $\varphi_{c_+}\varphi_{c_-}\varphi_s$, $\varphi_{c_+}{}^2\varphi_s$, ...) are not allowed because momentum conservation is not consistent with power counting.

The action for the collinear–soft interaction is

$$S_{cs} = \frac{g}{2}\int d^d x\, \varphi_{c_+}^2(x)\varphi_s(x) \tag{3.11}$$

(the c_-–soft interaction can be considered similarly). In coordinate space the region where $\varphi_{c_+}(x)$ lives is $x \sim (1, \lambda^{-2}, \lambda^{-1})Q^{-1}$. The region where $\varphi_s(x)$ lives is $x \sim (\lambda^{-2}, \lambda^{-2}, \lambda^{-2})Q^{-1}$. The characteristic region of x in the integral (3.11) is therefore collinear (Fig. 7).

The soft field $\varphi_s(x)$ varies little in the e_- direction within this region: $\varphi_s(x) \approx \varphi_s(\bar{x}_+)$, where $\bar{x}_+ \equiv \frac{1}{2} x_- e_+^\mu$ is the projection of x onto the e_+ axis. Derivatives acting on $\varphi_s(x)$ are $\partial_s \sim (\lambda^2, \lambda^2, \lambda^2)Q$, and we can expand

$$\varphi_s(x) = \varphi_s(\bar{x}_+) - \underbrace{\vec{x}_\perp \cdot \vec{\partial}_\perp}_{\mathcal{O}(\lambda)} \varphi_s(\bar{x}_+) + \frac{1}{2} \underbrace{x_+ \partial_-}_{\mathcal{O}(\lambda^2)} \varphi_s(\bar{x}_+) + \frac{1}{2} \underbrace{x_{\perp i} x_{\perp j} \partial_{\perp i} \partial_{\perp j}}_{\mathcal{O}(\lambda^2)} \varphi_s(\bar{x}_+) + \mathcal{O}(\lambda^3) .$$

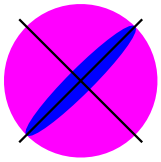


Figure 7: Collinear–soft interaction in coordinate space.

This is called multipole expansion, in analogy with electrodynamics. Therefore, the action (3.11) is

$$S_{cs} = \frac{g}{2} \int d^d x \, \varphi_{c_+}^2(x) \varphi_s(\bar{x}_+) + \mathcal{O}(\lambda) .$$

We can also understand this result from a slightly different point of view. Expressing the coordinate-space fields in the action (3.11) via the momentum-space ones we obtain

$$S_{cs} = \frac{g}{2} \int d^d x \frac{d^d k_{c_+1}}{(2\pi)^d} \frac{d^d k_{c_+2}}{(2\pi)^d} \frac{d^d k_s}{(2\pi)^d} e^{-i(k_{c_+1} + k_{c_+2} + k_s) \cdot x} \tilde{\varphi}_{c_+}(k_{c_+1}) \tilde{\varphi}_{c_+}(k_{c_+2}) \tilde{\varphi}_s(k_s) .$$

Here $k_{c_+1} + k_{c_+2} + k_s \sim (\lambda^2, 1, \lambda)Q$, and hence the characteristic $x \sim (1, \lambda^{-2}, \lambda^{-1})Q^{-1}$; for a soft momentum $k_s \sim (\lambda^2, \lambda^2, \lambda^2)Q$ we have

$$k_s \cdot x = \frac{1}{2} \underbrace{k_{s+} x_-}_{\mathcal{O}(1)} + \frac{1}{2} \underbrace{k_{s-} x_+}_{\mathcal{O}(\lambda^2)} - \underbrace{\vec{k}_{s\perp} \cdot \vec{x}_\perp}_{\mathcal{O}(\lambda)} .$$

In other words, the soft field φ_s, when interacting with the collinear field φ_{c_+}, effectively carries momentum $k_s = (k_{s+}, 0, \vec{0})$. The integral in $d^d k_s$ becomes

$$\int \frac{d^d k_s}{(2\pi)^d} e^{i k_{s+} x_-} \tilde{\varphi}_s(k_s) = \varphi_s(\bar{x}_+) .$$

Now we can write down the complete SCET Lagrangian:

$$\begin{aligned} L = {} & \frac{1}{2} (\partial_\mu \varphi_{c_+}(x)) (\partial^\mu \varphi_{c_+}(x)) - \frac{g}{3!} \varphi_{c_+}^3(x) \\ & + \frac{1}{2} (\partial_\mu \varphi_{c_-}(x)) (\partial^\mu \varphi_{c_-}(x)) - \frac{g}{3!} \varphi_{c_-}^3(x) \\ & + \frac{1}{2} (\partial_\mu \varphi_s(x)) (\partial^\mu \varphi_s(x)) - \frac{g}{3!} \varphi_s^3(x) \\ & - \frac{g}{2} \varphi_{c_+}^2(x) \varphi_s(\bar{x}_+) - \frac{g}{2} \varphi_{c_-}^2(x) \varphi_s(\bar{x}_-) + \mathcal{O}(\lambda) . \end{aligned} \tag{3.12}$$

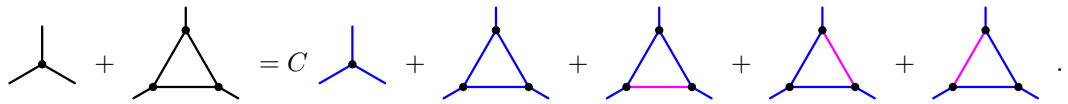
It is not exactly translation invariant; however, it is translation invariant up to $\mathcal{O}(\lambda)$. It is possible to include $\mathcal{O}(\lambda)$, $\mathcal{O}(\lambda^2)$, etc., correction terms to this Lagrangian; then it will become translation invariant up to higher powers of λ.

As discussed in Sect. 2, all quantities should be *completely* expanded in λ, i. e., each term should be proportional to some power λ^n, not a nontrivial function with all powers of λ; otherwise, the argument about the absence of double counting in dimensional regularization will not work. Therefore we should use not the local Lagrangian (3.10) (which contains all powers of λ) but the multipole-expanded nonlocal Lagrangian (3.12).

Generally speaking, coefficients in effective Lagrangians are obtained by matching, and can contain radiative corrections (from hard loops). But there are no loop corrections to coefficients in the SCET Lagrangian (3.12). For example, let's consider the c_+ collinear interaction, and suppose that it contains an unknown matching coefficient:

$$L_{c_+} = -\frac{g}{3!} C \varphi_{c_+}^3 \,, \quad C = 1 + C_1 g^2 + \cdots$$

We calculate the scattering amplitude with all 3 external momenta c_+ collinear both in the full theory and in the effective one. With one-loop accuracy



When all 3 external momenta are exactly parallel to e_+ (and hence on-shell), all loop diagrams vanish, and we obtain

$$C = 1 \,.$$

Let's now consider the current $J(x) = \frac{1}{2}\varphi^2(x)$ in the full theory in the kinematical situation when it annihilates one (or more) c_+ collinear particle(s) and creates one (or more) c_- collinear particle(s). In SCET it becomes a sum of 2-field, 3-field (and so on) operators: $J(x) = J_2(x) + J_3(x) + \cdots$, where symbolically

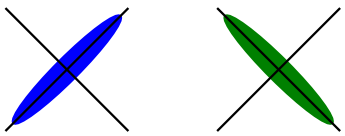


Figure 8: Coordinate-space regions where c_+ and c_- collinear fields live.

$$J_2 = C_2 \varphi_{c_+} \varphi_{c_-} \,, \quad J_3 = \frac{1}{2} C_3 \left[\varphi_{c_+}^2 \varphi_{c_-} + \varphi_{c_+} \varphi_{c_-}^2 \right] , \ldots$$

The field $\varphi_{c_+}(x)$ lives in the region $x \sim (1, \lambda^{-2}, \lambda^{-1}) Q^{-1}$ while $\varphi_{c_-}(x)$ – in $x \sim (\lambda^{-2}, 1, \lambda^{-1}) Q^{-1}$ (Fig. 8). The field $\varphi_{c_+}(x)$ varies quickly in the e_- direction: for $t \sim 1/Q$

$$\varphi_{c_+}(x + t e_-) = \varphi_{c_+}(x) + \underbrace{t \partial_-}_{\mathcal{O}(1)} \varphi_{c_+}(x) + \frac{1}{2} \underbrace{t^2 \partial_-^2}_{\mathcal{O}(1)} \varphi_{c_+}(x) + \cdots \,,$$

cannot be expanded in t. Similarly,

$$\varphi_{c_-}(x + t' e_+) = \varphi_{c_-}(x) + \underbrace{t' \partial_+}_{\mathcal{O}(1)} \varphi_{c_-}(x) + \frac{1}{2} \underbrace{t'^2 \partial_+^2}_{\mathcal{O}(1)} \varphi_{c_-}(x) + \cdots$$

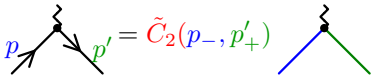
cannot be expanded in $t' \sim 1/Q$. It is natural to expect nonlocality of order Q^{-1} in J_2 (as well as J_3, etc.). We can expand $\varphi_{c_+}(x)$ in shifts in all directions except e_-, and $\varphi_{c_-}(x)$ – in all

directions except e_+:

$$J_2(x) = \int dt\, dt'\, C_2(t,t')\varphi_{c_+}(x+te_-)\varphi_{c_-}(x+t'e_+)$$

plus terms suppressed by powers of λ.

In momentum space, for on-shell momenta $p=(0,p_-,\vec{0})$ and $p'=(p'_+,0,\vec{0})$ we have the matching condition

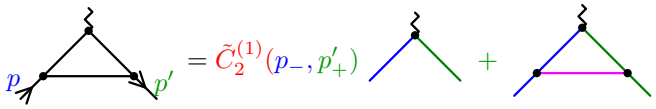


$$, \quad \tilde{C}_2(p_-,p'_+) = \int dt\, dt'\, e^{ip_-t - ip'_+t'} C_2(t,t')\,.$$

At the tree level there is no nonlocality:

$$\tilde{C}_2^{(0)}(p_-,p'_+) = 1\,, \quad C_2^{(0)}(t,t') = \delta(t)\delta(t')\,.$$

With 1-loop accuracy,



The SCET loop vanishes at on-shell momenta $p=(0,p_-,\vec{0})$, $p'=(p'_+,0,\vec{0})$, and the 1-loop correction to $\tilde{C}_2(p_-,p'_+)$ is given by the hard loop I_h (3.6):

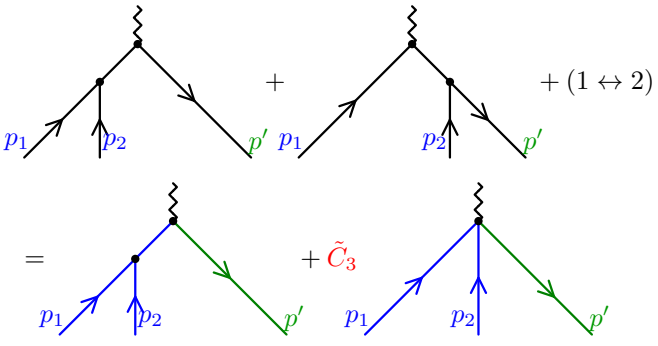
$$\tilde{C}_2^{(1)}(p_-,p'_+) = \frac{g^2}{(4\pi)^{d/2}} I_h(p_-p'_+) \tag{3.13}$$

(note that it depends only on the product $p_-p'_+$).

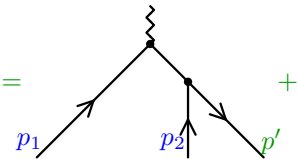
Similarly, the SCET operator J_3 is

$$J_3(x) = \frac{1}{2}\int dt_1\, dt_2\, dt'\, C_3(t_1,t_2,t')\varphi_{c_+}(x+t_1e_-)\varphi_{c_+}(x+t_2e_-)\varphi_{c_-}(x+t'e_+) + (+ \leftrightarrow -)\,.$$

The leading-order matching condition is



The first diagram on the second line is identical to the first diagram on the first line, and we may cancel them. After that, we may put the momenta on-shell, $p_1 = (0, p_{1-}, \vec{0})$, $p_2 = (0, p_{2-}, \vec{0})$, $p' = (p'_+, 0, \vec{0})$, and obtain

$\tilde{C}_3(p_{1-}, p_{2-}, p'_+) =$  $+ (1 \leftrightarrow 2) = \dfrac{g}{p_{2-}p'_+ - i0} + (1 \leftrightarrow 2)\,.$

In coordinate space,

$$\begin{aligned} C_3(t_1, t_2, t') &= \int \frac{dp_{1-}}{2\pi}\frac{dp_{2-}}{2\pi}\frac{dp'_+}{2\pi} e^{-ip_{1-}t_1 - ip_{2-}t2 + ip'_+t'}\,\tilde{C}_3(p_{1-}, p_{2-}, p'_+) \\ &= g\delta(t_1)\theta(-t_2)\theta(t') + (1 \leftrightarrow 2)\,. \end{aligned}$$

In other words,

$$J_3(x) = g\,\varphi_{c_+}(x) \int_{-\infty}^{0} dt\,\varphi_{c_+}(x + te_-) \int_0^{\infty} dt'\,\varphi_{c_-}(x + t'e_+)\,.$$

Incoming momenta p_- correspond to the operator $i\partial_-$; outgoing p'_+ – to $-i\partial_+$:

$$J_3(x) = g\,\varphi_{c_+}(x)\,\frac{1}{i\partial_- - i0}\varphi_{c_+}(x)\,\frac{1}{-i\partial_+ - i0}\varphi_{c_-}(x)\,.$$

Let's check:

$$\begin{aligned} &\int_{-\infty}^{0} dt\,\varphi(x + te_-) = \int \frac{d^dk}{(2\pi)^d} e^{-ik\cdot x}\tilde{\varphi}(k) \int_{-\infty}^{0} dt\, e^{-ik_-t + 0t} \\ &= \int \frac{d^dk}{(2\pi)^d}\frac{i}{k_- + i0} e^{-ik\cdot x}\tilde{\varphi}(k) = \frac{i}{i\partial_- + i0}\int \frac{d^dk}{(2\pi)^d} e^{-ik\cdot x}\tilde{\varphi}(k) = \frac{i}{i\partial_- + i0}\varphi(x)\,; \end{aligned}$$

similarly,

$$\int_0^{\infty} dt\,\varphi(x + te_+) = \frac{-i}{i\partial_+ - i0}\varphi(x)\,.$$

We can understand this relation also in the following way. Let a function $F(x)$ be defined as

$$F(x) = \int_{-\infty}^{0} dt\,\varphi(x + te_-)\,.$$

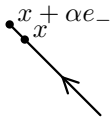


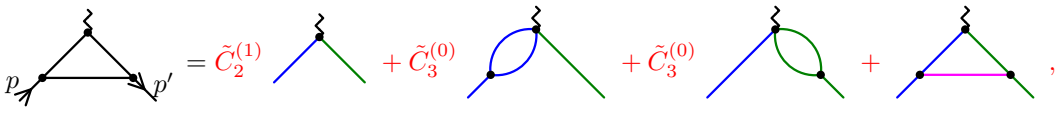
Figure 9: $F(x + \alpha e_-)$.

Then, for an infinitesimal α (Fig. 9),

$$F(x + \alpha e_-) = F(x) + \alpha\partial_- F(x) = \int_{-\infty}^{\alpha} dt\,\varphi(x + te_-) = F(x) + \alpha\varphi(x)\,,$$

and hence $\partial_- F(x) = \varphi(x)\,.$

Now we are ready to calculate the form factor with off-shell momenta $p = (p_+, p_-, \vec{0})$, $p' = (p'_+, p'_-, \vec{0})$ in SCET. At 1 loop



where $\tilde{C}_2^{(1)}$ is given by the formula (3.13). The c_+ collinear loop diagram (Fig. 10a) is

$$\frac{1}{2}\frac{g^2}{(4\pi)^{d/2}}\int\frac{d^dk}{i\pi^{d/2}}\frac{\tilde{C}_3(k_- + p_-, -k_-, p'_+)}{(-k^2 - i0)(-(k+p)^2 - i0)}$$
$$= \frac{g^2}{(4\pi)^{d/2}}\int\frac{d^dk}{i\pi^{d/2}}\frac{1}{(-k^2 - i0)(-(k+p)^2 - i0)(-p'_+k_- - i0)} = \frac{g^2}{(4\pi)^{d/2}}I_{c_+}\,,$$

where I_{c_+} is given by the formula (3.7); the c_- collinear loop is similar. In the soft loop diagram (Fig. 10b), $p = (p_+, p_-, \vec{0})$, $p' = (p'_+, p'_-, \vec{0})$, $k = (k_+, k_-, \vec{k}_\perp)$; momentum conservation holds up to $\mathcal{O}(\lambda)$, and

$$\frac{g^2}{(4\pi)^{d/2}}\int\frac{d^dk}{i\pi^{d/2}}\frac{1}{(-k^2 - i0)(-p_-(k_+ + p_+) - i0)(-p'_+(k_- + p'_-) - i0)} = \frac{g^2}{(4\pi)^{d/2}}I_s\,,$$

where I_s is given by the formula (3.8). Thus we have reproduced the result of the method of regions (Sect. 2) within SCET.

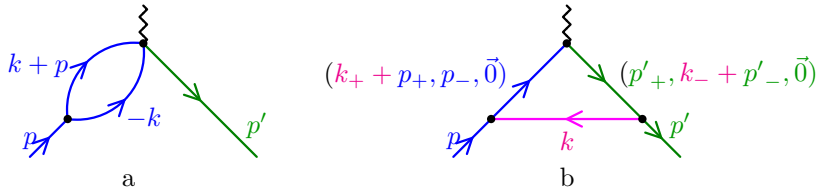


Figure 10: c_+ collinear (a) and soft (b) loop diagrams in SCET.

4 QCD

4.1 SQET Lagrangian

Now we consider massless QCD

$$L = \bar{\psi}i\not{D}\psi - \frac{1}{4}F^{a\mu\nu}F^a_{\mu\nu}\,,$$

where $igF^{\mu\nu} = [iD^\mu, iD^\nu]$ and flavor indices are assumed. We want to construct an effective theory with soft ($k_c \sim (\lambda^2, 1, \lambda)Q$) and collinear ($k_s \sim (\lambda^2, \lambda^2, \lambda^2)Q$) modes:

$$\psi \to \psi_c + \psi_s\,, \quad A^\mu \to A^\mu_c + A^\mu_s\,.$$

Of course, in any real physical problems there must be some other characteristic momentum in addition to k_c, otherwise we cannot say that a nearly light-like momentum k_c along e_+ has high energy: either the second nearly light-like momentum along e_- ($k_{c_-} \sim (q, \lambda^2, \lambda)Q$), or the heavy-quark momentum Mv ($v = e_0$), or something else. We'll not consider c_- collinear modes explicitly; results for them can be easily obtained by interchanging $+ \leftrightarrow -$.

The correlator of soft quark fields is

$$<T\psi_s(x_s)\bar\psi_s(0)> = \int \frac{d^4k}{(2\pi)^4} e^{-ik\cdot x} \frac{i\not k}{k^2+i0} \sim \lambda^6 ,$$

and hence

$$\psi_s \sim \lambda^3 ;$$

the correlator of soft gluon fields is

$$<TA_s^\mu(x_s)A_s^\nu(0)> = \int \frac{d^4k}{(2\pi)^4} e^{-ik\cdot x} \frac{i}{k^2+i0} \left[-g^{\mu\nu} + \xi\frac{k^\mu k^\nu}{k^2}\right] \sim \lambda^4 ,$$

and hence

$$A_s^\mu \sim \lambda^2$$

(note that the covariant derivative $iD_s^\mu = i\partial_s^\mu + gA_s^\mu \sim \lambda^2$ is homogeneous). The soft Lagrangian is

$$L_s = \bar\psi_s i\not D_s \psi_s - \frac{1}{4} F_s^{a\mu\nu} F^a_{s\mu\nu} ,$$

where $igF_s^{\mu\nu} = [iD_s^\mu, iD_s^\nu]$; it is $L_s \sim \lambda^4$.

The collinear quark field can be decomposed as

$$\psi_c = \xi + \eta , \quad \xi = \frac{\gamma_+\gamma_-}{4}\psi_c , \quad \eta = \frac{\gamma_-\gamma_+}{4}\psi_c . \tag{4.1}$$

The correlators of these fields are

$$<T\xi(x)\xi(0)> = \int \frac{d^4k}{(2\pi)^4} e^{-ik\cdot x} \frac{i}{k^2+i0} \frac{\gamma_+\gamma_-}{4} \underbrace{\not k}_{\frac{1}{2}k_-\gamma_+} \frac{\gamma_-\gamma_+}{4} \sim \lambda^2 ,$$

$$<T\eta(x)\eta(0)> = \int \frac{d^4k}{(2\pi)^4} e^{-ik\cdot x} \frac{i}{k^2+i0} \frac{\gamma_-\gamma_+}{4} \underbrace{\not k}_{\frac{1}{2}k_+\gamma_-} \frac{\gamma_+\gamma_-}{4} \sim \lambda^4 ,$$

and hence

$$\xi \sim \lambda , \quad \eta \sim \lambda^2 .$$

The correlator of collinear gluon fields is

$$<TA_c^\mu(x)A_c^\nu(0)> = \int \frac{d^4k}{(2\pi)^4} e^{-ik\cdot x} \frac{i}{k^2+i0} \left[-g^{\mu\nu} + \xi\frac{k^\mu k^\nu}{k^2}\right]$$

(ξ is the gauge parameter), and hence

$$<A_{c+}A_{c+}> \sim \lambda^4 , \quad <A_{c-}A_{c-}> \sim 1 , \quad <A_{c\perp}A_{c\perp}> \sim \lambda^2 ,$$

and $A_c \sim (\lambda^2, 1, \lambda)$ (note that the covariant derivative $iD_c^\mu = i\partial_c^\mu + gA_c^\mu \sim (\lambda^2, 1, \lambda)$ is homogeneous).

Substituting the decomposition (4.1) into the QCD Lagrangian we obtain

$$\begin{aligned} L &= i(\bar{\xi} + \bar{\eta}) \left(\frac{1}{2} D_+ \gamma_- + \frac{1}{2} D_- \gamma_+ + \not{D}_\perp \right) (\xi + \eta) \,, \\ &= \frac{i}{2} \bar{\xi} D_+ \gamma_- \xi + \frac{i}{2} \bar{\eta} D_- \gamma_+ \eta + i\bar{\xi} \not{D}_\perp \eta + i\bar{\eta} \not{D}_\perp \xi \,. \end{aligned}$$

The equation of motion

$$\not{D} \psi_c = \left(\frac{1}{2} D_+ \gamma_- + \frac{1}{2} D_- \gamma_+ + \not{D}_\perp \right) (\xi + \eta) = 0$$

is decomposed into

$$\gamma_+ \not{D} \psi_c = 2D_+ \xi + \not{D}_\perp \eta = 0 \,, \quad \gamma_- \not{D} \psi_c = 2D_- \eta + \not{D}_\perp \xi = 0 \,.$$

We can express the small field η via the leading field ξ:

$$\eta = -\frac{1}{2} \gamma_- \frac{1}{iD_- + i0} i \not{D}_\perp \xi \,, \quad \bar{\eta} = -\frac{1}{2} \bar{\xi} i \overleftarrow{\not{D}}_\perp \frac{1}{i\overleftarrow{D}_- + i0} \gamma_- \,.$$

Substituting this solution into the Lagrangian (or, equivalently, integrating out η) leads to

$$\begin{aligned} L = {} & \frac{1}{2} \bar{\xi} i D_+ \gamma_- \xi - \frac{1}{2} \bar{\xi} i \not{D}_\perp \frac{\gamma_-}{iD_- + i0} i \not{D}_\perp \xi - \frac{1}{2} \bar{\xi} i \overleftarrow{\not{D}}_\perp \frac{\gamma_-}{i\overleftarrow{D}_- + i0} i \not{D}_\perp \xi \\ & + \frac{1}{8} \bar{\xi} i \overleftarrow{\not{D}}_\perp \frac{\gamma_-}{i\overleftarrow{D}_- + i0} i D_- \gamma_+ \frac{\gamma_-}{D_-} \not{D}_\perp \xi \\ = {} & \frac{1}{2} \bar{\xi} i D_+ \gamma_- \xi + \frac{1}{2} \bar{\xi} i \not{D}_\perp \frac{1}{iD_- + i0} i \not{D}_\perp \gamma_- \xi \,. \end{aligned}$$

This Lagrangian contains different orders in λ. In order to obtain the leading-order Lagrangian we substitute $iD_- \to iD_{c-} = i\partial_- + gA_{c-}$, $iD_\perp \to iD_{c\perp} = i\partial_\perp + gA_{c\perp}$ and arrive at

$$\begin{aligned} L = {} & \bar{\psi}_s i \not{D}_s \psi_s - \frac{1}{4} F_s^{a\mu\nu} F_{s\mu\nu}^a \\ & + \frac{1}{2} \bar{\xi} \Bigg[i \underbrace{D_+}_{i\partial_+ + gA_{c+} + gA_{s+}(\bar{x}_+)} + i \not{D}_{c\perp} \frac{1}{iD_{c-} + i0} i \not{D}_{c\perp} \Bigg] \gamma_- \xi - \frac{1}{4} F_c^{a\mu\nu} F_{c\mu\nu}^a \,, \end{aligned} \tag{4.2}$$

where $\bar{x}_+ \equiv \frac{1}{2} x_- e_+^\mu$ (multipole expansion) and $igF_c^{\mu\nu} = [iD^\mu, iD^\nu]$, $iD^\mu = \frac{1}{2} iD_+ e_-^\mu + \frac{1}{2} iD_{c-} e_+^\mu + iD_{c\perp}^\mu$.

The SCET Lagrangian (4.2) is invariant with respect to soft gauge transformations $U_s(x) = e^{if_s^a(x)t^a}$ where the characteristic scale of U_s is $x_s \sim (\lambda^{-2}, \lambda^{-2}, \lambda^{-2})$:

$$\psi_s(x) \to U_s(x) \psi_s(x) \,, \quad A_s^\mu(x) \to U_s(x) A_s^\mu(x) U_s^+(x) - \frac{i}{g} \big(\partial^\mu U_s(x) \big) U_s^{-1}(x) \,.$$

The collinear fields transform as

$$\xi(x) \to U_s(\bar{x}_+)\xi(x)\,, \quad A_c^\mu(x) \to U_s(\bar{x}_+)A_c^\mu(x)U_s^{-1}(\bar{x}_-)\,,$$

because

$$U_s(x) = U_s(\bar{x}_+) - \underbrace{\vec{x}_\perp\cdot\vec{\partial}_\perp U_s(\bar{x}_+)}_{\mathcal{O}(\lambda)} + \mathcal{O}(\lambda^2)\,.$$

The term $\big(\partial^\mu U_s\big)U_s^{-1} \sim \lambda^2$ is not needed for A_{c-} and $A_{c\perp}$. The component A_{c+} only appears in D_+:

$$A_{c+}(x) + A_{s+}(\bar{x}_+) \to U_s(\bar{x}_+)\left[A_{c+}(x) + A_{s+}(\bar{x}_+)\right]U_s^{-1}(\bar{x}_+) + \frac{i}{g}U_s(\bar{x}_+)\big(\partial_+ U_s^{-1}(\bar{x}_+)\big)\,,$$

and $iD_+ \to U_s(\bar{x}_+)iD_+U_s^{-1}(\bar{x}_+)$.

The Lagrangian (4.2) is also invariant with respect to collinear gauge transformations $U_c(x) = e^{if_c^a(x)t^a}$ where the characteristic scale of U_c is $x_c \sim (1,\lambda^{-2},\lambda^{-1})$. These fast varying transformation cannot affect smooth soft fields:

$$\psi_s(x) \to \psi_s(x)\,, \quad A_s^\mu(x) \to A_s^\mu(x)\,.$$

The collinear fields transform as

$$\begin{aligned}
&\xi(x) \to U_c(x)\xi(x)\,,\\
&A_c^\mu(x) \to U_c(x)A_c^\mu(x)U_c^{-1}(x) + \frac{1}{g}U_c(x)\left[i\partial^\mu + \tfrac{1}{2}gA_{s+}(\bar{x}_+)e_-^\mu, U_c^{-1}(x)\right]\,.
\end{aligned}$$

For components we have

$$\begin{aligned}
A_{c\perp}(x) &\to U_c(x)A_{c\perp}(x)U_c^{-1}(x) + \frac{i}{g}U_c(x)\left(\partial_\perp U_c^{-1}(x)\right)\,,\\
A_{c-}(x) &\to U_c(x)A_{c-}(x)U_c^{-1}(x) + \frac{i}{g}U_c(x)\left(\partial_- U_c^{-1}(x)\right)\,,\\
A_{c+}(x) &\to U_c(x)A_{c+}(x)U_c^{-1}(x) + \frac{i}{g}U_c(x)\left[D_{s+}(\bar{x}_+), U_c^{-1}(x)\right]\,,
\end{aligned}$$

so that $iD_+ \to U_c(x)iD_+U_c^{-1}(x)$.

The SCET Lagrangian (4.2) is not Lorentz invariant – it explicitly contains the vectors e_+, e_-. However, these vectors are not uniquely defined by the physical problem. We may change them keeping soft momenta soft, and collinear momenta – collinear. All physical predictions remain intact (reparametrization invariance). This symmetry is generated by the following infinitesimal transformations:

- Lorentz boost $e_+ \to (1+\varepsilon)e_+$, $e_- \to (1-\varepsilon)e_-$: collinear momenta remain collinear ($k_+ \to (1+\varepsilon)k_+$, $k_- \to (1-\varepsilon)k_-$);
- $e_+ \to e_+$, $e_- \to e_- + \varepsilon_\perp$ (where $\varepsilon_\perp$ is an infinitesimal transverse vector):

$$k_- \to \underbrace{k_-}_{\mathcal{O}(1)} + \underbrace{k\cdot\varepsilon_\perp}_{\mathcal{O}(\lambda)}, \quad k_\perp = k - \tfrac{1}{2}(k\cdot e_+)e_- - \tfrac{1}{2}(k\cdot e_-)e_+ \to \underbrace{k_\perp}_{\mathcal{O}(\lambda)} - \underbrace{\tfrac{1}{2}k_+\varepsilon_\perp}_{\mathcal{O}(\lambda^2)} - \underbrace{\tfrac{1}{2}(k\cdot\varepsilon_\perp)e_+}_{\mathcal{O}(\lambda)};$$

- $e_+ \to e_+ + \lambda\varepsilon_\perp$, $e_- \to e_-$:

$$k_+ \to \underbrace{k_+}_{\mathcal{O}(\lambda^2)} + \underbrace{\lambda k\cdot\varepsilon_\perp}_{\mathcal{O}(\lambda^2)}, \quad k_\perp \to \underbrace{k_\perp}_{\mathcal{O}(\lambda)} - \underbrace{\tfrac{\lambda}{2}(k\cdot\varepsilon_\perp)e_-}_{\mathcal{O}(\lambda^2)} - \underbrace{\tfrac{\lambda}{2}k_-\varepsilon_\perp}_{\mathcal{O}(\lambda)}$$

  (this transformation mixes different orders in λ).

Of course, if there are also c_- collinear modes, the second transformation also has to contain $\lambda\varepsilon_\perp$, to keep c_- collinear momenta c_- collinear.

Wilson lines are widely used in SCET. Therefore we make a short digression about their properties. The Wilson line in QCD is defined as

$$[x', x] = P\exp ig\int_x^{x'} dy_\mu\, A^\mu(y)\,; \tag{4.3}$$



Figure 11: Wilson line.

it depends on a contour connecting x with x'. Any contour can be represented by a sequence of infinitesimal straight segments (Fig. 11); the path-ordered exponent in (4.3) is defined as the product of the infinitesimal Wilson lines, corresponding to these segments (from x to x'), arranged from right to left. An infinitesimal Wilson line transforms under a gauge transformation as

$$[x+dx, x] = 1 + igA^\mu(x)\,dx_\mu \to 1 + ig\left[U(x)A^\mu(x)U^{-1}(x) - \frac{i}{g}\left(\partial^\mu U(x)\right)U^{-1}(x)\right]dx_\mu$$
$$= U(x+dx)U^{-1}(x) + igU(x)A^\mu(x)U^{-1}(x)\,dx_\mu = U(x+dx)\left[1 + igA^\mu(x)\,dx_\mu\right]U^{-1}(x)\,,$$

and hence for any finite Wilson line we obtain

$$[x', x] \to U(x')[x', x]U^{-1}(x)\,.$$

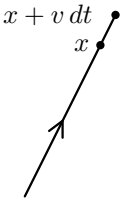


Figure 12: $W(x + v\,dt)$.

This means that, e. g., $\bar\psi(x')[x', x]\psi(x)$ is a gauge invariant operator. Let's define

$$W(x) = [x, x - \infty v] = P\exp ig\int_{-\infty}^0 dt\, v_\mu A^\mu(x + vt)\,.$$

If we consider only gauge transformations which are identical in the infinite past ($U(x - \infty v) = 1$), then $W(x) \to U(x)W(x)$, and $W^{-1}(x)\psi(x)$ (as well as $\bar\psi(x)W(x)$) is a gauge invariant operator. Let's extend this line (Fig. 12): $W(x + v\,dt) = [1 + igv\cdot A(x)\,dt]\,W(x)$, and hence $v\cdot\partial W(x) = igv\cdot A(x)\,W(x)$, or $v\cdot D\,W(x) = 0$.

Collinear quarks interact with soft gluons:

$$L_q = \frac{1}{2}\bar\xi(x)iD_+\gamma_-\xi(x)\,, \quad iD_+ = i\partial_+ + gA_{c+}(x) + gA_{s+}(\bar x_+) = iD_{c+} + gA_{s+}(\bar x_+)\,.$$

If we introduce the soft Wilson line (Fig. 13)

$$S(x) = P \exp ig \int_{-\infty}^{0} dt\, A_{s+}(x + e_+ t)$$

(where $D_{s+}S(x) = 0$) and redefine the collinear fields as

$$\xi(x) = S(\bar{x}_+)\xi_0(x)\,, \quad A_c^\mu(x) = S(\bar{x}_+)A_{c0}^\mu(x)S^{-1}(\bar{x}_+)\,,$$

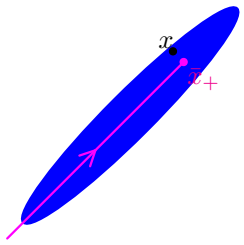


Figure 13: Soft Wilson line.

then

$$\begin{aligned} &iD_+\xi(x) \\ &= \big[S(\bar{x}_+)i\partial_+ + \big((i\partial_+ + gA_s(\bar{x}_+))S(\bar{x}_+)\big) + gS(\bar{x}_+)A_{c0+}(x)\big]\xi_0(x) = S(\bar{x}_+)iD_{c0+}\xi_0(x)\,, \end{aligned}$$

and the Lagrangian becomes

$$L_q = \frac{1}{2}\bar{\xi}_0(x)iD_{c0+}\xi_0(x)\,.$$

So, in terms of the new field $\xi_0(x)$ there is no interaction with soft gluons.

Similarly, collinear gluons interact with soft gluons: $F_c^{\mu\nu}$ in the Lagrangian (4.2) contains not only A_c^μ but also A_s^μ (because of D_+). The transformation to A_{c0}^μ leads to

$$iD_{c-} = i\partial_- + gS(\bar{x}_+)A_{c0-}(x)S^{-1}(\bar{x}_+) = S(\bar{x}_+)iD_{c0-}S^{-1}(\bar{x}_+)\,,$$

because $\partial_- S(\bar{x}_+) = 2\partial S(\bar{x}_+)/\partial x_+ = 0$; $iD_{c\perp} = S(\bar{x}_+)iD_{c0\perp}S^{-1}(\bar{x}_+)$; and

$$\begin{aligned} iD_+ &= S(\bar{x}_+)i\partial_+S^{-1}(\bar{x}_+) - S(\bar{x}_+)\big(i\partial_+S^{-1}(\bar{x}_+)\big) + gA_{s+}(\bar{x}_+) + gS(\bar{x}_+)A_{c0+}(x)S^{-1}(\bar{x}_+) \\ &= S(\bar{x}_+)iD_{c0+}S^{-1}(\bar{x}_+) \end{aligned}$$

because $S(\bar{x}_+)\big(i\partial_+S^{-1}(\bar{x}_+)\big) = -\big(i\partial_+S(\bar{x}_+)\big)S^{-1}(\bar{x}_+) = gA_{s+}(\bar{x}_+)$, $iD_{s+}S = (i\partial_+ + gA_{s+})S = 0$ (note that $iD_{c0+} = i\partial_+ + gA_{c0+}$ does not contain the soft gluon field). Therefore,

$$L_g = -\frac{1}{2}\,\mathrm{Tr}\, F_{c0\mu\nu}F_{c0}^{\mu\nu}\,,$$

where $F_c^{\mu\nu}(x) = S(\bar{x}_+)F_{c0}^{\mu\nu}(x)S^{-1}(\bar{x}_+)$, and $F_{c0}^{\mu\nu}$ does not contain the soft gluon field. So, in terms of the new field A_{c0}^μ there is no interaction with soft gluons.

Using the collinear Wilson line (Fig. 14)

$$W(x) = P \exp ig \int_{-\infty}^{0} dt\, A_{c-}(x + te_-)$$

we can redefine the collinear fields as

$$\xi(x) = W(x)\chi(x)\,, \quad \mathcal{A}^\mu(x) = W^{-1}(x)\big(iD_c^\mu W(x)\big)$$

(note that $\mathcal{A}_- = 0$, $\mathcal{A}_+ \sim \lambda^2$, $\mathcal{A}_\perp \sim \lambda$). Defining also the covariant derivative

$$i\mathcal{D}^\mu = W^{-1}(x)iD_c^\mu W(x) = i\partial^\mu + \mathcal{A}^\mu,$$

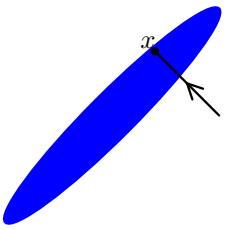


Figure 14: Collinear Wilson line.

we can rewrite the collinear quark Lagrangian in (4.2) as

$$L_q = \frac{1}{2}\bar\chi i\mathcal{D}_+\gamma_-\chi + \frac{1}{2}\bar\chi i\mathcal{D}\!\!\!/_\perp\frac{1}{i\partial_- + i0}i\mathcal{D}\!\!\!/_\perp\gamma_-\chi = \frac{1}{2}\bar\chi i\mathcal{D}_+\gamma_-\chi - \frac{i}{2}\bar\chi\gamma_- i\mathcal{D}\!\!\!/_\perp\int_{-\infty}^{0} dt\ (i\mathcal{D}\!\!\!/_\perp\chi)_{\,x+te_-}\,,$$

because $W^{-1}(x)iD_{c-}W(x) = i\partial_-$ and hence

$$W^{-1}(x)\frac{1}{iD_{c-}+i0}W(x) = \frac{1}{i\partial_-+i0}\,.$$

Nonlocality in e_- direction is $\sim Q^{-1}$. Similarly, the collinear gluon Lagrangian in (4.2) becomes

$$L_g = -\frac{1}{2g^2}\,\mathrm{Tr}\,\mathcal{F}_{\mu\nu}\mathcal{F}^{\mu\nu}\,,$$

where

$$W^{-1}F_{c\mu\nu}W = \mathcal{F}_{\mu\nu} = \frac{1}{g}(\partial_\mu\mathcal{A}_\nu - \partial_\nu\mathcal{A}_\mu - i[\mathcal{A}_\mu,\mathcal{A}_\nu])\,.$$

4.2 Vector quark current

Now we shall consider the quark vector current

$$J^\mu(x) = \bar\psi(x)\gamma^\mu\psi(x)$$

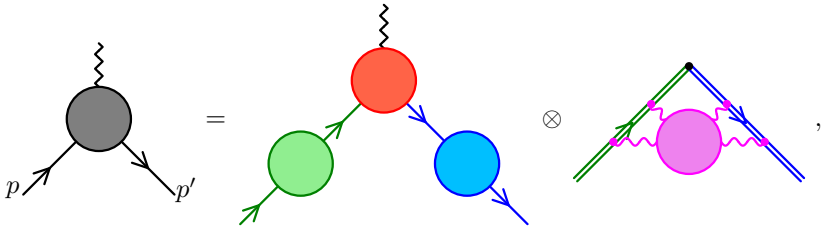
in the kinematical situation $c_- \to c_+$. Of course, we need both c_+ collinear fields (discussed in Sect. 4.1) and c_- collinear ones (all formulas for them can be easily obtained by the interchange $+ \leftrightarrow -$). The QCD field $\psi(x)$ becomes $S_-(\bar x_-)\chi_-(x)$ (where $\bar x_- = \frac{1}{2}x_+e_-$, $\gamma_-\chi_- = 0$); similarly, $\bar\psi(x)$ becomes $\bar\chi_+(x)S_+^+(\bar x_+)$ (where $\bar x_+ = \frac{1}{2}x_-e_+$, $\gamma_+\chi_+ = 0$). Similarly to Sect. 3.3,

$$J^\mu(x) = \int dt\,dt'\,C_V(t,t')\bar\chi_+(x+te_-)S_+^+(\bar x_+)S_-(\bar x_-)\gamma_\perp^\mu\chi_-(x+t'e_+) + \cdots$$

The integration region is $x^\mu \sim (1,1,\lambda^{-1})Q^{-1}$ (Fig. 8), and we can use the multipole expansion to get

$$J^\mu(x) = \int dt\,dt'\,C_V(t,t')\bar\chi_+(\bar x_- + x_\perp + te_-)S_+^+(0)S_-(0)\gamma_\perp^\mu\chi_-(\bar x_+ + x_\perp + t'e_+) + \cdots$$

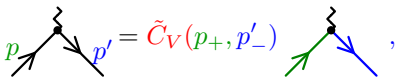
So, at the leading order in λ the matrix element of J^μ (the form factor) can be factorized,



to all orders in α_s. The matrix element of $S_+^+(0)S_-(0)$ is the soft factor S, the soft Wilson line with the cusp. The matching coefficient $\tilde{C}_V$ is the hard factor, and the propagators of χ_+ and χ_- produce the jet factors:

$$F(-q^2,-p^2,-p'^2) = \tilde{C}_V(-q^2)J_-(-p^2)J_+(-p'^2)S\left(\frac{(-p^2)(-p'^2)}{-q^2}\right).$$

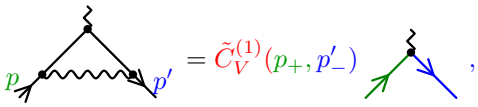
The coefficient C_V is obtained by matching the on-shell matrix elements in QCD and SCET: the quark momenta are $p=(p_+,0,\vec{0})$, $p'=(0,p'_-,\vec{0})$. At the tree level



and hence

$$\tilde{C}_V^{(0)}(p_+,p'_-) = 1\,, \quad C_V^{(0)}(t,t') = \delta(t)\delta(t')\,.$$

At 1 loop



because SCET loops vanish. The calculation of this loop diagram is similar to that of I_h (Sect. 3.2), the result is

$$\begin{aligned} C_V(-q^2) &= 1 - C_F\frac{g_0^2(-q^2)^{-\varepsilon}}{(4\pi)^{d/2}}\frac{\Gamma(1+\varepsilon)\Gamma^2(1-\varepsilon)}{\Gamma(1-2\varepsilon)}\left[\frac{2}{\varepsilon^2}+\frac{3+2\varepsilon}{\varepsilon(1-2\varepsilon)}\right] \\ &= 1 - C_F\frac{g_0^2(-q^2)^{-\varepsilon}}{(4\pi)^{d/2}}e^{-\gamma\varepsilon}\left(\frac{2}{\varepsilon^2}+\frac{3}{\varepsilon}-\frac{\pi^2}{6}+8+\mathcal{O}(\varepsilon)\right). \end{aligned}$$

Re-expressing this matching coefficient via the $\overline{\text{MS}}$ coupling $\alpha_s(\mu)$, we obtain

$$C_V(-q^2) = 1 - C_F\frac{\alpha_s(\mu)}{4\pi}\left(\frac{-q^2}{\mu^2}\right)^{-\varepsilon}\left(\frac{2}{\varepsilon^2}+\frac{3}{\varepsilon}-\frac{\pi^2}{6}+8\right).$$

The bare matching coefficient should be equal to $C_V(-q^2) = Z^{-1}C_V(-q^2,\mu)$, where the renormalized matching coefficient $C_V(-q^2,\mu)$ is finite at $\varepsilon\to 0$, and Z is a minimal renormalization constant (containing only negative powers of ε). We arrive at

$$\begin{aligned} Z &= 1 + C_F\left(\frac{2}{\varepsilon^2}-\frac{2}{\varepsilon}\log\frac{-q^2}{\mu^2}+\frac{3}{\varepsilon}\right)\frac{\alpha_s(\mu)}{4\pi}\,, \\ C_V(-q^2,\mu) &= 1 + C_F\left(-\log^2\frac{-q^2}{\mu^2}+3\log\frac{-q^2}{\mu^2}+\frac{\pi^2}{6}-8\right)\frac{\alpha_s(\mu)}{4\pi}\,. \end{aligned}$$

The bare matching coefficient does not depend on μ:

$$\frac{d\log C_V(-q^2)}{d\log\mu} = 0 = -\frac{d\log Z}{d\log\mu} + \frac{d\log C_V(-q^2,\mu)}{d\log\mu}\,.$$

The SCET vector current anomalous dimension is defined by

$$\frac{d\log Z}{d\log\mu} = \Gamma(\alpha_s(\mu))\log\frac{-q^2}{\mu^2} + \gamma_V(\alpha_s(\mu))\,;$$

the renormalized matching coefficient satisfies the renormalization group (RG) equation

$$\frac{d\log C_V(-q^2,\mu)}{d\log\mu} = \Gamma(\alpha_s(\mu))\log\frac{-q^2}{\mu^2} + \gamma_V(\alpha_s(\mu))\,. \tag{4.4}$$

Taking into account $d\log\alpha_s(\mu)/d\log\mu = -2\varepsilon + \mathcal{O}(\alpha_s)$, we obtain

$$\Gamma(\alpha_s) = 4C_F\frac{\alpha_s}{4\pi} + \mathcal{O}(\alpha_s^2)\,, \quad \gamma_V(\alpha_s) = -6C_F\frac{\alpha_s}{4\pi} + \mathcal{O}(\alpha_s^2)\,.$$

Here $\Gamma(\alpha_s)$ is called the light-like cusp anomalous dimension.

The solution of the RG equation (4.4) can be written as

$$C_V(-q^2,\mu) = U(\mu_0,\mu)C_V(-q^2,\mu_0)\,,$$

where the evolution factor $U(\mu_0,\mu)$ satisfies the equation

$$\frac{d\log U(\mu_0,\mu)}{d\log\mu} = \Gamma(\alpha_s(\mu))\log\frac{-q^2}{\mu^2} + \gamma_V(\alpha_s(\mu))$$

with the initial condition $U(\mu_0,\mu_0) = 1$. The anomalous dimensions have the form

$$\Gamma(\alpha_s) = \Gamma_0\frac{\alpha_s}{4\pi} + \Gamma_1\left(\frac{\alpha_s}{4\pi}\right)^2 + \cdots\,, \quad \gamma_V(\alpha_s) = \gamma_{V0}\frac{\alpha_s}{4\pi} + \gamma_{V1}\left(\frac{\alpha_s}{4\pi}\right)^2 + \cdots\,.$$

Dividing this equation by the evolution equation for $\alpha_s(\mu)$,

$$\frac{d\log\alpha_s(\mu)}{d\log\mu} = -2\beta(\alpha_s(\mu))\,, \quad \beta(\alpha_s) = \beta_0\frac{\alpha_s}{4\pi} + \beta_1\left(\frac{\alpha_s}{4\pi}\right)^2 + \cdots\,,$$

we obtain

$$\frac{d\log U(\mu_0,\mu)}{d\log\alpha_s} = -\frac{1}{2\beta(\alpha_s)}\left[\Gamma(\alpha_s)\left(\log\frac{-q^2}{\mu_0^2} - 2\log\frac{\mu}{\mu_0}\right) + \gamma_V(\alpha_s)\right]\,.$$

We substitute

$$\log\frac{\mu}{\mu_0} = -\int_{\alpha_s(\mu_0)}^{\alpha_s(\mu)}\frac{d\alpha_s}{\alpha_s}\frac{1}{2\beta(\alpha_s)}$$

and arrive at the solution

$$U(\mu_0,\mu) = \exp\left[S(\mu_0,\mu) - A_{\gamma_V}(\mu_0,\mu)\right]\left(\frac{-q^2}{\mu_0^2}\right)^{-A_\Gamma(\mu_0,\mu)}\,, \tag{4.5}$$

where

$$A_\gamma(\mu_0,\mu) = \int_{\alpha_s(\mu_0)}^{\alpha_s(\mu)}\frac{d\alpha_s}{\alpha_s}\frac{\gamma(\alpha_s)}{2\beta(\alpha_s)} = \frac{\gamma_0}{2\beta_0}\log r + \mathcal{O}(\alpha_s)\,,$$

$$S(\mu_0,\mu) = -\int_{\alpha_s(\mu_0)}^{\alpha_s(\mu)}\frac{d\alpha_s}{\alpha_s}\frac{\Gamma(\alpha_s)}{2\beta(\alpha_s)}\int_{\alpha_s(\mu_0)}^{\alpha_s}\frac{d\alpha_s'}{\alpha_s'}\frac{1}{\beta(\alpha_s')}$$

$$= \frac{\Gamma_0}{2\beta_0^2}\left[\frac{4\pi}{\alpha_s(\mu_0)}\left(\frac{r-1}{r} - \log r\right) + \left(\frac{\Gamma_1}{\Gamma_0} - \frac{\beta_1}{\beta_0}\right)(1 - r + \log r) + \frac{\beta_1}{2\beta_0}\log^2 r\right] + \mathcal{O}(\alpha_s)\,,$$

and $r = \alpha_s(\mu)/\alpha_s(\mu_0)$.

The soft function at 1 loop (Fig. 15) is

$$S^{(1)} = -2C_F \frac{g_0^2}{(4\pi)^{d/2}} (-q^2) I_s \,,$$

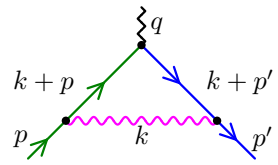


Figure 15: Soft function.

see Sect. 3.2. Therefore,

$$S(\Lambda_s^2) = 1 - 2C_F \frac{g_0^2 (\Lambda_s^2)^{-\varepsilon}}{(4\pi)^{d/2}} \Gamma(1-\varepsilon)\Gamma^2(\varepsilon)$$
$$= 1 - 2C_F \frac{\alpha_s(\mu)}{4\pi} \left(\frac{\Lambda_s^2}{\mu^2}\right)^{-\varepsilon} \left(\frac{1}{\varepsilon^2} + \frac{\pi^2}{4}\right) = Z_S^{-1} S(\Lambda_s^2, \mu) \,,$$

where

$$Z_S = 1 + 2C_F \left(\frac{1}{\varepsilon^2} - \frac{1}{\varepsilon} \log \frac{\Lambda_s^2}{\mu^2}\right) \frac{\alpha_s(\mu)}{4\pi} + \mathcal{O}(\alpha_s^2) \,,$$
$$S(\Lambda_s^2, \mu) = 1 - C_F \left(\log^2 \frac{\Lambda_s^2}{\mu^2} + \frac{\pi^2}{2}\right) \frac{\alpha_s(\mu)}{4\pi} + \mathcal{O}(\alpha_s^2) \,.$$

The renormalized soft function satisfies the RG equation

$$\frac{d \log S(\Lambda_s^2, \mu)}{d \log \mu} = \Gamma(\alpha_s(\mu)) \log \frac{\Lambda_s^2}{\mu^2} + \gamma_S(\alpha_s(\mu)) \,,$$

where

$$\gamma_S(\alpha_s) = 0 + \mathcal{O}(\alpha_s^2) \,.$$

To summarize: the quark form factor at the leading order in λ is equal to

$$F(-q^2, -p^2, -p'^2) = C_V(-q^2, \mu) J(-p^2, \mu) J(-p'^2, \mu) S(\Lambda_s^2, \mu) \,, \tag{4.6}$$

where

$$\Lambda_s^2 = \frac{(-p^2)(-p'^2)}{-q^2} \,.$$

It does not depend on μ:

$$\frac{d \log F(-q^2, -p^2, -p'^2)}{d \log \mu} = 0$$
$$= \frac{d \log C_V(-q^2, \mu)}{d \log \mu} + \frac{d \log J(-p^2, \mu)}{d \log \mu} + \frac{d \log J(-p'^2, \mu)}{d \log \mu} + \frac{d \log S(\Lambda_s^2, \mu)}{d \log \mu} \,.$$

The anomalous dimensions are

$$\frac{d \log C_V(-q^2, \mu)}{d \log \mu} = \Gamma(\alpha_s(\mu)) \log \frac{-q^2}{\mu^2} + \gamma_V(\alpha_s(\mu)) \,,$$
$$\frac{d \log J(-p^2, \mu)}{d \log \mu} = -\Gamma(\alpha_s(\mu)) \log \frac{-p^2}{\mu^2} - \gamma_J(\alpha_s(\mu)) \,,$$
$$\frac{d \log S(\Lambda_s^2, \mu)}{d \log \mu} = \Gamma(\alpha_s(\mu)) \log \frac{\Lambda_s^2}{\mu^2} + \gamma_S(\alpha_s(\mu)) \,,$$

where $\Gamma(\alpha_s)$ is the light-like cusp anomalous dimension. Therefore, the following condition has to be satisfied:

$$\Gamma(\alpha_s(\mu))\left[\log\frac{-q^2}{\mu^2} - \log\frac{-p^2}{\mu^2} - \log\frac{-p'^2}{\mu^2} + \log\frac{(-p^2)(-p'^2)}{(-q^2)\mu^2}\right] + \gamma_V(\alpha_s(\mu)) - 2\gamma_J(\alpha_s(\mu)) + \gamma_S(\alpha_s(\mu)) = 0\,.$$

This condition explains why the coefficient of the logarithm in each anomalous dimension is $\Gamma(\alpha_s)$.

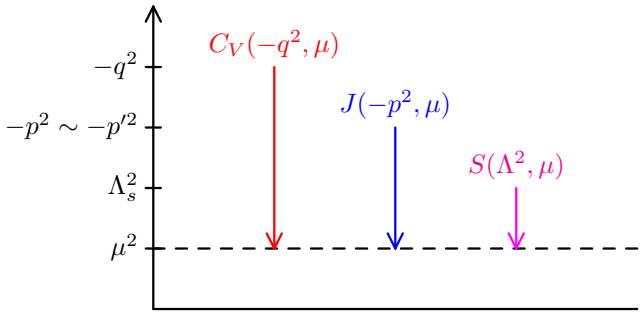


Figure 16: Running the factors in the factorization formula.

We have to use the same normalization scale μ in all factors in the factorization formula (4.6). However, in order to avoid large logarithms in perturbative series it is better to calculate $C_V(-q^2,\mu)$ at $\mu^2 \sim -q^2$; $J(-p^2,\mu)$ and $J(-p'^2,\mu)$ at $\mu^2 \sim -p^2 \sim -p'^2$; and $S(\Lambda_s^2,\mu)$ at $\mu^2 \sim \Lambda_s^2$. Then we use the RG equations to run these factors to a common μ^2 (Fig. 16).

5 Conclusion

In these lectures we discussed basics of SCET-I as applied to a single problem, the form factor with large $-q^2$ and small $-p^2 \sim -p'^2$. For applications of SCET to numerous physical problems, both in heavy quark physics and in high energy hadron collider physics, see [1, 2] and references cited therein.

I am grateful to the organizers of the Helmholtz–DIAS International Summer School "Quantum Field Theory at the Limits: from Strong Fields to Heavy Quarks" (Dubna, July 18–30) for inviting me.

References

[1] T. Becher, A. Broggio, A. Ferroglia, *Introduction to Soft-Collinear Effective Theory*, Lecture Notes in Physics **896**, Springer (2015) [arXiv:1410.1892 [hep-ph]].

[2] C. Bauer, I. W. Stewart, *The Soft-Collinear Effective Theory*, http://cources.edx.org/c4x/MITx/8.EFTx/asset/notes_scetnotes.pdf

[3] V. A. Smirnov, *Applied asymptotic expansions in momenta and masses*, Springer Tracts in Modern Physics **177**, Springer (2002).

[4] B. Jantzen, *Foundation and generalization of the expansion by regions*, JHEP **12** (2011) 076 [arXiv:1111.2589 [hep-ph]].

Distribution Amplitudes of Heavy Hadrons: Theory and Applications

Alexander Parkhomenko

P. G. Demidov Yaroslavl State University, Yaroslavl, Russia

DOI: http://dx.doi.org/10.3204/DESY-PROC-2016-04/Parkhomenko

The physics of heavy quarks becomes a very reach area of study thanks to an excellent operation of hadron colliders and B-factories and exciting results from them. Experimental data obtained allows to get some information about the heavy hadron dynamics. In this case, the models for the heavy hadron wave-functions are required to do theoretical predictions for concrete processes under study. In many cases, the light-cone description is enough to obtain theoretical estimates for heavy hadron decays. A discussion of the wave-functions of the B-meson and heavy bottom baryons in terms of the light-cone distribution amplitudes is given in this paper. Simple models for the distribution amplitudes are presented and their scale dependence is discussed. Moments of the distribution amplitudes which are entering the branching fractions of radiative, leptonic and semileptonic B-mesons decays are also briefly discussed.

1 Introduction

Physics of heavy hadrons, both experimental and theoretical, still remains a hot topic at present. From one side, the remarkable operation of the hadron collider LHC at CERN provides us with a lot of interesting and exciting results and, from the other side, many more results can be obtained from the B-factory at KEK which is under construction now and hopefully to be run in a year from now. Among the excellent achievements obtained at the LHC, there is the measurement of the rare purely leptonic decay $B_s \to \mu^+\mu^-$ by the LHCb and CMS collaborations [1] in a nice agreement with the theoretical expectations based on the Standard Model (SM) (see, for example, [2] and reference therein) and the evidence of the similar decay $B^0 \to \mu^+\mu^-$ seen by the same collaborations [1] is also in agreement with the SM predictions [2]. Let us note that both decays were considered as a clean candle into possible new physics at the flavor-physics frontue, when predicted branching fractions are substantially larger the SM expectations. At the statistics have been already collected at the LHC, it starts possible to make a detail combine analysis of the rare $B \to K^{(*)}\ell^+\ell^-$ decays, where $\ell = e$, μ, in the lepton-pair invariant mass squared and spherical angles. In particular, some quantities show a sizable deviation from theoretical predictions and these require theoretical explanation. The other semileptonic decay $B^+ \to \pi^+\mu^+\mu^-$ have been also observed at the LHC [3] and, on the Run-II statistics, for the first time partially integrated branching fraction over the lepton-pair invariant mass divided into 8 bins have been experimentally obtained [4] in a good agreement with the SM predictions. All these results need to be approved at the B-factory SuperKEKB after its operation will start and, in addition, one should wait new exciting results as several B-meson

decay modes, being unobservable at the LHC, can be measured by the Belle collaboration and are of great importance to get a complete picture of B-meson physics. Among them, one can specify the decays like $B \to K^{(*)}\nu\bar{\nu}$ and $B^0 \to \pi^0\ell^+\ell^-$.

In a difference to B-meson decays, the situation with bottom baryons is a little bit worser as the SuperKEKB machine is not designed for the Λ_b and heavier baryon production. So, the LHC is the only source for the bottom-baryon study for quite some time. As the result, only limited information about this part of the hadronic sector is available and a lot of theoretical predictions will wait their check for future experimental facilities. Interesting processes are the rare semileptonic decays $\Lambda_b \to \Lambda\ell^+\ell^-$ decays, where $\ell = e,\ \mu$, which are the baryonic realization of the flavor-changing neutral current transition $b \to s\ell^+\ell^-$, quite sensitive to induced by loop diagrams contributions from new physics.

Theoretical predictions for weak decays require some information about the dynamics of light quarks in heavy hadrons — $B_{(s)}$-meson and bottom baryon. Several approaches have been already worked out and, in some cases, experimentally checked like $B \to K^{(*)}\ell^+\ell^-$ decays, where $\ell = e,\ \mu$, both at B-factories at SLAC and KEK and at the hadron colliders at FNAL and CERN. Among them, factorization approaches are of priority. In particular, the Soft-Collinear Effective Theory (SCET) originally suggested for making prediction based on the idea of the energy separation of light degrees of freedom in weak decays, have become a powerful tool for other multiscale processes which are under intensive study at the LHC now. As a byproduct of this theory, one needs to know several moments of the heavy-hadron wave-function which are entering invariant amplitudes of decays. Moreover, even a shape of the heavy-hadron wave-function is required to determine the momentum-squared dependence of the transition form factors. So, a business connected with a study of the dynamical properties of the heavy-hadron wave-functions is a useful direction in theoretical high-energy physics and its basis and some applications, this lecture is devoted.

2 Light-Cone Distribution Amplitudes of B-Meson

The dynamics of a light quark inside a heavy meson is convenient to describe within the Heavy Quark Effective Theory (HQET) [5, 6, 7]. In this approach, the heavy antiquark is considered as an external source (either static or slowly moving in dependence on the frame specified) and the light quark completely determines the meson properties. So, HQET is a useful tool in theoretical analysis of heavy hadrons. As the heavy meson is very similar to the hydrogen atom (see Fig. 1), one should use the effective mass of heavy meson $\bar{\Lambda} = m_M - m_Q$ which is nothing else but the difference between the meson mass m_M and the heavy-quark mass m_Q. Applying the pole scheme for the heavy antiquark, one can get the estimate $\bar{\Lambda} \simeq 0.5$ GeV for the lowest-mass D- and B-mesons [8]. The analogy between the heavy meson and hydrogen atom can be extended even further taking into account the fact that in the limit of an infinitely large mass of the heavy antiquark the heavy-quark spin does not influence the light-quark dynamics and, so, decouples. Such an approximation is known as the Heavy-Quark-Symmetry (HQS) limit in which the heavy quark can be considered as a spinless particle. In working out the dynamical properties of the meson, one can assume the heavy quark to be a scalar particle and study the so-called "spinor" meson [9]. The realistic quantum numbers of the meson and its wave-function can be obtained after a contraction with the heavy-quark spin.

The bilocal operator interpolating the heavy meson in the valence quark-antiquark approx-

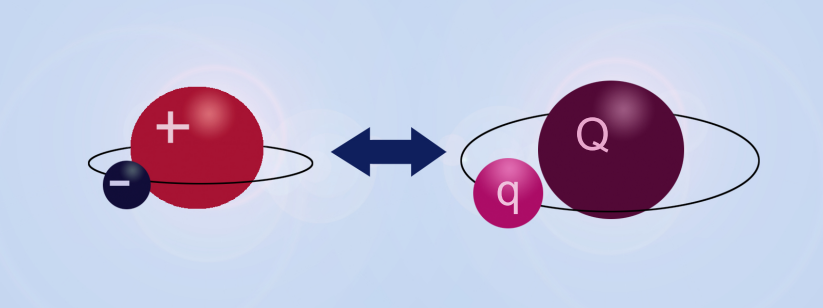


Figure 1: The similarity between the hydrogen atom (left) and heavy meson (right).

imation (the lowest Fock state) in the HQS limit is as follows [9]:

$$\widetilde{O}(z) = Q^*(0)\,\mathcal{P}\exp\left\{-ig_{\rm st}\int_0^z dz'^\mu A^a_\mu(z')\,\frac{\lambda^a}{2}\right\}q(z) = Q^*(0)\,E(0,z)\,q(z). \tag{1}$$

The link between the quarks is the path-ordered exponential called the Wilson line [10], where $A^a_\mu(z)$ is the gluonic field, $g_{\rm st}$ is the strong coupling, and λ^a $(a = 1,\ldots,8)$ are the Gell-Mann matrices. Sometimes it is convenient to use the notation: $A_\mu = A^a_\mu\lambda^a/2$.

In many exclusive decays of the B-meson only one projection of the light-quark momentum gives the dominant contribution into the decay amplitude. So, it is necessary to find such a direction and study the dependence of the meson quantities on the corresponding momentum projection. On this way, the light-cone representation of four-vectors appears to be very convenient. To get a corresponding decomposition, one needs to introduce a light cone and specify two light-like four-vectors on it, for example, $n^\mu_\pm = (1,0,0,\mp1)/\sqrt{2}$, where $n^2_\pm = 0$ and $(n_+n_-) = 1$. They can be related with physical vectors presented in a problem. In particular, if one assumes that the light quark in the bilocal operator (1) is a massless particle situated on the light cone and the gauge link is a straight line connecting its position with the origin, the four-vector n^μ_+ can be directed along this link. In this case, $dz'^\mu = dz'_-n^\mu_+$ in (1) and the variable z'_- specifies the position of the gluon field on the line. The decomposition of an arbitrary four-vector is as follows:

$$A^\mu = A_+n^\mu_- + A_-n^\mu_+ + A^\mu_\perp, \tag{2}$$

where $A_\pm = n^\mu_\pm A_\mu$ are two light-cone projections. Note that the scalar product $(A^a(z')dz') = A^a_+(z'_-)dz'_-$ in the exponential in (1) and turns out to be zero in the Fock-Schwinger gauge $A^a_+(z'_-) = 0$. In this gauge, adopted further in this paper, the gauge link becomes trivial, $E(0,z) = 1$, and the expression for the meson bilocal current (1) simplifies.

The meson-to-vacuum transition matrix element at $z^2 = 0$ [9] is of our interest:

$$\langle 0|Q^*(0)\,q(z)|M(v)\rangle = f_M\left\{\tilde\varphi_+(t) + [\tilde\varphi_-(t) - \tilde\varphi_+(t)]\,\frac{\hat z}{2t}\right\}U(v), \tag{3}$$

where f_M is a constant with the dimension of a mass, $t = (vz)$ is the time in the heavy-meson rest frame, where the meson four-velocity is $v^\mu = (1,0,0,0)$, the bispinor $U(v)$ is the non-relativistic wave-function of the "spinor-like" meson, and $\tilde\varphi_\pm(t)$ are the distribution amplitudes

(DAs) of the heavy meson. The Fourier transforms of DAs are usually required in constructing matrix elements of heavy meson decays:

$$\tilde{\varphi}_{\pm}(t) = \int_0^\infty d\omega\, \mathrm{e}^{-i\omega t} \phi_{\pm}(\omega). \tag{4}$$

In performing calculations, it is convenient to introduce the projection operator onto the $B^{(*)}$-meson state. Note that the heavy B- and B^*-mesons are degenerate in this approach. The B-meson-to-vacuum transition matrix element at $z^2 = 0$ in the real world after the heavy-quark spin is taken into account can be written in the form [9, 11]:

$$\langle 0|\bar{q}_\alpha(z)\, h_{v,\beta}(0)|\bar{B}^{(*)}(v)\rangle = \eta_{B^{(*)}} \frac{i f_{B^{(*)}} m_{B^{(*)}}}{4} \left[(1+\hat{v}) \left\{ \tilde{\varphi}_+^B(t) - \left[\tilde{\varphi}_+^B(t) - \tilde{\varphi}_-^B(t)\right] \frac{\hat{z}}{2t} \right\} \gamma_5(\hat{\varepsilon}) \right]_{\beta\alpha}, \tag{5}$$

where ε^μ is the polarization vector of the B^*-meson, $\eta_B = -1$ for the B-meson and $\eta_{B^*} = 1$ for the B^*-meson. The HQS gives the relations $f_{B^*} = f_B$ and $\tilde{\varphi}_\pm^{B^*}(t) = \tilde{\varphi}_\pm^B(t)$.

The projection operator onto the three-particle state can be also determined through the B-meson-to-vacuum transition matrix element at $z^2 = 0$ both for the "spinor-like" meson and after the spin of the heavy quark is switched on. For this matrix element one needs to introduce four distribution amplitudes [12]: $\tilde{\Psi}_A^B(t,u)$, $\tilde{\Psi}_V^B(t,u)$, $\tilde{X}_A^B(t,u)$, and $\tilde{Y}_A^B(t,u)$. The corresponding projection operator $\langle 0|\bar{q}_\alpha(z)\, G_{\lambda\rho}(uz)\, h_{v,\beta}(0)|\bar{B}(v)\rangle$ was also worked out and can be found in [13]: A similar projection operator for B^*-meson-to-vacuum transition matrix element at $z^2 = 0$ can be easily obtained from the above one after making the replacement $\gamma_5 \to \hat{\varepsilon}^*$ as in (5).

Equations of motion (EoM) for heavy and light quarks which are assumed to be on the mass shell result into relations among the B-meson DAs [12]:

$$\phi_+^B(\omega) + \omega \frac{d\phi_-^B(\omega)}{d\omega} = I(\omega), \quad \left(\omega - 2\bar{\Lambda}\right) \phi_+^B(\omega) + \omega\, \phi_-^B(\omega) = J(\omega), \tag{6}$$

where $I(\omega)$ and $J(\omega)$ are determined by the three-particle quark-antiquark-gluon DAs [12]. The Wandzura-Wilczek [9] relation follows from the first equation in (6) when $I(\omega) = 0$:

$$\phi_-^B(\omega) = \int_\omega^\infty \frac{\phi_+^B(\omega')}{\omega'}\, d\omega'. \tag{7}$$

The basic property of the B-meson DAs is their scale dependence and one needs to know corresponding evolution equations. For the leading B-meson DA, this equation was worked out by B. Lange and M. Neubert [14]:

$$\frac{d\phi_+^B(\omega;\mu)}{d\ln\mu} = -\frac{\alpha_{\rm st}(\mu)\, C_F}{\pi} \int_0^\infty d\omega'\, \gamma^{\rm LN}(\omega,\omega';\mu)\, \phi_+^B(\omega';\mu), \tag{8}$$

where $C_F = 4/3$. The Lange-Neubert anomalous dimension is as follows [14]:

$$\gamma^{\rm LN}(\omega,\omega';\mu) = \left(\ln\frac{\mu}{\omega} - \frac{5}{4}\right) \delta(\omega-\omega') - \Gamma_{\rm LN}(\omega',\omega), \tag{9}$$

$$\Gamma_{\rm LN}(\omega',\omega) = \left[\frac{\omega}{\omega'} \frac{\Theta(\omega'-\omega)}{\omega'-\omega} + \frac{\Theta(\omega-\omega')}{\omega-\omega'}\right]_\oplus. \tag{10}$$

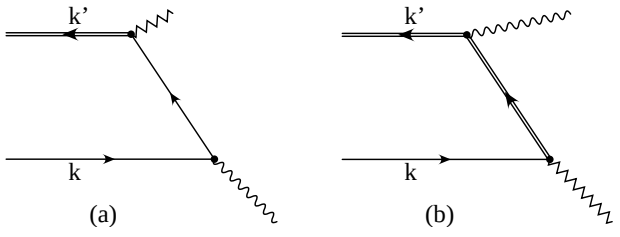


Figure 2: The $B^+ \to \ell^+ \nu_\ell \gamma$ decay amplitudes in the leading order in perturbation theory.

Here, the $\oplus$-convention is introduced:

$$\int_0^\infty d\omega' f(\omega') \left[\gamma(\omega', \omega)\right]_\oplus = \int_0^\infty d\omega' \left[f(\omega') - f(\omega)\right] \gamma(\omega', \omega). \tag{11}$$

It was also shown in [14] that the Lange-Neubert kernel factorizes in the space of moments:

$$\tilde{\Gamma}_{\rm LN}(N) = \int_0^\infty d\omega \left(\frac{\omega}{\omega'}\right)^{N-1} \Gamma_{\rm LN}(\omega', \omega) = -\Psi(N) - \Psi(-N) - 2\gamma_{\rm E}, \tag{12}$$

where $\gamma_{\rm E} = 0.577216$ is the Euler's constant and $\Psi(x) = \Gamma'(x)/\Gamma(x)$ is the digamma function. The analytic solution of the evolution equation can be written in the integral form as follows:

$$\phi_+^B(\omega;\mu) = \frac{1}{2\pi} \int_{-\infty}^{+\infty} dt\, \varphi_0(t)\, f(\omega, \mu, \mu_0, it). \tag{13}$$

It depends on the function $f(\omega, \mu, \mu_0, it)$ which can be calculated in the perturbation theory. The other function $\varphi_0(t)$ is arbitrary and fixed by the condition $\varphi_0(0) = \lambda_B^{-1}$ only. The shape of $\varphi_0(t)$ can be determined after a model for $\phi_+^B(\omega;\mu)$ is specified.

3 Applications of B-meson DAs

The B-meson distribution amplitudes, usually in the form of inverse moments, are entering the exclusive decay amplitudes of B-mesons. In this section some processes where the distribution amplitudes are important, are presented and briefly discussed.

3.1 $B^+ \to \ell^+ \nu_\ell \gamma$ Decay

Let us start the discussion with one of the most clean B-meson decay modes — the radiative leptonic $B^+ \to \ell^+ \nu_\ell \gamma$ decay. In the leading order in the perturbation theory, the decay amplitude is presented by two Feynman diagrams shown in Fig. 2 and can be written as follows:

$$\mathcal{M} = \frac{4G_F}{\sqrt{2}} V_{ub}^* \left\langle \gamma(p,\epsilon) \left| \bar{b}\gamma_\mu (1-\gamma_5)\, u \right| B^+(v) \right\rangle \left[\bar{u}(q_\ell)\gamma^\mu (1-\gamma_5)\, u(q_\nu)\right]. \tag{14}$$

The $B^+ \to \gamma$ transition matrix element entering this amplitude can be parameterized by two

form factors $F_V(E_\gamma)$ and $F_A(E_\gamma)$ [15]:

$$\begin{aligned}&\left\langle \gamma(p,\epsilon)\left|\bar{b}(0)\gamma^\mu\left(1-\gamma_5\right)u(0)\right|B^+(v)\right\rangle \\ &=\sqrt{4\pi\alpha}\left\{\varepsilon^{\mu\rho\sigma\tau}v_\rho p_\sigma\epsilon^*_\tau F_V(E_\gamma)-i\left[(vp)\epsilon^{*\mu}-(v\epsilon^*)p^\mu\right]F_A(E_\gamma)\right\},\end{aligned} \tag{15}$$

where $E_\gamma=(vp)=m_B\left(1-q^2/m_B^2\right)/2$ is the photon energy. The kinematical region of the process is determined by the condition $E_\gamma\gg\Lambda_{\rm QCD}$, with $\Lambda_{\rm QCD}$ being the QCD parameter, where perturbative QCD methods for exclusive processes can be applied.

It was demonstrated that in this order the factorization approach is applicable and the most convenient tool for the QCD factorization implementation is the Soft-Collinear Effective Theory (SCET) [16, 17, 18]. We are not going to discuss this theory in details but give the following references [19, 20], where a detail discussion of this theory can be found.

The differential width of the $B^+\to\ell^+\nu_\ell\gamma$ decay calculated within the SCET can be written in the form [21]:

$$\frac{d\Gamma}{dE_\gamma}=\frac{\alpha G_F^2 f_B^2|V_{ub}|^2m_B^4}{54\pi^2}\left(C_3^{\rm SCET}\right)^2\frac{x_\gamma\left(1-x_\gamma\right)}{\Lambda_B^2(E_\gamma)}, \tag{16}$$

where $x_\gamma=2E_\gamma/m_B$ is the reduced photon energy. The coefficient $C_3^{\rm SCET}$ results after matching QCD and SCET operators at the hard scale $\mu_F=m_B$:

$$C_3^{\rm SCET}=1+\frac{\alpha_s(m_B)C_F}{4\pi}\left[-2\log^2x_\gamma-2\,{\rm Li}_2(1-x_\gamma)+\frac{3x_\gamma-2}{x_\gamma-1}\log x_\gamma-6-\frac{\pi^2}{12}\right]. \tag{17}$$

The differential decay width (16) depends on non-perturbative parameters — the first inverse moment of the leading DA $\phi_+^B(k_+;\mu_F)$ and its logarithmic extensions in the form [21]:

$$\Lambda_B^{-1}(E_\gamma)=e^{-S(E_\gamma;\mu_F)}\int\frac{dk_+}{k_+}\,\phi_+^B(k_+;\mu_F)\left\{1+\frac{\alpha_sC_F}{4\pi}\left[\log^2\frac{2E_\gamma k_+}{\mu_F^2}-\frac{\pi^2}{12}-1\right]\right\}. \tag{18}$$

Here, the exponential factor $e^{-S(E_\gamma;\mu_F)}$ appears after resummation of large Sudakov logarithms. It should be noted that power corrections of order of $\mathcal{O}(1/m_B,1/(2E_\gamma))$ to the decay rate are also calculated recently [22].

The $B^+\to\ell^+\nu_\ell\gamma$ decay was a subject of intensive experimental searches on the B-factories at SLAC and KEK. In particular, the experimental analysis for the partial branching fraction in the photon-energy interval $E_\gamma^{\rm sig}=[1\ {\rm GeV},m_B/2]$ with the full dataset of $(771.6\pm10.6)\times10^6\ B\bar{B}$ pairs has been reported by the Belle collaboration recently [23]. The upper limits (@ 90% C. L.) presented are as follows: $\mathcal{B}(B^+\to e^+\nu_e\gamma)<6.1\times10^{-6}$, $\mathcal{B}(B^+\to\mu^+\nu_\mu\gamma)<3.4\times10^{-6}$, and $\mathcal{B}(B^+\to\ell^+\nu_\ell\gamma)<3.5\times10^{-6}$. The last one was translated into the restriction on the first inverse moment [23]:

$$\lambda_B=\left[\int_0^\infty\frac{dk_+}{k_+}\,\phi_+^B(k_+)\right]^{-1}>238\ {\rm MeV}. \tag{19}$$

This result is in good agreement with the theoretical estimates being within the interval []: 300 MeV $<\lambda_B<$ 600 MeV.

The related topic is the shape of the $B^+\to\gamma$ form factors entering the transition matrix element (15). Both the vector and axial-vector form factors with account of the soft contribution are known [24]. Neglecting radiative and $1/m_B$ corrections, the form factors are equal $F_V^{(0)}=$

$F_A^{(0)} = F_{B\to\gamma^*}^{(0)}$. The corresponding soft contribution is estimated by the LCSRs method [24]:

$$F_{B\to\gamma^*}^{(0)}(E_\gamma) = \frac{Q_u f_B m_B}{2E_\gamma \lambda_B(\mu)} + \frac{Q_u f_B m_B}{2E_\gamma}\int_0^{\omega_0} d\omega \left[\frac{2E_\gamma}{m_\rho^2}\, e^{-(2E_\gamma\omega - m_\rho^2)/M^2} - \frac{1}{\omega}\right]\phi_+^B(\omega,\mu), \quad (20)$$

where $Q_u = 2/3$ is the electric charge of the u-quark, M is the Borel parameter, and $m_\rho \simeq 775$ MeV is the ρ-meson mass [8]. Note that the isospin symmetry is implicitly assumed which means that the difference between the ρ- and ω-mesons is neglected. The soft part of the form factor (the second term in (20)) is also dependent on the other non-perturbative parameter — the effective threshold $s_0 = 1.2$ GeV, where $\omega_0 = s_0/(2E_\gamma)$. It was also demonstrated that a choice of a model for the B-meson DA influences a result for the form factor but this dependence is not substantial.

3.2 $B_q \to \gamma\gamma$ and $B_q \to \ell^+\ell^-\gamma$ Decays

The interesting problem within the SCET is the universality of non-perturbative effects in leptonic and radiative B-meson decays. Let us start with the radiative $B_q \to \gamma\gamma$ decay, where $q = d$ or s, the decay width of which can be written as follows [25]:

$$\Gamma = \frac{\alpha^2 G_F^2 f_B^2 m_B^5}{144\pi^3}\,|V_{tq}V_{tb}^*|^2\left|C_7^{\rm eff} C_9^{\rm SCET}\right|^2 \frac{1}{\Lambda_B^2(m_B/2)}. \quad (21)$$

Similar processes are the ones where one of the photons is virtual and decaying into the lepton pair. The differential decay width of $B_q \to \ell^+\ell^-\gamma$, where $\ell = e$, μ, has the form [25]:

$$\frac{d\Gamma}{dE_\gamma} = \frac{\alpha^3 G_F^2 f_B^2 m_B^4}{1728\pi^4}\,|V_{tq}V_{tb}^*|^2 \frac{x_\gamma(1-x_\gamma)}{\Lambda_B^2(E_\gamma)}\left[\left|C_9^{\rm eff} C_3^{\rm SCET} + \frac{2C_7^{\rm eff}}{1-x_\gamma}\, C_9^{\rm SCET}\right|^2 + \left|C_{10} C_3^{\rm SCET}\right|^2\right], \quad (22)$$

where $x_\gamma = 2E_\gamma/m_B$. The coefficient $C_3^{\rm SCET}$ (17) determines the differential width of the $B^+ \to \ell^+\nu_\ell\gamma$ decay while the decays considered above are dependent on the other coefficient $C_9^{\rm SCET}$ which also results after perturbative matching of QCD and SCET operators at the scale $\mu_F = m_B$:

$$C_9^{\rm SCET} = 1 + \frac{\alpha_s(m_B)C_F}{4\pi}\left[\log\frac{m_B^2}{\mu_R} - 2\log^2 x_\gamma + 2\log x_\gamma - 2\,{\rm Li}_2(1-x_\gamma) - 6 - \frac{\pi^2}{12}\right]. \quad (23)$$

These examples explicitly show the necessity to know two coefficients $C_3^{\rm SCET}$ and $C_9^{\rm SCET}$ only for performing theoretical analysis of the radiative and leptonic radiative B-mesons decays. As for the B-meson DAs, all three decays considered are dependent on $\Lambda_B^{-1}(\mu)$ (18) and this quantity can be independently determined from the analysis of each decay. This can be a good universality test of the soft contribution determined by the B-meson dynamics.

3.3 $B^+ \to \pi^+\ell^+\ell^-$ Decays

The other good example of the B-meson decays which are sensitive to the B-meson distribution amplitudes are rare semileptonic decays like the $B^+ \to P\,\ell^+\ell^-$ decay, where $P = \pi$, K, $\eta^{(\prime)}$ and $\ell = e$, μ. In this lecture some details of the $B^+ \to \pi^+\ell^+\ell^-$ decay are presented.

Detailed perturbative analysis in full kinematical region of q^2, the lepton-pair invariant mass squared, was undertaken in [26]. The differential branching fraction is as follows:

$$\frac{d\text{Br}\,(B^+\to\pi^+\ell^+\ell^-)}{dq^2}=\frac{G_F^2\alpha_{\rm em}^2\tau_B}{1024\pi^5 m_B^3}|V_{tb}V_{td}^*|^2\sqrt{\lambda(q^2)}\sqrt{1-\frac{4m_\ell^2}{q^2}}F(q^2). \tag{24}$$

This expression contains the dynamical function:

$$\begin{aligned}F(q^2) &= \frac{2}{3}\,\lambda(q^2)\left(1+\frac{2m_\ell^2}{q^2}\right)\left|C_9^{\rm eff}f_+(q^2)+\frac{2m_b}{m_B+m_\pi}\,C_7^{\rm eff}f_T(q^2)\right|^2 \\ &+ \frac{2}{3}\,\lambda(q^2)\left(1-\frac{4m_\ell^2}{q^2}\right)\left|C_{10}^{\rm eff}\right|^2 f_+^2(q^2)+\frac{4m_\ell^2}{q^2}\left(m_B^2-m_\pi^2\right)^2\left|C_{10}^{\rm eff}\right|^2 f_0^2(q^2),\end{aligned} \tag{25}$$

where $C_i^{\rm eff}$ are the effective Wilson coefficients which are specific combinations of Wilson coefficients entering the effective weak $b\to d$ Hamiltonian:

$$\mathcal{H}_{\rm eff}^{(b\to d)}=-\frac{4G_F}{\sqrt{2}}\left[V_{tb}^*V_{td}\sum_{i=1}^{10}C_i(\mu)\mathcal{O}_i(\mu)+V_{ub}^*V_{ud}\sum_{i=1}^{2}C_i(\mu)\Big(\mathcal{O}_i(\mu)-\mathcal{O}_i^{(u)}(\mu)\Big)\right]+\text{h. c.} \tag{26}$$

Here, G_F is the Fermi constant, $C_i(\mu)$ are Wilson coefficients, $\mathcal{O}_i(\mu)$ are the dimension-six operators, and V_{ij} are Cabibbo-Kobayashi-Maskawa (CKM) matrix elements. One can easily recognize that the products $V_{tb}^*V_{td}\sim V_{ub}^*V_{ud}\sim\lambda^3$ are of the same order in $\lambda=\sin\theta_C$, where θ_C is the Cabibbo angle.

The dynamical function (25) is depended on three form factors $f_+(q^2)$, $f_0(q^2)$, and $f_T(q^2)$ which are non-perturbative scalar functions of the momentum transfered squared. They are entering the vector and tensor $B\to\pi$ transition matrix elements. The Heavy-Quark Symmetry (HQS) is applicable in the large-recoil limit (small q^2-values) and relates these form factors [11]:

$$\begin{aligned}f_0(q^2) &= \left(\frac{m_B^2+m_\pi^2-q^2}{m_B^2}\right)\left[\left\{1+\frac{\alpha_s(\mu)C_F}{4\pi}\left(2-2L(q^2)\right)\right\}f_+(q^2)\right. \\ &+ \left.\frac{\alpha_s(\mu)C_F}{4\pi}\frac{m_B^2(q^2-m_\pi^2)}{(m_B^2+m_\pi^2-q^2)^2}\Delta F_\pi\right],\end{aligned} \tag{27}$$

$$\begin{aligned}f_T(q^2) &= \left(\frac{m_B+m_\pi}{m_B}\right)\left[\left(1+\frac{\alpha_s(\mu)C_F}{4\pi}\left(\ln\frac{m_b^2}{\mu^2}+2L(q^2)\right)\right)f_+(q^2)\right. \\ &- \left.\frac{\alpha_s(\mu)C_F}{4\pi}\frac{m_B^2}{m_B^2+m_\pi^2-q^2}\Delta F_\pi\right],\end{aligned} \tag{28}$$

where for simplicity the following quantities are introduced:

$$L(q^2)=\left(1+\frac{m_B^2}{m_\pi^2-q^2}\right)\ln\left(1+\frac{m_\pi^2-q^2}{m_B^2}\right),\qquad \Delta F_\pi=\frac{8\pi^2 f_B f_\pi}{N_c m_B\lambda_B}\left\langle\bar u^{-1}\right\rangle_\pi. \tag{29}$$

The last quantity ΔF_π contains the first inverse moments of π- and B-meson:

$$\left\langle\bar u^{-1}\right\rangle_\pi=\int du\frac{\phi_\pi(u)}{1-u},\qquad \lambda_B^{-1}\equiv\left\langle\bar\omega^{-1}\right\rangle_+=\int d\omega\frac{\phi_+^B(\omega)}{\omega}. \tag{30}$$

Only one form factor $f_+(q^2)$ is required for getting the q^2-distribution in this decay which can be fitted from the data on the $B \to \pi\ell^+\nu_\ell$ decays [26].

Within the factorization approach, it is also possible to calculate some types of power-suppressed corrections in the $B \to \pi\ell^+\ell^-$ decay, in particular, the annihilation contributions. This type of corrections contains the q^2-dependent first inverse moment of the sub-leading B-meson LCDA:

$$\lambda_{B,-}^{-1}(q^2) = \int_0^\infty \frac{\phi_-^B(\omega)\, d\omega}{\omega - q^2/M_B - i\epsilon}. \tag{31}$$

Note the specific feature of this moment: it is logarithmically divergent at $q^2 \to 0$ because the sub-leading LCDA $\phi_-^B(\omega)$ turns out to be constant at small ω, $\phi_-^B(\omega)|_{\omega\to 0} \sim \text{const}$. Nevertheless, such a fiture does not result a problem in the numerical analysis of the differential branching fraction as the kinematical lower cut $q^2 \geq 4m_\ell^2$ exists in the semileptonic $B \to \pi\ell^+\ell^-$ decay. Annihilation contributions of a similar type enter also in decay amplitudes of similar semileptonic $B \to V_\parallel \ell^+\ell^-$ decays, where $V_\parallel$ is the longitudinally polarized light vector meson [27]. Decays with a transversely polarized vector meson in the final state are dependent on $\phi_+^B(\omega)$ to the leading order. In the limit $q^2 = 0$, the corresponding branching fraction is finite and can be related with the branching ratios of rare radiative $B \to V\gamma$ decays.

3.4 Models for the B-Meson Distribution Amplitudes

The distribution amplitudes are non-perturbative quantities and usual perturbative methods of QFT [10] are inapplicable. The commonly used method of their calculation is the QCD Sum Rules [9, 28]. To combine these distribution amplitudes with hard kernels in amplitudes of physical processes, one needs to model them by some analytical expressions called the distribution amplitude models. At present, several models for the distribution amplitudes have been suggested. Two simplest ones are the exponential models [9]:

$$\phi_B^+(\omega) = \frac{\omega}{\omega_0^2}\, e^{-\omega/\omega_0}, \qquad \phi_B^-(\omega) = \frac{1}{\omega_0}\, e^{-\omega/\omega_0}, \tag{32}$$

where $\omega_0 = 2\bar{\Lambda}/3$, which appeared to be the most popular in physical applications, and the light-meson-like models [12]:

$$\phi_B^+(\omega) = \frac{\omega}{2\bar{\Lambda}^2}\, \theta(2\bar{\Lambda} - \omega), \qquad \phi_B^-(\omega) = \frac{2\bar{\Lambda} - \omega}{2\bar{\Lambda}^2}\, \theta(2\bar{\Lambda} - \omega), \tag{33}$$

which is also simple and explicitly based on the light-meson distribution amplitude. The energy dependence of these distribution amplitudes is presented in Fig. 3.

More involved models are the two-parametric model by Braun, Ivanov, and Korchemsky (BIK) [28] and improved exponential model by Lee and Neubert [29]. The later one matches the exponential behavior at low momenta of light quark and QCD-based behavior (the radiative tail) at large momenta. For these models the leading distribution amplitude only was studied while the non-leading amplitude was skipped.

As mentioned above, one needs moments of these amplitudes in getting decay widths of heavy mesons. Among moments, first inverse ones are of special interest. The uncertainty induced by a choice of the distribution amplitude model of the heavy meson on the semileptonic decay rates of B-mesons is also interesting to study which is not yet been worked out.

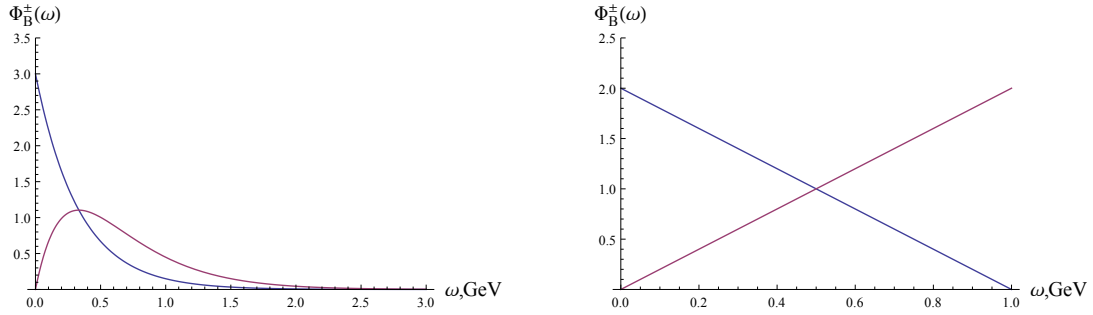


Figure 3: The energy dependence of of both leading and non-leading distribution amplitude models where the exponential ones are presented on the left panel and the light-meson-like models are on the right panel.

4 Light-Cone Distribution Amplitudes of Heavy Baryons

Light-cone distribution amplitudes (LCDAs) of heavy baryons are the transition matrix elements from the baryonic state to vacuum of non-local light-ray operators built off an effective heavy quark and two light quarks. The content of such operators supports a similarity in the construction of the heavy-baryon LCDAs to both the B-meson (within the HQET) [9, 28] and the nucleon (within QCD) [30, 31] LCDAs descriptions. An important simplifying feature of the operators containing one or more heavy quarks is an existence of the Heavy Quark Symmetry (HQS) which results into the decoupling of the heavy-quark spin from the system dynamics in the limit $m_Q \to \infty$, where m_Q is the heavy-quark mass. So, to understand the properties of heavy baryons in this limit, it is enough to switch off the heavy-quark spin and to introduce a total set of two-particle LCDAs corresponding to the light-quark system, called diquark, which quantum numbers completely determine a number of LCDAs and their asymptotic behavior.

In this simplified picture, there are the $SU(3)_F$ antitriplet of "scalar baryons" with the $J^P = 0^+$ spin-parity determined by the diquark spin-parity $j^p = 0^+$ and the $SU(3)_F$ sextet of "axial-vector baryons" with the $J^P = 1^+$ spin-parity which follows from the diquark spin-parity $j^p = 1^+$. It is reasonable to start with the description of the "scalar baryons" and then to generalize the procedure on the "axial-vector baryons". The changes originated by an account of the heavy-quark spin can be done after the total sets of the non-local operators and corresponding LCDAs are introduced in the decoupling limit. All these steps are discussed briefly in this section.

4.1 "Scalar Baryons"

The "scalar baryons" are combined into the $SU(3)_F$ antitriplet with $J^P = 0^+$ in which the light diquark states are also the scalar states with $j^p = 0^+$.

The set of the LCDAs is determined by the matrix elements between the baryonic state and

vacuum of the four independent non-local light-ray operators [32, 33, 34]:

$$\begin{aligned}
\epsilon^{abc}\langle 0|\left(q_1^a(t_1n)C\gamma_5\hat{n}q_2^b(t_2n)\right)h_v^c(0)|H(v)\rangle &= f_H^{(2)}\,\Psi_2(t_1,t_2), \\
\epsilon^{abc}\langle 0|\left(q_1^a(t_1n)C\gamma_5 q_2^b(t_2n)\right)h_v^c(0)|H(v)\rangle &= f_H^{(1)}\,\Psi_3^s(t_1,t_2), \\
\epsilon^{abc}\langle 0|\left(q_1^a(t_1n)C\gamma_5 i\sigma_{\bar{n}n}q_2^b(t_2n)\right)h_v^c(0)|H(v)\rangle &= 2f_H^{(1)}\,\Psi_3^\sigma(t_1,t_2), \\
\epsilon^{abc}\langle 0|\left(q_1^a(t_1n)C\gamma_5\hat{\bar{n}}q_2^b(t_2n)\right)h_v^c(0)|H(v)\rangle &= f_H^{(2)}\Psi_4(t_1,t_2),
\end{aligned} \tag{34}$$

where $q_i(x) = u(x)$, $d(x)$, $s(x)$ are the light-quark fields, $h_v(0)$ is the static heavy-quark field situated at the origin of the position-space frame, C is the charge conjugation matrix, n^μ and $\bar{n}^\mu$ are two light-like vectors normalized by the condition $(n\bar{n}) = 2$[1], and $\sigma_{\bar{n}n} = i\left(\hat{\bar{n}}\hat{n} - \hat{n}\hat{\bar{n}}\right)/2$. In addition, the frame is adopted where the heavy-meson velocity is related to the light-like vectors as follows: $v^\mu = (n^\mu + \bar{n}^\mu)/2$. The light-quark fields on the light cone are assumed to be multiplied by the Wilson lines:

$$q(tn) = [0,tn]\,q(tn) = \mathrm{P}\exp\left\{-ig_{\mathrm{st}}t\int_0^1 d\alpha n^\mu\,A_\mu(\alpha tn)\right\}q(tn) = \sum_{N=0}^{\infty}\frac{t^N}{N!}\,(n^\mu D_\mu)^N\,q(0),$$

where the following definition of the covariant derivative $D_\mu = \partial_\mu - ig_{\mathrm{st}}A_\mu$ is accepted. The static heavy-quark field living on the light cone also includes the Wilson line but of the other type with the time-like link [35]:

$$h_v(0) = \mathrm{P}\exp\left\{ig_{\mathrm{st}}\int_{-\infty}^0 d\alpha v^\mu\,A_\mu(\alpha v)\right\}\phi(-\infty),$$

with which it is connected with the sterile field $\phi(-\infty)$.

The couplings $f_H^{(i)}$ introduced in Eqs. (34) to make the LCDAs dimensionless are defined by local operators [36, 37, 38, 39]:

$$\begin{aligned}
\epsilon^{abc}\langle 0|\left(q_1^a(0)C\gamma_5 q_2^b(0)\right)h_v^c(0)|H(v)\rangle &= f_H^{(1)}, \\
\epsilon^{abc}\langle 0|\left(q_1^a(0)C\gamma_5\hat{v}q_2^b(0)\right)h_v^c(0)|H(v)\rangle &= f_H^{(2)}.
\end{aligned}$$

The scale dependences of these couplings are governed by the anomalous dimensions $\gamma^{(i)}$ of local operators as follows:

$$\frac{d\ln f_H^{(i)}(\mu)}{d\ln\mu} \equiv -\gamma^{(i)} = -\sum_k \gamma_k^{(i)}\,a^k(\mu), \qquad a(\mu) \equiv \frac{\alpha_s^{\overline{\mathrm{MS}}}(\mu)}{4\pi},$$

where the strong coupling is determined in the $\overline{\mathrm{MS}}$-scheme. This equation can be solved order by order in the $a(\mu)$-power expansion and in the NLO order, one can use the following formula:

$$f_H^{(i)}(\mu) = f_H^{(i)}(\mu_0)\left(\frac{\alpha_s(\mu)}{\alpha_s(\mu_0)}\right)^{\gamma_1^{(i)}/\beta_0}\left[1 - \frac{\alpha_s(\mu_0)-\alpha_s(\mu)}{4\pi}\,\frac{\gamma_1^{(i)}}{\beta_0}\left(\frac{\gamma_2^{(i)}}{\gamma_1^{(i)}} - \frac{\beta_1}{\beta_0}\right)\right],$$

where $\beta_{0,1}$ are the first two coefficient in the perturbative expansion of the β-function. As the evolution to the required scale can be easily done now, one needs to know numerical values of

[1]The definitions of n^μ and $\bar{n}^\mu$ differ by the factor $1/\sqrt{2}$ from the ones used in the previous section.

the couplings $f_H^{(i)}(\mu)$ at some representative scale μ_0, say $\mu_0 = 1$ GeV. As this scale is rather low to use the perturbation theory, non-perturbative techniques are necessary to calculate the value. In particular, the QCD sum rules method in NLO for the Λ_b-baryon results [39]:

$$f_{\Lambda_b}^{(1)}(\mu_0 = 1 \text{ GeV}) \simeq f_{\Lambda_b}^{(2)}(\mu_0 = 1 \text{ GeV}) \simeq 0.030 \pm 0.005 \text{ GeV}^3.$$

Non-relativistic constituent-quark picture of heavy baryons H suggests that $f_H^{(2)} \simeq f_H^{(1)}$ at low scales of order 1 GeV, and this expectation is supported by numerous QCD sum rule calculations [37, 36, 38, 39]. These couplings $f_H^{(i)}(\mu)$ cannot coincide at all scales because of different anomalous dimensions $\gamma^{(i)}$ of local operators.

Similar to the couplings $f_H^{(i)}(\mu)$, the LCDAs $\Psi_i(t_1, t_2)$ introduced in Eq. (34) are also scale-dependent functions. To find their scale evolution, it is convenient to make their Fourier transform to the momentum space:

$$\Psi(t_1, t_2) = \int_0^\infty d\omega_1 \int_0^\infty d\omega_2 \, e^{-it_1\omega_1 - it_2\omega_2} \psi(\omega_1, \omega_2) = \int_0^\infty \omega \, d\omega \int_0^1 du \, e^{-i\omega(t_1 u + t_2 \bar{u})} \, \widetilde{\psi}(\omega, u),$$

where $\bar{u} = 1 - u$. In the first representation $\omega_1 = u\omega$ and $\omega_2 = (1-u)\,\omega = \bar{u}\omega$ are the energies of the light quarks q_1 and q_2. The leading-order evolution equation for $\psi_2(\omega_1, \omega_2; \mu)$ can be derived by identifying the ultra-violet singularities of the one-gluon-exchange diagrams [32]. The evolution equation in the leading order is expressed in terms of two-particle kernels:

$$\mu \frac{d}{d\mu} \, \psi_2(\omega_1, \omega_2; \mu) = -\frac{\alpha_s(\mu)}{2\pi} \, \frac{4}{3} \left\{ \int_0^\infty d\omega_1' \, \gamma^{\rm LN}(\omega_1', \omega_1; \mu) \, \psi_2(\omega_1', \omega_2; \mu) \right.$$
$$\left. + \int_0^\infty d\omega_2' \, \gamma^{\rm LN}(\omega_2', \omega_2; \mu) \, \psi_2(\omega_1, \omega_2'; \mu) - \int_0^1 dv \, V(u, v) \, \psi_2(v\omega, \bar{v}\omega; \mu) + \frac{3}{2} \, \psi_2(\omega_1, \omega_2; \mu) \right\},$$

where the kernel $\gamma^{\rm LN}(\omega', \omega; \mu)$ controls the evolution of the B-meson LCDA [14] and $V(u, v)$ is the Efremov-Radyushkin-Brodsky-Lepage (ER-BL) kernel [40, 41]. The term $3\psi_2(\omega_1, \omega_2; \mu)/2$ results from the one-loop $f_H^{(2)}$ renormalization subtraction. The evolution equation above can be solved either numerically or semi-analytically [32, 34].

The next step in working out solutions of the heavy-baryon evolution equations analytically was undertaken in [42]. In particular, the eigenfunctions of the Lange-Neubert evolution kernel were found and used for a systematic implementation of the renormalization-group effects for both the B-meson and Λ_b-baryon wave-function evolutions. Based on these foundations, the new strategy to construct the LCDA models in accordance with the Wandzura-Wilczek-like relations was presented. As a possible extension of the above analysis in application to baryons, the classification of the non-local baryonic operators constructed from four particles (three quarks and a gluon) is required to work out equations involving explicitly the there-particle LCDAs and twist-four four-particle ones which should reduce to the Wandzura-Wilczek relations after four-particle LCDAs are neglected.

4.2 "Axial-Vector Baryons"

The "axial-vector baryons" are components of the $SU(3)_F$ sextet with $J^P = 1^+$ in which the light diquark states are the axial-vector states with $j^p = 1^+$. In a difference to the "scalar

baryons" case, one needs to consider the baryons with the longitudinal and transverse polarizations separately.

The set of the longitudinal LCDAs is determined by the matrix elements between the baryonic state with the appropriate polarization and vacuum of the four independent non-local light-ray operators [33, 34]:

$$\begin{aligned}
\epsilon^{abc}\langle 0|\left(q_1^a(t_1)C\,\hat{n}q_2^b(t_2)\right)h_v^c(0)|H(v,\varepsilon)\rangle &= (\bar{v}\varepsilon)\,f_H^{(2)}\,\Psi_2^{\parallel}(t_1,t_2)\\
\epsilon^{abc}\langle 0|\left(q_1^a(t_1)C\,q_2^b(t_2)\right)h_v^c(0)|H(v,\varepsilon)\rangle &= (\bar{v}\varepsilon)\,f_H^{(1)}\,\Psi_3^{\parallel s}(t_1,t_2)\\
\epsilon^{abc}\langle 0|\left(q_1^a(t_1)C\,i\sigma_{\bar{n}n}q_2^b(t_2)\right)h_v^c(0)|H(v,\varepsilon)\rangle &= 2\,(\bar{v}\varepsilon)\,f_H^{(1)}\,\Psi_3^{\parallel a}(t_1,t_2)\\
\epsilon^{abc}\langle 0|\left(q_1^a(t_1)C\,\hat{\bar{n}}q_2^b(t_2)\right)h_v^c(0)|H(v,\varepsilon)\rangle &= -\,(\bar{v}\varepsilon)\,f_H^{(2)}\,\Psi_4^{\parallel}(t_1,t_2)
\end{aligned}$$

where $\bar{v}^\mu = (\bar{n}^\mu - n^\mu)/2$ is the four-vector normalized as $(\bar{v}\bar{v}) = -1$ and orthogonal to the four-velocity $(v\bar{v}) = 0$. In the LCDA definitions above, the baryonic state is assumed to have a pure longitudinal polarization $\varepsilon_\parallel^\mu = \bar{v}^\mu$ and the prefactor on the r.h.s. is simply $(\bar{v}\varepsilon) = -1$.

The similar set of the transverse LCDAs is determined as follows [33, 34]:

$$\begin{aligned}
\epsilon^{abc}\langle 0|\left(q_1^a(t_1)C\,\gamma_\perp^\mu\hat{n}q_2^b(t_2)\right)h_v^c(0)|H(v,\varepsilon)\rangle &= f_H^{(2)}\,\Psi_2^{\perp}(t_1,t_2)\,\varepsilon_\perp^\mu\\
\epsilon^{abc}\langle 0|\left(q_1^a(t_1)C\,\gamma_\perp^\mu q_2^b(t_2)\right)h_v^c(0)|H(v,\varepsilon)\rangle &= f_H^{(1)}\,\Psi_3^{\perp s}(t_1,t_2)\,\varepsilon_\perp^\mu\\
\epsilon^{abc}\langle 0|\left(q_1^a(t_1)C\,\gamma_\perp^\mu i\sigma_{\bar{n}n}q_2^b(t_2)\right)h_v^c(0)|H(v,\varepsilon)\rangle &= 2f_H^{(1)}\,\Psi_3^{\perp a}(t_1,t_2)\,\varepsilon_\perp^\mu\\
\epsilon^{abc}\langle 0|\left(q_1^a(t_1)C\,\gamma_\perp^\mu\hat{\bar{n}}q_2^b(t_2)\right)h_v^c(0)|H(v,\varepsilon)\rangle &= f_H^{(2)}\,\Psi_4^{\perp}(t_1,t_2)\,\varepsilon_\perp^\mu
\end{aligned}$$

where $\gamma_\perp^\mu = \gamma^\mu - \left(\hat{\bar{n}}\hat{n} + \hat{n}\hat{\bar{n}}\right)/2$ and $\varepsilon_\perp^\mu = \varepsilon^\mu - \varepsilon_\parallel^\mu$ is the transverse polarization of the baryon.

4.3 Real Baryons

As far as all the sets of the LCDAs are determined, it necessary to generalize their definitions to real baryons which simply means that the spin of the heavy quark should be included into the baryon wave function. In other words, the r. h. s. of matrix elements of all non-local operators must be multiplied on the Dirac spinor $U(v)$ of the heavy quark h_v, satisfying the conditions: $\hat{v}\,U(v) = U(v)$ and $\overline{U}(v)\,U(v) = 1$. After these modifications, the "scalar baryons" transform to the baryons with the spin-parity $J^P = 1/2^+$ and the heavy-quark Dirac spinor $U(v)$ is nothing else but the heavy-baryon spinor $H(v)$, i. e. the spin of the heavy quark completely determines the spin structure of the heavy-baryon wave function. The case of "axial-vector baryons" is a little bit more complicated. It is well-known from quantum mechanics that the direct product of two angular momenta $j_1 = 1/2$ and $j_2 = 1$ is decomposed into two irreducible representations with the momenta $J_1 = 1/2$ and $J_2 = 3/2$. That is exactly the situation after the heavy-quark spin is switched on in the heavy baryon with the diquark in the axial-vector state $j^p = 1^+$:

$$\varepsilon_\mu\,U(v) = \left[\varepsilon_\mu\,U(v) - \frac{1}{3}\,(\gamma_\mu + v_\mu)\,\hat{\varepsilon}\,U(v)\right] + \frac{1}{3}\,(\gamma_\mu + v_\mu)\,\hat{\varepsilon}\,U(v) \equiv R_\mu^{3/2}(v) + \frac{1}{3}\,(\gamma_\mu + v_\mu)\,H(v).$$

As the result, there are two states with the spin-parities $J^P = 1/2^+$ and $J^P = 3/2^+$. The former one is described by the Dirac spinor $H(v)$ and for the $J^P = 3/2^+$ state the Rarita-Schwinger vector-spinor $R_\mu^{3/2}(v)$, which satisfies the relations $\hat{v}\,R_\mu^{3/2}(v) = R_\mu^{3/2}(v)$, $v^\mu\,R_\mu^{3/2}(v) = 0$, and $\gamma^\mu\,R_\mu^{3/2}(v) = 0$, is introduced.

4.4 QCD Sum Rules

In applications to a calculation of amplitudes with heavy baryons, one needs to know realistic models for LCDAs. Such models can be obtained by matching several few moments of LCDA models and the corresponding ones calculated by some non-perturbative methods, say by the QCD sum rules. The later method requires a calculation of a two-point correlator which involve the non-local light-ray operator and a suitable local current $J^{\Gamma'}(x)$. The general structure of the heavy-baryon local current can be chosen as follows:

$$\bar{J}^{\Gamma'}(x) = \epsilon^{abc} \left(\bar{q}_2^a(x) \left[A + B\,\hat{v}\right] \Gamma' C^T \bar{q}_1^b(x)\right) \bar{h}_v^c(x),$$

where A and B are two constants satisfying the constraint $A+B=1$ which accounts for an arbitrariness in the choice of a local current. The variation in $A \in [0,1]$ is adopted as a systematic error of numerical estimations. Note that the central value $A = B = 1/2$ corresponds to the constituent quark model picture [32]. The Dirac matrix Γ' is a suitable structure determined by the spin-parity of the baryon, in particular, $\Gamma' = \gamma_5$ for baryons from the $SU(3)_F$ antitriplet ($j^p = 0^+$) and $\Gamma' = \gamma_\parallel$, $\gamma_\perp$ for the $SU(3)_F$-sextet baryons with $j^p = 1^+$.

In calculations of the correlation functions, one tacitly assumes that baryons are bound states of quarks which are not free particles inside but couple by virtue of the gluonic field. So, light quark propagators $\tilde{S}_q(x)$, being very sensitive to the influence of the background gluonic field, should be modified accordingly while for the heavy quark this effect is sub-dominant and to leading order in the heavy-quark mass m_Q expansion can be neglected. To take effects of the QCD background inside baryons into account, the method of non-local condensates [43, 44, 45] is used. In this approach the light-quark propagator can be decomposed into two parts: the perturbative $S_q(x)$ and non-perturbative $\mathcal{C}_q(x)$ ones, and the later accumulates an information about the background inside the baryon in terms of non-local quark condensate $\langle \bar{q}(x) q(0) \rangle$.

To obtain the QCD sum rules, it is convenient to make the double Fourier transform of the correlation function:

$$\Pi_{\Gamma\Gamma'}(\omega_1, \omega_2; E) = i \int_{-\infty}^{\infty} \frac{dt_1\, dt_2}{(2\pi)^2}\, e^{i(\omega_1 t_1 + \omega_2 t_2)} \int d^4x\, e^{-iE(vx)}\, \langle 0 | \mathcal{O}^{\Gamma}(t_1, t_2)\, \bar{J}^{\Gamma'}(x) | 0 \rangle$$

As it is well-known from the QCD-SR analysis within the HQET, the heavy-quark condensate term is suppressed by $1/m_Q$ and absent in the Heavy-Quark Symmetry limit. So, the QCD Sum Rules can be read off after the phenomenological and perturbatively calculated considerations of the correlation function are equated based on the idea of the quark-hadron duality [46]:

$$|f_H|^2\, \psi^{\Gamma}(\omega, u)\, e^{-\bar{\Lambda}_H/\tau} = \mathbb{B}[\Pi](\omega, u; \tau, s_0),$$

where symbol $\mathbb{B}$ means the Borel-transform, $\bar{\Lambda}_H = m_H - m_Q$ is the effective baryon mass in the HQET, and s_0 is the momentum cutoff resulting from applying the quark-hadron duality. The explicit QCD-SRs for all the baryonic non-local operators can be found in [34].

The numerical values of first several moments of the bottom-baryon LCDAs estimated by the QCD-SRs are presented in [34]. These moments should be matched to the corresponding moments of the model functions for the LCDAs. The general presentation of the model functions for the b-baryon LCDAs is governed by their scale evolution and can be composed of the exponential part corresponding to the heavy-light interaction and the Gegenbauer polynomials to the light-light interaction. The order of the polynomials is determined by the twist of the

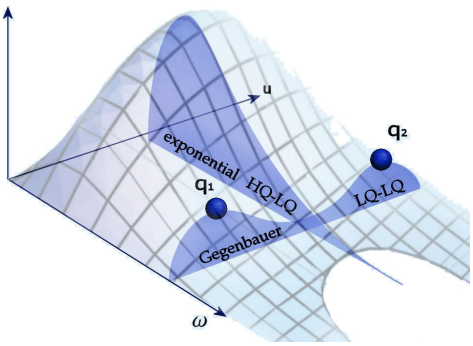


Figure 4: The general representation of the model functions for the heavy-baryon LCDAs with the ω-dependence specific for the B-meson LCDAs and the u-dependence in terms of an expansion in the Gegenbauer polynomials similar to the ones for the light mesons.

diquark system. Motivated by the analysis done for the Λ_b-baryon [32], the following simple models for the LCDAs have proposed [33, 34]:

$$\begin{aligned}
\tilde{\psi}_2(\omega,u) &= \omega^2 u(1-u)\sum_{n=0}^{2}\frac{a_n^{(2)}}{{\epsilon_n^{(2)}}^4}\,C_n^{3/2}(2u-1)\,\mathrm{e}^{-\omega/\epsilon_n^{(2)}},\\
\tilde{\psi}_{3s}(\omega,u) &= \frac{\omega}{2}\sum_{n=0}^{2}\frac{a_n^{(3)}}{{\epsilon_n^{(3)}}^3}\,C_n^{1/2}(2u-1)\,\mathrm{e}^{-\omega/\epsilon_n^{(3)}},\\
\tilde{\psi}_{3\sigma}(\omega,u) &= \frac{\omega}{2}\sum_{n=0}^{3}\frac{b_n^{(3)}}{{\eta_n^{(3)}}^3}\,C_n^{1/2}(2u-1)\,\mathrm{e}^{-\omega/\eta_n^{(3)}},\\
\tilde{\psi}_4(\omega,u) &= \sum_{n=0}^{2}\frac{a_n^{(4)}}{{\epsilon_n^{(4)}}^2}\,C_n^{1/2}(2u-1)\,\mathrm{e}^{-\omega/\epsilon_n^{(4)}}.
\end{aligned}$$

The qualitative behavior of the twist-2 LCDAs is presented in Fig. 4. The estimates of the parameters entering the theoretical models for the heavy-baryon LCDAs at the scale $\mu_0 = 1$ GeV can be found in [33, 34]. The $SU(3)_F$-symmetry breaking in LCDAs based on taking into account the s-quark difference from the u- and d-quarks is estimated to be approximately 15% [33, 34].

5 Conclusions

A brief introduction into the heavy hadron wave-functions is given in the present lecture. The discussion is started from the simplest hadronic system — the heavy meson which is the bound state of the light quark and the heavy antiquark. An example of such a system are the D- and B-mesons which are containing the heavy c- and b-antiquarks, respectively. In the HQET, the dynamics in the heavy mesons is mainly determined by a motion of the light quark while the heavy antiquark can be considered as a static source. In many cases, not all the light-quark

degrees of freedom are equally important and the dominant ones can be separated from the subdominant. Within this picture, it is possible to determine the so-called Light-Cone Distribution Amplitudes (LCDAs) of the heavy meson. Analysis shows that there are only two LCDAs in the lowest (two-particle) Fock decomposition and four more LCDAs in the three-particle heavy-meson state. The former two are mainly discussed in this lecture as well as their importance in calculations of branching fractions of radiative, leptonic and semileptonic B-meson decays. The last part is devoted to the bottom baryons which are the bound states of a heavy quark and two light ones. The total sets of the non-local light-ray operators for the ground-state heavy baryons with $J^P = 1/2^+$ and $J^P = 3/2^+$ are constructed in QCD in the heavy-quark limit. Matrix elements of these operators sandwiched between the heavy-baryon state and vacuum determine the LCDAs of different twist through the diquark current. Simple theoretical models for the LCDAs have been proposed and are briefly discussed. $SU(3)_F$ breaking effects result a correction of order 10%. Their application, for example, to transition matrix elements of heavy baryons is a good topic for future theoretical studies.

Acknowledgements

I would like to thank the organizers of the Helmholtz International Summer School for the invitation, skillful organization, and kind hospitality in Dubna. It is a pleasure to thank Ahmed Ali, Christian Hambrock, and Wei Wang for the collaboration on the topic of bottom baryons and Anna Kuznetsova for the help with the B-meson LCDA models. I acknowledge the support by the Russian Foundation for Basic Research (Project No. 15-02-06033-a).

References

[1] V. Khachatryan *et al.* [CMS and LHCb Collaborations], Nature **522**, 68 (2015) [arXiv:1411.4413].

[2] C. Bobeth *et al.*, Phys. Rev. Lett. **112**, 101801 (2014) [arXiv:1311.0903].

[3] R. Aaij *et al.* [LHCb Collaboration], JHEP **1212**, 125 (2012) [arXiv:1210.2645].

[4] R. Aaij *et al.* [LHCb Collaboration], JHEP **1510**, 034 (2015) [arXiv:1509.00414].

[5] A. V. Manohar and M. B. Wise, "Heavy quark physics," Camb. Monogr. Part. Phys. Nucl. Phys. Cosmol. **10**, 1 (2000).

[6] A. G. Grozin, "Heavy quark effective theory," Springer Tracts Mod. Phys. **201**, 1 (2004).

[7] T. Mannel, "Effective Field Theories in Flavor Physics," Springer Tracts Mod. Phys. **203**, 1 (2004).

[8] C. Patrignani *et al.* [Particle Data Group Collaboration], Chin. Phys. C **40**, 100001 (2016).

[9] A. G. Grozin and M. Neubert, Phys. Rev. **D55**, 272 (1997) [arXiv:hep-ph/9607366].

[10] M. E. Peskin and D. V. Schroeder, "An Introduction to quantum field theory," Reading, USA: Addison-Wesley (1995). 842 p.

[11] M. Beneke and T. Feldmann, Nucl. Phys. **B592**, 3 (2001) [arXiv:hep-ph/0008255].

[12] H. Kawamura, J. Kodaira, C. F. Qiao and K. Tanaka, Phys. Lett. **B523**, 111 (2001) [Erratum-ibid. **B536**, 344 (2002)] [arXiv:hep-ph/0109181].

[13] A. Khodjamirian, T. Mannel and N. Offen, Phys. Rev. **D75**, 054013 (2007) [arXiv:hep-ph/0611193]

[14] B. O. Lange and M. Neubert, Phys. Rev. Lett. **91** (2003) 102001 [arXiv:hep-ph/0303082].

[15] G. P. Korchemsky, D. Pirjol, and T. M. Yan, Phys. Rev. **D61**, 114510 (2000) [arXiv:hep-ph/9911427].

[16] C. W. Bauer, S. Fleming, D. Pirjol and I. W. Stewart, Phys. Rev. **D63**, 114020 (2001) [arXiv:hep-ph/0011336].

[17] C. W. Bauer, D. Pirjol and I. W. Stewart, Phys. Rev. **D65**, 054022 (2002) [arXiv:hep-ph/0109045].

[18] M. Beneke, A. P. Chapovsky, M. Diehl and T. Feldmann, Nucl. Phys. **B643**, 431 (2002) [arXiv:hep-ph/0206152].

[19] T. Becher, A. Broggio and A. Ferroglia, Lect. Notes Phys. **896**, pp. 1 (2015) [arXiv:1410.1892].

[20] A. Grozin, arXiv:1611.08828 (this Proceedings).

[21] S. Descotes-Genon and C. T. Sachrajda, Nucl. Phys. **B650**, 356 (2003) [arXiv:hep-ph/0209216].

[22] M. Beneke and J. Rohrwild, Eur. Phys. J. **C71**, 1818 (2011) [arXiv:1110.3228].

[23] A. Heller *et al.* [Belle Collaboration], Phys. Rev. **D91**, 112009 (2015) [arXiv:1504.05831].

[24] V. M. Braun and A. Khodjamirian, Phys. Lett. **B718**, 1014 (2013) [arXiv:1210.4453].

[25] S. Descotes-Genon and C. T. Sachrajda, Phys. Lett. **B557**, 213 (2003) [arXiv:hep-ph/0212162].

[26] A. Ali, A. Y. Parkhomenko, and A. V. Rusov, Phys. Rev. **D89**, 094021 (2014) [arXiv:1312.2523].

[27] M. Beneke, T. Feldmann and D. Seidel, Eur. Phys. J. C **41**, 173 (2005) doi:10.1140/epjc/s2005-02181-5 [hep-ph/0412400].

[28] V. M. Braun, D. Y. Ivanov and G. P. Korchemsky, Phys. Rev. **D69**, 034014 (2004) [arXiv:hep-ph/0309330].

[29] S. J. Lee and M. Neubert, Phys. Rev. D **72**, 094028 (2005) [arXiv:hep-ph/0509350].

[30] V. M. Braun, S. E. Derkachov, G. P. Korchemsky and A. N. Manashov, Nucl. Phys. **B553**, 355 (1999) [arXiv:hep-ph/9902375].

[31] V. Braun, R. J. Fries, N. Mahnke and E. Stein, Nucl. Phys. **B589**, 381 (2000) [Erratum-ibid. **B607**, 433 (2001)] [arXiv:hep-ph/0007279].

[32] P. Ball, V. M. Braun and E. Gardi, Phys. Lett. **B665**, 197 (2008) [arXiv:0804.2424].

[33] A. Ali, C. Hambrock, and A. Ya. Parkhomenko, Theor. Math. Phys. **170**, 2 (2012) [Teor. Mat. Fiz. **170**, 5 (2012)].

[34] A. Ali, C. Hambrock, A. Ya. Parkhomenko, and W. Wang, Eur. Phys. J. **C73**, 2302 (2013) [arXiv:1212.3280].

[35] G. P. Korchemsky and A. V. Radyushkin, Phys. Lett. **B279**, 359 (1992) [arXiv:hep-ph/9203222].

[36] A. G. Grozin and O. I. Yakovlev, Phys. Lett. **B285**, 254 (1992) [arXiv:hep-ph/9908364].

[37] E. Bagan, M. Chabab, H. G. Dosch and S. Narison, Phys. Lett. **B301** (1993) 243.

[38] S. Groote, J. G. Korner and O. I. Yakovlev, Phys. Rev. **D55** (1997) 3016 [arXiv:hep-ph/9609469].

[39] S. Groote, J. G. Korner and O. I. Yakovlev, Phys. Rev. **D56**, 3943 (1997) [arXiv:hep-ph/9705447].

[40] A. V. Efremov and A. V. Radyushkin, Theor. Math. Phys. **42**, 97 (1980) [Teor. Mat. Fiz. **42**, 147 (1980)]; Phys. Lett. **B94**, 245 (1980).

[41] G. P. Lepage and S. J. Brodsky, Phys. Lett. **B87**, 359 (1979); Phys. Rev. **D22** (1980) 2157.

[42] G. Bell, T. Feldmann, Y.-M. Wang and M. W. Y. Yip, JHEP **1311**, 191 (2013) [arXiv:1308.6114].

[43] S. V. Mikhailov and A. V. Radyushkin, JETP Lett. **43**, 712 (1986) [Pisma Zh. Eksp. Teor. Fiz. **43**, 551 (1986)].

[44] S. V. Mikhailov and A. V. Radyushkin, Phys. Rev. **D45**, 1754 (1992).

[45] A. P. Bakulev and S. V. Mikhailov, Phys. Rev. **D65**, 114511 (2002) [arXiv:hep-ph/0203046].

[46] M. A. Shifman, A. I. Vainshtein and V. I. Zakharov, Nucl. Phys. **B147**, 385 (1979); Nucl. Phys. **B147**, 448 (1979).

Search for light dark vector boson: NA64 experiment

S.N. Gninenko[1] *and N.V. Krasnikov*[1,2]

[1] INR RAS, 117312 Moscow, Russia
[2] Joint Institute for Nuclear Research, 141980 Dubna, Russia

DOI: http://dx.doi.org/10.3204/DESY-PROC-2016-04/Krasnikov

In this mini review we outline the main experimental and theoretical results related with the search for light vector boson proposed as a solution of the muon $g-2$ anomaly. In particular, we consider a model with infinite number of light vector bosons which can escape most of current experimental bounds. We describe also the NA64 experiment at CERN devoted to the search for light vector boson both in visible and invisible decay modes.

1 Introduction

The search for new physics beyond the SM can be divided into two categories. The first one is the search for new heavy particles and interactions at high energies, the so-called "energy frontier" research. Typical examples are LEP, Tevatron and LHC. The second type of research is the search for relatively light with masses $m \leq O(1)\ GeV$ new hypothetical particles. In this case an experiment needs to cross the "intensity frontier". The most famous example of light hypothetical particle is the axion [1], invented for the solution of strong CP-problem. Also there are models predicting the existence of light scalar, spin 1/2 and vector particles. In particular, models with light vector bosons [2] (vector portal) become rather popular now. Light vector boson can be mediator between our world and light dark matter particles [2]. Also light vector boson can explain [3] - [8] muon $(g-2)$ anomaly [9]. Recent claim [10] of the discovery of 17 MeV vector particle observed as a peak in e^+e^- invariant mass distribution in nuclear transitions makes the question of possible existence of light vector boson extremely interesting and important.

In this mini review we outline the main experimental and theoretical results related with the search for light vector boson. In particular. we consider a model with infinite number of light vector bosons which can escape most of current experimental bounds. We also describe the NA64 experiment at CERN devoted to the search for light vector boson both in visible and invisible decay modes.

2 Muon $g-2$ anomaly and the light Z' boson.

Recent precise measurement of the anomalous magnetic moment of the positive muon $a_\mu = (g-2)/2$ from Brookhaven AGS experiment 821 [9] gives result which is about 3.6σ higher [11]

than the Standard Model prediction

$$a_\mu^{exp} - a_\mu^{SM} = 288(80) \times 10^{-11} \tag{1}$$

This result may signal the existence of new physics beyond the Standard Model. New light (with a mass $m_{Z'} \leq O(1)\ GeV$) vector boson (dark photon) which couples very weakly with muon with $\alpha_{Z'} \sim O(10^{-8})$ can explain $(g-2)$ anomaly [3]-[8]. Vectorlike interaction of Z' boson with muon

$$L_{Z'} = g^{'} \bar{\mu} \gamma^\mu \mu Z'_\mu \tag{2}$$

leads to additional contribution to muon anomalous magnetic moment [12]

$$\delta a = \frac{\alpha^{'}}{2\pi} F(\frac{m_{Z'}}{m_\mu}), \tag{3}$$

where

$$F(x) = \int_0^1 dz \frac{[2z(1-z)^2]}{[(1-z)^2 + x^2 z]} \tag{4}$$

and $\alpha^{'} = \frac{(g^{'})^2}{4\pi}$. Equation (4) allows to determine the coupling constant $\alpha^{'}$ which explains the value (1) of muon anomaly. For $m_{Z'} \ll m_\mu$ one can find that

$$\alpha^{'} = (1.8 \pm 0.5) \times 10^{-8}. \tag{5}$$

For another limiting case $m_{Z'} \gg m_\mu$ the $\alpha^{'}$ is

$$\alpha^{'} = (2.7 \pm 0.7) \times 10^{-8} \times \frac{m_{Z'}^2}{m_\mu^2}. \tag{6}$$

But the postulation of the interaction (2) of the Z_μ boson with muon is not the end of the story. The main question: what about the interaction of the Z' boson with other quarks and leptons? The most general renormalizable Z' interaction with the SM fermions ψ_k ($\psi_k = e, \nu_e, u, d, ...$) has the form

$$L_{Z'} = g^{'} Z'_\mu J^\mu_{Z'}, \tag{7}$$

$$J^\mu_{Z'} = \sum_k [q_{Lk} \bar{\psi}_{Lk} \gamma^\mu \psi_{Lk} + q_{Rk} \bar{\psi}_{Rk} \gamma^\mu \psi_{Rk}], \tag{8}$$

where $\psi_{Lk,Rk} = \frac{1}{2}(1 \mp \gamma_5)\psi$ and q_{Lk}, q_{Rk} are the Z' charges of the ψ_{Lk}, ψ_{Rk} fermions. The Z' can interact with other beyond SM particles, for instance, with dark matter fermions χ

$$L_{Z',\chi} = g_D Z'_\mu \bar{\chi} \gamma^\mu \chi. \tag{9}$$

There are several models of the current $J^\mu_{Z'}$. In a model [13, 14] Z' interacts with photon A_μ due to kinetic mixing term[1]

$$L_{mix} = \frac{\epsilon}{2} F^{\mu\nu} Z'_{\mu\nu}. \tag{10}$$

As a result of the mixing (10) the field Z' interacts with the SM electromagnetic field $J^\mu_{EM} = \frac{2}{3}\bar{u}\gamma^\mu u - \frac{1}{3}\bar{d}\gamma^\mu d - \bar{e}\gamma^\mu e + ...$ with coupling constant $g^{'} = \epsilon e$ ($\alpha = \frac{e^2}{4\pi} = \frac{1}{137}$) .

[1]Here $F_{\mu\nu} = \partial_\mu A_\nu - \partial_\nu A_\mu$ and $Z'_{\mu\nu} = \partial_\mu Z'_\nu - \partial_\nu Z'_\mu$.

Other interesting scenario is the model [15] where Z' (the dark leptonic gauge boson) interacts with the SM leptonic current, namely

$$L_{Z'} = g'[\bar{e}\gamma^\nu e + \bar{\nu}_{eL}\gamma^\nu \nu_{eL} + \bar{\mu}\gamma^\nu \mu + \bar{\nu}_{\mu L}\gamma^\nu \nu_{\mu L} + \bar{\tau}\gamma^\nu \tau + \bar{\nu}_{\tau L}\gamma^\nu \nu_{\tau L}]Z'_\nu$$

In Refs. [3] - [5] for an explanation of $g-2$ muon anomaly a model where Z' interacts with $L_\mu - L_\tau$ current with an interaction

$$L_{Z'} = g'[\bar{\mu}\gamma^\nu \mu + \bar{\nu}_{\mu L}\gamma^\nu \nu_{\mu L} - \bar{\tau}\gamma^\nu \tau - \bar{\nu}_{\tau L}\gamma^\nu \nu_{\tau L}]Z'_\nu \tag{11}$$

has been proposed. The interaction (12) is free from γ_5-anomalies, it commutes with the SM gauge group and moreover it escapes (see next section) from the most restrictive current experimental bounds because the interaction (12) does not contain quarks and first generation leptons ν_e, e.

3 Model with infinite number of light Z' bosons

Here we consider model with infinite number of light vector bosons which can escape current experimental bounds. The models with infinite number of local fields have been considered in Refs.[16, 17, 18]. Note that notion of an unparticle, introduced by Georgi [19, 20] can be interpreted as a particular case of such models [16, 17, 21, 22, 23]. So we consider a model with infinite number of vector fields $Z'_{\mu n}$ with masses $m_{Z'_n}$. We introduce the "effective" vector field $Z'_\mu = \sum_n c_n {Z'_{\mu n}}^2$ and postulate the interaction of the electromagnetic field A_μ with the the effective field Z'_μ in the form of kinetic mixing term (10). As a result of mixing the effective field Z'_μ will interact with the SM electromagnetic current with coupling constant $g^{`} = \epsilon e$. The one-loop contribution to $\delta a$ is $\delta a = \sum_n |c_n^2| \frac{\alpha^{`}}{2\pi} F(\frac{m_{Z'_n}}{m_\mu})$. The effectic field Z'_μ represents the infinite number of vector resonances that helps to escape bounds related with the search for narrow resonance in e^+e^- invariant mass distribution [18]. We can speculate that the origin of the infinite number of local vector fields as a result of compactification of some additional dimension. Namely, we can imagine the model with vector field $Z'_\mu(x, x_5)$ living in five-dimensional world and interacting with the four-dimensional SM fields due to kinetic mixing term

$$L_{mix} = \frac{\epsilon}{2} F^{\mu\nu}(x) Z'_{\mu\nu}(x, x_5 = 0)$$

After compactification of the x_5 coordinate we obtain the model (10) with the interaction of the effective field Z' with the SM electromagnetic current.

4 Accelerator experimental bounds

4.1 Fixed target electron experiments

Fixed target experiments, APEX [24] and MAMI(Mainz Microtron) [25] searched for Z' in electron-nucleus scatterings using the Z' bremsstrahlung production $e^- Z \to e^- Z Z'$ and subsequent Z' decay into electron-positron pair $Z' \to e^+e^-$. The absence of the resonant peak

[2]Here c_n are some numbers

in the invariant e^+e^- mass spectrum allows to obtain upper limits on the Z' boson coupling constants g_{Ve}, g_{Ae} of the Z' with electron. The A1 collaboration excluded the masses $50\ MeV < M_{Z'} < 300\ MeV$ [25] for $g-2$ muon anomaly explanation in the model with equal muon and electon couplings of the Z' boson with a sensitivity to the mixing parameter up to $\epsilon^2 = 8 \times 10^{-7}$. APEX collaboration used $\sim 2\ GeV$ electron beam at Jefferson Laboratory and excluded masses $175\ MeV < M_{Z'} < 250\ MeV$ for $g-2$ muon anomaly explanation in the model with equal muon and electon couplings of the Z' boson.

4.2 e^+e^- experiments

BaBar experiment searched for both visible and invisible Z' decays in $\Upsilon(1S)$ decays [26, 27, 28]. A search for invisible $\Upsilon(1S)$ has been performed by reconstructing $\Upsilon(3S) \to \pi^+\pi^-\Upsilon(1S)$. The bound $Br(\Upsilon(1S) \to invisible) = (-1.6 \pm 1.4 \pm 1.6) \cdot 10^{-4}$ was found. Here the first uncertainty is statistical and the second systematic. In addition invisible decays can be searched for in radiative $\Upsilon(1S) \to \gamma +$ invisible decays. In particular, the decay $\Upsilon(1S) \to \gamma +$ invisible could proceed through production of a light scalar A followed the by its decay into invisible modes $\Upsilon(1S) \to \gamma + A$, $A \to$ invisible. The bound on $Br(\Upsilon(1S) \to \gamma +$ invisible) was obtained at the level $(0.5-24) \cdot 10^{-5}$ assuming a phase-space distribution for photon energy. Visible decays of light Z' bosons were searched for in the reaction $e^+e^- \to \gamma Z'$, $Z' \to l^+l^-(l = e, \mu)$ and Z' can be detected as resonances in the l^+l^- spectrum. For the model with the Z' boson interaction with the SM electomagnetic current values of the mixing strength $10^{-3} - 10^{-2}$ are excluded for $0.212\ GeV < m_{Z'} < 10\ GeV$.

Recently BaBar collaboration used the reaction $e^+e^- \to Z'\mu^+\mu^-$, $Z' \to \mu^+\mu^-$ to search for Z' boson. The use of this process allows to restrict directly the muon coupling $g_{V\mu}$ of Z' boson. The obtained results exclude the Z' model with the $L_\mu - L_\tau$ interaction as possible muon $(g-2)$ anomaly explanation for $m_{Z'} > 212MeV$ [29].

The KLOE detector experiment in Fraskati, at the DAΦNE Φ-factory searched for Z' in decays $\Phi \to \eta Z' \to \eta e^+e^-$ and $\Phi \to \gamma Z' \to \gamma\mu^+\mu^-$ [30]. Also the reaction $e^+e^- \to Z'\gamma \to e^+e^-\gamma$ has been used for the search for Z'. The obtained bounds are weaker than the NA48/2 [31] and MAMI [25] bounds.

4.3 Fixed target proton experiments

The most strongest bound comes from the NA-48/2 experiment [31]. The NA-48/2 experiment used simultaneous K^+ and K^- seconday beams produced by 400 GeV primary CERN SPS protons for the search for light Z' boson in π^0 decays [31]. The decays $K^\pm \to \pi^\pm\pi^0$ and $K^\pm \to \pi^0\mu^\pm\nu$ have been used to obtain tagged π^0 mesons. The decays $\pi^0 \to \gamma Z^`$, $Z' \to e^+e^-$ have been used for the search for Z' boson. Z' boson manifests itself as a narrow peak in the distribution of the e^+e^- invariant mass. spectrum. For the model when the Z' boson interacts with the SM electomagnetic current as $L_{int,Z'} = \epsilon e Z'_\mu J^\mu_{SM}$ the obtained bounds exclude the $(g-2)$ muon anomaly explanation for Z' boson masses $9MeV < m_{Z'} < 70\ MeV$ [31].

It should be noted that the decay width $\pi^0 \to \gamma Z'$ is proportional to $(g_{Vu}q_u - g_{Vd}q_d)^2 = (2g_{Vu} + g_{Vd})^2/9$ and for the models with nonuniversal Z'-boson couplings, for instance, for the model with $L_\mu - L_\tau$ interaction current the NA-48/2 bound [31] is not applicable.

4.4 Constraints from $K \to \pi + nothing$ decay

Light vector bosom Z' can be produced in the $K \to \pi Z'$ decay in full analogy with the SM decay $K \to \pi\gamma^*$ of K-meson into pion and virtual photon. For the model with the dominant Z' decay into invisible modes nontrivial bound on Z' boson mass and coupling constants arises. Namely, the BNL E949 experiment [32] combined with E787 results measured the $K^+ \to \pi^+\nu\bar{\nu}$ decay and gave upper bounds on the $Br(K^+ \to \pi^+ Z')$ decay as a function of the Z' mass in the assumption that invisible $Z' \to nothing$ decay dominates. The E949 + E787 bound leads to the bound on the Z' mass and coupling constants. For instance, in the model when Z' couple with the SM electromagnetic current and decays mainly into invisible modes(light dark matter) the muon $(g-2)$ anomaly explanation due to Z' is excluded for $M_{Z'} > 50\ MeV$ except the narrow region around $M_{Z'} = m_\pi$ [33] - [35]. Note that in the models with the Z' non electromagnetic current interaction, for instance in the model where the Z' interacts with the $L_\mu - L_\tau$ current, the bound from $K \to \pi + nothing$ decay decay does not work or it could be rather weak [34]. Recent result of NA64 collaboration [36] based on the use of the reaction $eZ \to eZZ'$, $Z' \to$ invisible gives the most powerful bound on dark matter Z' boson and excludes the region $M_{Z'} \leq 50\ GeV$ for muon $g-2$ anomaly explanation, see next section.

4.5 Bound from electron magnetic moment

The experimental and theoretical values for electron magnetic moment coincide at the 10^{-12} level of accuracy, namely [37]

$$\Delta a_e \equiv a_e^{exp} - a_e^{SM} = -(1.05 \pm 0.82) \times 10^{-12}\,. \tag{12}$$

The Z' boson contributes to the Δa_e at one loop level, see formulae (3,4). From the bound (13) it is possible to restrict the couplng constants g_{Ve} and g_{Ae}. For the model with equal muon and electron couplings $g_{Ve} = g_{V\mu}$ and $g_{Ae} = g_{A\mu} = 0$ the $(g-2)$ muon anomaly explanation due to Z' existence is excluded for $M_{Z'} \geq 15\ MeV$ [38].

4.6 Constraints from $\nu - e$ scatterings

If the Z' boson couples with electron neutrino current and electron - the strongest bound arises from Borexino experiment [40]. Borexino experiment detects the low energy solar neutrino through elastic scattering of neutrino and electron [40]. The Z' exchange modifies the SM elastic electron neutrino electron cross section that allows to obtain strong constraint on the Z' coupling constants with electron neutrino and electron [41]. The obtained bound on $|g_{V\nu_e} \cdot g_{Ve}|^{1/2}$ is about 10^{-6} for $m_{Z'} \leq 1\ MeV$ and about 10^{-4} for $m_{Z'} \leq 100\ MeV$. Borexino data exclude the $(g-2)$ muon anomaly explanation in the model with Z' interaction with leptonic current [15]. Also the Borexino data exclude the model with the Z' interaction with the $B-L$ current.

4.7 Bound from $\nu_\mu N \to \nu_\mu N \mu^+\mu^-$

The neutrino trident $\nu_\mu N \to \nu_\mu N + \mu^+\mu^-$ events allow to restrict a model where Z' interacts with $L_\mu - L_\tau$ current using the data of the CHARM [42] and the CCFR [43] experiments. The CCFR and CHARM data on $\nu_\mu N \to \nu_\mu N + \mu^+\mu^-$ production exclude the $g-2$ muon anomaly explanation for Z'-boson mass $m_{Z'} \geq 400\ MeV$ [44].

4.8 Beam dump experiments

The results of beam dump experiments E137 [45], E141 [46] at SLAC and E774 [47] at FNAL have been used [2] to constrain the couplings of light gauge boson Z'. In recent paper [48] MiniBooNE-DM collaboration have obtained bound on $Y = \epsilon^2\alpha'(\frac{m_\chi}{m_{Z'}})^4 \leq 10^{-8}$.

5 NA64 experiment at CERN. The first results

The NA64 experiment [49] at CERN is a fixed-target experiment searching for dark sector particles at the CERN Super Proton Synchrotron(SPS). If new light boson Z' exists it could be produced in the reaction of high-energy electrons scattering off nuclei. The NA64 experiment uses the bremsstrahlung reaction $eZ \to eZZ'$ for the search for Z' boson. Both visible $Z' \to e^+e^-$ and invisible $Z' \to$ invisible decays can be used for the search for Z' boson. Also the use of the secondary muon beams for the search for Z' boson in the reaction $\mu Z \to \mu ZZ'$ [50] is planned in the near future.

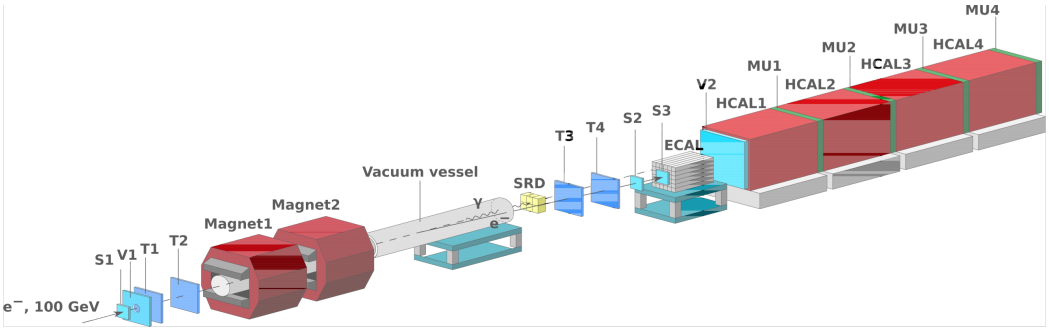


Figure 1: Schematic illustration of the setup to search for $Z' \to$ invisible decays for the bremsstrahlung Z' produced in the reaction of $eZ \to eZZ'$ of 100 GeV e^- incident on the active ECAL target [36].

The NA64 detector has two modifications for the search for both visible and invisible Z' decays. Here we outline the main features of NA64 detector used for the search for invisible Z' decays. The NA64 detector is schematically shown in Fig.1. The experiment employes the optimized 100 GeV electron secondary beam from CERN SPS. The detector utilises the beam defining scintillator (Sc) counters $S1 - S3$ and veto $V1$, and magnetic spectrometer consisting of two successive dipole magnets and a low-material-budget tracker. The tracker is a set of two upstream Micromegas chambers ($T1, T2$) and two downstream GEM stations ($T3, T4$) allowing the measurements of electron momenta with the precision $\delta p/p \approx 0.01$ [51]. The magnets also serves as an effective filter rejecting the low energy component of beam. To enhance the electron identification the synchrotron radiation (SR) emitted by electrons is used for their effective tagging. A 15 m long vacuum vessel between the magnets and the electromagnetic calorimeter (ECAL) is installed to minimize absorption of the SR photons detected immediately at the downstream end of the vessel with a SR detector (SRD), which is eihther an array of $Bi_4Ge_3O_{12}$(BGO) cristals of a $PbSc$ sandwich calorimeter of a very fine segmentation [52]. By using the SRD, the initial level of the hadron contamination in the beam $\pi/e \leq 10^{-2}$ is

further suppressed by a factor $\approx 10^{-3}$. The detector is also equipped with an active target, which is an electromagnetic calorimeter for measurement of the electron energy deposition E_{ECAL} with the accuracy $\delta E_{ECAL}/E_{ECAL} \approx 0.1/\sqrt{E_{ECAL}}$. The ECAL is a matrix of 6×6 Shashlik-type modules assembled from Pb ans Sc plates with wave length shifting fiber read-out. Each module has ≈ 40 radiation length. Downstream of ECAL the detector is equipped with a high-efficiency veto counter $V2$ and a massive, hermetic hadronic calorimeter (HCAL) of a ≈ 30 nuclear lengths. The HCAL serves as an effective veto to detect muons of hadronic secondairies produced in the $e^- A$ interactions in the target. The HCAL energy resolutions is $\delta E_{HCAL}/E_{HCAL} \approx 0.6/\sqrt{E_{HCAL}}$. Four muon plane counters MU1 - MU4, located between the HCAL modules are used for the muon identification in the final state.

The method of the search for Z' is as follows [36]. As a result of the reaction $e^- Z \to eZZ'$ of the Z' electroproduction on nuclei with subsequent Z' decay $Z' \to \chi\chi$ into dark matter particles χ we expect events whose signature is a single electromagnetic (EM) shower in the target with energy E_e accompanied by a significant missing energy $E_{miss} = E_0 - E_e$ above those expected from backgrounds. Here we assume that dark matter particles traverse the detector without interaction or visible decays in order to give a missing energy signature. No other assumptions on the nature of the $Z' \to$ invisible decay are made. Other signature of the signal event is small energy deposited in HCAL.

During summer 2016 run NA64 experiment collected approximately 2.75×10^9 electrons on target [36]. Candidate events were requested to have the missing energy in the range $50 < E_{miss} < 100\ GeV$, which was selected based on the calculation of the energy spectrum of Z' emitted in the reaction $eZ \to eZZ'$ by e^- from the EM shower generated by electron beam in the target [53]. Zero events have been observed and as a consequence the 90% $C.L.$ upper limit for the average number of signal events $N_{Z'} = 2.3$ has been derived. The obtained results [36] exclude the invisible Z' as an explanation of the muon anomaly with masses $m_{Z'} \leq 100\ MeV$ in the model with the Z' inreraction with the SM electromagnetic current, see Fig.2. Only small mass region around $m_{Z'} = m_\pi$ is still allowed. The future NA64 runs with $\geq 5 \times 10^{10}$ electrons on target can test the remaining mass region around $m_{Z'} = m_\pi$.

5.1 Conclusions

Current experimental data restrict rather strongly the explanation of the $g-2$ muon anomaly due to existence of new light gauge boson but not completely eliminate it. The most popular model where Z' interacts with the SM electromagnetic current due to mixing $\frac{\epsilon}{2} F_{\mu\nu} Z^{\mu\nu}$ term is excluded except its modification in which the invisible decay Z' dominates. In this case the narrow mass region around $m_{Z'} \sim m_\pi$ is still allowed. The Borexino data on neutrino electron elastic scattering exclude the models with Z' interaction with both leptonic current and $B-L$ currents. The interaction of the $Z^{`}$ boson with $L_e - L_\mu$ current is excluded for $m_{Z'} \geq 214\ MeV$. The review of nonaccelerator bounds can be found in Ref.[54].

Acknowledgments

We are indebted to V.A.Matveev for usefull discussions and comments.

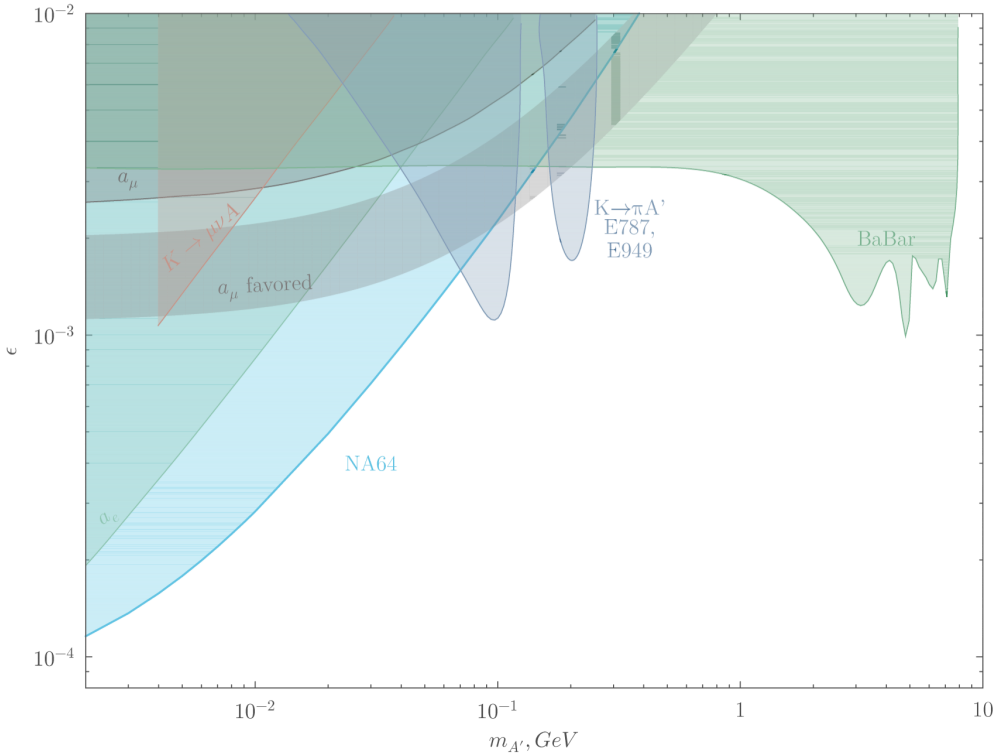


Figure 2: The NA64 90 % C.L. exclusion region in the ($m_{Z'}$, ϵ) plane. Constraints from BaBar and E787 + E949 experiments, as well the muon $(g-2)$ favoured area are also shown [36].

References

[1] R.D.Peccei and H.R.Quinn, Phys.Rev.Lett. **38** 1440 (1977);
S.Weinberg, Phys.Rev.Lett., **40** 223 (1978)
F.Wilczek, Phys.Rev.Lett., **40** 279 (1978).

[2] As a recent review, see for example:
Jim Alexander et al., arXiv:hep-ph/1608.08632 (2016).

[3] S.N.Gninenko and N.V.Krasnikov, Phys. Lett. **B513**, 119 (2001).

[4] S.Baek et al., Phys.Rev. **D64**, 055006 (2001).

[5] E.Ma, D.Roy and S.Roy, Phys.Lett. **B525**, 101 (2002).

[6] P.Fayet, Phys.Rev. **D75**, 115017 (2007).

[7] M.Pospelov, Phys.Rev. **D80**, 095002 (2009),

[8] J.Heeck, and W.Rodejohann, Phys.Rev. **D84**, 075007 (2011).

[9] J.Beringer et al., [Particle Data Group Collaboration], Phys.Rev. **D86**, 010001 (2012) and partial update for the 2014 edition (http://pdg.lbl.gov). G.W.Benett et al., [Muon G-2 Collaboration], Phys.Rev. **D73** 072003 (2006);
H.N.Brown et al., arXiv:hep-ex/0102017(2001).

[10] A.Krasznahorsky et al., Phys.Rev.Lett. **116** 042501 (2016).

[11] K.A.Olive et al.,(Particle Data Group), Chinese Physics **C38** 90001 (2014).

[12] As a review, see for example:
F.Jegelehner and A.Nyffeler, Phys.Repts. **C477** 1 (2009).

[13] B.Holdom, Phys.Lett. **B178**, 65 (1986).

[14] K.R.Dienes, C.F.Kolda and J.March-Russell, Nucl.Phys. **B492** 104 (1997).

[15] Hye-Sung Lee, arXiv:hep-ph/1408.4256 (2014).

[16] N.V.Krasnikov, Phys.Lett. **B325** 430 (1994).

[17] N.V.Krasnikov, Int.J.Mod.Phys. **A 22** 5117 (2007).

[18] N.V.Krasnikov, Mod.Phys.Lett. **A23** 3233 (2008).

[19] H.Georgi, Phys.Rev.Lett. **98** 221601 (2007).

[20] H.Georgi, Phys.Lett. **B 650** 275 (2007).

[21] M.A.Stephanov, Phys.Rev. **D 76** 035008 (2007).

[22] Patricio Gaete and Euro Spallucci, Phys.Lett. **B661** 319 (2008).

[23] H.Nikolic, Mod.Phys.Lett. **A23** 2645 (2008).

[24] S.Abrahamyan et al., Phys.Rev.Lett. **107** 191804 (2011).

[25] H.Merkel et al. (A1 Collaboration), Phys.Rev.Lett. **112** 2218002 (2014).

[26] BaBar Collab. (B.Aubert et al.), Nucl.Instr.Meth. **A479** 1 (2002).

[27] J.P.Lees et al.(BaBar) Phys.Rev.Lett. **113** 201801 (2014).

[28] As a review, see for example:
B. Echenard, Mod.Phys.Lett. **27** 1230016 (2012).

[29] J.P.Lees et al. (BaBar Collaboration), Phys.Reb. **D 94** 011102 (2016) (2016).

[30] As a recent review, see:
E. Perez del Rio, Dark Forces Searches at KLOE-2, arXiv:1602.0492 (2016).

[31] NA48/2 Collab. (J.R.Batley et al.), Phys.Lett. **B476** 178 (2015).

[32] A.V.Artamonov et al. (BNL-E249 Collaboration), Phys.Rev. **D79** 092004 (2009).

[33] M.Pospelov, Phys.Rev. **D80** 095002 (2009).

[34] H.Davoudiasl, H.S.Lee and W.J.Marciano, Phys.Rev. **D89** 095006 (2014).

[35] R.Essig et al., J.High Energy Phys. **11** 167 (2013).

[36] D.Banerjee et al., (NA64 Collaboration) Phys.Rev.Lett. **118** 011802 (2017).

[37] R.Aoyamma et al., Phys.Rev.Lett. **109** 111807 (2012).

[38] H.Davoudiasl, H.S.Lee and W.J.Marciano, Phys.Rev. **D86** 095009 (2012);
M.Endo, K.Hamaguchi and G.Mishima, Phys.Rev. **D86** 095029 (2012).

[39] G.Bellini et al., Phys.Rev.Lett. **107** 141302 (2011).

[40] G.Bellini et al., Phys.Rev.Lett. **107**, 141302 (2011).

[41] R.Harnik, J.Kopp and P.A.N.Machado, JCAP **07** 026 (2012);
R.Laha, B.Dasgupta and J.F.Beacom, Phys.Rev. **D89** 093025 (2012).

[42] D.Geiregat et al. [CHARM-II collaboration], Phys.Lett. **B245** 1271 (1990).

[43] S.R.Mishra et al.[CCFR collaboration], Phys.Rev.Lett. **66**, 3117 (1991).

[44] W.Almannsofer, S.Gori, M.Pospelov and I.Yavin, Phys.Rev.Lett. **113** 091801 (2014).

[45] J.D.Bjorken et al., Phys.Rev. **D38** 3375 (1988).

[46] E.H.Riordan et al., Phys.Rev.Lett. **59** 775 (1997).

[47] A.Bross et al., Phys.Rev.Lett. **67** 2942 (1991).

[48] A.A.Aguillar-Arevalo et al., arXiv:hep-ex/1702.02688 (2017).

[49] S.Andreas et al., arXiv:hep-ph/1312.3309(2013).

[50] S.N.Gninenko, N.V.Krasnikov and V.A.Matveev, Phys.Rev. **D91** 095015 (2015).

[51] D.Banerjee, P.Crivelli and A.Rubbia, Adv.High Energy Phys. **2015** 105730 (2015).

[52] S.N.Gninenko, Phys.Rev. **D89** 075008 (2014).

[53] S.N.Gninenko, N.V.Krasnikov, M.M.Kirsanov and D.V.Kirpichnikov, Phys.Rev. **D94** 095025 (2016).

[54] As a recent review, see:
Y.S.Jeong, C.S.Kim and H.S.Lee, Int.J.Mod.Phys. **A31** (2016).

Recent results on B-physics and multiquark states from LHCb

Bernardo Adeva[1]

[1]University of Santiago de Compostela, Campus Sur, E-15782 Santiago de Compostela, Spain

On behalf of the LHCb collaboration

DOI: http://dx.doi.org/10.3204/DESY-PROC-2016-04/Adeva

A review is made of recent results on flavour physics and multiquark states by the LHCb experiment. These cover a wide range of topics discussed at the School, which are briefly summarized here, with reference to the relevant publications. The topics range from a complete review of the $B^0_{(s)} - \bar{B}^0_{(s)}$ meson oscillations, with and without CP violation, with a specific discussion of CPT non conservation, to axion and inflaton searches at a hadron collider. Results on rare decays and weak anomalies are also summarized, and a follow-up is made of the charmonium-pentaquark discovery and of recent findings on tetraquark-like states.

1 B-meson mixing, CP- and CPT-violation

Only four long-lived neutral mesons exist in Nature: K^0, D^0, B^0, and B^0_s. Their particle-antiparticle oscillations are important assets to constrain models beyond the Standard Model of Particle Physics (SM), because they probe high masses through quantum fluctuations in the vacuum polarization diagrams. Under CPT conservation, the mixing matrix contains 5 real observables: $m_{H,L}$, $\Gamma_{H,L}$, and the CP-violating phase ϕ, where $\Delta m \equiv m_H - m_L$ and $\Delta\Gamma \equiv \Gamma_L - \Gamma_H$ are the mass and lifetime differences between the two mass eigenstates. As discussed at the School (see this communication on Indico), the oscillation can be observed either in self-tagging modes (only accessible from B^0 or $\bar{B}^0$) or in CP-eigenstates, where interference between mixing and decay amplitudes is possible.

Using semimuonic decays and flavour tagging at production and decay times, the LHCb experiment has performed a measurement of the mass difference between the B^0 mass eigenstates [1]: $\Delta m_d = (0.5050 \pm 0.0021 \pm 0.0010)\, ps^{-1}$. A much faster oscillation is observed with the B^0_s meson [2], seen by LHCb from hadron decays such as $B^0_s \to D^-_s \pi^+$, with $D_s \to \phi(K^+K^-)\pi^-$. These measurements are the most precise to date, and both agree with the SM prediction.

Concerning CP-violation in the mixing, earlier non-zero observations at the Tevatron [3] have been reassessed recently, including LHCb results from non CP-symmetric pp collisions at the LHC. LHCb has succeeded in separating the contributions from the B^0_s [4] and B^0 [5] mesons in the semimuonic asymmetries, with the results $a^s_{SL} = (0.39 \pm 0.25 \pm 0.20)\%$ and $a^d_{SL} = (-0.02 \pm 0.19 \pm 0.30)\%$, showing consistency with the SM prediction of null asymmetry.

An important test of the Kobayashi-Maskawa theory is measuring the very small CP-

violating phase that arises from the unitarity triangle having a very short side:

$$V_{us}^* V_{ub} (\approx 0) + V_{cs}^* V_{cb} + V_{ts}^* V_{tb} = 0$$

which is given by the phase difference between the last two terms, called β_s. This can only be achieved at hadron colliders, mainly by using the golden channel $B_s^0 \to J/\psi\phi$. The result reported by LHCb from the above channel is further improved when adding together the information from the $B_s^0 \to J/\psi\pi^+\pi^-$ final states [6], yielding the final measurement: $\phi_s^{c\bar{c}s} = -2\beta_s = -10 \pm 39$ mrad [7]. The time analysis of the CP-asymmetry, performed with an average resolution of $46 fs$ at LHCb, provides as a by-product the lifetime difference between the mass eigenstates $\Delta\Gamma_s$. With leading precision from LHCb, overall agreement is found among the different collider experiments (ATLAS, CMS, D0, CDF and LHCb). World averaged values are found: $\phi_s^{c\bar{c}s} = -33 \pm 33$ mrad and $\Delta\Gamma_s = 88 \pm 20$ ns^{-1}, in very good agreement with the SM predictions of: $\phi_s^{c\bar{c}s} = -37.6 \pm 0.8$ mrad and $\Delta\Gamma_s = 88 \pm 20$ ns^{-1}. Further improvement will require assessment of higher order corrections, related to penguin loop diagrams [8, 9].

In addition, recent major contributions have been performed to the standard unitarity triangle of the CKM matrix: $V_{ud}^* V_{ub} + V_{cd}^* V_{cb} + V_{td}^* V_{tb} = 0$, defined by the phases β and γ, by providing direct measurements of γ from the BaBar, BELLE, and LHCb experiments [10, 11, 12]. The combined measurement of γ by LHCb from tree-level diagrams [12], that handles together the interference parameters from all decays of the generic form $B \to DK$, has provided the most accurate result: $\gamma = (70.9^{+7.1}_{-8.5})^\circ$. It is worth mentioning that γ is the only CP-violating phase that can be determined from tree-level diagrams alone, and can therefore be used as a reference candle for the SM contribution, when compared to additional measurements to come that may be sensitive to loop diagrams. Concerning the β phase, LHCb has recently contributed to the already existing very precise measurements by BaBar and BELLE [13], with the new result [14]: $S = \sin^2(2\beta) = 0.731 \pm 0.035 \pm 0.020$, and with a constraint to the cosine term of the time dependent asymmetry: $C = -0.038 \pm 0.032 \pm 0.005$.

The level of precision attained in $B - \bar{B}$ oscillations opens the possibility to explore CPT violation, which would imply Lorentz non invariance [15]. The so-called Standard Model Extension (SME) postulates interactions that would destabilize the vacuum and spontaneously generate a non-zero vacuum expectation value (VEV) of Lorentz tensors [16]. Should the masses ($\delta m \neq 0$) or lifetimes ($\delta\Gamma \neq 0$) of B and $\bar{B}$ mesons not be equal, a phase angle shift in the $B - \bar{B}$ asymmetry oscillation would be observed through the complex number [17]:

$$z = \frac{\delta m - i\delta\Gamma/2}{\Delta m - i\Delta\Gamma/2}$$

Given the fact that the denominator is quite small as compared with the B-meson masses (either B^0 or B_s^0), the figure of merit may become, in relative terms, comparable to the ratio $m_W/M_P \approx 10^{-17}$ of Planck mass effects at the electroweak scale. Since the numerator of z depends on the 4-velocity $\beta^\mu = \gamma(1, \vec{\beta})$ of the meson as $\beta^\mu \Delta a_\mu$ [16], the sensitivity is enhanced by an additional factor of 20 at LHCb, once the LHC beam location is specified on the Earth's rotating frame. The time analysis revealed no significant periodicities, and Δa_μ was determined, for B^0 and B_s^0, with precisions of order 10^{-15} and 10^{-14} GeV, respectively [17]. The following constraints were obtained: Re$z = -0.022 \pm 0.033 \pm 0.005$ and Im$z = -0.022 \pm 0.011 \pm 0.002$.

2 Rare b-decays and weak anomalies

Final states with dileptons are a particularly sensitive probe to search for contributions of Wilson operators in precision tests of flavor-changing neutral currents (FCNC) in $b \to s$ and $b \to d$ transitions, beyond those of the Standard Model at loop level. Well known examples are the very rare decays $B^0_{(s)} \to \mu^+\mu^-$ and exclusive $b \to s\mu^+\mu^-$ processes.

A joint effort has been performed by the LHCb and CMS experiments at the LHC [18] to assess the elusive $B^0_{(s)} \to \mu^+\mu^-$ decays, under scrutiny for many years at several accelerator facilities. Taking into account the distinct geometrical acceptance and resolution properties of both experiments, the combination of the data has resulted in the final discovery of the $B_s \to \mu^+\mu^-$ mode with branching fraction $\mathcal{B}(B_s \to \mu^+\mu^-) = (2.8^{+0.7}_{-0.8}) \times 10^{-9}$ and in a 3σ effect for $B^0 \to \mu^+\mu^-$, with $\mathcal{B}(B^0 \to \mu^+\mu^-) = (3.9^{+1.6}_{-1.4}) \times 10^{-10}$. The fit for the ratios of the branching fractions relative to their SM predictions yields $\mathcal{S}^{B_s}_{SM} = 0.76^{+20}_{-18}$ and $\mathcal{S}^{B^0}_{SM} = 3.7^{+1.6}_{-1.4}$. The measurements are compatible with the respective SM predictions at the 1.2σ and 2.2σ level, when computed from the one-dimensional hypothesis tests. Finally, the fit for the ratio of branching fractions yields $\mathcal{R} = 0.14^{+0.08}_{-0.06}$, which is compatible with the SM at the 2.3σ level.

Rare $b \to s\mu^+\mu^-$ FCNC's are only allowed in the SM by calculable electroweak penguin and box diagrams, open to contributions of new heavy particles (extra Z' bosons, or new Higgs particles, among them). The angular observables of the decay $B^0 \to K^{*0}(K^+\pi^-)\mu^+\mu^-$ are characterized by 6 amplitudes: $\mathcal{A}^{L,R}_{0,\parallel,\perp}$, related to the three helicity states of the K^{*0} and the two chiralities (L,R) of the dimuon system. The full set of 9 (CP-averaged) observables was analized by LHCb in 2013 as function of $q^2(\mu^+\mu^-)$, showing statistical agreement with the SM predictions in all of them, except in the particular observable:

$$P'_5 = \sqrt{2}\mathrm{Re}(\mathcal{A}^L_0\mathcal{A}^{L*}_\perp - \mathcal{A}^R_0\mathcal{A}^{R*}_\perp)/\sqrt{F_L(1-F_L)} \quad \text{with} \quad F_L = |\mathcal{A}^L_0|^2 + |\mathcal{A}^R_0|^2$$

which showed a local discrepancy of 3.7σ [19]. Possible interpretations of this discrepancy and consistency of all $b \to s\mu^+\mu^-$ transitions were widely discussed in the literature, and LHCb has updated the above result with the full $3fb^{-1}$ data sample from the LHC Run-1, and performed a global fit to all observables, in order to better assess the difference with respect to the SM predictions. A discrepancy in the P'_5 observable within the interval $2 < q^2 < 6\,\mathrm{GeV}^2$ was confirmed with the new data [20]. Such discrepancy has also been observed in a recent measurement by the Belle experiment [21]. Various theoretical analyses [22, 23] showed that the difference can consistently be accounted for by modifying the real part of the coefficients C_9 and C_{10} associated with the (V,A) Wilson operators in $b \to s\mu^+\mu^-$ transitions:

$$\mathcal{O}_9 \equiv (\bar{s}\gamma_\mu b_L)(\bar{\mu}\gamma^\mu\mu) \qquad \mathcal{O}_{10} \equiv (\bar{s}\gamma_\mu b_L)(\bar{\mu}\gamma^\mu\gamma^5\mu)$$

Because C_{10} is already being constrained by the $B_s \to \mu^+\mu^-$ branching fraction, LHCb has performed a global χ^2-fit to all angular observables and determined the best-fit value to be displaced from the SM prediction of 4.27 by $\Delta\mathrm{Re}C_9 = -1.04 \pm 0.25$ (3.4σ significance) [20]. This shift could be caused by an unexpectedly high hadronic effect that changes the SM predictions, or by contributions to the decay from non-SM vector particles.

An additional topic that has attracted a great deal of interest from various experiments, including LHCb, is lepton universality. It is well known that gauge interactions in the SM are flavor-universal at tree level, and all flavor-dependent interactions originate from the Yukawa couplings to the Higgs boson. It is actually the smallness of neutrino masses that makes lepton

interactions go universal for e, μ, τ, and the only uncertainty in ratios of semileptonic decays must come from the different lepton masses. Two such ratios are particularly sensitive to physics beyond the SM, and have drawn specific recent attention from experiments. They are defined as follows:

$$R_K = \frac{\int_{q^2_{min}}^{q^2_{max}} [d\Gamma(B^+ \to K^+\mu^+\mu^-/dq^2)]dq^2}{\int_{q^2_{min}}^{q^2_{max}} [d\Gamma(B^+ \to K^+e^+e^-/dq^2)]dq^2} \qquad R_{D^{(*)}} = \frac{\Gamma(B \to D^{(*)}\tau\nu_\tau)}{\Gamma(B \to D^{(*)}\mu\nu_\mu)}$$

The first ratio is essentially free of all hadronic uncertainties, notably form factors, and was measured by LHCb in the interval $1 < q^2 < 6\ GeV^2$ [24], which excludes the J/ψ region and the region above $\psi(2s)$, affected by broad charmonium resonances. To cope with the very different bremsstrahlung properties of electrons and muons, LHCb takes strong advantage from the copious J/ψ production in the control channel $B^+ \to J/\psi(l^+l^-)K^+$, to cancel potential sources of systematics (assuming e, μ universality in $J/\psi \to l^+l^-$). The value $R_K = 0.745^{+0.090}_{-0.074} \pm 0.036$ is obtained, which is only 2.6σ from the SM prediction of unity within $\mathcal{O}(10^{-3})$ uncertainty, but suggestive of a possible deviation. No new measurements have been issued since then, for this important observable.

In an influential publication made by the BaBar experiment in 2013 [25], both ratios R_D and R_{D^*} were reported to have anomalously high values, exceeding the SM expectation by more than 3σ. Universality breakup by the τ lepton is particularly sensitive to new physics contributions, mainly from two Higgs doublet models (2HDM). In these models, scalar contributions $S_{L,R}$ from Wilson operators $(\bar{c}P_{L,R}b)(\bar{\tau}P_L\nu_\tau)$ with $P_{L,R} \equiv (1 \mp \gamma_5)/2$, make the helicity amplitudes H_s of $B \to D^{(*)}\tau\nu_\tau$ receive distinct extra contributions from D and D^* mesons (from their different spin), such that [25]:

$$H_s^{2HDM} \approx H_s^{SM}\left(1 + (S_R \pm S_L)\frac{q^2}{m_\tau(m_b \mp m_c)}\right)$$

In fact, the BaBar measurements appear to exclude 2HDM's where $S_L = 0$ (the so-called type II model, present in minimal Supersymmetry), in the full range of the $\tan\beta - m_{H^\pm}$ plane, but are compatible with more general 2HDM's having $|S_R + S_L| < 1.4$.

Reconstruction of τ leptons is challenging in pp collisions, including muonic decays, because of the presence of three final state neutrinos, and the lack of the energy constraint that is provided by the beam energy in e^+e^- machines. Yet LHCb has performed, for the first time at a hadron collider, the reconstruction of a $b \to \tau$ decay signal, leading to a measurement of R_{D^*} [26]. The three-body decay $D^{*+} \to D^0(K^-\pi^-)\pi^+$ was chosen, that produces identical reconstruction topologies in the τ and μ final states, when subject to the ratio:

$$R_{D^*} = \frac{\Gamma(\bar{B}^0 \to D^{*+}\tau^-(\mu^-\bar{\nu}_\mu\nu_\tau)\bar{\nu}_\tau)}{\Gamma(\bar{B}^0 \to D^{*+}\mu^-\bar{\nu}_\mu)}$$

where the B^0 rest-frame variables m^2_{miss}, E^*_μ, $q^2 = (p_B - p_D)^2$ are measured from the estimation of $\vec{p}_B$ achieved with charged particles. Control samples of the different backgrounds allow precise corrections to the signal yield.

The LHCb result: $\mathcal{R}(D^*) = 0.336 \pm 0.027 \pm 0.030$ [26] confirms the excess to the SM value of 0.252 ± 0.003 found by BaBar. The fit also extracts form factor parameters that appear to agree with world averages. Two further independent measurements of $\mathcal{R}(D^*)$ have been issued by the Belle experiment [27, 28], that indicate consistency with LHCb results. The world average of

measurements in the $(\mathcal{R}(D^*), \mathcal{R}(D))$ plane [29] currently shows a 3.9σ deviation with respect to the SM expectation. This exciting situation is clearly calling for new measurements, both at hadron colliders and e^+e^- machines. Given the feasibility of τ reconstruction at LHCb, a wealth of new measurements are forseen using other B-hadrons, such as B_s ,B_c, and Λ_b, that will soon help understand the picture.

Other very rare decays, sensitive to new particles beyond the SM, have been recently examined by LHCb, in particular the three-body decay $B^\pm \to \pi^\pm\mu^+\mu^-$. The ratio of its branching fraction to the more precisely measured kaon decay has been determined, in the regions $1.0 < q^2 < 6.0\,\mathrm{GeV}^2$ and $15.0 < q^2 < 22.0\,\mathrm{GeV}^2$ separately [30]. We quote the latter result:

$$\frac{\mathcal{B}(B^\pm \to \pi^\pm\mu^+\mu^-)}{\mathcal{B}(B^\pm \to K^\pm\mu^+\mu^-)} = 0.037 \pm 0.008 \pm 0.001$$

which implies a total branching fraction: $\mathcal{B}(B^\pm \to \pi^\pm\mu^+\mu^-) = (1.83 \pm 0.24 \pm 0.05) \times 10^{-8}$, with CP asymmetry: $\mathcal{A}_{CP}(B^\pm \to \pi^\pm\mu^+\mu^-) = -0.11 \pm 0.12 \pm 0.01$ [30]. These are the most precise measurements of these observables to date. In addition, the differential branching fraction with respect to the dimuon invariant mass squared was measured for the first time [30], and found to be consistent with SM theoretical predictions [31, 32, 33]. The ratio of branching fractions above has been used for a precision determination of $|V_{td}/V_{ts}|$ where the form factor uncertainties are greatly reduced [34]. In fact, independent extractions of $|V_{td}/V_{ts}|$ from different sources, such as rare B decays, B^0 and B_s^0 oscillation frequencies, and CKM unitarity, constitute a sensitive test of the SM and its possible extensions, including the Minimal Flavor Violation hypothesis (MFV) [35].

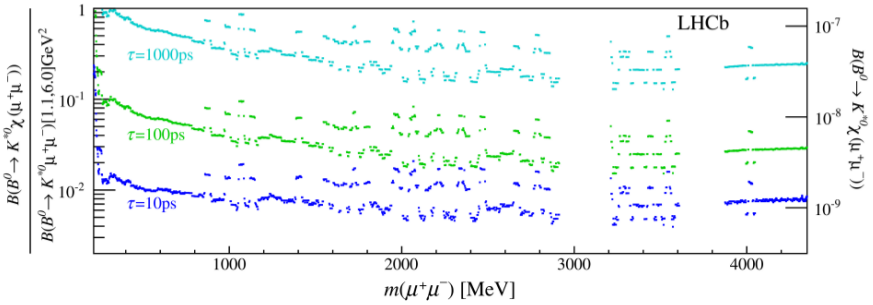
3 Hidden-sector searches

Dark matter (DM) may arise from quasi-stable particles in the Supersymmetry breaking sector at 1-10 TeV scale, that interact feably with all known particles. On the other hand, spontaneous breaking of the Peccei-Quinn symmetry, which is a U(1) rotation of the right-handed u,d-type quarks, leads to a light pseudo Nambu-Goldstone boson, the axion (χ). Its observation would provide fundamental understanding of why CP-violation is not seen in strong interactions [36]. The axion has been postulated to explain the e^+ excess observed in cosmic ray experiments [37, 38], because TeV-scale DM would decay into axions and get therefore long lived. This axion-like particle should then be light (GeV scale), in order to couple mainly to e and μ.

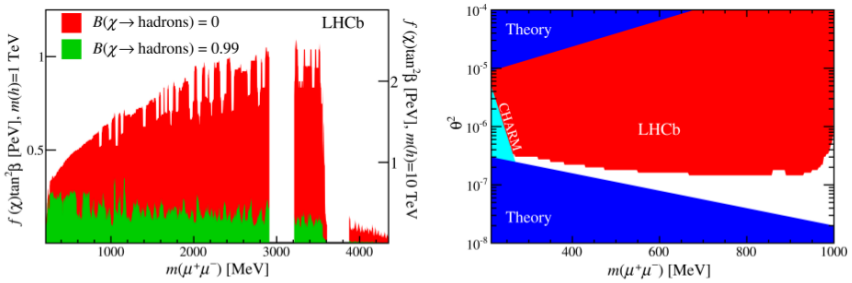
A possibility to detect the axion at high energy accelerators has been put forward [39], through its mixing with a CP-odd Higgs boson A^0 (either in Supersymmetry or in 2HDM's) with vacuum expectation values (VEV): $< H_{1,2} >= v_{1,2}$. The top quark can host this portal through flavor-changing neutral current (FCNC) loop decays such $b \to s\chi$, with amplitude [39]:

$$\mathcal{M}(b \to s\chi) = -\sin\theta\mathcal{M}(b \to sA^0) \qquad \tan\theta = n\frac{v_{EW}}{f_\chi \tan\beta} \quad \tan\beta \equiv \frac{v_1}{v_2}$$

where f_χ is the axion decay constant and $v_{EW} = \sqrt{v_1^2 + v_2^2}$, where $n = 2$ (DFSZ axion, [40, 41]) or $n = 1$ (NMSSM [42]). For large values of the axion decay constant, this particle does not decay at its production vertex, so its detection must involve wide range vertexing, combined with high $\mu^+\mu^-$ mass resolution, in order to search for narrow states in $b \to s\mu\mu$. To this end, $B^0 \to K^{*0}\mu^-\mu^-$ was chosen by LHCb.



(a) Upper limits at 95% CL for the indicated ratios in the left and right axes. Excluding the region near $2m_\mu$, the relative limits for $\tau < 10$ ps are between 0.005-0.05 and all relative limits for $\tau < 1000$ ps are less than 1.



(b) Exclusion regions at 95% C.L: (left) constraints on the axion model of Ref. [39]; (right) constraints on the mixing angle squared θ^2 of the inflaton model of Ref. [43]. The regions excluded by the theory [43] and by the CHARM experiment [46] are also shown.

Similar methodological principles, using the above decay, govern the search for a χ field responsible for an inflationary period at the early Universe, that may have generated the baryon asymmetry observed today. The portal is provided in this case by its mixing with the SM Higgs boson, and the associated inflaton particle is expected to have a mass in the range $270 \lesssim m(\chi) \lesssim 1800\,\text{MeV}$ [43]. Above the dimuon threshold, its lifetime is a strong function of the mass, and it rapidly falls down from being long-lived ($10^{-6}s$) to the $10\,ps$ region.

The LHCb experiment has determined the product of branching fractions [44]:

$$\mathcal{B}(B^0 \to K^{*0}\chi(\mu^+\mu^-)) \equiv \mathcal{B}(B^0 \to K^{*0}\chi) \times \mathcal{B}(\chi \to \mu^+\mu^-)$$

which is measured relative to $\mathcal{B}(B^0 \to K^{*0}\mu^+\mu^-)$, within a normalization region that is taken from prompt decays and restricted by $1.1 < m^2(\mu^+\mu^-) < 6.0\ GeV^2$. Many uncertainties cancel when doing this normalization, including some concerning hidden-sector theory.

The $m(\mu^+\mu^-)$ distribution was scanned for an excess of χ signal candidates over the expected background. The dimuon mass resolution is less than 8 MeV for the entire range, and it is as small as 2 MeV below 220 MeV. The $\chi \to \mu^+\mu^-$ decay vertex is permitted, but not required, to be displaced from the $B^0 \to K^{*0}\chi$ decay vertex. Two regions of reconstructed dimuon lifetime,

$\tau(\mu^+\mu^-)$ are defined for each mass $m(\chi)$: a prompt region $|\tau(\mu^+\mu^-)| < 3\sigma$, and a displaced region with larger distances. The lifetime resolution σ is about 0.2 ps for $m(\mu^+\mu^-) \gtrsim 250\,\text{MeV}$ and 1ps near $2m_\mu$. Narrow resonances are vetoed to avoid contamination from unassociated dimuon and K^{*0} resonances.

Upper limits on $\mathcal{B}(B^0 \to K^{*0}\chi(\mu^+\mu^-))/\mathcal{B}(B^0 \to K^{*0}\mu^+\mu^-)$ are set at 95% confidence level for several values of $\tau(\chi)$, as shown in Fig. 1a. As $\tau(\chi) \gtrsim 10$ ps, the limits become less stringent, since the probability of a χ boson decaying within the vertex detector (about 1m long) decreases. Fig. 1a shows exclusion regions for the DFSZ [40, 41] axion model of Ref. [39], set in the limit of large Higgs-doublet VEV's, $\tan\beta \gtrsim 3$, for charged-Higgs masses $m_H = 1\,\text{TeV}$ and $m_H = 10\,\text{TeV}$. Fig. 1b shows the results for two extreme cases: $\mathcal{B}(\chi \to \text{hadrons}) = 0$ and 0.99. While $\mathcal{B}(\chi \to \mu^+\mu^-)$ is 100 times larger when $\mathcal{B}(\chi \to \text{hadrons}) = 0$, $\tau(\chi)$ is also larger, which results in the model probing the region where the upper limits are weaker. The constraints are loose for $m(\chi) > 2m_\tau$, since the axion preferentially decays to $\tau^+\tau^-$ if kinematically allowed. Fig. 1b also shows exclusion regions for the inflaton model of Ref. [43], which only considers $m_\chi < 1$ GeV. The branching fraction into hadrons is taken directly from Ref. [45]. Constraints are placed on the mixing angle between the Higgs and the inflaton fields, θ, which exclude most of the previously allowed region.

In summary, no evidence for a narrow signal is observed, and upper limits are placed on $\mathcal{B}(B^0 \to K^{*0}\chi(\mu^+\mu^-))/\mathcal{B}(B^0 \to K^{*0}\mu^+\mu^-)$. This is the first dedicated search over a large mass range for a hidden-sector boson in a decay mediated by a $b \to s$ transition at leading order, and the most sensitive search to date over the entire accessible mass range. Stringent constraints are placed on theories that predict the existence of additional scalar or axial-vector fields.

4 Pentaquark states

Five-quark states of matter, beyond the simple quark model picture, have been an inspiring case of QCD models for five decades, ever since they were first conjectured by Gell-Man and Zweig in 1964 [47]. However no convincing findings were established at the onset of the LHC operation [51]. After processing a total integrated luminosity of 3 fb^{-1} of 8 TeV pp collisions at the LHC, the LHCb experiment collected a sample of over 26000 events of the three-body decay $\Lambda_b \to J/\psi(\mu^+\mu^-)K^-p$. As a consequence of the triggering on displaced vertices, of the large acceptance for low p_T dimuons, and of the 2-3 MeV mass resolution in the two-particle combinations of this final state, the background under this signal is nearly zero.

Analysis of the Dalitz plot showed that, in addition to a large number of known resonant Λ^* structures in the K^-p mass, an unexpected feature in the $J/\psi p$ mass was present. In order to investigate whether the above structure can be attributed to a reflection from the Λ^* resonances or not, a full amplitude fit was performed by LHCb to the $\Lambda_b^0 \to J/\psi K^-p$ decay [48], that included interference between two decay chains: the standard $\Lambda_b \to J/\psi\Lambda^*$, $\Lambda^* \to K^-p$, and the exotic $\Lambda_b \to P_c^+K^-$, $P_c^+ \to J/\psi p$, where P_c^+ represents a pentaquark state with given spin-parity asignment J^P. All possible known Λ^* states were tried (up to 13 different J^P combinations, with spins ranging from 1/2 to 9/2).

A significant Λ^* production recoiling against the J/ψ is observed, and the data cannot be satisfactorily described without including two Breit-Wigner shaped resonances in the $J/\psi p$ invariant mass distribution. Adding one pentaquark state improves the fit by $\Delta(-2\ln\mathcal{L}) = 14.7^2$, and the addition of a second P_c^+ state causes a further decrease of the likelihood of $\Delta(-2\ln\mathcal{L}) = 11.6^2$. The model with both P_c^+ states together has a 18.7σ significance. These structures can-

not be accounted for by reflections from $J/\psi\Lambda^*$ resonances or other known sources. Interpreted as resonant states they must have minimal quark content $c\bar{c}uud$, and can therefore be called charmonium pentaquark states. The lighter state $P_c(4380)^+$ has a mass of $4380 \pm 8 \pm 29$ MeV and a width of $205 \pm 18 \pm 86$ MeV, while the heavier state $P_c(4450)^+$ has a mass of $4449.8 \pm 1.7 \pm 2.5$ MeV and a width of $39 \pm 5 \pm 19$ MeV. The best-fit asignments are $J^P = (3/2^-, 5/2^+)$, but the combinations $(5/2^-, 3/2^+)$ and $(3/2^+, 5/2^-)$ cannot be excluded. All other J^P combinations are excluded with high significance.

It is found that the interference between two opposite parity P_c^+ states is needed to explain the observed asymmetric distribution of the P_c^+ helicity angle (angle of the J/ψ in the P_c^+ rest frame), which appears to be correlated with the mass of the K^-p system. As a consequene, the opposite sign of the parity of the two states is highly significant. In addition, the analysis of the phase of the Breit-Wigner amplitudes as function of $m(J\psi p)$ shows unambiguous counterclockwise rotation, as expected for a true resonance, in the case of $P_c^+(4450)$, and it is well compatible with such behaviour in the case of $P_c^+(4380)$.

The above analysis was later confirmed by a model independent approach to the same data, with minimal assumptions about K^-p contributions [49]. It has been demostrated with more than 9σ significance that the $\Lambda_b \to J/\psi K^-p$ decays cannot be described with K^-p sources alone, and that $J/\psi p$ contributions play a dominant role in this incompatibility [49].

The above pentaquark states have been re-assessed by LHCb in the Cabibbo suppressed channel $\Lambda_b \to J/\psi\pi^-p$, with measured 8.2% relative branching fraction, in a more recent publication [50]. A full amplitude model was carried out, following the lines of the previous $\Lambda_b \to J/\psi K^-p$ amplitude model, and a significantly better description of the data was achieved by either including the two P_c^+ observed in $\Lambda_b \to J/\psi K^-p$, or the $Z_c(4200)$ state reported by Belle and LHCb. The total significance was 3.1σ when both types of exotics were included. Within the statistical and systematic errors, the $\Lambda_b \to J/\psi\pi^-p$ data are consistent with the $P_c(4380)^+$ and $P_c(4450)^+$ production rates expected from the previous observation in $\Lambda_b \to J/\psi K^-p$. Assuming $Z_c(4200)$ is negligible, a 3.3σ significance is found for both P_c^+ states together.

5 Exotic $J/\psi\phi$ states

LHCb has performed the first full amplitude analysis of a sample of 4289 ± 151 $B^+ \to J/\psi\phi K^+$ decays, with $J/\psi \to \mu^+\mu^-$ and $\phi \to K^+K^-$, obtained with the $3fb^{-1}$ integrated luminosity of the LHC Run-1 [52]. A good description of the data in the 6D phase space, composed of invariant masses and decay angles, is obtained. The data cannot be described by a model that contains only excited kaon states decaying into ϕK^+, and four structures are observed [52], each with significance over 5σ. The J^{PC} quantum numbers of these structures and their significance within the fit model are indicated in Table 1.

The K^{*+} amplitude model extracted from the data is consistent with expectations from the quark model and from the previous experimental results in such resonances. The model includes signicant contributions from a number of expected kaon excitations, including the first observation of the $K^*(1680)^+ \to \phi K^+$ transition. The J^{PC} quantum numbers of the X(4140) structure have been determined to be 1^{++}. This has a large impact on its possible interpretations, in particular ruling out 0^{++} or 2^{++} $D_s^{*+}D_s^{*-}$ molecular models. The X(4140) width is substantially larger than previously determined. As discussed in [53], the data indicate that this structure is possibly an effect due to the below-threshold $D_s^{\pm}D_s^{*\mp}$ cusp. The near coincidence

	Mass (MeV)	Width	J^{PC}	nσ
X(4140)	$4146.5 \pm 4.5^{+4.6}_{-2.8}$	$83 \pm 21^{+21}_{-14}$	1^{++}	8.4 / 5.7
X(4274)	$4273.3 \pm 8.3^{+17.2}_{-3.6}$	$56 \pm 11^{+8}_{-11}$	1^{++}	6.0 / 5.8
X(4500)	$4506.0 \pm 11^{+12}_{-15}$	$92 \pm 21^{+21}_{-20}$	0^{++}	6.1 / 4.0
X(4700)	$4704.0 \pm 10^{+14}_{-24}$	$120 \pm 31^{+42}_{-33}$	0^{++}	5.6 / 4.1

Table 1: Summary of resonance parameters and quantum numbers of the $J/\psi\phi$ structures, with their significance $n\sigma$ (resonance/J^{PC}).

of the $D_s^{\pm}D_s^{*\mp}$ and $J/\psi\phi$ mass thresholds provides suitable conditions for the rearrangement of $(c\bar{s})(\bar{c}s)$ to $(c\bar{c})(\bar{s}s)$.

The existence of the X(4274) structure has been established with a significance of $6.0\,\sigma$, and its quantum numbers determined to be 1^{++}. Due to interference effects, the data peak above the pole mass, underlining the importance of proper amplitude analysis. Molecular bound states or cusps cannot account for the observed J^{PC} assignment. A hybrid charmonium state would have $J^{PC} = 1^{-+}$. A discussion of its feasibility in various tetraquark models and lattice QCD calculations can be found in Refs. [52, 53]

The high $J/\psi\phi$ mass region was investigated for the first time with good sensitivity and shows very significant structures, which can be described as two 0^{++} resonances: X(4500) and X(4700). Its possible concordance with predicted virtual $D_s^{*+}D_s^{*-}$ states is also discussed in [52]. None of the observed $J/\psi\phi$ states is consistent with the state seen in the two-photon collisions by the Belle collaboration [54].

References

[1] The LHCb collaboration, R. Aaij et al. arXiv:1604.03475 (2016)

[2] The LHCb collaboration, R. Aaij et al. N. J. Phys. **15** (2013) 053021

[3] The D0 collaboration, V. M. Abazov et al., PRL **105** (2010) 081801

[4] The LHCb collaboration, arXiv: 1605.09768 (2016), submitted to PRL

[5] The LHCb collaboration, R. Aaij et al. , Phys. Rev. Lett. **114**, 041601 (2015)

[6] The LHCb collaboration, R. Aaij et al. , Phys. Lett. **B736**, 186 (2014)

[7] The LHCb collaboration, R. Aaij et al. , Phys. Rev. Lett. **114** 041801 (2015)

[8] The LHCb collaboration, JHEP **11** (2015) 082

[9] K. De Bruyn R. Fleischer, JHEP **03** (2015) 145

[10] The BaBar collaboration, Phys. Rev. **D87** (2013) 052015.

[11] The Belle collaboration, arXiv: 1301.2033.

[12] LHCb-PAPER-2016-032, in preparation.

[13] The Review of Particle Physics, C. Patrignani et al., Chin. Phys. **C40**, 100001 (2016).

[14] The LHCb collaboration, PRL **115**, 031601 (2015)

[15] O. Greenberg, Phys. Rev. Lett. **89** (2002) 231602

[16] D. Colladay and V. A. Kostelecky, Phys. Rev. **D58** (1998) 116002

[17] The LHCb Collaboration, R. Aaij et al. , Phys. Rev. Lett. **116** (2016) 241601

[18] The CMS and LHCb collaborations, Nature Letter **522** (2015) 68.
[19] The LHCb collaboration, R. Aaij et al., arXiv:1304.6325.
[20] The LHCb collaboration, R. Aaij et al., JHEP **02** (2016) 104.
[21] The Belle collaboration, arXiv: 1604.04042.
[22] S. Descotes-Genon et al., JHEP **12** (2014) 125.
[23] W. Altmannshofer S. Straub, Eur. Phys. **J C75** (2015) 382.
[24] The LHCb collaboration, PRL **113** (2014) 151601
[25] The Babar collavoration, PRD **88** (2013) 072012, also PRL 109 101802
[26] The LHCb collaboration, R. Aaij et al. PRL **115**, 111803 (2015)
[27] Belle Collaboration, M. Huschle et al. , Phys. Rev. **D92**, 072014 (2015).
[28] Belle Collabaration, Y. Sato et al., arXiv:1607.07923.
[29] V. Vagnoni, ICHEP 2016, Chicago August 3-10.
[30] The LHCb collaboration, R. Aaij et al. JHEP **10** (2015) 034.
[31] A. Ali, A. Parkhomenko, A. Rusov, Phys. Rev. **D89** (2014),
[32] Fermilab Lattice and MILC collaborations, J. A. Bailey et al. arXiv:1507.01618
[33] C. Hambrock, A. Khodjiamiriam and A. Rusov, arXiv:1506.07760.
[34] Fermilab Lattice and MILC collaborations, Daping Du et al. arXiv: 1510.02349 (2016)
[35] T. Blake, G. Lanfranchi, D.M. Straub, arXiv:1606.0091 (2016)
[36] R. D. Peccei and H. R. Quinn, Phys. Rev. Lett. **38**, 1440 (1977).
[37] O. Adriani et al. (PAMELA collaboration), Phys. Rev. Lett. **111**, 081102 (2013).
[38] M. Aguilar et al. (AMS collaboration), Phys. Rev. Lett. **113**, 121102 (2014).
[39] M. Freytsis, Z. Ligeti, and J. Thaler Phys. Rev. **D 81**, 034001 (2010).
[40] M. Dine, W. Fischler, and M. Srednicki, Phys. Lett. B **104**, 199 (1981).
[41] A. R. Zhitnitsky, Sov. J. Nucl. Phys. **31**, 260 (1980).
[42] L. J. Hall and T. Watari, Phys. Rev. D. **70** (2004) 115001.
[43] F. Bezrukov, and D. Gorbunov, J. High Energy Phys. **05** 010 (2010).
[44] The LHCb collaboration, R. Aaij et al., Phys. Rev. Lett. **115**, 161802 (2015).
[45] F. Bezrukov and D. Gorbunov, Phys. Lett. **B736**, 494 (2014).
[46] F. Bergsma et al. (CHARM collaboration), Phys. Lett. **B157**, 458 (1985).
[47] M. Gell-Man, Phys. Lett. **8**, 214 (1964), G. Zweig, Report No. CERN-TH-401.
[48] The LHCb collaboration, R. Aaij et al., Phys. Rev. Lett. **115**, 072001 (2015).
[49] The LHCb collaboration, R. Aaij et al., arXiv:1604.05708 (2016).
[50] The LHCb collaboration, R. Aaij et al., arXiv:1606.06999 (2016).
[51] K. H. Hicks Eur. Phys. J. **H37** (2012).
[52] The LHCb collaboration, R. Aaij et al., arXiv:1606.07895 (2016), submitted to PRL.
[53] The LHCb collaboration, R. Aaij et al., LHCb-PAPER-2016-019, arXiv:1606.07898, submitted to PRD.
[54] Belle collaboration, C. P. Shen et al. Phys. Rev. Lett. **104** (2010) 1120045, arXiv:0912.2383.

Search for Resonances and New Physics

Nuno T. Leonardo

Laboratório de Instrumentação e Física Experimental de Partículas, Lisbon, Portugal

DOI: http://dx.doi.org/10.3204/DESY-PROC-2016-04/Leonardo

The appearance of new resonances is a most spectacular means by which physics beyond the standard model may be revealed at the LHC. Searches are conducted for bumps in mass spectra exploring a multitude of final states. Results are presented spanning from sub-GeV to multi-TeV scales.

1 Introduction

The Large Hadron Collider (LHC) is currently the world's energy and intensity frontier hadron accelerator, providing collisions at record center-of-mass energies and high luminosities. The LHC along with its detectors is allowing to collect unique datasets of unprecedented size, quality, and potential for physics discovery.

The LHC has completed in early 2013 its first running phase (Run1) and the experiments have collected data sets of proton-proton (pp) collisions at centre-of-mass energies of 7 and 8 TeV with integrated luminosities of about 5 and 20 fb^{-1}, respectively. After an upgrade period for both accelerator and detectors, the second data taking period (Run2) started in mid 2015 at 13TeV, and the experiments had collected already in excess of 15 fb^{-1} at the time the school took place in Dubna. In addition to its main pp programme, the LHC provides collisions involving heavy ions. Valuable datasets of lead-lead (PbPb) and proton-lead (pPb) collisions have been gathered, at centre-of-mass energies per nucleon pair of 2.76 and 5.02 TeV.

Analyses of the collected data have produced a rich set of physics results. These include detailed measurements of a variety of processes, and extensive searches, both indirect and direct, for new particles. The discoveries achieved so far include new particle states and new processes. Among many others these count the observation of a new resonance, compatible with the Higgs boson, and of an ultra-rare process (B_s meson decay into two muons) in pp collisions, and of sequential meson melting of quark-antiquark bound states in PbPb collisions. The results attained in Run1 have lead to the corroboration of the standard model of particle physics (SM) as an extremely successful effective theory and to the exclusion of large, relevant regions of the parameter space available for proposed scenarios extending the SM.

The exploration of the datasets being collected at the new record energy of 13TeV, as well as the ones that will be gathered over the next decades with enhanced accelerator and detectors (the High-Luminosity LHC phase), hold the enormous potential of detecting New Physics, beyond the SM, thus allowing for ground-breaking advancements in our understanding of Nature at the most fundamental level.

2 Detection

The collisions are produced at the center of the detectors – ATLAS, CMS, ALICE and LHCb – that register the debris of the collisions used to reconstruct and study the involved physics processes. ATLAS and CMS are general-purpose detectors, while ALICE and LHCb are specialised in the study of collisions with heavy ions and of processes involving b and c quarks, respectively.

Figure 1 illustrates the particle reconstruction process at CMS. The central feature of the CMS apparatus is a superconducting solenoid of 6m internal diameter, providing a magnetic field of 3.8T. Within the solenoid volume are a silicon pixel and strip tracker, a lead tungstate crystal electromagnetic calorimeter (ECAL), and a brass and scintillator hadron calorimeter (HCAL), each composed of a barrel and two endcap sections. Forward calorimeters extend the pseudorapidity coverage provided by the barrel and endcap detectors. Muons are measured in gas-ionisation detectors embedded in the steel flux-return yoke outside the solenoid.

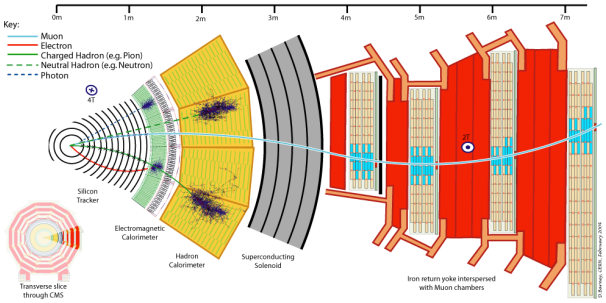


Figure 1: Illustration of particle reconstruction in a general-purpose detector (CMS).

Information from the various elements of the detector is used to reconstruct and identify the stable particles produced in the collisions, by what is dubbed a particle-flow algorithm. The energy of photons is directly obtained from the ECAL measurement, corrected for zero-suppression effects. The energy of electrons is determined from a combination of the electron momentum at the primary interaction vertex as determined by the tracker, the energy of the corresponding ECAL cluster, and the energy sum of all bremsstrahlung photons spatially compatible with originating from the electron track. The energy of muons is obtained from the curvature of the corresponding track. The energy of charged hadrons is determined from a combination of their momentum measured in the tracker and the matching ECAL and HCAL energy deposits, corrected for zero-suppression effects and for the response function of the calorimeters to hadronic showers. Finally, the energy of neutral hadrons is obtained from the corresponding corrected ECAL and HCAL energies. Figure 2 displays reconstructed collision events. In addition to the underlying event, pairs of energetic muon, electron, photon, and jet candidates are featured.

The LHC collisions (bunch crossings) occur at a rate of 40 million times per second. Only a small fraction of which is read out and selected in real time to be recorded for later analysis. The filtering involved is a critical step, and is implemented by a two-tiered trigger system. The first level (L1), composed of custom hardware processors, uses information from the calorimeters and muon detectors to select events at a rate of around 100kHz within a time interval of less than 4μs. The second level, known as the high-level trigger (HLT), consists of a farm of processors running a version of the full event reconstruction software optimised for fast processing, and reduces the event rate to less than 1kHz before data storage.

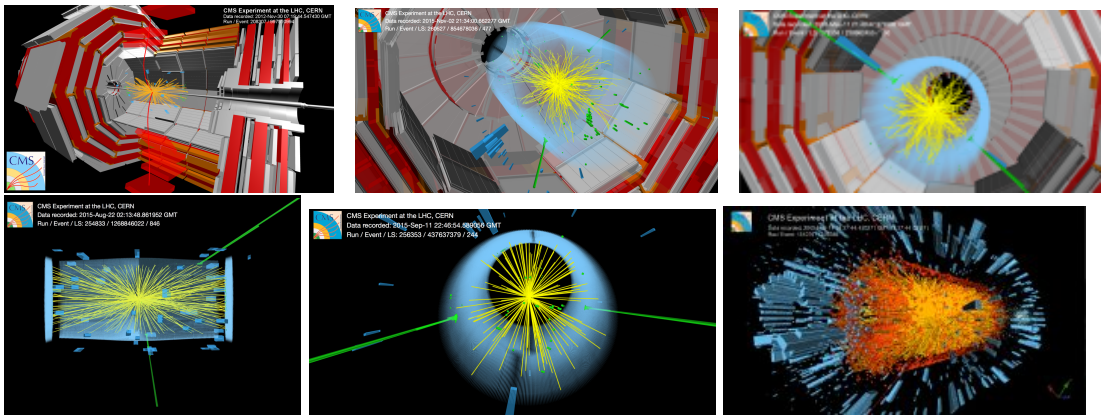


Figure 2: Collision events displaying the following featured candidates (ordered left-to-right, top-to-bottom): di-muon, di-electron, di-photon, di-jet, di-photon with the solenoid turned-off, all in pp collisions, and di-muon in a PbPb collision.

3 Low-mass resonances

Muon signals are cleanly reconstructed, with high accuracy down to low transverse momentum (p_{T}), reaching precisions of 1-2% in the central CMS detector. The probability of misidentifying other particles (hadrons) as muons is low, down to the permill level. Figure 3 displays the di-muon mass spectrum, obtained with data collected in 2016 at 13TeV. It illustrates the ability of the detector to precisely explore a wide-range of particle energies and masses across the spectrum, from the light vector mesons, ω, ϕ, to quarkonia ($J/\psi, \Upsilon$), to the Z^0 vector boson and well beyond it. Note that in order to display the precision achieved across different orders of magnitude, the graph is constructed with a variable width binning in doubly log scales.

Multi-muon signals are explored extensively. Coupled with other particles and vertex-displacement criteria, they form the baseline for online selection of heavy flavors at the general-purpose detectors. In addition to generic, high-p_{T} double-muon trigger algorithms, shown in light gray, Fig. 3 highlights dedicated algorithms, with low-p_{T} thresholds, in specific mass windows.

Quarkonia, heavy quark-antiquark bound states, are extensively explored, forming a laboratory in which to study the strong interaction and, in particular, the mechanisms of hadron production. Precision measurements of produc-

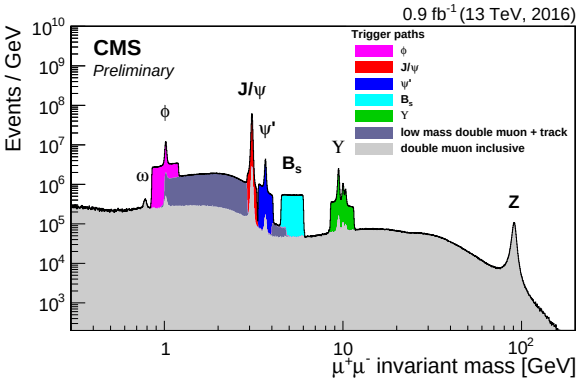


Figure 3: Di-muon mass spectrum.

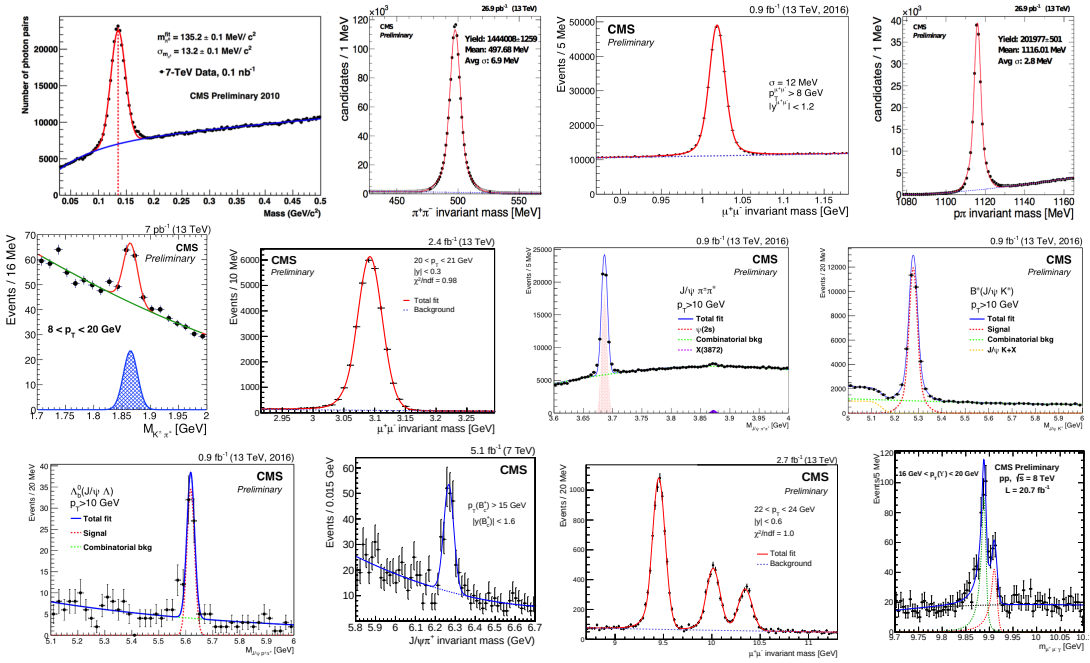


Figure 4: Selected hidden and open flavour resonances, from 0.1 to 10 GeV (ordered from left-to-right, top-to-bottom): π^0, K^0_s, $\phi(1020)$, Λ, D^0, J/ψ, ψ' and X(3872), B^+, Λ^0_b, B^+_c, Υ(nS), χ_b.

tion cross sections and polarisations are performed, which are in turn jointly used to constrain parameters of QCD effective models (e.g. non-relativistic QCD). The properties of hadrons containing b-quarks, identified by their characteristic long lifetimes and corresponding measurable displacement in the detector, are explored in detail which result is high precision tests of

the SM. Figure 4 shows a selection of hadronic signals.

Various final states, involving muons, photons, and light hadrons, are employed to search for new resonant states at low mass. The outcome of these searches includes the first experimental observation of new meson and baryon states, specifically excited states of the χ_b, B_c, or Ξ_b hadrons, as shown in Fig. 5. These observations involve relatively complex decay topologies, of up to six final state particles and four distinct displaced vertices, or low-energy photon conversion to electron-positron pairs in the material of the inner detector.

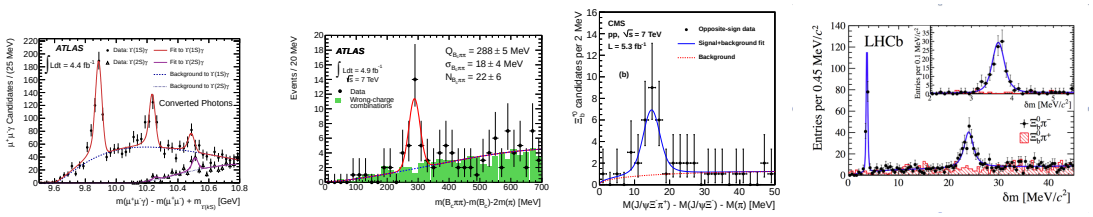


Figure 5: New low-mass resonances (anticipated) (ordered left-to-right): $\chi_b(3P)$; $B_c(2S)$; Ξ_b^{*0}; $\Xi_b^{\prime -}$ and Ξ_b^{*-}.

In addition to searching for structures directly in mass spectra, multi-body final-state hadronic decays are explored to search for new resonant structures in the decay products. For example, the decay $B^+ \to \psi\phi K^+$ is used to explore possible structures in the $\psi\phi$ invariant mass. As displayed in Fig. 6, enhancements in the $J/\psi\phi$ spectrum have been identified by

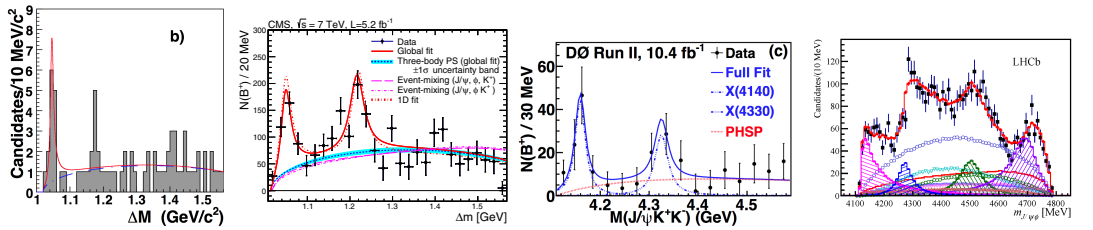


Figure 6: New low-mass resonances (unanticipated). Structures in the $J/\psi\phi$ mass spectra identified at 4.140, 4.274, 4.500, 4.700 GeV.

different experiments, between 4 and 5 GeV. These are unanticipated structures that add to the growing list of candidates for exotic, hadronic particles, which started to be formed with the observation of the X(3872) by Belle more than a decade ago. Further data should allow measurements of their properties and contribute to a clarification of their nature.

The decay process $\Lambda_b^0 \to J/\psi pK$ is explored to tag the $J/\psi p$ final state. A full amplitude analysis of the process achieves a best description of the data, shown in Fig. 7, with the addition of two new states, with masses near 4.4GeV. These new resonances decaying strongly into $J/\psi p$ should have a minimum quark content of $c\bar{c}uud$, thus being hidden-charm pentaquark candidates (labeled P_c^+). The high-yield $B_s^0 \to J/\psi\phi$ channel is explored to search for new, prompt states. Evidence of an excess in the $B_s^0\pi$ invariant mass has been reported, which could be interpreted as an open-beauty tetraquark candidate. However, independent confirmation of the excesses has not been achieved.

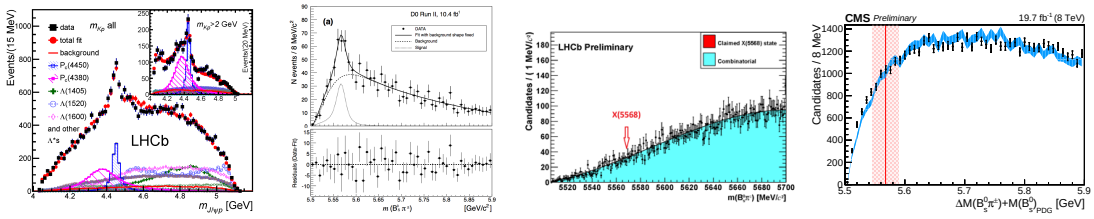


Figure 7: New low-mass resonances (unconfirmed). (leftmost) observation of two pentaquark candidates with masses about 4.4GeV; (others) evidence and search for a tetraquark candidate with mass of about 5.6 GeV.

The complementary study of the strong sector is achieved by exploring collisions involving heavy nuclei. Exclusive measurements of a variety of particle states in heavy-ion collisions have been or will be achieved for the first time at the LHC, which serve as precious hard probes of the hot and dense medium. These include heavy-flavor states, such as b and c quark hadrons, W and Z bosons, and eventually the top quark. Among a large set of unique results achieved, a Run1 highlight is the observation of sequential quarkonium suppression – a spectacular indication of quark-gluon plasma (QGP) formation at the LHC. The relative suppression of the three Υ(nS) states offer sa rare picture of a clear effect in a complex environment – as shown in Fig. 8, not only is each Υ state suppressed in PbPb compared to pp collisions, but the excited states are significantly more suppressed.

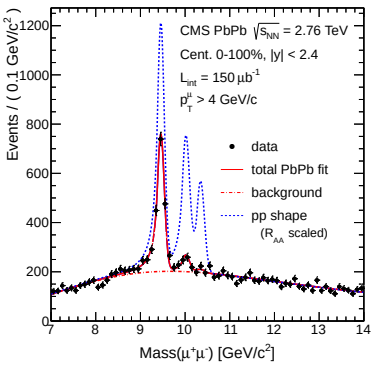


Figure 8: Observation of onia sequential suppression.

The exploration of low-mass spectra in pp collisions involves also the search for new light elementary particles. A search is performed for pair production of new light bosons (a) decaying to pairs of isolated di-muons. One production mechanism for these new bosons is in the decay chain of a Higgs boson (h): $h \to 2a + X \to 4\mu + X$, where X denotes possible additional particles from cascade decays of the Higgs boson. The data mass spectrum is shown in Fig. 9 and does not feature any significant addition beyond the resonance states $\omega, \rho, \phi, \mathrm{J}/\psi$ that are here backgrounds for the analysis. While the search is designed to be model independent, a range of BSM scenarios predict this decay topology, including the next-to-minimal supersymmetric standard model (NMSSM) and models with hidden or dark sectors. Production limits are placed in the context of these benchmark BSM scenarios.

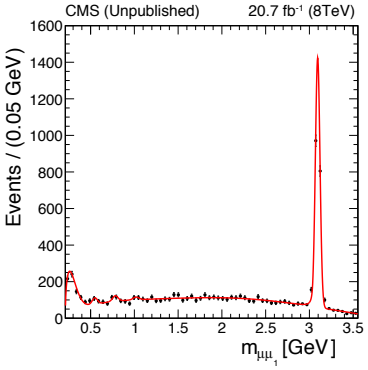


Figure 9: Search for pairs of resonances $h \to 2a \to 4\mu$.

The study of electroweak decays of heavy-flavored hadrons continues to provide stringent SM tests. A class

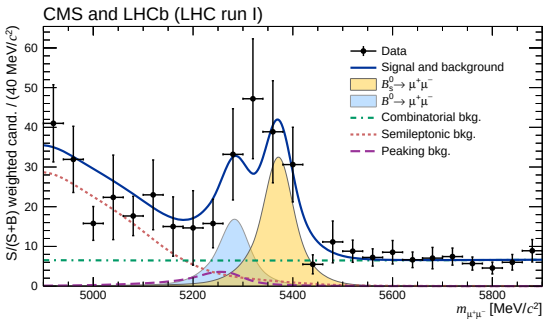


Figure 10: Observation of $B_s^0 \to \mu\mu$.

of processes that is particularly sensitive to BSM effects is provided by rare decays. The study of $B \to K^{(*)}\mu\mu$ decays have resulted in deviations at the 3σ level relative to theory predictions (which are however made challenging due to hadronic form factors). The theoretically clean, ultra-rare processes $B_{(d)}^0 \to \mu\mu$ are extremely suppressed in the SM and therefore particularly sensitive to BSM effects. Their search has spanned about three decades across different experiments in different colliders. SM-level sensitivity is attained only with the LHC. The separate analyses of the Run1 datasets collected by the CMS and LHCb experiments resulted in 4.3σ and 4.0σ evidence for the B_s^0 decay, respectively, while the combined fit to the two datasets, performed by the collaborations and shown in Fig. 10, yielded a significance in excess of 6σ. While the analysis was optimised for the B_s^0 search, an excess was also obtained at the 3σ-level for the B^0 decay, which is however more directly affected by the estimation of the contribution from b-hadron two-body hadronic decays when muons are misidentified that peak in the signal region. The analysis result is compatible with the SM, and exclude vast regions of the parameter space of BSM models. The result is regarded as one of the flagship discoveries of LHC Run1.

4 Intermediate-mass resonances

Isolated leptons allow to reconstruct the SM vector bosons W and Z, across the different collisions energies and systems provided by the LHC, as shown in Fig. 11. These serve as standard

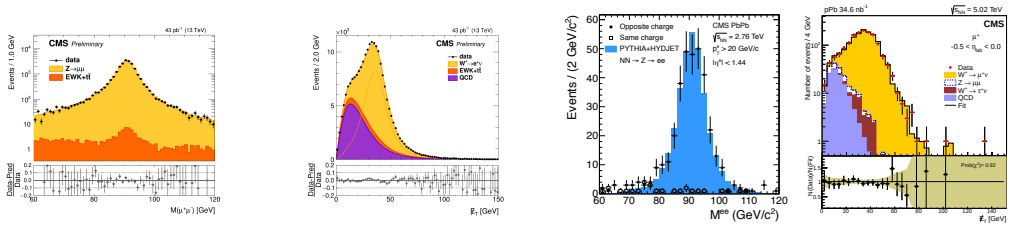


Figure 11: Vector bosons reconstruction. Ordered left-to-right: $Z^0 \to \mu\mu$ and $W^\pm \to e\nu_e$, in pp; $Z^0 \to ee$, in PbPb collisions; $W^\pm \to \mu\nu_\mu$, in pPb collisions.

candles for detector and simulation calibration at high p_T, references for searches of heavier

(BSM) gauge bosons, and as final-state particles in searches for heavier resonances. Precision measurements of production and decay are carried out in pp collisions. The vector bosons have now been observed for the first time also in collisions involving nuclei. They serve as colourless probes that remain unaffected by the hot and dense QCD medium produced, and thus as control for processes expected to be heavily modified in the nuclear media.

One of the original goals of the LHC physics program was the clarification of the electroweak symmetry breaking mechanism. The ATLAS and CMS collaborations first reported the discovery of a new boson in 2012, at a mass of abut 125 GeV. The experimental evidence collected since is consistent with the particle being the Higgs boson, the quantum of the scalar field postulated by the Higgs mechanism. Figure 12 shows the 2-photon and 4-muon mass spectra obtained with recent data, illustrating the boson's re-discovery in Run2. The measurement of the particle's properties with improving precision, also exploring rarer channels, will continue to be pursued with priority with the increasing dataset.

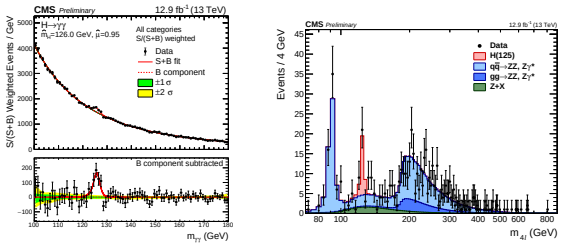


Figure 12: Higgs (LHC Run2) re-discovery.

The new scalar, along with the vector bosons, is explored in the search for BSM effects, via the study of or search for rare or SM-forbidden production and decay modes. The Higgs searches are further extended to higher mass ranges, as also illustrated in Fig. 12 (for the lepton channel). The search for heavier di-photon resonances is similarly explored, as in Fig. 13.

Much excitement was raised by a modest excess at a mass of about 750 GeV in the di-photon data collected in 2015. This raised discussions about possible explanations in terms of new physics and the possible production of a new, BSM particle decaying to two photons. The (local) statistical significance of the excess was between 3σ and 4σ for the ATLAS and CMS experiments, reducing to 2σ and less once the effect of searching under multiple signal hypotheses is considered (global significance). However, at mass and widths corresponding to the largest deviations from the background-only hypothesis in the 2015 data, no large excess is observed in the 2016 data.

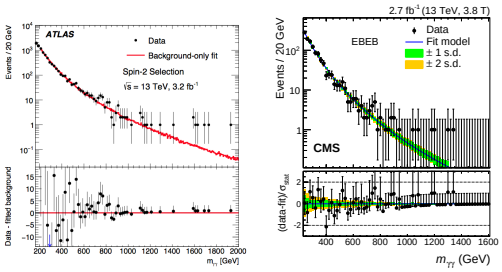


Figure 13: An excess at 750 GeV ?

The main reason for the original 750 GeV excitement was arguably that compatible excesses were detected by two independent experiments in the first place. However, in general, fluctuations at similar level should not come as a surprise – considering the large number of searches for new particles that are performed, we are guaranteed to occasionally see excesses in some regions of some analyses purely from statistical fluctuations of the data.

5 High-mass resonances

The search for massive resonances is pursued similarly in a multitude of ways.

Many BSM models require new particles that couple to quarks and gluons and can be observed as resonances in the di-jet mass spectrum. The spectrum arises from the scattering of partons at high p_T and is predicted by QCD to fall smoothly with increasing di-jet mass. The search for new resonances is pursued in a model-independent way, by inspecting the spectrum shown in Fig. 14, here probed up to 8 TeV, and hunting for bumps. No significant excess is observed and predicted signals from narrow gluon-gluon, quark-gluon, and quark-quark resonances are shown therein with cross sections equal to the observed upper limits at 95% CL.

The di-lepton spectra, shown in Fig. 15 for opposite-sign muons, electrons, muon-electron, and taus, is searched also for high-mass resonance states. No clear, significant excesses above the SM backgrounds are found, and limits are placed on benchmark BSM models.

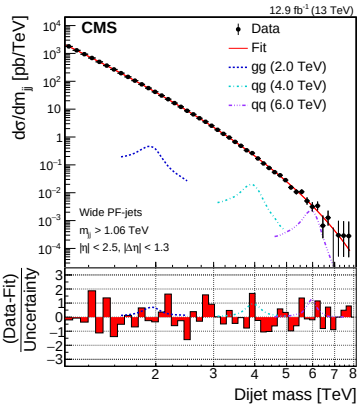


Figure 14: Di-jet spectrum.

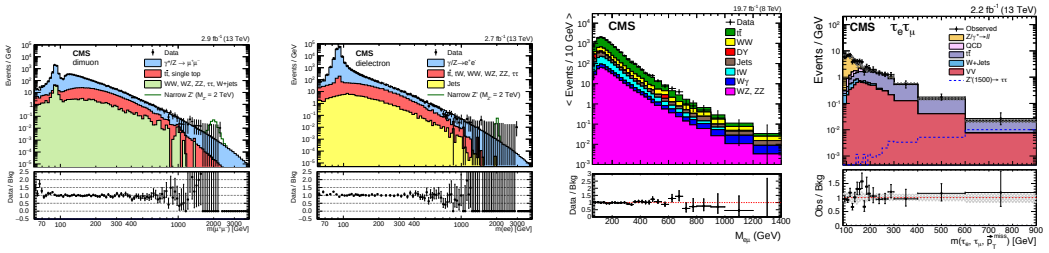


Figure 15: Searches for high-mass resonances in di-lepton spectra: $\mu\mu, ee, \mu e, \tau\tau$.

BSM resonances are searched for also in their decays to di-bosons, including the new scalar (H), as shown in Fig. 16. Sufficiently massive resonances tend to produce highly Lorentz-boosted objects, which yield collimated decay products; when these are partially or fully merged into single jets, methods to analyse jet substructure and suitable jet-tagging techniques are employed.

When no significant excess is observed in the data, exclusion limits on specific benchmark models are placed. Figure 17 provides an overall summary of the exclusion limits achieved in the context of the specified categories of BSM scenarios. The analysis of the 8TeV data and specially of the initial 13TeV data recently collected results in exclusion limits of around several TeV.

6 Exotic resonances

With the goal of 'leaving no stone unturned', searches are performed exploring less conventional signatures. These tend also to often require less orthodox analysis strategies, such as dedicated

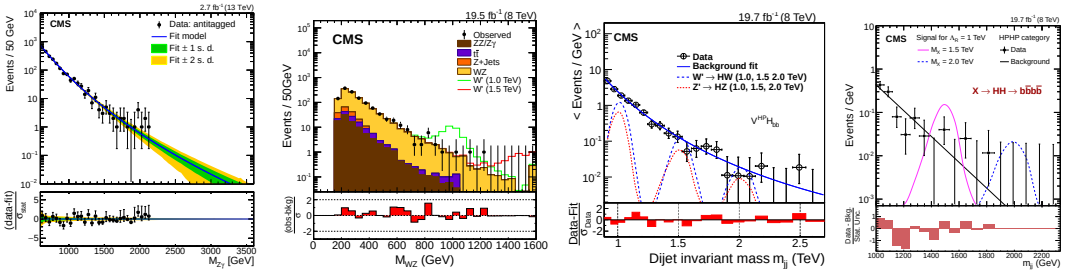


Figure 16: Searches for new, massive resonances in the di-boson spectra: $Z\gamma, WZ, HW, HH$. Specific candidate BSM states are also overlaid, for illustration purposes, which are however not corroborated by the data.

approaches to trigger selection and event processing and reconstruction. One may opt to collect data in a dedicated stream that reads out only selected sub-detector elements instead of the full event (data scouting). One may select events un-asynchronously with the LHC collisions (in between bunch-crossings, in order to collect exotic particles with highly delayed decays). Or search for resonances that, being sufficiently long lived, would have time to travel away from the collision point and decay at a highly displaced vertex – as BSM scenarios such as hidden valleys and stealth or RPV or displaced SUSY among others would have it. The exclusion limits are summarised in Fig. 17 also for some of these more exotic scenarios.

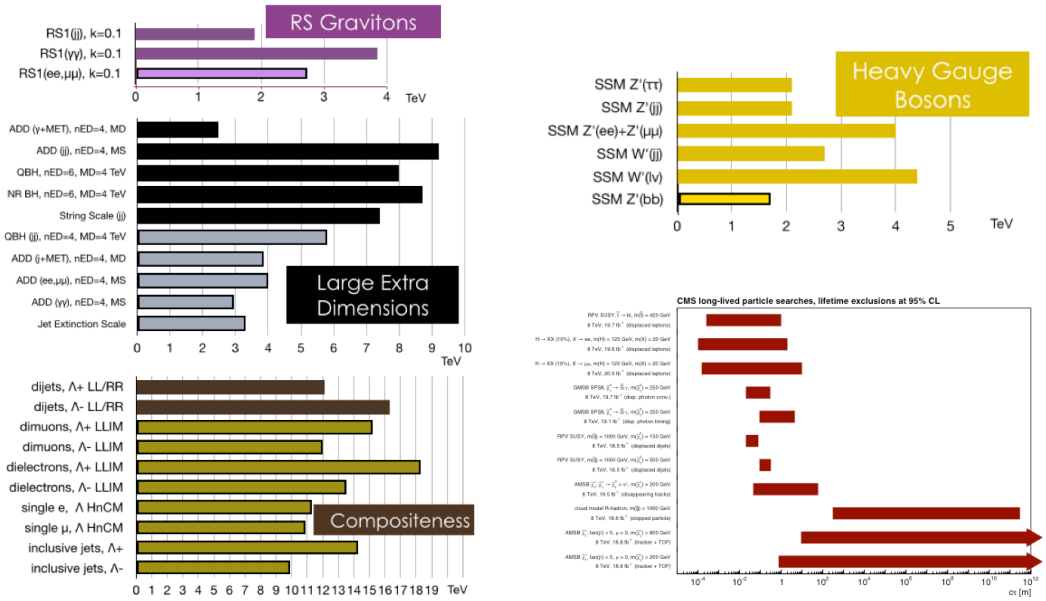


Figure 17: Summary of current 95% CL upper exclusion limits on the mass of new resonances in various BSM scenarios.

7 Conclusion

The LHC and its detectors have had an extremely successful first running period, and are initiating its second data-taking period at higher collision energies. Various new resonances – both anticipated and unexpected – have been discovered. In addition, new processes and phenomena have been observed, and old ones probed to unprecedented precision. The standard model has in the process been reinforced as an extremely successful effective theory. The bulk of the LHC data that will be gathered over the coming years and decade carry the promise and potential of detecting what physics lies beyond it – the overarching goal we pursue.

Acknowlegements:
The author acknowledges support by grants FCT IF/01454/2013/CP1172/CT0003 and CERN/FP/123601/2011, Portugal. He wishes to thank the organisers for the Lecture invitation and the wonderful gathering in Dubna.

General references

[1] ATLAS Collaboration public results,
`https://twiki.cern.ch/twiki/bin/view/AtlasPublic`

[2] CDF Collaboration public results,
`https://www-cdf.fnal.gov/physics/physics.html`

[3] CMS Collaboration public results,
`http://cms-results.web.cern.ch/cms-results/public-results/publications/`

[4] D∅ Collaboration public results,
`http://www-d0.fnal.gov/d0_publications`

[5] LHCb Collaboration public results,
`http://lhcbproject.web.cern.ch/lhcbproject/Publications/LHCbProjectPublic/Summary_all.html`

New results on the XYZ states and B-decays from Belle

Makoto Takizawa[1,2,3,4]

[1]Showa Pharmaceutical University, Machida, Tokyo, 194-8543, Japan
[2]Theoretical Research Division, Nishina Center, RIKEN, Wako, Saitama 351-0198, Japan
[3]J-PARC Branch, KEK Thery Center, IPNS, KEK, Tokai, Ibaraki, 319-1106, Japan
[4]On behalf of the Belle Collaboration

DOI: http://dx.doi.org/10.3204/DESY-PROC-2016-04/Takizawa

We present the recent results on the XYZ states and B-decays measured by the Belle detector at the KEKB e^+e^- collider.

1 Introduction

The Belle experiment ran at the KEKB [1] e^+e^- asymmetric energy collider between 1999 and 2010 and the total integrated luminosity reached 1040 fb^{-1}. Most of the data were taken at the energy of the $\Upsilon(4S)$ resonance in order to study the B physics, but other energy data were taken as listed in Table 1. The physics events were detected by the general purpose Belle spectrometer [2], which consists of a silicon vertex detector, a central drift chamber, an array of aerogel Cherenkov counters, a barrel-like arrangement of time-of-flight scintillation counters and an electromagnetic calorimeter. Arrays of resistive plate counters interspersed in the iron yoke is used for the identification of muons and K_L mesons. The physics achievements from the Belle experiment until 2012 are reviewed in Ref. [3] and the physics results from the B-factories until 2014 are reviewed in Ref. [4].

Concerning the XYZ states, Particle Data Group (PDG) uses the naming X for all XYZ states. On the other hand, in the many literatures, the Y's are used for the states of $J^{PC} = 1^{--}$ with the energy range of the charmonia but seem not to be considered as the charmonia. As for the Z_c's (Z_b's), the Z_c's (Z_b's) are the meson states including $c\bar{c}$ ($b\bar{b}$) with electric charge, and therefore, the minimal quark content for Z_c^+ is $c\bar{c}u\bar{d}$. The Z_c's and Z_b's are considered as isospin 1 states and there exist the neutral states with same isospin multiplet. Such states are also called Z states. We use the X for all other types of the exotic mesons. The recent status of XYZ states is reviewed in Ref. [5].

2 Bottomonium-like hadrons

2.1 Anomalous $\Upsilon(nS)\pi^+\pi^-$ (n=1,2,3) production near $\Upsilon(5S)$ resonance

The $\Upsilon(10860)$ resonance is the $J^{PC} = 1^{--}$ state with the mass of 10876 ± 11 MeV/c^2 and the width of 55 ± 28 MeV. The main component of this resonance is considered as the 5th excited

Resonance	On-peak luminosity (fb^{-1})	Off-peak luminosity (fb^{-1})	Number of resonances
$\Upsilon(1S)$	5.7	1.8	102×10^6
$\Upsilon(2S)$	24.9	1.7	158×10^6
$\Upsilon(3S)$	2.9	0.25	11×10^6
$\Upsilon(4S)$	711.0	89.4	772×10^6
$\Upsilon(5S)$	121.4	1.7	7.1×10^6
Scan		27.6	

Table 1: Summary of the luminosity of the Belle experiment. "On-peak" means the energy is just at the resonance points and "Off-peak" means the energy is 60 MeV below the resonance points. "Scan" means the energy is scanned between the $\Upsilon(4S)$ and $\Upsilon(6S)$ resonances.

state (including the ground state) of the orbital angular moment $L = 0$ bottomonium, and therefore, sometimes called $\Upsilon(5S)$. Its mass is above the open bottom threshold and the decays to $B\bar{B}$, $B\bar{B}^*$, $B^*\bar{B}^*$ and $B_s\bar{B}_s$ have been observed. In 2008, Belle reported the first observation of $e^+e^- \to \Upsilon(1S)\pi^+\pi^-$, $\Upsilon(2S)\pi^+\pi^-$ and first evidence for $e^+e^- \to \Upsilon(3S)\pi^+\pi^-$, $\Upsilon(1S)K^+K^-$ near the peak of the $\Upsilon(5S)$ resonance at $\sqrt{s} \sim 10.87$ GeV [6]. The $\Upsilon(nS)$ was detected through the $\Upsilon(nS) \to \mu^+\mu^-$ decay mode. Signal candidates were identified using the kinematic variable ΔM, defined as the difference between $M(\mu^+\mu^-\pi^+\pi^-)$ or $M(\mu^+\mu^-K^+K^-)$ and $M(\mu^+\mu^-)$ for pion or kaon modes. The signal events should be concentrated at $\Delta M = \sqrt{s} - M_{\Upsilon(nS)}$ and results are given in Fig. 1. By analyzing the data and assuming the $\Upsilon(5S)$ to be the sole

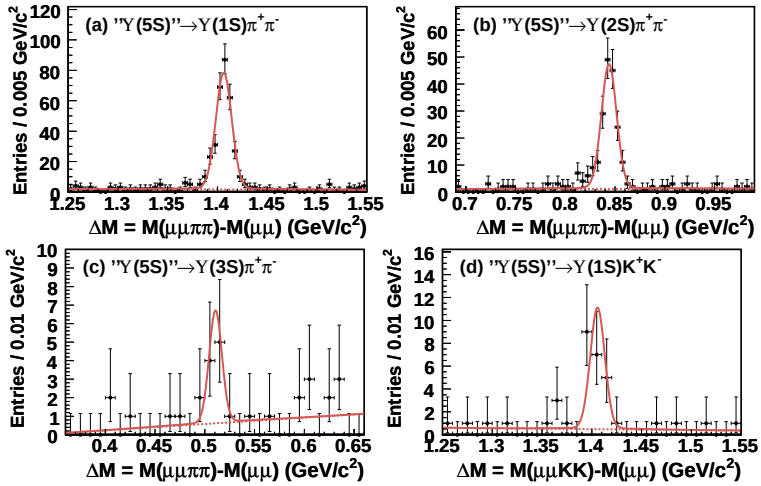


Figure 1: The ΔM distributions for (a) $\Upsilon(1S)\pi^+\pi^-$, (b) $\Upsilon(2S)\pi^+\pi^-$, (c) $\Upsilon(3S)\pi^+\pi^-$, and (d) $\Upsilon(1S)K^+K^-$ with the fit results superimposed. The dashed curves show the background components in the fits. Figures are taken from Ref. [6]

source of the observed events, the partial decay widths have been obtained. The results are summarized in Table 2. The measured partial widths , of order $0.6 - 0.9$ MeV, are more than 2 orders of magnitude larger than the corresponding partial widths for $\Upsilon(4S)$, $\Upsilon(3S)$ or $\Upsilon(2S)$

Process	N_s	Σ	Γ(MeV)
$\Upsilon(1S)\pi^+\pi^-$	325^{+20}_{-19}	20σ	$0.59 \pm 0.04 \pm 0.09$
$\Upsilon(2S)\pi^+\pi^-$	186 ± 15	14σ	$0.85 \pm 0.07 \pm 0.16$
$\Upsilon(3S)\pi^+\pi^-$	$10.5^{+4.0}_{-3.3}$	3.2σ	$0.52^{+0.20}_{-0.17} \pm 0.10$
$\Upsilon(1S)K^+K^-$	$20.2^{+5.2}_{-4.5}$	4.9σ	$0.067^{+0.017}_{-0.015} \pm 0.013$

Table 2: Signal yield (N_s), significance (Σ) and the partial widths (Γ) for $\Upsilon(5S) \to \Upsilon(nS)\pi^+\pi^-$ and $\Upsilon(1S)K^+K^-$ are also given. The first uncertainty is statistical, and the second is systematic.

decays. The unexpectedly large partial widths disagree with the expectation for a pure $b\bar{b}$ state, and therefore, the $\Upsilon(5S)$ is one of the strong candidates for the exotic hadron.

In order to understand the nature of the $\Upsilon(5S)$ state, Belle measured the production cross sections for $e^+e^- \to \Upsilon(1S)\pi^+\pi^-$, $\Upsilon(2S)\pi^+\pi^-$ and $\Upsilon(3S)\pi^+\pi^-$ as a function of $\sqrt{s}$ between 10.83 GeV and 11.02 GeV [7]. The enhancements of the production cross sections were observed in all three final states. A fit using a Breit-Wigner resonance shape yields a peak mass of $[10888.4^{+2.7}_{-2.6}(\text{stat}) \pm 1.2(\text{syst})]$ MeV/c^2 and a width of $[30.7^{+8.3}_{-7.0}(\text{stat}) \pm 3.1(\text{syst})]$ MeV. Recently, new measurements have been performed with including not only $\Upsilon(10860)$ but also $\Upsilon(11020)$ [8]. The results are $M_{10860} = (10891.1 \pm 3.2^{+0.6}_{-1.7})$ MeV/c^2, $\Gamma_{10860} = (53.7^{+7.1\,+1.3}_{-5.6\,-5.4})$ MeV, $M_{11020} = (10987.5^{+6.4\,+9.0}_{-2.5\,-2.1})$ MeV/c^2 and $\Gamma_{11020} = (61^{+9\,+2}_{-19\,-20})$ MeV.

2.2 First observation of the P-wave spin-singlet bottomonium states

The $h_b(nP)$ states are the P-wave spin-singlet bottomonium. In 2012, Belle reported the first observations of the $h_b(1P)$ and $h_b(2P)$ produced via $e^+e^- \to \pi^+\pi^- h_b(nP)$ using a 121.4 fb^{-1} data sample collected at energies near the $\Upsilon(5S)$ resonance [9]. The $h_b(nP)$ states were observed in the $\pi^+\pi^-$ missing mass spectrum defined as $M^2_{miss} \equiv (P_{\Upsilon(5S)} - P_{\pi^+\pi^-})^2$, where $P_{\Upsilon(5S)}$ is the 4-momentum of the $\Upsilon(5S)$ determined from the beam momenta and $P_{\pi^+\pi^-}$ is the 4-momentum of the $\pi^+\pi^-$ system. The M_{miss} spectrum is divided into three adjacent regions with boundaries at $M_{miss} = 9.3$, 9.8, 10.1, and 10.45 GeV/c^2 and fitted separately in each region. In the third region, prior to fitting, the contribution due to the $K^0_S \to \pi^+\pi^-$ is subtracted. In Fig. 2, the M_{miss} spectrum after subtraction of both the combinatoric and $K^0_S \to \pi^+\pi^-$ contributions is shown with the fitted signal functions. The measured masses of $h_b(1P)$ and $h_b(2P)$ are $M = (9898.2^{+1.1+1.0}_{-1.0-1.1})$ MeV/c^2 and $M = (10259.8 \pm 0.6^{+1.4}_{-1.0})$ MeV/c^2, respectively. Using the world average masses of the $\chi_{bJ}(nP)$ states, the P-wave hyperfine splittings are determined to be $\Delta M_{\rm HF} = (+1.7 \pm 1.5)$ and $(+0.5^{+1.6}_{-1.2})$ MeV/c^2, respectively. The significances of the $h_b(1P)$ and $h_b(2P)$ are 5.5 σ and 11.2 σ, respectively.

The hadronic transition $\Upsilon(4S) \to \eta h_b(1P)$ and the radiative decay $h_b(1P) \to \gamma\eta_b(1S)$ have been observed [10]. The measured branching fractions are $\mathcal{B}[\Upsilon(4S) \to \eta h_b(1P)] = (2.18 \pm 0.11 \pm 0.18) \times 10^{-3}$ and $\mathcal{B}[h_b(1P) \to \gamma\eta_b(1S)] = (56 \pm 8 \pm 4)\%$.

2.3 First observation of two charged bottomonium-like resonances; $Z_b(10610)^\pm$ and $Z_b(10650)^\pm$

In 2012, Belle reported the first observations of two narrow charged bottomonium-like resonances in the mass spectra of the $\pi^\pm\Upsilon(nS)$ $(n = 1, 2, 3)$ and $\pi^\pm h_b(mP)$ $(m = 1, 2)$ pairs

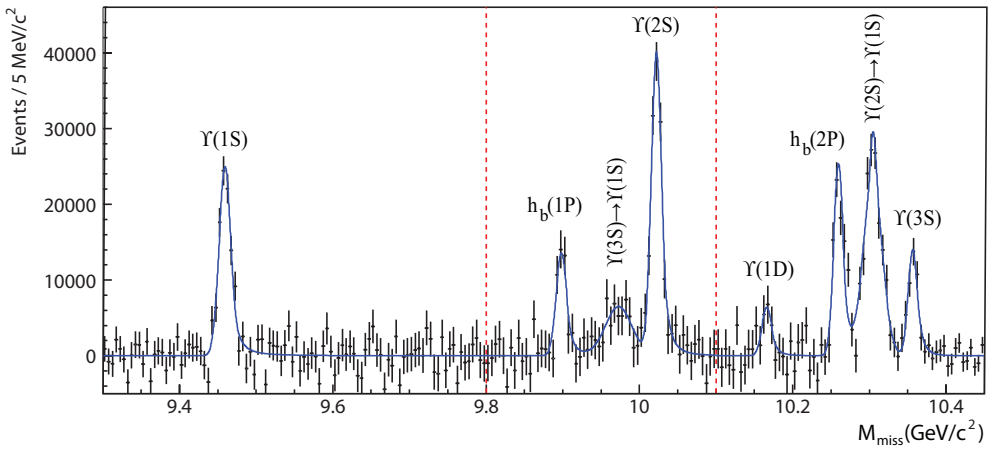


Figure 2: The M_{miss} spectrum with the combinatoric background and K^0_S contribution subtracted (points with errors) and signal component of the fit function overlaid (smooth curve). The vertical lines indicate boundaries of the fit regions. Figure is taken from Ref. [9]

that were produced in association with a single charged pion in $\Upsilon(5S)$ decays [11]. Amplitude analyses of the three-body $\Upsilon(5S) \to \Upsilon(nS)\pi^+\pi^-$ decays were performed by means of unbinned maximum likelihood fits to two-dimensional $M^2[\Upsilon(nS)\pi^+]$ vs $M^2[\Upsilon(nS)\pi^-]$ Dalitz distributions. Two peaks were observed in the $\Upsilon(nS)\pi^\pm$ system near 10.61 GeV/c^2 and 10.65 GeV/c^2. The statistical significance of the two peaks exceeded 10σ for all $\Upsilon(nS)\pi^+\pi^-$ channels. Similarly, two peaks were observed in the $h_b(mP)\pi^\pm$ system. The significance of the $Z_b(10610)^\pm$ and $Z_b(10650)^\pm$ is 16.0σ [5.6σ] for the $h_b(1P)$ [$h_b(2P)$]. Weighted averages of the mass and width are $M = 10607.2 \pm 2.0$ MeV/c^2, $\Gamma = 18.4 \pm 2.4$ MeV for the $Z_b(10610)^\pm$ and $M = 10652.2 \pm 1.5$ MeV/c^2, $\Gamma = 11.5 \pm 2.2$ MeV for the $Z_b(10650)^\pm$, where statistical and systematic errors are added in quadrature. Recent amplitude analysis of the three-body $\Upsilon(nS)\pi^+\pi^-$ final states strongly favored $I^G(J^P) = 1^+(1^+)$ quantum-number assignments [12]. Since the minimal quark content is $b\bar{b}u\bar{d}$ [$b\bar{b}d\bar{u}$] for the Z_b^+ [Z_b^-], the $Z_b(10610)^\pm$ and $Z_b(10650)^\pm$ are the genuine exotic hadrons. The measured masses of two states are a few MeV/c^2 above the thresholds for the open bottom channels $B^*\bar{B}$ (10604.46 MeV/c^2) and $B^*\bar{B}^*$ (10650.2 MeV/c^2). This suggests that these states have a hadronic molecular-type structure.

2.4 First observation of $Z_b(10610)^0$

Belle reported the first observation of the neutral partner of the $Z_b(10610)^\pm$, the $Z_b(10610)^0$ decaying to $\Upsilon(2,3S)\pi^0$ with a 6.5σ significance using a Dalits analysis of $\Upsilon(5S) \to \Upsilon(2,3S)\pi^0\pi^0$ decays [13]. The measured mass of the $Z_b(10610)^0$ is $M = (10609 \pm 4 \pm 4)$ MeV/c^2, that is consistent with the mass of the corresponding charged state, the $Z_b(10610)^\pm$. This suggests that the isospin symmetry breaking is small for $Z_b(10610)$'s and an admixture of the $b\bar{b}$ component in $Z_b(10610)^0$ is small.

3 Charmonium-like hadrons

3.1 $Y(4260)$, $Y(4360)$ and $Y(4660)$

The $Y(4260)$ state was first observed by the BaBar Collaboration in the initial-state-radiation (ISR) process $e^+e^- \to \gamma_{\rm ISR}\pi^+\pi^- J/\psi$ [14] and then confirmed by the CLEO [15] and Belle experiments [16, 17] using the same technique. The cross section of $e^+e^- \to \pi^+\pi^- J/\psi$ are given in Fig. 3 The quantum number of the $Y(4260)$ resonances is $J^{PC} = 1^{--}$. However, the

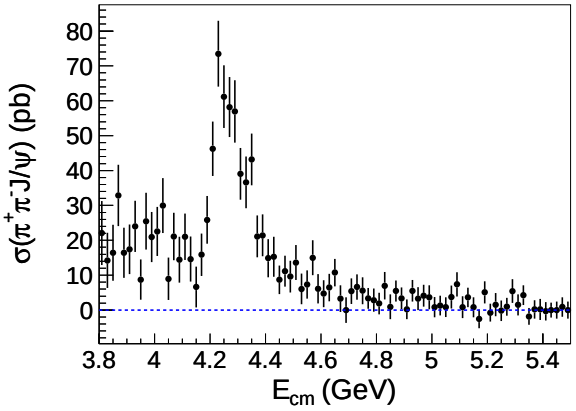


Figure 3: The measured $e^+e^- \to \pi^+\pi^- J/\psi$ cross section for c.m. energies between 3.8 and 5.5 GeV after background subtraction. The errors are statistical only. Figure is taken from Ref. [17]

properties of the $Y(4260)$ resonance are rather different from those of other known $J^{PC} = 1^{--}$ charmonium states in the same mass range. Since it is well above the $D\bar{D}$ threshold, it is expected to decay into $D^{(*)}\bar{D}^{(*)}$ dominantly. In fact, no significant enhancement is observed in $D^{(*)}\bar{D}^{(*)}$ final states. On the other hand, $\Gamma(Y(4260) \to \pi^+\pi^- J/\psi) > 1.6$ MeV at 90% CL, which is much larger than the typical charmonium state, i.e., $\Gamma(\psi(3770) \to \pi^+\pi^- J/\psi) = 53 \pm 8$ keV.

In 2007, Belle reported the observation of two resonance structures in $e^+e^- \to \pi^+\pi^-\psi(2S)$ via initial-state radiation [18]. The masses and widths of the two resonances ($Y(4360)$ and $Y(4660)$) are $M_1 = 4361 \pm 9 \pm 9$ MeV/c^2, $\Gamma_1 = 74 \pm 15 \pm 10$ MeV and $M_2 = 4664 \pm 11 \pm 5$ MeV/c^2, $\Gamma_2 = 48 \pm 15 \pm 3$ MeV, respectively, if the mass spectrum is parametrized with the coherent sum of two Breit-Wigner functions. The statistical significance of the first peak is more than 8σ and that of the second peak is 5.8σ. In 2015, using full data sample of the Belle experiment, $Y(4360)$ and $Y(4660)$ states have been studied [19] and the measured cross section is given in Fig. 4. Likewise $Y(4260)$, $Y(4360)$ and $Y(4660)$ are not observed in $D^{(*)}\bar{D}^{(*)}$ channels. $Y(4260)$ has rather large partial decay width to the $\pi^+\pi^- J/\psi$ final state, but has quite small partial decay width to the $\pi^+\pi^-\psi(2S)$ final state. Conversely, $Y(4360)$ and $Y(4660)$ have large partial decay width to the $\pi^+\pi^-\psi(2S)$ final state, but have small partial decay width to the $\pi^+\pi^- J/\psi$ final state. These facts suggest that $Y(4260)$, $Y(4360)$ and $Y(4660)$ are not simple charmonium states, and therefore, are the candidates for the exotic hadrons.

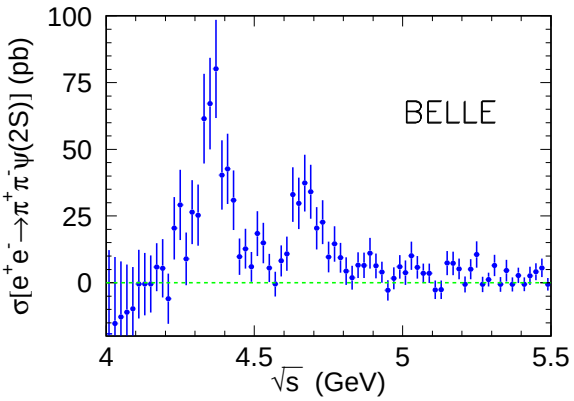


Figure 4: The measured $e^+e^- \to \pi^+\pi^-\psi(2S)$ cross section for c.m. energies between 4.0 and 5.5 GeV after background subtraction. Figure is taken from Ref. [19]

3.2 $Z_c(3900)$

The $J^{PC} = 1^{--}$ state $Y(4260)$ has rather large decay width to the $\pi^+\pi^- J/\psi$ and it is similar to the $J^{PC} = 1^{--}$ state $\Upsilon(10860)$ has rather large decay width to the $\pi^+\pi^-\Upsilon(1S)$. In the $\Upsilon(10860)$ decay, the charged bottomonium-like states $Z_b(10610)$ and $Z_b(10650)$ were observed as described in Sect. 2.3. Likewise $\Upsilon(10860)$, whether the $Y(4260)$ decay to the charged charmonium-like state was the issue of the discussion. Recently, BESIII reported [20], and Belle confirmed [17], the observation of a charged resonance-like structure in the $\pi^+ J/\psi$ invariant mass distribution for $e^+e^- \to \pi^+\pi^- J/\psi$ events collected at $\sqrt{s} = 4.26$ GeV, dubbed the $Z_c(3900)$. The mass and width determined by BESIII are $M = (3899.0 \pm 3.6 \pm 4.9)$ MeV/c^2 and $\Gamma = (46 \pm 10 \pm 20)$ MeV, respectively with more than 8σ statistical significance. Those by Belle are $M = (3894.5 \pm 6.6 \pm 4.5)$ MeV/c^2 and $\Gamma = (63 \pm 24 \pm 26)$ MeV, respectively with 5.2σ significance. The fit results of the distribution of $M_{\rm max}(\pi J/\psi)$, the maximum of $M(\pi^+ J/\psi)$ and $M(\pi^- J/\psi)$ by Belle are given in Fig. 5. Recently, BESIII reported on a study of the process $e^+e^- \to \pi^\pm (D\bar{D}^*)^\mp$ at $\sqrt{s} = 4.26$ GeV using a 525 pb^{-1} data sample collected with the BESIII detector at BEPCII storage ring. A distinct charged structure dubbed $Z_c(3885)$ is observed with more than 18σ significance [21]. The measured mass and width are $M = (3883.9 \pm 1.5 \pm 4.2)$MeV/c^2 and $\Gamma = (24.8 \pm 3.3 \pm 11.0)$ MeV, respectively. The fitted $Z_c(3885)$ mass is marginally (2σ) inconsistent with that of the $Z_c(3900)$, and therefore, it is an issue of the discussion whether the $Z_c(3885)$ structure is identical with the $Z_c(3900)$ structure.

Since the mass of $Z_c(3885)$ or $Z_c(3900)$ is close to the $D^0\bar{D}^{*-}$ threshold, there are suggestions that these states are the virtual $D\bar{D}^*$ molecule-like structure, i,e., a charmed-sector analog of the $Z_b(10610)$. However, the situation is not so simple. Because of the heavy quark symmetry, the interaction between $B^{(*)}$ and $\bar{B}^{(*)}$ is considered to be similar to that between $D^{(*)}$ and $\bar{D}^{(*)}$. On the other hand, the size of the kinetic energy term of the $D\bar{D}^*$ system is about 2.7 times larger than that of the $B\bar{B}^*$ system due to the reduced mass difference. Therefore, simultaneous explanation of the $Z_b(10610)$ and $Z_c(3900)$ structures are rather difficult.

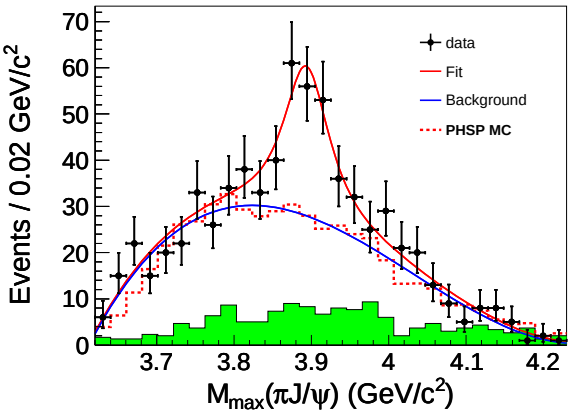


Figure 5: Unbinned maximum likelihood fit to the distribution of the $M_{\max}(\pi J/\psi)$. Points with error bars are data, the curves are the best fit, the dashed histogram is the phase space distribution and the shaded histogram is the non-$\pi^+\pi^- J/\psi$ background estimated from the normalized J/ψ sidebands. Figure is taken from Ref. [17]

4 B decays

The B-meson properties have been studied for understanding the CP violation phenomena and the results from the B-factories have been summarized in Ref. [4]. The energy frontier experiment the Large Hadron Collider (LHC) at CERN started the $\sqrt{s} = 7$ TeV operation in 2010. Then, the observation of the boson has been reported on July 4th, 2012 and later it was identified as the Standard Model (SM) Higgs boson. In 2015, the $\sqrt{s} = 13$ TeV operation at LHC started. However, up to now, no new phenomena beyond the SM (BSM) have been observed.

In such a situation, the intensity frontier experiments are attracting attention since such experiments may have the possibility to access to much higher energy scale phenomena. The deviations from the SM predictions have been measured in the semileptonic B decays to τ leptons and the angular observables of the $B \to K^* \ell^+ \ell^-$ decays with $\ell = e, \mu$. In order to observe the BSM phenomena, the observables should be predicted very accurately in the SM. Otherwise the small contributions from the BSM phenomena are easily masked by the uncertainties of the SM predictions. The uncertainties of the SM predictions are mostly come from the strong interaction parts. In this two B-decay modes in question, there is single hadron in the initial and final states and therefore no initial and final state interactions by the strong interaction exist.

4.1 $\mathcal{R}(D^*)$ and $\mathcal{R}(D)$

The ratio $\mathcal{R}(D^{(*)}) = \mathcal{B}(\bar{B} \to D^{(*)}\tau^-\bar{\nu}_\tau)/\mathcal{B}(\bar{B} \to D^{(*)}\ell^-\bar{\nu}_\ell)$, with $\ell = e, \mu$ has much attention since it is sensitive to the Charged Higgs boson contributions, which is the BSM phenomena. It is naively understood that the Charged Higgs boson coupling to the τ lepton is stronger than that to the electron or muon because of the large mass of the τ lepton. By taking the ratio of the branching fractions, the theoretical as well as experimental uncertainties have been

reduced. The SM predictions are $\mathcal{R}(D^*) = 0.252 \pm 0.003$ [22] and $\mathcal{R}(D) = 0.300 \pm 0.008$ [23]. On the other hand, experimental results are as follows. *BABAR* reported $\mathcal{R}(D^*) = 0.332 \pm 0.024 \pm 0.018$ and $\mathcal{R}(D) = 0.440 \pm 0.058 \pm 0.042$ with a semileptonic tagging method [24]. Belle used a hadronic tagging method and the results are $\mathcal{R}(D^*) = 0.293 \pm 0.038 \pm 0.015$ and $\mathcal{R}(D) = 0.375 \pm 0.064 \pm 0.026$ [25]. In LHCb experiment, the multidimensional fit to kinematics distributions of the candidate $\bar{B}^0$ decays gave $\mathcal{R}(D^*) = 0.336 \pm 0.027 \pm 0.030$ [26]. Recently Belle performed the measurement of $\mathcal{R}(D^*)$ using the semileptonic tagging method and the result was $\mathcal{R}(D^*) = 0.302 \pm 0.030 \pm 0.011$ [27]. In the experimental results, the first errors are statistical ones and the second errors are systematical ones. All the experimental results are consistent with each other.

The Heavy Flavor Averaging Group (HFAG) summarized these results and reported them on their web page. The averages are $\mathcal{R}(D^*) = 0.316 \pm 0.016 \pm 0.010$ and $\mathcal{R}(D) = 0.397 \pm 0.040 \pm 0.028$, which exceed the SM predictions by 1.9σ and 3.3σ, respectively. The combined analysis shows that the deviation from the SM prediction is 4σ, which is summarized in Fig. 6.

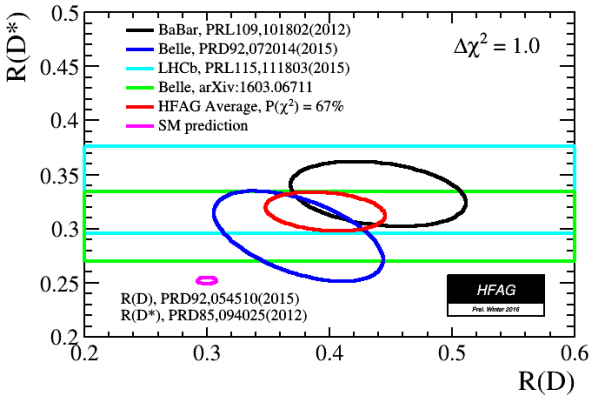


Figure 6: Summary of the theoretical as well as experimental results of $\mathcal{R}(D^*)$ and $\mathcal{R}(D)$. Figure is taken from HFAG web site http://www.slac.stanford.edu/xorg/hfag/semi/winter16/winter16_dtaunu.html

4.2 τ lepton polarization in $\bar{B} \to D^* \tau^- \bar{\nu}_\tau$ decay

Although I did not mention this subject on my lecture at the summer school, in this subsection, I would like to report Belle's new results on the τ lepton polarization and $\mathcal{R}(D^*)$ in $\bar{B} \to D^* \tau^- \bar{\nu}_\tau$ decay with $\tau \to \pi \nu_\tau$ and $\tau \to \rho \nu_\tau$ using the hadronic tagging method [28]. The τ lepton polarization is defined as $P_\tau(D^*) = [\Gamma^+(D^*) - \Gamma^-(D^*)]/[\Gamma^+(D^*) + \Gamma^-(D^*)]$, where $\Gamma^\pm(D^*)$ denotes the decay rate of $\bar{B} \to D^* \tau^- \bar{\nu}_\tau$ with a τ helicity of $\pm 1/2$. The $P_\tau(D^*)$ is considered to be sensitive to the BSM physics. The $P_\tau(D^*)$ can be measured from the angular distributions in the two-body hadronic τ decays.

The result is $P_\tau(D^*) = -0.36 \pm 0.51^{+0.21}_{-0.16}$, which is consistent with the SM prediction $P_\tau(D^*) = -0.497 \pm 0.013$ [29]. This analysis gave the independent measurement of the $\mathcal{R}(D^*)$ in the two-body hadronic τ decay modes. The result $\mathcal{R}(D^*) = 0.27 \pm 0.035^{+0.028}_{-0.025}$ is consistent with the SM prediction.

4.3 Lepton-flavor-dependent angular analysis of $B \to K^*\ell^+\ell^-$

The $B \to K^*\ell^+\ell^-$ decay involves the quark transition $b \to s\ell^+\ell^-$, a flavor-changing neutral current that is forbidden at tree level in the SM. There may be sizable contributions from the BSM phenomena and the LHCb reported the 3.4σ deviation from the SM prediction in the angular dependent observable P_5' measured by the $B^0 \to K^{*0}\mu^+\mu^-$ decay [30]. The definition of P_5' is given in Ref. [30]. Recently, Belle performed the measurements of these angular dependent observables in not only the $B^0 \to K^{*0}\mu^+\mu^-$, but also the $B^\pm \to K^{*\pm}\mu^+\mu^-$, $B^0 \to K^{*0}e^+e^-$ and $B^\pm \to K^{*\pm}e^+e^-$ decay modes [31]. The results are compatible with SM predictions, where the largest discrepancy is 2.6σ in P_5' for the muon channels as shown in Fig. 7.

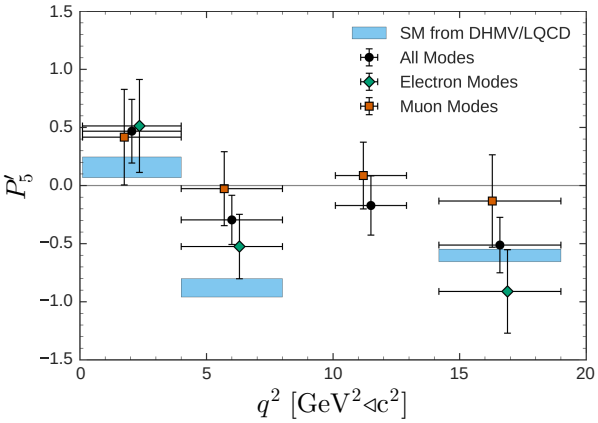


Figure 7: The theoretical as well as experimental results of P_5'. Figure is taken from Ref. [31].

5 Summary

The recent results on the hadron spectroscopy measured by the Belle detector at the KEKB e^+e^- collider have been reviewed. We have focused on the bottomonium-like and charmonium-like mesons having the unanticipated properties from the $q\bar{q}$ structures.

Although the data taking of the Belle experiment was finished on June 30, 2010, there may be rich hadron physics to be analyzed in Belle data. Quantum numbers, production rates, decay rates, etc. have not been to be determined for many higher resonance states, which should be measured. As discussed in this talk, many states may not have the simple quark-gluon structures but have the rich structures. In order to clarify the structures of such exotic hadrons, any suggestion from the theorists is very welcome.

So far, physics beyond the Standard Model has not been observed. In order to observe BSM phenomena, the more accurate and less uncertain SM predictions of the observables as well as the more precise experimental measurements are necessary.

The SuperKEKB/Belle II experiment will start data taking on the end of 2017. The designed luminosity is 40 times bigger than the KEKB-factory/Belle. Please await our new data from the SuperKEKB-/Belle II.

References

[1] S. Kurokawa and E. Kikutani, Nucl. Instrum. Methods Phys. Res., Sect. **A** 499, 1 (2003).

[2] A. Abashian et al. (Belle Collaboration), Nucl. Instrum. Methods Phys. Res., Sect. **A** 479, 117 (2002) and references therein.

[3] J. Brodzicka et al. (Belle Collaboration), Prog. Theor. Exp. Phys. **2012** 04D001 (2012).

[4] A. J. Bevan et al., Eur. Phys. J. **C74** 3026 (2014).

[5] X. Liu, Chin. Sci. Bull. **54** 3815 (2014).

[6] K.-F. Chen et al. (Belle Collaboration), Phys. Rev. Lett. **100** 112001 (2008).

[7] K.-F. Chen et al. (Belle Collaboration), Phys. Rev. **D82** 091106(R) (2010).

[8] D. Santel et al. (Belle Collaboration), Phys. Rev. **D93** 011101(R) (2016).

[9] I. Adachi et al. (Belle Collaboration), Phys. Rev. Lett. **108** 032001 (2012).

[10] IU. Tamponi et al. (Belle Collaboration), Phys. Rev. Lett. **115** 142001 (2015).

[11] A. Bondar et al. (Belle Collaboration), Phys. Rev. Lett. **108** 122001 (2012).

[12] A. Garmash et al. (Belle Collaboration), Phys. Rev. **D91** 072003 (2015).

[13] P. Krokovny et al. (Belle Collaboration), Phys. Rev. **D88** 052016 (2013).

[14] B. Aubert et al. (BaBar Collaboration), Phys. Rev. Lett. **95** 142001 (2005).

[15] Q. He et al. (CLEO Collaboration), Phys. Rev. **D74** 091104(R) (2006).

[16] C. Z. Yuan et al. (Belle Collaboration), Phys. Rev. Lett. **99** 182004 (2007).

[17] Z. Q. Liu et al. (Belle Collaboration), Phys. Rev. Lett. **110** 252002 (2013).

[18] X. L. Wang et al. (Belle Collaboration), Phys. Rev. Lett. **99** 142002 (2007).

[19] X. L. Wang et al. (Belle Collaboration), Phys. Rev. **D91** 112007 (2015).

[20] M. Ablikim et al. (BESIII Collaboration), Phys. Rev. Lett. **110** 252001 (2013).

[21] M. Ablikim et al. (BESIII Collaboration), Phys. Rev. Lett. **112** 022001 (2014).

[22] S. Fajfer, J. F. Kamenik, and I. Nisandzic, Phys. Rev. **D85** 094025 (2012).

[23] H. Na et al., Phys. Rev. **D92** 054410 (2015).

[24] J. P. Lees et al., (BaBar Collaboration), Phys. Rev. **D88** 072012 (2013).

[25] M. Huschle et al., (Belle Collaboration), Phys. Rev. **D92** 072014 (2015).

[26] R. Aaij et al., (LHCb Collaboration), Phys. Rev. Lett. **115** 111803 (2015).

[27] Y. Sato et al., (Belle Collaboration), Phys. Rev. **D94** 0720007 (2016).

[28] S. Hirose et al., (Belle Collaboration), arXiv:1612.00529 [hep-ex].

[29] M. Tanaka and R. Watanabe, Phys. Rev. **D87** 034028 (2013).

[30] R. Aaij et al., (LHCb Collaboration), JHEP **02** 104 (2016).

[31] S. Wehle et al., (Belle Collaboration), arXiv:1612.005014 [hep-ex].

Multiquark Hadrons - Current Status and Issues

Ahmed Ali *

Deutsches Elektronen-Synchrotron DESY,
D-22607 Hamburg, Germany
*E-mail: ahmed.ali@desy.de

DOI: http://dx.doi.org/10.3204/DESY-PROC-2016-04/Ali

Multiquark states having four and five valence quarks, called tetraquarks and pentaquarks, respectively, are now firmly established experimentally, with the number of such independent states increasing steadily over the years. They represent a new facet of QCD, but the underlying dynamics is currently poorly understood. I review some selected aspects of data and discuss several competing phenomenological models put forward to accommodate them.

1 Introduction

Ever since the discovery of the state $X(3872)$ by Belle in 2003 [1], a large number of multiquark states has been discovered in particle physics experiments, conducted at the electron-positron and hadron colliders. They are exotic, having J^{PC} quantum numbers not allowed for $q\bar{q}$ states, or have too small a decay width for their mass, and, in some cases, their decay distributions have unfamiliar features not seen before. Most of them are quarkonium-like states, in that they have a $(c\bar{c})$ or a $(b\bar{b})$ component in their Fock space. A good fraction of them are electrically neutral but some are singly-charged. Examples are $X(3872)(J^{PC} = 1^{++})$, $Y(4260)(J^{PC} = 1^{--})$, $Z_c(3900)^{\pm}(J^P = 1^+)$, $P_c(4450)^{\pm}(J^P = 5/2^+)$, in the hidden charm sector, and $Z_b(10610)^{\pm}(J^P = 1^+)$ and $Z_b(10650)^{\pm}(J^P = 1^+)$, in the hidden bottom sector. The numbers in the parentheses are their masses in MeV. Of these, $P_c(4450)^{\pm}(J^P = 5/2^+)$ is a pentaquark state, as its discovery mode $P_c(4450)^+ \to J/\psi p$ [2] requires a minimal valence quark content $c\bar{c}uud$. The others are tetraquark states, with characteristic decays, such as $X(3872) \to J/\psi\pi^+\pi^-$, $Y(4260) \to J/\psi\pi^+\pi^-$, $Z_c(3900)^+ \to J/\psi\pi^+$, and $Z_b(10610)^+ \to h_b(1P, 2P)\pi^{\pm}, \Upsilon(1S, 2S)\pi^+$. The charmonia sector and the observed neutral charmonium-like exotic states are shown in Fig. 1, and the observed charged charmonium-like states are displayed in Fig. 2. No doubly-charged multiquark hadron has been seen so far, though some are expected, such as $[\bar{c}\bar{u}][sd] \to D_s^-\pi^-$, in the diquark scenario discussed below.

Deciphering the underlying dynamics of the multiquark states is a formidable challenge and several models have been proposed to accommodate them. I discuss them briefly in the next section for the tetraquark mesons, and will discuss one of them - the diquark model - in some details in section 3. Current data and models for the observed pentaquarks are discussed briefly in section 4, and the diquark model for pentaquarks is discussed at some length in section 5, including a number of predictions to be tested in forthcoming experiments. A summary is given

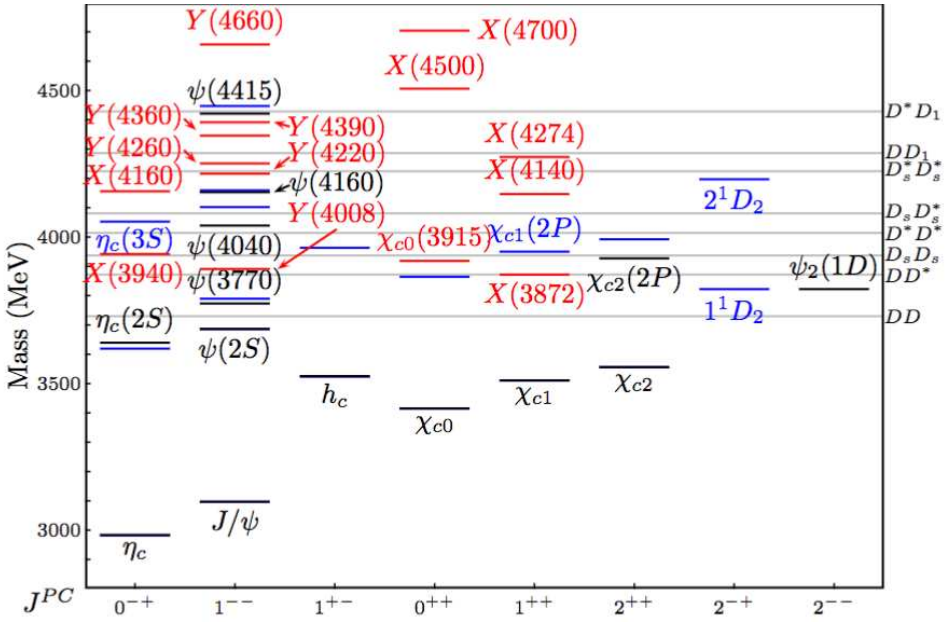


Figure 1: Charmonia and Charmonium-like neutral exotic sector. Black lines represent observed charmonium levels, blue lines are predicted charmonia levels and red lines are exotic states. Two-particle meson thresholds are indicated on the right (from [3]).

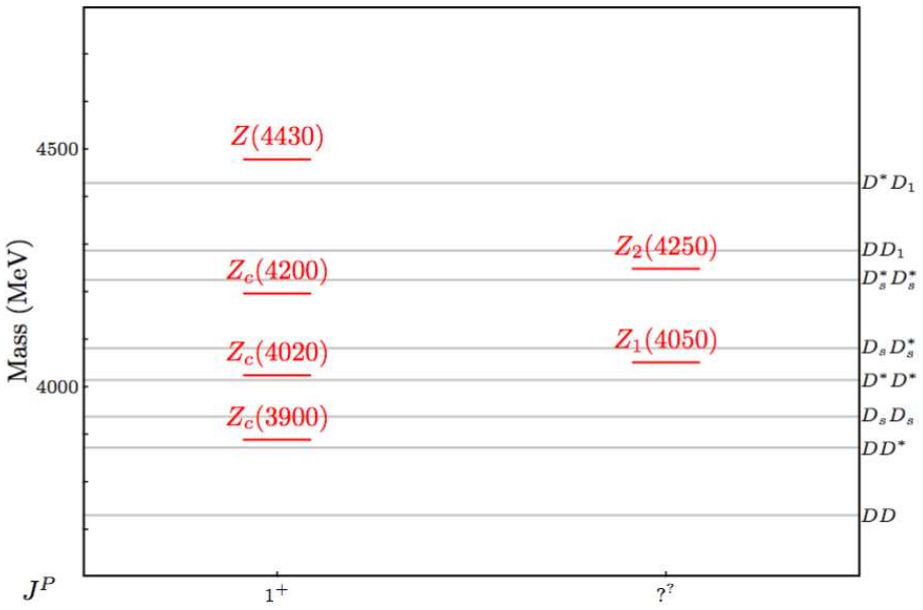


Figure 2: Observed charged exotic charmonium sector. Two-particle meson thresholds are indicated on the right (from [3]).

in section 6.

2 Models for Tetraquarks

Several explicit kinematic and dynamical mechanisms have been devised to accommodate the exotic spectroscopy. They go by the names: cusps, hadroquarkonia, hybrids, hadron molecules, and compact diquarks. They are briefly explained below.

2.1 Tetraquarks as Cusps

In the cusp interpretation of tetraquarks [4, 5], it is assumed that threshold re-scatterings are enough to describe the data, and as such there is no need for poles in the scattering matrix. This approach has been invoked to explain the origin of the charged states $Z_c(3900)[D\bar{D}^*]$, $Z_c(4025)[D^*\bar{D}^*]$, $Z_b(1610)[B\bar{B}^*]$, and $Z_b(10650)[B^*\bar{B}^*]$, as they lie just above the indicated thresholds. Discussed long ago by Wigner [6] in the context of the non-relativistic two-body scattering theory, and stressed more recently by Törnqvist [7] in an attempt to understand the low-lying scalar meson $q\bar{q}$ nonet, and by Bugg [8], in interpreting the resonances as synchronized artefacts, this effect has to do with the behavior of scattering cross-sections $\sigma(E)$ near thresholds, say $E = E_0$. The cross-section remains finite as one approaches E_0 from above or below, but the slope $d\sigma(E)/dE$ shows a discontinuity, which can result in a "cusp", as $\sigma(E)$ is continued below E_0. It is related to the self-energy threshold singularity, in that the expression for the imaginary part of the self-energy $\mathrm{Im}\Pi(s)$ is zero for $\sqrt{s}$ below the threshold and turns on rapidly once the threshold is crossed[1]. Here $\Pi(s)$ is the self-energy of of a particle coupled to two intermediate states. The resulting enhancements by cusps can mimic genuine S-matrix poles (resonances). However, they can be distinguished by studying the phase motions of the amplitudes. Representing a resonance by a Breit-Wigner amplitude, $f(s) = \Gamma/2/(M - \sqrt{s} - i\Gamma/2)$, the magnitude and phase vary with $\sqrt{s}$, according to a circular trajectory in the Argand diagram. Cusps, on the other hand, have characteristically different dependence on $\sqrt{s}$. Using the variable $z = c(m_A + m_B - \sqrt{s})$, where A and B are the intermediate states, and c is a normalizing constant, one can show that the imaginary part of a cusp amplitude is zero for positive z (i.e., below threshold) and turns on rapidly as the threshold is crossed, reflecting essentially the function $erfc(\sqrt{z})$, which governs $\mathrm{Im}(\Pi(s))$. This phase motion differs from that of a genuine Breit-Wigner. We will illustrate this in the context of the pentaquark $P_c(4450)^+$ later in section 4.

2.2 Tetraquarks as hadroquarkonia

This mechanism is motivated by analogy with the hydrogen atom. In the hadroquarkonium model, a $Q\bar{Q}$ ($Q = c, b$) forms the hard core surrounded by light matter (light $q\bar{q}$ in the case of tetraquarks and qqq for pentaquarks), with the two systems bound by a van der Walls type force. For example, the hadrocharmonium core may consist of the $J/\psi, \psi'$ or χ_c, and the light $q\bar{q}$ degrees of freedom can be combined to accommodate the observed hadrons [9]. A variation on this theme is that the hard core quarkonium could be in a color-adjoint representation, in which case the light degrees of freedom are also a color-octet to form an overall singlet. Hadroquarkonium models have conceptual problems, in that if the binding force is weak, the

[1] Here E and $\sqrt{s}$ are used interchangeably.

question is why the system remains stable for long enough a time to be identified as a distinct state. If the force is strong, it is not clear why the $Q\bar{Q}$ core and the light degrees of freedom don't rearrange themselves as a pair of heavy mesons ($D\bar{D}^*, B\bar{B}^*$ etc.). This would then suppress the appearance of the states $(J/\psi, h_c)\pi\pi$ in their decays, which, in fact, are the discovery modes of many such exotic multiquark states.

2.3 Tetraquarks as hybrids

Next are hybrid models, the basic idea of which dates back to circa 1994 [10] based on the QCD-inspired flux-tubes, which predict exotic $J^{\rm PC}$ states of both the light and heavy quarks. Hybrids are hadrons formed from valence quarks and gluons, for example, consisting of $Q\bar{Q}g$. States dominated by gluons form glueballs, which are firm predictions of QCD, but have proven to be elusive experimentally. What has emerged from the current lattice-QCD computations [11] is that non-perturbative gluons, the object of interest in constructing the hybrids, are quasiparticles having $J^{PC} = 1^{+-}$ with an excitation energy of approximately 1 GeV. This would put the lightest charmonium multiplets at around 4200 MeV. Extensive studies of such hybrids have been carried out on the lattice by the Hadron Spectrum Collaboration [12], though for a heavy pion mass, $m_\pi \sim 400$ MeV and at fixed lattice spacing. Several states in this computation are identified as charmonium hybrid multiplets, having the quantum numbers $J^{PC} = 0^{-+}, 1^{--}, 2^{-+}, 1^{-+}$, with their masses ($M$) estimated to lie in the range $M - M_{\eta_c} \simeq 1200 - 1400$ MeV. Very much along the same lines, but much earlier, a hybrid interpretation was advanced for the $J^{\rm PC} = 1^{--}$ state $Y(4260)$, which has a small e^+e^- annihilation cross section [13, 14, 15]. In the meanwhile, hybrids have been offered as templates for other exotic hadrons as well [16, 17]. They have been put on firmer theoretical footings in the framework of effective field theories [18]. Despite all these theoretical advances, which are impressive and may eventually provide reliable quantitative predictions, an unambiguous hybrid candidate has yet to be identified in the current experiments. Advances in lattice QCD techniques, enabling a firm phenomenological profiles of the glueballs and the $Q\bar{Q}g$ hybrids, and dedicated experiments, such as the GlueX [19] and $\bar{\rm P}$ANDA [20], may change this picture dramatically.

2.4 Tetraquarks as hadron molecules

A very popular approach assumes that the tetraquark (pentaquark) states are meson-meson (meson-baryon) bound states, with an attractive residual van der Waals force generated by mesonic exchanges [21]. This hypothesis is in part supported by the closeness of the observed exotic hadron masses to their respective two-particle thresholds, as can be seen in Figs. 1 and 2. In many cases, this leads to a very small binding energy, which imparts the exotic hadrons very large hadronic radii, following from the Heisenberg uncertainty principle. This is best illustrated by the $X(3872)$, which has an S-wave coupling to $D^*\bar{D}$ (and its conjugate) and has a binding energy $\mathcal{E}_X = M_{X(3872)} - M_{D^{*0}} - M_{\bar{D}^0} = +0.01 \pm 0.18$ MeV. Such a hadron molecule will have a large mean square separation of the constituents $\langle r_X \rangle \propto 1/\sqrt{\mathcal{E}_X} \simeq 10$ fm, where the quoted radius corresponds to a binding energy $\mathcal{E}_X = 0.15$ MeV. This would lead to small production cross-sections in hadronic collisions [22], contrary to what has been observed in a number of experiments at the Tevatron and the LHC. In some theoretical constructs, this problem is mitigated by making the hadron molecules complicated by invoking a hard (point-like) core. In that sense, such models resemble hadroquarkonium models, discussed above. In

yet others, rescattering effects are invoked to substantially increase the cross-sections [23]. A crucial test is the p_T-spectrum of the exotic hadrons in question in prompt production processes at the LHC.

The hadron molecular picture is plausible in explaining some aspects of the current data, namely the lack of experimental evidence of a quartet of exotic states, almost degenerate in mass with the $X(3872)$, containing a light quark-antiquark pair $q\bar{q}$, $q = u, d$, leading to the formation of $I = 1$ and $I = 0$ multiplets. These multiplets are anticipated in the diquark picture, discussed below. However, in the molecular picture, due to the exchange of a pion providing the main binding, and pion being an isospin-1 meson, not all isospin configurations will bind. In line with this, no resonant structure is seen near the $D^0\bar{D}^0$ threshold, consistent with the inadmissibility of a strong interaction coupling of three pseudo-scalars $D^0\bar{D}^0\pi^0$ due to parity conservation. On the other hand, the case for hadron molecules is weak for those exotics whose masses are well above the respective thresholds. For example, the $Z_c(3900)^+$ is a case in point in which the mass lies 20 MeV above the $D\bar{D}^*$ threshold, which, incidentally, is also its main decay mode. This is hard to accommodate in the hadron molecular picture. Theoretical interest in hadron molecules has remained unabated, and there exists a vast and growing literature on this topic with ever increasing sophistication, a sampling of which is referenced here [24, 25, 26, 27, 28, 29, 30].

2.5 Tetraquarks as compact diquark-antidiquark mesons

Last, but by no means least, on this list are QCD-based interpretations in which tetraquarks and pentaquarks are genuinely new hadron species in which a color-nonsinglet diquark is the essential building block [31, 32, 33]. In the large N_c limit of QCD, tetraquarks, treated as diquark-antidiquark mesons, are shown to exist [34, 35, 36] as poles in the S-matrix. They may have narrow widths in this approximation, and hence they are reasonable candidates for multiquark states. First attempts to study multiquark states using Lattice QCD have been undertaken [37, 38, 39, 40, 41] in which correlations involving four-quark operators are studied numerically. Evidence of tetraquark states in the sense of S-matrix poles using these methods is still lacking. Establishing the signal of a resonance requires good control of the background. In the lattice QCD simulations of multiquark states, this is currently not the case. This may be traced back to the presence of a number of nearby hadronic thresholds and to lattice-specific issues, such as an unrealistic pion mass. More powerful analytic and computational techniques are needed to draw firm conclusions.

In the absence of reliable first principle calculations, approximate phenomenological methods are the way forward. In that spirit, an effective Hamiltonian approach has been often used [31, 32, 42, 43, 44, 45], in which tetraquarks are assumed to be diquark-antidiquark objects, bound by gluonic exchanges (pentaquarks are diquark-diquark-antiquark objects). This allows one to work out the spectroscopy and some aspects of tetraquark decays. Heavy quark symmetry is a help in that it can be used for the heavy-light diquarks relating the charmonia-like states to the bottomonium-like counterparts. As detailed below, diquark models anticipate a very rich spectroscopy of tetraquarks and pentaquarks, only a small part of which has been possibly observed experimentally. Hence, diquark models are in dire need of dynamical selection rules to reduce the number of observable states. The underlying dynamics is complex and the current theoretical framework, in which the parameters of the effective Hamiltonian subsume the dynamics, is obviously inadequate. I will discuss the phenomenology of the diquark picture in the next section to test how far such models go in describing the observed exotic hadrons

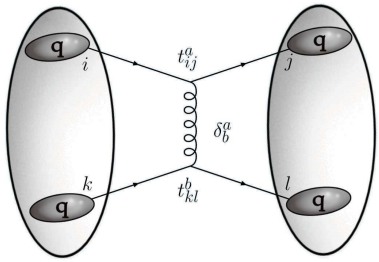


Figure 3: One-gluon exchange diagram for diquarks.

and other properties measured in current experiments.

For recent in-depth reviews of all the models discussed above and the theoretical techniques employed, see [3, 46, 47, 48].

3 The Diquark Model

The basic assumption of this model is that diquarks are tightly bound colored objects and they are the building blocks for forming tetraquark mesons and pentaquark baryons. Diquarks, for which we use the notation $[qq]_c$, and interchangeably $\mathcal{Q}$, have two possible SU(3)-color representations. Since quarks transform as a triplet $\mathsf{3}$ of color SU(3), the diquarks resulting from the direct product $\mathsf{3} \otimes \mathsf{3} = \bar{\mathsf{3}} \oplus \mathsf{6}$, are thus either a color anti-triplet $\bar{\mathsf{3}}$ or a color sextet $\mathsf{6}$. The leading diagram based on one-gluon exchange is shown in Fig. 3. The product of the SU(3)-matrices in Fig. 3 can be decomposed as

$$t^a_{ij} t^a_{kl} = -\frac{2}{3} \underbrace{(\delta_{ij}\delta_{kl} - \delta_{il}\delta_{kj})/2}_{\text{antisymmetric: projects } \bar{\mathbf{3}}} + \frac{1}{3} \underbrace{(\delta_{ij}\delta_{kl} + \delta_{il}\delta_{kj})/2}_{\text{symmetric: projects } \mathbf{6}} . \tag{1}$$

The coefficient of the antisymmetric $\bar{\mathsf{3}}$ representation is $-2/3$, reflecting that the two diquarks bind with a strength half as strong as between a quark and an antiquark, in which case the corresponding coefficient is $-4/3$. The symmetric $\mathsf{6}$ on the other hand has a positive coefficient, $+1/3$, reflecting a repulsion. Thus, in working out the phenomenology, a diquark is assumed to be an $SU(3)_c$-antitriplet, with the antidiquark a color-triplet. With this, we have two color-triplet fields, quark q_3 and anti-diquark $\overline{\mathcal{Q}}$ or $[\bar{q}\bar{q}]_3$, and two color-antitriplet fields, antiquark $\bar{q}_{\bar{3}}$ and diquark $\mathcal{Q}$ or $[qq]_{\bar{3}}$, from which the spectroscopy of the conventional and exotic hadrons is built. However, the quarks and diquarks differ in an essential point, namely the former are point-like objects but the latter are composite and have a hadronic size. It has crucial importance in determining the electromagnetic and strong couplings, and hence for the production cross-sections in leptonic and hadronic collisions.

Since quarks are spin-1/2 objects, a diquark has two possible spin-configurations, spin-0, with the two quarks in a diquark having their spin-vectors anti-parallel, and spin-1, in which case the two quark spins are aligned, as shown in Fig. 4. They were given the names "good diquarks" and "bad diquarks", respectively, by Jaffe [49], implying that in the former case, the two quarks bind, and in the latter, the binding is not as strong. There is some support of this pattern from lattice simulations for light diquarks [50], in which correlations are studied in

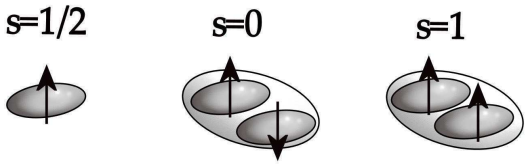


Figure 4: Quark and diquark spins.

terms of the spatial distribution of the two quarks forming the diquark in the background of the static quark. Phenomenological expectations that QCD dynamics favors the formation of good (spin-0) diquarks in color anti-triplet configuration is verified. It is exceedingly important to study on the lattice such correlations in two-point functions, involving tetraquarks, which have been attempted but with inconclusive results so far. However, as the spin-degree of freedom decouples in the heavy quark systems, as can be shown explicitly in heavy quark effective theory context for heavy mesons and baryons [51], we expect that this decoupling will also hold for heavy-light diquarks $[Q_i q_j]_{\bar{3}}$ with $Q_i = c, b; q_j = u, d, s$. So, for the heavy-light diquarks, both the spin-1 and spin-0 configurations are present. Also, the diquarks in heavy baryons (such as Λ_b and Ω_b), consisting of a heavy quark and a light diquark, both $j^p = 0^+$ and $j^p = 1^+$ quantum numbers of the diquark are needed to accommodate the observed baryon spectrum.

In this writeup, we will be mostly discussing heavy-light diquarks, though heavy-heavy diquarks $[QQ]_{\bar{3}}$ ($Q = c, b$), and the resulting tetraquark states $[QQ]_{\bar{3}}[\bar{Q}\bar{Q}]_3$ are also anticipated and discussed in the literature [52]. Following the discussion above, we construct the interpolating diquark operators for the two spin-states of such diquarks (here $Q = c, b$) [32]:

$$\begin{array}{rrrcl} \text{Scalar} & 0^+: & \mathcal{Q}_{i\alpha} & = & \epsilon_{\alpha\beta\gamma}(\bar{Q}_c^{\beta}\gamma_5 q_i^{\gamma} - \bar{q}_{i_c}^{\beta}\gamma_5 Q^{\gamma}), \qquad {\scriptstyle \alpha,\,\beta,\,\gamma:\ SU(3)_C \text{ indices}} \\ \text{Axial-Vector} & 1^+: & \vec{\mathcal{Q}}_{i\alpha} & = & \epsilon_{\alpha\beta\gamma}(\bar{Q}_c^{\beta}\vec{\gamma} q_i^{\gamma} + \bar{q}_{i_c}^{\beta}\vec{\gamma} Q^{\gamma}). \end{array}$$

In the non-relativistic (NR) limit, these states are parametrized by Pauli matrices: $\Gamma^0 = \frac{\sigma_2}{\sqrt{2}}$ (Scalar 0^+), and $\vec{\Gamma} = \frac{\sigma_2\vec{\sigma}}{\sqrt{2}}$ (Axial-Vector 1^+). We will characterize a tetraquark state with total angular momentum J by the state vector $|s_{\mathcal{Q}}, s_{\bar{\mathcal{Q}}};\ J\rangle$ showing the diquark spin $s_{\mathcal{Q}}$ and the antidiquark spin $s_{\bar{\mathcal{Q}}}$. There is no consensus on their names. We use the symbols X_J for J^{++}, Z for $J^{PC} = 1^{+-}$, and Y for $J^{PC} = 1^{--}$ states. Thus, the tetraquarks with the following diquark-spin and angular momentum J have the Pauli forms:

$$\begin{aligned} |0_{\mathcal{Q}}, 0_{\bar{\mathcal{Q}}};\ 0_J\rangle &= \Gamma^0 \otimes \Gamma^0, \\ |1_{\mathcal{Q}}, 1_{\bar{\mathcal{Q}}};\ 0_J\rangle &= \frac{1}{\sqrt{3}}\Gamma^i \otimes \Gamma_i, \\ |0_{\mathcal{Q}}, 1_{\bar{\mathcal{Q}}};\ 1_J\rangle &= \Gamma^0 \otimes \Gamma^i, \\ |1_{\mathcal{Q}}, 0_{\bar{\mathcal{Q}}};\ 1_J\rangle &= \Gamma^i \otimes \Gamma^0, \\ |1_{\mathcal{Q}}, 1_{\bar{\mathcal{Q}}};\ 1_J\rangle &= \frac{1}{\sqrt{2}}\varepsilon^{ijk}\Gamma_j \otimes \Gamma_k. \end{aligned} \tag{2}$$

Whenever necessary, we will put a subscript c or b to distinguish the $c\bar{c}$ and $b\bar{b}$ states.

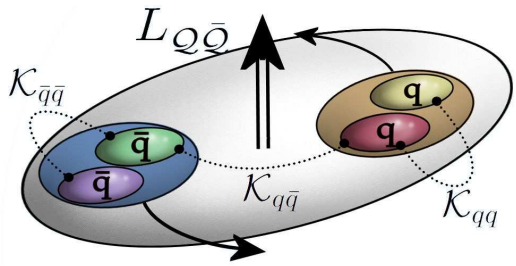


Figure 5: Schematic diagram of a tetraquark in the diquark-antidiquark picture.

3.1 Non-relativistic Hamiltonian for Tetraquarks with hidden charm

For the heavy quarkonium-like exotic hadrons, we work in the non-relativistic limit and use the following effective Hamiltonian to calculate the tetraquark mass spectrum [32, 42]

$$H_{\rm eff} = 2m_{\mathcal{Q}} + H_{SS}^{(qq)} + H_{SS}^{(q\bar{q})} + H_{SL} + H_{LL}, \tag{3}$$

where $m_{\mathcal{Q}}$ is the diquark mass, the second term above is the spin-spin interaction involving the quarks (or antiquarks) in a diquark (or anti-diquark), the third term depicts spin-spin interactions involving a quark and an antiquark in two different shells (i.e., in the two different diquark configurations), with the fourth and fifth terms being the spin-orbit and the orbit-orbit interactions, involving the quantum numbers of the tetraquark, respectively. For the S-states, these last two terms are absent. For illustration, we consider the case $Q = c$ and display the individual terms in $H_{\rm eff}$:

$$\begin{aligned}
H_{SS}^{(qq)} &= 2(\mathcal{K}_{cq})_{\bar{3}}[(\mathbf{S}_c \cdot \mathbf{S}_q) + (\mathbf{S}_{\bar{c}} \cdot \mathbf{S}_{\bar{q}})], \\
H_{SS}^{(q\bar{q})} &= 2(\mathcal{K}_{c\bar{q}})(\mathbf{S}_c \cdot \mathbf{S}_{\bar{q}} + \mathbf{S}_{\bar{c}} \cdot \mathbf{S}_q) + 2\mathcal{K}_{c\bar{c}}(\mathbf{S}_c \cdot \mathbf{S}_{\bar{c}}) + 2\mathcal{K}_{q\bar{q}}(\mathbf{S}_q \cdot \mathbf{S}_{\bar{q}}), \\
H_{SL} &= 2A_{\mathcal{Q}}(\mathbf{S}_{\mathcal{Q}} \cdot \mathbf{L} + \mathbf{S}_{\bar{\mathcal{Q}}} \cdot \mathbf{L}), \\
H_{LL} &= B_{\mathcal{Q}} \tfrac{L_{\mathcal{Q}\bar{\mathcal{Q}}}(L_{\mathcal{Q}\bar{\mathcal{Q}}}+1)}{2}.
\end{aligned} \tag{4}$$

Here $(\mathcal{K}_{cq})_{\bar{3}}$ parametrizes the spin-spin interaction between the charm c and the light quark q within a diquark in a color anti-triplet configuration, and the $(\mathcal{K}_{i\bar{j}}$ parametrize the spin-spin strengths between the quarks i and the antiquark $\bar{j}$, in the color-singlet configuration involving two different diquarks. The parameters $A_{\mathcal{Q}}$ and $B_{\mathcal{Q}}$ characterize the strength of the spin-orbit and the orbital angular force, respectively.
The usual angular momentum algebra then yields the following form:

$$\begin{aligned}
H_{\rm eff} &= 2m_{\mathcal{Q}} + \frac{B_{\mathcal{Q}}}{2}\langle L^2\rangle - 2a\langle L\cdot S\rangle + 2\kappa_{qc}\big[\langle s_q \cdot s_c\rangle + \langle s_{\bar{q}} \cdot s_{\bar{c}}\rangle\big] \\
&= 2m_{\mathcal{Q}} - aJ(J+1) + \left(\frac{B_{\mathcal{Q}}}{2} + a\right)L(L+1) + aS(S+1) - 3\kappa_{qc} \\
&\quad + \kappa_{qc}\big[s_{qc}(s_{qc}+1) + s_{\bar{q}\bar{c}}(s_{\bar{q}\bar{c}}+1)\big].
\end{aligned} \tag{5}$$

The effective Hamiltonian given above can be used for the tetraquark states involving a $b\bar{b}$ pair, with appropriate rescaling of the parameters.

Table 1: S-wave tetraquark states involving a $Q\bar{Q}$ pair in the two bases and their masses in the diquark model.

Label	J^{PC}	$\|s_{qQ}, s_{\bar{q}\bar{Q}}; S, L\rangle_J$	$\|s_{q\bar{q}}, s_{Q\bar{Q}}; S', L'\rangle_J$	Mass
X_0	0^{++}	$\|0,0;0,0\rangle_0$	$\big(\|0,0;0,0\rangle_0 + \sqrt{3}\|1,1;0,0\rangle_0\big)/2$	$M_{00} - 3\kappa_{qQ}$
X_0'	0^{++}	$\|1,1;0,0\rangle_0$	$\big(\sqrt{3}\|0,0;0,0\rangle_0 - \|1,1;0,0\rangle_0\big)/2$	$M_{00} + \kappa_{qQ}$
X_1	1^{++}	$\big(\|1,0;1,0\rangle_1 + \|0,1;1,0\rangle_1\big)/\sqrt{2}$	$\|1,1;1,L'\rangle_1$	$M_{00} - \kappa_{qQ}$
Z	1^{+-}	$\big(\|1,0;1,0\rangle_1 - \|0,1;1,0\rangle_1\big)/\sqrt{2}$	$\big(\|1,0;1,L'\rangle_1 - \|0,1;1,L'\rangle_1\big)/\sqrt{2}$	$M_{00} - \kappa_{qQ}$
Z'	1^{+-}	$\|1,1;1,0\rangle_1$	$\big(\|1,0;1,L'\rangle_1 + \|0,1;1,L'\rangle_1\big)/\sqrt{2}$	$M_{00} + \kappa_{qQ}$
X_2	2^{++}	$\|1,1;2,0\rangle_2$	$\|1,1;2,L'\rangle_2$	$M_{00} + \kappa_{qQ}$

Table 2: P-wave ($J^{PC} = 1^{--}$) tetraquark states involving a $Q\bar{Q}$ pair in the two bases and their masses in the diquark model.

Label	$\|s_{qQ}, s_{\bar{q}\bar{Q}}; S, L\rangle_J$	$\|s_{q\bar{q}}, s_{Q\bar{Q}}; S', L'\rangle_J$	Mass
Y_1	$\|0,0;0,1\rangle_1$	$\big(\|0,0;0,1\rangle_1 + \sqrt{3}\|1,1;0,1\rangle_1\big)/2$	$M_{00} - 3\kappa_{qQ} + B_Q$
Y_2	$\big(\|1,0;1,1\rangle_1 + \|0,1;1,1\rangle_1\big)/\sqrt{2}$	$\|1,1;1,L'\rangle_1$	$M_{00} - \kappa_{qQ} + 2a + B_Q$
Y_3	$\|1,1;0,1\rangle_1$	$\big(\sqrt{3}\|0,0;0,1\rangle_1 - \|1,1;0,1\rangle_1\big)/2$	$M_{00} + \kappa_{qQ} + B_Q$
Y_4	$\|1,1;2,1\rangle_1$	$\|1,1;2,L'\rangle_1$	$M_{00} + \kappa_{qQ} + 6a + B_Q$
Y_5	$\|1,1;2,3\rangle_1$	$\|1,1;2,L'\rangle_1$	$M_{00} + \kappa_{qQ} + 16a + 6B_Q$

3.2 Low-lying S and P-wave tetraquark states in the $c\bar{c}$ and $b\bar{b}$ sectors

The states in the diquark-antidiquark basis $|s_{qQ}, s_{\bar{q}\bar{Q}}; S, L\rangle_J$ and in the $Q\bar{Q}$ and $q\bar{q}$ basis $|s_{q\bar{q}}, s_{Q\bar{Q}}; S', L'\rangle_J$ are related by Fierz transformation. The positive parity S-wave tetraquarks are given in terms of the six states listed in Table 1 (charge conjugation is defined for neutral states). These states are characterized by the quantum number $L = 0$, hence their masses depend on just two parameters M_{00}, the diquark mass, and κ_{qQ}, leading to several predictions to be tested against experiments. The P-wave states are listed in Table 2. The first four of them have $L = 1$, and the fifth has $L = 3$, and hence is expected to be significantly heavier.
The parameters appearing on the r.h. columns of Tables 1 and 2 can be determined using the masses of some of the observed X, Y, Z states, and their numerical values are given in Table 3. Some parameters in the $c\bar{c}$ and $b\bar{b}$ sectors can also be related using the heavy quark mass scaling [53].
Typical errors on the masses due to parametric uncertainties are estimated to be about 30 MeV. Of course, this assumes that the effective Hamiltonian framework is a good approximation, and the error from this assumption is hard to quantify. There are several predictions in the charmonium-like sector, which, with the values of the parameters given in the tables above, are in the right ball-park [2]. It should be remarked that these input values, in particular for the quark-quark couplings in a diquark, κ_{qQ}, are larger than in the earlier determinations by Maiani *et al.* [32].In the modified scheme [42], the parameters ($\kappa_{i\bar{j}}$ are set to zero, eliminating the $H_{SS}^{(q\bar{q})}$ term in the effective Hamiltonian. With this, better agreement is reached with experiments

[2] I thank Satoshi Mishima for providing these estimates.

Table 3: Numerical values of the parameters in $H_{\rm eff}$, obtained using some of the S and P-wave tetraquarks as input.

	charmonium-like	bottomonium-like
M_{00} [MeV]	3957	10630
κ_{qQ} [MeV]	67	23
B_Q [MeV]	268	329
a [MeV]	52.5	26

Table 4: X, Y, Z hadron masses from experiments and in the diquark-model.

		charmonium-like		bottomonium-like	
Label	J^{PC}	State	Mass [MeV]	State	Mass [MeV]
X_0	0^{++}	—	3756	—	10562
X_0'	0^{++}	—	4024	—	10652
X_1	1^{++}	$X(3872)$	3890	—	10607
Z	1^{+-}	$Z_c^+(3900)$	3890	$Z_b^{+,0}(10610)$	10607
Z'	1^{+-}	$Z_c^+(4020)$	4024	$Z_b^+(10650)$	10652
X_2	2^{++}	—	4024	—	10652
Y_1	1^{--}	$Y(4008)$	4024	$Y_b(10891)$	10891
Y_2	1^{--}	$Y(4260)$	4263	$Y_b(10987)$	10987
Y_3	1^{--}	$Y(4290)$ (or $Y(4220)$)	4292	—	10981
Y_4	1^{--}	$Y(4630)$	4607	—	11135
Y_5	1^{--}	—	6472	—	13036

assuming that diquarks are more tightly bound than suggested from the analysis of the baryons in the diquark-quark picture. Despite this success, the continued experimental absence of the two lowest-lying 0^{++} states, called X_0 and X_0', is puzzling. Perhaps, they are below the threshold for strong decays and decay weakly, and thus have not been looked for. Alternative calculations of the tetraquark spectrum based on diquark-antidiquark model have been carried out in other phenomenological schemes [54], and in the QCD sum rule framework [55, 56]. All of them share the common feature with the effective Hamiltonian approach discussed here, namely they anticipate a very rich tetraquark spectroscopy. So, if the diquark picture has come to stay, some dynamical selection rules are required to better understand the observed spectrum.

The exotic bottomonium-like states are currently rather sparse. The reason for this is that quite a few exotic candidates charmonium-like states were observed in the decays of B-hadrons. This mode is obviously not available for the hidden $b\bar{b}$ states. They can only be produced in hadro- and electroweak high energy processes. Tetraquark states with a single b quark can, in principle, also be produced in the decays of the B_c mesons, as pointed out recently [57]. As the $c\bar{c}$ and $b\bar{b}$ cross-section at the LHC are very large, we anticipate that the exotic spectroscopy involving the open and hidden heavy quarks is an area where significant new results will be reported by all the LHC experiments. Measurements of the production and decays of exotica, such as transverse-momentum distributions and polarization information, will go a long way in understanding the underlying dynamics.

As a side remark, we mention that recently there has been a lot of excitement due to the D0 observation [58] of a narrow structure $X(5568)$, consisting of four different quark flavors ($bdus$), found through the $B_s^0\pi^\pm$ decay mode. However, this has not been confirmed by the LHCb collaboration [59], despite the fact that LHCb has 20 times larger B_s^0 sample than that of D0. This would have been the first discovery of an open b-quark tetraquark state. They are anticipated in the compact tetraquark picture [57], and also in the hadron molecule framework [60].

We now discuss the three observed exotic states in the bottomonium sector in detail. The hidden $b\bar{b}$ state $Y_b(10890)$ with $J^{\rm P}=1^{--}$ was discovered by Belle in 2007 [61] in the process $e^+e^-\to Y_b(10890)\to(\Upsilon(1S),\Upsilon(2S),\Upsilon(3S))\pi^+\pi^-$ just above the $\Upsilon(5S)$. The branching ratios measured are about two orders of magnitude larger than anticipated from similar dipionic transitions in the lower $\Upsilon(nS)$ states and in the ψ' (for a review and references to earlier work, see Brambilla *et al* [62]). Also the dipion invariant mass distributions in the decays of Y_b are marked by the presence of the resonances $f_0(980)$ and $f_2(1270)$. This state was interpreted as a $J^{\rm PC}=1^{--}$ P-wave tetraquark [43, 44]. Subsequent to this, a Van Royen-Weiskopf formalism was used [45] in which direct electromagnetic couplings with the diquark-antidiquark pair of the Y_b was assumed. Due to the P-wave nature of the $Y_b(10890)$, with a commensurate small overlap function, the observed small production cross-section in $e^+e^-\to b\bar{b}$ is expected. In the tetraquark picture, the $Y_b(10890)$ is the $b\bar{b}$ analogue of the $c\bar{c}$ state $Y_c(4260)$, also a P-wave, which is likewise found to have a very small production cross-section, but decays readily into $J/\psi\pi^+\pi^-$. Hence, the two have very similar production and decay characteristics.

The current status of $Y_b(10890)$ is, however, unclear. Subsequent to its discovery, Belle undertook high-statistics scans to measure the ratio $R_{b\bar{b}}=\sigma(e^+e^-\to b\bar{b})/\sigma(e^+e^-\to\mu^+\mu^-)$, and also more precisely the ratios $R_{\Upsilon(nS)\pi^+\pi^-}=\sigma(e^+e^-\to\Upsilon(nS)\pi^+\pi^-)/\sigma(e^+e^-\to\mu^+\mu^-)$. They are shown in Fig. 6 and Fig. 7, respectively. The two masses, $M(5S)_{b\bar{b}}$ measured through $R_{b\bar{b}}$, and $M(Y_b)$, measured through $R_{\Upsilon(nS)\pi^+\pi^-}$, now differ by slightly more than 2σ, $M(5S)_{b\bar{b}}-M(Y_b)=-9\pm4$ MeV. From the mass difference alone, these two could very well be just one and the same state, namely the canonical $\Upsilon(5S)$ - an interpretation adopted by the Belle

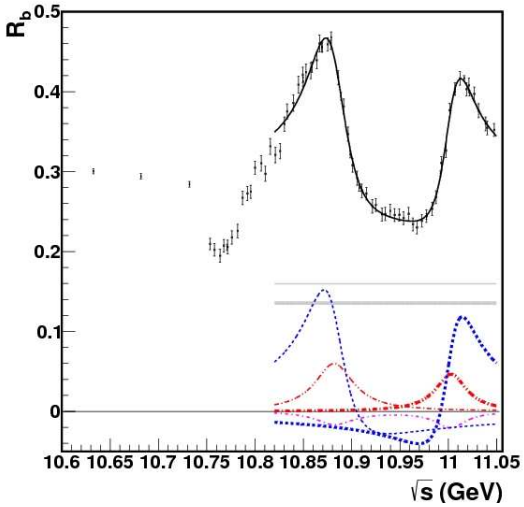


Figure 6: The ratio $R_b = \sigma(e^+e^- \to b\bar{b})/\sigma(e^+e^- \to \mu^+\mu^-)$ in the $Y(10860)$ and $Y(11020)$ region. The components of the fit are depicted in the lower part of the figure: total (solid curve), constant $|A_{ic}|^2$ (thin), $|A_c|^2$ (thick): for $\Upsilon(5S)$ (thin) and $\Upsilon(6S)$ (thick): $|f|^2$ (dot-dot-dash), cross terms with A_c (dashed), and two-resonance cross term (dot-dash). Here, A_c and A_{ic} are coherent and incoherent continuum terms, respectively (from Belle [63]).

collaboration [63]. On the other hand, it is now the bookkeeping of the branching ratios measured at or near the $\Upsilon(5S)$, which is puzzling. This is reflected in the paradox that *direct production* of the $B^{(*)}\bar{B}^{(*)}$ as well as of $B_s\bar{B}_s^{(*)}$ states have essentially no place in the Belle accounting [63], even though these reactions have measured cross sections, first observed by CLEO [74]. The branching ratios of the $\Upsilon(5S)$ measured by Belle are already saturated by the exotic states $(\Upsilon(nS)\pi^+\pi^-, h_b(mP)\pi^+\pi^-, Z_b(10610)^\pm\pi^\mp, Z_b(10650)^\pm\pi^\mp$ and their isospin partners). The reason for this mismatch is not clear, and is attributed by Belle to the inadequate modeling of R_b due to several thresholds in this energy reason. In our opinion, an interpretation of the Belle data based on two resonances $\Upsilon(5S)$ and $Y_b(10890)$ is more natural, with $\Upsilon(5S)$ having the decays expected for the bottomonium S-state above the $B^{(*)}\bar{B}^{(*)}$ threshold, and the decays of $Y_b(10890)$, a tetraquark, being the source of the exotic states seen. As data taking starts in a couple of years in the form of a new and expanded collaboration, Belle-II, cleaning up the current analysis in the $\Upsilon(5S)$ and $\Upsilon(6S)$ region should be one of their top priorities.

Thus, the hypothesis that $\Upsilon(5S)$ and $Y_b(10890)$, while having the same $J^{\rm PC} = 1^{--}$ quantum numbers and almost the same mass, are *different* states, is still not completely ruled out. As already mentioned, this is hinted by the drastically different decay characteristics of the dipionic transitions involving the lower quarkonia S-states, such as $\Upsilon(4S) \to \Upsilon(1S)\pi^+\pi^-$, on one hand, and similar decays of the Y_b, on the other. These anomalies are seen both in the decay rates and in the dipion invariant mas spectra in the $\Upsilon(nS)\pi^+\pi^-$ modes. The large branching ratios of $Y_b \to \Upsilon(nS)\pi^+\pi^-$, as well as of $Y(4260) \to J/\psi\pi^+\pi^-$, are due to the Zweig-allowed nature of these transitions, as the initial and final states have the same valence quarks. The final state $\Upsilon(nS)\pi^+\pi^-$ in Y_b decays requires the excitation of a $q\bar{q}$ pair from the vacuum. Since, the light scalars σ_0, $f_0(980)$ are themselves tetraquark candidates [64, 65], they are expected to show

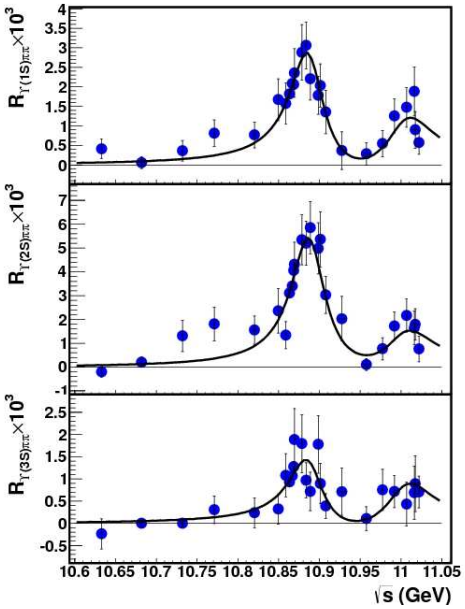


Figure 7: The ratio $R_{\Upsilon(nS)\pi^+\pi^-} = \sigma(e^+e^- \to \Upsilon(nS)\pi^+\pi^-)/\sigma(e^+e^- \to \mu^+\mu^-)$ in the $Y(10860)$ and $Y(11020)$ region (from Belle [63]).

up in the $\pi^+\pi^-$ invariant mass distributions, as opposed to the corresponding spectrum in the transition $\Upsilon(4S) \to \Upsilon(1S)\pi^+\pi^-$ (see Fig. 8). Subsequent discoveries [66] of the charged states $Z_b^+(10610)$ and $Z_b^+(10650)$, found in the decays $\Upsilon(5S)/Y_b \to Z_b^+(10610)\pi^-, Z_b^+(10650)\pi^-$, leading to the final states $\Upsilon(1S)\pi^+\pi^-$, $\Upsilon(2S)\pi^+\pi^-$, $\Upsilon(3S)\pi^+\pi^-$, $h_b(1P)\pi^+\pi^-$ and $h_b(2P)\pi^+\pi^-$, give credence to the tetraquark interpretation, as discussed below.

3.3 Heavy-Quark-Spin Flip in $\Upsilon(10890) \to h_b(1P, 2P)\pi\pi$

The cross-section $\sigma(e^+e^- \to (h_b(1P), h_b(2P)\pi^+\pi^-)$ measured by Belle [67] is shown in Fig. 9, providing clear evidence of the production in the $\Upsilon(10860)$ and $\Upsilon(11020)$ region. We summarize the relative rates and strong phases measured by Belle [66] in the process $\Upsilon(10890) \to \Upsilon(nS)\pi^+\pi^-, h_b(mP)\pi^+\pi^-$, with $n = 1, 2, 3$ and $m = 1, 2$ in Table 5. For ease of writing we shall use the notation Z_b and Z_b' for the two charged Z_b states. Here no assumption is made about the nature of $\Upsilon(10890)$, it can be either $\Upsilon(5S)$ or Y_b. Of these, the decay $\Upsilon(10890) \to \Upsilon(1S)\pi^+\pi^-$ involves both a resonant (i.e., via Z/Z') and a direct component, but the other four are dominated by the resonant contribution. One notices that the relative normalizations are very similar and the phases of the $(\Upsilon(2S), \Upsilon(3S))\pi^+\pi^-$ differ by about 180° compared to the ones in $(h_b(1P, h_b(2P))\pi^+\pi^-$. At the first sight this seems to violate the heavy-quark-spin conservation, as in the initial state $s_{b\bar{b}} = 1$, which remains unchanged for the $\Upsilon(nS)$ in the final state, i.e., it involves an $s_{b\bar{b}} = 1 \to s_{b\bar{b}} = 1$ transition, but as $s_{b\bar{b}} = 0$ for the $h_b(mP)$, this involves an $s_{b\bar{b}} = 1 \to s_{b\bar{b}} = 0$ transition, which should have been suppressed, but is not supported by data. It has been shown that this contradiction is only apparent [53]. Expressing the states Z_b and Z_b' in the basis of definite $b\bar{b}$ and light quark $q\bar{q}$ spins, it becomes evident that both the Z_b and

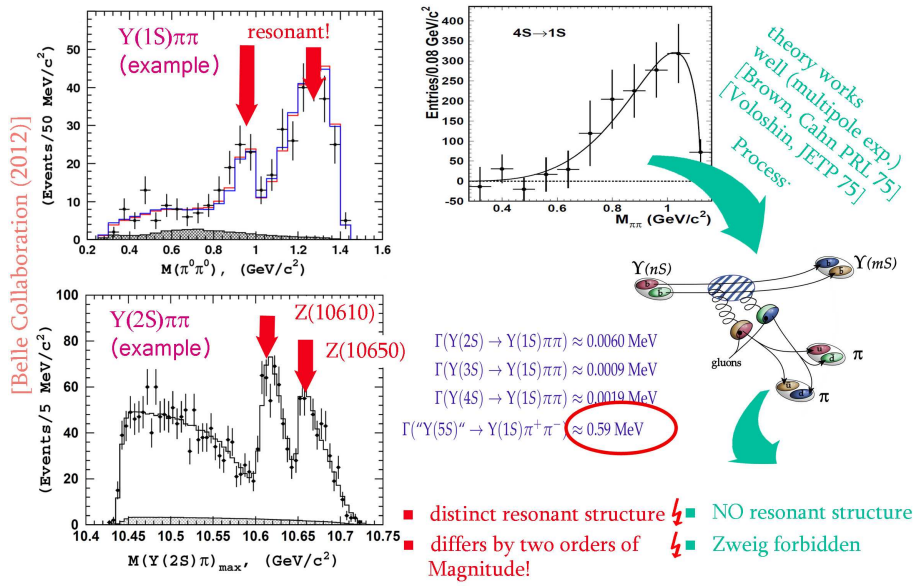


Figure 8: Dipion invariant mass distribution in $\Upsilon(10890) \to \Upsilon(1S)\pi^0\pi^0$ (upper left frame); the resonances indicated in the dipion spectrum correspond to the $f_0(980)$ and $f_2(1270)$; the resonances $Z(10610)$ and $Z(10650)$ are indicated in the $\Upsilon(2S)\pi^+$ invariant mass distribution from $\Upsilon(10890) \to \Upsilon(2S)\pi^+\pi^-$ (lower left frame). The data are from the Belle collaboration [66]. The upper right hand frame shows the dipion invariant mass distribution in $\Upsilon(4S) \to \Upsilon(1S)\pi^+\pi^-$, and the theoretical curve (with the references) is based on the Zweig-forbidden process shown below. The measured decay widths from $\Upsilon(nS) \to \Upsilon(1S)\pi^+\pi^-$ $nS = 2S, 3S, 4S$ and $\Upsilon(10890) \to \Upsilon(1S)\pi^+\pi^-$ are also shown.

Table 5: Relative normalizations and phases for $s_{b\bar{b}} : 1 \to 1$ and $1 \to 0$ transitions in $\Upsilon(10890)$ decays [66].

Final State	$\Upsilon(1S)\pi^+\pi^-$	$\Upsilon(2S)\pi^+\pi^-$	$\Upsilon(3S)\pi^+\pi^-$	$h_b(1P)\pi^+\pi^-$	$h_b(2P)\pi^+\pi^-$
Rel. Norm.	$0.57 \pm 0.21^{+0.19}_{-0.04}$	$0.86 \pm 0.11^{+0.04}_{-0.10}$	$0.96 \pm 0.14^{+0.08}_{-0.05}$	$1.39 \pm 0.37^{+0.05}_{-0.15}$	$1.6^{+0.6+0.4}_{-0.4-0.6}$
Rel. Phase	$58 \pm 43^{+4}_{-9}$	$-13 \pm 13^{+17}_{-8}$	$-9 \pm 19^{+11}_{-26}$	187^{+44+3}_{-57-12}	$181^{+65+74}_{-105-109}$

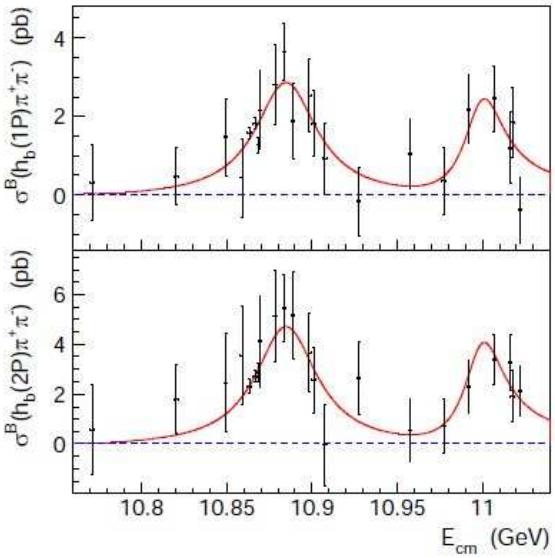


Figure 9: $\sigma(e^+e^- \to h_b(1P)\pi^+\pi^-)$ and $\sigma(e^+e^- \to h_b(2P)\pi^+\pi^-)$-in the $Y(10860)$ and $Y(11020)$ region(from Belle [67]).

Z_b' have $s_{b\bar{b}} = 1$ and $s_{b\bar{b}} = 0$ components,

$$|Z_b\rangle = \frac{|1_{q\bar{q}}, 0_{b\bar{b}}\rangle - |0_{q\bar{q}}, 1_{b\bar{b}}\rangle}{\sqrt{2}}, \quad |Z_b'\rangle = \frac{|1_{q\bar{q}}, 0_{b\bar{b}}\rangle + |0_{q\bar{q}}, 1_{b\bar{b}}\rangle}{\sqrt{2}} \tag{6}$$

Defining (g is the effective couplings at the vertices $\Upsilon\, Z_b\, \pi$ and $Z_b\, h_b\, \pi$)

$$\begin{aligned} g_Z &\equiv g(\Upsilon \to Z_b\pi)g(Z_b \to h_b\pi) \propto -\alpha\beta\langle h_b|Z_b\rangle\langle Z_b|\Upsilon\rangle, \\ g_{Z'} &\equiv g(\Upsilon \to Z_b'\pi)g(Z_b' \to h_b\pi) \propto \alpha\beta\langle h_b|Z_b'\rangle\langle Z_b'|\Upsilon\rangle, \end{aligned} \tag{7}$$

we note that within errors, Belle data is consistent with the heavy quark spin conservation, which requires $g_Z = -g_{Z'}$. The two-component nature of the Z_b and Z_b' is also the feature which was pointed out earlier for Y_b in the context of the direct transition $Y_b(10890) \to \Upsilon(1S)\pi^+\pi^-$. To determine the coefficients α and β, one has to resort to $s_{b\bar{b}}$: $1 \to 1$ transitions

$$\Upsilon(10890) \to Z_b/Z_b' + \pi \to \Upsilon(nS)\pi\pi \ (n = 1, 2, 3). \tag{8}$$

The analogous effective couplings are

$$\begin{aligned} f_Z &= f(\Upsilon \to Z_b\pi)f(Z_b \to \Upsilon(nS)\pi) \propto |\beta|^2\langle\Upsilon(nS)|0_{q\bar{q}}, 1_{b\bar{b}}\rangle\langle 0_{q\bar{q}}, 1_{b\bar{b}}|\Upsilon\rangle, \\ f_{Z'} &= f(\Upsilon \to Z_b'\pi)f(Z_b' \to \Upsilon(nS)\pi) \propto |\alpha|^2\langle\Upsilon(nS)|0_{q\bar{q}}, 1_{b\bar{b}}\rangle\langle 0_{q\bar{q}}, 1_{b\bar{b}}|\Upsilon\rangle. \end{aligned} \tag{9}$$

Dalitz analysis indicates that $\Upsilon(10890) \to Z_b/Z_b' + \pi \to \Upsilon(nS)\pi\pi$ $(n = 1, 2, 3)$ proceed mainly through the resonances Z_b and Z_b', though $\Upsilon(10890) \to \Upsilon(1S)\pi\pi$ has a significant direct component, expected in tetraquark interpretation of $\Upsilon(10890)$ [45]. A comprehensive analysis of

the Belle data including the direct and resonant components is required to test the underlying dynamics, which yet to be carried out. However, parametrizing the amplitudes in terms of two Breit-Wigners, one can determine the ratio α/β from $\Upsilon(10890) \to Z_b/Z_b' + \pi \to \Upsilon(nS)\pi\pi$ ($n = 1, 2, 3$). For the $s_{b\bar{b}} : 1 \to 1$ transition, we get for the averaged quantities:

$$\overline{\text{Rel.Norm.}} = 0.85 \pm 0.08 = |\alpha|^2/|\beta|^2; \quad \overline{\text{Rel.Phase}} = (-8 \pm 10)^\circ. \tag{10}$$

For the $s_{b\bar{b}} : 1 \to 0$ transition, we get

$$\overline{\text{Rel.Norm.}} = 1.4 \pm 0.3; \quad \overline{\text{Rel.Phase}} = (185 \pm 42)^\circ. \tag{11}$$

Within errors, the tetraquark assignment with $\alpha = \beta = 1$ is supported, i.e.,

$$|Z_b\rangle = \frac{|1_{bq}, 0_{\bar{b}\bar{q}}\rangle - |0_{bq}, 1_{\bar{b}\bar{q}}\rangle}{\sqrt{2}}, \quad |Z_b'\rangle = |1_{bq}, 1_{\bar{b}\bar{q}}\rangle_{J=1}, \tag{12}$$

and

$$|Z_b\rangle = \frac{|1_{q\bar{q}}, 0_{b\bar{b}}\rangle - |0_{q\bar{q}}, 1_{b\bar{b}}\rangle}{\sqrt{2}}, \quad |Z_b'\rangle = \frac{|1_{q\bar{q}}, 0_{b\bar{b}}\rangle + |0_{q\bar{q}}, 1_{b\bar{b}}\rangle}{\sqrt{2}}. \tag{13}$$

It is interesting that similar conclusion was drawn in the 'molecular' interpretation [68] of the Z_b and Z_b'.
The Fierz rearrangement used in obtaining second of the above relations would put together the $b\bar{q}$ and $q\bar{b}$ fields, yielding

$$|Z_b\rangle = |1_{b\bar{q}}, 1_{\bar{b}q}\rangle_{J=1}, \quad |Z_b'\rangle = \frac{|1_{b\bar{q}}, 0_{q\bar{b}}\rangle + |0_{b\bar{q}}, 1_{q\bar{b}}\rangle}{\sqrt{2}}. \tag{14}$$

Here, the labels $0_{b\bar{q}}$ and $1_{\bar{q}b}$ could be viewed as indicating B and B^* mesons, respectively, leading to the prediction $Z_b \to B^*\bar{B}^*$ and $Z_b' \to B\bar{B}^*$, which is not in agreement with the Belle data [66]. However, this argument rests on the conservation of the light quark spin, for which there is no theoretical foundation. Hence, this last relation is not reliable. Since $Y_b(10890)$ and $\Upsilon(5S)$ are rather close in mass, and there is an issue with the unaccounted *direct production* of the $B^*\bar{B}^*$ and $B\bar{B}^*$ states in the Belle data collected in their vicinity, we conclude that the experimental situation is still in a state of flux and look forward to its resolution with the consolidated Belle-II data.

The exotic hadrons having $J^{\rm PC} = 1^{--}$ can be produced at the Tevatron and LHC via the Drell-Yan process [69] $pp(\bar{p}) \to \gamma^* \to V + ...$ The cases $V = \phi(2170), Y(4260), Y_b(10890)$ have been studied [69]. With the other two hadrons already discussed earlier, we recall that $\phi(2170)$ was first observed in the ISR process $e^+e^- \to \gamma_{\rm ISR} f_0(980)\phi(1020)$ by BaBaR [70] and later confirmed by BESII [71] and Belle [72]. Drenska *et al.* [73] interpreted $\phi(1270)$ as a P-wave tetraquark $[sq][\bar{s}\bar{q}]$. Thus, all three vector exotica are assumed to be the first orbital excitation of diquark-antidiquark states with a hidden $s\bar{s}$, $c\bar{c}$ and $b\bar{b}$ quark content, respectively. As all three have very small branching ratios in a dilepton pair, they should be searched for in the decay modes in which they have been discovered, and these are $\phi(2170) \to f_0(980)\phi(1020) \to \pi^+\pi^-K^+K^-$, $Y(4260) \to J/\psi\pi^+\pi^- \to \mu^+\mu^-\pi^+\pi^-$ and $Y_b(10890) \to \Upsilon(nS)\pi^+\pi^- \to \mu^+\mu^-\pi^+\pi^-$. Thus, they involve four charged particles, which can be detected at hadron colliders. The cross sections for the processes $p\bar{p}(p) \to \phi(2170)(\to \phi(1020)f_0(980) \to$

$K^+K^-\pi^+\pi^-$), $p\bar{p}(p) \to Y(4260)(\to J/\psi\pi^+\pi^- \to \mu^+\mu^-\pi^+\pi^-)$, and $p\bar{p}(p) \to Y_b(10890)(\to \Upsilon(1S,2S,3S)\pi^+\pi^- \to \mu^+\mu^-\pi^+\pi^-)$, at the Tevatron ($\sqrt{s} = 1.96$ TeV) and the LHC are computed in [69]. All these processes have measurable rates, and they should be searched for at the LHC.

Summarizing the tetraquark discussion, we note that there are several puzzles in the X, Y, Z sector, and the underlying dynamics is not understood. Apart from the rich spectrum in the diquark scenario and the continued absence of many predicted states, they involve the nature of the observed states $J^{PC} = 1^{--}$, $Y(4260)$ and $Y(10890)$, and whether they are related with each other. Also, whether $Y(10890)$ and $\Upsilon(5S)$ are one and the same particle is still an open issue. In principle, both $Y(4260)$ and $Y(10890)$ can be produced at the LHC and measured through the $J\psi\pi^+\pi^-$ and $\Upsilon(nS)\pi^+\pi^-$ ($nS = 1S, 2S, 3S$) modes, respectively. Their hadroproduction cross-sections are unfortunately uncertain, but their (normalized) transverse momentum distributions will be quite revealing. As they are both $J^{PC} = 1^{--}$ hadrons, they can also be produced via the Drell-Yan mechanism and detected through their signature decay modes. The tetraquark interpretation of the charged exotics Z_b and Z_b' leads to a straight forward understanding of the relative rates and strong phases of the heavy quark spin non-flip and spin-flip transitions in the decays $\Upsilon(10890) \to \Upsilon(nS)\pi^+\pi^-$ and $\Upsilon(10890) \to h_b(mP)\pi^+\pi^-$, respectively. In the tetraquark picture, the corresponding hadrons in the charm sector Z_c and Z_c' are related to their $b\bar{b}$ counterparts.

4 Pentaquarks

Pentaquarks remained elusive for almost a decade under the shadow of the botched discoveries of $\Theta(1540)$, $\Phi(1860)$, $\Theta_c(3100)$. The sentiment of the particle physics community is reflected in the terse 2014 PDG review [75], which characterizes them as false alarms. This has definitely changed by the observation of $J/\psi p$ resonances consistent with pentaquark states in $\Lambda_b^0 \to J/\psi K^- p$ decays by the LHCb collaboration [2]:

$$pp \to b\bar{b} \to \Lambda_b X; \Lambda_b \to K^- J/\psi p. \tag{15}$$

The measured distributions in the invariant masses m_{Kp} and $m_{J/\psi p}$ are shown in Fig. 10 together with a model comparison with two P_c^+ states. A statistically good fit of the $m_{J/\psi p}$ distribution is consistent with the presence of two resonant states, henceforth called $P_c(4450)^+$ and $P_c(4380)^+$, with the following characteristics

$$M = 4449.8 \pm 1.7 \pm 2.5 \text{ MeV}; \quad \Gamma = 39 \pm 5 \pm 19 \text{ MeV}, \tag{16}$$

and

$$M = 4380 \pm 8 \pm 29 \text{ MeV}; \quad \Gamma = 205 \pm 18 \pm 86 \text{ MeV}. \tag{17}$$

Both of these states carry a unit of baryonic number and have the valence quarks $P_c^+ = \bar{c}cuud$. The preferred $J^{\rm P}$ assignments are $5/2^+$ for the $P_c(4450)^+$ and $3/2^-$ for the $P_c(4380)^+$.

Doing an Argand-diagram analysis in the (Im A^{P_c} - Re A^{P_c}) plane, the phase change in the amplitude is consistent with a resonance for the $P_c(4450)^+$, but less so for the $P_c(4380)^+$, as shown in Fig. 11. The phase diagram for the $P_c(4380)^+$ state needs further study with more data, but the resonant character of the $P_c(4450)^+$ state is established beyond doubt. This will be contrasted with the corresponding phase diagram resulting from the assumption that $P_c(4450)^+$ is a kinematically-induced cusp state.

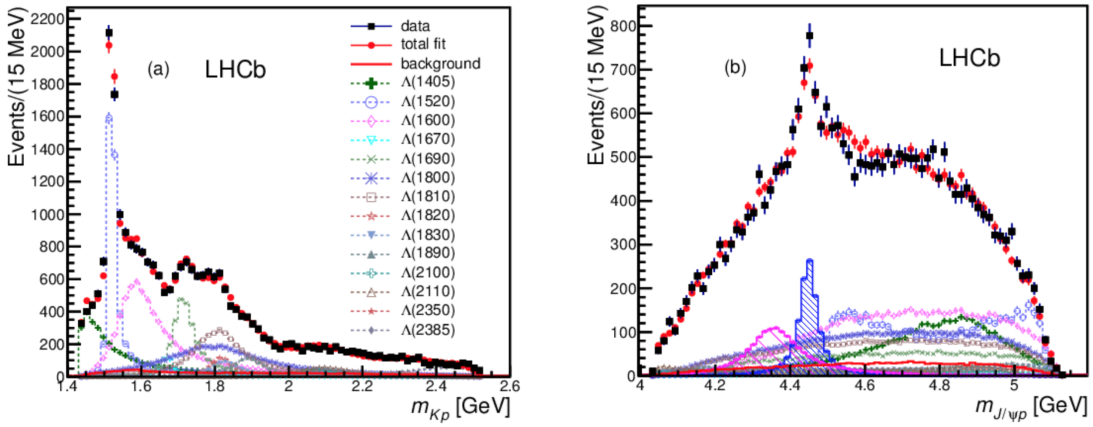


Figure 10: Fit projections for (a) m_{Kp} and (b) $m_{J/\psi p}$ distributions for the reduced Λ^* model with two P_c^+ states, $P_c(4450)$ blue (open) squares with shaded histogram and $P_c(4380)^+$ with (purple) filled squares. Each Λ^* component is also shown. (from LHCb [2]).

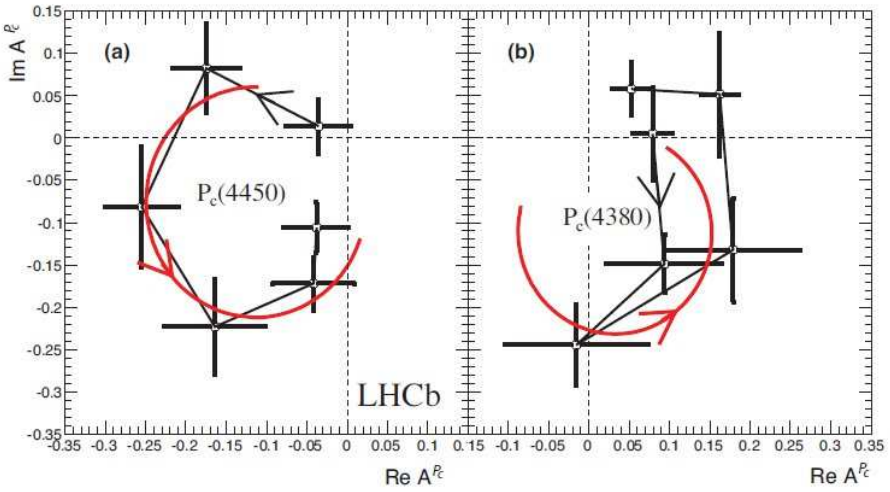


Figure 11: Fitted values of the real and imaginary parts of the amplitudes for the $(3/2^-, 5/2^+)$ assignments for (a) the $P_c(4450)^+$ state and (b) the $P_c(4380)^+$ state, each divided into six $m_{J/\psi p}$ bins of equal width between $-\Gamma$ and $+\Gamma$ shown in the Argand diagrams as connected points with error bars. The solid (red) curves are the predictions from the Breit-Wigner formula for the same mass range with $M(\Gamma)$ of 4450(39) MeV and 4380 (205) MeV, respectively. (from LHCb [2]).

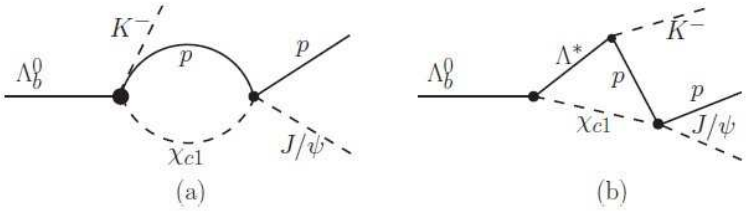


Figure 12: The two scattering diagrams discussed in the text [78].

Following a pattern seen for the tetraquark candidates, namely their proximity to respective thresholds, such as $D\bar{D}^*$ for the $X(3872)$, $B\bar{B}^*$ and $B^*\bar{B}^*$ for the $Z_b(10610)$ and $Z_b(10650)$, respectively, also the two pentaquark candidates $P_c(4380)$ and $P_c(4450)$ lie close to several charm meson-baryon thresholds [76]. The $\Sigma_c^{*+}\bar{D}^0$ has a threshold of 4382.3 ± 2.4 MeV, tantalizingly close to the mass of $P_c(4380)^+$. In the case of $P_c(4450)^+$, there are several thresholds within striking distance, $\chi_{c1}p(4448.93 \pm 0.07), \Lambda_c^{*+}\bar{D}^0(4457.09 \pm 0.35), \Sigma_c^+\bar{D}^{*0}(4459.9 \pm 0.9)$, and $\Sigma_c^+\bar{D}^0\pi^0(4452.7 \pm 0.5)$, where the masses are in units of MeV. This has led to a number of hypotheses to explain the two P_c states:

- $P_c(4380)$ and $P_c(4450)$ are baryocharmonia [77].
- Rescattering-induced kinematic effects are mimicking the resonances [78, 79, 80, 81].
- They are open charm-baryon and charm-meson bound states [82, 83, 84, 85, 86].
- They are compact diquark-diquark-antiquark states [87, 88, 89, 90, 91, 92, 93, 94], with each component being a $\bar{3}$, yielding a color-singlet $\bar{c}[cq][qq]$ state. Another possibility is via the sequential formation of compact color triplets, making up diquark-triquark systems, yielding also color-singlet states [95, 96].

In the baryocharmonium picture, the P_c states are hadroquarkonium-type composites of J/ψ and excited nucleon states similar to the known resonances $N(1440)$ and $N(1520)$. Photoproduction of the P_c states in $\gamma + p$ collisions is advocated as sensitive probe of this mechanism [77]. We shall discuss below the interpretation of pentaquarks as scattering-induced kinematic effects, and as meson-baryon molecules, but review the compact diquark-based models in quite some detail.

4.1 Pentaquarks as rescattering-induced kinematic effects

Kinematic effects can result in a narrow structure around the $\chi_{c1}p$ threshold. Two possible mechanisms shown in Fig. 12 are:
(a) 2-point loop with a 3-body production $\Lambda_b^0 \to K^-\,\chi_{c1}\,p$ followed by the rescattering process $\chi_{c1}\,p \to J/\psi\,p$, and
(b) in which $K^-\,p$ is produced from an intermediate Λ^* and the proton rescatters with the χ_{c1} into a $J/\psi\,p$, as shown below.

The amplitude for Fig. (a) can be expressed as

$$G_\Lambda(E) = \int \frac{d^3q}{(2\pi)^3} \frac{\vec{q}^2 f_\Lambda(\vec{q}^2)}{E - m_p - m_{\chi_{c1}} - \vec{q}^2/(2\mu)}, \tag{18}$$

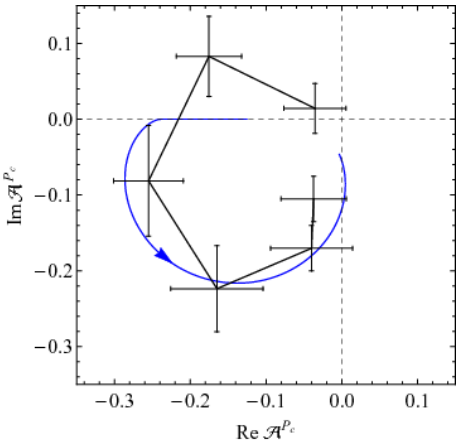


Figure 13: Fitted values of the real and imaginary parts of the amplitudes for the $P_c(4450)^+$ using a Breit-Wigner formula with $M(\Gamma)$ of 4450(39) MeV [2]. The directed curve (blue) is the fit in the cusp model. (from [78]).

where μ is the reduced mass and $f_\Lambda(\vec{q}^2) = \exp(-2\vec{q}^2/\Lambda^2)$ is a form factor to regularize the loop integral. Fitting the Argand diagram for the $P_c(4450)^+$ with $\mathcal{A}_{(a)} = N(b + G_\Lambda(E))$ determines the normalization N, the constant background b, and Λ. The integral can be solved analytically [78]

$$G_\Lambda(E) = \frac{\mu\Lambda}{(2\pi)^{3/2}}(k^2 + \Lambda^2/4) + \frac{\mu k^3}{2\pi}\exp^{-2k^2/\Lambda^2}\left[erfc(\frac{\sqrt{2}k}{\Lambda}) - i\right] \tag{19}$$

where $k = \sqrt{2\mu(E - m_1 - m_2 + i\epsilon)}$. This function has a characteristic phase motion reflecting the error function, as shown in Fig. 13. It differs from the Breit-Wigner fit, which is in excellent agreement with the LHCb data [2]. The cusp-based fit also shows a counter-clockwise behavior in the Argand diagram, but not for the two data points where the imaginary part of the cusp amplitude is zero. The absolute value of the amplitude in the cusp approach shows a resonant behavior, which can be made to peak even more sharply at $\mathrm{Re}\sqrt{s} = 4450$ MeV, if the amplitude for Fig. 12 (b) is included and assumed dominated by the $\Lambda^*(1890)$-exchange. However, it is the phase motion, which is decisive in distinguishing a dynamical Breit-Wigner (or, for that matter a Flatte [97] type) resonance and a kinematic-induced cusp behavior. More data is needed to completely settle this difference in the case of $P_c(4450)^+$, but currently the Breit-Wigner fit is the preferred description.

4.2 Pentaquarks as meson-baryon molecules

In the hadronic molecular interpretation, one identifies the $P_c(4380)^+$ with $\Sigma_c(2455)\bar{D}^*$ and the $P_c(4450)^+$ with $\Sigma_c(2520)\bar{D}^*$, which are bound by a pion exchange. The underlying interaction

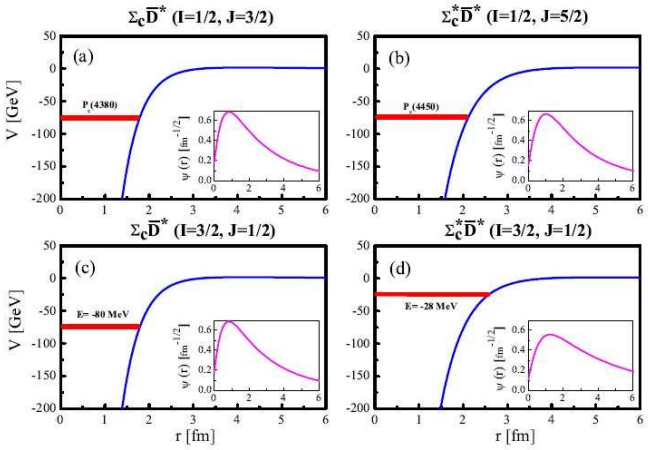


Figure 14: Effective potentials, V (GeV), energy levels, thick (red) lines, and wave-functions, $\psi(r)$, of the $\Sigma_c^{(*)}\bar{D}^*$ system (from [85]).

can be expressed in terms of the effective Lagrangians [85]:

$$\mathcal{L}_{\mathcal{P}} = ig\mathrm{Tr}\left[\bar{H}_a^{(\bar{Q})}\,\gamma^\mu\,A^\mu_{ab}\,\gamma_5 H_b^{(\bar{Q})}\right],$$
$$\mathcal{L}_{\mathcal{S}} = -\frac{3}{2}g_1\epsilon^{\mu\lambda\nu\kappa}v_\kappa\mathrm{Tr}\left[\bar{\mathcal{S}}_\mu\,A_\nu\,\mathcal{S}_\lambda\right], \qquad (20)$$

which are built using the heavy quark and chiral symmetries. Here $H_a^{(\bar{Q})} = [P_a^{*(\bar{Q})\,\mu}\gamma_\mu - P_a^{(\bar{Q})}\gamma_5](1-\not{v})/2$ is a pseudoscalar and vector charmed meson multiplet (D, D^*), v being the four-velocity vector $v = (0, \vec{1})$, $\mathcal{S}_\mu = 1/\sqrt{3}(\gamma_\mu + v_\mu)\gamma^5\mathcal{B}_6 + \mathcal{B}^*_{6\mu}$ stands for the charmed baryon multiplet, with $\mathcal{B}_6$ and $\mathcal{B}^*_{6\mu}$ corresponding to the $J^P = 1/2^+$ and $J^P = 3/2^+$ in 6_F flavor representation, respectively. A_μ is an axial-vector current, containing a pion chiral multiplet, defined as $A_\mu = 1/2(\xi^\dagger\partial_\mu\xi - \xi\partial_\mu\xi^\dagger)$, with $\xi = \exp(i\mathbb{P}/f_\pi)$, with $\mathbb{P}$ an $SU(2)$ matrix containing the pion field, and $f_\pi = 132$ MeV. This interaction Lagrangian is used to work out effective potentials, energy levels and wave-functions of the $\Sigma_c^{(*)}\bar{D}^*$ systems, shown in Fig. 14. In this picture, $P_c(4380)^+$ is a $\Sigma_c\bar{D}^*$ $(I = 1/2,\, J = 3/2)$ molecule, and $P_c(4450)^+$ is a $\Sigma_c^*\bar{D}^*$ $(I = 1/2,\, J = 5/2)$ molecule.

Apart from accommodating the two observed pentaquarks, this framework predicts two additional hidden-charm molecular pentaquark states, $\Sigma_c\bar{D}^*$ $(I = 3/2,\, J = 1/2)$ and $\Sigma_c^*\bar{D}^*$ $(I = 3/2,\, J = 1/2)$, which are isospin partners of $P_c(4380)^+$ and $P_c(4450)^+$, respectively, decaying into $\Delta(1232)J/\psi$ and $\Delta(1232)\eta_c$. In addition, a rich pentaquark spectrum of states for the hidden-bottom $(\Sigma_b B^*, \Sigma_b^* B^*)$, B_c-like $(\Sigma_c B^*, \Sigma_c^* B^*)$ and $(\Sigma_b\bar{D}^*, \Sigma_b^*\bar{D}^*)$ with well-defined (I, J) is predicted.

5 Pentaquarks in the compact diquark models

In the pioneering work by Maiani *et al.* [87] on the pentaquark interpretation of the LHCb data on $\Lambda_b^0 \to J/\psi\; p\; K^-$ decay, which is mainly discussed here, the assigned internal quantum numbers are: $P_c^+(4450) = \{\bar{c}[cu]_{s=1}[ud]_{s=0}; L_{\mathcal{P}} = 1, J^{\mathrm{P}} = \frac{5}{2}^+\}$ and $P_c^+(4380) = \{\bar{c}[cu]_{s=1}[ud]_{s=1}; L_{\mathcal{P}} =$

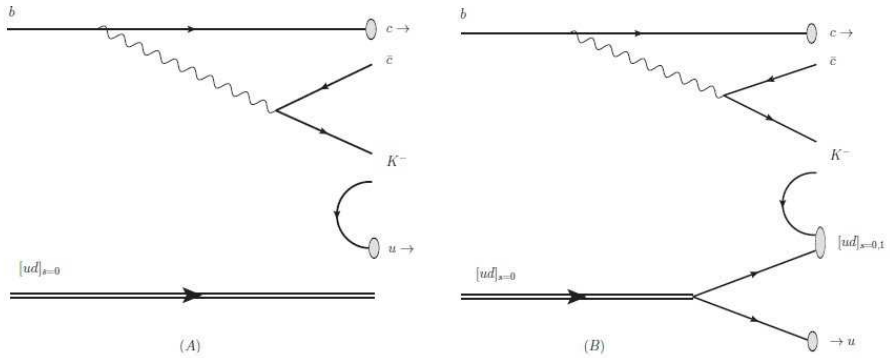


Figure 15: Two mechanisms for the decays $\Lambda_b^0 \to J/\psi K^- p$ in the pentaquark picture (from [87].

$0, J^{\rm P} = \frac{3}{2}^-\}$. Taking into account the mass differences due to the orbital angular momentum and the light diquark spins, the observed mass difference between the two P_c^+ states of about 70 MeV is reproduced. The crucial assumption is that the two diagrams for the decay $\Lambda_b^0 \to J/\psi\ p\ K^-$ in which the ud-spin in Λ_b^0 goes over to the $[ud]$-diquark spin in the pentaquark, Fig. 15(A), and the one in which the ud-spin is shared among the final state pentaquark and a meson, generating a light diquark $[ud]$ having spin-0 and spin-1, Fig. 15(B), are treated at par. This is a dynamical assumption, and remains to be tested.

5.1 $SU(3)_F$ structure of pentaquarks

Concentrating on the quark flavor of the pentaquarks $\mathbb{P}_c^+ = \bar{c}cuud$, they are of two different types [87]:

$$\mathbb{P}_u = \epsilon^{\alpha\beta\gamma} \bar{c}_\alpha\, [cu]_{\beta,s=0,1}\, [ud]_{\gamma,s=0,1}, \tag{21}$$

$$\mathbb{P}_d = \epsilon^{\alpha\beta\gamma} \bar{c}_\alpha\, [cd]_{\beta,s=0,1}\, [uu]_{\gamma,s=1}, \tag{22}$$

the difference being that the $\mathbb{P}_d$ involves a $[uu]$ diquark, and the Pauli exclusion principle implies that this diquark has to be in an $SU(3)_F$-symmetric representation. This leads to two distinct $SU(3)_F$ series of pentaquarks

$$\begin{aligned} \mathbb{P}_A &= \epsilon^{\alpha\beta\gamma}\, \{\bar{c}_\alpha\, [cq]_{\beta,s=0,1}\, [q'q'']_{\gamma,s=0}, L\} = \mathbf{3} \otimes \bar{\mathbf{3}} = \mathbf{1} \oplus \mathbf{8}, \\ \mathbb{P}_S &= \epsilon^{\alpha\beta\gamma}\, \{\bar{c}_\alpha\, [cq]_{\beta,s=0,1}\, [q'q'']_{\gamma,s=1}, L\} = \mathbf{3} \otimes \mathbf{6} = \mathbf{8} \oplus \mathbf{10}. \end{aligned} \tag{23}$$

For S waves, the first and the second series have the angular momenta

$$\mathbb{P}_A(L=0): \quad J = 1/2(2),\ 3/2(1), \tag{24}$$

$$\mathbb{P}_S(L=0): \quad J = 1/2(3),\ 3/2(3),\ 5/2(1), \tag{25}$$

where the multiplicities are given in parentheses. One assigns $\mathbb{P}(3/2^-)$ to the $\mathbb{P}_A$ and $\mathbb{P}(5/2^+)$ to the $\mathbb{P}_S$ series of pentaquarks [87].

The decay amplitudes of interest can be generically written as

$$\mathcal{A} = \left\langle \mathcal{PM} \left| H_{\rm eff}^W \right| \mathcal{B} \right\rangle, \tag{26}$$

where, $H_{\rm eff}^W$ is the effective weak Hamiltonian inducing the Cabibbo-allowed $\Delta I = 0, \Delta S = -1$ transition $b \to c\bar{c}s$, and the Cabibbo-suppressed $\Delta S = 0$ transition $b \to c\bar{c}d$. The $SU(3)_F$ based analysis of the decays $\Lambda_b \to \mathbb{P}^+ K^- \to (J/\psi\, p)K^-$ goes as follows. With respect to $SU(3)_F$, $\Lambda_b(bud) \sim \bar{3}$ and it is an isosinglet $I = 0$. Thus, the weak non-leptonic Hamiltonian for $b \to c\bar{c}q$ $(q = s, d)$ decays is:

$$H_{\rm eff}^W = \frac{4G_F}{\sqrt{2}} \left[V_{cb}V_{cq}^*(c_1 O_1^{(q)} + c_2 O_2^{(q)}) \right]. \tag{27}$$

Here, G_F is the Fermi coupling constant, V_{ij} are the CKM matrix elements, and c_i are the Wilson coefficients of the operators $O_1^{(q)}$ $(q = d,\ s)$, defined as

$$O_1^{(q)} = (\bar{q}_\alpha c_\beta)_{V-A}(\bar{c}_\alpha b_\beta)_{V-A}; \quad O_2^{(q)} = (\bar{q}_\alpha c_\alpha)_{V-A}(\bar{c}_\beta b_\beta)_{V-A}, \tag{28}$$

where α and β are $SU(3)$ color indices, and $V - A = 1 - \gamma_5$ reflects that the charged currents are left-handed, and the penguin amplitudes are ignored. With M a nonet of $SU(3)$ light mesons (π, K, η, η'), the weak transitions $\langle \mathbb{P}, M|H_{\rm W}|\Lambda_b\rangle$ requires $\mathbb{P} + M$ to be in $8 \oplus 1$ representation. Recalling the $SU(3)$ group multiplication rule

$$\begin{aligned} 8 \otimes 8 &= 1 \oplus 8 \oplus 8 \oplus 10 \oplus \bar{10} \oplus 27, \\ 8 \otimes 10 &= 8 \oplus 10 \oplus 27 \oplus 35, \end{aligned} \tag{29}$$

the decay $\langle \mathbb{P}, M|H_{\rm W}|\Lambda_b\rangle$ can be realized with $\mathbb{P}$ in either an octet $\mathtt{8}$ or a decuplet $\mathtt{10}$. The discovery channel $\Lambda_b \to \mathbb{P}^+ K^- \to J/\psi p K^-$ corresponds to $\mathbb{P}$ in an octet $\mathtt{8}$.

5.2 An effective Hamiltonian for the hidden charm pentaquarks

Keeping the basic building blocks of the pentaquarks to be quarks and diquarks, we follow here the template in which the two P_c states are assumed to be made from four quarks, consisting of two highly correlated diquark pairs, and an antiquark. For the present discussion, it is an anti-charm quark $\bar{c}$ which is correlated with the two diquarks $[cq]$ and $[q'q'']$, where q, q', q'' can be u or d. The tetraquark formed by the diquark-diquark $([cq]_{\bar{\mathtt{3}}}[q'q'']_{\bar{\mathtt{3}}})$ is a color-triplet object, following from $\bar{\mathtt{3}} \times \bar{\mathtt{3}} = \bar{\mathtt{6}} + \mathtt{3}$, with orbital and spin quantum numbers, denoted by $L_{\mathcal{QQ}}$ and $S_{\mathcal{QQ}}$, which combines with the color-anti-triplet $\bar{\mathtt{3}}$ of the $\bar{c}$ to form an overall color-singlet pentaquark, with the corresponding quantum numbers $L_{\mathcal{P}}$ and $S_{\mathcal{P}}$. This is shown schematically in Fig. 16.

An effective Hamiltonian based on this picture is constructed [94], extending the underlying tetraquark Hamiltonian developed for the X, Y, Z states [32]. It involves the constituent diquarks masses, $m_{[cq]}$, $m_{[q'q'']}$, the spin-spin interactions between the quarks in each diquark shell, and the spin-orbit and orbital angular momentum of the tetraquarks. To this are added the charm quark mass m_c, the spin-orbit and the orbital terms of the pentaquarks.

$$H = H_{[\mathcal{QQ}']} + H_{\bar{c}[\mathcal{QQ}']} + H_{S_{\mathcal{P}}L_{\mathcal{P}}} + H_{L_{\mathcal{P}}L_{\mathcal{P}}}, \tag{30}$$

where the diquarks $[cq]$ and $[q'q'']$ are denoted by $\mathcal{Q}$ and $\mathcal{Q}'$ having masses $m_{\mathcal{Q}}$ and $m_{\mathcal{Q}'}$, respectively. $L_{\mathcal{P}}$ and $S_{\mathcal{P}}$ are the orbital angular momentum and the spin of the pentaquark state, and the quantities $A_{\mathcal{P}}$ and $B_{\mathcal{P}}$ parametrize the strength of their spin-orbit and orbital angular momentum couplings, respectively. The individual terms in the Hamiltonian (30) are given in [94].

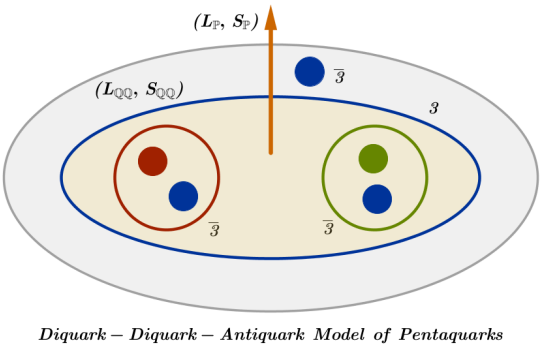


Figure 16: $SU(3)$-color quantum numbers of the diquarks, tetraquark and antiquark are indicated, together with the orbital and spin quantum numbers of the tetraquark and pentaquark [94]

.

The mass formula for the pentaquark state with the ground state tetraquark ($L_{\mathcal{QQ}'} = 0$) can be written as

$$M = M_0 + \frac{B_{\mathcal{P}}}{2} L_{\mathcal{P}}(L_{\mathcal{P}}+1) + 2A_{\mathcal{P}} \frac{J_{\mathcal{P}}(J_{\mathcal{P}}+1) - L_{\mathcal{P}}(L_{\mathcal{P}}+1) - S_{\mathcal{P}}(S_{\mathcal{P}}+1)}{2} + \Delta M \qquad (31)$$

where $M_0 = m_{\mathcal{Q}} + m_{\mathcal{Q}'} + m_c$ and ΔM is the mass term that arises from different spin-spin interactions. With the tetraquark in $L_{\mathcal{QQ}'} = 1$, one has to add the two terms given above with their coefficients $A_{\mathcal{QQ}'}$ and $B_{\mathcal{QQ}'}$. In this work, we restrict ourselves to the S-wave tetraquarks.

For $L_{\mathcal{P}} = 0$, the pentaquark states are classified in terms of the diquarks spins, $S_{\mathcal{Q}}$ and $S_{\mathcal{Q}'}$; the spin of anti-charm quark is $S_{\bar{c}} = 1/2$. There are four S-wave pentaquark states for $J^P = \frac{3}{2}^-$ and a single state with $J^P = \frac{5}{2}^-$. For $J^P = \frac{3}{2}^-$, we have the following states[3]:

$$\begin{aligned}
|0_{\mathcal{Q}}, 1_{\mathcal{Q}'}, \frac{1}{2}_{\bar{c}}; \frac{3}{2}\rangle_1 &= \frac{1}{\sqrt{2}}[(\uparrow)_c(\downarrow)_q - (\downarrow)_c(\uparrow)_q](\uparrow)_{q'}(\uparrow)_{q''}(\uparrow)_{\bar{c}} \\
|1_{\mathcal{Q}}, 0_{\mathcal{Q}'}, \frac{1}{2}_{\bar{c}}; \frac{3}{2}\rangle_2 &= \frac{1}{\sqrt{2}}[(\uparrow)_{q'}(\downarrow)_{q''} - (\downarrow)_{q'}(\uparrow)_{q''}](\uparrow)_c(\uparrow)_q(\uparrow)_{\bar{c}} \\
|1_{\mathcal{Q}}, 1_{\mathcal{Q}'}, \frac{1}{2}_{\bar{c}}; \frac{3}{2}\rangle_3 &= \frac{1}{\sqrt{6}}(\uparrow)_c(\uparrow)_q\{2(\uparrow)_{q'}(\uparrow)_{q''}(\downarrow)_{\bar{c}} - [(\uparrow)_{q'}(\downarrow)_{q''} + (\downarrow)_{q'}(\uparrow)_{q''}](\uparrow)_{\bar{c}}\} \\
|1_{\mathcal{Q}}, 1_{\mathcal{Q}'}, \frac{1}{2}_{\bar{c}}; \frac{3}{2}\rangle_4 &= \sqrt{\frac{3}{10}}[(\uparrow)_c(\downarrow)_q + (\downarrow)_c(\uparrow)_q](\uparrow)_{q'}(\uparrow)_{q''}(\uparrow)_{\bar{c}} - \sqrt{\frac{2}{15}}(\uparrow)_c(\uparrow)_q\{(\uparrow)_{q'}(\uparrow)_{q''}(\downarrow)_{\bar{c}} \\
&\quad + [(\uparrow)_{q'}(\downarrow)_{q''} + (\downarrow)_{q'}(\uparrow)_{q''}](\uparrow)_{\bar{c}}\}, \qquad (32)
\end{aligned}$$

and the spin representation corresponding to $J^P = \frac{5}{2}^-$ state is:

$$|1_{\mathcal{Q}}, 1_{\mathcal{Q}'}, \frac{1}{2}_{\bar{c}}; \frac{5}{2}\rangle = (\uparrow)_c(\uparrow)_q(\uparrow)_{q'}(\uparrow)_{q''}(\uparrow)_{\bar{c}}\,. \qquad (33)$$

[3]For a similar classification in the diquark-triquark picture, see[96].

Table 6: S (P)- wave pentaquark states $\mathcal{P}_{X_i}$ $(\mathcal{P}_{Y_i})$ and their spin- and orbital angular momentum quantum numbers. The subscripts $\mathcal{Q}$ and $\mathcal{Q}'$ represent the heavy $[cq]$ and light $[q'q'']$ diquarks, respectively. In the expressions for the masses of the $\mathcal{P}_{Y_i}$ states, the terms $M_{\mathcal{P}_{X_i}} = M_0 + \Delta M_i$ with $i = 1, ..., 5$.

Label	$\lvert S_\mathcal{Q}, S_{\mathcal{Q}'}; L_\mathcal{P}, J^P\rangle_i$	Mass	Label	$\lvert S_\mathcal{Q}, S_{\mathcal{Q}'}; L_\mathcal{P}, J^P\rangle_i$	Mass
$\mathcal{P}_{X_1}$	$\lvert 0_\mathcal{Q}, 1_{\mathcal{Q}'}, 0; \frac{3}{2}^-\rangle_1$	$M_0 + \Delta M_1$	$\mathcal{P}_{Y_1}$	$\lvert 0_\mathcal{Q}, 1_{\mathcal{Q}'}, 1; \frac{5}{2}^+\rangle_1$	$M_{\mathcal{P}_{X_1}} + 3A_\mathcal{P} + B_\mathcal{P}$
$\mathcal{P}_{X_2}$	$\lvert 1_\mathcal{Q}, 0_{\mathcal{Q}'}, 0; \frac{3}{2}^-\rangle_2$	$M_0 + \Delta M_2$	$\mathcal{P}_{Y_2}$	$\lvert 1_\mathcal{Q}, 0_{\mathcal{Q}'}, 1; \frac{5}{2}^+\rangle_2$	$M_{\mathcal{P}_{X_2}} + 3A_\mathcal{P} + B_\mathcal{P}$
$\mathcal{P}_{X_3}$	$\lvert 1_\mathcal{Q}, 1_{\mathcal{Q}'}, 0; \frac{3}{2}^-\rangle_3$	$M_0 + \Delta M_3$	$\mathcal{P}_{Y_3}$	$\lvert 1_\mathcal{Q}, 1_{\mathcal{Q}'}, 1; \frac{5}{2}^+\rangle_3$	$M_{\mathcal{P}_{X_3}} + 3A_\mathcal{P} + B_\mathcal{P}$
$\mathcal{P}_{X_4}$	$\lvert 1_\mathcal{Q}, 1_{\mathcal{Q}'}, 0; \frac{3}{2}^-\rangle_4$	$M_0 + \Delta M_4$	$\mathcal{P}_{Y_4}$	$\lvert 1_\mathcal{Q}, 1_{\mathcal{Q}'}, 1; \frac{5}{2}^+\rangle_4$	$M_{\mathcal{P}_{X_4}} + 3A_\mathcal{P} + B_\mathcal{P}$
$\mathcal{P}_{X_5}$	$\lvert 1_\mathcal{Q}, 1_{\mathcal{Q}'}, 0; \frac{5}{2}^-\rangle_5$	$M_0 + \Delta M_5$	$\mathcal{P}_{Y_5}$	$\lvert 1_\mathcal{Q}, 1_{\mathcal{Q}'}, \frac{1}{2}_{\bar{c}}, 1; \frac{5}{2}^+\rangle_5$	$M_{\mathcal{P}_{X_5}} - 2A_\mathcal{P} + B_\mathcal{P}$

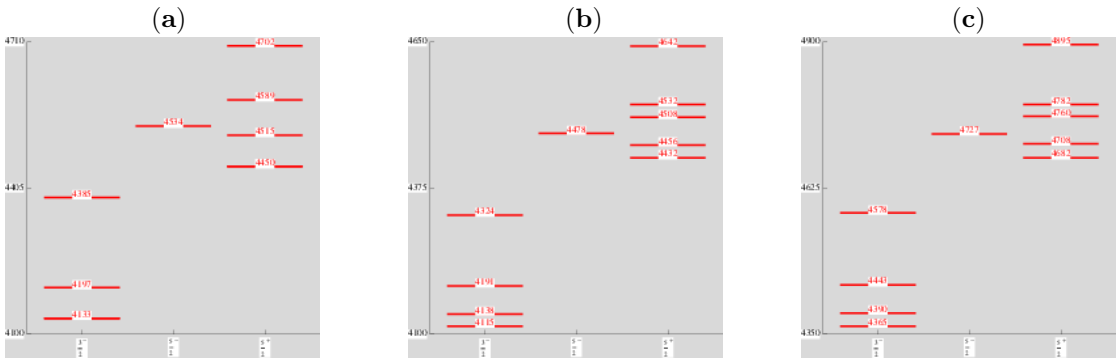


Figure 17: Mass Spectrum (in MeV) of the lowest S- and P-wave pentaquark states in the diquark-diquark-antiquark picture for the charmonium sector for the flavor content (a) $\bar{c}[cq][qq]$, (b) $\bar{c}[cq][sq]$, and (c) $\bar{c}[cs][qq]$. (from [94])

The masses for the four S-wave pentaquark states with $J^P = \frac{3}{2}^-$ and a single state with $J^P = \frac{5}{2}^-$ are given in Table 6, where we label the states as $\mathcal{P}_{X_i}$. The corresponding five P-wave pentaquark states with $L_\mathcal{P} = 1$ and $J^P = \frac{5}{2}^+$ are labeled as $\mathcal{P}_{Y_i}$ in Table 6. ΔM_i are defined in [94], where also the various input parameters are given. The resulting mass spectrum with the quark flavor content $\bar{c}[cq][qq]$, $\bar{c}[cq][sq]$, and $\bar{c}[cs][qq]$, characterized by $c_i (i = 1, 2, 3)$, respectively, is shown in Fig. 17. The above figure shows that the spectrum of pentaquark states in the compact diquark model is very rich. For comparison with the current LHC data, only the left frame in Fig. 17 is relevant. Apart from the other predicted states, there is a state, $\mathcal{P}_{X_4}$, which is predicted to have a mass 4385 MeV, having the quantum numbers $|1_\mathcal{Q}, 1_{\mathcal{Q}'}, 0; \frac{3}{2}^-\rangle$. This agrees with the mass of the observed state $P_c^+(4380)$. Likewise, the state $P_c^+(4550)$, having $J^P = \frac{5}{2}^+$ can be identified with the state $\mathcal{P}_{Y_2}$ in the firs t row of Table 6, having the quantum numbers $|1_\mathcal{Q}, 0_{\mathcal{Q}'}, 1; \frac{5}{2}^+\rangle$. We recall that these two states have the same internal

quantum numbers as assumed by Maiani *et al.* [87]:

$$P_c(4380)^+ = \mathbb{P}^+(3/2^-) = \{\bar{c}\,[cq]_{s=1}[q'q'']_{s=1}, L=0\}\,,$$
$$P_c(4450)^+ = \mathbb{P}^+(5/2^+) = \{\bar{c}\,[cq]_{s=1}[q'q'']_{s=0}, L=1\}\,. \quad (34)$$

5.3 b-baryonn decays to pentaquarks and heavy quark symmetry

The pentaquark states reported by the LHCb are produced in Λ_b^0 decays, $\Lambda_b^0 \to \mathcal{P}^+\, K^-$, where $\mathcal{P}$ denotes a generic pentaquark state. QCD has a symmetry in the heavy quark limit, i.e., for $m_b \gg \Lambda_{\rm QCD}$, b-quark becomes a static quark and the light diquark spin becomes a good quantum number, constraining the states which can otherwise be produced. The b-baryon decays to pentaquarks having a $c\bar{c}$ component are also presumably subject to the selection rules following from the heavy quark symmetry. Thus, the state $\mathcal{P}_{X_4}$ (identified with $P_c(4380)^+$ in [87]) is unlikely to be produced in Λ_b decays, as it has the "wrong" light-diquark spin number. On the other hand, there is a lower mass state $\mathcal{P}_{X_2}$ present in the spectrum, having the correct flavor and spin quantum numbers $|1_Q, 0_{Q'}, 0; \frac{3}{2}^-\rangle$, with a mass of about 4130 MeV, which we expect to be produced in Λ_b decays. One could argue that the mass estimates following from the assumed effective Hamiltonian are in error by a larger amount than quoted in [94]. However, as already stated, the mass difference between the $J^P = \frac{5}{2}^+$ and $J^P = \frac{3}{2}^-$ pentaquarks, having the right quantum numbers $|1_{\mathcal{Q}}, 0_{\mathcal{Q}'}, 1; \frac{5}{2}^+\rangle$ and $|1_{\mathcal{Q}}, 0_{\mathcal{Q}'}, 0; \frac{3}{2}^-\rangle$ is expected to be around 340 MeV, yielding a mass for the lower-mass $J^P = \frac{3}{2}^-$ pentaquark state of about 4110 MeV. The two estimates are compatible with each other, and we advocate to search for this state in the LHCb data. Among the ten states listed in Table 6, only the ones called $\mathcal{P}_{X_2}$ and $\mathcal{P}_{Y_2}$ are allowed as the Λ_b decay products.

5.4 Weak decays with $\mathbb{P}$ in Decuplet representation

Decays involving the decuplet `10` pentaquarks may also occur, if the light diquark pair having spin-0 $[ud]_{s=0}$ in Λ_b gets broken to produce a spin-1 light diquark $[ud]_{s=1}$. In this case, one would also observe the decays of Λ_b, such as

$$\Lambda_b \to \pi \mathbb{P}_{10}^{(S=-1)} \to \pi(J/\psi\Sigma(1385)),$$
$$\Lambda_b \to K^+ \mathbb{P}_{10}^{(S=-2)} \to K^+(J/\psi\Xi^-(1530)).$$

These decays are, however, disfavored by the heavy-quark-spin-conservation selection rules. The extent to which this rule is compatible with the existing data on B-meson and Λ_b decays can be seen in the PDG entries. Whether the decays of the pentaquarks are also subject to the same selection rules is yet to be checked, but on symmetry grounds, we do expect it to hold. Hence, the observation (or not) of these decays will be quite instructive.

Apart from $\Lambda_b(bud)$, several other b-baryons, such as $\Xi_b^0(usb)$, $\Xi_b^-(dsb)$ and $\Omega_b^-(ssb)$ undergo weak decays. These b-baryons are characterized by the spin of the light diquark, as shown below, making their isospin (I) and strangeness (S) quantum numbers explicit as well as their light diquark $j^{\rm P}$ quantum numbers. The c-baryons are likewise characterized similarly.
Examples of bottom-strange b-baryon in various charge combinations, respecting $\Delta I = 0$, $\Delta S = -1$ are:

$$\Xi_b^0(5794) \to K(J/\psi\Sigma(1385)),$$

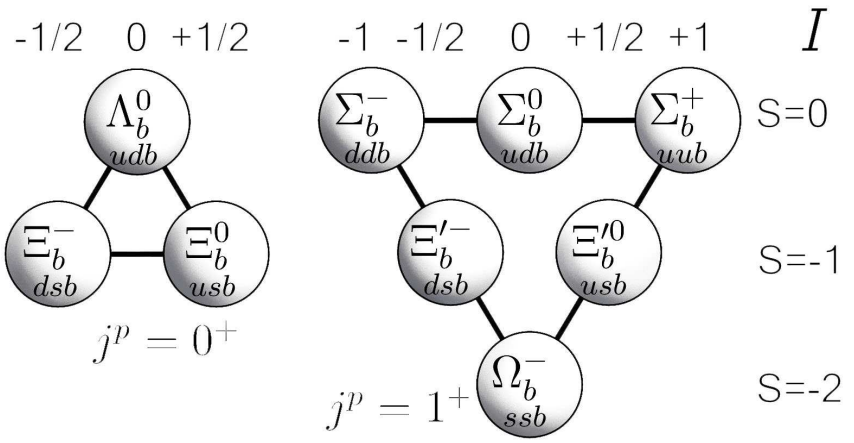


Figure 18: b-baryons with the light diquark spins $j^p = 0^+$ (left) and $j^p = 1^+$ (right).

which corresponds to the formation of the pentaquarks with the spin configuration $\mathbb{P}_{10}(\bar{c}\,[cq]_{s=0,1}\,[q's]_{s=0,1})$ with $(q, q' = u, d)$.
Above considerations have been extended involving the entire $SU(3)_F$ multiplets entering the generic decay amplitude $\langle \mathcal{P}\mathcal{M}|H_{\rm eff}|\mathcal{B}\rangle$, where $\mathcal{B}$ is the $SU(3)_F$ antitriplet b-baryon, shown in the left frame of Fig. 18, $\mathcal{M}$ is the 3×3 pseudoscalar meson matrix

$$\mathcal{M}_i^j = \begin{pmatrix} \frac{\pi^0}{\sqrt{2}} + \frac{\eta_8}{\sqrt{6}} & \pi^+ & K^+ \\ \pi^- & -\frac{\pi^0}{\sqrt{2}} + \frac{\eta_8}{\sqrt{6}} & K^0 \\ K^- & \bar{K}^0 & -\frac{2\eta_8}{\sqrt{6}} \end{pmatrix},$$

and $\mathcal{P}$ is a pentaquark state belonging to an octet with definite J^P, denoted as a 3×3 matrix J^P, $\mathcal{P}_j^i(J^{\rm P})$,

$$\mathcal{P}_i^j\left(J^P\right) = \begin{pmatrix} \frac{P_{\Sigma^0}}{\sqrt{2}} + \frac{P_\Lambda}{\sqrt{6}} & P_{\Sigma^+} & P_p \\ P_{\Sigma^-} & -\frac{P_{\Sigma^0}}{\sqrt{2}} + \frac{P_\Lambda}{\sqrt{6}} & P_n \\ P_{\Xi^-} & P_{\Xi^0} & -\frac{P_\Lambda}{\sqrt{6}} \end{pmatrix},$$

or a decuplet $\mathcal{P}_{ijk}$ (symmetric in the indices), with $\mathcal{P}_{111} = \Delta_{10}^{++}, ..., \mathcal{P}_{333} = \Omega_{10}^-$. (see Guan-Nan Li *et al.* [88] for a detailed list of the component fields and $SU(3)_F$-based relations among decay widths). The two observed pentaquarks are denoted as $P_p(3/2^-)$ and $P_p(5/2^+)$.

Estimates of the $SU(3)$ amplitudes require a dynamical model, which will be lot more complex to develop than the factorization-based models for the two-body B-meson decays, but, as argued in the literature, SU(3) symmetry can be used to relate different decay modes. Using heavy quark symmetry, which reduces the number of Feynman diagrams to be calculated, they are worked out in [94]. Thus, the decay $\Lambda_b^0 \to J/\psi p K^-$ and $\Lambda_b^0 \to J/\psi p \pi^-$ have just one dominant Feynman diagram each, the one in which the $[ud]$ diquark in Λ_b^0 retains its spin. The ratio of the branching fraction $\mathcal{B}(\Lambda_b^0 \to J/\psi p \pi^)/\mathcal{B}(\Lambda_b^0 \to J/\psi p K^-) = 0.0824 \pm 0.0024 \pm 0.0042$ [98] is consistent with the expectations from Cabibbo suppression. This ratio

should also hold for the resonating part of the amplitudes, namely if one replaces the $J/\psi p$ by $P_c(4450)^+$, and like wise for the $J^P = 3/2^-$ P_c^+ state. This is hinted by the current LHCb measurements [99].

Examples of the weak decays in which the initial b-baryon has a spin-1 light diquark, i.e. $j^{\rm P} = 1^+$, which is retained in the transition, are provided by the Ω_b decays. The $s\bar{s}$ pair in Ω_b is in the symmetric $\mathsf{6}$ representation of $SU(3)_F$ with spin 1 and is expected to produce decuplet pentaquarks in association with a ϕ or a kaon [87]

$$\Omega_b(6049) \to \phi(J/\psi\,\Omega^-(1672)), K(J/\psi\,\Xi(1387)).$$

These correspond, respectively, to the formation of the following pentaquarks ($q = u,\, d$)

$$\mathbb{P}_{10}^-(\bar{c}\,[cs]_{s=0,1}\,[ss]_{s=1}), \mathbb{P}_{10}(\bar{c}\,[cq]_{s=0,1}\,[ss]_{s=1}).$$

These transitions are expected on firmer theoretical footings, as the initial $[ss]$ diquark in Ω_b is left unbroken. Again, a lot more transitions can be found relaxing this condition, which would involve a $j^{\rm P} = 1^+ \to 0^+$ light diquark, but they are anticipated to be suppressed.

6 Summary

In summary, with the discoveries of the X, Y, Z and P_c states a new era of hadron spectroscopy is upon us. In addition to the well-known $q\bar{q}$ mesons and qqq baryons, there is increasing evidence that the hadronic world is multi-layered, in the form of tetraquark mesons, pentaquark baryons, and likely also the hexaquarks (or H dibaryons) [100]. However, the underlying dynamics is far from being understood, and the real issue is how the various constituents of an exotic multiquark state rearrange themselves. The two competing pictures are hadron molecules and compact diquak models, with $Q\bar{Q}g$ hybrids and glueballs also anticipated. Thresholds near the resonances do play a role in the phenomenology, and in some cases kinematic-induced cusp effects may also be a viable template. It is plausible, perhaps rather likely, that no single mechanism fits all the observable states, and the exotic hadrons may find their abode in competing theoretical frameworks. The case of diquark models in this context was reviewed here in more detail. Existence proof on the lattice of diquark correlations in some of the tetra- and pentaquark states discussed here would be a breakthrough and keenly awaited. In the meanwhile, phenomenological models built within constrained theoretical frameworks are unavoidable. They and experiments will guide us how to navigate through this uncharted territory.

7 Acknowledgments

I would like to thank the local organizers of the Helmholtz school "Quantum Field Theory at the Limits: From Strong Fields to Heavy Quarks", and JINR for their warm hospitality. Helpful discussions with Sören Lange, Luciano Maiani, Antonello Polosa, and Sheldon Stone are thankfully acknowledged. Thanks are also due to Sheldon Stone for craefully reading the manuscript.

References

[1] S.-K. Choi *et al.* (Belle Collaboration), Phys. Rev. Lett. **91**, 262001 (2003).

[2] R. Aaij *et al.* [LHCb Collaboration], Phys. Rev. Lett. **115** (2015) 072001 [arXiv:1507.03414 [hep-ex]].

[3] A. Esposito, A. Pilloni and A. D. Polosa, arXiv:1611.07920 [hep-ph].

[4] E. S. Swanson, Int. J. Mod. Phys. E **25**, no. 07, 1642010 (2016) doi:10.1142/S0218301316420106 [arXiv:1504.07952 [hep-ph]].

[5] E. S. Swanson, Phys. Rev. D **91** (2015) no.3, 034009 [arXiv:1409.3291 [hep-ph]].

[6] E. P. Wigner, Phys. Rev. **73**, 1002 (1948).

[7] N. A. Tornqvist, Z. Phys. C **68**, 647 (1995) [hep-ph/9504372].

[8] D. V. Bugg, J. Phys. G **35**, 075005 (2008) [arXiv:0802.0934 [hep-ph]].

[9] S. Dubynskiy and M. B. Voloshin, Phys. Lett. B **666**, 344 (2008) [arXiv:0803.2224 [hep-ph]].

[10] F. E. Close and P. R. Page, Nucl. Phys. B **443**, 233 (1995) [hep-ph/9411301].

[11] J. J. Dudek, Phys. Rev. D **84**, 074023 (2011) [arXiv:1106.5515 [hep-ph]].

[12] S. M. Ryan, EPJ Web Conf. **130**, 01002 (2016).

[13] F. E. Close and P. R. Page, Phys. Lett. B **628**, 215 (2005) [hep-ph/0507199].

[14] E. Kou and O. Pene, Phys. Lett. B **631**, 164 (2005) [hep-ph/0507119].

[15] S. L. Zhu, Phys. Lett. B **625**, 212 (2005) [hep-ph/0507025].

[16] C. A. Meyer and E. S. Swanson, Prog. Part. Nucl. Phys. **82**, 21 (2015) [arXiv:1502.07276 [hep-ph]].

[17] M. R. Pennington, EPJ Web Conf. **113** (2016) 01014 [arXiv:1509.02555 [nucl-th]].

[18] M. Berwein, N. Brambilla, J. Tarrs Castell and A. Vairo, Phys. Rev. D **92** (2015) no.11, 114019 [arXiv:1510.04299 [hep-ph]].

[19] H. Al Ghoul *et al.* [GlueX Collaboration], AIP Conf. Proc. **1735**, 020001 (2016) [arXiv:1512.03699 [nucl-ex]].

[20] M. F. M. Lutz *et al.* [PANDA Collaboration], arXiv:0903.3905 [hep-ex].

[21] N. A. Tornqvist, Z. Phys. C **61**, 525 (1994) [hep-ph/9310247]; E. Braaten and M. Kusunoki, Phys. Rev. D **69**, 074005 (2004) [hep-ph/0311147]; F. E. Close and P. R. Page, Phys. Lett. B **578**, 119 (2004) [hep-ph/0309253]; E. S. Swanson, Phys. Rept. **429**, 243 (2006) [hep-ph/0601110]; M. Cleven, F. K. Guo, C. Hanhart and U. G. Meissner, Eur. Phys. J. A **47**, 120 (2011) [arXiv:1107.0254 [hep-ph]].

[22] C. Bignamini, B. Grinstein, F. Piccinini, A. D. Polosa and C. Sabelli, Phys. Rev. Lett. **103**, 162001 (2009) [arXiv:0906.0882 [hep-ph]].

[23] P. Artoisenet and E. Braaten, Phys. Rev. D **81**, 114018 (2010) [arXiv:0911.2016 [hep-ph]].

[24] T. Gutsche, M. Kesenheimer and V. E. Lyubovitskij, Phys. Rev. D **90**, no. 9, 094013 (2014) [arXiv:1410.0259 [hep-ph]].

[25] M. Cleven, arXiv:1405.4195 [hep-ph].

[26] F.-K. Guo, C. Hanhart, Y. S. Kalashnikova, P. Matuschek, R. V. Mizuk, A. V. Nefediev, Q. Wang and J.-L. Wynen, Phys. Rev. D **93**, no. 7, 074031 (2016) [arXiv:1602.00940 [hep-ph]].

[27] P. Artoisenet, E. Braaten and D. Kang, Phys. Rev. D **82**, 014013 (2010) [arXiv:1005.2167 [hep-ph]].

[28] C. Hanhart, Y. S. Kalashnikova and A. V. Nefediev, Eur. Phys. J. A **47**, 101 (2011) [arXiv:1106.1185 [hep-ph]].

[29] C. Meng, J. J. Sanz-Cillero, M. Shi, D. L. Yao and H. Q. Zheng, Phys. Rev. D **92**, no. 3, 034020 (2015) [arXiv:1411.3106 [hep-ph]].

[30] T. Barnes, F. E. Close and E. S. Swanson, Phys. Rev. D **91**, no. 1, 014004 (2015) [arXiv:1409.6651 [hep-ph]].

[31] L. Maiani, F. Piccinini, A. D. Polosa and V. Riquer, Phys. Rev. Lett. **93** (2004) 212002 [hep-ph/0407017].

[32] L. Maiani, F. Piccinini, A. D. Polosa and V. Riquer, Phys. Rev. D **71**, 014028 (2005) [hep-ph/0412098].

[33] S. J. Brodsky, D. S. Hwang and R. F. Lebed, Phys. Rev. Lett. **113**, no. 11, 112001 (2014) [arXiv:1406.7281 [hep-ph]].

[34] S. Weinberg, Phys. Rev. Lett. **110**, 261601 (2013) [arXiv:1303.0342 [hep-ph]].

[35] M. Knecht and S. Peris, Phys. Rev. D **88**, 036016 (2013) [arXiv:1307.1273 [hep-ph]].

[36] G. Rossi and G. Veneziano, JHEP **1606**, 041 (2016) [arXiv:1603.05830 [hep-th]].

[37] M. Padmanath, C. B. Lang and S. Prelovsek, Phys. Rev. D **92**, no. 3, 034501 (2015) [arXiv:1503.03257 [hep-lat]].

[38] A. Hosaka, T. Iijima, K. Miyabayashi, Y. Sakai and S. Yasui, PTEP **2016**, no. 6, 062C01 (2016) [arXiv:1603.09229 [hep-ph]].

[39] C. DeTar, PoS LeptonPhoton **2015**, 023 (2016) [arXiv:1511.06884 [hep-lat]].

[40] Y. Chen *et al.*, Phys. Rev. D **89**, no. 9, 094506 (2014) [arXiv:1403.1318 [hep-lat]].

[41] Y. Ikeda *et al.* [HAL QCD Collaboration], Phys. Rev. Lett. **117**, no. 24, 242001 (2016) [arXiv:1602.03465 [hep-lat]].

[42] L. Maiani, F. Piccinini, A. D. Polosa and V. Riquer, Phys. Rev. D **89**, 114010 (2014) [arXiv:1405.1551 [hep-ph]].

[43] A. Ali, C. Hambrock, I. Ahmed and M. J. Aslam, Phys. Lett. B **684**, 28 (2010) [arXiv:0911.2787 [hep-ph]].

[44] A. Ali, C. Hambrock and M. J. Aslam, Phys. Rev. Lett. **104**, 162001 (2010) Erratum: [Phys. Rev. Lett. **107**, 049903 (2011)] [arXiv:0912.5016 [hep-ph]].

[45] A. Ali, C. Hambrock and S. Mishima, Phys. Rev. Lett. **106**, 092002 (2011) [arXiv:1011.4856 [hep-ph]].

[46] R. A. Briceno *et al.*, Chin. Phys. C **40** (2016) no.4, 042001 [arXiv:1511.06779 [hep-ph]].

[47] H. X. Chen, W. Chen, X. Liu and S. L. Zhu, Phys. Rept. **639**, 1 (2016) [arXiv:1601.02092 [hep-ph]].

[48] R. F. Lebed, R. E. Mitchell and E. S. Swanson, arXiv:1610.04528 [hep-ph].

[49] R. L. Jaffe, Phys. Rept. **409**, 1 (2005) [hep-ph/0409065].

[50] C. Alexandrou, P. de Forcrand and B. Lucini, Phys. Rev. Lett. **97**, 222002 (2006) [hep-lat/0609004].

[51] A. V. Manohar and M. B. Wise, Camb. Monogr. Part. Phys. Nucl. Phys. Cosmol. **10**, 1 (2000).

[52] M. Karliner, J. L. Rosner and S. Nussinov, arXiv:1611.00348 [hep-ph]; Z. G. Wang, arXiv:1701.04285 [hep-ph]; Y. Bai, S. Lu and J. Osborne, arXiv:1612.00012 [hep-ph].

[53] A. Ali, L. Maiani, A. D. Polosa and V. Riquer, Phys. Rev. D **91**, no. 1, 017502 (2015) [arXiv:1412.2049 [hep-ph]].

[54] D. Ebert, R. N. Faustov and V. O. Galkin, Phys. Lett. B **634**, 214 (2006) [hep-ph/0512230].

[55] M. Nielsen, F. S. Navarra and S. H. Lee, Phys. Rept. **497**, 41 (2010) [arXiv:0911.1958 [hep-ph]].

[56] R. Albuquerque, S. Narison, F. Fanomezana, A. Rabemananjara, D. Rabetiarivony and G. Randriamanatrika, Int. J. Mod. Phys. A **31**, no. 36, 1650196 (2016) [arXiv:1609.03351 [hep-ph]].

[57] A. Ali, L. Maiani, A. D. Polosa and V. Riquer, Phys. Rev. D **94**, no. 3, 034036 (2016) [arXiv:1604.01731 [hep-ph]].

[58] V. M. Abazov *et al.* [D0 Collaboration], Phys. Rev. Lett. **117** (2016) no.2, 022003 [arXiv:1602.07588 [hep-ex]].

[59] The LHCb Collaboration [LHCb Collaboration], LHCb-CONF-2016-004, CERN-LHCb-CONF-2016-004.

[60] S. S. Agaev, K. Azizi and H. Sundu, Eur. Phys. J. Plus **131**, no. 10, 351 (2016) [arXiv:1603.02708 [hep-ph]].

[61] K. F. Chen *et al.* [Belle Collaboration], Phys. Rev. Lett. **100**, 112001 (2008) [arXiv:0710.2577 [hep-ex]].

[62] N. Brambilla *et al.*, Eur. Phys. J. C **71**, 1534 (2011) [arXiv:1010.5827 [hep-ph]].

[63] D. Santel *et al.* [Belle Collaboration], Phys. Rev. D **93** (2016) no.1, 011101 [arXiv:1501.01137 [hep-ex]].

[64] G. 't Hooft, G. Isidori, L. Maiani, A. D. Polosa and V. Riquer, Phys. Lett. B **662**, 424 (2008) [arXiv:0801.2288 [hep-ph]].

[65] A. H. Fariborz, R. Jora and J. Schechter, Phys. Rev. D **77**, 094004 (2008) [arXiv:0801.2552 [hep-ph]].

[66] A. Bondar *et al.* [Belle Collaboration], Phys. Rev. Lett. **108**, 122001 (2012) [arXiv:1110.2251 [hep-ex]].

[67] R. Mizuk *et al.* [Belle Collaboration], Phys. Rev. Lett. **117**, no. 14, 142001 (2016) [arXiv:1508.06562 [hep-ex]].

[68] A. E. Bondar *et al.*, Phys. Rev. D **84**, 054010 (2011) [arXiv:1105.4473 [hep-ph]].

[69] A. Ali and W. Wang, Phys. Rev. Lett. **106**, 192001 (2011) [arXiv:1103.4587 [hep-ph]].

[70] B. Aubert *et al.* [BaBar Collaboration], Phys. Rev. D **74**, 091103 (2006) [hep-ex/0610018].

[71] M. Ablikim *et al.* [BES Collaboration], Phys. Rev. Lett. **100**, 102003 (2008) [arXiv:0712.1143 [hep-ex]].

[72] C. P. Shen *et al.* [Belle Collaboration], Phys. Rev. D **80**, 031101 (2009) [arXiv:0808.0006 [hep-ex]].

[73] N. V. Drenska, R. Faccini and A. D. Polosa, Phys. Lett. B **669**, 160 (2008) [arXiv:0807.0593 [hep-ph]].

[74] K.A. Olive *et al.* (Particle Data Group), Chinese Phys., **C 38**, 090001 (2014).

[75] See the review by G. C.Wohl in K.A. Olive *et al.* (Particle Data Group), Chinese Phys.,**C 38**, 090001 (2014).

[76] T. J. Burns, Eur. Phys. J. A **51** (2015) no.11, 152 [arXiv:1509.02460 [hep-ph]].

[77] V. Kubarovsky and M. B. Voloshin, Phys. Rev. D **92**, no. 3, 031502 (2015) [arXiv:1508.00888 [hep-ph]].

[78] F. K. Guo, U. G. Meiner, W. Wang and Z. Yang, Phys. Rev. D **92**, no. 7, 071502 (2015) [arXiv:1507.04950 [hep-ph]].

[79] X. H. Liu, Q. Wang and Q. Zhao, Phys. Lett. B **757** (2016) 231 [arXiv:1507.05359 [hep-ph]].

[80] M. Mikhasenko, arXiv:1507.06552 [hep-ph].

[81] U. G. Meiner and J. A. Oller, Phys. Lett. B **751**, 59 (2015) [arXiv:1507.07478 [hep-ph]].

[82] H. X. Chen, W. Chen, X. Liu, T. G. Steele and S. L. Zhu, Phys. Rev. Lett. **115**, no. 17, 172001 (2015) [arXiv:1507.03717 [hep-ph]].

[83] J. He, Phys. Lett. B **753**, 547 (2016) [arXiv:1507.05200 [hep-ph]].

[84] L. Roca, J. Nieves and E. Oset, Phys. Rev. D **92**, no. 9, 094003 (2015) [arXiv:1507.04249 [hep-ph]].

[85] R. Chen, X. Liu, X. Q. Li and S. L. Zhu, Phys. Rev. Lett. **115**, no. 13, 132002 (2015) [arXiv:1507.03704 [hep-ph]].

[86] C. W. Xiao and U.-G. Meiner, Phys. Rev. D **92**, no. 11, 114002 (2015) [arXiv:1508.00924 [hep-ph]].

[87] L. Maiani, A. D. Polosa and V. Riquer, Phys. Lett. B **749**, 289 (2015) [arXiv:1507.04980 [hep-ph]].

[88] G. N. Li, X. G. He and M. He, JHEP **1512**, 128 (2015) [arXiv:1507.08252 [hep-ph]].

[89] A. Mironov and A. Morozov, JETP Lett. **102**, no. 5, 271 (201 [arXiv:1507.04694 [hep-ph]].

[90] V. V. Anisovich, M. A. Matveev, J. Nyiri, A. V. Sarantsev and A. N. Semenova, arXiv:1507.07652 [hep-ph].

[91] R. Ghosh, A. Bhattacharya and B. Chakrabarti, arXiv:1508.00356 [hep-ph].

[92] Z. G. Wang, Eur. Phys. J. C **76**, no. 2, 70 (2016) [arXiv:1508.01468 [hep-ph]].

[93] Z. G. Wang and T. Huang, Eur. Phys. J. C **76**, no. 1, 43 (2016) [arXiv:1508.04189 [hep-ph]].

[94] A. Ali, I. Ahmed, M. J. Aslam and A. Rehman, Phys. Rev. D **94**, no. 5, 054001 (2016) [arXiv:1607.00987 [hep-ph]].

[95] R. F. Lebed, Phys. Lett. B **749**, 454 (2015) [arXiv:1507.05867 [hep-ph]].

[96] R. Zhu and C. F. Qiao, Phys. Lett. B **756**, 259 (2016) [arXiv:1510.08693 [hep-ph]].

[97] S. M. Flatte, Phys. Lett. **63B**, 224 (1976). doi:10.1016/0370-2693(76)90654-7

[98] R. Aaij *et al.* [LHCb Collaboration], JHEP **1407**, 103 (2014) [arXiv:1406.0755 [hep-ex]].

[99] R. Aaij *et al.* [LHCb Collaboration], Phys. Rev. Lett. **117**, no. 8, 082003 (2016) Addendum: [Phys. Rev. Lett. **117**, no. 10, 109902 (2016)] [arXiv:1606.06999 [hep-ex]].

[100] L. Maiani, A. D. Polosa and V. Riquer, Phys. Lett. B **750**, 37 (2015) [arXiv:1508.04459 [hep-ph]].

Heavy Quark Symmetry and Hidden Charm Pentaquarks

Ahmed Ali[1], *Ishtiaq Ahmed*[2], *M. Jamil Aslam*[3] *and Abdur Rehman*[2*]

[1] Deutsches Elektronen-Synchrotron DESY, D-22607 Hamburg, Germany
[2] National Centre for Physics, Quaid-i-Azam University Campus, Islamabad 45320, Pakistan
[3] Physics Department, Quaid-i-Azam University, Islamabad 45320, Pakistan

DOI: http://dx.doi.org/10.3204/DESY-PROC-2016-04/Rehman

We report on the role of the heavy quark symmetry (HQS) in understanding the hidden charm pentaquarks, $P_c^+(4380)$ and $P_c^+(4450)$, observed by LHCb in $\Lambda_b^0 \to J/\psi\ p\ K^-$ decays, in the compact diquark-diquark-antiquark picture. In the HQS-limit, only the state $P_c^+(4450)$ is expected to be produced. Within this picture, we employ $SU(3)_F$ symmetry to discuss the mass spectrum and decays of the related pentaquark states $\bar{c}[cq][q'q'']$ with $q, q', q'' \in [u, d, s]$. Some of these pentaquarks are expected to be produced in b-baryon decays and we work out their relative decay widths.

1 Introduction

The states $P_c^+(4380)(J^P = \frac{3}{2}^-)$ and $P_c^+(4450)(J^P = \frac{5}{2}^+)$ are recently observed by the LHCb collaboration [1] with the possible quark contents $c\bar{c}uud$ in the decay mode $\Lambda_b^0 \to J/\psi\ p\ K^-$, having the masses $4380 \pm 8 \pm 29$ MeV and $4449.8 \pm 1.7 \pm 2.5$ MeV and decay widths $205 \pm 18 \pm 86$ MeV and $39 \pm 5 \pm 19$ MeV, respectively. Their dynamics is far from being understood, and a number of theoretical models has been put forward in the literature to accommodate them, summarized briefly in [2]. We concentrate here on the compact pentaquark picture with the structure diquark-diquark-anti-charm quark [3, 4]. To be specific, we follow here the framework by Maiani *et al.* [3]. Their assigned spin and angular quantum numbers are: $P_c^+(4450) = \{\bar{c}[cu]_{s=1}[ud]_{s=0}; L_{\mathcal{P}} = 1, J^{\rm P} = \frac{5}{2}^+\}$ and $P_c^+(4380) = \{\bar{c}[cu]_{s=1}[ud]_{s=1}; L_{\mathcal{P}} = 0, J^{\rm P} = \frac{3}{2}^-\}$. We have argued in [5] that the lower-mass state $P_c^+(4380)$, which has the light diquark with spin-1, i.e., $[ud]_{s=1}$, is unlikely to be produced in Λ_b decays due to the heavy quark symmetry (HQS). The point is that in the HQS-limit, the spin-degree of freedom of the light diquark in Λ_b becomes a good quantum number. Hence, the state $P_c^+(4380)$, with the above quantum numbers, can only be produced if the spin-0 diquark in Λ_b^0 is broken. Current data on Λ_b^0 decays suggest HQS as a diagnostic tool: the decays preserving this symmetry have significantly large branching ratios compared to the ones that violate it [6]. Therefore, this allows only the higher mass sate $P_c^+(4450)$ to be produced in Λ_b^0 decays.

We calculate the mass spectrum of the pentaquarks, $\bar{c}[cq][q'q'']$ with $q, q', q'' \in [u, d, s]$ in an effective Hamiltonian approach proposed by Maiani *et al.* for the interpretation of exotic states in the meson sectors [7, 8], extending it to the pentaquark sector. Making use of the

*Speaker. This proceeding is based on Ref. [5].

Table 1: S (P)- wave pentaquark states $\mathcal{P}_{X_i}$ ($\mathcal{P}_{Y_i}$) and their spin- and orbital angular momentum quantum numbers. The subscripts $\mathcal{Q}$ and $\mathcal{Q}'$ represent the heavy $[cq]$ and light $[q'q'']$ diquarks, respectively. In the expressions for the masses of the $\mathcal{P}_{Y_i}$ states, the terms $M_{\mathcal{P}_{X_i}} = M_0 + \Delta M_i$ with $i = 1, ..., 5$.

Label	$\lvert S_{\mathcal{Q}}, S_{\mathcal{Q}'}; L_{\mathcal{P}}, J^P\rangle_i$	Mass	Label	$\lvert S_{\mathcal{Q}}, S_{\mathcal{Q}'}; L_{\mathcal{P}}, J^P\rangle_i$	Mass
$\mathcal{P}_{X_1}$	$\lvert 0_{\mathcal{Q}}, 1_{\mathcal{Q}'}, 0; \frac{3}{2}^-\rangle_1$	$M_0 + \Delta M_1$	$\mathcal{P}_{Y_1}$	$\lvert 0_{\mathcal{Q}}, 1_{\mathcal{Q}'}, 1; \frac{5}{2}^+\rangle_1$	$M_{\mathcal{P}_{X_1}} + 3A_{\mathcal{P}} + B_{\mathcal{P}}$
$\mathcal{P}_{X_2}$	$\lvert 1_{\mathcal{Q}}, 0_{\mathcal{Q}'}, 0; \frac{3}{2}^-\rangle_2$	$M_0 + \Delta M_2$	$\mathcal{P}_{Y_2}$	$\lvert 1_{\mathcal{Q}}, 0_{\mathcal{Q}'}, 1; \frac{5}{2}^+\rangle_2$	$M_{\mathcal{P}_{X_2}} + 3A_{\mathcal{P}} + B_{\mathcal{P}}$
$\mathcal{P}_{X_3}$	$\lvert 1_{\mathcal{Q}}, 1_{\mathcal{Q}'}, 0; \frac{3}{2}^-\rangle_3$	$M_0 + \Delta M_3$	$\mathcal{P}_{Y_3}$	$\lvert 1_{\mathcal{Q}}, 1_{\mathcal{Q}'}, 1; \frac{5}{2}^+\rangle_3$	$M_{\mathcal{P}_{X_3}} + 3A_{\mathcal{P}} + B_{\mathcal{P}}$
$\mathcal{P}_{X_4}$	$\lvert 1_{\mathcal{Q}}, 1_{\mathcal{Q}'}, 0; \frac{3}{2}^-\rangle_4$	$M_0 + \Delta M_4$	$\mathcal{P}_{Y_4}$	$\lvert 1_{\mathcal{Q}}, 1_{\mathcal{Q}'}, 1; \frac{5}{2}^+\rangle_4$	$M_{\mathcal{P}_{X_4}} + 3A_{\mathcal{P}} + B_{\mathcal{P}}$
$\mathcal{P}_{X_5}$	$\lvert 1_{\mathcal{Q}}, 1_{\mathcal{Q}'}, 0; \frac{5}{2}^-\rangle_5$	$M_0 + \Delta M_5$	$\mathcal{P}_{Y_5}$	$\lvert 1_{\mathcal{Q}}, 1_{\mathcal{Q}'}, \frac{1}{2}_{\bar{c}}, 1; \frac{5}{2}^+\rangle_5$	$M_{\mathcal{P}_{X_5}} - 2A_{\mathcal{P}} + B_{\mathcal{P}}$

HQS, one can accommodate the $\{\bar{c}[cu]_{s=1}[ud]_{s=0}; L_{\mathcal{P}} = 1, J^{\rm P} = \frac{5}{2}^+\}$ state $P_c(4450)$ but not the state $P_c(4380)$, that has $\{\bar{c}[cu]_{s=1}[ud]_{s=1}; L_{\mathcal{P}} = 0, J^{\rm P} = \frac{3}{2}^-\}$. Thus, if confirmed by independent analysis and more data, one has to find a different interpretation of the state $P_c(4380)$. However, the pentaquark spectrum is rich enough to accommodate a $J^{\rm P} = \frac{3}{2}^-$ state, which can be reached in the decays $\Lambda_b^0 \to J/\psi\, p\, K^-$ consistent with the HQS-based selection rules, albeit with a lower mass. Using the mass difference $m[\Lambda_c^+(2625); J^P = \frac{3}{2}^-] - m[\Lambda_c^+(2286); J^P = \frac{1}{2}^+] \simeq 341$ MeV, the mass of this $J^P = 3/2^-$ state is estimated by us to be in the range 4110-4130 MeV. We work out the mass spectrum of the pentaquarks related by $SU(3)_F$. Some of these pentaquarks will be produced in weak decays of b-baryons. Combining HQS and the $SU(3)_F$ symmetry results in strikingly simple relations among these decay amplitudes, and the resulting relative decay widths are presented here.

This report is organized as follows: In section II, we provide mass formula for the pentaquark states having the quark flavors $\bar{c}[cq][q'q'']$, with $q, q', q'' = u, d, s$, assuming isospin symmetry within diquark model. In section III, the amplitude and the effective Hamiltonian for the b-baryon decays into pentaquarks, obeying the HQS and $SU(3)_F$ symmetry are provided. In the last section, we conclude our work.

2 Spectrum of the $\bar{c}[cq][q'q'']$ pentaquarks, with $q, q', q'' = u, d, s$

The mass formula for the pentaquark state with the ground state tetraquark ($L_{\mathcal{Q}\mathcal{Q}'} = 0$) can be written as [5]

$$M = M_0 + \frac{B_{\mathcal{P}}}{2} L_{\mathcal{P}}(L_{\mathcal{P}} + 1) + 2A_{\mathcal{P}} \frac{J_{\mathcal{P}}(J_{\mathcal{P}} + 1) - L_{\mathcal{P}}(L_{\mathcal{P}} + 1) - S_{\mathcal{P}}(S_{\mathcal{P}} + 1)}{2} + \Delta M \qquad (1)$$

where $M_0 = m_{\mathcal{Q}} + m_{\mathcal{Q}'} + m_c$, and ΔM is a mass term which arises from different spin-spin interactions. For the tetraquark in $L_{\mathcal{Q}\mathcal{Q}'} = 1$, one has to add two more terms in Eq. (1) with their coefficients $A_{\mathcal{Q}\mathcal{Q}'}$ and $B_{\mathcal{Q}\mathcal{Q}'}$ (see Eq. (5) of ref. [5]). In this work, we restrict ourselves to the S-wave tetraquarks while for the pentaquarks the S (P)- wave states, called $\mathcal{P}_{X_i}$ ($\mathcal{P}_{Y_i}$), are listed in Table 1. In the caption of Table 1, ΔM_i (i runs from 1 to 4) are the mass splitting terms that arise after diagonalizing the 4×4 matrix, whereas ΔM_5 is given in Eq.(12) of Ref. [5].

Table 2: Masses of the $\mathcal{P}_{X_i}$ and $\mathcal{P}_{Y_i}$ states (in MeV) formed through different diquark-diquark-anti-charm quark combinations in type-I model of tetraquarks. The quoted errors are obtained from the uncertainties in the input parameters in the effective Hamiltonian. Flavor labels c_i $(i = 1, ..., 5)$ correspond to quark contents given below (with $q = u$ or d). (From [5]).

$\mathcal{P}_{X_i}$	$\mathcal{P}_{X_1}$	$\mathcal{P}_{X_2}$	$\mathcal{P}_{X_3}$	$\mathcal{P}_{X_4}$	$\mathcal{P}_{X_5}$
$c_1 : \bar{c}[cq][qq]$	4133 ± 55	4133 ± 55	4197 ± 55	4385 ± 55	4534 ± 55
$c_2 : \bar{c}[cq][sq]$	4115 ± 58	4138 ± 47	4191 ± 53	4324 ± 47	4478 ± 47
$c_3 : \bar{c}[cs][qq]$	4365 ± 55	4390 ± 42	4443 ± 49	4578 ± 43	4727 ± 42
$c_4 : \bar{c}[cs][sq]$	4313 ± 47	4382 ± 45	4434 ± 51	4568 ± 46	4721 ± 45
$c_5 : \bar{c}[cq][ss]$	4596 ± 47	4664 ± 46	4721 ± 51	4853 ± 46	5006 ± 45
$\mathcal{P}_{Y_i}$	$\mathcal{P}_{Y_1}$	$\mathcal{P}_{Y_2}$	$\mathcal{P}_{Y_3}$	$\mathcal{P}_{Y_4}$	$\mathcal{P}_{Y_5}$
$c_1 : \bar{c}[cq][qq]$	4450 ± 57	4450 ± 57	4515 ± 57	4702 ± 58	4589 ± 56
$c_2 : \bar{c}[cq][sq]$	4432 ± 61	4456 ± 50	4508 ± 56	4642 ± 50	4532 ± 48
$c_3 : \bar{c}[cs][qq]$	4682 ± 57	4708 ± 46	4760 ± 52	4895 ± 47	4782 ± 44
$c_4 : \bar{c}[cs][sq]$	4603 ± 51	4699 ± 49	4752 ± 54	4885 ± 49	4776 ± 47
$c_5 : \bar{c}[cq][ss]$	4913 ± 51	4981 ± 49	5038 ± 54	5170 ± 49	5061 ± 47

In our predictions for the pentaquark masses, some common parameters are fixed from the XYZ states, under the assumption that they are diquark-antidiquark states for both type-I [8] and type-II models [7]. To fix the unknown parameter $B_{\mathcal{P}}$, involving the pentaquark orbital angular momentum, we identify the state $|1_{\mathcal{Q}}, 0_{\mathcal{Q}'}, 1; \frac{5}{2}^+\rangle_2$ with the pentaquark state $\frac{5}{2}^+$ having a mass 4450 MeV and $L_{\mathcal{P}} = 1$ which yields 160 MeV and 220 MeV for $B_{\mathcal{P}}$ in the type-I and type-II models, respectively. However, in Table 2, we present only the results of type-I model as they have been used in the forthcoming discussions. We note that the states $\mathcal{P}_{X_4}$ and $\mathcal{P}_{Y_2}$ have the spin- and angular momentum quantum numbers, which correspond to the assignments for $P_c^+(4380)$ and $P_c^+(4450)$, respectively, in the paper by Maiani *et al.* [3].

3 Estimate of the ratios of weak b-baryon decays into pentaquarks

The general amplitude for the decay under consideration can be written as

$$\mathcal{A} = \left\langle \mathcal{P}\mathcal{M} \left| H_{\rm eff}^W \right| \mathcal{B} \right\rangle , \tag{2}$$

where $\mathcal{B}$ is a flavor anti-triplet b-baryon with the light quark spin $j^P = 0^+$ (the flavor sextet b-baryons with $j^P = 0^+$ are denoted by $\mathcal{C}$). $\mathcal{M}$ is a light pseudoscalar meson in the $SU(3)_F$ octet, and $\mathcal{P}$ is the final state pentaquark, while, $H_{\rm eff}^W$ is the effective weak Hamiltonian inducing the Cabibbo-allowed $\Delta I = 0, \Delta S = -1$ transition $b \to c\bar{c}s$, and the Cabibbo-suppressed $\Delta S = 0$ transition $b \to c\bar{c}d$,

$$H_{\rm eff}^W = \frac{4G_F}{\sqrt{2}}\left[V_{cb}V_{cq}^*(c_1O_1^{(q)} + c_2O_2^{(q)})\right]. \tag{3}$$

Here, G_F is the Fermi coupling constant, $V_{cb}V_{cq}^*$ are the CKM matrix elements, and $c_1(c_2)$ are the Wilson coefficients of the operators $O_1^{(q)}(O_2^{(q)})$ $(q = d,\ s)$, defined as

$$O_1^{(q)} = (\bar{q}_\alpha c_\beta)_{V-A}(\bar{c}_\alpha b_\beta)_{V-A};\quad O_2^{(q)} = (\bar{q}_\alpha c_\alpha)_{V-A}(\bar{c}_\beta b_\beta)_{V-A}, \tag{4}$$

where α and β are $SU(3)$ color indices, and $V - A = \gamma^\mu(1 - \gamma_5)$ reflects that the charged currents are left-handed.

While calculating the absolute decay rates is a formidable challenge, estimates of the ratios of the decay widths can be obtained using $SU(3)_F$ symmetry. They were worked out in [5], and are given in Tables 3 and 4. We note that the $\Delta S = 0$ transitions are suppressed by a factor $|V_{cd}^*/V_{cs}^*|^2 \simeq 0.05$ compared to $\Delta S = 1$ transitions. In the HQS-limit, the decays $\Lambda_b^0 \to J/\psi\ p\ K^-$ and $\Lambda_b^0 \to J/\psi\ p\ \pi^-$ have just one Feynman diagram each, as this is the only diagram in which the $[ud]$ diquark in Λ_b retains its spin. The one, in which the $[ud]$ diquark is split, giving rise to the interference term discussed in [9], is suppressed by $1/m_b$. The relative branching fractions $\mathcal{B}(\Lambda_b^0 \to J/\psi\ p\ \pi^-)/\mathcal{B}(\Lambda_b^0 \to J/\psi\ p\ K^-) = 0.0824 \pm 0.0024 \pm 0.0042$ [10] is consistent with the expectation from Cabibbo suppression. Whether this ratio also holds for the pentaquark states is being studied by the LHCb. Curent measurements, while still preliminary, suggest that this is the case.

Table 3: Estimate of the ratios of the decay widths $\Gamma(\mathcal{B}(\mathcal{C}) \to \mathcal{P}^{5/2}\mathcal{M})/\Gamma(\Lambda_b^0 \to P_p^{5/2}K^-)$ (from [5]).

$\Delta S = 1$			
Decay Process	$\Gamma/\Gamma(\Lambda_b^0 \to P_p^{5/2}K^-)$	Decay Process	$\Gamma/\Gamma(\Lambda_b^0 \to P_p^{5/2}K^-)$
$\Lambda_b \to P_p^{\{Y_2\}_{c_1}} K^-$	1	$\Xi_b^- \to P_{\Sigma^-}^{\{Y_2\}_{c_2}} \bar{K}^0$	2.07
$\Lambda_b \to P_n^{\{(Y_2\}_{c_1}} \bar{K}^0$	1	$\Xi_b^0 \to P_{\Sigma^+}^{\{Y_2\}_{c_2}} K^-$	2.07
$\Lambda_b \to P_{\Lambda^0}^{\{Y_2\}_{c_3}} \eta'$	0.03	$\Lambda_b \to P_{\Lambda^0}^{\{Y_2\}_{c_3}} \eta$	0.19
$\Xi_b^- \to P_{\Sigma^0}^{\{Y_2\}_{c_2}} K^-$	1.04	$\Xi_b^- \to P_{\Lambda^0}^{\{Y_2\}_{c_2}} K^-$	0.34
$\Omega_b^- \to P_{\Xi_{10}^-}^{\{Y_3\}_{c_5}} \bar{K}^0$	0.14	$\Omega_b^- \to P_{\Xi_{10}^0}^{\{Y_3\}_{c_5}} K^-$	0.14
$\Delta S = 0$			
Decay Process	$\Gamma/\Gamma(\Lambda_b^0 \to P_p^{5/2}K^-)$	Decay Process	$\Gamma/\Gamma(\Lambda_b^0 \to P_p^{5/2}K^-)$
$\Lambda_b \to P_p^{\{Y_2\}_{c_1}} \pi^-$	0.08	$\Lambda_b \to P_n^{\{Y_2\}_{c_1}} \pi^0$	0.04
$\Lambda_b \to P_n^{\{Y_2\}_{c_1}} \eta$	0.01	$\Lambda_b \to P_n^{\{Y_2\}_{c_1}} \eta'$	0
$\Xi_b^- \to P_{\Xi^-}^{\{Y_2\}_{c_4}} K^0$	0.02	$\Xi_b^- \to P_{\Sigma^0}^{\{Y_2\}_{c_2}} \pi^-$	0.08
$\Xi_b^- \to P_{\Sigma^-}^{\{Y_2\}_{c_2}} \eta$	0.02	$\Xi_b^- \to P_{\Sigma^-}^{\{Y_2\}_{c_2}} \eta'$	0.01
$\Xi_b^- \to P_{\Sigma^-}^{\{Y_2\}_{c_2}} \pi^0$	0.08	$\Xi_b^0 \to P_{\Sigma^0}^{\{Y_2\}_{c_2}} \pi^0$	0.04
$\Xi_b^0 \to P_{\Lambda^0}^{\{X_2\ (Y_2)\}_{c_2}} \eta$	0.01	$\Xi_b^0 \to P_{\Lambda^0}^{\{Y_2\}_{c_2}} \eta'$	0.01
$\Xi_b^0 \to P_{\Lambda^0}^{\{Y_2\}_{c_2}} \pi^0$	0.01	$\Omega_b^- \to P_{\Xi_{10}^-}^{\{Y_3\}_{c_5}} \pi^0$	0.01
$\Omega_b^- \to P_{\Xi_{10}^0}^{\{Y_3\}_{c_5}} \pi^-$	0.02		

Table 4: Estimate of the ratios of the decay widths $\Gamma(\mathcal{B}(\mathcal{C}) \to \mathcal{P}^{3/2}\mathcal{M})/\Gamma(\Lambda_b^0 \to P_p^{\{X_2\}_{c_1}} K^-)$ transitions (from [5]).

$\Delta S = 1$			
Decay Process	$\Gamma/\Gamma(\Lambda_b^0 \to P_p^{\{X_2\}_{c_1}} K^-)$	Decay Process	$\Gamma/\Gamma(\Lambda_b^0 \to P_p^{\{X_2\}_{c_1}} K^-)$
$\Lambda_b \to P_p^{\{X_2\}_{c_1}} K^-$	1	$\Xi_b^- \to P_{\Sigma^-}^{\{X_2\}_{c_2}} \bar{K}^0$	1.38
$\Lambda_b \to P_n^{\{X_2\}_{c_1}} \bar{K}^0$	1	$\Xi_b^0 \to P_{\Sigma^+}^{\{X_2\}_{c_2}} K^-$	1.38
$\Lambda_b \to P_{\Lambda^0}^{\{X_2\}_{c_3}} \eta'$	0.17	$\Lambda_b \to P_{\Lambda^0}^{\{X_2\}_{c_3}} \eta$	0.22
$\Xi_b^- \to P_{\Sigma^0}^{\{X_2\}_{c_2}} K^-$	0.69	$\Xi_b^- \to P_{\Lambda^0}^{\{X_2\}_{c_2}} K^-$	0.23
$\Omega_b^- \to P_{\Xi_{10}^-}^{\{X_3\}_{c_5}} \bar{K}^0$	0.24	$\Omega_b^- \to P_{\Xi_{10}^0}^{\{X_3\}_{c_5}} K^-$	0.24
$\Delta S = 0$			
Decay Process	$\Gamma/\Gamma(\Lambda_b^0 \to P_p^{\{X_2\}_{c_1}} K^-)$	Decay Process	$\Gamma/\Gamma(\Lambda_b^0 \to P_p^{\{X_2\}_{c_1}} K^-)$
$\Lambda_b \to P_p^{\{X_2\}_{c_1}} \pi^-$	0.06	$\Lambda_b \to P_n^{\{X_2\}_{c_1}} \pi^0$	0.03
$\Lambda_b \to P_n^{\{X_2\}_{c_1}} \eta$	0.01	$\Lambda_b \to P_n^{\{X_2\}_{c_1}} \eta'$	0.01
$\Xi_b^- \to P_{\Xi^-}^{\{X_2\}_{c_4}} K^0$	0.02	$\Xi_b^- \to P_{\Sigma^0}^{\{X_2\}_{c_2}} \pi^-$	0.03
$\Xi_b^- \to P_{\Sigma^-}^{\{X_2\}_{c_2}} \eta$	0.02	$\Xi_b^- \to P_{\Sigma^-}^{\{X_2\}_{c_2}} \eta'$	0.01
$\Xi_b^- \to P_{\Sigma^-}^{\{X_2\}_{c_2}} \pi^0$	0.04	$\Xi_b^0 \to P_{\Sigma^0}^{\{X_2\}_{c_2}} \pi^0$	0.02
$\Xi_b^0 \to P_{\Lambda^0}^{\{X_2\}_{c_2}} \eta$	0	$\Xi_b^0 \to P_{\Lambda^0}^{\{X_2\}_{c_2}} \eta'$	0
$\Xi_b^0 \to P_{\Lambda^0}^{\{X_2\}_{c_2}} \pi^0$	0.01	$\Omega_b^- \to P_{\Xi_{10}^-}^{\{X_3\}_{c_5}} \pi^0$	0.01
$\Omega_b^- \to P_{\Xi_{10}^0}^{\{X_3\}_{c_5}} \pi^-$	0.02		

4 Conclusion

The decay $\Lambda_b^0 \to \mathcal{P}_{X_4} K^-$ is suppressed due to the HQS selection rules. Therefore, the state $\mathcal{P}_{X_4}$, having the quantum numbers $\{\bar{c}[cu]_{s=1}[ud]_{s=1}; L_{\mathcal{P}} = 0, J^{\rm P} = \frac{3}{2}^-\}$, identified as $P_c^+(4380)$ in the compact diquark picture, is unlikely to be produced. Instead, we identify $\mathcal{P}_{X_2}$ as the HQS-favored state in the mass range 4110-4130 MeV and look forward to the forthcoming data and analysis. Combining the $SU(3)_F$ -symmetry with HQS provides simplified predictive relations, which will be helpful in the future searches of the hidden charm pentaquarks in b-baryon decays.

5 Acknowledgments

We would like to thank the organisers of *Quantum Field Theory at the Limits: from Strong Fields to Heavy Quarks* for their hospitality in Dubna.

References

[1] R. Aaij *et al.* [LHCb Collaboration], *Observation of $J/\psi\, p$ Resonances Consistent with Pentaquark States in $\Lambda_b^0 \to J/\psi K^- p$ Decays*, Phys. Rev. Lett. **115** (2015) 072001 [arXiv:1507.03414].

[2] A. Ali, arXiv:1605.05954 [hep-ph].

[3] L. Maiani, A. D. Polosa and V. Riquer, *The New Pentaquarks in the Diquark Model*, Phys. Lett. B **749**, 289 (2015) [arXiv:1507.04980].

[4] G. N. Li, X. G. He and M. He, JHEP **1512**, 128 (2015) [arXiv:1507.08252]; A. Mironov, A. Morozov, JETP Lett. **102**, 271 (2015) [arXiv:1507.04694]; A.V. Anisovich et al., [arXiv:1507.07652]; R. Ghosh, A. Bhattacharya, B. Chakrabarti, [arXiv:1508.00356]; Zhi-Gang Wang, Eur. Phys. J. C **76**, 70 (2016) [arXiv:1508.01468]; Zhi-Gang Wang, Tao Huang, Eur. Phys. J. C **76**, 43 (2016) [arXiv:1508.04189]; Zhi-Gang Wang, Eur. Phys. J. C **76**, 142 (2016) [arXiv: 1509.06436]; Hua-Xing Chen, Wei Chen, Xiang Liu and Shi-Lin Zhu, [arXiv: 1601.02092].

[5] A. Ali, I. Ahmed, M. Jamil Aslam, A. Rehman, *Heavy quark symmetry and weak decays of the b-baryons in pentaquarks with a $c\bar{c}$ component*, Phys. Rev. D **94** (2016), 054001 [arXiv:1607.00987].

[6] K. A. Olive *et al.* [Particle Data Group], Chin. Phys. C **38**, 090001 (2014). doi:10.1088/1674-1137/38/9/090001

[7] L. Maiani, F. Piccinini, A. D. Polosa and V. Riquer, *The Z(4430) and a New Paradigm for Spin Interactions in Tetraquarks*, Phys. Rev. D **89**, 114010 (2014) [arXiv:1405.1551 [hep-ph]].

[8] L. Maiani, F. Piccinini, A. D. Polosa and V. Riquer, *Diquark-antidiquarks with hidden or open charm and the nature of X(3872)*, Phys. Rev. D **71**, 014028 (2005) [hep-ph/0412098].

[9] H. Y. Cheng and C. K. Chua, Phys. Rev. D **92**, no. 9, 096009 (2015) doi:10.1103/PhysRevD.92.096009 [arXiv:1509.03708 [hep-ph]].

[10] R. Aaij *et al.* [LHCb Collaboration], JHEP **1407**, 103 (2014) doi:10.1007/JHEP07(2014)103 [arXiv:1406.0755 [hep-ex]].

XYZ mesons and Glueballs: effects of the quark-gluon mixing

Nikolai Kochelev

Institute of Modern Physics, Chinese Academy of Science, Lanzhou 730000, China and Bogoliubov Laboratory of Theoretical Physics, Joint Institute for Nuclear Research, Dubna, Moscow Region, 141980, Russia

DOI: http://dx.doi.org/10.3204/DESY-PROC-2016-04/Kochelev

We present the new developments in the physics of XYZ mesons and glueballs and discuss the connection between properties of the XYZ mesons and glueballs, and the structure of the QCD vacuum. It is shown that the mixing between quark and gluon degree of freedoms induced by the nontrivial topological structure of the QCD vacuum might affect strongly the properties of the exotic hadrons. A new interpretation of the XYZ mesons as the mixing between radial excitations of light quark-antiquark systems and states with heavy quark content is suggested. We introduce also a new mechanism of quarkonia production in hadron-hadron collisions coming from the mixing of light and heavy quark sectors of QCD. This mechanism is based on the nontrivial topological structure of the QCD vacuum and might explain the polarization puzzle in inclusive J/Ψ production in high energy reactions. The possibility of big changes of the scalar and pseudoscalar glueball masses in the hot gluonic plasma is established and their consequences in the phase structure of QCD analyzed.

1 Introduction

Nowadays the study of the exotic hadrons is one of the hottest topics of hadron physics. Within the quark model the ordinary mesons are considered as bound states of quark-antiquark pairs and baryons are three-quark bound states. However, more complicated states which include additional quarks and/or valence gluons are not forbidden by QCD. There were three big waves in the history of the exotic hadrons. The first wave was created by the pioneering papers by Jaffe [1, 2] on spectroscopy of the four quark $q^2\bar{q}^2$ states within MIT bag model with light u, d, s quarks. These states we call now light tetraquarks. The second wave was created by the prediction of the $udud\bar{s}$ strange pentaquark state with very small width within the chiral soliton model [3]. The third and last wave was generated by the Belle Collaboration discovery of the $X(3872)$ meson with very small width and the mass near DD^* threshold [4]. Now we have many candidates for exotic tetraquark states with heavy quark content which are called the XYZ mesons. There are also several candidates for the heavy pentaquarks (see, for example, the recent reviews [5, 6]). A lot of the different microscopical models have been suggested to explain their unusual properties. We discuss a new approach to the XYZ mesons based on the possibility of a large mixing between radial excitations in the light quark and antiquark system and states with heavy quark content. Such mixing might be induced by the nonperturbative

quark-gluon interaction related to the nontrivial topological structure of the QCD vacuum. The second part of this review is devoted to the modern status of glueballs which are the bound states of the gluons. We discuss the properties of these exotic hadrons including the possibility of the existence of the three-gluon bound states. And finally, we show that glueballs can influence strongly the properties of Quark-Gluon Plasma.

2 The exotic XYZ mesons

One of the main problems of the exotic hadron spectroscopy is the possibility of large mixings between exotic and nonexotic hadrons with the same quantum numbers. This mixing does not allow, in the most cases, to separate exotic states from the ordinary hadrons. The instantons, the strong fluctuations of the vacuum gluon fields, induce t'Hooft's multiquark interaction which can lead to the strong mixing of the different quark flavors (see review [15]). Due to the specific structure of t'Hooft's interaction it can violate the OZI rule in the channels with the quantum numbers 0^{-+} and 0^{++} as shown in Fig.1a. Since the instanton corresponds to a subbarrier transition between vacua with the different topological charge, the natural energy scale of this violation is related to the height of the potential barrier between these vacua. This height is given by the energy of the so-called sphaleron $E_{sph} = 3\pi/4\alpha_s(\rho_c)\rho_c \approx 2.8$ GeV with $\rho_c \approx 0.3$ fm being the average instanton size in the QCD vacuum [16]. For higher mass excitations one can expect that the instanton-anti-instanton molecules give an important contribution to the mixing between states with different quark flavors. Examples of such mixing between light quark-antiquark states and states with heavy quarks are shown in the Figs.1b, c and Fig.2. The nonperturbative interaction which governs that mixing is the quark-gluon effective interaction induced by instantons [17, 18]

$$\mathcal{L}_I = -i\frac{g_s\mu_a}{4M_q}\,\bar{q}\sigma^{\mu\nu}t^a q\,G^a_{\mu\nu} \tag{1}$$

where $G^a_{\mu\nu}$ is the gluon field strength, M_q is the effective mass of the light $u-, d-$ quarks in the vacuum and μ_a is the anomalous quark chromomagnetic moment (AQCM). An extension

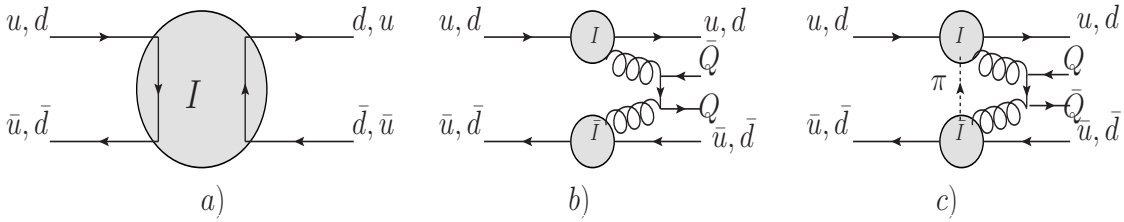


Figure 1: a) low energy mixing between light quarks induced by single instanton or anti-instanton , b) high energy mixing between light quarks and heavy quarks Q induced by the instanton-anti-instanton molecules and c) additional mixing induced by an additional pion exchange which is shown by the dashed line.

of Eq.1 which preserves the chiral symmetry was suggested by Polyakov and has the following form [9]

$$\mathcal{L}_I = -i\frac{g_s\mu_a}{4M_q}\bar{q}\sigma^{\mu\nu}t^a e^{i\gamma_5\vec{\tau}\cdot\vec{\phi}_\pi/F_\pi}qG^a_{\mu\nu}, \tag{2}$$



Figure 2: Additional mixing between heavy and light quarks in the $I = 0$ channel.

where $F_\pi = 93$ MeV is the pion decay constant [1]. Within the instanton model, the value of AQCM is [18]

$$\mu_a = -\frac{3\pi(M_q\rho_c)^2}{4\alpha_s(\rho_c)} \approx -0.38 \tag{3}$$

for $M_q \approx 170$ MeV in mean field approximation.

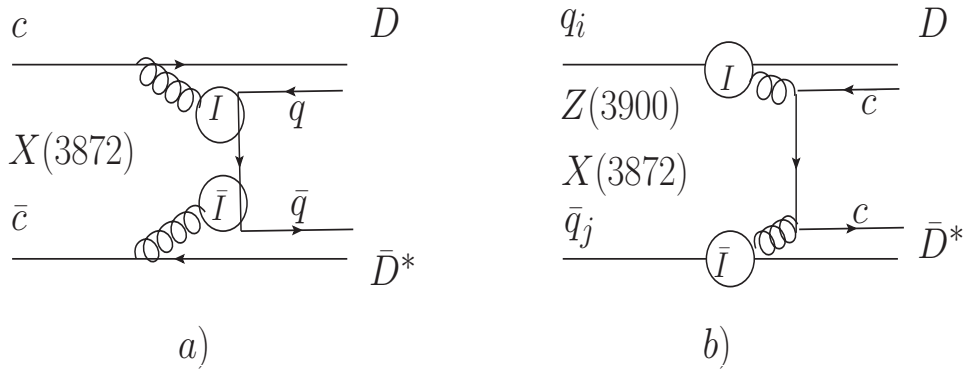


Figure 3: a) Mixing $c\bar{c}$ core with $D\bar{D}^*$ state, b) mixing the light radial excited state with $D\bar{D}^*$

In general, a high radially excited state of a light quark-antiquark system can mix easily with states which have a heavy quark content, if they have the same quantum numbers and approximately the same mass. It might be that the $X(3872)$ and the $Z_c(3900)$ are result of the mixing of molecular states and/or tetraquark charmed hidden states with high radial excitations of a light quark system, by the mechanism shown in Fig.1b, c and Fig.3b. A recent paper in the spirit of this idea was presented by Coito [13]. In the case of such mixing one should observe the decays of the XYZ mesons to final states without heavy quarks. The absence of these decay modes in present experiments might be related to the existence of many nodes in the wave function of the light quark system. One can estimate, for example, that light quark $q\bar{q}$ systems with radial numbers $n_r \sim 7 - 8$ have approximately the same mass as the $X(3872)$ and the $Z_c(3900)$. The many node structure of the wave function might lead to a very small overlap of the initial and final wave functions in the decay. These strong effect of the many nodes in wave function in decays is well known phenomenon. In particular, Brodsky and Karliner in [14] used it to explain the small rate of $\Psi(2S) \to \rho\pi$ in comparison with $J/\Psi \to \rho\pi$. Therefore, the

[1] For simplicity we consider only the $N_F = 2$ case.

mixing of high excited states in light quark-antiquark systems with heavy quark states might be behind of the unusual properties of XYZ mesons.

3 The J/Ψ polarization puzzle

There is a longstanding problem to explain the absence of transverse polarization of J/Ψ in the inclusive production at high energy. The transverse polarization was predicted by perturbative QCD and it comes from the fragmentation of on-shell gluon to charm-anticharm pair (see review [19]). Such polarization is in disagreement with the measurement at TEVATRON [20] and at LHC [21, 22]. In a recent paper the polarization of gluons in the constituent quark induced

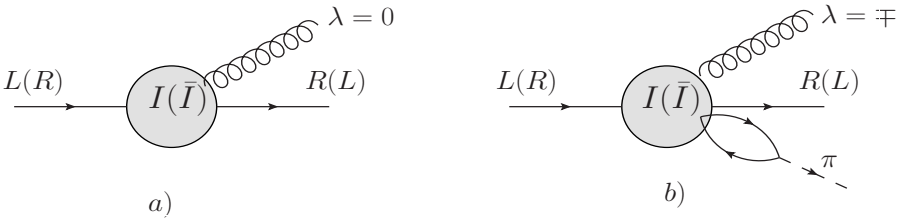


Figure 4: Diagram a) shows the quark-gluon vertex generated by the instanton, and diagram b) describes the quark-gluon-pion vertex induced by the instanton.

by instantons was calculated [23]. The diagram without pion, Fig.4a, produces no polarization of the gluons [9]. However, the diagram with an additional pion, Fig.4b, leads to polarization of the gluons. In this case the instanton and anti-instanton provide a polarization of opposite sign. The contribution of the instantons to the J/Ψ polarization in proton-proton collisions is presented in Fig.5. It is evident, that such mechanism leads to a longitudinal polarization of the J/Ψ because the perturbative vertex with a hard gluon does not change the helicity of the charm quark. From the another side, one can consider this new mechanism as the contribution

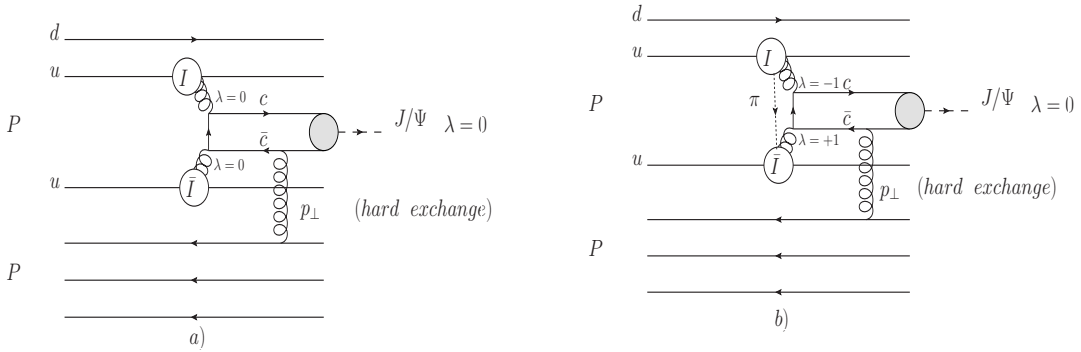


Figure 5: Example of diagrams which lead to the longitudinal polarization of J/Ψ induced by instanton-anti-instanton pair a) without pion exchange and b) with pion exchange.

to the inclusive production of the quarkonia coming from the mixing of light quarks with a state having heavy quark content.

4 Glueballs

The glueballs, the bound states of the gluons, are now widely under discussion (see the reviews [24, 25]). Different approaches including MIT bag model, several types of the constituent models, holographic QCD, QCD sum rule methods and the lattice simulation were used to extract the information on the spectrum and quantum numbers of the glueballs. One direct way based on the first principals of QCD to calculate the glueball spectrum are lattice calculations. At the present, the old [26] and more recent lattice calculations [27] in quenched QCD, i.e. the theory without quarks, are in the agreement and the result for the low mass of the glueballs in pure $SU(3)_c$ is

$$M(0^{++}) \approx\ 1.7\ GeV, M(2^{++}) \approx\ 2.4\ GeV, M(0^{-+}) \approx\ 2.6\ GeV$$

One of the interesting features of lattice calculations is that in the unquenched QCD with light quarks the result for the lowest mass of glueballs practically does not change [28]

$$M(0^{++}) = 1.795(60)\ GeV, \quad M(2^{++}) = 2.620(50)\ GeV,$$

for 2+1 flavor and $m_\pi = 360$ MeV. A more recent result for $N_f = 2$ and $m_\pi \approx 580$ MeV is [29]

$$M(0^{++}) = 1.624(141)GeV, M(0^{-+}) = 2.738(153)GeV,\ M(2^{++}) = 2.516(95)GeV.$$

There are many candidates for the glueball states. For the scalar glueballs we have the following mesons

$$f_0(600), \quad f_0(980), \quad f_0(1370), \quad f_0(1500), \quad f_0(1710), \quad f_0(1790),$$

For pseudoscalar glueball the candidates are

$$\eta(1405), \quad X(1835), \quad X(2120), \quad X(2370), \quad X(2500)$$

In the case of the tensor glueballs there are two candidates

$$f_J(2220), \quad f_2(2340).$$

One of the main problems of the glueball spectroscopy is the possible large mixings of the glueballs with ordinary and exotic quark states which leads to the difficulties in disentangling the glueballs in the experiments (see recent discussion in [30]). The example of such mixing is presented in Fig.6. The contribution of the mixing presented in Fig.6a was considered in [31] within the QCD sum rule method, and it was shown to be very important. One of the suitable ways to avoid this problem and obtain a clear prediction for the glueballs is to study the glueballs with exotic quantum numbers. $J^{PC} = 0^{--}, 0^{+-}, 1^{-+}, 2^{+-}, etc\ldots$ which cannot mix with ordinary quark-antiquark states. However, the calculation of the masses and decay modes of these exotic glueballs is very difficult because one should consider states with a large number of gluons. For example, Lattice calculations give a very large mass $M_G = 5.17$ GeV with a large uncertainty for the 0^{--} exotic three-gluon glueball. The first attempt to calculate the masses of the glueballs with exotic quantum number was done in ref. [32, 33] within the QCD sum rule approach and a rather small mass for 0^{--} glueball was found. However in a recent paper [34], it was shown that the interpolation current for the gluonic state used in [32, 33] has an anomaly and cannot be applied for the glueball calculations. In ref. [34] a new interpolating current for the 0^{--} glueball has been suggested. The derived QCD sum rules are consistent

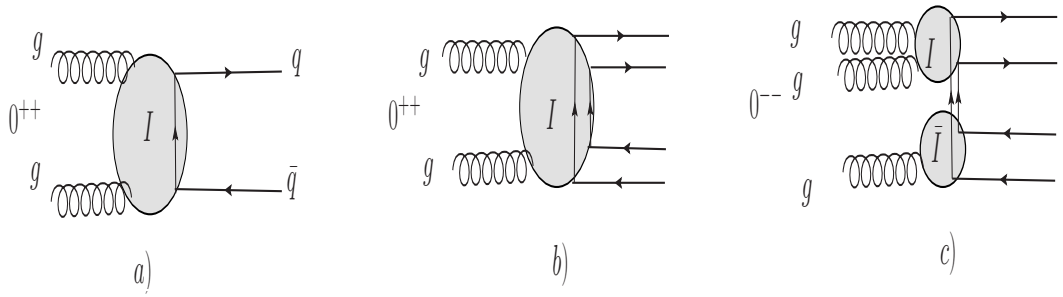


Figure 6: a) Mixing 0^{++} glueball with a quark-antiquark state, b) mixing of this glueball with a tetraquark, and c) mixing of the exotic three gluon 0^{--} state with an exotic tetraquark.

and stable. The resulting value for the mass of the 0^{--} glueball state is $M_G = 6.3^{+0.8}_{-1.1}$ GeV and an upper limit for the total width $\Gamma_G \leq 235$ MeV has been obtained. It has been also argued that the mixing of this glueball state with 0^{--} tetraquark is expected to be very small. Therefore, the exotic 0^{--} glueball can be considered a pure gluon state. At the present, the Belle Collaboration is searching for this state [35].

5 Glueballs in Quark-Gluon Plasma

In experiments at RHIC and LHC a new type of nuclear matter the so-called strongly interacted quark-gluon plasma has been discovered (see review [38]). It behaves as a liquid and does not have the expected gas-like behavior. There are many experiments planned at the running and future facilities to investigate the properties of such new matter. It is very important from the point of view of theory of the strong interactions to find the fundamental reason which leads to such behavior of quark-gluon matter. One possible way is to investigatethe simpler case of pure Gluodynamics, the theory without quarks. Recently very precise lattice results for the Equation of State (EoS) of this theory at finite T below and above the deconfinement temperature T_c were presented [39]. They challenge our understanding of QCD dynamics at finite temperatures. One of the puzzles is a very spectacular behavior of the trace anomaly, $I/T^4 = (\epsilon - 3p)/T^4$, as a function of T. In particular, just above T_c it rapidly grows untill $T_G \approx 1.1T_c$ and then it decays as $I/T^4 \sim 1/T^2$ untill $T \approx 5T_c$. A mechanism which can explain such anomalous behavior has been suggested in ref. [40]. The mechanism is based on the possibility of a large change of the glueball masses above the T_c. The starting point is the relation between the lowest scalar glueball mass, m_G, and the gluon condensate, $G^2 =< 0|\ \frac{\alpha_s}{\pi} G^a_{\mu\nu} G^a_{\mu\nu}|0 >$ at $T = 0$, which appears naturally in the dilaton approach [41]

$$m_G^2 f_G^2 = \frac{11 N_c}{6} < 0|\frac{\alpha_s}{\pi} G^a_{\mu\nu} G^a_{\mu\nu}|0 >, \tag{4}$$

where f_G is the glueball coupling constant to gluons. Lattice calculations show that the gluon condensate decreases roughly by a factor two at $T = T_c$ due to the strong suppression of its electric component, while slightly above T_c the condensate vanishes very rapidly due to the cancellation between its magnetic and electric components [42]. The temperature behavior of the condensate at $T_G \geq T \geq T_c$ can be described by the equation [43]

$$G^2(T) = G^2\left[1 - \left(\frac{T}{T_G}\right)^n\right]$$

and the mass of scalar and pseudoscalar glueballs for $T_G \geq T \geq T_c$ are given by

$$m(T) = m_0\sqrt{1 - \left(\frac{T}{T_G}\right)^4}.$$

The possible dynamical reason for the decrease of scalar and pseudoscalar glueball masses above T_c is the strong attraction between gluons induced by instanton-antiinstanton molecules shown in Fig.7. Such a molecular structure of the instanton vacuum is expected above T_c For the quark-antiquark channel the effect of the instanton-antiinstanton induced interaction was discussed in [45] and it was shown to be strong. For the gluon-gluon interaction the effect should be even stronger because it is enhanced by factor $S_0^2 \approx 10^2$, where $S_0 \approx 10$ is the instanton action. The rapid decrease of the scalar and preudoscalar glueball masses above

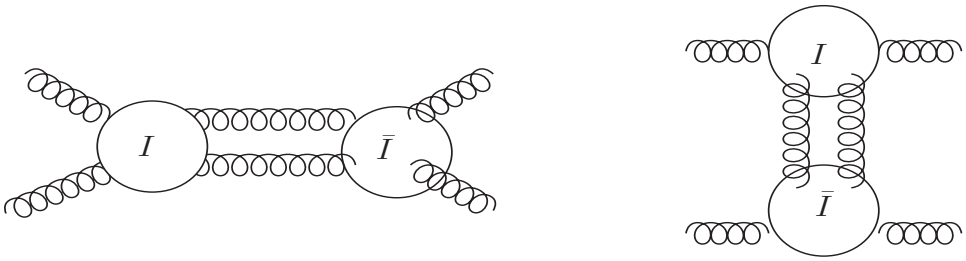


Figure 7: Gluon-gluon interaction induced by instanton-antiinstanton molecules.

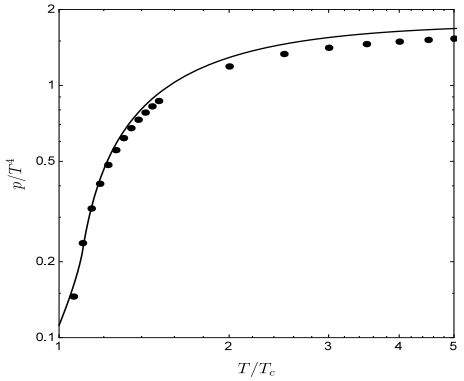


Figure 8: The pressure p/T^4 as the function of T/T_c in comparison with the lattice data [39].

T_c leads to a large contribution of these glueballs to the pressure of the gluon plasma and the sum of the glueball and free gluon contributions describe the lattice data very well as shown in Fig.8. Given these results we can describe three different phases of gluon matter [40]. The first phase is the confinement regime at $T < T_c$ and is described by a gas of massive glueballs.

The second phase appears just above T_c at $T_G \geq T \geq T_c$, where $T_G \approx 1.1T_c$. In this phase the main contribution to the EoS is coming from the very light scalar and pseudoscalar glueballs. Above the $T_G \approx 1.1T_c$ the third phase appears, a mixed phase of massless gluons and point-like scalar-pseudoscalar massless glueballs. The existence of such phases can be checked in high multiplicity events in relativistic heavy ion collisions where an abundant production of glueballs is expected [36, 37]. The most simple way is to look for the change of the scalar and pseudoscalar glueball masses in the two pion and three pion channels, correspondingly, as a function of multiplicity. Finally it should be also mentioned that the mixing between quark and gluon states can change strongly above T_c due to the transition between single instanton induced mixing to the mixing produced by instanton-antiinstanton molecules.

6 Conclusion

The exotic hadrons carry a very important information on the structure of the strong interactions and the properties of the exotic hadrons are very sensitive to the nonperturbative structure of QCD. We have shown that the XYZ mesons can arise as the result of a nonperturbative mixing between different configurations with and without heavy quark content. We have furthermore suggested a new mechanism for heavy quarkonia production at high energy which can be related to such mixing. We have also discussed the modern status of the glueballs and their mixing with quarkonia. Finally, we have predicted a drastic change of the scalar and pseudoscalar glueball masses above the deconfinement temperature in the gluonic plasma which has very exciting consequences at the level of the possible phase transitions at very high temperatures.

Acknowledgments

I would like to thank Alexander Dorokhov, Sergo Gerasimov, Mikhail Ivanov, Ernst-Michael Ilgenfritz, Makoto Oka, Pengming Zhang, Bing-Song Zou and, especially, Vicente Vento for useful discussions. I am grateful to Ahmed Ali and Michail Ivanov for the invitation to give a talk about exotic hadrons at Helmholtz - DIAS International Summer School "Quantum Field Theory at the Limits: from Strong Fields to Heavy Quarks", 18-30 July 2016, Dubna, Russia. This work has been supported by the Chinese Academy of Sciences President's International Fellowship Initiative (Grant No. 2013T2J0011), the Japan Society for the Promotion of Science (Grant No.S16019) and was initiated through the series of APCTP-BLTP JINR Joint Workshops.

References

[1] R. L. Jaffe, Phys. Rev. D **15** (1977) 267.

[2] R. L. Jaffe, Phys. Rev. D **15** (1977) 281.

[3] D. Diakonov, V. Petrov and M. V. Polyakov, Z. Phys. A **359** (1997) 305

[4] S. K. Choi *et al.* [Belle Collaboration], Phys. Rev. Lett. **91** (2003) 262001

[5] S. L. Olsen, arXiv:1611.01277 [hep-ex].

[6] R. F. Lebed, R. E. Mitchell and E. S. Swanson, arXiv:1610.04528 [hep-ph].

[7] S. L. Olsen, PoS Bormio 050 (2015) [arXiv:1511.01589 [hep-ex]].

[8] T. Schäfer and E.V. Shuryak, Rev. Mod. Phys. **70** (1998) 1323.

[9] D. Diakonov, Prog. Part. Nucl. Phys. **51** (2003) 173.

[10] J. Balla, M. V. Polyakov and C. Weiss, Nucl. Phys. B **510**, 327 (1998).

[11] N. Kochelev, H. J. Lee, B. Zhang and P. Zhang, Phys. Rev. D **92**, no. 3, 034025 (2015).

[12] N. Kochelev, H. J. Lee, Y. Oh, B. Zhang and P. Zhang, arXiv:1510.00472 [hep-ph].

[13] S. Coito, Phys. Rev. D **94** (2016) no.1, 014016

[14] S. J. Brodsky and M. Karliner, Phys. Rev. Lett. **78** (1997) 4682

[15] T. Schafer and E. V. Shuryak, Rev. Mod. Phys. **70**, 323 (1998) [arXiv:hep-ph/9610451].

[16] D. Diakonov, Prog. Part. Nucl. Phys. **51** (2003) 173

[17] N. I. Kochelev, Phys. Lett. B **426** (1998) 149

[18] N. Kochelev, Phys. Part. Nucl. Lett. **7** (2010) 326

[19] S. Brodsky, G. de Teramond and M. Karliner, Ann. Rev. Nucl. Part. Sci. **62** (2012) 1 [Ann. Rev. Nucl. Part. Sci. **62** (2011) 2082]

[20] A. Abulencia *et al.* [CDF Collaboration], Phys. Rev. Lett. **99** (2007) 132001

[21] R. Aaij *et al.* [LHCb Collaboration], Eur. Phys. J. C **73** (2013) no.11, 2631

[22] S. Chatrchyan *et al.* [CMS Collaboration], Phys. Lett. B **727** (2013) 381

[23] N. Kochelev, H. J. Lee, B. Zhang and P. Zhang, Phys. Lett. B **757** (2016) 420

[24] V. Mathieu, N. Kochelev and V. Vento, Int. J. Mod. Phys. E **18** 1 (2009).

[25] W. Ochs, J. Phys. G **40**, 043001 (2013)

[26] C. J. Morningstar and M. J. Peardon, Phys. Rev. D **60**, 034509 (1999)

[27] Y. Chen *et al.*, Phys. Rev. D **73** (2006) 014516

[28] E. Gregory, A. Irving, B. Lucini, C. McNeile, A. Rago, C. Richards and E. Rinaldi, JHEP **1210** (2012) 170

[29] Talk given by Y.Chen at Lattice 2016, Southampton, July 24-30.

[30] V. Vento, Eur. Phys. J. A **52** (2016) no.1, 1

[31] D. Harnett, R. T. Kleiv, K. Moats and T. G. Steele, Nucl. Phys. A **850** (2011) 110

[32] C. F. Qiao and L. Tang, Phys. Rev. Lett. **113**, no. 22, 221601 (2014)

[33] L. Tang and C. F. Qiao, Nucl. Phys. B **904** (2016) 282

[34] A. Pimikov, H. J. Lee, N. Kochelev and P. Zhang, arXiv:1611.08698 [hep-ph].

[35] S. Jia *et al.* [Belle Collaboration], arXiv:1611.07131 [hep-ex].

[36] V. Vento, Phys. Rev. D **75**, 055012 (2007)

[37] H. Stoecker *et al.*, J. Phys. G **43**, no. 1, 015105 (2016)

[38] E. Shuryak, arXiv:1412.8393 [hep-ph].

[39] S. Borsanyi, G. Endrodi, Z. Fodor, S. D. Katz and K. K. Szabo, JHEP **1207** (2012) 056.

[40] N. Kochelev, Eur. Phys. J. A **52** (2016) no.7, 186

[41] J. R. Ellis and J. Lanik, Phys. Lett. B **150** (1985) 289.

[42] S. H. Lee and K. Morita, Phys. Rev. D **79** (2009) 011501.

[43] D. E. Miller, Phys. Rept. **443** (2007) 55.

[44] E. V. Shuryak and I. Zahed, Phys. Rev. D **70** (2004) 054507.

[45] G. E. Brown, C. H. Lee, M. Rho and E. Shuryak, Nucl. Phys. A **740**, 171 (2004)

[46] E. M. Ilgenfritz and E. V. Shuryak, Nucl. Phys. B **319**, 511 (1989)).

Hadrons and Multiquark States in Holographic QCD

Valery E. Lyubovitskij[1,2,3,4], *Thomas Gutsche*[1], *Ivan Schmidt*[2]

[1]Institut für Theoretische Physik, Universität Tübingen,
Kepler Center for Astro and Particle Physics,
Auf der Morgenstelle 14, D–72076 Tübingen, Germany
[2]Departamento de Física y Centro Científico Tecnológico de Valparaíso (CCTVal), Universidad Técnica Federico Santa María, Casilla 110-V, Valparaíso, Chile
[3]Department of Physics, Tomsk State University, 634050 Tomsk, Russia
[4]Laboratory of Particle Physics, Tomsk Polytechnic University, 634050 Tomsk, Russia

DOI: http://dx.doi.org/10.3204/DESY-PROC-2016-04/Lyubovitskij

We discuss hadrons and multiquark states in holographic QCD. This approach is based on an action which describes hadron structure with broken conformal and chiral invariance and incorporates confinement through the presence of a background dilaton field. According to the gauge/gravity duality the five-dimensional boson and fermion fields propagating in AdS space are dual to four-dimensional fields leaving on the surface of AdS sphere, which correspond to hadrons. In this picture hadronic wave functions — basics blocks of hadronic properties — are dual to the profiles of AdS fields in the fifth (holographic) dimension, which is identified with scale variable. As applications we consider properties of hadrons and multiquark states from unified point of view: mass spectrum, form factors, parton, transverse momentum, Wigner and Husimi distributions.

1 Introduction

Recent decades have been marked by significant progress in derivation and application of holographic QCD approaches based on the gauge/gravity duality [1]. The duality has several manifistations. Two most important of them are: 1) matching between partion functions in two approaches gives relation between parameters of string and $SU(N)$ Yang-Mills (YM) theories; 2) conformal group acting in the boundary theory is isomorphic to $SO(4,2)$ group, which is the isometry group of the AdS_5 space. In particular, the string parameters g_s - coupling, l_s - length, and R - the AdS radius are related to the YM theory parameters g_{YM} - coupling, 't Hooft coupling $\lambda = g_{YM}^2 N$ as $2\pi g_s = g_{_{YM}}^2$ and $\frac{R^4}{l_s^4} = 2\, g_{_{YM}}^2\, N$. There are two imporant limits in case of dual theories: 1) 't Hooft limit (large N at λ fixed) $g_{YM} = \frac{\lambda}{N} \ll 1$, which corresponds to $g_s \ll 1$ (tree-level perturbative string theory). In this case we say that the "Conformal Field side" of duality works; 2) Strong coupling limit $\lambda \gg 1$, which means $l_s \ll R$. In this case we say that "String Theory side" of the duality works. AdS/QCD approaches are derived from AdS/CFT ones upon breaking of conformal invariance. According to the dictionary, the AdS/QCD or holographic QCD (HQCD) is an approximation to QCD attempting to model hadronic physics in terms of fields/strings living in extra dimensions - AdS space. HQCD models reproduce main features of QCD at low and high energies: chiral

symmetry, confinement, power scaling of hadron form factors. One should stress that the extra 5th dimension has clear physical interpretation as the scale. AdS/QCD approaches are divided on two types: 1) top-down approaches – low-energy approximation of string theory trying to find a gravitational background with features similar to QCD (e.g. Sakai-Sugimoto model); 2) bottom-up approaches – more phenomenological ones, using the features of QCD to construct 5d dual theory including gravity on AdS space. In order to go towards to QCD one should: i) break conformal invariance and generate mass gap, ii) via Kaluza-Klein decomposition of the five-dimensional AdS fields introduce a tower of normalized bulk fields (Kaluza-Klein modes) dual to hadronic wave functions. Bottom-up AdS/QCD approaches have two main realizations of breaking of conformal invariance and introducing confinement — hard-wall and soft-wall versions. In the hard-wall approach the AdS geometry is cutted by two branes — ultraviolet (UV) ($z = \epsilon \to 0$) and infrared (IR) ($z = z_{\rm IR}$). Hard-wall model gives incorrect linear dependence of hadron masses on angular momentum. This approach is analogue of the quark bag model [2] and similar to the covariant constituent quark model with infrared confinement developed in Ref. [3]. In the soft-wall model the soft cutoff of the AdS space is introduced via background dilaton field [4]-[10]. The advantage of this approach is that it gives analytical solution of equation of motion for the bulk profiles of AdS fields and produces Regge behavior of hadronic masses: $M_H^2 \sim J(L)$.

In this paper we consider holographic approach based on soft-wall approach developed by us in Refs. [5]-[10]. We report the applications of our approach to the properties of hadrons and multiquark states. In particular, we present results for hadronic mass spectra, form factors and parton, transverse momentum, Wigner and Husimi distributions [5]-[10].

2 Approach

Here we briefly review our approach. First, we specify the five-dimensional AdS metric:

$$\begin{aligned} ds^2 = g_{MN} dx^M dx^N &= \eta_{ab}\, e^{2A(z)}\, dx^a dx^b = e^{2A(z)}\, (\eta_{\mu\nu} dx^\mu dx^\nu - dz^2)\,, \\ \eta_{\mu\nu} &= {\rm diag}(1,-1,-1,-1,-1)\,, \end{aligned} \tag{1}$$

where M and $N = 0, 1, \cdots, 4$ are the space-time (base manifold) indices, $a = (\mu, z)$ and $b = (\nu, z)$ are the local Lorentz (tangent) indices, and g_{MN} and η_{ab} are curved and flat metric tensors, respectively, which are related by the vielbein $\epsilon^a_M(z) = e^{A(z)}\, \delta^a_M$ as $g_{MN} = \epsilon^a_M \epsilon^b_N \eta_{ab}$. Here z is the holographic coordinate, R is the AdS radius, and $g = |{\rm det} g_{MN}|$. In the following we restrict ourselves to a conformal-invariant metric with $A(z) = \log(R/z)$.

The relevant AdS/QCD actions for the boson and fermion field of spin J are [5]-[7]

$$\begin{aligned} S_B &= \int d^4x dz\, \sqrt{g}\, e^{-\varphi(z)} \Big[\mathcal{D}_M \Phi_{M_1 \cdots M_J}(x,z) \mathcal{D}^M \Phi^{M_1 \cdots M_J}(x,z) \\ &- \Big((\mu^B_J)^2 + U^B_J(z) \Big)\, \Phi_{M_1 \cdots M_J}(x,z) \Phi^{M_1 \cdots M_J}(x,z) \Big]\,, \end{aligned} \tag{2}$$

$$\begin{aligned} S_F &= S^+_F + S^-_F\,, \quad S^\pm_F = \int d^4x dz\, \sqrt{g}\, e^{-\varphi(z)} \sum_{i=+,-} \Big[\bar\Psi^\pm_{M_1 \cdots M_J}(x,z) i \mathcal{D}^\pm_M \Psi^{\pm\, M_1 \cdots M_J}(x,z) \\ &\mp \bar\Psi^\pm_{M_1 \cdots M_J}(x,z) \Big((\mu^F_J)^2 + U^F_J(z) \Big) \Psi^{\pm\, M_1 \cdots M_J}(x,z) \end{aligned} \tag{3}$$

where $\mathcal{D}_M$ and $\mathcal{D}^{\pm}_M$ are the covariant derivative (including external vector and axial fields) acting on boson $\Phi_{M_1\cdots M_J}$ and fermion $\Psi^{\pm}_{M_1\cdots M_J}$ fields, respectively. $\Psi^{\pm}_{M_1\cdots M_J}$ is the pair of bulk fermion fields, which are the holographic analogues of the left- and right-chirality fermion operators in the 4D theory. $\varphi(z)=\kappa^2 z^2$ is the dilaton field with κ being a free scale parameter. The quantities μ^B_J and μ^F_J are the bulk boson and fermion masses related to the conformal dimensions (Δ^B_J, Δ^F_J) of the spin-J AdS boson and fermion fields, respectively

$$(\mu^B_J R)^2=\Delta^B_J(\Delta^B_J-4)\,,\quad \mu^F_J R=\Delta^F_J-2 \tag{4}$$

As was shown in Refs. [11] and [6] the field dimensions Δ^B_J and Δ^F_J are related to twist-dimension $\tau_{B/F}$ of hadronic operators as

$$\Delta^B_J=\tau_B=2+L\,,\quad \Delta^F_J=\tau_F+\frac{1}{2}=\frac{7}{2}+L\,. \tag{5}$$

where $L=\max|L_z|$ is the maximal value of the z component of the quark orbital angular momentum in hadron [11]: $U^B_J(z)=4\varphi(z)(J-1)/R^2$ and $U^F_J(z)=\varphi(z)/R$ are the effective dilaton potentials. Note the choice of quadratic dilaton profile and potentials $U^B_J(z)$ and $U^F_J(z)$ is necessary in order to guarantee correct Regge behavior of hadronic mass spectra and asymptotic power scaling of hadronic factors at large momenta transfer in agreement with quark counting rules [5]-[10].

Notice that the fermion masses and the effective potentials corresponding to the fields Ψ^+ and Ψ^- have opposite signs according to the P-parity transformation. The absolute sign of the fermion mass is related to the chirality of the boundary operator. According to our conventions the QCD operators $\mathcal{O}_R$ and $\mathcal{O}_L$ have positive and negative chirality, and therefore the mass terms of the bulk fields Ψ^+ and Ψ^- have absolute signs "plus" and "minus", respectively.

One of the main advantages of the soft-wall AdS/QCD model is that the most of the calculations can be done analytically. In a first step, we show how in this approach the hadron wave functions and spectrum are generated. We follow the procedure pursued in Refs. [5]-[7]. We drop the external vector and axial fields in covariant derivatives, turn to the tangent space with Lorentz signature, where the AdS fields are rescaled as

$$\Phi_{\mu_1\cdots\mu_J}=e^{\varphi(z)/2+A(z)J}\phi_{\mu_1\cdots\mu_J}\,,\quad \Psi^{\pm}_{\mu_1\cdots\mu_J}=e^{\varphi(z)/2+A(z)(J-1/2)}\psi^{\pm}_{\mu_1\cdots\mu_J}\,. \tag{6}$$

Next we split the fermion field into left- and right-chirality components

$$\psi^{\pm}_{\mu_1\cdots\mu_J}(x,z)=\psi^{\pm\,L}_{\mu_1\cdots\mu_J}(x,z)+\psi^{\pm\,R}_{\mu_1\cdots\mu_J}(x,z) \tag{7}$$

and perform Kaluza-Klein (KK) expansion for $\phi_{\mu_1\cdots\mu_J}(x,z)$ and $\psi^{\pm\,L/R}_{\mu_1\cdots\mu_J}(x,z)$

$$\begin{aligned}\phi_{\mu_1\cdots\mu_J}(x,z) &= \sum_n \phi_{n\,\mu_1\cdots\mu_J}(x)\,F_{n\tau}(z)\,,\\ \psi^{\pm\,L/R}_{\mu_1\cdots\mu_J}(x,z) &= \frac{1}{\sqrt{2}}\sum_n \psi^{L/R}_{n\,\mu_1\cdots\mu_J}(x)\,G^{\pm\,L/R}_{n\tau}(z)\,,\end{aligned} \tag{8}$$

where the tower of the KK fields $\phi_{n\,\mu_1\cdots\mu_J}(x)$ is dual to four-dimensional fields describing mesons with spin J, while KK fields $\psi^{L/R}_{n\,\mu_1\cdots\mu_J}(x)$ are dual left/right-chirality fermion fields describing baryons with spin J. The number n corresponds to the radial quantum number. The set of

functions $F_{n\tau}(z)$ are the profiles of boson AdS fields in holographic direction, which are dual to the mesonic wave functions with twist τ and radial quantum number n. In case of baryon we have four sets of such profiles dual to baryonic wave functions, which satisfy to the following relation (due P- and C-invariance) $G^{\pm\,R}_{n\tau}(z) = \mp G^{\mp\,L}_{n\tau}(z)$. Then it is convenient to rescale the boson and fermion profiles as

$$F_{n\tau}(z) = e^{-3/2A(z)}\, f_{n\tau}(z)\,, \quad G^{\pm\,R/L}_{n\tau}(z) = e^{-2A(z)}\, g^{\pm\,R/L}_{n\tau}(z) \tag{9}$$

in order derive the Schrödinger-type equation of motions (EOMs) for the wave functions $f_{n\tau}$ and $g^{\pm\,L/R}_{n\tau}(z)$

$$\Big[-\partial_z^2 + \frac{4L^2-1}{4z^2} + \kappa^4 z^2 + 2\kappa^2(J-1)\Big]\, f_{n\tau}(z) \;=\; M^2_{B,n\tau J}\; f_{n\tau}(z) \tag{10}$$

and

$$\left[-\partial_z^2 + \kappa^4 z^2 + 2\kappa^2\Big(m \mp \frac{1}{2}\Big) + \frac{m(m\pm 1)}{z^2}\right]\, g^{L/R}_{n\tau}(z) \;=\; M^2_{F,n\tau}\; g^{L/R}_{n\tau}(z)\,, \tag{11}$$

where $m = \tau - 3/2$; $M_{B,n\tau J}$ and $M_{F,n\tau}$ are the masses of bosons and fermions dual to corresponding hadrons (mesons and baryons) with specific values of quantum numbers.

Above EOMs have analytical solutions for both wave functions

$$\begin{aligned}
f_{n\tau}(z) &= \sqrt{\frac{2\Gamma(n+1)}{\Gamma(n+\tau-1)}}\; \kappa^{\tau-1}\; z^{\tau-3/2}\; e^{-\kappa^2 z^2/2}\; L_n^{\tau-2}(\kappa^2 z^2)\,,\\
g^{L}_{n\tau}(z) &= \sqrt{\frac{2\Gamma(n+1)}{\Gamma(n+\tau)}}\; \kappa^{\tau}\; z^{\tau-1/2}\; e^{-\kappa^2 z^2/2}\; L_n^{\tau-1}(\kappa^2 z^2)\,,\\
g^{R}_{n\tau}(z) &= \sqrt{\frac{2\Gamma(n+1)}{\Gamma(n+\tau-1)}}\; \kappa^{\tau-1}\; z^{\tau-3/2}\; e^{-\kappa^2 z^2/2}\; L_n^{\tau-2}(\kappa^2 z^2)
\end{aligned} \tag{12}$$

and mass spectrum $M^2_{B,n\tau J} = 4\kappa^2\Big(n + \frac{\tau+J}{2} - 1\Big)$ and $M^2_{F,n\tau} = 4\kappa^2\Big(n+\tau-1\Big)$. Therefore, our main idea is to find the solutions for the bulk profiles of the AdS field in the z–direction, and then calculate the physical properties of hadrons in terms of the bulk profiles of AdS fields dual to hadronic wave functions. In this way both mass spectrum and dynamical hadronic properties like form factors and parton distributions will be calculated from a unified point of view based on the solutions of the Schrödinger-type EOMs (12). One can see that the bulk profiles of AdS fields have the correct scaling behavior for small z, which leads to correct power behavior of calculated hadronic form factors at large Q^2. Another important property of the bulk profiles is that they vanish at large z (confinement). Up to now we discussed the solutions of EOMs for the bulk profiles on its mass shell $p^2 = M^2$. In case when we go beyond mass shell, we can calculate so-called bulk-to-boundary propagators describing the behavior of bulk profiles at arbitrary p^2, which are necessary for calculation of momentum dependence of matrix elements in our approach. In particular, the bulk-to-boundary propagator for the vector AdS field dual to electromagnetic field is given in analytical form in terms of the Gamma $\Gamma(n)$ and Tricomi $U(a,b,z)$ functions: $V(Q,z) = \Gamma\Big(1+\frac{Q^2}{4\kappa^2}\Big)U\Big(\frac{Q^2}{4\kappa^2}, 0, \kappa^2 z^2\Big)$. The

bulk-to-boundary propagator $V(Q,z)$ obeys the normalization condition $V(0,z)=1$ consistent with gauge invariance and fulfils the following ultraviolet (UV) and infrared (IR) boundary conditions: $V(Q,0)=1\,,\quad V(Q,\infty)=0$. The UV boundary condition corresponds to the local (structureless) coupling of the electromagnetic field to matter fields, while the IR boundary condition implies that the vector field vanishes at $z=\infty$. E.g. a generic expression for the meson form factor is given in the form integral over z variable of the product of $V(Q,z)$ and bulk profiles corresponding to the wave functions of initial (in) and final (fin) meson

$$F_M(Q^2)=\int\limits_0^\infty dz V(Q,z) f_{\rm in}(z) f_{\rm fin}(z)\,. \tag{13}$$

Another advantage of our approach is a possibility to constraint the form of light-front wave functions (see detailed discussion in Refs. [5]-[10]) from matching of matrix elements of physical processes in AdS/QCD and Light-Front QCD. The idea of such matching was proposed in Ref. [11]. Next step is inclusion of effects of quark masses in agreement with constraints imposed by chiral symmetry and heavy quark effective theory.

3 Applications

One of the nice features of our approach is that we can derive effective light-front wave functions (LFWFs) using matrix elements for physical processes calculated in AdS/QCD. In particular, the nucleon LFWFs are set up as

$$\begin{aligned}
\psi^+_{+q}(x,\mathbf{k}_\perp) &= \varphi^{(1)}_q(x,\mathbf{k}_\perp)\,,\quad \psi^+_{-q}(x,\mathbf{k}_\perp) \;=\; -\frac{k^1+ik^2}{xM_N}\,\varphi^{(2)}_q(x,\mathbf{k}_\perp)\,,\\
\psi^-_{+q}(x,\mathbf{k}_\perp) &= \frac{k^1-ik^2}{xM_N}\,\varphi^{(2)}_q(x,\mathbf{k}_\perp)\,,\quad \psi^-_{-q}(x,\mathbf{k}_\perp) \;=\; \varphi^{(1)}_q(x,\mathbf{k}_\perp)\,,\\
\varphi^{(1)}_q(x,\mathbf{k}_\perp) &= \frac{4\pi}{M_N}\sqrt{\frac{q_v(x)+\delta q_v(x)}{2}}\,\sqrt{D^{(1)}_q(x)}\exp\left[-\frac{\mathbf{k}^2_\perp}{2M^2_N}D^{(1)}_q(x)\right],\\
\varphi^{(2)}_q(x,\mathbf{k}_\perp) &= \frac{4\pi}{M_N}\sqrt{\frac{q_v(x)-\delta q_v(x)}{2}}\,D^{(2)}_q(x)\exp\left[-\frac{\mathbf{k}^2_\perp}{2M^2_N}D^{(2)}_q(x)\right].
\end{aligned} \tag{14}$$

Here M_N is the nucleon mass.

Our functions $\varphi^{(1)}_q$ and $\varphi^{(2)}_q$ are normalized as

$$\begin{aligned}
\int\frac{d^2\mathbf{k}_\perp}{16\pi^3}\left[\varphi^{(1)}_q(x,\mathbf{k}_\perp)\right]^2 &= \frac{q_v(x)+\delta q_v(x)}{2}\,,\\
\int\frac{d^2\mathbf{k}_\perp}{16\pi^3}\,\frac{\mathbf{k}^2_\perp}{M^2_N}\left[\varphi^{(2)}_q(x,\mathbf{k}_\perp)\right]^2 &= \frac{q_v(x)-\delta q_v(x)}{2}\,,\\
\int\limits_0^1 dx\int\frac{d^2\mathbf{k}_\perp}{16\pi^3}\left[\varphi^{(1)}_q(x,\mathbf{k}_\perp)\right]^2 &= \frac{n_q+g^q_A}{2}\,,\\
\int\limits_0^1 dx\int\frac{d^2\mathbf{k}_\perp}{16\pi^3}\,\frac{\mathbf{k}^2_\perp}{M^2_N}\left[\varphi^{(2)}_q(x,\mathbf{k}_\perp)\right]^2 &= \frac{n_q-g^q_A}{2}\,,
\end{aligned} \tag{15}$$

where n_q is the number of u or d valence quarks in the proton and g_A^q is the axial charge of a quark with flavor $q = u$ or d.

Using these LFWFs one can calculate electromagnetic form factors, transverse momentum, Wigner and Husimi distributions, etc. Analytic experessions for these quantities can be found in Ref. [10]. In Figs. 1-4 we plot the results for the x-dependence of the unpolarized and polarized PDFs, TMDs, Wigner and Husimi distributions, and indicate selected results for the quark and nucleon electromagnetic form factors. We use the results for the NLO helicity-independent and helicity-dependent parton distributions at $\mu^2_{\rm NLO} = 0.40$ GeV^2 from Refs. [12] as input. Next in Figs. 5-7 we show our prediction for the deuteron electromagnetic form factors and structure functions.

Acknowledgements

The authors thank Stan Brodsky, Lev Lipatov, Oleg Teryaev, Werner Vogelsang, and Marat Siddikov for useful discussions. This work was supported by the German Bundesministerium für Bildung und Forschung (BMBF) under Project 05P2015 - ALICE at High Rate (BMBF-FSP 202): "Jet- and fragmentation processes at ALICE and the parton structure of nuclei and structure of heavy hadrons", by Heisenberg-Landau Program, by Tomsk State University Competitiveness Improvement Program and the Russian Federation program "Nauka" (Contract No. 0.1526.2015, 3854), by CONICYT (Chile) Research Project No. 80140097 and under Grants No. 7912010025, 1140390 and FB-0821. VEL would like to thank Departamento de Física y Centro Científico Tecnológico de Valparaíso (CCTVal), Universidad Técnica Federico Santa María, Valparaíso, Chile for warm hospitality. In memory of my parents (VEL).

References

[1] J. M. Maldacena, "The large N limit of superconformal field theories and supergravity," Adv. Theor. Math. Phys. **2**, 231 (1998) [Int. J. Theor. Phys. **38**, 1113 (1999)].

[2] P. N. Bogolubov, "On a Model of quasiindependent quarks," Ann. Inst. H. Poincare Phys. Theor. **8**, 163 (1968); A. Chodos, R. L. Jaffe, K. Johnson, C. B. Thorn and V. F. Weisskopf, "A New Extended Model of Hadrons," Phys. Rev. D **9**, 3471 (1974).

[3] T. Branz, A. Faessler, T. Gutsche, M. A. Ivanov, J. G. Korner and V. E. Lyubovitskij, "Relativistic constituent quark model with infrared confinement," Phys. Rev. D **81**, 034010 (2010).

[4] A. Karch, E. Katz, D. T. Son and M. A. Stephanov, "Linear Confinement and AdS/QCD," Phys. Rev. D **74**, 015005 (2006); S. J. Brodsky and G. F. de Teramond, "Hadronic spectra and light-front wavefunctions in holographic QCD," Phys. Rev. Lett. **96**, 201601 (2006); O. Andreev, "$1/q^2$ corrections and gauge / string duality," Phys. Rev. D **73**, 107901 (2006)

[5] T. Branz, T. Gutsche, V. E. Lyubovitskij, I. Schmidt and A. Vega, "Light and heavy mesons in a soft-wall holographic approach," Phys. Rev. D **82**, 074022 (2010); A. Vega, I. Schmidt, T. Branz, T. Gutsche and V. E. Lyubovitskij, "Meson wave function from holographic models," Phys. Rev. D **80**, 055014 (2009); T. Gutsche, V. E. Lyubovitskij,

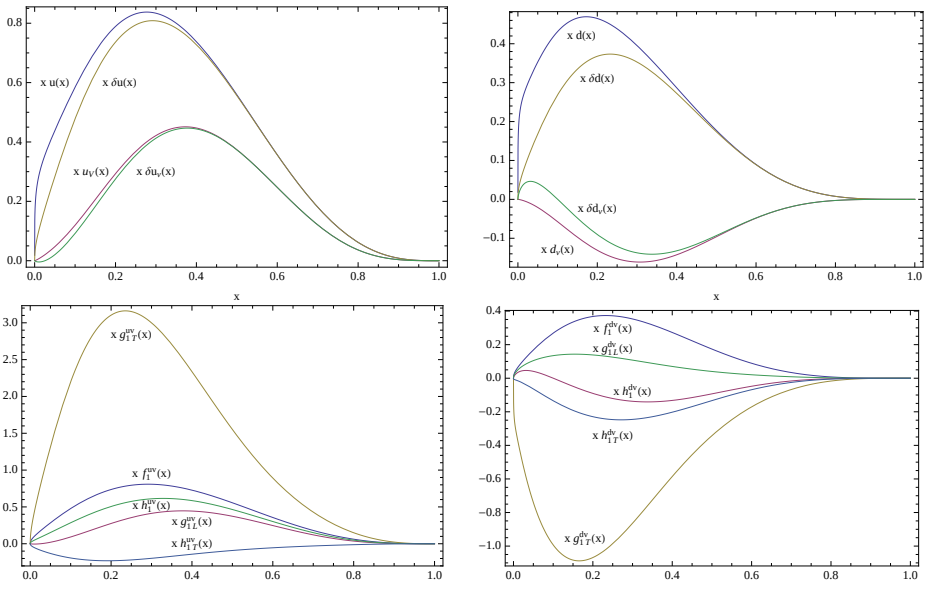


Figure 1: Quark PDFs and TMDs.

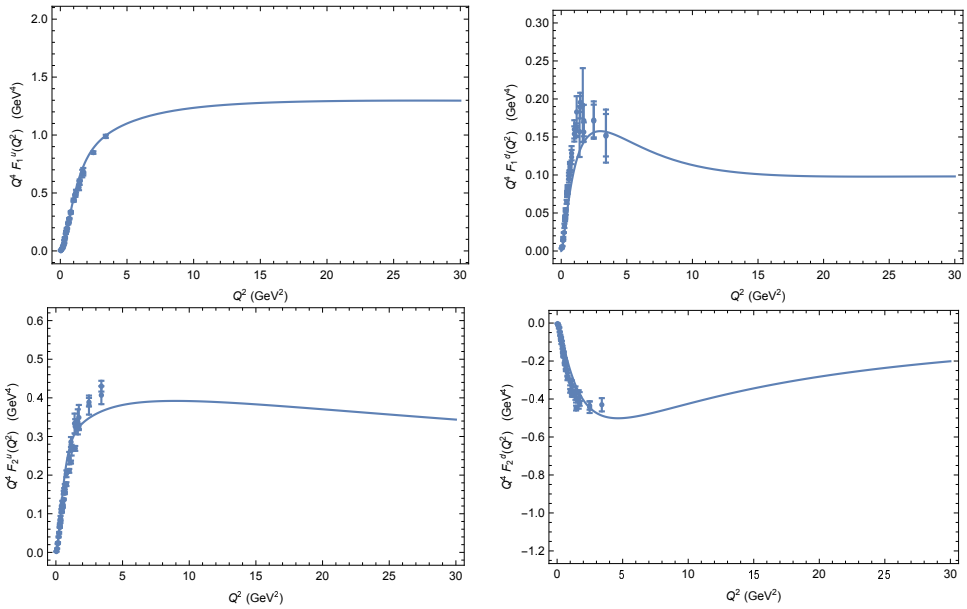


Figure 2: Dirac and Pauli Quark EM Form Factors multiplied by Q^4.

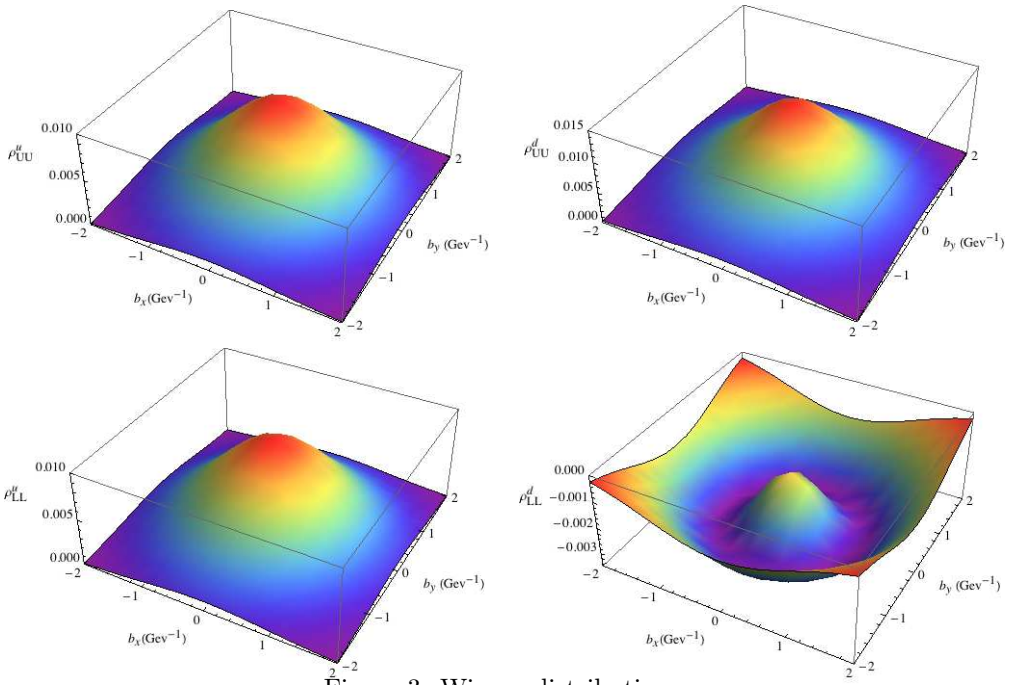


Figure 3: Wigner distributions.

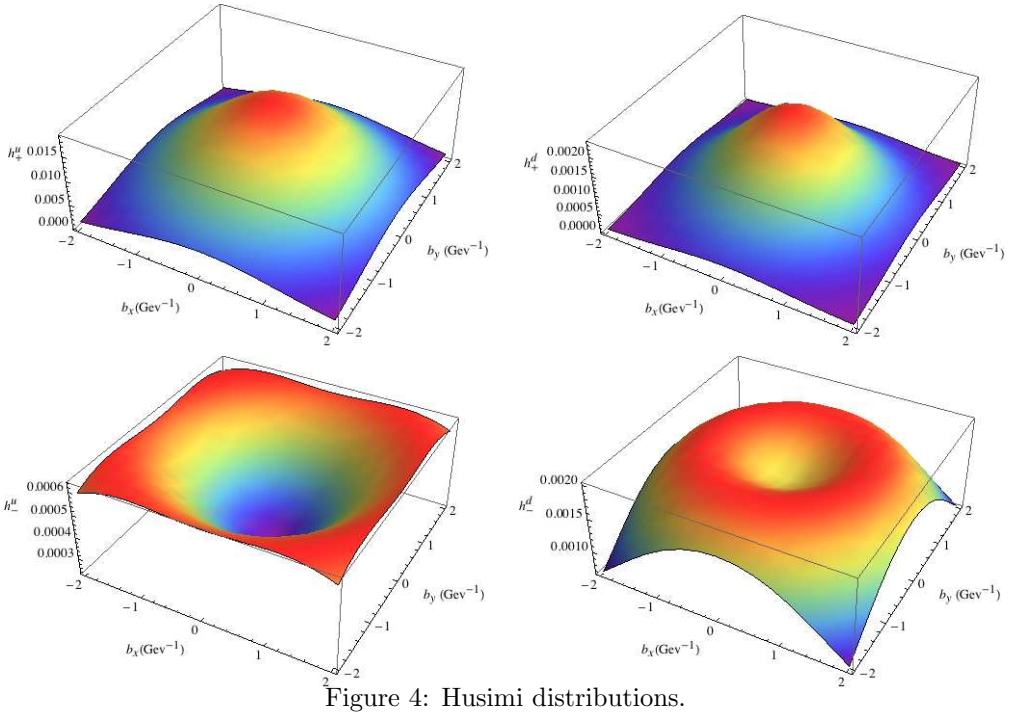


Figure 4: Husimi distributions.

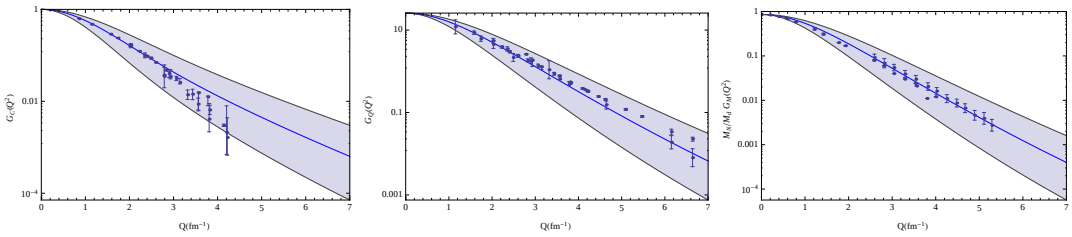


Figure 5: Deuteron charge G_C, quadrupole G_Q and magnetic G_M form factors.

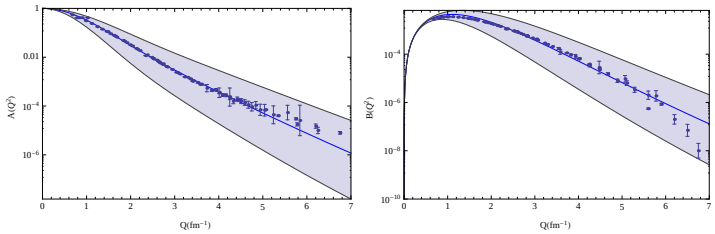


Figure 6: Deuteron structure functions A and B.

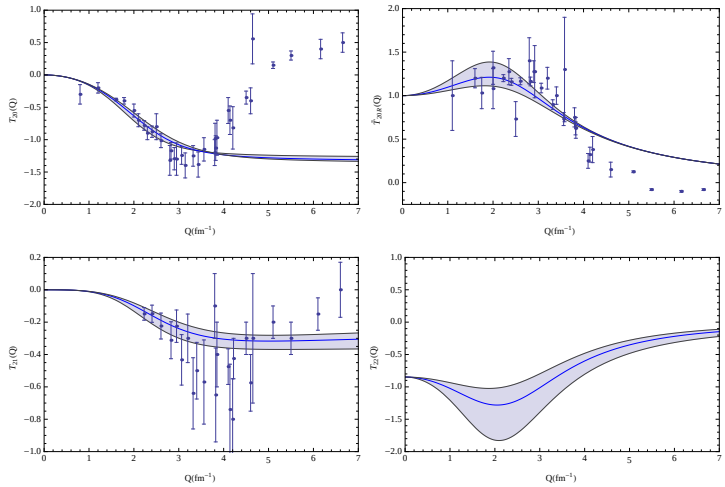


Figure 7: Deuteron tensor-polarized structures T_{20}, $\tilde{T}_{20R}$, T_{21} and T_{22}.

I. Schmidt and A. Vega, "Chiral Symmetry Breaking and Meson Wave Functions in Soft-Wall AdS/QCD," Phys. Rev. D **87**, 056001 (2013).

[6] T. Gutsche, V. E. Lyubovitskij, I. Schmidt and A. Vega, "Dilaton in a soft-wall holographic approach to mesons and baryons," Phys. Rev. D **85**, 076003 (2012).

[7] T. Gutsche, V. E. Lyubovitskij, I. Schmidt and A. Vega, "Nucleon structure including high Fock states in AdS/QCD," Phys. Rev. D **86**, 036007 (2012); A. Vega, I. Schmidt, T. Gutsche, V. E. Lyubovitskij, "Generalized parton distributions in AdS/QCD," Phys. Rev. D **83**, 036001 (2011); T. Gutsche, V. E. Lyubovitskij, I. Schmidt and A. Vega, "Nucleon resonances in AdS/QCD," Phys. Rev. D **87**, 016017 (2013).

[8] T. Gutsche, V. E. Lyubovitskij, I. Schmidt and A. Vega, "Light-front potential for heavy quarkonia constrained by the holographic soft-wall model," Phys. Rev. D **90**, 096007 (2014); "Light-front quark model consistent with Drell-Yan-West duality and quark counting rules," Phys. Rev. D **89**, 054033 (2014) Erratum: [Phys. Rev. D **92**, 019902 (2015)]; "Nucleon structure in a light-front quark model consistent with quark counting rules and data," Phys. Rev. D **91**, 054028 (2015) "Nuclear physics in soft-wall AdS/QCD: Deuteron electromagnetic form factors," Phys. Rev. D **91**, 114001 (2015); "Pion light-front wave function, parton distribution and the electromagnetic form factor," J. Phys. G **42**, 095005 (2015); A. Vega, I. Schmidt, T. Gutsche and V. E. Lyubovitskij, "Nonperturbative contribution to the strange-antistrange asymmetry of the nucleon sea," Phys. Rev. D **93**, 056001 (2016).

[9] T. Gutsche, V. E. Lyubovitskij and I. Schmidt, "Deuteron electromagnetic structure functions and polarization properties in soft-wall AdS/QCD," arXiv:1607.04124 [hep-ph], Phys. Rev. D (in print).

[10] T. Gutsche, V. E. Lyubovitskij and I. Schmidt, "Nucleon parton distributions in a light-front quark model," arXiv:1610.03526 [hep-ph].

[11] S. J. Brodsky, G. F. de Teramond, "Hadronic spectra and light-front wavefunctions in holographic QCD," Phys. Rev. Lett. **96**, 201601 (2006); S. J. Brodsky and G. F. de Teramond, "Light-Front Dynamics and AdS/QCD Correspondence: The Pion Form Factor in the Space- and Time-Like Regions," Phys. Rev. D **77**, 056007 (2008).

[12] M. Gluck, E. Reya and A. Vogt, "Dynamical parton distributions revisited," Eur. Phys. J. C **5**, 461 (1998); M. Gluck, E. Reya, M. Stratmann and W. Vogelsang, "Models for the polarized parton distributions of the nucleon," Phys. Rev. D **63**, 094005 (2001).

Heavy quark production at the LHC in the Parton Reggeization Approach

Anton Karpishkov, Maxim Nefedov, Vladimir Saleev, Alexandra Shipilova

Samara National Research University, Moskovskoe Shosse, 34, 443086, Samara, Russia

DOI: http://dx.doi.org/10.3204/DESY-PROC-2016-04/Saleev

We present the general introduction to the Parton Reggeization Approach and discuss some new results on large-p_T production for heavy quarks at the LHC. We concentrate here on study of different correlation spectra for $b\bar{b}-$jet pairs, $D\bar{D}-$meson pairs and $DD-$meson pairs.

1 Introduction

Study of the production of mesons, containing c and b quarks in hadronic collisions, persists as a topic of considerable interest both in theoretical and experimental communities of high energy physics. Production of the heavy-quark jets and D or B mesons is a good testing ground for the advanced computational techniques in perturbative Quantum Chromodynamics (pQCD), because the mass of the heavy quark provides a lower bound for the hard scale of the process, $\mu \geqslant 2m_{c/b} \gg \Lambda_{QCD}$. Therefore, one can expect that higher-order perturbative corrections in $\alpha_s(\mu)$ can be taken under control. On the other hand, due to the large center-of-mass energy of the modern hadron colliders, most notably the LHC, c and b quarks are produced copiously. Huge statistics allows experimental collaborations to perform the measurements of a large variety of *correlation* observables. These observables are differential in such variables as invariant mass of a pair of reconstructed hadrons (M), azimuthal angle between their transverse momenta ($\Delta\phi$) or distance in rapidity between the reconstructed hadrons (Δy).

Due to the nontrivial kinematical cuts on the phase-space of reconstructed hadrons, these correlation observables become multi-scale quantities. The conventional formalism of the Collinear Parton Model (CPM) is most suitable for the calculation of single-scale observables, and therefore leads to a significant radiative corrections for the above mentioned correlation spectra. The aim of Parton Reggeization Approach (PRA), which will be described below, is to introduce the gauge-invariant scheme of QCD-factorization, which will take into account the leading part of higher-order corrections, which are needed to describe the above mentioned correlation observables, already in the leading order (LO), and to improve, in such a way, order-by-order stability of the predictions.

Moreover, in many measurements, the heavy hadrons are produced with significant transverse momentum $p_T \gg m_{c/b}$. In this kinematics, the higher-order corrections are enhanced by the "fragmentation" logarithms $\log(p_T/m_{c/b})$, which should be resummed into the scale-dependent parton to hadron Fragmentation Functions (FF) $F_{i\to\mathcal{H}}(z,\mu^2)$, where z is the fraction of the momentum of the parent parton i, which is carried by the hadron $\mathcal{H}$. Not only

the $c/b \to \mathcal{H}_{c/b}$ fragmentation function become enhanced, but also a sizable $g \to \mathcal{H}_{c/b}$ fragmentation function is generated by the Dokshitzer-Gribov-Lipatov-Altarelli-Parisi (DGLAP) evolution of fragmentation functions. The gluon channel has to be taken into account due to the huge cross-section of the production of gluons at hadron colliders.

The outline of the current contribution is the following: in the Sec. 2 the general scheme of LO PRA calculations is described, in the Sec. 3 some new results on the heavy-flavor production, obtained in the LO of PRA are outlined.

2 Parton Reggeization Approach at the Leading Order

The standard alternative to the exact order-by-order treatment of the additional radiation within the CPM is the method of QCD Monte-Carlo (MC) generators, such as PYTHIA or HERWIG. The latter is based on the MC-simulation of DGLAP evolution and the property of collinear factorization of matrix elements in QCD, which allows one to take into account the radiation of additional partons with $p_T \ll \mu$ within the Leading Logarithmic Approximation (LLA). Strictly speaking, this method is inapplicable for the simulation of radiation of additional partons with $p_T \sim \mu$, since collinear factorization of QCD matrix elements is not valid in this region. Above-mentioned correlation observables are strongly sensitive to the radiation of additional hard partons, and description of this observables therefore depends on the *ad-hoc* scheme of treatment of the hard radiation,[1] which is implemented in particular MC generator.

To improve the collinear approximation in the region of $p_T \sim \mu$, PRA relies on another factorization theorem for QCD matrix elements, namely, factorization in the Multi-Regge Kinematics (MRK), see Ref. [1] for the review. In the MRK, the final state partons may be grouped into clusters, which are highly separated in rapidity, but the transverse momenta of partons in this clusters may be arbitrarily high. The scheme of LO calculations in the PRA is based on the certain approximate expression for QCD matrix element with the emission of two partons additionally to ones, required by the LO hard subprocess. This approximate expression smoothly interpolates between collinear and Regge limits for the emission of additional partons, and allows us to improve the description of radiations of additional hard partons on the solid theoretical grounds. Below, we will briefly outline the main steps of derivation of the factorization formula of the PRA for gluon-initiated processes.

To derive the factorization formula of the LO PRA, let's consider the following auxiliary hard subprocess:

$$g(p_1) + g(p_2) \to g(k_1) + q\bar{q}(P_{\mathcal{A}}) + g(k_2), \tag{1}$$

where the pair of heavy quarks $q = c/b$ with the four-momentum $P_{\mathcal{A}}$ and two additional gluons has been produced in the collision of two on-shell gluons $p_{1,2}^2 = 0$. In the Multi-Regge limit, when $\mathbf{k}_{T1}^2$, $\mathbf{k}_{T2}^2$ and $\mathbf{P}_{\mathcal{A}T}^2$ are $\ll \hat{s} = (p_1+p_2)^2$, and the rapidity gaps between produced particles $\Delta y(k_1, P_{\mathcal{A}}) \gg 1$ and $\Delta y(P_{\mathcal{A}}, k_2) \gg 1$, amplitude of the subprocess (1) is known to exhibit the t-channel factorization, presented diagrammatically in the Fig. 1 (left panel). This factorized form of the MRK amplitude is usually represented in terms of effective, gauge-invariant degrees of freedom of high energy QCD, Reggeized gluons ($R_\pm$) and Reggeized quarks ($Q_\pm$), which can be collectively denoted as *Reggeized partons*. Reggeized partons propagate in the t-channel between the effective vertices of the production of particles or clusters of particles, which are

[1] Such scheme usually includes boosts and rotations of the matrix element with *on-shell* initial-state partons and the so-called recoiling scheme. The latter restores overall momentum conservation in the event.

highly separated in rapidity. The MRK amplitude of the process (1) can be written as:

$$\begin{aligned}\mathcal{M} &= g_s^2 \left(\Gamma_{\mu\nu-}(p_1,-k_1) f_{a_1 b_1 c_1} \varepsilon_\mu^{a_1}(p_1) \varepsilon_\mu^{b_1 \star}(k_1)\right) \times \frac{1}{2q_1^2} \mathcal{A}^{c_1 c_2} \frac{1}{2q_2^2} \\ &\times \left(\Gamma_{\mu\nu+}(p_2,-k_2) f_{a_2 b_2 c_2} \varepsilon_\mu^{a_2}(p_2) \varepsilon_\mu^{b_2 \star}(k_2)\right) \end{aligned} \tag{2}$$

where $g_s^2 = 4\pi\alpha_s$ is the squared coupling constant of QCD, $q_{1,2} = p_{1,2} - k_{1,2}$, $\mathcal{A}^{c_1 c_2}$ is the effective vertex of the process $R_+ R_- \to q\bar{q}$, and the effective $R_\mp gg$-vertex reads [1, 2, 3]:

$$\Gamma_{\mu\nu\mp}(k_1,k_2) = 2g_{\mu\nu} k_1^\pm + (2k_2 + k_1)_\mu n_\nu^\pm - (2k_1 + k_2)_\nu n_\mu^\pm - \frac{(k_1+k_2)^2}{k_1^\pm} n_\mu^\pm n_\nu^\pm, \tag{3}$$

where $k_{1,2}$ are (incoming) four-momenta of gluons. The vectors $n_+^\mu = P_2^\mu/\sqrt{S}$ and $n_-^\mu = P_1^\mu/\sqrt{S}$ are related with the four-momenta of colliding protons $P_{1,2}^\mu$: $P_{1,2}^2 = 0$, $S = 2P_1P_2$. These vectors allows one to define the Sudakov (or light-cone) decomposition of the arbitrary four-vector: $k^\mu = \left(n_+^\mu k^- + n_-^\mu k^+\right)/2 + k_T^\mu$, where $n_\pm k_T = 0$, $k_\pm = n_\pm k$, $n_+ n_- = 2$ and $k_\pm = k^\pm$.

Effective vertex (3) describes the interaction of a gluon, with large k^+ or k^- light-cone momentum component with the Reggeized gluon $R_\mp$. The latter carries only one light-cone component of momentum q^+ for R_+ and q^- for R_-, and therefore, the other light-cone components of momenta of the gluons is conserved: $k_1^\pm + k_2^\pm = 0$ for the interaction with $R^\mp$ respectively. Taking this conditions into account, it is easy to see, that for the on-shell external gluons $k_{1,2}^2 = 0$ the vertex (3) satisfies Slavnov-Taylor identities $k_1^\mu \varepsilon^\nu(k_2)\Gamma_{\mu\nu\mp}(k_1,k_2) = 0$ and $\varepsilon^\mu(k_1) k_2^\nu \Gamma_{\mu\nu\mp}(k_1,k_2) = 0$, which guarantees the gauge invariance of the $R_\pm gg$-scattering amplitude.

The effective production vertex $\mathcal{A}^{c_1 c_2}$ is the Green's function of interaction of Reggeized gluons with ordinary QCD gluons and quarks, with amputated propagators of Reggeons. The effective vertex for the hard subprocess with the arbitrary number of quarks and gluons in the final state can be constructed, using the formalism of the Lipatov's effective action for Multi-Regge processes in QCD [2, 3], and it will be *gauge invariant* for arbitrary values of virtualities of incoming Reggeons $q_{1,2}^2$, provided that the above-mentioned constraints on the light-cone components of momenta of the Reggeons $R_\pm$ and $Q_\pm$ are fulfilled.

Contracting the vertex (3) with polarization vectors of on-shell gluons, squaring it and summing over the helicities, one obtains the following simple result:

$$\sum_{\lambda,\lambda'} \left|\Gamma_{\mu\nu\pm}(k_1,-k_2)\varepsilon_\mu(k_1,\lambda)\varepsilon_\mu^\star(k_2,\lambda')\right|^2 = 8(k_1^\mp)^2, \tag{4}$$

which allows one to rewrite the squared amplitude (2) summed (averaged) over the spin and color quantum numbers of the final-state (initial-state) particles in the following form:

$$\overline{|\mathcal{M}|^2} = \frac{4g_s^4}{q_1^2 q_2^2} \tilde{P}_{gg}(z_1)\tilde{P}_{gg}(z_2) \frac{\overline{|\mathcal{A}_{PRA}|^2}}{z_1 z_2}, \tag{5}$$

where the squared PRA amplitude is defined as:

$$\overline{|\mathcal{A}_{PRA}|^2} = \left(\frac{q_1^+ q_2^-}{4(N_c^2-1)\sqrt{t_1 t_2}}\right)^2 \left[\mathcal{A}_{c_1 c_2}^\star \mathcal{A}^{c_1 c_2}\right]. \tag{6}$$

In the Eqns. (5) and (6) we denote $t_{1,2} = \mathbf{q}^2_{T1,2}$, also we have introduced the light-cone momentum fractions $z_1 = q_1^+/p_1^+$, $z_2 = q_2^-/p_2^-$ and the PRA gluon-gluon splitting function $\tilde{P}_{gg}(z) = 2C_A(1-z)/z$. To derive these expressions one has to take into account, that $q^2_{1,2} = -\mathbf{q}^2_{T1,2}/(1-z_{1,2})$.

Kinematically, the MRK limit $|\Delta y(k_{1,2}, P_{\mathcal{A}})| \gg 1$ corresponds to the situation when $z_{1,2} \ll 1$, while the transverse momenta $t_1 \sim t_2 \sim \mathbf{p}^2_{T\mathcal{A}}$ can be non-negligible, and the effective production amplitude (6) explicitly and non-trivially depends on $t_{1,2}$ in this limit.

The opposite limit $t_{1,2} \to 0$ in the Eq. (5), corresponds to the traditional collinear factorization of QCD amplitudes. The known properties of collinear factorization for the squared QCD amplitude of the subprocess (1) are correctly reproduced by the Eq. (5) in the region $z_{1,2} \ll 1$, since the PRA splitting function $\tilde{P}_{gg}(z)$ correctly reproduces the small-z asymptotic of the full DGLAP splitting function $P_{gg}(z) = 2C_A\left((1-z)/z + z/(1-z) + z(1-z)\right)$, and the following relation holds for the squared PRA amplitude (6):

$$\int\limits_0^{2\pi} \frac{d\phi_1 d\phi_2}{(2\pi)^2} \lim_{t_{1,2}\to 0} \overline{|\mathcal{A}_{PRA}|^2} = \overline{|\mathcal{M}_{CPM}|^2}, \tag{7}$$

where $\overline{|\mathcal{M}_{CPM}|^2}$ is the squared amplitude of the corresponding subprocess with on-shell partons in the initial state (e. g. $gg \to q\bar{q}$ in the case at hand). One can observe, that to reproduce the collinear limit for any $z_{1,2}$, it is enough just to substitute the PRA splitting function in the Eq. (5) by the exact expression.

Finally, we define the *modified MRK (mMRK) approximation* for the squared matrix element of the subprocess (1) by the Eq. (5) with the substitution $\tilde{P}_{gg}(z) \to P_{gg}(z)$, and we apply this approximation to all values of $t_{1,2}$ and $z_{1,2}$. Numerical evidence (see Ref. [4] for the case of Reggeized gluons and the Refs. [5, 6] for the case of Reggeized quarks) suggests, that such approximation for matrix element is very good for the simulation of additional hard radiation outside of the final-state collinear region.

To derive the factorization formula for the cross-section, we substitute the mMRK approximation for the matrix element (5) to the standard formula of collinear factorization, integrated over the phase-space of additional partons:

$$d\sigma = \int \frac{dk_1^+ d^2\mathbf{k}_{T1}}{2k_1^+} \int \frac{dk_2^- d^2\mathbf{k}_{T2}}{2k_2^-} \int\limits_0^1 d\tilde{x}_1 d\tilde{x}_2 \; f_g(\tilde{x}_1,\mu^2) f_g(\tilde{x}_2,\mu^2) \cdot \frac{\overline{|\mathcal{M}|^2}}{2S\tilde{x}_1\tilde{x}_2} d\Phi_{\mathcal{A}},$$

where $f_g(x,\mu^2)$ are the standard Parton Distribution Functions of CPM, $\tilde{x}_1 = p_1^+/P_1^+$, $\tilde{x}_2 = p_1^-/P_1^-$, and $d\Phi_{\mathcal{A}}$ is the element of Lorentz-invariant phase space for the partons in the final state of the hard subprocess. Finally, one can change the variables of integration in the last expression as follows: $(\tilde{x}_1, k_1^+, \mathbf{k}_{T1}) \to (x_1, z_1, \mathbf{q}_{T1})$ and $(\tilde{x}_2, k_2^-, \mathbf{k}_{T2}) \to (x_2, z_2, \mathbf{q}_{T2})$, where the variables $x_{1,2}$ are defined as $x_1 = q_1^+/P_1^+$, $x_2 = q_2^-/P_2^-$, and rewrite it in a following form:

$$d\sigma = \int\limits_0^1 \frac{dx_1}{x_1} \int \frac{d^2\mathbf{q}_{T1}}{\pi} \tilde{\Phi}_g(x_1,t_1,\mu^2) \int\limits_0^1 \frac{dx_2}{x_2} \int \frac{d^2\mathbf{q}_{T2}}{\pi} \tilde{\Phi}_g(x_2,t_2,\mu^2) \cdot \frac{\overline{|\mathcal{A}_{PRA}|^2}}{2Sx_1x_2} d\Phi_{\mathcal{A}}, \tag{8}$$

where the "tree-level" unintegrated PDF (unPDF) has the form:

$$\tilde{\Phi}_g(x,t,\mu^2) = \frac{\alpha_s}{(2\pi)} \int\limits_x^1 \frac{dz}{t}\ P_{gg}(z)\cdot\frac{x}{z} f_g\left(\frac{x}{z},\mu^2\right). \tag{9}$$

The Eq. (8) is nothing but the well-known formula of the k_T-factorization of the cross-section [7], but integrals over $t_{1,2}$ and z in the Eqns. (8) and (9) are logarithmically divergent for $t \to 0$ and $z \to 1$. This divergence can be regulated if one properly takes into account the leading doubly-logarithmic corrections $\sim \left(\alpha_s \log^2(t/\mu^2)\right)^n$ from all orders of perturbation theory [8]. Here we follow the approach of Kimber, Martin and Ryskin (KMR) [9], where the unPDF is constructed to satisfy the normalization condition: $\int\limits_0^{\mu^2} dt\ \Phi_i(x,t,\mu^2) = x f_i(x,\mu^2)$, which ensures approximate normalization of the results for single-scale observables, obtained in k_T-factorization, on the corresponding LO CPM results. In the KMR approach, the $z \to 1$-singularity is regulated by the condition of rapidity ordering of the last emitted parton with the particles, produced in the hard subprocess. The last condition is natural from the point of view of our mMRK approximation, since only in this kinematic region it provides good approximation for the exact QCD matrix element.

The last important conceptual point is related with the Eq. (8). As a result of the derivation, presented above, the flux factor for the off-shell initial-state partons with virtualities $t_{1,2}$ is shown to coincide with the flux factor, which one has in CPM: $2Sx_1x_2 = (2S\tilde{x}_1\tilde{x}_2)\cdot z_1 z_2$. This result holds both in the collinear and in the Regge limits. Also this flux factor is shown to be compatible with the KMR unPDFs, since the Eq. (9) reproduces the "tree-level" structure of the KMR unPDFs (without Sudakov formfactor), and the flux factor is purely kinematical quantity, which could be determined on a basis of consideration of tree-level amplitudes only, without any need to take into account the loop corrections.

3 Heavy quark production at the LHC

3.1 Production of $b\bar{b}-$jet pairs in the LO PRA

To describe inclusive $b\bar{b}$-jet cross section in the LO approximation of the PRA, we need to consider gluon fusion subprocesses of $b\bar{b}$-quark pair production, which is dominating at high energies, i.e. $R_+ + R_- \to b + \bar{b}$. The amplitude of this process is obtained accordingly Feynman rules of Lipatov's effective theory [3] and the squared amplitude can be taken in analytical form from Ref. [10]. In the Figs. 2 and 3, we demonstrate a good agreement between LO PRA and data from ATLAS Collaboration [11] for invariant mass, azimuthal angle difference and $\chi = \exp|y_1 - y_2|$ spectra of $b\bar{b}-$dijets. Here and in the following, all calculations has been done with the use of the LO KMR model for unPDFs [9], and the LO MSTW-2008 PDF set [12] is used as the collinear input for the KMR formula.

3.2 Production of $D\bar{D}(DD)-$meson pairs in the LO PRA

To describe the hadronization stage we should use the fragmentation model, in which transition from the parton i, which was produced in hard interaction, to the $D(\bar{D})$ meson is described by

corresponding fragmentation functions $F_{i\to D(\bar{D})}(z,\mu^2)$ at the scale μ^2. In the case of $D\bar{D}(DD)$-meson pair production the fragmentation formula has the following form:

$$\frac{d\sigma(p+p\to D+\overline{D}+X)}{dp_{DT}dy_D dp_{\overline{D}T}dy_{\overline{D}}}=\sum_{ij}\int_0^1\frac{dz_1}{z_1}\int_0^1\frac{dz_2}{z_2}F_{i\to D}(z_1,\mu^2)F_{j\to\overline{D}}(z_2,\mu^2)\times$$
$$\times\frac{d\sigma(p+p\to i(k_i=p_D/z_1)+j(k_j=p_{\overline{D}(D)}/z_2)+X)}{dk_{iT}dy_i dk_{jT}dy_j}, \qquad (10)$$

where subprocesses $R_+ + R_- \to c+\bar{c}$ and $R_+ + R_- \to g+g$ contribute in $D\bar{D}$-production, and subprocess $R_+ + R_- \to g+g$ contributes in DD-production. In our calculations we use the LO FFs from Ref. [14]. These FFs satisfy two desirable properties: at first, their μ^2-scaling violation is governed by DGLAP evolution equations; and secondly – they are universal.

In Fig. 4, the predicted in the LO PRA spectra of D^0D^- pairs differential in azimuthal angle difference, transverse momentum, rapidity distance and invariant mass of the pair are shown in comparison with the data [15], obtained by LHCb Collaboration. One can observe, that description of these two-particle spectra in PRA match experimental data better than in the NLO calculations of CPM in all kinematical regions (see the comparison between theory and data in [15]). The similar result is obtained in case of $B\bar{B}-$meson pair production at the LHC, as it is shown in the right panel of Fig. 1. In case of production of two *identical* D mesons, we also obtain good agreement with the data (see Fig. 5), taking into account only gluon to $D-$meson fragmentation mechanism. Let us note that $DD-$meson pair production can not be described at all in the LO single-parton-scattering approximation of CPM (which is usually taken to be $gg\to c\bar{c}+c\bar{c}$) and the double-parton-scattering (DPS) production mechanism has been suggested to describe these data [19]. However, the kinematical region where DPS dominates coincides with the domain where the PRA gives large additional contribution to the CPM. As we have obtained, there is no place for DPS contribution if we are working already in the LO of PRA.

Acknowledgements

The work was supported by Russian Foundation for Basic Research through the Grant No 14-02-00021, and by the Ministry of Education and Science of Russia under Competitiveness Enhancement Program of Samara University for 2013-2020.

References

[1] L. N. Lipatov, Phys. Rep. **286** 131 (1997).

[2] L. N. Lipatov, Nucl. Phys. **B452** 369 (1995); L. N. Lipatov and M. I. Vyazovsky, Nucl. Phys. **B597** 399 (2001).

[3] E. N. Antonov, L. N. Lipatov, E. A. Kuraev, and I. O. Cherednikov, Nucl. Phys. **B721** 111 (2005).

[4] J. R. Andersen, V. Del Duca and C. D. White, JHEP **0902** 015 (2009).

[5] F. Hautmann, M. Hentschinski and H. Jung, Nucl. Phys. **B865** 54 (2012).

[6] M. Nefedov and V. Saleev, Phys. Rev. **D92** 094033 (2015).

[7] L. V. Gribov, E. M. Levin, and M. G. Ryskin, Phys. Rept. **100** 1 (1983); J. C. Collins and R. K. Ellis, Nucl. Phys. **B360** 3 (1991); S. Catani, M. Ciafaloni, and F. Hautmann, Nucl. Phys. **B366** 135 (1991).

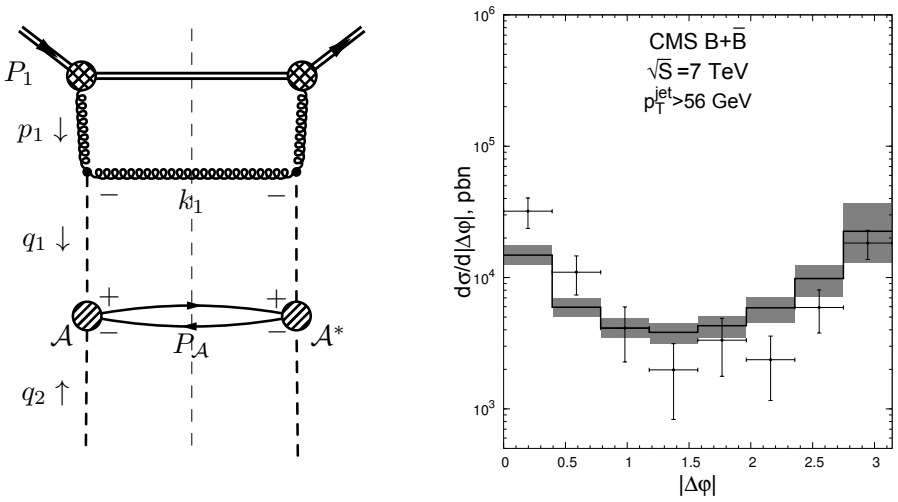


Figure 1: Left panel: Diagrammatic representation of the MRK-asymptotics of the squared amplitude of the subprocess (1). The dashed lines denote Reggeized gluons ($R_\pm$). Part of the diagram, containing the interaction of the gluon $g(p_2)$ with the Reggeized gluon $R_+(q_2)$ is not shown for brevity. Right panel: the spectrum of $B\bar{B}$-meson pair as a funcion of the azimuthal angle difference between them, the the data from CMS Collaboration [18].

[8] Yu. L. Dokshitzer, D.I. Diakonov and S. I. Troyan, Phys. Rep. **58** 269 (1980).

[9] M. A. Kimber, A. D. Martin, and M. G. Ryskin, Phys. Rev. **D63**, 114027 (2001); A. D. Martin, M. G. Ryskin and G. Watt, Eur. Phys. J. **C 66**, 163 (2010).

[10] M. A. Nefedov, V. A. Saleev, and A. V. Shipilova, Phys.Rev. **D87** 094030 (2013).

[11] ATLAS Collaboration, G. Aad*et al.*, Eur. Phys. J. **C71** 1846 (2011).

[12] A. D. Martin, W. J. Stirling, R. S. Thorne and G. Watt, Eur. Phys. J. **C63** 189 (2009).

[13] V. A. Saleev, and A. V. Shipilova, Phys.Rev. **D86** 034032 (2012); A. V. Karpishkov, M. A. Nefedov, V. A. Saleev, and A. V. Shipilova, Int.J.Mod.Phys. **A30** 1550023 (2015);

[14] B. A. Kniehl, G. Kramer, I. Schienbein, and H. Spiesberger, *Phys. Rev.* **D84** 094026 (2011).

[15] LHCb Collaboration, R. Aaij *et al.*, JHEP **06**, 141 (2012).

[16] A. V. Karpishkov, M. A. Nefedov, V. A. Saleev, and A. V. Shipilova, Phys. Rev. **D91** 054009 (2015).

[17] R. Maciula, V. A. Saleev, A. V. Shipilova, A. Szczurek, Phys. Lett. B **758** 458 (2016); A. V. Karpishkov, V. A. Saleev, and A. V. Shipilova, Phys.Rev. **D94** 114012 (2016).

[18] CMS Collaboration, JHEP **03** 136 (2011).

[19] LHCb Collaboration, R. Aaij et al. , JHEP **03** 108 (2014).

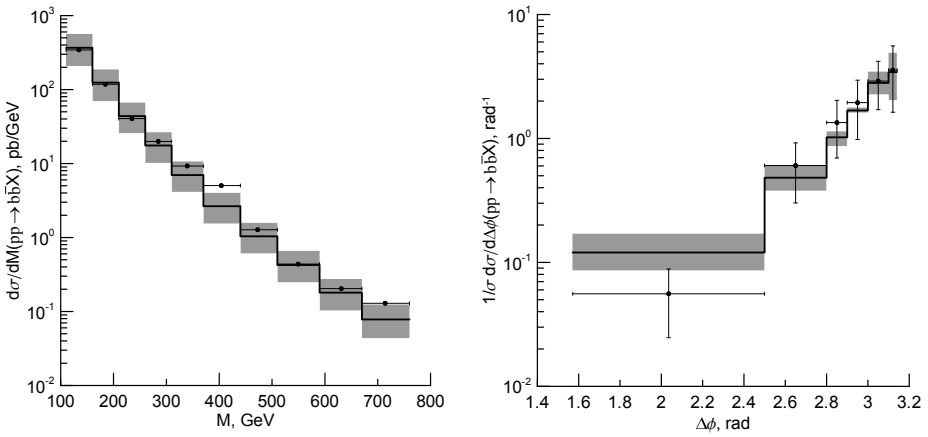


Figure 2: The $b\bar{b}$-dijet cross-section as a function of dijet invariant mass M and as a function of the azimuthal angle difference between the two jets for b-jets with $p_T > 40$ GeV, $|y| < 2.1$. The data are from ATLAS Collaboration [11], the solid line corresponds to KMR unPDF, the shaded bands indicate the theoretical uncertainties.

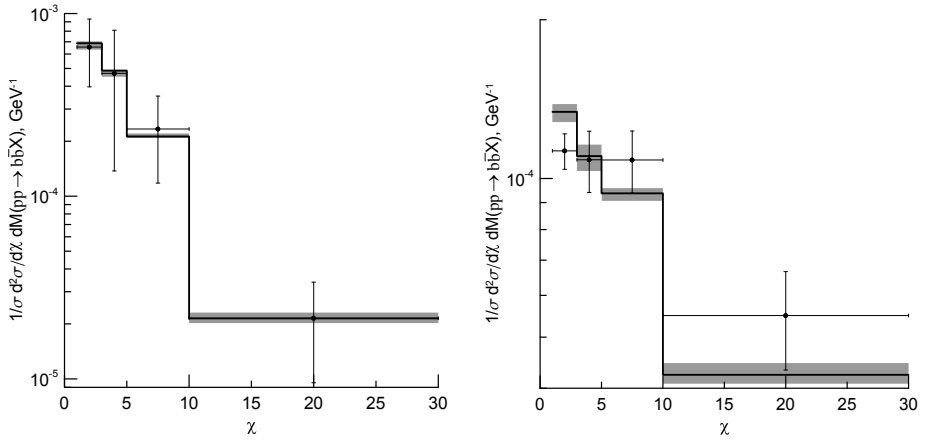


Figure 3: The $b\bar{b}$-dijet cross-section as a function of χ for b-jets with $p_T > 40$ GeV, $|y| < 2.1$ and $|y_{boost}| = \frac{1}{2}|y_1 + y_2| < 1.1$, for dijet invariant mass range $110 < M < 370$ GeV and $370 < M < 850$ GeV. The data are from ATLAS Collaboration [11].

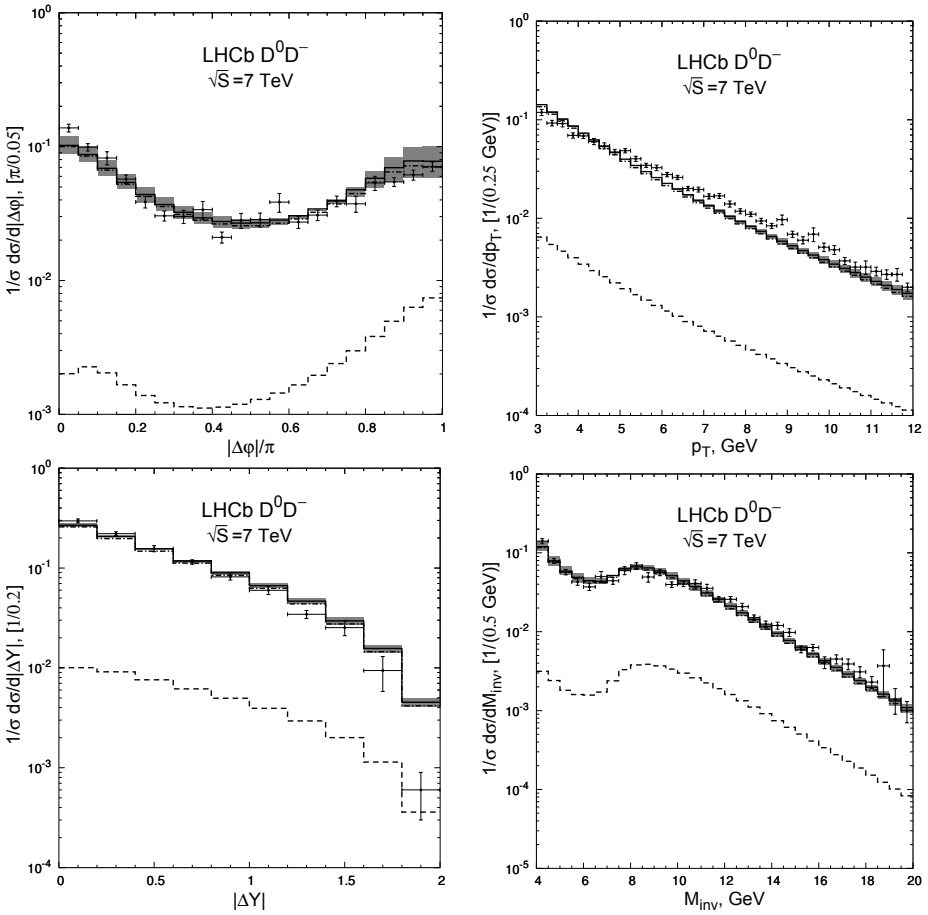


Figure 4: The spectra of D^0D^- pairs differential in azimuthal angle difference (left, top), transverse momentum (right, top), rapidity distance (left, bottom) and invariant mass of the pair (right, bottom) at the $2 < y < 4$ and $\sqrt{S} = 7$ TeV. The LHCb data at LHC are from the Ref. [15]. Dashed line represents the contribution of gluon fragmentation in gluon-gluon fusion, dash-dotted line – the c-quark fragmentation contribution in gluon-gluon fusion, solid line is their sum.

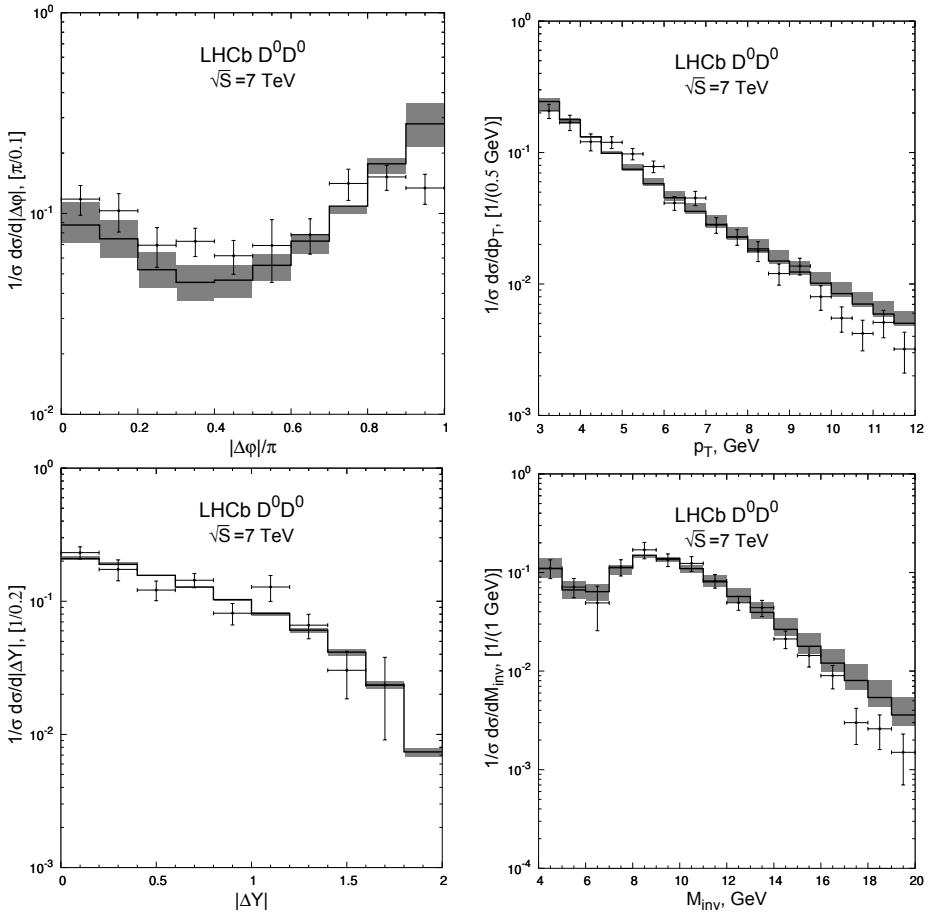


Figure 5: The spectra of D^0D^0 pairs differential in azimuthal angle difference (left, top), transverse momentum (right, top), rapidity distance (left, bottom) and invariant mass of the pair (right, bottom) at the $2 < y < 4$ and $\sqrt{S} = 7$ TeV. The LHCb data at LHC are from the Ref. [15]. Solid line represents the leading contribution of gluon fragmentation in gluon-gluon fusion.

The physics of Heavy Quark Distributions in Hadrons: Collider Tests

G.I. Lykasov[1], A.V. Lipatov[1,2], Yu.Yu. Stepanenko[2]

[1] *Joint Institute for Nuclear Research, Dubna 141980, Moscow region, Russia*
[2] *Skobeltsyn Institute of Nuclear Physics, Moscow State University, 119991 Moscow, Russia*
[3] *Gomel State University, Gomel 246019, Republic of Belarus*

DOI: http://dx.doi.org/10.3204/DESY-PROC-2016-04/Lykasov

We consider an observable very sensitive to the non-zero intrinsic charm (IC) contribution to the proton density. It is the ratio between the differential cross sections of the photon or Z-boson and c-jet production in the pp collision, $\gamma(Z)+c$, and the $\gamma(Z)$ and the b-jet production. It is shown that this ratio can be approximately flat or increasing at large $\gamma(Z)$ transverse momenta p_T and their pseudo-rapidities $1.5<\eta<2.4$ if the IC contribution is taken into account. On the contrary, in the absence of the IC this ratio decreases as p_T grows. We also present the ratios of the cross sections integrated over p_T as a function of the IC probability w. It is shown that these ratios are mostly independent on the theoretical uncertainties, and such predictions could therefore be much more promising for the search for the intrinsic charm signal at the LHC compared to the predictions for p_T-spectra, which significantly depend on these uncertainties.

1 Introduction

The hypothesis of the *intrinsic* (or valence-like) heavy quark component, the quark Fock state $|uudQ\bar{Q}\rangle$[1, 2, 3, 4] in a proton suggested by Brodsky with coauthors[1, 2] (BHPS model) is intensively discussed in connection with an opportunity to verify it experimentally[5, 6, 7, 8, 9, 10, 11, 12, 13]. Up to now, there is a long-standing debate about the possible existence of the *intrinsic* charm (IC) and *intrinsic* strange (IS) quarks in a proton[7]. Thorough theoretical and experimental studies of these intrinsic heavy quark components would be very important for the experiments performed at the LHC.

Recently it was shown that the possible existence of the intrinsic heavy quark components in the proton can be seen not only in the inclusive heavy flavor production at high energies[8], but also in the semi-inclusive production of prompt photons or vector bosons accompanied by heavy quark jets[9, 11]. An experimental hint on possible existence of the IC contribution was observed in the Tevatron experiment on the prompt photon production in the association of the c and b jets in the $p\bar{p}$ annihilation at $\sqrt{s}=1.98$ TeV[14, 15]. It was shown that the description of the Tevatron data within the perturbative QCD (pQCD) could be significantly improved if the IC contributions were taken into account The photon transverse momentum (p_T) spectrum in the $\gamma+c$ production and the ratio of the spectra in the $\gamma+c$ and $\gamma+b$ production measured at the Tevatron[16] are better described within the BHPS model[1, 2], which includes the IC

contributions. According to the pQCD calculations[17], in the absence of the IC contribution this ratio decreases, when p_T grows, while the Tevatron data show its flat behavior at large $p_T \geq 100$ GeV[16].

The possible IC signal can also be observed in the hard pp production of the gauge bosons Z or W accompanied by heavy flavors. As it was shown[11], the ratio of the $Z + c$ and W + heavy jet production cross sections maximizes the sensitivity to the IC component of the proton. Our early predictions about a possible intrinsic charm signal in the production of prompt photons or gauge bosons accompanied by heavy flavor jets concerned their transverse momenta distributions in the mid-rapidity region of pp collisions at the LHC energies[9, 11]. It was obtained with the IC probability about $w = 3.5\%$, which is the upper limit being due to constraints from the HERA data on the deep inelastic scattering. However, the upper limit of the IC probability in a proton is still very actively debated[7]. Therefore, in the present paper we focus mainly on the predictions for searching at any w for the IC signal in the observables, which are very little sensitive to the theoretical uncertainties, namely, the ratios between the $\gamma(Z) + c$ and $\gamma(Z) + b$ cross sections in pp collisions at the LHC energies. An important advantage of these observables is that many theoretical uncertainties, for example, heavy quark masses, the factorization and/or renormalization scales, are canceled, as will be demonstrated below. We show that the measure of these ratios is much more promising for the search for the IC signal.

Below we perform the calculations in two ways. First, we use the parton-level Monte Carlo event generator MCFM[18], which implements the NLO pQCD calculations of associated Z boson and heavy flavor jet production. The detailed description of the MCFM routine is available[18]. To generate the prompt photon and heavy jet production cross sections, we apply the k_T-factorization approach[19, 20], which becomes a commonly recognized tool in the high energy phenomenology. Our main motivation is that it gives a better description of the Tevatron data compared to the NLO pQCD calculations[17], as it was claimed[14, 15]. We apply this approach to the associated Z and heavy jet production to perform an independent cross-check of our results[1].

The outline of our paper is the following. In Sections 2 and 3 we recall basic ideas with a brief review of calculation steps. In Section 4 we present the numerical results of our calculations and a discussion. Finally, Section 5 contains our conclusions.

2 Intrinsic charm density in a proton as a function of IC probability w

According to[6, 10, 21], the intrinsic charm distribution at the starting scale μ_0^2 as a function of x can be presented in the following approximated form:

$$c_{int}(x, \mu_0^2) = c_0 w x^2 \left[(1-x)(1+10x+x^2) + 6x(1+x)\ln(x)\right], \quad (1)$$

where w is the probability to find the Fock state $|uudc\bar{c}\rangle$ in the proton, c_0 is the normalization constant and the masses of the light quarks and the nucleon are neglectedable compared to the charm quark mass. The inclusion of the non-zero nucleon mass leads to a more complicated

[1] Unfortunately, the MCFM routine does not produce the prompt photon and heavy jet production cross sections.

analytic form[23]. According to the BHPS model[1, 2], the charm density in a proton is the sum of the *extrinsic* and *intrinsic* charm densities,

$$xc(x,\mu_0^2) = xc_{ext}(x,\mu_0^2) + xc_{int}(x,\mu_0^2). \quad (2)$$

The *extrinsic*, or ordinary quarks and gluons are generated on a short-time scale associated with the large-transverse-momentum processes. Their distribution functions satisfy the standard QCD evolution equations. Contrariwise, the *intrinsic* quarks and gluons can be associated with a bound-state hadron dynamics and one believes that they have a non-perturbative origin. It was argued [2] that existence, for example, of *intrinsic* heavy quark pairs $c\bar{c}$ and $b\bar{b}$ within the proton state can be due to the gluon-exchange and vacuum-polarization graphs.

The charm density $xc(x,\mu^2)$ at an arbitrary scale μ^2 is calculated using the Dokshitzer-Gribov-Lipatov-Altarelli-Parisi (DGLAP) equations[22]. Let us stress that both the intrinsic part xc_{int} and extrinsic one xc_{ext} depend on μ^2. In the general case, there is some mixing between two parts of Eq.(2) during the DGLAP evolution. However, such mixing is negligible [10, 33], especially at large μ^2 and x. It can be seen from comparison of our calculations of charmed quark denspiies presented in Fig. (1), where this mixing was included within the CTEQ [24] set, and Fig.(2) of [10], when the mixing between two parts of the charm density was neglected. Our results on the total charm density $xc(x,\mu^2)$ are in good agreement with the calculations of [10] at the whole kinematical region of x because at $x < 0.1$ the IC contribution xc_{int} is much smaller than the *extrinsic* one xc_{ext}. Therefore, one can apply the DGLAP evolution separately to the first part $xc_{ext}(x,\mu_0^2)$ and the second part $xc_{int}(x,\mu_0^2)$ of (2), as it was done in [10]. Such calculations were done by the CTEQ[24] and CT14[25] groups at some fixed values of the IC probability w. Namely, the CTEQ group used $w = 1\%$ and $w = 3.5\%$, and CT14 used $w = 1\%$ and $w = 2\%$. Note that, according to the recent paper [23], the lifetime

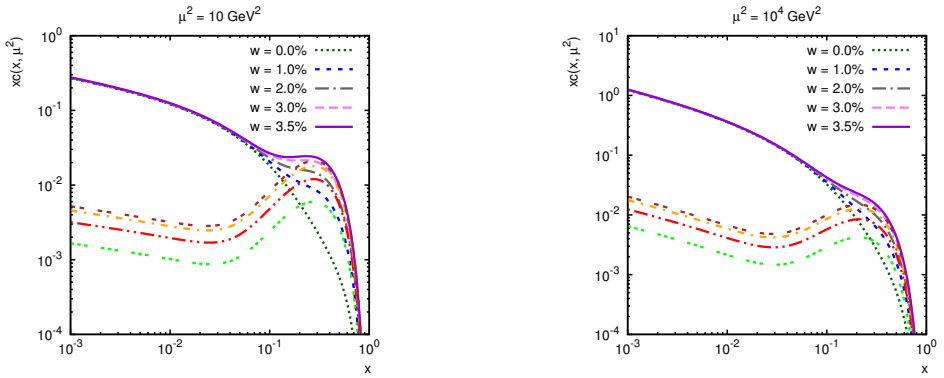


Figure 1: The charmed quark densities as a function of x and w at $\mu^2 = 10$ GeV^2 (top) and $\mu^2 = 10^4$ GeV^2 (bottom). The triple dashed line is the IC contriubion at $w = 1\%$, dash-double-dotted line corresponds to $w = 2\%$, dosh-dotted curve corresponds to $w = 3\%$ and double dashed corresponds to $w = 3.5$ %.

of the *intrinsic* charm should be more than the interaction time, at least, by a factor 5, when the quark Fock-state can be observed with the satisfactory accuracy. The ratio of these times is proprtional to Q^2 or p_T^2 [23]. We will analyze the hard processes of $\gamma(Z)$ production associated with heavy jets at LHC energies and kinematics, when the life time of the *intrinsic* charm is

much larger than the interaction time, at $p_T^2 \geq 10^4$ GeV^2, where the *intrinsic* charm could be resolved.

Taking into account that the IC probability w enters into (2) as a constant in front of the function dependent on x and μ^2, one can suggest a simple relation at any $w \leq w_{\max}$:

$$xc_{int}(x,\mu^2) = \frac{w}{w_{\max}} xc_{int}(x,\mu^2)|_{w=w_{\max}}. \tag{3}$$

Actually, that is the linear interpolation between two charm densities at the scale μ^2, obtained at $w = w_{\max}$ and $w = 0$. Later we adopt the charm distribution function from the CTEQ66M set[24]. We assume $w_{\max} = 3.5\%$ everywhere, which corresponds to the CTEQ66c1 set[24]. Additionally, we performed the three-point interpolation of the charmed quark distributions (over $w = 0$, $w = 1\%$ and $w = 3.5\%$, which correspond to the CTEQ66M, CTEQ66c0 and CTEQ66c1 sets, respectively). These results differ from the ones based on (3) by no more than 0.5%, thus giving us the confidence in our starting point.

Below we apply the charmed quark density obtained by (2) and (3) to calculate the total and differential cross sections of associated prompt photon or Z boson and heavy flavor jet production, $\gamma(Z)+Q$, at the LHC conditions. The suggested procedure to calculate $xc_{int}(x,\mu^2)$ at any $w \leq w_{\max}$ allows us to reduce significantly the time for the calculation of these observables.

3 Theoretical approaches to the associated $\gamma(Z) + Q$ production

As was mentioned above, we perform the numerical calculations of the associated $\gamma(Z)+Q$ production cross sections using the parton-level Monte Carlo event generator MCFM within the NLO pQCD as well as the k_T-factorization QCD approach. The MCFM is able to calculate the processes, that involve the gauge bosons Z or W (see[18] for more information). In contrast to our early study of these processes[11] within the MCFM, we use this generator to calculate the differential and total cross sections of the $Z + c$ and $Z + b$ production in the pp collision and their ratio as a function w.

The k_T-factorization approach[19, 20] is based on the small-x Balitsky-Fadin-Kuraev-Lipatov (BFKL)[26] gluon dynamics and provides solid theoretical grounds for the effects of the initial gluon radiation and the intrinsic parton transverse momentum[2]. Our main motivation to use here the k_T-factorization formalism is that its predictions for the associated $\gamma + Q$ production better agree with the Tevatron data compared to the NLO pQCD (see[14, 15]). The consideration is mainly based on the $\mathcal{O}(\alpha\alpha_s)$ off-shell (depending on the transverse momenta of initial quarks and gluons) quark-gluon Compton-like scattering subprocess, see Fig. 2(a). Within this approach the transverse momentum dependent (TMD) parton densities include many high order corrections, while the partonic amplitudes are calculated within the leading order (LO) of QCD. The off-shell quark-gluon Compton scattering amplitude is calculated within the reggeized parton approach[27, 28, 29] based on the effective action formalism[31], which ensures the gauge invariance of the obtained amplitudes despite the off-shell initial quarks and gluons[3]. The TMD parton densities are calculated using the Kimber-Martin-Ryskin (KMR) approach, currently developed within the NLO[30]. This approach is the formalism to construct the TMD quark and

[2] A detailed description of the k_T-factorization approach can be found, for example, in reviews[30].

[3] Here we use the expressions derived earlier[32].

gluon densities from the known conventional parton distributions. The key assumption is that the k_T dependence appears at the last evolution step, so that the DGLAP evolution can be used up to this step. Numerically, for the input we used parton densities derived in Section 2. Other details of these calculations are explained in[32]. To improve the k_T-factorization predictions at

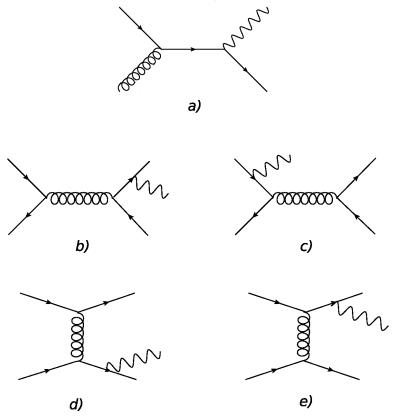


Figure 2: The $\mathcal{O}(\alpha\alpha_s)$ (a) and $\mathcal{O}(\alpha\alpha_s^2)$ (b) — (e) contributions to the $\gamma(Z) + Q$ production taken into account in the k_T-factorization calculations.

high transverse momenta, we take into account some $\mathcal{O}(\alpha\alpha_s^2)$ contributions, namely $q\bar{q} \to VQ\bar{Q}$ and $qQ \to VqQ$ ones, where V denotes the photon or the Z boson, see Fig. 2(b) — (e). These contributions are significant at large x and therefore can be calculated in the usual collinear QCD factorization scheme. Thus, we rely on the combination of two techniques that is most suitable.

4 Results and discussion

In our calculations we follow the conclusion obtained in our papers[9, 11] that the IC signal in the hard processes discussed here can be detected at ATLAS or CMS of the LHC in the forward rapidity region $1.5 < |\eta| < 2.4$ and $p_T > 50$ GeV. Additionally, we require $|\eta(Q)| < 2.4$ and $p_T(Q) > 25$ GeV, where $\eta(Q)$ and $p_T(Q)$ are the pseudo-rapidity and transverse momentum of the heavy quark jet in a final state, as was done in[9, 11].

The p_T-spectrum ratios $\sigma(\gamma + c)/\sigma(\gamma + b)$ and $\sigma(Z + c)/\sigma(Z + b)$ versus p_T at different w are presented in [33, 13]. It was shown that in the absence of the IC contribution the ratio $\sigma(\gamma + c)/\sigma(\gamma + b)$ is about 3 at $p_T \sim 100$ GeV and decreases down to 2 at $p_T \sim 500$ GeV. This behavior is the same for both energies $\sqrt{s} = 8$ TeV and $\sqrt{s} = 13$ TeV. If one takes into account the IC contributions, this ratio becomes approximately flat at $w = 2\%$ or even increasing up to about 4 at $w = 3.5\%$. It is very close to the Tevatron data[16]: the constant ratio $\sigma(\gamma + c)/\sigma(\gamma + b) \sim 3.5 - 4.5$ measured in the $p\bar{p}$ collisions at $110 < p_T < 300$ GeV and $\sqrt{s} = 1.96$ TeV. However, this agreement cannot be treated as the IC indication due to huge experimental uncertainties (about 50%) and rather different kinematical conditions. If the IC contribution is included, the ratio $\sigma(Z + c)/\sigma(Z + b)$ also increases by a factor about 2

at $w = 3.5\%$, when the Z boson transverse momentum grows from 100 GeV to 500 GeV (see Fig. 4). In the absence of the IC terms this ratio slowly decreases.

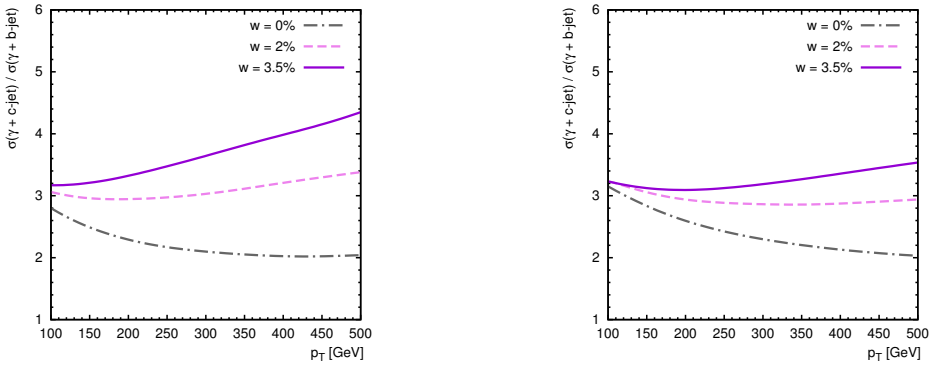


Figure 3: The cross section ratio of the $\gamma + c$ production to the $\gamma + b$ one in the pp collision calculated as a function of the photon transverse momentum p_T at $\sqrt{s} = 8$ TeV (left) and $\sqrt{s} = 13$ TeV (right) within the k_T-factorization approach. The kinematical conditions are described in the text

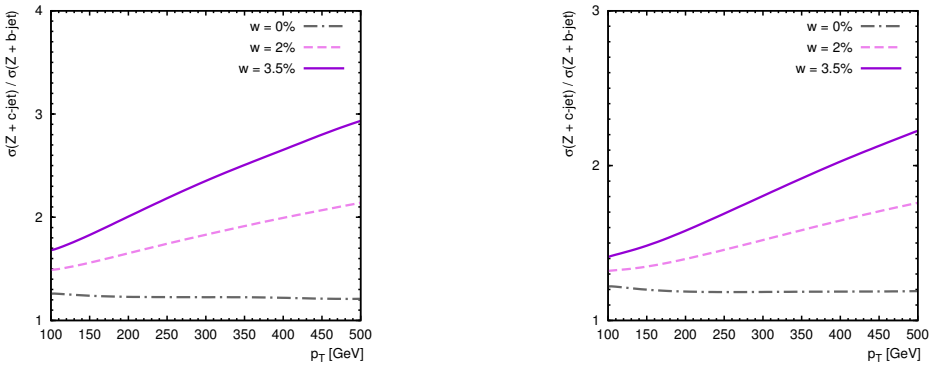


Figure 4: The cross section ratio of the $Z + c$ production to the $Z + b$ one in the pp collision calculated as a function of the Z boson transverse momentum p_T at $\sqrt{s} = 8$ TeV (top) and $\sqrt{s} = 13$ TeV (bottom) within the k_T-factorization approach. The kinematical conditions are described in the text.

In [33, 13] other observables were presented, where was shown that i t could be useful to detect the IC signal were analyzed, namely, the cross sections and their ratios integrated over $p_T > p_T^{\min}$, where $p_T^{\min} = 100$, 200 and 300 GeV for $\sqrt{s} = 8$ TeV and $p_T^{\min} = 200$, 300 and 400 GeV for $\sqrt{s} = 13$ TeV. All the p_T-spectra have a significant scale uncertainty as is shown in[11]. According to[11], the ratio between the cross sections for the $Z + Q$ and $W + Q$ production in the pp collision is less sensitive to the scale variation calculated within the MCFM. Nevertheless, the uncertainty in this ratio at large $p_T > 250$ GeV is about 40 — 50%. In the present paper we check these results for the ratios $\sigma(\gamma + c)/\sigma(\gamma + b)$ and $\sigma(Z + c)/\sigma(Z + b)$.

In Figs. 5 and 6 we present these ratios versus the IC probability w calculated at different scales, when the cross sections of $\gamma(Z) + Q$ production are integrated within the different intervals of transverse momentum. One can see a very small QCD scale uncertainty, especially at $\sqrt{s} = 13$ TeV (bottom right), which is less than 1%. In contrast, the scale uncertainty for the integrated $\gamma(Z) + Q$ cross sections (see Figs. 5 and 6, top) is significant and amounts to about 30 — 40%.

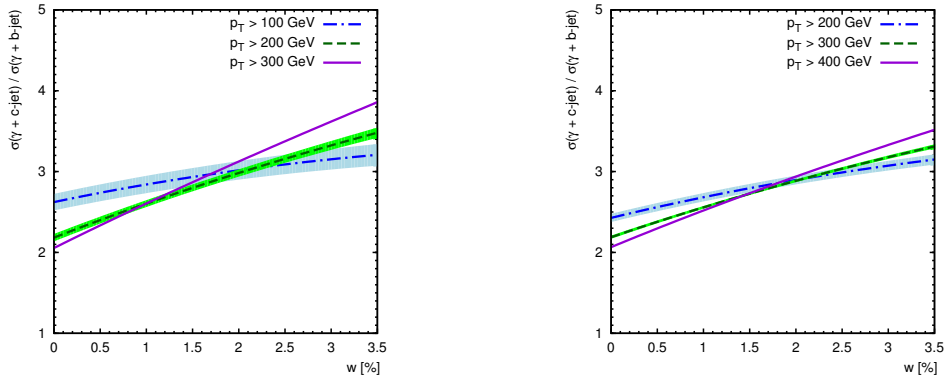


Figure 5: The cross section ratio of the associated $\gamma + c$ and $\gamma + b$ production in the pp collision as a function of w integrated over the photon transverse momenta $p_T > p_T^{\min}$ for different $p_T^{\min}$ at $\sqrt{s} = 8$ TeV (top) and $\sqrt{s} = 13$ TeV (bottom). The calculations were done using the k_T-factorization approach. The bands correspond to the usual scale variation as it is described in the text.

The sizable difference between the scale uncertainties for the ratios $\sigma(Z+Q)/\sigma(W+Q)$ and $\sigma(Z+c)/\sigma(Z+b)$ is due to the different matrix elements for the $Z+Q$ and $W+Q$ production in pp collisions, while the matrix elements for the $Z+c$ and $Z+b$ production are the same. It is important that the calculated ratios $\sigma(\gamma+c)/\sigma(\gamma+b)$ and $\sigma(Z+c)/\sigma(Z+b)$ can be used to determine the IC probability w from the future LHC data. Moreover, these ratios are practically independent of the uncertainties of our calculations: actually, the curves corresponding to the usual scale variations as described above coincide with each other (see Figs. 5 and 6, bottom). Therefore, we can recommend these observables as a test for the hypothesis of the IC component inside the proton.

5 Conclusion

The transverse momentum spectra of the prompt photons and Z bosons produced in association with the c or b jets in pp collisions are calculated using the MCFM (NLO pQCD) and the k_T-factorization approach at the LHC energies and pseudo-rapidites $1.5 < \eta < 2.4$ using PDFs with and without the IC contribution. It is shown that these two approaches give similar results. We found that the contribution of the intrinsic charm can give a significant signal in the ratios $\sigma(\gamma + c)/\sigma(\gamma + b)$ and $\sigma(Z + c)/\sigma(Z + b)$ at forward pseudo-rapidities $(1.5 < \eta < 2.4)$ corresponding to the ATLAS and CMS facilities. If the IC contributions are taken into account, the ratio $\sigma(\gamma+c)/\sigma(\gamma+b)$ as a function of the photon transverse momentum is approximately flat or increases at $p_T > 100$ GeV. The similar flat behavior of this ratio was

observed in the $p\bar{p}$ annihilation at the Tevatron. In the absence of the IC contributions this ratio decreases. Similarly, the ratio $\sigma(Z+c)/\sigma(Z+b)$ increases when the Z boson transverse momentum grows if the IC contribution is included and slowly decreases in the absence of the IC terms. We argued that the ratio of the cross sections $\gamma(Z)+c$ and $\gamma(Z)+b$ integrated over $p_T > p_T^{\min}$ with $p_T^{\min} \geq 100$ GeV can be used to determine the IC probability from the future LHC data. The advantage of the proposed ratios is that the theoretical uncertainties are very small, while the uncertainties for the p_T-spectra of photons or Z bosons produced in association with the c or b jets are large. Therefore, the search for the IC signal by analyzing the ratio $\sigma(\gamma/Z+c)/\sigma(\gamma/Z+b)$ can be more promising.

6 Acknowledgments

We thank S.J. Brodsky, A.A. Glasov and D. Stump for extremely helpful discussions and recommendations in the study of this topic. The authors are grateful to H. Jung, P.M. Nadolsky for very useful discussions and comments. The authors are also grateful to L. Rotali for very constructive discussions. This work was supported in part by grant of the President of Russian Federation NS-7989.2016.2. A.V.L. is grateful to the DESY Directorate for the support within the framework of the Moscow — DESY project on Monte-Carlo implementation for HERA — LHC.

References

[1] S. Brodsky, P. Hoyer, C. Peterson, N. Sakai, Phys. Lett. B **93**, 451 (1980).

[2] S. Brodsky, C. Peterson, N. Sakai, Phys. Rev. D **23**, 2745 (1981).

[3] B.W. Harris, J. Smith, R. Vogt, Nucl. Phys. B **461**, 181 (1996).

[4] M. Franz, M.V. Polyakov, K. Goeke, Phys. Rev. D **62**, 074024 (2000).

[5] S. Brodsky, F. Fleuret, C. Hadjidakis, J. Landsberg, Phys. Rep. **522**, 239 (2013).

[6] S. Brodsky, A. Kusina, F. Lyonnet, I. Schienbein, H. Spiesberger, Adv. High Energy Phys. **2015**, 231547 (2015).

[7] S. Brodsky, S. Gardner, Phys. Rev. Lett. **116**, 019101 (2016).

[8] G.I. Lykasov, V.A. Bednyakov, A.F. Pikelner, N.I. Zimin, Eur. Phys. Lett. **99**, 21002 (2012).

[9] V.A. Bednyakov, M.A. Demichev, G.I. Lykasov, T. Stavreva, M. Stockton, Phys. Lett. B **728**, 602 (2014).

[10] S. Rostami, A. Khorramian, A. Aleedanceshvar, M. Goharipour, arXiv:1510.0842 [hep-ph]; J.Phys., G43, 055001 (2016).

[11] P.-H. Beauchemin, V.A. Bednyakov, G.I. Lykasov, Yu.Yu. Stepanenko, Phys. Rev. D **92**, 034014 (2015).

[12] NNPDF Collaboration, arXiv:1605.06515 [hep-ph]

[13] S.J.Brodsky, V.A.Bednyakov, G.I.Lykasov, J.Smiesko, S.Tokar, Prog.Part.Nucl.Phys., **93**, 108 (2017); arXiv:1612.01351[hep-ph].

[14] D0 Collaboration, Phys. Lett. B **714**, 32 (2014).

[15] CDF Collaboration, Phys. Rev. Lett. **111**, 042003 (2013).

[16] D0 Collaboration, Phys. Lett. B **719**, 354 (2013).

[17] T. Stavreva, J.F. Owens, Phys. Rev. D **79**, 054017 (2009).

[18] J.M. Campbell, R.K. Ellis, Phys. Rev. **D** 65, 113007 (2002); http://mcfm.fnal.gov

[19] L.V. Gribov, E.M. Levin, M.G. Ryskin, Phys. Rep. **100**, 1 (1983);

[20] S. Catani, M. Ciafoloni, F. Hautmann, Nucl. Phys. B **366**, 135 (1991);
J.C. Collins, R.K. Ellis, Nucl. Phys. B **360**, 3 (1991).

[21] J. Pumplin, Phys. Rev. D **73**, 114015 (2006).

[22] V.N. Gribov, L.N. Lipatov, Sov.J. Nucl. Phys. **15**, 438 (1972);
L.N. Lipatov, Sov. J. Nucl. Phys. **20**, 94 (1975);
G. Altarelli, G. Parisi, Nucl. Phys. B **126**, 298 (1977);
Yu.L. Dokshitzer, Sov. Phys. JETP **46**, 641 (1977).

[23] J. Bluemlein, Phys.Lett. B **753**, 619 (2016), arXiv:1511.00229 [hep-ph].

[24] P.M. Nadolsky, H.-L. Lai, Q.-H. Cao, J. Huston, J. Pumplin, D. Stump, W.-K. Tung, C.-P. Yuan, Phys. Rev. D **78**, 013004 (2008).

[25] S. Dulat, T.-J. Hou, J. Gao, M. Guzzi, J. Huston, P.M. Nadolsky, J. Pumplin, C. Schmidt, D. Stump, C.-P. Yuan, Phys. Rev. D **93**, 033006 (2016).

[26] E.A. Kuraev, L.N. Lipatov, V.S. Fadin, Sov. Phys. JETP **44**, 443 (1976);
E.A. Kuraev, L.N. Lipatov, V.S. Fadin, Sov. Phys. JETP **45**, 199 (1977);
I.I. Balitsky, L.N. Lipatov, Sov. J. Nucl. Phys. **28**, 822 (1978).

[27] L.N. Lipatov, M.I. Vyazovsky, Nucl. Phys. B **597**, 399 (2001).

[28] A.V. Bogdan, V.S. Fadin, Nucl. Phys. B **740**, 36 (2006).

[29] M. Hentschinski, A. Sabio Vera, Phys. Rev. D **85**, 056006 (2012);
M. Hentschinski, Nucl. Phys. B **859**, 129 (2012);
G. Chachamis, M. Hentschinski, J.D. Madrigal Martinez, A. Sabio Vera, Nucl. Phys. B **861**, 133 (2012).

[30] B. Andersson *et al.* (Small-x Collaboration), J. Andersen *et al.* (Small-x Collaboration), Eur. Phys. J. C **48**, 53 (2006).

[31] L.N. Lipatov, Nucl. Phys. B **452**, 369 (1995); Phys. Rept. **286**, 131 (1997).

[32] A.V. Lipatov, M.A. Malyshev, arXiv:1606.02696 [hep-ph].

[33] A.V.Lipatov, G.I.Lykasov,Yu.Yu.Stepanenko, V.A.Bednyakov, Phys.Rev. **D94**, 053011 (2016) , arXiv:1606.04882 [hep-ph].

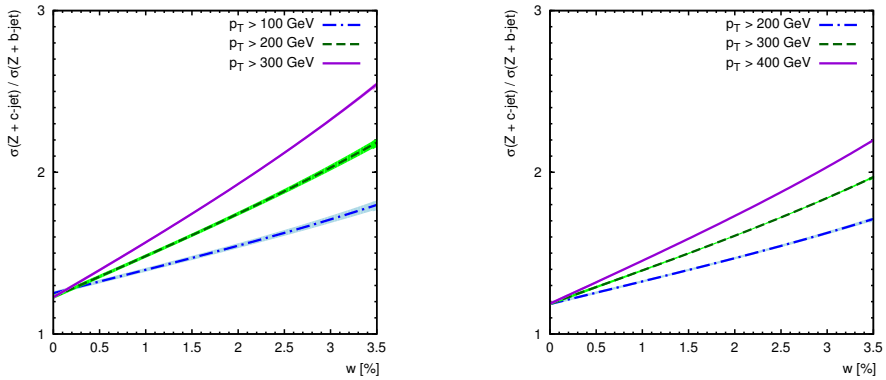


Figure 6: The cross section ratio of the associated $Z+c$ and $Z+b$ production in the pp collision as a function of w integrated over the Z boson transverse momenta $p_T > p_T^{\rm min}$ for different $p_T^{\rm min}$ at $\sqrt{s} = 8$ TeV (top) and $\sqrt{s} = 13$ TeV (bottom). The calculations were done using the k_T-factorization approach. The bands correspond to the usual scale variation as it is described in the text.

The interference effects of multi-channel pion-pion scattering in final states of charmonia and bottomonia decays

Yu.S. Surovtsev[1], *P. Bydžovský*[2], *T. Gutsche*[3], *R. Kamiński*[4], *V.E. Lyubovitskij*[3,5,6], *M. Nagy*[7]

[1]Bogoliubov Laboratory of Theoretical Physics, Joint Institute for Nuclear Research, Dubna 141980, Russia
[2]Nuclear Physics Institute, Czech Academy of Sciences, Řež near Prague 25068, Czech Republic
[3]Institut für Theoretische Physik, Universität Tübingen, Kepler Center for Astro and Particle Physics, Auf der Morgenstelle 14, D–72076 Tübingen, Germany
[4]Institute of Nuclear Physics, Polish Academy of Sciences, Cracow 31342, Poland
[5]Department of Physics, Tomsk State University, 634050 Tomsk, Russia
[6]Mathematical Physics Department, Tomsk Polytechnic University, Lenin Avenue 30, 634050 Tomsk, Russia
[7]Institute of Physics, Slovak Academy of Sciences, Bratislava 84511, Slovak Republic

DOI: http://dx.doi.org/10.3204/DESY-PROC-2016-04/Surovtsev

There is presented a unified analysis of all available data on the decays $\Upsilon(mS) \to \Upsilon(nS)\pi\pi$ ($m > n$, $m = 2,3,4,5$, $n = 1,2,3$), $J/\psi \to \phi(\pi\pi, K\overline{K})$, and $\psi(2S) \to J/\psi\pi\pi$ and the data on isoscalar S-wave processes $\pi\pi \to \pi\pi, K\overline{K}, \eta\eta$. The multi-channel $\pi\pi$ scattering is described in our model-independent approach based on analyticity and unitarity and using an uniformization procedure. It is shown that the basic shape of dipion mass distributions in the two-pion transitions of both charmonia and bottomonia states are explained by an unified mechanism based on the contribution of the $\pi\pi$, $K\overline{K}$ and $\eta\eta$ coupled channels including their interference.

1 Introduction

The extensive study of the properties of scalar mesons is important for the most profound topics concerning the QCD vacuum, because both sectors affect each other due to possible "direct" transitions between them. Obviously, those transitions influence the f_0-meson parameters, enlarging, in first turn, a total width of the $f_0(500)$ in comparison with its decay widths, i.e. the former contains some information on the QCD vacuum. The problem of a unique structure interpretation of the scalar mesons is far away from being solved completely [1].

In the 3-channel analysis of data on the isoscalar S-wave multi-channel $\pi\pi$ scattering ($\pi\pi \to \pi\pi, K\overline{K}, \eta\eta$), which was performed in our model-independent approach based on analyticity, unitarity and on the use of the uniformization procedure [2], we obtained two solutions for resonance parameters, which distinguish themselves mainly in the $f_0(500)$ width. Expansion of the analysis via the inclusion of the decays $J/\psi \to \phi(\pi\pi, K\overline{K})$ with data from the Mark III and DM2 Collaborations has changed a little the parameters of some resonances but two solutions

remained [3]. The further expansion of the above combined analysis with adding the data on $J/\psi \to \phi\pi\pi$ from the BES II Collaboration, which are given in the wider region of the $\pi\pi$ mass spectrum, helped to narrow down the $f_0(500)$ solution to the one with the larger width; other resonance parameters were practically not changed [4]. In Ref.[4] the data on $J/\psi \to \phi\pi\pi$ from the BES II are described to about 1.2 GeV. For expanding the description to higher energies, the amplitude for $\pi\pi \to \eta\eta$ should be taken into account. From experiment only the modulus of this amplitude is known. It is needed to know the phase shift of $\eta\eta$ scattering amplitude. We hope to obtain this description under reasonable assumptions. This is worth to pursue because this will give additional information on the $f_0(1370)$ (there are doubts whether it exists or not) and on the interesting 1500-MeV region.

Generally, a possibility of combined analysis of the isoscalar S-wave multi-channel $\pi\pi$ scattering and the decays $J/\psi \to \phi(\pi\pi, K\overline{K})$ and also the two-pion transitions among bottomonia is related to the expected fact that the is related to the expected fact that pairs of pseudo-scalar mesons are produced in S wave and only they undergo final state interactions, whereas the final quarkonium remains a spectator [4, 5, 6].

The above expansion of the combined analysis, in first turn, aimed at the further study of properties of scalar mesons. On the other hand, it was interesting to explain the unexpected (and even enigmatic) behavior of the dipion spectra in the decays $\Upsilon(mS) \to \Upsilon(nS)\pi\pi$ ($m > n, m = 3, 4, 5, n = 1, 2, 3$) — a bell-shaped form in the near-$\pi\pi$-threshold region [especially for the $\Upsilon(3S) \to \Upsilon(1S)\pi^+\pi^-$ and $\Upsilon(4S) \to \Upsilon(2S)\pi^+\pi^-$], smooth dips near a dipion mass of 0.7 GeV in $\Upsilon(3S) \to \Upsilon(1S)(\pi^+\pi^-, \pi^0\pi^0)$, of 0.6 GeV in $\Upsilon(4S, 5S) \to \Upsilon(1S)\pi^+\pi^-$ and of about 0.44 GeV in $\Upsilon(4S) \to \Upsilon(2S)\pi^+\pi^-$, and also sharp dips of about 1 GeV in the $\Upsilon(4S, 5S) \to \Upsilon(1S)\pi^+\pi^-$ transitions.

We considered practically all available data on the two-pion transitions of Υ mesons from the ARGUS, CLEO, CUSB, Crystal Ball, Belle, and *BaBar* Collaborations – $\Upsilon(mS) \to \Upsilon(nS)\pi\pi$ ($m > n$, $m = 2, 3, 4, 5$, $n = 1, 2, 3$) – and also the data on decays $J/\psi \to \phi(\pi\pi, K\overline{K})$ and $\psi(2S) \to J/\psi\pi\pi$ from the Mark III, DM2 and BES II Collaborations to analyze contributions of multi-channel $\pi\pi$ scattering in the final-state interactions. We have shown that all peculiarities of the $\pi\pi$ mass spectra are explained by the unified way via the interference of contributions of the $\pi\pi$-scattering amplitude and the analytically-continued $\pi\pi \to K\overline{K}$ and $\pi\pi \to \eta\eta$ amplitudes.

These results are based on our previous conclusions on wide resonances [4, 7, 8]: If a wide resonance cannot decay into a channel which opens above its mass, but the resonance is strongly coupled to this channel, then one should consider this resonance as a multi-channel state.

2 The amplitudes for multi-channel $\pi\pi$ scattering

When analysing the 3-channel $\pi\pi$ scattering, we considered the reactions $\pi\pi \to \pi\pi, K\overline{K}, \eta\eta$, because it was shown [7] that namely these coupled channels needed for obtaining correct values of f_0-resonance parameters.

The 3-channel S-matrix is determined on the 8-sheeted Riemann surface. The matrix elements S_{ij}, where $i, j = 1, 2, 3$ denote channels, have the right-hand cuts along the real axis of the s complex plane (s is the invariant total energy squared), starting with the channel thresholds s_i ($i = 1, 2, 3$), and the left-hand cuts related to the crossed channels.

Resonances are described on the Riemann surface using the formulas of analytic continuations of the S-matrix elements to all sheets. The formulas allow to express the matrix elements

on the unphysical sheets by means of the matrix elements on the physical sheet that have only the resonance zeros (aside the real axis), at least, around the physical region [2]. Using these formulas and assuming the resonance zeros on sheet I, we can obtain an arrangement of poles and zeros of the resonance on the whole Riemann surface (pole cluster of resonance).

Let us explain in the 2-channel example how pole cluster describing resonance arises. In the 1-channel consideration of the scattering $1 \to 1$ the main model-independent contribution of resonance is given by a pair of conjugate poles on sheet II and by a pair of conjugate zeros on sheet I at the same points of complex energy in S_{11}. (Conjugate poles and zeros are needed for real analyticity.) In the 2-channel consideration of the processes $1 \to 1$, $1 \to 2$ and $2 \to 2$, we have

$$
\begin{aligned}
&S_{11}^{\mathrm{II}} = \frac{1}{S_{11}^{\mathrm{I}}}, && S_{11}^{\mathrm{III}} = \frac{S_{22}^{\mathrm{I}}}{S_{11}^{\mathrm{I}} S_{22}^{I} - (S_{12}^{\mathrm{I}})^2}, && S_{11}^{\mathrm{IV}} = \frac{S_{11}^{\mathrm{I}} S_{22}^{\mathrm{I}} - (S_{12}^{\mathrm{I}})^2}{S_{22}^{I}},\\
&S_{22}^{\mathrm{II}} = \frac{S_{11}^{\mathrm{I}} S_{22}^{\mathrm{I}} - (S_{12}^{\mathrm{I}})^2}{S_{11}^{\mathrm{I}}}, && S_{22}^{\mathrm{III}} = \frac{S_{11}^{\mathrm{I}}}{S_{11}^{\mathrm{I}} S_{22}^{\mathrm{I}} - (S_{12}^{\mathrm{I}})^2}, && S_{22}^{\mathrm{IV}} = \frac{1}{S_{22}^{\mathrm{I}}},\\
&S_{12}^{\mathrm{II}} = \frac{i S_{12}^{\mathrm{I}}}{S_{11}^{\mathrm{I}}}, && S_{12}^{\mathrm{III}} = \frac{-S_{12}^{\mathrm{I}}}{S_{11}^{\mathrm{I}} S_{22}^{\mathrm{I}} - (S_{12}^{\mathrm{I}})^2}, && S_{12}^{\mathrm{IV}} = \frac{i S_{12}^{\mathrm{I}}}{S_{22}^{\mathrm{I}}}.
\end{aligned}
$$

In S_{11} a resonance is represented by a pair of conjugate poles on sheet II and by a pair of conjugate zeros on sheet I and also by a pair of conjugate poles on sheet III and by a pair of conjugate zeros on sheet IV at the same points of complex energy if a coupling of channels is absent ($S_{12} = 0$). If the resonance decays into both channels and/or takes part in exchanges in crossing channels, the coupling of channels arises ($S_{12} \neq 0$). Then positions of the poles on sheet III (and of corresponding zeros on sheet IV) turn out to be shifted with respect to positions of zeros on sheet I. Thus we obtain the pole cluster in the 2-channel case.

In the 3-channel case, there are *7 types* of resonances corresponding to 7 possible situations when there are resonance zeros on sheet I only in S_{11} – (**a**); S_{22} – (**b**); S_{33} – (**c**); S_{11} and S_{22} – (**d**); S_{22} and S_{33} – (**e**); S_{11} and S_{33} – (**f**); S_{11}, S_{22} and S_{33} – (**g**).
The resonance of every type which is related to its nature is represented by the pair of complex-conjugate pole clusters.

In order to allow for the Riemann surface structure and the representation of resonances by the pole clusters, we make a conformal map of the 8-sheeted Riemann surface, on which the three-channel S matrix is determined, onto the plane of uniformization of the $\pi\pi$-scattering S-matrix element S_{11}. This is made using the uniformizing variable [8]: $w = (\sqrt{(s-s_2)s_3} + \sqrt{(s-s_3)s_2})/\sqrt{s(s_3-s_2)}$ ($s_2 = 4m_K^2$ and $s_3 = 4m_\eta^2$), in which we have neglected the $\pi\pi$-threshold branch point and allowed for the $K\overline{K}$- and $\eta\eta$-threshold branch points and left-hand branch point at $s = 0$ related to the crossed channels.

The S-matrix elements are taken as the products $S = S_B S_{res}$ where S_{res} represents the main (*model-independent*) contribution of resonances, given by the pole clusters; S_B is the background part which contains possible remaining small (*model-dependent*) contributions of resonances and allows for influence of channels not taken explicitly into account in the uniformizing variable.

To obtain the pole clusters describing resonances, it is convenient to use the Le Couteur –

Newton relations [9] which have the following form on the w-plane:

$$S_{11}=\frac{d^*(-w^*)}{d(w)},\qquad S_{22}=\frac{d(-w^{-1})}{d(w)},\qquad S_{33}=\frac{d(w^{-1})}{d(w)},\tag{1}$$
$$S_{11}S_{22}-S_{12}^2=\frac{d^*(w^{*-1})}{d(w)},\quad S_{11}S_{33}-S_{13}^2=\frac{d^*(-w^{*-1})}{d(w)},\quad S_{22}S_{33}-S_{23}^2=\frac{d(-w)}{d(w)}.$$

The $d(w)$ function for the resonance part in these relations is $d_{res}(w)=w^{-\frac{M}{2}}\prod_{r=1}^{M}(w+w_r^*)$ with M a number of resonance zeros. For the background part S_B, the d-function has the form

$$d_B=\exp[-i\sum_{n=1}^{3}\frac{\sqrt{s-s_n}}{2m_n}(\alpha_n+i\beta_n\theta(s-s_n))]\tag{2}$$
$$\alpha_n=a_{n1}+a_{n\sigma}\frac{s-s_\sigma}{s_\sigma}\theta(s-s_\sigma)+a_{nv}\frac{s-s_v}{s_v}\theta(s-s_v),$$
$$\beta_n=b_{n1}+b_{n\sigma}\frac{s-s_\sigma}{s_\sigma}\theta(s-s_\sigma)+b_{nv}\frac{s-s_v}{s_v}\theta(s-s_v)$$

with s_σ the $\sigma\sigma$ threshold and s_v the effective threshold of three cannels $\eta\eta'$, $\rho\rho$, $\omega\omega$. These thresholds are determined in the analysis.

When performing our combined analysis, data for the multi-channel $\pi\pi$ scattering were taken from many papers (see Refs. in our paper [4]). Satisfactory description of the multi-channel $\pi\pi$ scattering is obtained with the total $\chi^2/\text{ndf}\approx 1.16$. The preferred scenario found is when the $f_0(500)$ is described by the cluster of type (**a**); the $f_0(1370)$, $f_0(1500)$ and $f_0(1710)$ with type (**c**); and $f_0'(1500)$ by type (**g**); the $f_0(980)$ is represented only by the pole on sheet II and a shifted pole on sheet III. The obtained pole-clusters for the resonances are shown in Table 1. Generally, the wide multi-channel states are most adequately represented by poles,

Table 1: The pole clusters for resonances on the $\sqrt{s}$-plane. $\sqrt{s_r}=\mathrm{E}_r-i\Gamma_r/2$.

Sheet		$f_0(500)$	$f_0(980)$	$f_0(1370)$	$f_0(1500)$	$f_0'(1500)$	$f_0(1710)$
II	E_r	521.6±12.4	1008.4±3.1			1512.4±4.9	
	$\Gamma_r/2$	467.3±5.9	33.5±1.5			287.2±12.9	
III	E_r	552.5±17.7	976.7±5.8	1387.2±24.4		1506.1±9.0	
	$\Gamma_r/2$	467.3±5.9	53.2±2.6	167.2±41.8		127.8±10.6	
IV	E_r			1387.2±24.4		1512.4±4.9	
	$\Gamma_r/2$			178.2±37.2		215.0±17.6	
V	E_r			1387.2±24.4	1493.9±3.1	1498.8±7.2	1732.8±43.2
	$\Gamma_r/2$			261.0±73.7	72.8±3.9	142.3±6.0	114.8±61.5
VI	E_r	573.4±29.1		1387.2±24.4	1493.9±5.6	1511.5±4.3	1732.8±43.2
	$\Gamma_r/2$	467.3±5.9		250.0±83.1	58.4±2.8	179.3±4.0	111.2±8.8
VII	E_r	542.5±25.5			1493.9±5.0	1500.4±9.3	1732.8±43.2
	$\Gamma_r/2$	467.3±5.9			47.8±9.3	99.9±18.0	55.2±38.0
VIII	E_r				1493.9±3.2	1512.4±4.9	1732.8±43.2
	$\Gamma_r/2$				62.2±9.2	298.4±14.5	58.8±16.4

because the poles give the main model-independent effect of resonances and are rather stable characteristics for various models, whereas masses and total widths are very model-dependent for wide resonances [10]. The masses, widths, and the coupling constants of resonances should

be calculated using the poles on sheets II, IV and VIII, because only on these sheets the analytic continuations have the forms [2]: $\propto 1/S_{11}^{\rm I}$, $\propto 1/S_{22}^{\rm I}$ and $\propto 1/S_{33}^{\rm I}$, respectively, i.e., the pole positions of resonances are at the same points of the complex-energy plane, as the resonance zeros on the physical sheet, and are not shifted due to the coupling of channels.

The obtained background parameters are: $a_{11} = 0.0$, $a_{1\sigma} = 0.0199$, $a_{1v} = 0.0$, $b_{11} = b_{1\sigma} = 0.0$, $b_{1v} = 0.0338$, $a_{21} = -2.4649$, $a_{2\sigma} = -2.3222$, $a_{2v} = -6.611$, $b_{21} = b_{2\sigma} = 0.0$, $b_{2v} = 7.073$; $b_{31} = 0.6421$, $b_{3\sigma} = 0.4851$; $b_{3v} = 0$; $s_\sigma = 1.6338$ GeV^2, $s_v = 2.0857$ GeV^2.

The small (zero for the elastic region) values of the $\pi\pi$ scattering background parameters (obtained after allowing for the left-hand branch-point at $s = 0$) confirms our assumption $S = S_B S_{res}$ and also that the representation of multi-channel resonances by the pole clusters on the uniformization plane is good and quite sufficient. This also shows that the consideration of the left-hand branch-point at $s = 0$ in the uniformizing variable partly solves a problem of some approaches (see, e.g., Ref. [11]) where the wide-resonance parameters are strongly controlled by the non-resonant background. Another important conclusion related to a practically zero background in $\pi\pi$ scattering and to the fact that the contribution to the $\pi\pi$ scattering amplitude from the crossed channels is given by allowing for the left-hand branch-point at $s = 0$ in the uniformizing variable and the meson-exchange contributions in the left-hand cuts: The zero background in the elastic-scattering region is obtained only when taking into account the left-hand branch-point in the uniformizing variables (both in the 2-channel analysis of processes $\pi\pi \to \pi\pi, K\overline{K}$ [10] and in the 3-channel analysis of processes $\pi\pi \to \pi\pi, K\overline{K}, \eta\eta$). This indicates that the ρ- and $f_0(500)$-meson exchange contributions in the left-hand cut practically cancel each other due to gauge invariance.

Let us explain how this is related to the gauge invariance. The propagator of vector particle is $D_{\mu\nu} = -(g_{\mu\nu} - k_\mu k_\nu/m_v^2)/(k^2 - m_v^2)$, of scalar particle $D = 1/(k^2 - m_s^2)$. In the particle exchange processes $k^2 < 0$. Therefore, the scalar-particle exchange leads to an attraction. In the case of the vector exchanged particle one can choose that gauge when in the numerator of propagator "works" only g_{00}. This leads to an repulsion of the scattering particles in the given gauge. Due to gauge invariance this effect extends to arbitrary gauges. To the point, the fact, that the mass terms in the corresponding Hamiltonians are $-\frac{1}{2}m_v^2V^2$ for the vector meson and $\frac{1}{2}m_s^2S^2$ for the scalar one, is a reflection of opposite nature of interactions due to the vector- and scalar-meson exchanges. One can show allowing for gauge invariance that the vector- and scalar-meson exchanges contribute with opposite signs. Therefore, the practically zero background in $\pi\pi$ scattering is an additional confirmation that the $f_0(500)$, observed in the analysis as the pole cluster of type **(a)**, is indeed a particle (though very wide), not some dynamically formed resonance. Therefore, one must consider at least in the background the coupled $\sigma\sigma$ channel which is not taken into account explicitly in the uniformizing variable w. In this connection it is reasonable to interpret the effective threshold at $s_\sigma = 1.6338$ GeV^2 in the background phase-shift of the $\pi\pi$ scattering amplitude as related to the $\sigma\sigma$ channel. Only in this channel we have obtained a non-zero background phase-shift in $\pi\pi$ scattering ($a_{1\sigma} = 0.0199$).

Further, since studying the decays of charmonia and bottomonia, we investigated the role of the individual f_0 resonances in contributing to the shape of the di-pion mass distributions in these decays, firstly we studied their role in forming the energy dependence of amplitudes of reactions $\pi\pi \to \pi\pi, K\overline{K}, \eta\eta$. In this case we switched off only those resonances [$f_0(500)$, $f_0(1370)$, $f_0(1500)$ and $f_0(1710)$], removal of which can be somehow compensated by correcting the background (maybe, with elements of the pseudo-background) to have the more-or-less acceptable description of the multi-channel $\pi\pi$ scattering. Below we therefore considered description of the multi-channel $\pi\pi$ scattering for two more cases: 1) first, when leaving out a minimal set of

the f_0 mesons consisting of the $f_0(500)$, $f_0(980)$, and $f_0'(1500)$, which is sufficient to achieve a description of the processes $\pi\pi \to \pi\pi, K\overline{K}, \eta\eta$ with a total $\chi^2/\mathrm{ndf} \approx 1.20$. 2) Second, from the above-indicated three mesons only the $f_0(500)$ can be omitted while still obtaining a reasonable description of multi-channel $\pi\pi$ scattering (though with appearance of a pseudo-background) with the total $\chi^2/\mathrm{ndf} \approx 1.43$. In Fig. 1 the obtained description of processes $\pi\pi \to \pi\pi, K\overline{K}, \eta\eta$ is shown. The solid lines correspond to contribution of all relevant f_0-resonances; the dotted, of the $f_0(500)$, $f_0(980)$, and $f_0'(1500)$; the dashed, of the $f_0(980)$ and $f_0'(1500)$. One can see

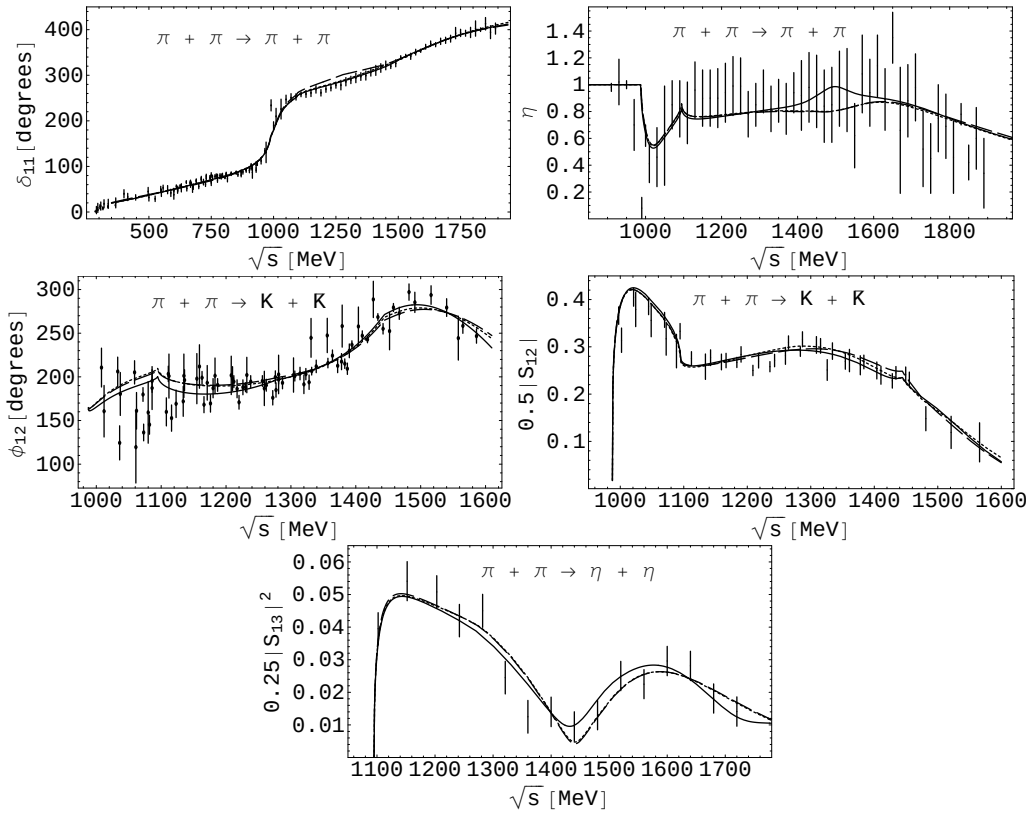


Figure 1: The phase shifts and moduli of the S-matrix element in the S-wave $\pi\pi$-scattering (upper panel), in $\pi\pi \to K\overline{K}$ (middle panel), and the squared modulus of the $\pi\pi \to \eta\eta$ S-matrix element (lower figure).

that the curves are quite similar in all three cases.

3 The contribution of multi-channel $\pi\pi$ scattering in the final states of decays of Ψ- and Υ-meson families

In the combined analysis, for the decay $J/\psi \to \phi\pi^+\pi^-$ the data were taken from Mark III, DM2 and BES II Collaborations; for $\psi(2S) \to J/\psi(\pi^+\pi^-$ and $\pi^0\pi^0)$ — from Mark II and

Crystal Ball(80) (see Refs. in [4]). For $\Upsilon(2S) \to \Upsilon(1S)(\pi^+\pi^-$ and $\pi^0\pi^0)$ data were used from ARGUS, CLEO, CUSB and Crystal Ball Collaborations; for $\Upsilon(3S) \to \Upsilon(1S)(\pi^+\pi^-, \pi^0\pi^0)$ and $\Upsilon(3S) \to \Upsilon(2S)(\pi^+\pi^-, \pi^0\pi^0)$ — from CLEO; for $\Upsilon(4S) \to \Upsilon(1S, 2S)\pi^+\pi^-$ — from *BaBar* and Belle; for $\Upsilon(5S) \to \Upsilon(1S, 2S, 3S)\pi^+\pi^-$ — from Belle Collaboration [12].

The di-meson mass distributions in the quarkonia decays are calculated using a formalism analogous to that proposed in Ref. [5] for the decays $J/\psi \to \phi(\pi\pi, K\overline{K})$ and $V' \to V\pi\pi$ $(V = \psi, \Upsilon)$ which is extended with allowing for amplitudes of transitions between the $\pi\pi$, $K\overline{K}$ and $\eta\eta$ channels in decay formulas. The decay amplitudes are related with the scattering amplitudes T_{ij} $(i, j = 1 - \pi\pi, 2 - K\overline{K}, 3 - \eta\eta)$ as follows

$$F\big(J/\psi \to \phi\pi\pi\big) = c_1(s)T_{11} + \Big(\frac{\alpha_2}{s - \beta_2} + c_2(s)\Big)T_{21} + c_3(s)T_{31}, \tag{3}$$

$$F\big(\psi(2S) \to \psi(1S)\pi\pi\big) = d_1(s)T_{11} + d_2(s)T_{21} + d_3(s)T_{31}, \tag{4}$$

$$F\big(\Upsilon(mS) \to \Upsilon(nS)\pi\pi\big) = e_1^{(mn)}T_{11} + e_2^{(mn)}T_{21} + e_3^{(mn)}T_{31}, \tag{5}$$
$$m > n,\ m = 2, 3, 4, 5,\ n = 1, 2, 3$$

where $c_i = \gamma_{i0} + \gamma_{i1}s$, $d_i = \delta_{i0} + \delta_{i1}s$ and $e_i^{(mn)} = \rho_{i0}^{(mn)} + \rho_{i1}^{(mn)}s$; indices m and n correspond to $\Upsilon(mS)$ and $\Upsilon(nS)$, respectively. The free parameters α_2, β_2, γ_{i0}, γ_{i1}, δ_{i0}, δ_{i1}, $\rho_{i0}^{(mn)}$ and $\rho_{i1}^{(mn)}$ depend on the couplings of J/ψ, $\psi(2S)$, and $\Upsilon(mS)$ to the channels $\pi\pi$, $K\overline{K}$ and $\eta\eta$. The pole term in the first equation in front of T_{21} is an approximation of possible ϕK states, not forbidden by OZI rules. The amplitudes T_{ij} are expressed through the S-matrix elements $S_{ij} = \delta_{ij} + 2i\sqrt{\rho_i\rho_j}T_{ij}$ where $\rho_i = \sqrt{1 - s_i/s}$ and s_i is the reaction threshold.

The di-meson mass distributions in the decay analysis were calculated using the relation $N|F|^2\sqrt{(s - s_1)[m_\psi^2 - (\sqrt{s} - m_\phi)^2][m_\psi^2 - (\sqrt{s} + m_\phi)^2]}$ for the decay $J/\psi \to \phi\pi\pi$ and with analogous relations for $\psi(2S) \to \psi(1S)\pi\pi$ and $\Upsilon(mS) \to \Upsilon(nS)\pi\pi$. The normalization to the experiment, N, is determined in the analysis.

A satisfactory description of all considered processes (including $\pi\pi \to \pi\pi, K\overline{K}, \eta\eta$) was obtained with the total $\chi^2/\text{ndf} \approx 1.24$; for the $\pi\pi$ scattering, $\chi^2/\text{ndf} \approx 1.15$.

Results for the distributions are shown in Figs. 2-4 with the same notation as in Fig. 1. Here the effects of omitting some resonance are more apparent than in Fig. 1.

4 Conclusions and Discussion

The combined analysis was performed for the data on isoscalar S-wave processes $\pi\pi \to \pi\pi, K\overline{K}, \eta\eta$ and on the decays of the charmonia — $J/\psi \to \phi\pi\pi$, $\psi(2S) \to J/\psi\,\pi\pi$ — and of the bottomonia — $\Upsilon(mS) \to \Upsilon(nS)\pi\pi$ $(m > n,\ m = 2, 3, 4, 5,\ n = 1, 2, 3)$ from the ARGUS, Crystal Ball, CLEO, CUSB, DM2, Mark II, Mark III, BES II, *BaBar*, and Belle Collaborations.

It is shown that the di-pion mass spectra in the above-indicated decays of charmonia and bottomonia are explained by the unified mechanism which is based on our previous conclusions on wide resonances [4, 7] and is related to contributions of the $\pi\pi$, $K\overline{K}$ and $\eta\eta$ coupled channels including their interference. It is shown that in the final states of these decays (except $\pi\pi$ scattering) the contribution of coupled processes, e.g., $K\overline{K}, \eta\eta \to \pi\pi$, is important even if these processes are energetically forbidden.

It was also very useful to consider the role of individual f_0 resonances in contributions to the di-pion mass distributions in the indicated decays. For example, it is seen that the sharp dips

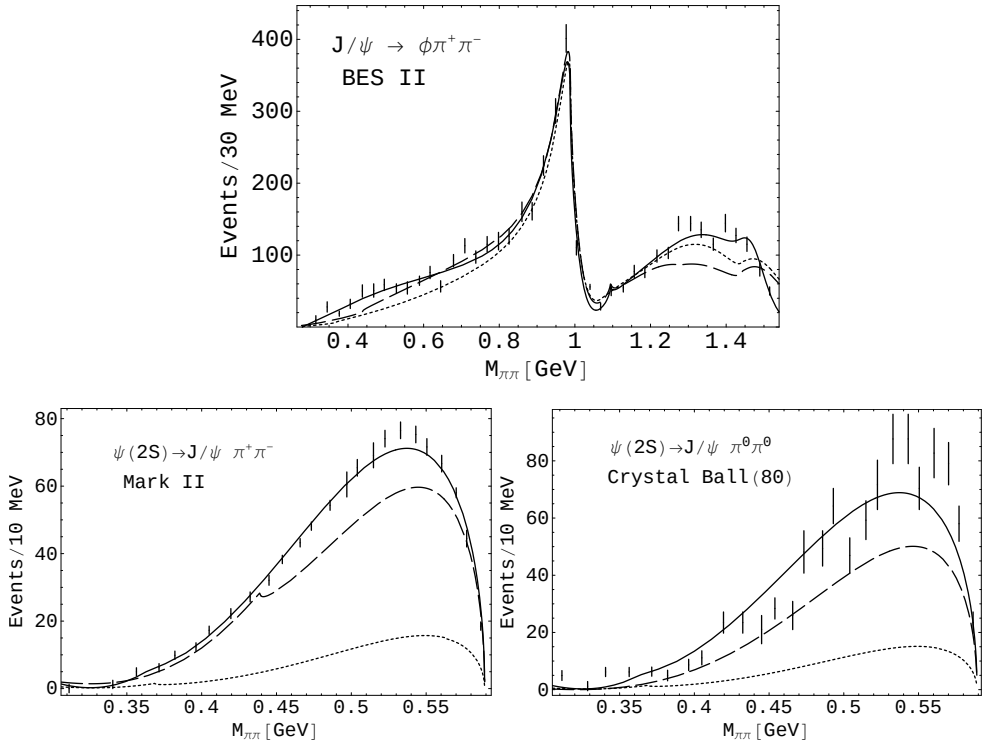


Figure 2: The decays $J/\psi \to \phi\pi\pi$ and $\psi(2S) \to J/\psi\pi\pi$. The solid lines correspond to contribution of all relevant f_0-resonances; the dotted, of the $f_0(500)$, $f_0(980)$, and $f_0'(1500)$; the dashed, of the $f_0(980)$ and $f_0'(1500)$.

near 1 GeV in the $\Upsilon(4S, 5S) \to \Upsilon(1S)\pi^+\pi^-$ decays are related with the $f_0(500)$ contribution to the interfering amplitudes of $\pi\pi$ scattering and $K\overline{K}, \eta\eta \to \pi\pi$ processes. Namely consideration of this role of the $f_0(500)$ allows us to make a conclusion on existence of the sharp dip at about 1 GeV in the di-pion mass spectrum of the $\Upsilon(4S) \to \Upsilon(1S)\pi^+\pi^-$ decay where, unlike $\Upsilon(5S) \to \Upsilon(1S)\pi^+\pi^-$, the scarce data do not permit to draw such conclusions yet.

Also, a manifestation of the $f_0(1370)$ turned out to be interesting and unexpected. First, in the satisfactory description of the $\pi\pi$ spectrum of decay $J/\psi \to \phi\pi\pi$, the second large peak in the 1.4-GeV region can be naively explained as the contribution of the $f_0(1370)$. We have shown that this is not right – the constructive interference between the contributions of the $\eta\eta$ and $\pi\pi$ and $K\overline{K}$ channels plays the main role in formation of the 1.4-GeV peak. This is quite in agreement with our earlier conclusion that the $f_0(1370)$ has a dominant $s\bar{s}$ component [7].

On the other hand, it turned out that the $f_0(1370)$ contributes considerably in the near-$\pi\pi$-threshold region of many di-pion mass distributions, especially making the threshold bell-shaped form of the di-pion spectra in the decays $\Upsilon(mS) \to \Upsilon(nS)\pi\pi$ $(m > n, m = 3, 4, 5, n = 1, 2, 3)$. This fact confirms, first, the existence of the $f_0(1370)$ (up to now there is no firm conviction if it exists or not). Second, that the exciting role of this meson in making the threshold bell-shaped form of the di-pion spectra can be explained as follows: the $f_0(1370)$, being predominantly the $s\bar{s}$ state [4] and practically not contributing to the $\pi\pi$-scattering amplitude, influences noticeably

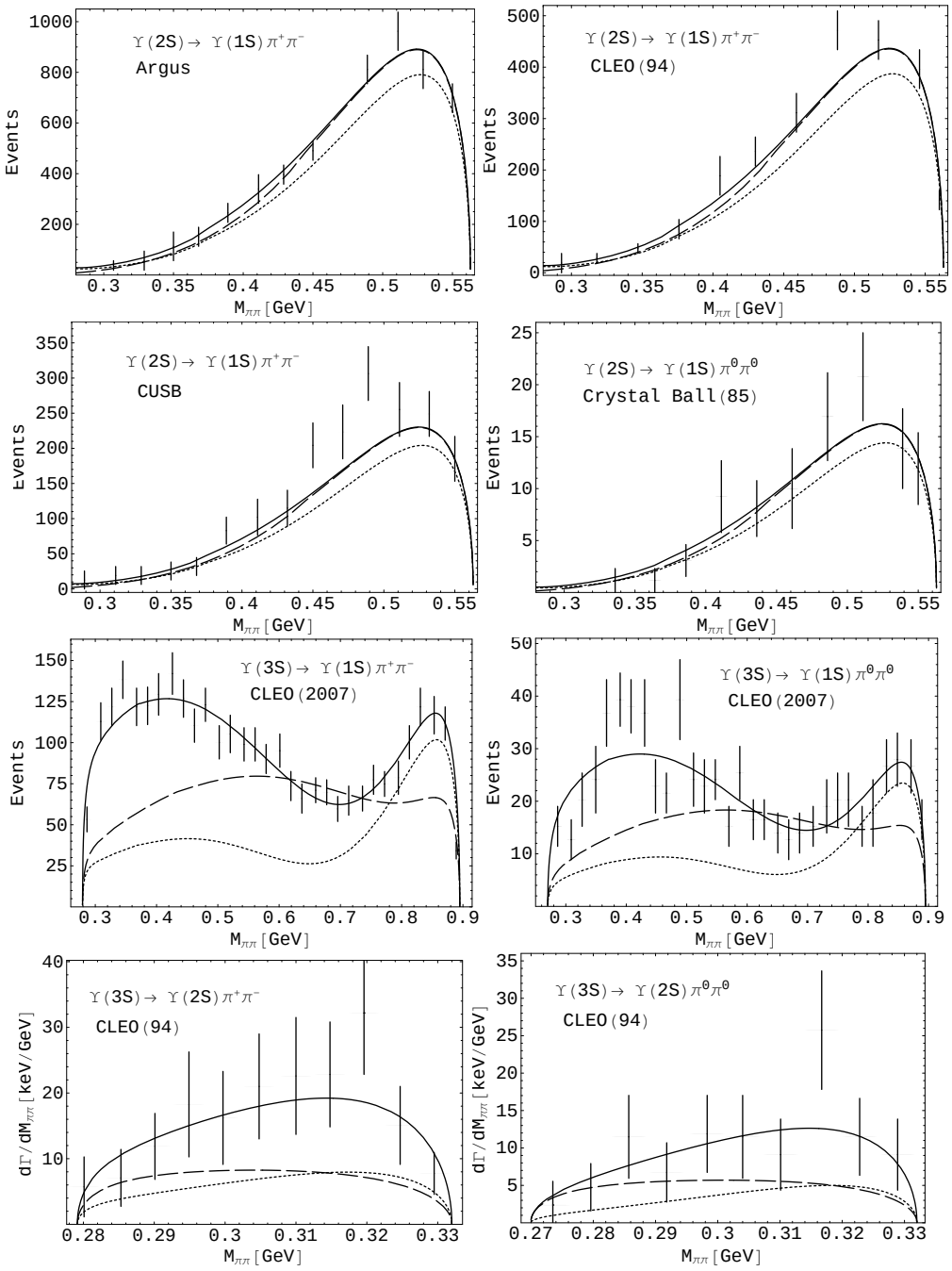


Figure 3: The decays $\Upsilon(2S) \to \Upsilon(1S)\pi\pi$ (two upper panels), $\Upsilon(3S) \to \Upsilon(1S)\pi\pi$ (middle panel) and $\Upsilon(3S) \to \Upsilon(2S)\pi\pi$ (lower panel).

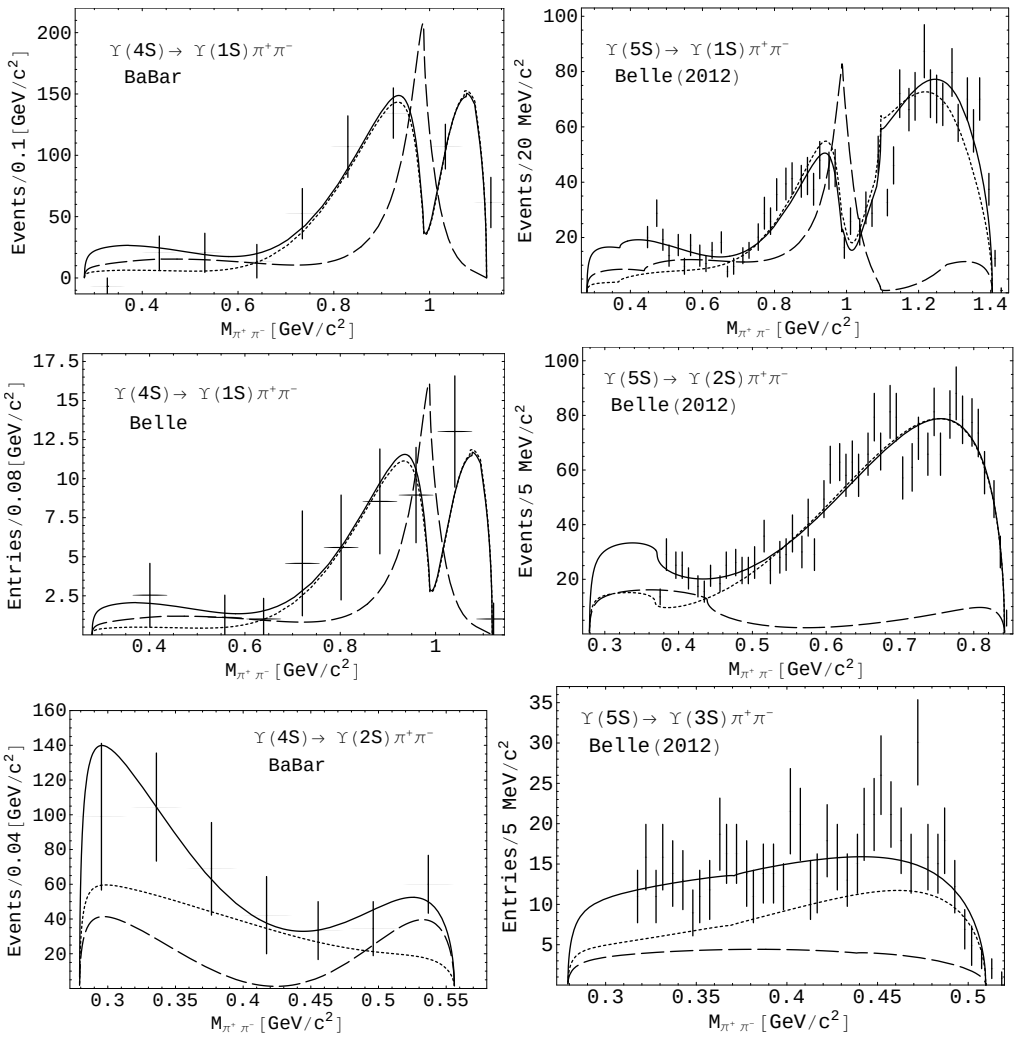


Figure 4: The decays $\Upsilon(4S) \to \Upsilon(1S, 2S)\pi^+\pi^-$ (left-hand) and $\Upsilon(5S) \to \Upsilon(ns)\pi^+\pi^-$ $(n = 1, 2, 3)$ (right-hand).

the $K\overline{K}$ scattering; e.g., it was shown that the $K\overline{K}$-scattering length is very sensitive to whether this state does exist or not [10]. The interference of contributions of the $\pi\pi$-scattering amplitude and the analytically-continued $\pi\pi \to K\overline{K}$ and $\pi\pi \to \eta\eta$ amplitudes lead to the observed results.

It is important that we have performed a combined analysis of available data on the processes $\pi\pi \to \pi\pi, K\overline{K}, \eta\eta$, on decays of charmonia and of bottomonia. The convincing description of practically all available data on two-pion transitions of the Ψ and the Υ mesons confirmed all our previous conclusions on the scalar mesons [4].

This work was supported in part by the Heisenberg-Landau Program, by the Votruba-Blokhintsev

Program for Cooperation of Czech Republic with JINR, by the Grant Agency of the Czech Republic (grant No. P203/15/04301), by the Grant Program of Plenipotentiary of Slovak Republic at JINR, by the Bogoliubov-Infeld Program for Cooperation of Poland with JINR, by the BMBF (Project 05P2015, BMBF-FSP 202), by Tomsk State University Competitiveness Improvement Program, the Russian Federation program "Nauka" (Contract No. 0.1526.2015, 3854), by Slovak Grant Agency VEGA under contract No.2/0197/14, and by the Polish National Science Center (NCN) grant DEC-2013/09/B/ST2/04382.

References

[1] K. A. Olive et al. (PDG), Chin. Phys. C **38**, 090001 (2014).

[2] Yu.S. Surovtsev, P. Bydžovský and V.E. Lyubovitskij, Phys. Rev. **D85**, 036002 (2012).

[3] Yu.S. Surovtsev *et al.*, PoS(Baldin ISHEPP XXI) 056-1-20. Conference: C12-09-10.4, Contributions.

[4] Yu.S. Surovtsev *et al.*, Phys. Rev. D **89**, 036010 (2014).

[5] D. Morgan and M.R. Pennington, Phys. Rev. D **48**, 1185 (1993); **48**, 5422 (1993).

[6] Yu.S. Surovtsev *et al.*, Phys. Rev. D **91**, 037901 (2015).

[7] Yu. S. Surovtsev *et al.*, J. Phys. G: Nucl. Part. Phys. **41**, 025006 (2014).

[8] Yu.S . Surovtsev *et al.*, Phys. Rev. D **86**, 116002 (2012).

[9] K.J. Le Couteur, Proc. R. London, Ser. A **256**, 115 (1960); R.G. Newton, J. Math. Phys. **2**, 188 (1961).

[10] Yu.S. Surovtsev, D. Krupa and M. Nagy, Eur. Phys. J. A **15**, 409 (2002).

[11] N.N. Achasov and G.N. Shestakov, Phys. Rev. D **49**, 5779 (1994).

[12] H. Albrecht *et al.* (ARGUS Collaboration), Phys. Lett. B **134**, 137 (1984); D. Besson *et al.* (CLEO Collaboration), Phys. Rev. D **30**, 1433 (1984); V. Fonseca *et al.* (CUSB Collaboration), Nucl. Phys. B **242**, 31 (1984); D. Gelphman *et al.* (Crystal Ball Collaboration), Phys. Rev. D **32**, 2893 (1985); D. Cronin-Hennessy *et al.* (CLEO Collaboration), Phys. Rev. D **76**, 072001 (2007); F. Butler *et al.* (CLEO Collaboration), Phys. Rev. D **49**, 40 (1994); B. Aubert *et al.* (BaBar Collaboration), Phys. Rev. Lett. **96**, 232001 (2006); A. Sokolov *et al.* (Belle Collaboration), Phys. Rev. D **75**, 071103 (2007); A. Bondar *et al.* (Belle Collaboration), Phys. Rev. Lett. **108**, 122001 (2012).

Relativistic Description of Baryon Properties

D. Ebert[1], *R. N. Faustov*[2], *V. O. Galkin*[2]

[1]Institut für Physik, Humboldt–Universität zu Berlin, Newtonstr. 15, D-12489 Berlin, Germany
[2]Institute of Informatics in Education, FRC CSC RAS, Vavilov Str. 40, 119991 Moscow, Russia

DOI: http://dx.doi.org/10.3204/DESY-PROC-2016-04/Galkin

Properties of heavy and strange baryons are investigated in the framework of the relativistic quark-diquark picture. It is assumed that two quarks in a baryon form a diquark and baryon is considered as the bound quark-diquark system. The relativistic effects and diquark internal structure are consistently taken into account. Calculations are performed up to rather high orbital and radial excitations of heavy and strange baryons. On this basis the Regge trajectories are constructed. The rates of semileptonic decays of heavy baryons are calculated. The obtained results agree well with available experimental data.

The convincing evidence of the existence of diquark correlations in hadrons has been collected. Thus recently several charged charmonium- and bottomonium-like states were discovered. They should be inevitably multiquark, at least four quark — tetraquark, states. One of the most successful pictures of such tetraquark states is the diquark-antidiquark model [1]. In the light meson sector it has been argued for a long time that mesons forming the inverted lightest scalar nonet can be well described as tetraquarks treated as diquark-antidiquark bound states [2]. In the baryon sector it is well known that the number of observed excited states both in the light and heavy sectors is considerably lower than the number of excited states predicted in the three-quark picture [3]. The introduction of diquarks significantly reduces this number since in such a picture some of degrees of freedom are frozen and thus the number of possible excitations is substantially smaller.

Here we study spectroscopy and weak decays of heavy and strange baryons in the relativistic quark-diquark picture in the framework of the quasipotential approach. The interaction of two quarks in a diquark and the quark-diquark interaction in a baryon are described by the diquark wave function Ψ_d of the bound quark-quark state and by the baryon wave function Ψ_B of the bound quark-diquark state respectively, which satisfy the relativistic quasipotential equation of the Schrödinger type [4]

$$\left(\frac{b^2(M)}{2\mu_R} - \frac{\mathbf{p}^2}{2\mu_R}\right)\Psi_{d,B}(\mathbf{p}) = \int \frac{d^3q}{(2\pi)^3} V(\mathbf{p},\mathbf{q};M)\Psi_{d,B}(\mathbf{q}), \tag{1}$$

where the relativistic reduced mass and the center-of-mass system relative momentum squared on mass shell are

$$\mu_R = \frac{M^4 - (m_1^2 - m_2^2)^2}{4M^3}, \qquad b^2(M) = \frac{[M^2 - (m_1+m_2)^2][M^2 - (m_1-m_2)^2]}{4M^2},$$

and M is the bound state mass (diquark or baryon), $m_{1,2}$ are the masses of quarks (q_1 and q_2) which form the diquark or of the diquark (d) and quark (q) which form the baryon (B), and $\mathbf{p}$ is their relative momentum.

The quasipotentials $V(\mathbf{p},\mathbf{q};M)$ of the quark-quark or quark-diquark interaction are constructed with the help of the QCD-motivated off-mass-shell scattering amplitude, projected onto the positive energy states. The effective quark interaction is taken to be the sum of the usual one-gluon exchange term and the mixture of long-range vector and scalar linear confining potentials with the mixing coefficient ε. It is also assumed that the vector confining potential contains not only the Dirac term but the Pauli term, thus introducing the anomalous chromomagnetic quark moment κ. The explicit expressions for the quasipotentials are given in Ref. [5].

In the nonrelativistic limit the usual Cornell-like potential is reproduced

$$V(r) = -\frac{4}{3}\frac{\alpha_s}{r} + Ar + B, \tag{2}$$

where α_s is the QCD coupling constant with freezing [2].

All parameters of the model such as quark masses, parameters of the linear confining potential A and B, the mixing coefficient ε and anomalous chromomagnetic quark moment κ were fixed previously from calculations of meson and baryon properties [4, 5]. The constituent quark masses $m_u = m_d = 0.33$ GeV, $m_s = 0.5$ GeV, $m_c = 1.55$ GeV, $m_b = 4.88$ GeV and the parameters of the linear potential $A = 0.18$ GeV^2 and $B = -0.3$ GeV have the usual values of quark models. The value of the mixing coefficient of vector and scalar confining potentials $\varepsilon = -1$ has been determined from the consideration of the heavy quark expansion for the semileptonic heavy meson decays and charmonium radiative decays [4]. The universal Pauli interaction constant $\kappa = -1$ has been fixed from the analysis of the fine splitting of heavy quarkonia ^3P_J-states [4]. Note that the long-range chromomagnetic contribution to the potential, which is proportional to $(1+\kappa)$, vanishes for the chosen value of $\kappa = -1$.

First we calculate masses and form factors of the diquarks and the vertex $\langle d(P)|J_\mu|d(Q)\rangle$ of the diquark-gluon interaction which is parameterized by the form factor

$$F(r) = 1 - e^{-\xi r - \zeta r^2}, \tag{3}$$

that takes the internal diquark structure into account. The values of diquark masses and parameters ξ and ζ are given in Refs. [5, 6]

Next we calculate the masses of heavy and strange baryons as the bound states of a quark and diquark. The results of calculations can be found in Refs. [5, 6]. Here, as an example, we give in Tables 1,2 the comparison of our predictions for the mass spectra of the Λ_c and Λ with other theoretical estimates and available experimental data. From these tables we see that our diquark model predicts appreciably less states than the three-quark approaches. The differences become apparent with the growth of the orbital and radial excitations in the baryon. Our model reproduces correctly all masses of the well established 4- and 3-star resonances and most of the 2- and 1-star states. Let us emphasize that the experimental mass of the $\frac{1}{2}^-$ 4-star $\Lambda(1405)$ is naturally reproduced if this state is considered as the first orbital excitation $1P$ in the strange quark-light scalar diquark picture of Λ baryons. The rather low mass of this state represents difficulties for most of the three-quark models [7, 8, 9], which predict its mass about 100 MeV higher than experimental value.

We calculated masses of both orbitally and radially excited heavy and strange baryons up to rather high excitation numbers. This makes it possible to construct the heavy baryon Regge trajectories both in the (J, M^2) and in the (n_r, M^2) planes: (a) The (J, M^2) Regge trajectory: $J = \alpha M^2 + \alpha_0$; (b) The (n_r, M^2) Regge trajectory: $n_r = \beta M^2 + \beta_0$, where α, β are the slopes

J^P	Experiment [10]			Theory			
	State	Status	Mass	our	[11]	[3]	[7]
$\frac{1}{2}^+$	Λ_c	***	2286.46	2286	2286	2286	2265
	$\Lambda_c(2765)$	*	2766.6	2769	2766	2791	2775
				3130	3112	3154	3170
				3437	3397		
$\frac{1}{2}^-$	$\Lambda_c(2595)$	***	2592.3	2598	2591	2625	2630
	$\Lambda_c(2940)$	***	2939.3	2983	2989		2780
				3303	3296		2830
$\frac{3}{2}^-$	$\Lambda_c(2625)$	***	2628.1	2627	2629	2636	2640
				3005	3000		2840
				3322	3301		2885
$\frac{3}{2}^+$				2874	2857	2887	2910
				3189	3188	3120	3035
$\frac{5}{2}^+$	$\Lambda_c(2880)$	***	2881.53	2880	2879	2887	2910
				3209	3198	3125	3140
$\frac{5}{2}^-$				3097	3075	2872	2900
$\frac{7}{2}^-$				3078	3092		3125
$\frac{7}{2}^+$				3270	3267		3175
$\frac{9}{2}^+$				3284	3280		
$\frac{9}{2}^-$				3444			
$\frac{11}{2}^-$				3460			

Table 1: Comparison of theoretical predictions for masses of the Λ_c baryons (in MeV).

and α_0, β_0 are intercepts. In Figs. 1,2 we plot the Regge trajectories in the (J, M^2) plane for charmed and strange baryons. Straight lines were obtained by the χ^2 fit of calculated values. The fitted slopes and intercepts of the Regge trajectories can be found in Refs [5, 6]. We see that the calculated heavy and strange baryon masses lie on the linear trajectories, which are parallel and equidistant.

Let us consider weak decays of baryons. The simplest case is the semileptonic decay of the bottom baryon to the charmed baryon, since in this case the model independent considerations based on heavy quark effective theory (HQET) can be applied. To calculate the heavy baryon decay rate it is necessary to determine the corresponding matrix element of the weak current between baryon states, which in the quasipotential approach is given by [14]

$$\langle\Lambda_{Q'}(p_{Q'})|J^W_\mu|\Lambda_Q(p_Q)\rangle = \int\frac{d^3p\,d^3q}{(2\pi)^6}\bar\Psi_{\Lambda_{Q'}\,\mathbf{p}_{Q'}}(\mathbf{p})\Gamma_\mu(\mathbf{p},\mathbf{q})\Psi_{\Lambda_Q\,\mathbf{p}_Q}(\mathbf{q}), \tag{4}$$

where $\Gamma_\mu(\mathbf{p},\mathbf{q})$ is the two-particle vertex function and $\Psi_{\Lambda\,\mathbf{p}_Q}$ are the baryon ($\Lambda = \Lambda_Q, \Lambda_{Q'}$) wave functions projected onto the positive energy states of quarks and boosted to the moving reference frame with momentum $\mathbf{p}_Q$. The wave function of the moving baryon $\Psi_{\Lambda_Q\,\mathbf{p}_Q}$ is connected with the wave function in the rest frame $\Psi_{\Lambda_Q\,\mathbf{0}}$ by the transformation [14]

$$\Psi_{\Lambda_Q\,\mathbf{p}_Q}(\mathbf{p}) = D^{1/2}_Q(R^W_{L_{\mathbf{p}_Q}})D^{\mathcal{I}}_d(R^W_{L_{\mathbf{p}_Q}})\Psi_{\Lambda_Q\,\mathbf{0}}(\mathbf{p}), \qquad \mathcal{I} = 0, 1, \tag{5}$$

J^P	Experiment [10]			Theory					
	State	Status	Mass	Our	[7]	[8]	[9]	[12]	[13]
$\frac{1}{2}^+$	Λ	****	1115.683 ± 0.006	1115	1115	1108	1136	1116	1149 ± 18
	$\Lambda(1600)$	***	$1560 - 1600$	1615	1680	1677	1625	1518	1807 ± 94
	$\Lambda(1710)$	*	1713 ± 13						
	$\Lambda(1810)$	***	$1750 - 1810$	1901	1830	1747	1799	1666	2112 ± 54
				1972	1910	1898		1955	2137 ± 69
				1986	2010	2077		1960	
				2042	2105	2099			
				2099	2120	2132			
$\frac{3}{2}^+$	$\Lambda(1890)$	****	$1850 - 1890$	1854	1900	1823		1896	1991 ± 103
				1976	1960	1952			2058 ± 139
				2130	1995	2045			2481 ± 111
				2184	2050	2087			
				2202	2080	2133			
$\frac{5}{2}^+$	$\Lambda(1820)$	****	$1815 - 1820$	1825	1890	1834		1896	
	$\Lambda(2110)$	***	$2090 - 2110$	2098	2035	1999			
				2221	2115	2078			
				2255	2115	2127			
				2258	2180	2150			
$\frac{7}{2}^+$	$\Lambda(2020)$	*	≈ 2020	2251	2120	2130			
				2471		2331			
$\frac{9}{2}^+$	$\Lambda(2350)$	***	$2340 - 2350$	2360		2340			
$\frac{1}{2}^-$	$\Lambda(1405)$	****	$1405.1^{+1.3}_{-1.0}$	1406	1550	1524	1556	1431	1416 ± 81
	$\Lambda(1670)$	****	$1660 - 1670$	1667	1615	1630	1682	1443	1546 ± 110
	$\Lambda(1800)$	***	$1720 - 1800$	1733	1675	1816	1778	1650	1713 ± 116
				1927	2015	2011		1732	2075 ± 249
				2197	2095	2076		1785	
				2218	2160	2117		1854	
$\frac{3}{2}^-$	$\Lambda(1520)$	****	1519.5 ± 1.0	1549	1545	1508	1556	1431	1751 ± 40
	$\Lambda(1690)$	****	$1685 - 1690$	1693	1645	1662	1682	1443	2203 ± 106
				1812	1770	1775		1650	2381 ± 87
	$\Lambda(2050)$	*	2056 ± 22	2035	2030	1987		1732	
				2319	2110	2090		1785	
	$\Lambda(2325)$	*	≈ 2325	2322	2185	2147		1854	
				2392	2230	2259		1928	
				2454	2290	2275		1969	
$\frac{5}{2}^-$	$\Lambda(1830)$	****	$1810 - 1830$	1861	1775	1828	1778	1785	
				2136	2180	2080			
				2350	2250	2179			
$\frac{7}{2}^-$	$\Lambda(2100)$	****	$2090 - 2100$	2097	2150	2090			
				2583	2230	2227			
$\frac{9}{2}^-$				2665		2370			

Table 2: Comparison of theoretical predictions and experimental data for the masses of the Λ states (in MeV).

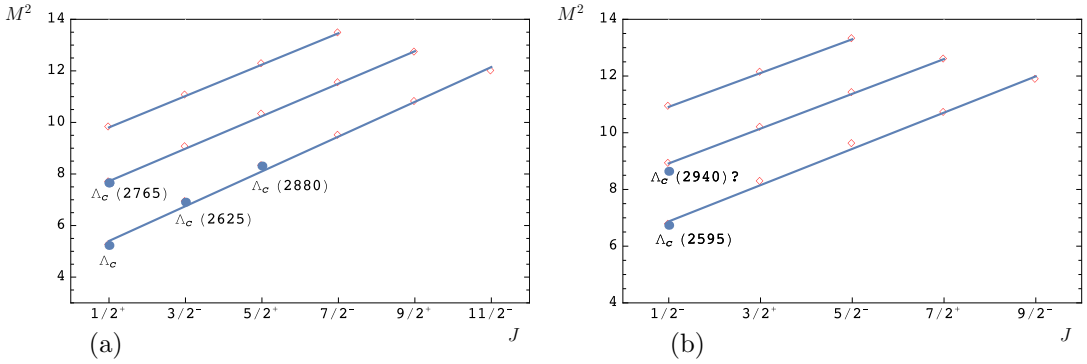


Figure 1: Parent and daughter (J, M^2) Regge trajectories for the Λ_c baryons with natural $(P = (-1)^{J-1/2})$ (a) and unnatural $(P = (-1)^{J+1/2})$ (b) parities. Diamonds are predicted masses. Available experimental data are given by dots with particle names; M^2 is in GeV^2.

where R^W is the Wigner rotation, $L_{\mathbf{p}}$ is the Lorentz boost from the baryon rest frame to a moving one, and $D^{1/2}(R)$, $D^{\mathcal{I}}(R)$ are rotation matrices of the quark and diquark spins.

The hadronic matrix elements for the semileptonic decay $\Lambda_Q \to \Lambda_{Q'}$ are parameterized in terms of six invariant form factors:

$$\begin{aligned}
\langle \Lambda_{Q'}(v')|V^\mu|\Lambda_Q(v)\rangle &= \bar{u}_{\Lambda_{Q'}}(v')\Big[F_1(w)\gamma^\mu + F_2(w)v^\mu + F_3(w)v'^\mu\Big]u_{\Lambda_Q}(v),\\
\langle \Lambda_{Q'}(v')|A^\mu|\Lambda_Q(v)\rangle &= \bar{u}_{\Lambda_{Q'}}(v')\Big[G_1(w)\gamma^\mu + G_2(w)v^\mu + G_3(w)v'^\mu\Big]\gamma_5 u_{\Lambda_Q}(v),
\end{aligned} \tag{6}$$

where $u_{\Lambda_Q}(v)$ and $u_{\Lambda_{Q'}}(v')$ are Dirac spinors of the initial and final baryon with four-velocities v and v', respectively; $w = v\cdot v' = (M^2_{\Lambda_Q} + M^2_{\Lambda_{Q'}} - q^2)/(2M_{\Lambda_Q}M_{\Lambda_{Q'}})$. In the heavy quark limit $m_Q \to \infty$ $(Q = b, c)$ the form factors (6) can be expressed through the single Isgur-Wise function $\zeta(w)$

$$F_1(w) = G_1(w) = \zeta(w), \qquad F_2(w) = F_3(w) = G_2(w) = G_3(w) = 0. \tag{7}$$

At subleading order of the heavy quark expansion the form factors are given by [14]

$$\begin{aligned}
F_1(w) &= \zeta(w) + \left(\frac{\bar\Lambda}{2m_Q} + \frac{\bar\Lambda}{2m_{Q'}}\right)\Big[2\chi(w) + \zeta(w)\Big], \qquad \bar\Lambda = M_{\Lambda_Q} - m_Q,\\
G_1(w) &= \zeta(w) + \left(\frac{\bar\Lambda}{2m_Q} + \frac{\bar\Lambda}{2m_{Q'}}\right)\Big[2\chi(w) + \frac{w-1}{w+1}\zeta(w)\Big],\\
F_2(w) &= G_2(w) = -\frac{\bar\Lambda}{2m_{Q'}}\frac{2}{w+1}\zeta(w), \qquad F_3(w) = -G_3(w) = -\frac{\bar\Lambda}{2m_Q}\frac{2}{w+1}\zeta(w).
\end{aligned} \tag{8}$$

The resulting expressions for the semileptonic decay $\Lambda_Q \to \Lambda_{Q'}$ form factors up to subleading order in $1/m_Q$ in our model are the following [14]

$$\begin{aligned}
F_1(w) &= \zeta(w) + \left(\frac{\bar\Lambda}{2m_Q} + \frac{\bar\Lambda}{2m_{Q'}}\right)[2\chi(w) + \zeta(w)]\\
&\quad +4(1-\varepsilon)(1+\kappa)\left[\frac{\bar\Lambda}{2m_{Q'}}\frac{1}{w-1} - \frac{\bar\Lambda}{2m_Q}(w+1)\right]\chi(w),
\end{aligned}$$

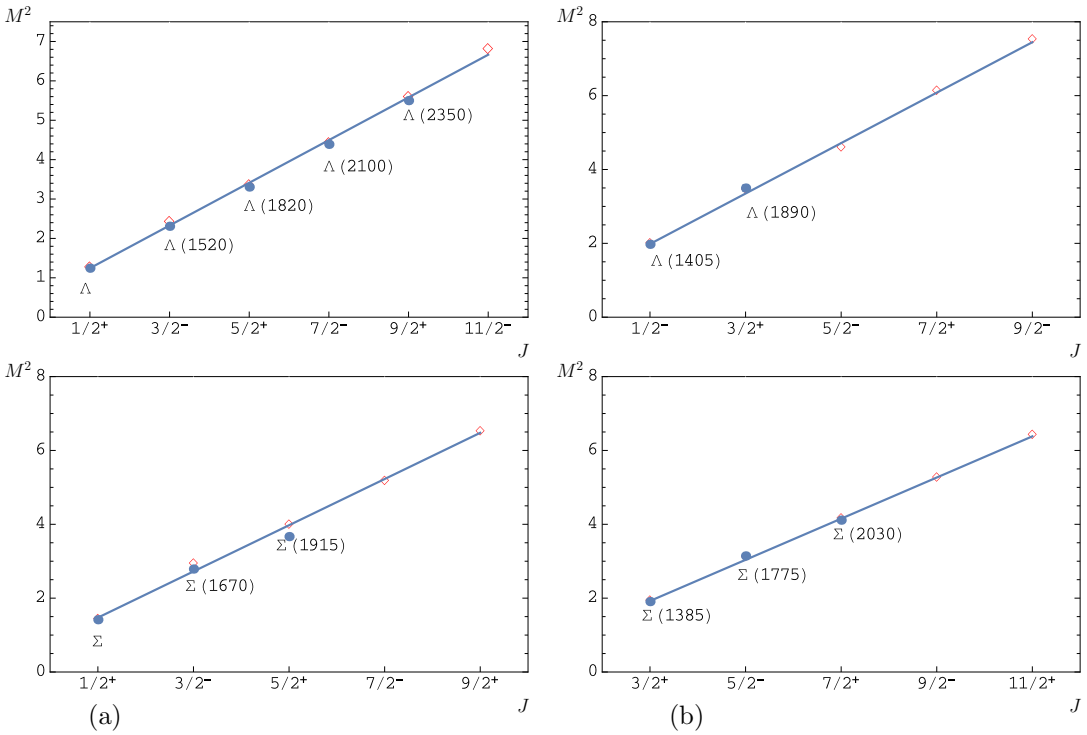


Figure 2: Same as in Fig. 1 but for the Λ and Σ baryons.

$$
\begin{aligned}
G_1(w) &= \zeta(w) + \left(\frac{\bar\Lambda}{2m_Q} + \frac{\bar\Lambda}{2m_{Q'}}\right)\left[2\chi(w) + \frac{w-1}{w+1}\zeta(w)\right] - 4(1-\varepsilon)(1+\kappa)\frac{\bar\Lambda}{2m_Q}w\chi(w),\\
F_2(w) &= -\frac{\bar\Lambda}{2m_{Q'}}\frac{2}{w+1}\zeta(w) - 4(1-\varepsilon)(1+\kappa)\left[\frac{\bar\Lambda}{2m_{Q'}}\frac{1}{w-1} + \frac{\bar\Lambda}{2m_Q}w\right]\chi(w),\\
G_2(w) &= -\frac{\bar\Lambda}{2m_{Q'}}\frac{2}{w+1}\zeta(w) - 4(1-\varepsilon)(1+\kappa)\frac{\bar\Lambda}{2m_{Q'}}\frac{1}{w-1}\chi(w),\\
F_3(w) &= -G_3(w) = -\frac{\bar\Lambda}{2m_Q}\frac{2}{w+1}\zeta(w) + 4(1-\varepsilon)(1+\kappa)\frac{\bar\Lambda}{2m_Q}\chi(w),
\end{aligned}
\tag{9}
$$

where the leading order Isgur-Wise function of heavy baryons

$$
\zeta(w) = \lim_{m_Q\to\infty}\int\frac{d^3p}{(2\pi)^3}\Psi_{\Lambda_{Q'}}\left(\mathbf{p} + 2\epsilon_d(p)\sqrt{\frac{w-1}{w+1}}\,\mathbf{e_\Delta}\right)\Psi_{\Lambda_Q}(\mathbf{p}),
\tag{10}
$$

$\mathbf{e_\Delta} = \mathbf{\Delta}/\sqrt{\mathbf{\Delta}^2}$, $\mathbf{\Delta} = M_{\Lambda_{Q'}}\mathbf{v}' - M_{\Lambda_Q}\mathbf{v}$, $\epsilon_d(p) = \sqrt{\mathbf{p}^2 + M_d^2}$ and the subleading function

$$
\chi(w) = -\frac{w-1}{w+1}\lim_{m_Q\to\infty}\int\frac{d^3p}{(2\pi)^3}\frac{\bar\Lambda - \epsilon_d(p)}{2\bar\Lambda}\Psi_{\Lambda_{Q'}}\left(\mathbf{p} + 2\epsilon_d(p)\sqrt{\frac{w-1}{w+1}}\,\mathbf{e_\Delta}\right)\Psi_{\Lambda_Q}(\mathbf{p}).
\tag{11}
$$

These functions were calculated using our model wave functions of the Λ_b and Λ_c baryons obtained in their mass spectrum calculations.

For $(1-\varepsilon)(1+\kappa)=0$ the HQET results (8) are reproduced. This can be achieved either setting $\varepsilon=1$ (pure scalar confinement) or $\kappa=-1$. In our model we need vector confining contribution and therefore use the latter option. This consideration gives us additional, based on the HQET, justification for fixing one of the main parameters of the model κ.

The $1/m_Q$ corrections turn out to be rather large, significantly larger than for the heavy-to-heavy mesons transitions. This is the consequence of the larger value of the expansion parameter $\bar{\Lambda}$. Indeed in the case of baryon decays the parameter $\bar{\Lambda}$ is determined by the light diquark energies, while for meson decays it is determined by light quark energies. Therefore consideration of such decays without the heavy quark expansion can significantly improve the precision of predictions. Also such an expansion cannot be applied for the heavy-to-light $\Lambda_b\to p$ weak transitions, since the final baryon contains only light u and d quarks.

It is important to note that both $\Lambda_b\to\Lambda_c l\nu_l$ and $\Lambda_b\to pl\nu_l$ decays have a broad kinematical range. The square of the momentum transfer to the lepton pair q^2 varies from 0 to $q^2_{\rm max}\approx 12$ GeV^2 for decays to Λ_c and from 0 to $q^2_{\rm max}\approx 22$ GeV^2 for decays to p. As a result the recoil momentum of the final baryon $|\mathbf{\Delta}|$ is almost always significantly larger than the relative quark momentum in the baryon. Thus one can neglect small relative momentum $|\mathbf{p}|$ with respect to the recoil momentum $|\mathbf{\Delta}|$ in the energies of quarks in energetic final baryons and replace $\epsilon_q(p+\Delta)\equiv\sqrt{m_q^2+(\mathbf{p}+\mathbf{\Delta})^2}$ by $\epsilon_q(\Delta)\equiv\sqrt{m_q^2+\mathbf{\Delta}^2}$. It is important to point out that we keep the quark mass in the energies $\epsilon_q(\Delta)$. Thus the resulting expressions are valid both for the heavy-to-light and heavy-to-heavy Λ_b baryon decays. Such replacement is made only in the subleading vertex function $\Gamma^{(2)}_\mu(\mathbf{p},\mathbf{q})$, which takes into account contributions of the intermediate negative-energy states [15], and permits us to perform one of the integrations using the quasipotential equation. As a result, the weak decay matrix elements are expressed through the usual overlap integral of initial and final baryon wave functions. The subleading contributions are proportional to the ratios of baryon binding energies, which are small, to the quark energies and thus turn out to be also small numerically. Therefore we obtain reliable expressions for the form factors in the whole accessible kinematical range [15]. The largest uncertainty, which turns out to be small numerically, occurs for the heavy-to-light transitions in the narrow region near zero recoil of the final light baryon, where the above discussed replacement is less justified. Let us emphasize that we consistently take into account all relativistic corrections including boosts of the baryon wave functions from the rest frame to the moving one. For numerical calculations of the form factors we use the quasipotential wave functions of the Λ_b, Λ_c and p baryons obtained in their mass spectra calculations. We plot the baryon decay form factors in Figs. 3 and 4.

The total decay rates and branching ratios are given in Table 3 in comparison with the results of other theoretical approaches [16, 17, 18, 19, 20, 21, 22] and available experimental data [10]. For absolute values we use the following CKM values $|V_{cb}|=(3.90\pm0.15)\times10^{-2}$, $|V_{ub}|=(4.05\pm0.20)\times10^{-3}$ extracted from our previous analysis of the heavy B and B_s meson decays [23]. In this table we also give our predictions for the average values of the forward-backward asymmetry of the charged lepton $\langle A_{FB}\rangle$, the convexity parameter $\langle C_F\rangle$ and the longitudinal polarization of the final baryon $\langle P_L\rangle$. Note that lattice calculations [22] give somewhat lower predictions for the branching ratios normalized by the square of the corresponding CKM matrix element for $\Lambda_b\to\Lambda_c$ transitions but give higher results for $\Lambda_b\to p$ transitions than other approaches. The lattice determination of form factors is done in the region of small recoils of the final baryon $q^2\sim q^2_{\rm max}$ and then their values are extrapolated to the whole kinematical region, which is broad especially for the heavy-to-light $\Lambda_b\to pl\nu_l$ decay. In our model we explicitly determine the form factor q^2 dependence in the whole kinematical range without

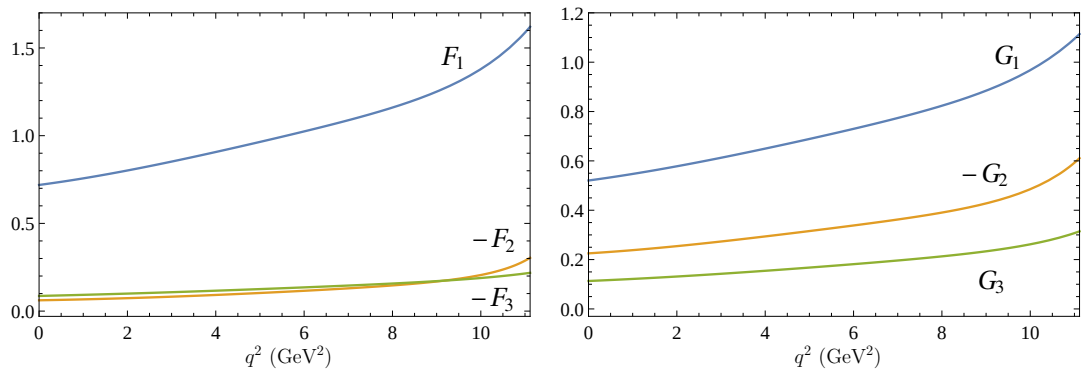


Figure 3: Form factors of the weak $\Lambda_b \to \Lambda_c$ transition.

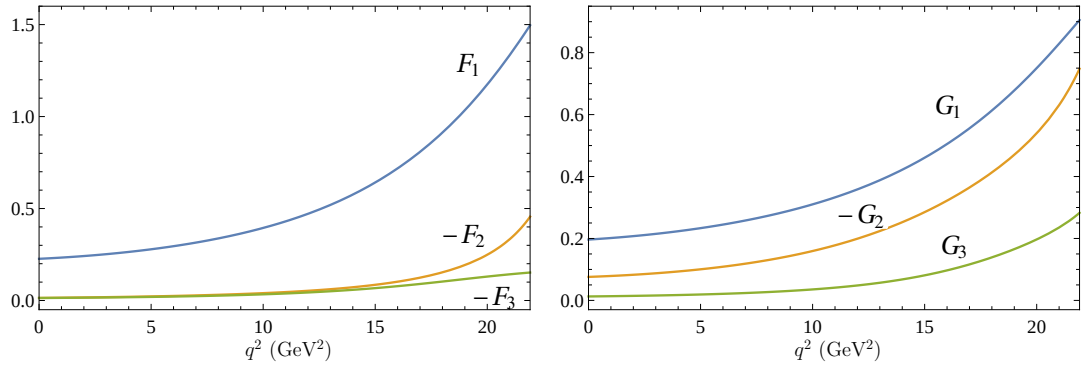


Figure 4: Form factors of the weak $\Lambda_b \to p$ transition.

extrapolations.

Recently the LHCb collaboration [24] measured the ratio of the heavy-to-heavy and heavy-to-light semileptonic Λ_b decays in the limited interval of q^2

$$R_{\Lambda_c p} = \frac{\int_{15\,\mathrm{GeV}^2}^{q^2_{max}} \frac{d\Gamma(\Lambda_b \to p \mu \nu_\mu)}{dq^2} dq^2}{\int_{7\,\mathrm{GeV}^2}^{q^2_{max}} \frac{d\Gamma(\Lambda_b \to \Lambda_c \mu \nu_\mu)}{dq^2} dq^2}. \tag{12}$$

Such a measurement is very important since it allows us for the first time to extract the ratio of CKM matrix elements $|V_{ub}|/|V_{cb}|$ from the Λ_b baryon decays and compare it to the corresponding ratio determined from B and B_s meson decays. Our prediction for the ratio $R_{\Lambda_c p}$ in comparison with the lattice result [22] and experimental value is given in Table 4. From this table we see that our value of the coefficient in front of $|V_{ub}|^2/|V_{cb}|^2$ is significantly lower than the lattice one. This is the result of the deviation of our calculation (and other quark model calculations) from lattice predictions for normalized by the square of CKM matrix element value for heavy-to-heavy and heavy-to-light semileptonic Λ_b decays (see Table 3). This deviation even increases in the ratio.

Comparing our result for $R_{\Lambda_c p}$ with experimental data [24] we can extract the ratio of the

Parameter	our	[16, 17]	[18]	[19]	[20]	[21]	[22]	Exp. [10]
$\Lambda_b \to \Lambda_c l \nu_l$								
Γ (ns^{-1})	44.2		53.9					
$\Gamma/\lvert V_{cb}\rvert^2$ (ps^{-1})	29.1						$21.5 \pm 0.8 \pm 1.1$	
Br (%)	6.48	6.9		4.83	6.3			$6.2^{+1.4}_{-1.2}$
$\langle A_{FB} \rangle$	0.195	0.18						
$\langle C_F \rangle$	-0.57	-0.63						
$\langle P_L \rangle$	-0.80	-0.82						
$\Lambda_b \to \Lambda_c \tau \nu_\tau$								
Γ (ns^{-1})	13.9		20.9					
$\Gamma/\lvert V_{cb}\rvert^2$ (ps^{-1})	9.11						$7.15 \pm 0.15 \pm 0.27$	
Br (%)	2.03	2.0		1.63				
$\langle A_{FB} \rangle$	-0.021	-0.0385						
$\langle C_F \rangle$	-0.09	-0.10						
$\langle P_L \rangle$	-0.71	-0.72						
$\Lambda_b \to p l \nu_l$								
$\Gamma/\lvert V_{ub}\rvert^2$ (ps^{-1})	18.7	13.3	7.55				$25.7 \pm 2.6 \pm 4.6$	
Br (10^{-4})	4.5	2.9		3.89	2.54	$4.0^{+2.3}_{-2.0}$		
$\langle A_{FB} \rangle$	0.346	0.388						
$\Lambda_b \to p \tau \nu_\tau$								
$\Gamma/\lvert V_{ub}\rvert^2$ (ps^{-1})	12.1	9.6	6.55				$17.7 \pm 1.3 \pm 1.6$	
Br (10^{-4})	2.9	2.1		2.75				
$\langle A_{FB} \rangle$	0.185	0.220						

Table 3: Comparison of theoretical predictions for the Λ_b semileptonic decay parameters with available experimental data.

Ratio	our	[19]	[22]	Experiment (LHCb) [24]
$R_{\Lambda_c p}$	$(0.78 \pm 0.08)\frac{\lvert V_{ub}\rvert^2}{\lvert V_{cb}\rvert^2}$	0.0101	$(1.471 \pm 0.095 \pm 0.109)\frac{\lvert V_{ub}\rvert^2}{\lvert V_{cb}\rvert^2}$	$(1.00 \pm 0.04 \pm 0.08) \times 10^{-2}$

Table 4: Predictions for the ratio of baryon decay rates.

CKM matrix elements. Using our model value we find

$$\frac{|V_{ub}|}{|V_{cb}|} = 0.113 \pm 0.011|_{\rm theor} \pm 0.006|_{\rm exp}, \tag{13}$$

which is in good agreement with the experimental ratio of these matrix elements extracted from inclusive decays [10]

$$\frac{|V_{ub}|_{\rm incl}}{|V_{cb}|_{\rm incl}} = 0.105 \pm 0.006, \tag{14}$$

and with the corresponding ratio found in our previous analysis of exclusive semileptonic B and B_s meson decays [$|V_{cb}| = (3.90 \pm 0.15) \times 10^{-2}$, $|V_{ub}| = (4.05 \pm 0.20) \times 10^{-3}$] [23]

$$\frac{|V_{ub}|}{|V_{cb}|} = 0.104 \pm 0.012. \tag{15}$$

On the other hand, the lattice value for the ratio $R_{\Lambda_c p}$ gives

$$\frac{|V_{ub}|}{|V_{cb}|} = 0.083 \pm 0.004 \pm 0.004, \tag{16}$$

which is in agreement with the corresponding CKM matrix element ratio extracted from the comparison of lattice predictions with data on exclusive B meson decays, but more than 3σ lower than the ratio extracted from inclusive B meson decays (14).

In summary, we demonstrated that spectroscopy and weak decays of heavy and strange baryons can be well described in the relativistic quark model based on the quark-diquark picture of baryons.

The authors are grateful to A. Ali, M. Ivanov, J. Körner V. Lyubovitskij and V. Matveev for valuable discussions and support. We thank the organizers of the Helmholtz International Summer School "Quantum Field Theory at the Limits: from Strong Fields to Heavy Quarks" for the invitation to participate in such a pleasant and productive meeting.

References

[1] D. Ebert, R. N. Faustov and V. O. Galkin, Phys. Lett. B **634**, 214 (2006); Eur. Phys. J. C **58**, 399 (2008).

[2] D. Ebert, R. N. Faustov and V. O. Galkin, Eur. Phys. J. C **60**, 273 (2009).

[3] V. Crede and W. Roberts, Rept. Prog. Phys. **76**, 076301 (2013).

[4] D. Ebert, V. O. Galkin and R. N. Faustov, Phys. Rev. D **57**, 5663 (1998) Erratum: [Phys. Rev. D **59**, 019902 (1999)]; Phys. Rev. D **67**, 014027 (2003).

[5] D. Ebert, R. N. Faustov and V. O. Galkin, Phys. Rev. D **84**, 014025 (2011).

[6] R. N. Faustov and V. O. Galkin, Phys. Rev. D **92**, no. 5, 054005 (2015).

[7] S. Capstick and N. Isgur, Phys. Rev. D **34**, 2809 (1986).

[8] U. Loring, B. C. Metsch and H. R. Petry, Eur. Phys. J. A **10**, 447 (2001).

[9] T. Melde, W. Plessas and B. Sengl, Phys. Rev. D **77**, 114002 (2008).

[10] K.A. Olive *et al.* (Particle Data Group), Chin. Phys. C, **38**, 090001 (2014).

[11] B. Chen, K. W. Wei and A. Zhang, Eur. Phys. J. A **51**, 82 (2015).

[12] E. Santopinto and J. Ferretti, Phys. Rev. C **92**, no. 2, 025202 (2015).

[13] G. P. Engel *et al.* [BGR Collaboration], Phys. Rev. D **87**, no. 7, 074504 (2013).

[14] D. Ebert, R. N. Faustov and V. O. Galkin, Phys. Rev. D **73**, 094002 (2006).

[15] R. N. Faustov and V. O. Galkin, Phys. Rev. D **94**, no. 7, 073008 (2016); Eur. Phys. J. C **76**, 628 (2016).

[16] T. Gutsche, M. A. Ivanov, J. G. Körner, V. E. Lyubovitskij, P. Santorelli and N. Habyl, Phys. Rev. D **91**, no. 7, 074001 (2015) Erratum: [Phys. Rev. D **91**, no. 11, 119907 (2015)].

[17] T. Gutsche, M. A. Ivanov, J. G. Körner, V. E. Lyubovitskij and P. Santorelli, Phys. Rev. D **90**, no. 11, 114033 (2014); Phys. Rev. D **93**, no. 3, 034008 (2016).

[18] M. Pervin, W. Roberts and S. Capstick, Phys. Rev. C **72**, 035201 (2005).

[19] R. Dutta, Phys. Rev. D **93**, no. 5, 054003 (2016).

[20] H. W. Ke, X. Q. Li and Z. T. Wei, Phys. Rev. D **77**, 014020 (2008); Z. T. Wei, H. W. Ke and X. Q. Li, Phys. Rev. D **80**, 094016 (2009).

[21] A. Khodjamirian, C. Klein, T. Mannel and Y.-M. Wang, JHEP **1109**, 106 (2011).

[22] W. Detmold, C. Lehner and S. Meinel, Phys. Rev. D **92**, no. 3, 034503 (2015).

[23] D. Ebert, R. N. Faustov and V. O. Galkin, Phys. Rev. D **75**, 074008 (2007); R. N. Faustov and V. O. Galkin, Mod. Phys. Lett. A **27**, 1250183 (2012); Eur. Phys. J. C **74**, no. 6, 2911 (2014).

[24] R. Aaij *et al.* [LHCb Collaboration], Nature Phys. **11**, 743 (2015).

Spectroscopy and Regge Trajectories of Light Mesons

D. Ebert[1], *R. N. Faustov*[2], *V. O. Galkin*[2]

[1]Institut für Physik, Humboldt–Universität zu Berlin, Newtonstr. 15, D-12489 Berlin, Germany
[2]Institute of Informatics in Education, FRC CSC RAS, Vavilov Str. 40, 119991 Moscow, Russia

DOI: http://dx.doi.org/10.3204/DESY-PROC-2016-04/Faustov

Masses of light tetraquarks are obtained in the diquark-antidiquark picture. Such exotic states can be identified with the known light scalar mesons forming an SU(3) nonet (σ meson $f_0(600)$, κ meson $K_0^*(800)$, $f_0(980)$ and $a_0(980)$). Mass spectra of light (u,d,s) quark-antiquark mesons are calculated within the QCD-motivated relativistic quark model.The relativistic treatment of the light quark dynamics results in mass spectra which agree well with available experimental data for the masses of the most well-established states. Their Regge trajectories exhibit linearity and equidistance.

The consistent theoretical understanding of the light meson sector remains an important problem already for many years [1]. An extensive analysis of the data on highly excited light non-strange meson states up to a mass of 2400 MeV collected by Crystal Barrel experiment at LEAR (CERN) has been published. Classification of these new data requires better theoretical description of light meson mass spectra. This is especially important, since light exotic states (such as tetraquarks, glueballs, hybrids) within quantum chromodynamics (QCD) are expected to have masses in this range. Particular interest is focused on scalar mesons, their properties and abundance. A generally accepted consistent picture has not yet emerged. Experimental and theoretical evidence for the existence of $f_0(600)(\sigma)$, $K_0^*(800)(\kappa)$, $f_0(980)$ and $a_0(980)$ indicates that lightest scalars form a complete $SU(3)$ flavour nonet. A peculiar feature of their mass spectrum is the inversion of the mass ordering, which cannot be naturally understood in the $q\bar{q}$ picture. This fact stimulated various alternative interpretations of light scalars as four quark states (tetraquarks) in particular diquark-antidiquark bound states. The proximity of f_0/a_0 to the $K\bar{K}$ threshold led to the $K\bar{K}$ molecular picture.

In the quasipotential approach and diquark-antidiquark picture of tetraquarks the interaction of two quarks in a diquark and the diquark-antidiquark interaction in a tetraquark are described by the diquark wave function (Ψ_d) of the bound quark-quark state and by the tetraquark wave function (Ψ_T) of the bound diquark-antidiquark state, respectively. These wave functions satisfy the quasipotential equation of the Schrödinger type [2]

$$\left(\frac{b^2(M)}{2\mu_R}-\frac{\mathbf{p}^2}{2\mu_R}\right)\Psi_{d,T}(\mathbf{p})=\int\frac{d^3q}{(2\pi)^3}V(\mathbf{p},\mathbf{q};M)\Psi_{d,T}(\mathbf{q}), \tag{1}$$

where the relativistic reduced mass is

$$\mu_R=\frac{E_1E_2}{E_1+E_2}=\frac{M^4-(m_1^2-m_2^2)^2}{4M^3}, \tag{2}$$

State J^{PC}	Diquark content	Theory mass	Experiment $I=0$	mass	$I=1$	mass
$(qq)(\bar{q}\bar{q})$						
0^{++}	$S\bar{S}$	596	$f_0(600)$ (σ)	400-1200		-
$1^{+\pm}$	$(S\bar{A} \pm \bar{S}A)/\sqrt{2}$	672				
0^{++}	$A\bar{A}$	1179	$f_0(1370)$	1200-1500		
1^{+-}	$A\bar{A}$	1773				
2^{++}	$A\bar{A}$	1915	$f_2(1910)$ $f_2(1950)$	1903(9) 1944(12)		
$(qs)(\bar{q}\bar{s})$						
0^{++}	$S\bar{S}$	992	$f_0(980)$	980(10)	$a_0(980)$	984.7(12)
1^{++}	$(S\bar{A} + \bar{S}A)/\sqrt{2}$	1201	$f_1(1285)$	1281.8(6)	$a_1(1260)$	1230(40)
1^{+-}	$(S\bar{A} - \bar{S}A)/\sqrt{2}$	1201	$h_1(1170)$	1170(20)	$b_1(1235)$	1229.5(32)
0^{++}	$A\bar{A}$	1480	$f_0(1500)$	1505(6)	$a_0(1450)$	1474(19)
1^{+-}	$A\bar{A}$	1942	$h_1(1965)$	1965(45)	$b_1(1960)$	1960(35)
2^{++}	$A\bar{A}$	2097	$f_2(2010)$ $f_2(2140)$	2011(70) 2141(12)	$a_2(1990)$ $a_2(2080)$	2050(45) 2100(20)
$(ss)(\bar{s}\bar{s})$						
0^{++}	$A\bar{A}$	2203	$f_0(2200)$	2189(13)		-
1^{+-}	$A\bar{A}$	2267	$h_1(2215)$	2215(40)		-
2^{++}	$A\bar{A}$	2357	$f_2(2340)$	2339(60)		-

Table 1: Masses of light unflavored diquark-antidiquark ground state ($\langle \mathbf{L}^2 \rangle$=0) tetraquarks (in MeV) and possible experimental candidates. S and A denote scalar and axial vector diquarks.

and E_1, E_2 are given by

$$E_1 = \frac{M^2 - m_2^2 + m_1^2}{2M}, \quad E_2 = \frac{M^2 - m_1^2 + m_2^2}{2M}. \tag{3}$$

Here, $M = E_1 + E_2$ is the bound-state mass (diquark or tetraquark), $m_{1,2}$ are the masses of quarks ($q = u, d$ and s) which form the diquark or of the diquark (d) and antidiquark ($\bar{d}'$) which form the light tetraquark (T), and $\mathbf{p}$ is their relative momentum. In the center-of-mass system the relative momentum squared on mass shell reads

$$b^2(M) = \frac{[M^2 - (m_1 + m_2)^2][M^2 - (m_1 - m_2)^2]}{4M^2}. \tag{4}$$

The kernel $V(\mathbf{p}, \mathbf{q}; M)$ in Eq. (1) is the quasipotential operator of the quark-quark or diquark-antidiquark interaction. It is constructed with the help of the off-mass-shell scattering amplitude, projected onto the positive-energy states. For the quark-quark interaction in a diquark we use the relation $V_{qq} = V_{q\bar{q}}/2$ arising under the assumption of an octet structure of the interaction from the difference in the qq and $q\bar{q}$ colour states. An important role in this construction is played by the Lorentz structure of the confining interaction. In our analysis of mesons, while constructing the quasipotential of the quark-antiquark interaction, we assumed that the effective interaction is the sum of the usual one-gluon exchange term and a mixture of long-range vector and scalar linear confining potentials, where the vector confining potential

State J^P	Diquark content	Theory mass	Experiment $I=\frac{1}{2}$	mass
$(qq)(\bar{s}\bar{q})$ or $(sq)(\bar{q}\bar{q})$				
0^+	$S\bar{S}$	730	$K_0^*(800)$ (κ)	672(40)
1^+	$(S\bar{A}\pm\bar{S}A)/\sqrt{2}$	1057		
0^+	$A\bar{A}$	1332	$K_0^*(1430)$	1425(50)
1^+	$A\bar{A}$	1855		
2^+	$A\bar{A}$	2001	$K_2^*(1980)$	1973(26)

Table 2: Masses of strange diquark-antidiquark ground state ($\langle\mathbf{L}^2\rangle$=0) tetraquarks (in MeV) and possible experimental candidates. S and A denote scalar and axial vector diquarks.

contains the Pauli term. We use the same conventions for the construction of the quark-quark and diquark-antidiquark interactions in the tetraquark.

At the first step, we take the masses and form factors of the light diquarks from the previous consideration of light diquarks in heavy baryons. At the second step, we calculate the masses of light tetraquarks considered as the bound states of a light diquark and antidiquark.

The obtained mass spectra of ground state light tetraquarks are presented in Tables 1 and 2. We see that the diquark-antidiquark picture can provide a natural explanation for the inversion of masses of light scalar 0^+ mesons. Indeed all lightest experimentally observed scalar mesons $f_0(600)$ (σ), $K_0^*(800)$ (κ), $f_0(980)$ and $a_0(980)$ can be interpreted in our model as light tetraquarks composed from a scalar diquark and antidiquark $(S\bar{S})$. Therefore, the $f_0(980)$ and $a_0(980)$ tetraquarks contain, in comparison to the $q\bar{q}$ picture, an additional pair of strange quarks which gives a natural explanation why their masses are heavier than the strange $K_0^*(800)$ (κ).

The other scalar tetraquark states can be composed from an axial vector diquark and antidiquark $(A\bar{A})$. Their masses are predicted to be approximately 600 MeV heavier than the $S\bar{S}$ tetraquarks (S is a scalar diquark). The diquark-antidiquark composition also naturally explains the experimentally observed proximity of masses of the unflavored $a_0(1450)$, $f_0(1500)$ and strange $K_0^*(1430)$ scalars.

The calculated masses of light unflavoured and strange $(q\bar{q})$ mesons are given in Tables 3 and 4 taken form Ref. [3]. As already discussed above, the scalar sector presents a special interest due to its complexity and the abundance of experimentally observed light states. We see from Table 3 that the masses of the lightest $q\bar{q}$ scalar mesons have values about 1200 MeV. This confirms our conclusion [2] that light scalar mesons, $f_0(600)$ (σ), $K_0^*(800)$ (κ), $f_0(980)$ and $a_0(980)$, with masses below 1 GeV should be described as light tetraquarks consisting from scalar diquark and antidiquark. Moreover the predicted masses of the scalar tetraquarks composed from axial-vector diquark and antidiquark [2] have masses in the same range as the lowest $q\bar{q}$ scalar mesons. The obtained results for the masses indicate that $a_0(1450)$ should be predominantly a tetraquark state which predicted [2] mass 1480 MeV is within experimental error bars of $M_{a_0(1450)} = 1474 \pm 19$ MeV. The exotic scalar state $X(1420)$ from the "Further States" Section [4] could be its isotensor partner. On the other hand $s\bar{q}(1^3P_0)$ interpretation is favored for $K_0^*(1430)$ (see Table 4). This picture naturally explains the experimentally observed proximity of masses of the unflavoured $a_0(1450)$ and $f_0(1500)$ with the strange $K_0^*(1430)$. Therefore one could expect an additional predominantly $q\bar{q}$ isovector state a_0 with the mass about 1200 MeV, though it was not observed in several experiments.

Some of the Regge trajectories both in (M^2,J) and (M^2, n_r) planes (M is the mass, J is the spin and n_r is the radial quantum number of the meson state) are shown in Figs. 1-7.

		Theory	Experiment				Theory	Experiment	
$n^{2S+1}L_J$	J^{PC}	$q\bar{q}$	$I=1$	mass	$I=0$	mass	$s\bar{s}$	$I=0$	mass
1^1S_0	0^{-+}	154	π	139.57			743		
1^3S_1	1^{--}	776	ρ	775.49(34)	ω	782.65(12)	1038	φ	1019.455(20)
1^3P_0	0^{++}	1176	a_0	1474(19)	f_0	1200-1500	1420	f_0	1505(6)
1^3P_1	1^{++}	1254	a_1	1230(40)	f_1	1281.8(6)	1464	f_1	1426.4(9)
1^3P_2	2^{++}	1317	a_2	1318.3(6)	f_2	1275.1(12)	1529	f_2'	1525(5)
1^1P_1	1^{+-}	1258	b_1	1229.5(32)	h_1	1170(20)	1485	h_1	1386(19)
2^1S_0	0^{-+}	1292	π	1300(100)	η	1294(4)	1536	η	1476(4)
2^3S_1	1^{--}	1486	ρ	1465(25)	ω	1400-1450	1698	φ	1680(20)
1^3D_1	1^{--}	1557	ρ	1570(70)	ω	1670(30)	1845		
1^3D_2	2^{--}	1661					1908		
1^3D_3	3^{--}	1714	ρ_3	1688.8(21)	ω_3	1667(4)	1950	φ_3	1854(7)
1^1D_2	2^{-+}	1643	π_2	1672.4(32)	η_2	1617(5)	1909	η_2	1842(8)
2^3P_0	0^{++}	1679			f_0	1724(7)	1969		
2^3P_1	1^{++}	1742	a_1	1647(22)			2016	f_1	1971(15)
2^3P_2	2^{++}	1779	a_2	1732(16)	f_2	1755(10)	2030	f_2	2010(70)
2^1P_1	1^{+-}	1721					2024		
3^1S_0	0^{-+}	1788	π	1816(14)	η	1756(9)	2085	η	2103(50)
3^3S_1	1^{--}	1921	ρ	1909(31)	ω	1960(25)	2119	φ	2175(15)
1^3F_2	2^{++}	1797			f_2	1815(12)	2143	f_2	2156(11)
1^3F_3	3^{++}	1910	a_3	1874(105)			2215	f_3	2334(25)
1^3F_4	4^{++}	2018	a_4	2001(10)	f_4	2018(11)	2286		
1^1F_3	3^{+-}	1884					2209	h_3	2275(25)
2^3D_1	1^{--}	1895	ρ	1909(31)			2258	ω	2290(20)
2^3D_2	2^{--}	1983	ρ_2	1940(40)	ω_2	1975(20)	2323		
2^3D_3	3^{--}	2066					2338		
2^1D_2	2^{-+}	1960	π_2	1974(84)	η_2	2030(20)	2321		
3^3P_0	0^{++}	1993	a_0	2025(30)	f_0	1992(16)	2364	f_0	2314(25)
3^3P_1	1^{++}	2039	a_1	2096(123)			2403		
3^3P_2	2^{++}	2048	a_2	2050(42)	f_2	2001(10)	2412	f_2	2339(60)
3^1P_1	1^{+-}	2007	b_1	1960(35)	h_1	1965(45)	2398		
4^1S_0	0^{-+}	2073	π	2070(35)	η	2010(50)	2439		
4^3S_1	1^{--}	2195	ρ	2265(40)	ω	2205(30)	2472		
1^3G_3	3^{--}	2002	ρ_3	1982(14)	ω_3	1945(20)	2403		
1^3G_4	4^{--}	2122	ρ_4	2230(25)	ω_4	2250(30)	2481		
1^3G_5	5^{--}	2264	ρ_5	2300(45)	ω_5	2250(70)	2559		
1^1G_4	4^{-+}	2092					2469		
3^3D_1	1^{--}	2168	ρ	2149(17)			2607		
3^3D_2	2^{--}	2241	ρ_2	2225(35)	ω_2	2195(30)	2667		
3^3D_3	3^{--}	2309	ρ_3	2300(60)	ω_3	2278(28)	2727		
3^1D_2	2^{-+}	2216	π_2	2245(60)	η_2	2248(20)	2662		
2^3F_2	2^{++}	2091	a_2	2100(20)	f_2	2141(12)	2514		

Table 3: Masses of excited light unflavored mesons (in MeV).

		Theory	Experiment				Theory	Experiment	
$n^{2S+1}L_J$	J^{PC}	$q\bar{q}$	$I=1$	mass	$I=0$	mass	$s\bar{s}$	$I=0$	mass
2^3F_3	3^{++}	2191	a_3	2070(20)			2585		
2^3F_4	4^{++}	2284			f_4	2320(60)	2657		
2^1F_3	3^{+-}	2164	b_3	2245(50)			2577		
4^3P_0	0^{++}	2250			f_0	2189(13)	2699		
4^3P_1	1^{++}	2286	a_1	2270(50)	f_1	2310(60)	2729		
4^3P_2	2^{++}	2297	a_2	2280(30)	f_2	2297(28)	2734		
4^1P_1	1^{+-}	2264	b_1	2240(35)	h_1	2215(40)	2717		
2^3G_3	3^{--}	2267	ρ_3	2260(20)	ω_3	2255(15)	2743		
2^3G_4	4^{--}	2375					2819		
2^3G_5	5^{--}	2472					2894		
2^1G_4	4^{-+}	2344	π_4	2250(15)	η_4	2328(30)	2806		
5^1S_0	0^{-+}	2385	π	2360(25)	η	2320(15)	2749		
5^3S_1	1^{--}	2491					2782		
1^3H_4	4^{++}	2234	a_4	2237(5)	f_J	2231.1(35)	2634		
1^3H_5	5^{++}	2359					2720		
1^3H_6	6^{++}	2475	a_6	2450(130)	f_6	2465(50)	2809		
1^1H_5	5^{+-}	2328					2706		

Table 3: Masses of excited light unflavored mesons (in MeV)(continued).

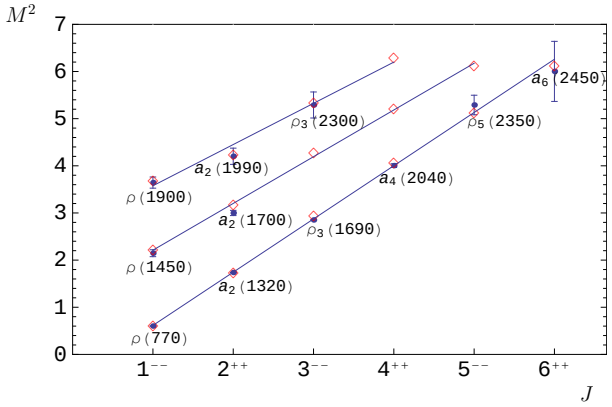


Figure 1: Parent and daughter (J, M^2) Regge trajectories for isovector light mesons with natural parity (ρ). Diamonds are predicted masses. Available experimental data are given by dots with error bars and particle names. M^2 is in GeV^2.

We see that the calculated light meson masses fit nicely to the linear trajectories. These trajectories are almost parallel and equidistant. It is important to note that the quality of fitting the π meson Regge trajectories is significantly improved if the ground state π is excluded from the fit. In the kaon case omitting the ground state also improves the fit but not so dramatically as for the pion. The corresponding trajectories are shown in Figs. 4 and 5 by dashed lines. This indicates the special role of the pion originating from the chiral symmetry breaking. The fitted

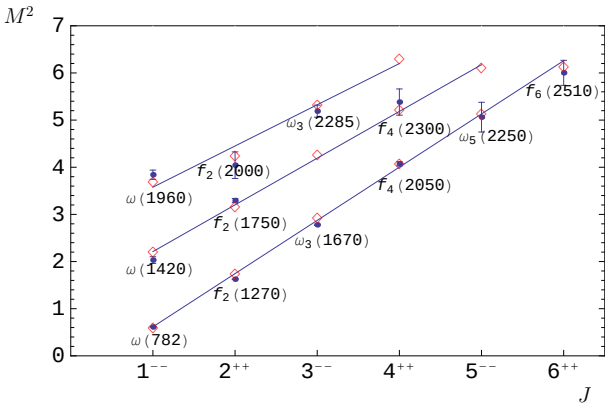


Figure 2: Same as in Fig. 1 for isoscalar light $q\bar{q}$ mesons with natural parity (ω).

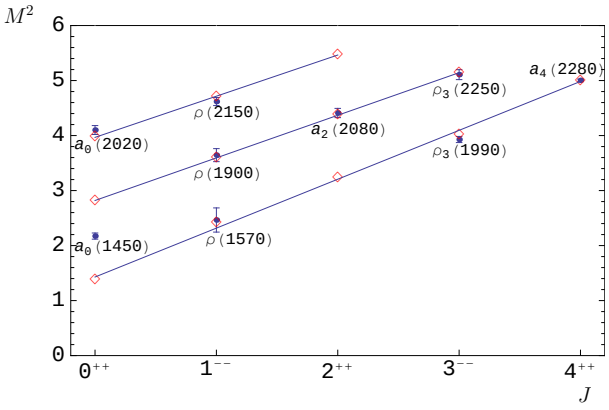


Figure 3: Same as in Fig. 1 for isovector light $q\bar{q}$ mesons with natural parity (a_0).

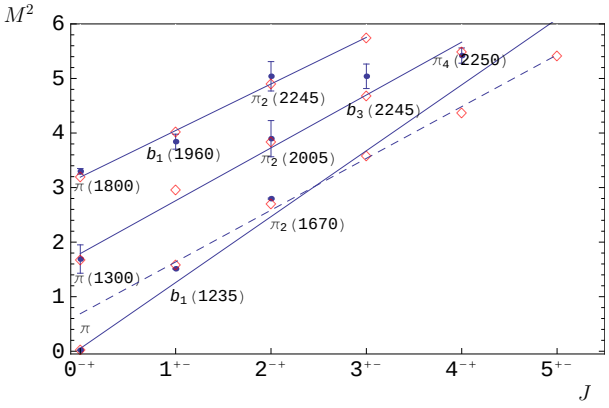


Figure 4: Same as in Fig. 1 for isovector light mesons with unnatural parity (π). Dashed line corresponds to the Regge trajectory, fitted without π.

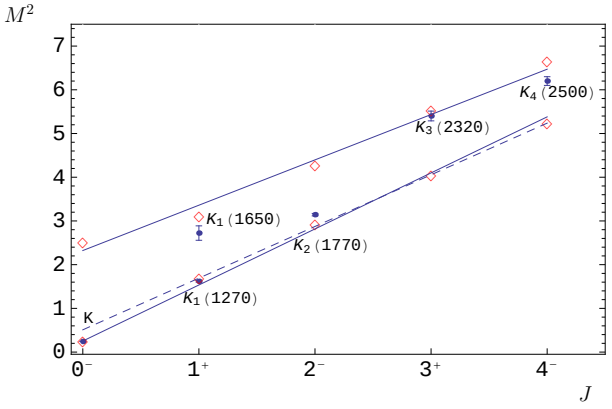


Figure 5: Same as in Fig. 1 for isodublet light mesons with unnatural parity (K). Dashed line corresponds to the Regge trajectory, fitted without K.

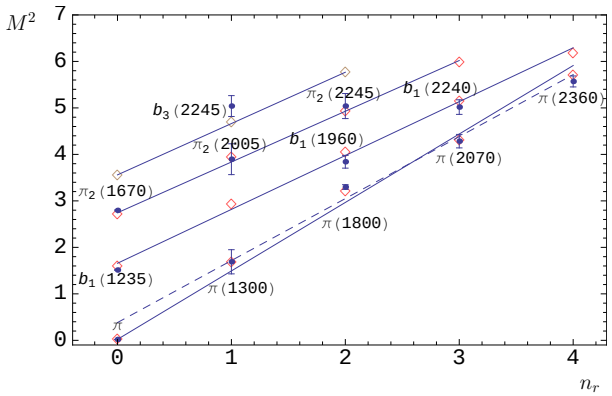


Figure 6: The (n_r, M^2) Regge trajectories for spin-singlet isovector mesons π, b_1, π_2 and b_3 (from bottom to top). Notations are the same as in Fig. 1. The dashed line corresponds to the Regge trajectory, fitted without π.

		Theory	Experiment				Theory	Experiment	
$n^{2S+1}L_J$	J^P	$q\bar{s}$	$I=1/2$	mass	$n^{2S+1}L_j$	J^P	$q\bar{s}$	$I=1/2$	mass
1^1S_0	0^-	482	K	493.677(16)	3^1S_0	0^-	2065		
1^3S_1	1^-	897	K^*	891.66(26)	3^3S_1	1^-	2156		
1^3P_0	0^+	1362	K_0	1425(50)	2^3D_1	1^-	2063		
1^3P_2	2^+	1424	K_2^*	1425.6(15)	2^3D_3	3^-	2182		
$1P_1$	1^+	1412	K_1	1403(7)	$2D_2$	2^-	2163	K_2	2247(17)
$1P_1$	1^+	1294	K_1	1272(7)	$2D_2$	2^-	2066		
2^1S_0	0^-	1538			3^3P_0	0^+	2160		
2^3S_1	1^-	1675	K^*		3^3P_2	2^+	2206		
1^3D_1	1^-	1699	K^*	1717(27)	$3P_1$	1^+	2200		
1^3D_3	3^-	1789	K_3^*	1776(7)	$3P_1$	1^+	2164		
$1D_2$	2^-	1824	K_2	1816(13)	1^3G_3	3^-	2207		
$1D_2$	2^-	1709	K_2	1773(8)	1^3G_5	5^-	2356	K_5^*	2382(24)
2^3P_0	0^+	1791			$1G_4$	4^-	2285		
2^3P_2	2^+	1896			$1G_4$	4^-	2255		
$2P_1$	1^+	1893			2^3F_4	4^+	2436		
$2P_1$	1^+	1757	K_1	1650(50)	$2F_3$	3^+	2348	K_3	2324(24)
1^3F_2	2^+	1964	K_2^*	1973(26)	2^3G_5	5^-	2656		
1^3F_4	4^+	2096	K_4^*	2045(9)	$2G_4$	4^-	2575	K_4	2490(20)
$1F_3$	3^+	2080							
$1F_3$	3^+	2009							

Table 4: Masses of excited strange mesons (in MeV).

slopes and intercepts of the Regge trajectories are given in Tables 5 and 6.

It can be seen in Figs. 1 and 3 that $\rho(1700)$ and $a_0(1450)$ do not lie on the corresponding Regge trajectories. This further confirms our previous conclusion that $a_0(1450)$ should be predominantly a tetraquark state and suggests the possible exotic nature of $\rho(1700)$.

From the comparison of the slopes in Tables 5, 6 we see that the α values are systematically larger than the β ones. The ratio of their mean values is about 1.3 both for the light $q\bar{q}$ isovector and $s\bar{s}$ mesons. Such ratio is lower than predictions of the QCD string model $\alpha/\beta = 2$ and massless Salpeter equation $\alpha/\beta = \pi/2$ [3]. The mean value of the slope $\beta \sim 0.85$ GeV^{-2} for isovector mesons is about two times larger than the result of the above mentioned models, namely, $\beta = 1/(4\pi A) \approx 0.44$ GeV^{-2}, for $A = 0.18$ GeV^2 used in our approach.

The assignment of the experimentally observed states to the corresponding Regge trajectories in our model based on their masses and J^{PC} values (see Figs. 1-7) is slightly different from the previous phenomenological analysis [5, 6] based on the equal values for the slopes α and β. However the number of states, for which such correspondence is found, is approximately the same. Future experimental data will shed further light on this issue.

In summary, we presented the masses of the ground state light tetraquarks in the diquark-antidiquark picture, the mass spectra and Regge trajectories of light $q\bar{q}$ mesons. In distinction with previous phenomenological treatments, we used the dynamical approach based on the relativistic quark model. Both diquark and tetraquark masses were obtained by numerical solution of the quasipotential wave equations. The diquark structure was taken into account by using diquark-gluon form factors in terms of diquark wave functions. It is important to

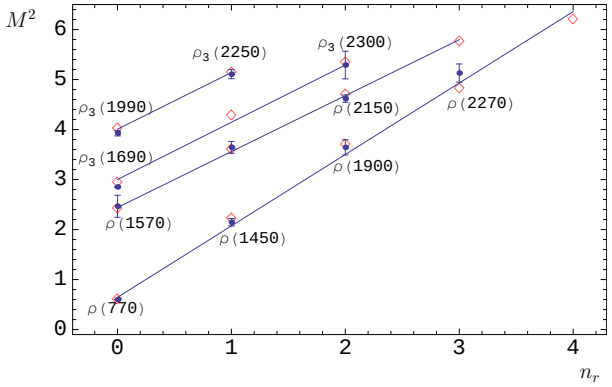


Figure 7: The (n_r, M^2) Regge trajectories for spin-triplet isovector mesons $\rho(^3S_1)$, $\rho(^3D_1)$, $\rho_3(^3D_3)$ and $\rho_3(^3G_3)$ (from bottom to top). Notations are the same as in Fig. 1.

Trajectory	natural parity		unnatural parity	
	α (GeV^{-2})	α_0	α (GeV^{-2})	α_0
$q\bar{q}$	ρ		π	
parent	0.887 ± 0.008	0.456 ± 0.018	$0.828 \pm 0.057^*$	$-0.025 \pm 0.034^*$
daughter 1	1.009 ± 0.019	-1.232 ± 0.074	1.031 ± 0.063	-1.846 ± 0.217
daughter 2	1.144 ± 0.113	-3.092 ± 0.540	1.171 ± 0.009	-3.737 ± 0.042
$q\bar{q}$	a_0		a_1	
parent	1.125 ± 0.035	-1.607 ± 0.104	1.014 ± 0.036	-0.658 ± 0.120
daughter 1	1.291 ± 0.003	-3.640 ± 0.011	1.148 ± 0.012	-2.497 ± 0.050
daughter 2	1.336 ± 0.022	-5.300 ± 0.102	1.154 ± 0.014	-3.798 ± 0.007
$q\bar{s}$	K^*		K	
parent	0.839 ± 0.004	0.318 ± 0.012	$0.780 \pm 0.022^\dagger$	$-0.197 \pm 0.036^\dagger$
daughter	0.942 ± 0.046	-1.532 ± 0.209	0.964 ± 0.072	-2.240 ± 0.296
$s\bar{s}$	φ		$\eta_{s\bar{s}}$	
parent	0.728 ± 0.011	0.234 ± 0.034	0.715 ± 0.023	-0.444 ± 0.068
daughter 1	0.721 ± 0.089	-1.072 ± 0.047	0.718 ± 0.032	-1.786 ± 0.157
daughter 2	0.684 ± 0.039	-2.047 ± 0.226	0.729 ± 0.010	-3.174 ± 0.057

* fit without π: $\alpha = (1.053 \pm 0.059)$ GeV^{-2} , $\alpha_0 = -0.725 \pm 0.170$
† fit without K: $\alpha = (0.846 \pm 0.013)$ GeV^{-2} , $\alpha_0 = -0.431 \pm 0.042$

Table 5: Fitted parameters of the (J, M^2) parent and daughter Regge trajectories for light mesons with natural and unnatural parity ($q = u, d$).

Meson	β (GeV^{-2})	β_0	Meson	β (GeV^{-2})	β_0
$q\bar{q}$			$s\bar{s}$		
π	$0.679 \pm 0.023^*$	$-0.018 \pm 0.014^*$	$\eta_{s\bar{s}}$	0.559 ± 0.009	-0.315 ± 0.026
$\rho(^3S_1)$	0.700 ± 0.023	-0.451 ± 0.060	φ	0.597 ± 0.009	-0.662 ± 0.031
a_0	0.830 ± 0.032	-1.214 ± 0.109	f_0	0.566 ± 0.009	-1.156 ± 0.039
a_1	0.840 ± 0.037	-1.401 ± 0.134	f_1	0.561 ± 0.013	-1.224 ± 0.058
b_1	0.863 ± 0.030	-1.431 ± 0.106	h_1	0.575 ± 0.015	-1.292 ± 0.066
$a_2(^3P_2)$	0.867 ± 0.036	-1.585 ± 0.134	f_2	0.581 ± 0.007	-1.370 ± 0.031
$\rho(^3D_1)$	0.894 ± 0.013	-2.182 ± 0.050			
π_2	0.916 ± 0.032	-2.514 ± 0.134			
$\rho_3(^3D_3)$	0.874 ± 0.041	-2.623 ± 0.189			
$a_2(^3F_2)$	0.891 ± 0.010	-2.881 ± 0.043			
a_3	0.890 ± 0.014	-3.254 ± 0.066			
b_3	0.906 ± 0.015	-3.225 ± 0.071			
a_4	0.899 ± 0.016	-3.672 ± 0.084			

* fit without π: $\beta = (0.750 \pm 0.032)$ GeV^{-2}, $\beta_0 = -0.287 \pm 0.109$

Table 6: Fitted parameters of the (n_r, M^2) Regge trajectories for light mesons.

emphasize that, in our analysis, we did not introduce any free adjustable parameters but used their values fixed from our previous considerations of hadron properties. It was found that the lightest scalar mesons $f_0(600)$ (σ), $K_0^*(800)$ (κ), $f_0(980)$ and $a_0(980)$ can be naturally described in our model as diquark-antidiquark bound systems, while the lightest scalar (1^3P_0) $q\bar{q}$ states have masses above 1 GeV.

The authors are grateful to M. Ivanov, V. Lyubovitskij and V. Matveev for valuable discussions and support. We thank the the organizers of the Helmholtz International Summer School "Quantum Field Theory at the Limits: from Strong Fields to Heavy Quarks" for the invitation to participate in such a pleasant and productive meeting.

References

[1] T. Branz, A. Faessler, T. Gutsche, M. A. Ivanov, J. G. Korner and V. E. Lyubovitskij, Phys. Rev. D **81**, 034010 (2010).

[2] D. Ebert, R. N. Faustov and V. O. Galkin, Eur. Phys. J. C **60**, 273 (2009).

[3] D. Ebert, R. N. Faustov and V. O. Galkin, Phys. Rev. D **79**, 114029 (2009).

[4] K.A. Olive *et al.* (Particle Data Group), Chin. Phys. C, **38**, 090001 (2014).

[5] A. V. Anisovich, V. V. Anisovich and A. V. Sarantsev, Phys. Rev. D **62**, 051502 (2000); V. V. Anisovich, L. G. Dakhno, M. A. Matveev, V. A. Nikonov and A. V. Sarantsev, Phys. Atom. Nucl. **70**, 450 (2007).

[6] S. S. Afonin, Phys. Rev. C **76**, 015202 (2007).

Non-Leptonic Two-Body Decays of Charmed Mesons and CP Violation

Pietro Santorelli

Dipartimento di Fisica "E. Pancini" - Università di Napoli Federico II
Complesso Universitario di Monte Sant'Angelo, Via Cintia
I-80126 Napoli Italy
& INFN, Sezione di Napoli, Napoli Italy

DOI: http://dx.doi.org/10.3204/DESY-PROC-2016-04/Santorelli

The nonleptonic two body decays of the D and D_s mesons represent a key subject to study possible effects of CP violation. The attention for these decay modes was triggered four years ago by the results of measurements of the difference between CP asymmetries in charged KK and $\pi\pi$ final state, $\Delta a_{\rm CP}$. Although the measured $\Delta a_{\rm CP}$ is now compatible with zero the nonleptonic decays of charmed mesons into a pair of light mesons is an interesting subject for many reasons. Here we discuss phenomenological models to study the decays into two pseudoscalar mesons.

1 Introduction

The study of nonleptonic decays of charmed mesons is particularly interesting for many reasons.

- These decays give us the possibility to study the CP violation effects in the case of a quark of up-type. In fact the Singly Cabibbo Suppressed (SCS) decay amplitudes receive contribution from current-current operators and from penguin operators with different weak phases. This is the necessary condition to reveal CP violating effects. In fact it is possible to show that the amplitudes for SCS decay modes can be written as

$$\mathcal{A}^{SCS} = \frac{1}{2}(V_{cs}^* V_{us} - V_{cd}^* V_{ud}) A^{(1,2)}\, e^{\imath\delta} - \frac{1}{2} V_{cb}^* V_{ub} A^{(P)}\, e^{\imath\delta'}\,, \tag{1}$$

  where the $A^{(1,2)}$ and $A^{(P)}$ are the tree and the penguin amplitudes, respectively. While δ and δ' are strong phases. The related CP direct asymmetry is

$$a_{\rm CP} = \frac{|\mathcal{A}|^2 - |\bar{\mathcal{A}}|^2}{|\mathcal{A}|^2 + |\bar{\mathcal{A}}|^2} = \eta A^2 \lambda^4 \sin(\delta - \delta') \left[\frac{A^{(P)}}{A^{(1,2)}}\right] \approx (6 \times 10^{-4})\ \sin(\delta - \delta') \left[\frac{A^{(P)}}{A^{(1,2)}}\right]. \tag{2}$$

  The estimation of $a_{\rm CP}$ requires the calculation of the strong phases, which are expected to be large due to the presence of resonances with masses near to the mass of D mesons, and hadronic amplitudes, $A^{(P)}$ and $A^{(1,2)}$.

- The calculation of the hadronic amplitudes represents a very challenging goal. The mass of the charm quark is not enough large to benefit from the powerful approach of Heavy

Quark Effective Theory [1]. Neither it is possible to use the Chiral Perturbation Theory because the charm mass it too large respect the scale of the strong interactions. The only available first principle calculational method remains the lattice, but for now this approach is not reliable for the charmed mesons. Meanwhile, these processes are studied by phenomenological models.

In the following we will consider the decays of D and D_s mesons in two pseudoscalar mesons in the framework of the Standard Model and in particular we will focus our attention on the use of $SU(3)_F$ symmetry. This approach dates back to the discovery of the J/ψ meson [2, 3, 4, 5]. However, we limit ourself to review literature on the subject after 2012, the year of the first experimental measurements of $\Delta a_{\rm CP} = a_{\rm CP}(D^0 \to K^+K^-) - a_{\rm CP}(D^0 \to \pi^+\pi^-)$ [6, 7] [1]. The first large measured value of $\Delta a_{\rm CP}$ triggered a lot of research devoted to understand this result. There was two different and well motivated positions respect to the compatibility of the data with the Standard Model. Many authors supported the idea that direct CP violation of the order of 1% in the charm sector is a clear sign of New Physics effects [13]. Many others [14] have arguments in favor of the possibility to account for large CP violation effects in the Standard Model as a consequence of large phases coming from Final State interaction (FSI).

2 The $D \to PP$ decay modes and $SU(3)_F$ symmetry

The decays of D and D_s mesons into two light ones can, in principle, be studied by assuming $SU(3)_F$ flavour symmetry. In the case of two pseudoscalar mesons the idea is to classify the final states as the symmetric part of product of the two octets[2], which classifies the pions, kaons and the η_8

$$PP \sim (\mathbf{8} \otimes \mathbf{8})_S = \mathbf{1} \oplus \mathbf{8} \oplus \mathbf{27}\,. \tag{3}$$

The D mesons can be regarded as members of a anti-triplet of $SU(3)_F$, $(D^0, D^+, D_s) \sim \overline{\mathbf{3}}$; while, being the effective hamiltonian responsible of charm decays made of three light quark fields and one charm field, it is given by the tensor product

$$\mathcal{H} \sim \mathbf{3} \otimes \overline{\mathbf{3}} \otimes \mathbf{3} \sim \mathbf{3} \oplus \mathbf{3'} \oplus \overline{\mathbf{6}} \oplus \mathbf{15}\,. \tag{4}$$

The physical amplitudes in this approach are given by

$$\langle PP|\,\mathcal{H}\,|D\rangle \sim \langle \mathbf{1} \oplus \mathbf{8} \oplus \mathbf{27}|\,\left(\mathbf{3} \oplus \overline{\mathbf{6}} \oplus \mathbf{15}\right)\,\left|\overline{\mathbf{3}}\right\rangle\,. \tag{5}$$

The Wigner-Eckart theorem allow us to write all the amplitudes (corresponding to well defined initial and final state, they are fixed by their values of the isospin, and hypercharge operators) in terms of three unknown Reduced Matrix Elements (RME)[3]

$$\langle \mathbf{8}|\,|\mathbf{15}\,|\left|\overline{\mathbf{3}}\right\rangle\,, \quad \langle \mathbf{27}|\,|\mathbf{15}\,|\left|\overline{\mathbf{3}}\right\rangle\,, \quad \langle \mathbf{8}|\,|\overline{\mathbf{6}}\,|\left|\overline{\mathbf{3}}\right\rangle\,. \tag{6}$$

Therefore, in the limit of symmetry, the theoretical description of all these decay modes requires to fix 5 unknown parameters (they became 9 if we include the contribution of the **3** representation). Anyway, by looking at the experimental data it is easy to understand that the $SU(3)_F$

[1] See also [8, 9] and the more recent LHCb measurements [10, 11, 12]

[2] We are considering just the octect, if we want to consider also the η and η' we should take into account another singlet, in our approximation we should assume $\eta = \eta_8$.

[3] We are neglecting the part of the Hamiltonian transforming as **3** because it is proportional to the Cabibbo-Kobayashy-Maskawa terms $V_{cb}^* V_{ub}$. The inclusion of this term add two new RME.

flavour symmety is strongly violated. In fact, for example, the relations [15, 16]

$$\begin{aligned} A(D^0 \to K^+ K^-) &= -A(D^0 \to \pi^+ \pi^-)\,, & (7)\\ a_{CP}^{dir}(K^+ K^-) &= -a_{CP}^{dir}(\pi^+ \pi^-)\,, & (8)\\ \tan\theta_C\, A(D^+ \to \bar{K}^0 \pi^+) &= \sqrt{2}\, A(D^+ \to \pi^0 \pi^+)\,, & (9)\\ Br(D^0 \to K^+ \pi^-) &= \tan^4(\theta_C)\, Br(D^0 \to K^- \pi^+)\,, & (10)\\ A(D^0 \to K^0 \overline{K}^0) &= 0\,, & (11) \end{aligned}$$

dictated by the $SU(3)_F$ symmetry are at odds with data [17]. The linear breaking of the symmetry has been discussed in [18, 19], where the authors wrote the new operators appearing in the analysis for $m_s \neq m_{u,d}$ and identify 15 new RMEs. At the end if we take into account also the linear breaking of $SU(3)_F$, the description of the $D \to PP$ modes needs 18 RME (neglecting the contribution of the penguin operators, **3**), while the decay channels are 17. In [18] the authors show that only 13 RMEs are independent and so the (real) free parameters in this approach (they are 25) can be fixed by a fit to the 17 experimental branching ratios, 8 CP direct asymmetries and the data on the strong phase, $\delta_{K\pi}$. In this framework, all the available experimental data have been used to fix the free parameters and one cannot give any prediction. However, the compatibility with the experimental data is useful to assess the validity of the theoretical approach.

3 The topological amplitudes approach and $SU(3)_F$

As we have seen in the previous section, the linear breaking of $SU(3)_F$ can be consistently included into the analysis of the amplitudes at the cost of a number of real parameters larger than the number of the branching ratios. An alternative way to study these decay modes involves topological amplitudes which are characterized by the flavour flow in the decays [20, 21, 22, 23]. In [24] the $D \to PP$ modes are studied by combining topological amplitude approach and $SU(3)_F$ assumptions. It is shown that a map can be constructed between the topological amplitudes and the reduced amplitudes characterized by $SU(3)_F$ representation. This map can accommodate also the linear corrections to $SU(3)_F$ symmetry due to $m_s \neq m_{u,d}$. Moreover, to reduce the number of free parameters, the Tree (T) and Annihilation (A) amplitudes are evaluated in the factorization assumption by considering and fitting $1/N_c^2$ corrections to them. Here the constraints on the strength of $1/N_c$ corrections and on the maximal size of linear $SU(3)_F$ breaking allow to fix the 27 free parameters by fitting 16 measured branching ratios and one strong phase.

Concerning the calculation and the capability to predict CP asymmetries in this approach, we should remember that the CP violating part of the decay amplitudes are suppressed and so any procedure which consists in fitting branching ratios cannot determine them. Furthermore, once identified the topological amplitudes contributing to the decay amplitudes, one can construct sum rules of direct CP asymmetries in such a way a cancellation between the unknown amplitudes occurs. In [25] the unknown penguin (P) and penguin annihilation (PA) topological amplitudes disappear by conveniently combine the following CP asymmetries

sum rule 1: $a_{\rm CP}(D^0 \to \pi^+\pi^-)$, $a_{\rm CP}(D^0 \to \pi^0\pi^0)$ and $a_{\rm CP}(D^0 \to K^+K^-)$,

sum rule 2: $a_{\rm CP}(D^+ \to K^+\bar{K}^0)$, $a_{\rm CP}(D_s \to K^0\pi^+)$ and $a_{\rm CP}(D_s \to K^+\pi^0)$,

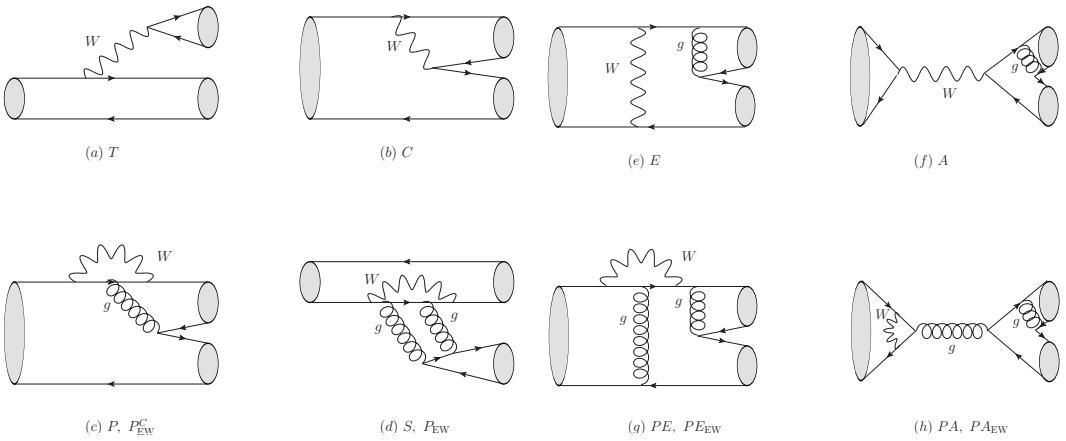


Figure 1: All the possible, non negligible, flavor diagrams: (a) color allowed tree, T; (b) color-suppressed tree C; (c) QCD-penguin P; (d) QCD-penguin singlet S; (e) Exchange E; (f) Annihilation A; (g) QCD-penguin exchange PE; (h) QCD-penguin annihilation PA.

a numerical analysis of the correlation between two asymmetries starting from the experimental data on the last one is done in [25].

4 A pure topological approach to the $D \to PP$ modes

In ref. [26] the analisys of the SCS decay modes and the corresponding CP direct asymmetries are studied by the use of the topological amplitudes approach [20, 21, 22, 23]. Possible contributing diagrams can be found in Fig. 1.

The $SU(3)_F$ symmetry breaking effects has been considered by introducing five parameters depending on the final state. Amplitudes and SU(3) breaking parameters are fixed by fitting SCS decay modes of D and D_s mesons and the related CP asymmetries. The final states with η and η' has been taken into account. We refer to the article for a detailed discussion on the fit procedure. However, by putting some constraints on the parameters as suggested by the result of the analysis on the CF in Ref. [27], in their fit *case II* [26] they have a smaller number of free parameters (respect to the experimental data) and so they are able to give predictions for direct CP asymmetries

$$\begin{aligned} a_{CP}(D^0 \to \pi^+\pi^-) &= +3.3 \times 10^{-4}, \\ a_{CP}(D^0 \to K^+K^-) &= -7.3 \times 10^{-4}, \\ a_{CP}(D^0 \to \bar{K}^0 K^0) &= -5.8 \times 10^{-4}, \\ a_{CP}(D^0 \to \pi^0\eta) &= -4.7 \times 10^{-4}, \\ a_{CP}(D^0 \to \pi^0\eta') &= -3.3 \times 10^{-4}, \end{aligned} \tag{12}$$

which are compatible with the most recent experimental data [17, 28]

5 Factorization and Final state interactions

The naive factorization has been shown that is unable to reproduce the experimental data on the decays of D and D_s mesons into final states with two mesons. Moreover, an important role in this kind of processes is played by the FSI. In the paper [29] the FSI in the decay of D mesons into two pseudoscalar mesons have been studied by assuming, as in [15], that FSI effects are dominated by resonances close to the mass of D mesons. Resonances with isospin 0, 1 and 1/2 near the D mass exist and them may contribute to rescatterings among different channels in these respective isospin states and enhance/suppress some of the decay rates. A modified factorization approximation is assumed which is similar to the QCD-factorization in two body decays of B meson [1]. In this case the non factorizable terms are parameterized in the Wilson coefficient and are considered free parameters and fixed by a fit to experimental branching ratios. In [29] the W-exchange and W-annihilation contributions are taken into account and their strengths are obtained from phenomenological fits to the data. The agreement with the available experimental data is quite good (cfr Tables IV, V and VI in ref [29]) but the data on the branching ratios cannot constraint the penguin operators contributions and so it is not possible to give predictions on the direct CP asymmetries in these channels.

However, it is interesting to test the validity of this approach by considering a more general treatment based on $SU(3)_F$. In [30, 31, 32], by taking into account high-order perturbation expansion in $SU(3)_F$ breaking has been shown by Gronau that some relations between amplitudes receive contributions which are suppressed by powers of U-spin and Isospin breaking parameters. In particular, a class of D^0 decays related by U-spin symmetry has been identified and relations between their amplitudes are constructed in such a way symmetry breaking terms modify them at fourth order in U-spin and at first order in isospin breaking and second order in U-spin breaking. In fact, if we consider the ratios

$$\begin{aligned}
R_1 &\equiv \frac{|A(D^0\to K^+\pi^-)|}{|A(D^0\to \pi^+K^-)|\tan^2\theta_C}\ ,\\
R_2 &\equiv \frac{|A(D^0\to K^+K^-)|}{|A(D^0\to \pi^+\pi^-)|}\ ,\\
R_3 &\equiv \frac{|A(D^0\to K^+K^-)|+|A(D^0\to \pi^+\pi^-)|}{|A(D^0\to \pi^+K^-)|\tan\theta_C+|A(D^0\to K^+\pi^-)|\tan^{-1}\theta_C}\ ,\\
R_4 &\equiv \sqrt{\frac{|A(D^0\to K^+K^-)||A(D^0\to \pi^+\pi^-)|}{|A(D^0\to \pi^+K^-)||A(D^0\to K^+\pi^-)|}}\ ,
\end{aligned} \tag{13}$$

it is possible to show that the R_i are not mutually independent and that they obey the following identity

$$R_4 = R_3\sqrt{\frac{1-[(R_2-1)/(R_2+1)]^2}{1-[(R_1-1)/(R_1+1)]^2}}\ . \tag{14}$$

In the limit of $SU(3)_F$ $R_i = 1$ and ΔR defined by

$$\Delta R \equiv R_3 - R_4 + \frac{1}{8}\left[\left(\sqrt{2R_1-1}-1\right)^2-\left(\sqrt{2R_2-1}-1\right)^2\right] = \mathcal{O}(\epsilon_1^4,\epsilon_2^4)+\mathcal{O}(\delta_1\epsilon_1^2,\delta_2\epsilon_2^2)\ , \tag{15}$$

is different from zero by terms of the order $\mathcal{O}(\epsilon_1^4,\epsilon_2^4)$ and $\mathcal{O}(\delta_1\epsilon_1^2,\delta_2\epsilon_2^2)$, where ϵ_i and δ_i are U-spin and Isospin breaking terms, respectively. In the case of the results obtained in [29] they

have

$$\Delta R = -0.000013 \pm 0.006\,. \tag{16}$$

6 FSI phases as main sources of $SU(3)_F$ breaking

In ref [15, 33] large phase differences are obtained by fitting experimental data in the factorization improved approximation for the D meson decays into PS, PP and PV final state. In this approach the large $SU(3)_F$ violation are essentially consequences of the large phases. Following the same line of thinking, in [34] we have studied the SCS decays of D mesons into a pair of pseudoscalar mesons by assuming an exact $SU(3)_F$ symmetry for the decay amplitudes. The effective hamiltonian for $|\Delta C| = 1$ and $\Delta S = 0$ transforms as a triplet and so is responsible of the transition of the D^0 (which is an U-spin singlet) into two different U-spin triplets. The first one is part of the octet representation of $SU(3)_F$ the second is in the 27 representation. Thus there are two free parameters to be fixed. Concerning the phases, they are related with the Isospin of the final state, and so we have δ_1 which is related to the state with $I = 1$ in the octet, and δ_0, δ_0' and ϕ which are related to the $I = 0$ in the octet and in the singlet representations; ϕ represents the mixing angle. In conclusion, in this approach there are six different free parameters to describe the D^0 SCS decays and we have shown that a good fit to the data can be obtained [34].

In ref. [35] we are extending the previous approach by considering also the D^+ and D_s SCS modes and all the Cabibbo Favoured (CF) and the Double Cabibbo Suppressed (DCS) decay modes. The $SU(3)_F$ violation in the CF and DCS decay modes of D^0 cannot be ascribed only to the strong phase which, in analogy to the previous ones, we called $\delta_{1/2}$. Thus, we have introduced a free parameter, K, taking into account, in the amplitudes, the non-conservation of the strangeness violating $SU(3)_F$ currents. Moreover, the $SU(3)_F$ symmetry require the introduction of two new parameters. At the end this approach contains eleven free parameters to describe D meson decays into two pseudoscalar mesons without the η and η' in the final state. Preliminary result of the fit to the experimental branching ratios can be found in the Table 1.
The test suggested by Gronau [32] gives, for this model, $\Delta R = 0.0030 \pm 0.0004$ (cfr. eq. (15)).

The CP violating part of the amplitudes, in this approach, depend essentially on two unknown parameters that cannot be determined by the branching ratios. However, they can be extracted from the experimental data on $\Delta a_{\rm CP}$ and so predictions of CP asymmetries for final state with kaons and pions can be done [35].

7 $a_{\rm CP}(D^0 \to K_S\, K_S)$

The decay mode $D^0 \to K^0\, \bar{K}^0$ is interesting because, as was pointed out many years ago in [15], the tree level amplitude $A(D^0 \to K^0\, \bar{K}^0)$ vanish in the limit of $SU(3)_F$ but this is not true if we look at the penguin contributions. The fact that the ratio of the penguin to the tree amplitude could be large implies that the CP asymmetry (cfr eq. (2)) may be enhanced at observable level [36]. The penguin annihilation term and the exchange contribution (relevant for the calculation) are estimated by a perturbative approach and by using the results of a fit to all D decays in two pseudoscalar mesons, respectively. They give [36]

$$\left|a_{\rm CP}(D^0 \to K_S\, K_S)\right| \leqslant 1.1\% \quad (95\%\ \text{C.L.})\,. \tag{17}$$

Channel	Fit ($\times 10^{-3}$)	Exp. ($\times 10^{-3}$)
CF		
$\mathrm{BR}(D^+ \to \pi^+ K_S)$	15.72 ± 0.41	15.3 ± 0.6
$\mathrm{BR}(D^+ \to \pi^+ K_L)$	14.34 ± 0.37	14.6 ± 0.5
$\mathrm{BR}(D^0 \to \pi^+ K^-)$	39.31 ± 0.40	39.3 ± 0.4
$\mathrm{BR}(D^0 \to \pi^0 K_S)$	11.9 ± 0.33	12.0 ± 0.4
$\mathrm{BR}(D^0 \to \pi^0 K_L)$	9.39 ± 0.27	10.0 ± 0.7
$\mathrm{BR}(D_s^+ \to K^+ K_S)$	15.0 ± 0.5	15.0 ± 0.5
SCS		
$\mathrm{BR}(D^0 \to \pi^+ \pi^-)$	1.42 ± 0.03	1.421 ± 0.025
$\mathrm{BR}(D_0^+ \to \pi^0 \pi^0)$	0.83 ± 0.04	0.826 ± 0.035
$\mathrm{BR}(D^+ \to \pi^+ \pi^0)$	1.22 ± 0.06	1.24 ± 0.06
$\mathrm{BR}(D^0 \to K^+ K^-)$	4.02 ± 0.06	4.01 ± 0.07
$\mathrm{BR}(D^0 \to K_S K_S)$	0.17 ± 0.04	0.18 ± 0.04
$\mathrm{BR}(D^+ \to K^+ K_S)$	2.89 ± 0.12	2.95 ± 0.15
$\mathrm{BR}(D_s^+ \to \pi^0 K^+)$	1.03 ± 0.04	0.63 ± 0.21
$\mathrm{BR}(D_s^+ \to \pi^+ K_S)$	1.24 ± 0.06	1.22 ± 0.06
DCS		
$\mathrm{BR}(D^+ \to \pi^0 K^+)$	0.155 ± 0.005	0.189 ± 0.025
$\mathrm{BR}(D^0 \to \pi^- K^+)$	0.140 ± 0.003	0.1399 ± 0.0027

Table 1: In the second column the branching ratios used in the fit, in the last column the predictions for the values obtained for the fitted values of the parameters.

In a previous analysis [37] the upper bound

$$\left|a_{\mathrm{CP}}(D^0 \to K_S\, K_S)\right| \lesssim \frac{2|V_{cb}V_{ub}|}{\varepsilon|V_{cs}V_{us}|} \sim 0.6\%\,, \tag{18}$$

is obtained which is in fairly good agreement with eq. (17). Here, ε is a measure of the $SU(3)_F$ breaking. Finally, by assuming similar magnitude for two different matrix elements in [18] the relation

$$\left|a_{\mathrm{CP}}(D^0 \to K_S\, K_S)\right| \lesssim \frac{3}{2}\,\Delta a_{\mathrm{CP}} \tag{19}$$

has been given. However, this prediction cannot be considered reliable because, as stressed in [36], $a_{\mathrm{CP}}(D^0 \to K_S\, K_S)$ and Δa_{CP} involve different topological amplitudes.

From the experimental point of view, we have the following measurements

$$\begin{aligned}
a_{\mathrm{CP}}(D^0 \to K_S K_S) &= (-23 \pm 19)\%, && \text{CLEO (2001)[38]} \\
a_{\mathrm{CP}}(D^0 \to K_S K_S) &= (-2.9 \pm 5.2 \pm 2.2)\%, && \text{LHCb (2015)[39]} \\
a_{\mathrm{CP}}(D^0 \to K_S K_S) &= (-0.2 \pm 1.53 \pm 0.17)\% && \text{Belle (2016)[40]}
\end{aligned} \tag{20}$$

and so the asymmetry is compatible with zero.

8 Summary

We have reviewed approaches to study the nonleptonic decays of D and D_s mesons into two pseudoscalar mesons. We have seen that the use of the $SU(3)_F$ symmetry alone, even if it allows a consistent description of the branching ratios when symmetry breaking is considered, cannot give predictions on the CP asymmetries, due to the large number of RME. However, physical considerations and/or some other approximations (like, for example, improved factorization) can, together with a model to take into account FSI, give not only a good description of the measured branching fractions but also reliable predictions on CP asymmetries.

Acknowledgements

It is a pleasure to thank F. Buccella, E. Franco, M. Lusignoli, A. Paul, A. Pugliese and L. Silvestrini for collaboration and discussions. Many thanks also to M.A. Ivanov for discussions.

References

[1] M. Beneke, G. Buchalla, M. Neubert and C. T. Sachrajda, Phys. Rev. Lett. **83** (1999) 1914 [hep-ph/9905312].

[2] G. Altarelli, N. Cabibbo and L. Maiani, Nucl. Phys. B **88** (1975) 285.

[3] R. L. Kingsley, S. B. Treiman, F. Wilczek and A. Zee, Phys. Rev. D **11** (1975) 1919. doi:10.1103/PhysRevD.11.1919

[4] R. L. Kingsley, S. B. Treiman, F. A. Wilczek and A. Zee, Phys. Rev. D **12** (1975) 106. doi:10.1103/PhysRevD.12.106

[5] C. Quigg, Z. Phys. C **4** (1980) 55. doi:10.1007/BF01477308

[6] T. Aaltonen *et al.* [CDF Collaboration], Phys. Rev. Lett. **109** (2012) 111801 [arXiv:1207.2158 [hep-ex]].

[7] R. Aaij *et al.* [LHCb Collaboration], Phys. Rev. Lett. **108** (2012) 111602 [arXiv:1112.0938 [hep-ex]].

[8] B. R. Ko [Belle Collaboration], PoS ICHEP **2012** (2013) 353 [arXiv:1212.1975 [hep-ex]].

[9] B. Aubert *et al.* [BaBar Collaboration], Phys. Rev. Lett. **100** (2008) 061803 [arXiv:0709.2715 [hep-ex]].

[10] R. Aaij *et al.* [LHCb Collaboration], Phys. Lett. B **723** (2013) 33 [arXiv:1303.2614 [hep-ex]].

[11] R. Aaij *et al.* [LHCb Collaboration], JHEP **1407** (2014) 041 [arXiv:1405.2797 [hep-ex]].

[12] R. Aaij *et al.* [LHCb Collaboration], JHEP **1504** (2015) 043 [arXiv:1501.06777 [hep-ex]].

[13] Y. Grossman, A. L. Kagan and Y. Nir, Phys. Rev. D **75** (2007) 036008 doi:10.1103/PhysRevD.75.036008 [hep-ph/0609178]. G. Isidori, J. F. Kamenik, Z. Ligeti and G. Perez, Phys. Lett. B **711** (2012) 46 [arXiv:1111.4987 [hep-ph]]. K. Wang and G. Zhu, Phys. Lett. B **709** (2012) 362 [arXiv:1111.5196 [hep-ph]]. G. Hiller, Y. Hochberg and Y. Nir, Phys. Rev. D **85** (2012) 116008 [arXiv:1204.1046 [hep-ph]]. G. F. Giudice, G. Isidori and P. Paradisi, JHEP **1204** (2012) 060 [arXiv:1201.6204 [hep-ph]]. W. Altmannshofer, R. Primulando, C. T. Yu and F. Yu, JHEP **1204** (2012) 049 [arXiv:1202.2866 [hep-ph]]. C. H. Chen, C. Q. Geng and W. Wang, Phys. Rev. D **85** (2012) 077702 [arXiv:1202.3300 [hep-ph]]. O. Gedalia, J. F. Kamenik, Z. Ligeti and G. Perez, Phys. Lett. B **714** (2012) 55 [arXiv:1202.5038 [hep-ph]]. T. Mannel and N. Uraltsev, JHEP **1303** (2013) 064 [arXiv:1205.0233 [hep-ph]]. B. Keren-Zur, P. Lodone, M. Nardecchia, D. Pappadopulo, R. Rattazzi and L. Vecchi, Nucl. Phys. B **867** (2013) 394 [arXiv:1205.5803 [hep-ph]]. R. Barbieri, D. Buttazzo, F. Sala and D. M. Straub, JHEP **1210** (2012) 040 [arXiv:1206.1327 [hep-ph]]. A. D. Dolgov, S. I. Godunov, A. N. Rozanov and M. I. Vysotsky, JETP Lett. **96** (2012) 290 [arXiv:1206.6652 [hep-ph]]. C. Delaunay, J. F. Kamenik, G. Perez and L. Randall, JHEP **1301** (2013) 027 [arXiv:1207.0474 [hep-ph]].

[14] M. Golden and B. Grinstein, Phys. Lett. B **222** (1989) 501, D. Pirtskhalava and P. Uttayarat, Phys. Lett. B **712** (2012) 81 [arXiv:1112.5451 [hep-ph]]; B. Bhattacharya, M. Gronau and J. L. Rosner, Phys. Rev. D **85** (2012) 054014 [arXiv:1201.2351 [hep-ph]]; T. Feldmann, S. Nandi and A. Soni, JHEP **1206** (2012) 007 [arXiv:1202.3795 [hep-ph]]; J. Brod, Y. Grossman, A. L. Kagan and J. Zupan, JHEP **1210** (2012) 161 [arXiv:1203.6659 [hep-ph]]; H. -Y. Cheng and C. -W. Chiang, Phys. Rev. D **86** (2012) 014014 [arXiv:1205.0580 [hep-ph]]. See also [16, 18, 34, 37]

[15] F. Buccella, M. Lusignoli, G. Miele, A. Pugliese and P. Santorelli, Phys. Rev. D **51** (1995) 3478 [hep-ph/9411286]; see also F. Buccella, M. Lusignoli, G. Mangano, G. Miele, A. Pugliese and P. Santorelli, Phys. Lett. B **302** (1993) 319 [hep-ph/9212253].

[16] E. Franco, S. Mishima and L. Silvestrini, JHEP **1205** (2012) 140 doi:10.1007/JHEP05(2012)140 [arXiv:1203.3131 [hep-ph]].

[17] C. Patrignani *et al.* [Particle Data Group Collaboration], Chin. Phys. C **40** (2016) no.10, 100001.

[18] G. Hiller, M. Jung and S. Schacht, Phys. Rev. D **87** (2013) no.1, 014024 [arXiv:1211.3734 [hep-ph]].

[19] G. Hiller, M. Jung and S. Schacht, PoS EPS **-HEP2013** (2013) 371 [arXiv:1311.3883 [hep-ph]].

[20] L. L. Chau, Phys. Rept. **95** (1983) 1.

[21] L. L. Chau and H. Y. Cheng, Phys. Rev. Lett. **56** (1986) 1655.

[22] L. L. Chau and H. Y. Cheng, Phys. Rev. D **36** (1987) 137.

[23] L. L. Chau and H. Y. Cheng, Phys. Lett. B **280** (1992) 281.

[24] S. Mller, U. Nierste and S. Schacht, Phys. Rev. D **92** (2015) no.1, 014004 [arXiv:1503.06759 [hep-ph]].

[25] S. Mller, U. Nierste and S. Schacht, Phys. Rev. Lett. **115** (2015) no.25, 251802 [arXiv:1506.04121 [hep-ph]].

[26] R. Dhir, C. S. Kim and S. Oh, Int. J. Mod. Phys. A **30** (2015) no.17, 1550104 [arXiv:1504.02556 [hep-ph]].

[27] H. Y. Cheng and C. W. Chiang, Phys. Rev. D **85** (2012) 034036 Erratum: [Phys. Rev. D **85** (2012) 079903] [arXiv:1201.0785 [hep-ph]].

[28] Y. Amhis *et al.* [Heavy Flavor Averaging Group (HFAG) Collaboration], arXiv:1412.7515 [hep-ex].

[29] A. Biswas, N. Sinha and G. Abbas, Phys. Rev. D **92** (2015) no.1, 014032 [arXiv:1503.08176 [hep-ph]].

[30] M. Gronau, Phys. Lett. B **730** (2014) 221 Addendum: [Phys. Lett. B **735** (2014) 282] [arXiv:1311.1434 [hep-ph]].

[31] M. Gronau, Phys. Rev. D **90** (2014) no.11, 117901 [arXiv:1410.7255 [hep-ph]].

[32] M. Gronau, Phys. Rev. D **91** (2015) no.7, 076007 [arXiv:1501.03272 [hep-ph]].

[33] F. Buccella, M. Lusignoli and A. Pugliese, Phys. Lett. B **379** (1996) 249 [hep-ph/9601343].

[34] F. Buccella, M. Lusignoli, A. Pugliese and P. Santorelli, Phys. Rev. D **88** (2013) no.7, 074011 [arXiv:1305.7343 [hep-ph]].

[35] F. Buccella, E. Franco, A. Paul, P. Santorelli and L. Silvestrini, in preparation.

[36] U. Nierste and S. Schacht, Phys. Rev. D **92** (2015) no.5, 054036 [arXiv:1508.00074 [hep-ph]].

[37] J. Brod, A. L. Kagan and J. Zupan, Phys. Rev. D **86** (2012) 014023 [arXiv:1111.5000 [hep-ph]].

[38] G. Bonvicini *et al.* [CLEO Collaboration], Phys. Rev. D **63** (2001) 071101 [hep-ex/0012054].

[39] R. Aaij *et al.* [LHCb Collaboration], JHEP **1510** (2015) 055 [arXiv:1508.06087 [hep-ex]].

[40] A. Abdesselam *et al.*, arXiv:1609.06393 [hep-ex].

Analyzing New Physics in $\bar{B}^0 \to D^{(*)}\tau^-\bar{\nu}_\tau$

C. T. Tran[1,2], *M. A. Ivanov*[1], *J. G. Körner*[3]

[1]Bogoliubov Laboratory of Theoretical Physics JINR, 141980 Dubna, Russia
[2]Moscow Institute of Physics and Technology, 141700 Dolgoprudny, Russia
[3]PRISMA Cluster of Excellence, Institut für Physik, Johannes Gutenberg-Universität, D-55099 Mainz, Germany

DOI: http://dx.doi.org/10.3204/DESY-PROC-2016-04/Tran

We discuss possible new physics (NP) effects beyond the standard model (SM) in the exclusive decays $\bar{B}^0 \to D^{(*)}\tau^-\bar{\nu}_\tau$. Starting with a model-independent effective Hamiltonian including non-SM four-Fermi operators, we show how to obtain experimental constraints on different NP scenarios and investigate their effects on a large set of physical observables. The $\bar{B}^0 \to D^{(*)}$ transition form factors are calculated in the full kinematic q^2 range by employing the covariant confined quark model developed by our group.

1 Introduction

The exclusive semileptonic decays $\bar{B}^0 \to D^{(*)}\tau^-\bar{\nu}_\tau$ have been measured by the *BABAR* [1], Belle [2], and LHCb [3] collaborations in an effort to unravel the well-known $R_{D^{(*)}}$ puzzle which has persisted for several years (see [4, 5, 6] and references therein). The current world averages of the ratios are $R_D = 0.406 \pm 0.050$ and $R_{D^*} = 0.311 \pm 0.016$, which exceed the SM predictions of $R_D = 0.300 \pm 0.008$ [7] and $R_{D^*} = 0.252 \pm 0.003$ [8] by 2.1σ and 3.6σ, respectively.

The excess of $R(D^{(*)})$ over SM predictions has attracted a great deal of attention in the particle physics community and has led to many theoretical studies looking for NP explanations. Some studies focus on specific NP models including two-Higgs-doublet models [9], leptoquark models [10], and other extensions of the SM. Other studies adopt a model-independent approach, in which a general effective Hamiltonian for the $b \to c\ell\nu$ transition in the presence of NP is imposed to investigate the impact of various NP operators on different physical observables [11]. Most of the theoretical studies rely on the heavy quark effective theory (HQET) [12] to evaluate the hadronic form factors, which are expressed through a few universal functions in the heavy quark limit (HQL). In the present analysis, we employ an alternative approach to calculate the NP-induced hadronic transitions based on the covariant confined quark model (CCQM), which has been developed in some earlier papers by us (see [13] and references therein).

Here we follow the authors of [11] to include NP operators in the effective Hamiltonian and investigate their effects on physical observables of the decays $\bar{B}^0 \to D^{(*)}\ell^-\bar{\nu}_\ell$. We define a full set of form factors corresponding to SM+NP operators and calculate them by employing the CCQM. In the CCQM the transition form factors can be determined in the full range of momentum transfer, making the calculations straightforward without any extrapolation. This provides an opportunity to investigate NP operators in a self-consistent manner, and independently from the HQET. We first constrain the NP operators using experimental data

on the ratios of branching fractions, then analyze their effects on various observables. We also derive the fourfold angular distribution for the cascade decay $\bar{B}^0 \to D^{*+}(\to D^0\pi^+)\tau^-\bar{\nu}_\tau$ to analyze the polarization of the D^* meson in the presence of NP.

2 Effective operators and helicity amplitudes

Assuming that all neutrinos are left-handed and that NP effects only influence leptons of the third generation, the effective Hamiltonian for the quark-level transition $b \to c\tau^-\bar{\nu}_\tau$ is given by

$$\mathcal{H}_{eff} = \frac{4G_F}{\sqrt{2}} V_{cb} \left[\mathcal{O}_{V_L} + \sum_{X=S_L,S_R,V_L,V_R,T_L} X\mathcal{O}_X \right],$$

where the four-Fermi operators $\mathcal{O}_X$ are defined as $(i = L, R)$

$$\begin{aligned} \mathcal{O}_{V_i} &= (\bar{c}\gamma^\mu P_i b)\,(\bar{\tau}\gamma_\mu P_L \nu_\tau)\,, \\ \mathcal{O}_{S_i} &= (\bar{c} P_i b)\,(\bar{\tau} P_L \nu_\tau)\,, \\ \mathcal{O}_{T_L} &= (\bar{c}\sigma^{\mu\nu} P_L b)\,(\bar{\tau}\sigma_{\mu\nu} P_L \nu_\tau)\,. \end{aligned}$$

Here, $\sigma_{\mu\nu} = i\left[\gamma_\mu, \gamma_\nu\right]/2$, $P_{L,R} = (1 \mp \gamma_5)/2$ are the left and right projection operators, and X's are the complex Wilson coefficients governing the NP contributions, which are equal to zero in the SM.

The invariant form factors describing the hadronic transitions $\bar{B}^0 \to D$ and $\bar{B}^0 \to D^*$ are defined as follows:

$$\begin{aligned} \langle D(p_2)|\bar{c}\gamma^\mu b|\bar{B}^0(p_1)\rangle &= F_+(q^2)P^\mu + F_-(q^2)q^\mu, \\ \langle D(p_2)|\bar{c}b|\bar{B}^0(p_1)\rangle &= (m_1+m_2)F^S(q^2), \\ \langle D(p_2)|\bar{c}\sigma^{\mu\nu}(1-\gamma^5)b|\bar{B}^0(p_1)\rangle &= \frac{iF^T(q^2)}{m_1+m_2}\left(P^\mu q^\nu - P^\nu q^\mu + i\varepsilon^{\mu\nu Pq}\right), \\ \langle D^*(p_2)|\bar{c}\gamma^\mu(1\mp\gamma^5)b|\bar{B}^0(p_1)\rangle &= \frac{\epsilon^\dagger_{2\alpha}}{m_1+m_2}\Big[\mp g^{\mu\alpha} Pq A_0(q^2) \pm P^\mu P^\alpha A_+(q^2) \\ &\quad \pm q^\mu P^\alpha A_-(q^2) + i\varepsilon^{\mu\alpha Pq} V(q^2)\Big], \\ \langle D^*(p_2)|\bar{c}\gamma^5 b|\bar{B}^0(p_1)\rangle &= \epsilon^\dagger_{2\alpha} P^\alpha G^S(q^2), \\ \langle D^*(p_2)|\bar{c}\sigma^{\mu\nu}(1-\gamma^5)b|\bar{B}^0(p_1)\rangle &= -i\epsilon^\dagger_{2\alpha}\Big[\left(P^\mu g^{\nu\alpha} - P^\nu g^{\mu\alpha} + i\varepsilon^{P\mu\nu\alpha}\right) G_1^T(q^2) \\ &\quad + \left(q^\mu g^{\nu\alpha} - q^\nu g^{\mu\alpha} + i\varepsilon^{q\mu\nu\alpha}\right) G_2^T(q^2) \\ &\quad + \left(P^\mu q^\nu - P^\nu q^\mu + i\varepsilon^{Pq\mu\nu}\right) P^\alpha \frac{G_0^T(q^2)}{(m_1+m_2)^2}\Big], \end{aligned}$$

where $P = p_1 + p_2$, $q = p_1 - p_2$, and ϵ_2 is the polarization vector of the D^* meson which satisfies the condition $\epsilon_2^\dagger \cdot p_2 = 0$. The particles are on their mass shells: $p_1^2 = m_1^2 = m_{\bar{B}^0}^2$ and $p_2^2 = m_2^2 = m_{D^{(*)}}^2$.

Using the helicity technique first described in [14] and further discussed in our recent papers [4, 5], one obtains the ratio of branching fractions $R_{D^{(*)}}(q^2)$ as follows:

$$R_{D^{(*)}}(q^2) = \left(\frac{q^2 - m_\tau^2}{q^2 - m_\mu^2}\right)^2 \frac{\mathcal{H}_{tot}^{D^{(*)}}}{\sum\limits_n |H_n|^2 + \delta_\mu\big(\sum\limits_n |H_n|^2 + 3|H_t|^2\big)},$$

$$
\begin{aligned}
\mathcal{H}^D_{tot} &= |1+g_V|^2\left[|H_0|^2+\delta_\tau(|H_0|^2+3|H_t|^2)\right]+\frac{3}{2}|g_S|^2|H^S_P|^2\\
&\quad +3\sqrt{2\delta_\tau}\mathrm{Re}g_S H^S_P H_t+8|T_L|^2(1+4\delta_\tau)|H_T|^2+12\sqrt{2\delta_\tau}\mathrm{Re}T_L H_0 H_T,\\
\mathcal{H}^{D^*}_{tot} &= (|1+V_L|^2+|V_R|^2)\Big[\sum_n|H_n|^2+\delta_\tau\Big(\sum_n|H_n|^2+3|H_t|^2\Big)\Big]+\frac{3}{2}|g_P|^2|H^S_V|^2\\
&\quad -2\mathrm{Re}V_R\big[(1+\delta_\tau)(|H_0|^2+2H_+H_-)+3\delta_\tau|H_t|^2\big]-3\sqrt{2\delta_\tau}\mathrm{Re}g_P H^S_V H_t\\
&\quad +8|T_L|^2(1+4\delta_\tau)\sum_n|H^n_T|^2-12\sqrt{2\delta_\tau}\mathrm{Re}T_L\sum_n H_n H^n_T.
\end{aligned}
$$

Here, $\delta_\ell = m^2_\ell/2q^2$ is the helicity flip factor, $g_V \equiv V_L + V_R$, $g_S \equiv S_L + S_R$, $g_P \equiv S_L - S_R$, and the index n runs through $(0,+,-)$. The definition of the hadronic helicity amplitudes H in terms of the invariant form factors is presented in the Appendix of [6]. Note that we do not consider interference terms between different NP operators since we assume the dominance of only one NP operator besides the SM contribution.

3 Form factors in the CCQM

As has been discussed in detail in [5] we calculate the current-induced $B \to D^{(*)}$ transitions from their one-loop quark diagrams. As a result the various form factors in our model are represented by threefold integrals which are calculated by using FORTRAN codes in the full kinematical momentum transfer region $0 \le q^2 \le q^2_{max} = (m_{\bar{B}^0} - m_{D^{(*)}})^2$. Our numerical results for the form factors are well represented by a double-pole parametrization

$$F(q^2) = \frac{F(0)}{1 - as + bs^2}, \quad s = \frac{q^2}{m^2_1}.$$

The parameters of the form factors for the $\bar{B}^0 \to D$ and $\bar{B}^0 \to D^*$ transitions are listed in Table 1. We also list the zero-recoil values of the form factors for comparison with the

	$\bar{B}^0 \to D^*$								$\bar{B}^0 \to D$			
	A_0	A_+	A_-	V	G^S	G^T_0	G^T_1	G^T_2	F_+	F_-	F^S	F^T
$F(0)$	1.62	0.67	−0.77	0.77	−0.50	−0.073	0.73	−0.37	0.79	−0.36	0.80	0.77
a	0.34	0.87	0.89	0.90	0.87	1.23	0.90	0.88	0.75	0.77	0.22	0.76
b	−0.16	0.057	0.070	0.075	0.060	0.33	0.074	0.065	0.039	0.046	−0.098	0.043
$F(q^2_{\rm max})$	1.91	0.99	−1.15	1.15	−0.74	−0.13	1.10	−0.55	1.14	−0.53	0.89	1.11
$F^{HQL}(q^2_{\rm max})$	1.99	1.12	−1.12	1.12	−0.62	0	1.12	−0.50	1.14	−0.54	0.88	1.14

Table 1: Parameters of the dipole approximation for $\bar{B}^0 \to D^{(*)}$ form factors. Zero-recoil values of the form factors are also listed for comparison with the HQET.

corresponding HQET results which can e.g. be found in [5]. The agreement between the two sets of zero-recoil values is within 10%. It is worth mentioning that we obtain a nonzero result for the form factor G^T_0 at zero recoil, which is predicted to vanish in the HQET.

We note that in [4] the HQL in our approach was explored in great detail for the heavy-to-heavy $\bar{B}^0 \to D^{(*)}$ transitions. In [4] we also calculated the Isgur-Wise function and considered the near-recoil behavior of the form factors. A brief discussion of the subleading corrections to

the HQL arising from finite quark masses can be found in Appendix B of [5]. Finally, we briefly discuss some error estimates within our model. We fix our model parameters (the constituent quark masses, the infrared cutoff, and the hadron size parameters) by minimizing the functional $\chi^2 = \sum_i \frac{(y_i^{\rm expt} - y_i^{\rm theor})^2}{\sigma_i^2}$ where σ_i is the experimental uncertainty. If σ is too small then we take its value of 10%. Moreover, we observed that the errors of the fitted parameters are of the order of 10%. Thus we estimate the model uncertainties to lie within 10%.

4 Experimental constraints

Within the SM (without any NP operators) our model calculation yields $R(D) = 0.267$ and $R(D^*) = 0.238$, which are consistent with other SM predictions given in [7, 8] within 10%.

Assuming the dominance of only one NP operator at a time (besides the SM one), we compare the calculated ratios $R_{D^{(*)}}$ with the current experimental data $R_D = 0.406 \pm 0.050$ and $R_{D^*} = 0.311 \pm 0.016$ and obtain the allowed regions for the NP couplings as shown in Fig. 1.

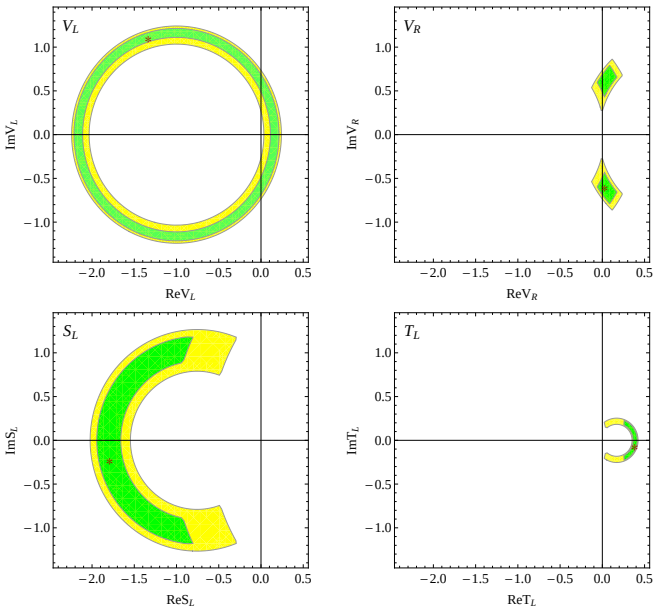


Figure 1: Constraints on the Wilson coefficients V_L, V_R, S_L, and T_L within 1σ (green, dark) and 2σ (yellow, light). No value of S_R is allowed within 2σ. The best-fit value in each case is denoted with the symbol $*$.

It is important to note that while determining these regions, we also take into account a theoretical error of 10% for the ratios $R(D^{(*)})$. The vector operators $\mathcal{O}_{V_{L,R}}$ and the left scalar operator $\mathcal{O}_{S_L}$ are favored while there is no allowed region for the right scalar operator $\mathcal{O}_{S_R}$ within 2σ. Therefore we will not consider $\mathcal{O}_{S_R}$ in what follows. The tensor operator $\mathcal{O}_{T_L}$ is less favored, but it can still well explain the current experimental results. In each allowed region at 2σ we find the best-fit value for each NP coupling. The best-fit couplings read $V_L = -1.33 + i1.11$, $V_R = 0.03 - i0.60$, $S_L = -1.79 - i0.22$, $T_L = 0.38 - i0.06$, and are marked with an asterisk.

5 The cascade decay $\bar{B}^0 \to D^{*+}(\to D^0\pi^+)\tau^-\bar{\nu}_\tau$ and the angular observables

5.1 The fourfold distribution

In order to analyze NP effects on the polarization of the D^* meson one uses the cascade decay $\bar{B}^0 \to D^{*+}(\to D^0\pi^+)\tau^-\bar{\nu}_\tau$. A detailed derivation of the fourfold angular distribution (without NP) can be found in our paper [15]. The three angles θ, θ^*, and χ in the distribution are defined in Fig. 2 One has

$$\frac{d^4\Gamma(\bar{B}^0 \to D^{*+}(\to D^0\pi^+)\tau^-\bar{\nu}_\tau)}{dq^2 d\cos\theta d\chi d\cos\theta^*} = \frac{9}{8\pi}|N|^2 J(\theta,\theta^*,\chi),$$

where

$$|N|^2 = \frac{G_F^2|V_{cb}|^2|\mathbf{p_2}|q^2 v^2}{(2\pi)^3 12 m_1^2}\mathcal{B}(D^* \to D\pi).$$

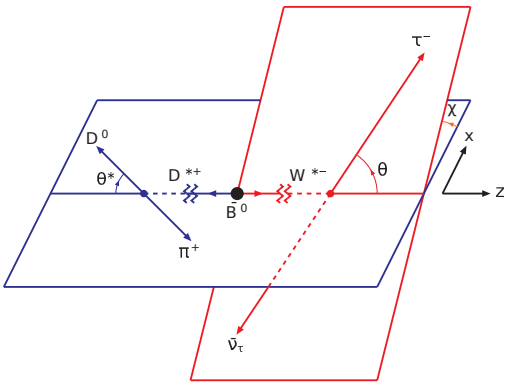


Figure 2: Definition of the angles θ, θ^* and χ in the cascade decay $\bar{B}^0 \to D^{*+}(\to D^0\pi^+)\tau^-\bar{\nu}_\tau$.

The full angular distribution $J(\theta,\theta^*,\chi)$ is written as

$$\begin{aligned} J(\theta,\theta^*,\chi) &= J_{1s}\sin^2\theta^* + J_{1c}\cos^2\theta^* + (J_{2s}\sin^2\theta^* + J_{2c}\cos^2\theta^*)\cos 2\theta \\ &+ J_3\sin^2\theta^*\sin^2\theta\cos 2\chi + J_4\sin 2\theta^*\sin 2\theta\cos\chi \\ &+ J_5\sin 2\theta^*\sin\theta\cos\chi + (J_{6s}\sin^2\theta^* + J_{6c}\cos^2\theta^*)\cos\theta \\ &+ J_7\sin 2\theta^*\sin\theta\sin\chi + J_8\sin 2\theta^*\sin 2\theta\sin\chi + J_9\sin^2\theta^*\sin^2\theta\sin 2\chi, \end{aligned}$$

where $J_{i(a)}$ $(i = 1,\ldots,9; a = s,c)$ are the angular observables. Their explicit expressions in terms of helicity amplitudes and Wilson coefficients can be found in our paper [5]. The fourfold distribution allows one to define a large set of observables which can help probe NP in the decay. First, by integrating the angular decay distribution over all angles one obtains

$$\frac{d\Gamma(\bar{B}^0 \to D^*\tau^-\bar{\nu}_\tau)}{dq^2} = |N|^2 J_{\rm tot} = |N|^2(J_L + J_T),$$

where $J_L = 3J_{1c} - J_{2c}$ and $J_T = 2(3J_{1s} - J_{2s})$ are the longitudinal and transverse polarization amplitudes of the D^* meson. In Fig. 3 we present the q^2 dependence of the rate ratios $R_{D^{(*)}}(q^2)$ in different NP scenarios. It is interesting to note that unlike the vector and scalar operators, which tend to increase both ratios, the tensor operator can lead to a decrease of the ratio $R(D^*)$ for $q^2 \gtrsim 8$ GeV^2. Moreover, while the ratio $R(D^*)$ is minimally sensitive to the scalar coupling S_L (in comparison with other couplings, i.e. $V_{L,R}$, T_L), the ratio $R(D)$ shows maximal sensitivity to S_L. These behaviors can help discriminate between different NP operators.

5.2 The $\cos\theta$ distribution, the forward-backward asymmetry, and the lepton-side convexity parameter

We define a normalized angular decay distribution $\widetilde{J}(\theta^*, \theta, \chi)$ through

$$\widetilde{J}(\theta^*, \theta, \chi) = \frac{9}{8\pi} \frac{J(\theta^*, \theta, \chi)}{J_{\rm tot}},$$

where $J_{\rm tot} = 3J_{1c} + 6J_{1s} - J_{2c} - 2J_{2s}$. The normalized angular decay distribution $\widetilde{J}(\theta^*, \theta, \chi)$ obviously integrates to 1 after $\cos\theta^*$, $\cos\theta$, and χ integration. By integrating the fourfold distribution over $\cos\theta^*$ and χ one obtains the differential $\cos\theta$ distribution which is described by a tilted parabola. The normalized form of the parabola reads

$$\widetilde{J}(\theta) = \frac{a + b\cos\theta + c\cos^2\theta}{2(a + c/3)}.$$

The linear coefficient $b/2(a + c/3)$ can be projected out by defining a forward-backward asymmetry given by

$$\begin{aligned} &\mathcal{A}_{FB}(q^2) \\ &= \frac{[\int_0^1 - \int_{-1}^0] d\cos\theta \, d\Gamma/d\cos\theta}{[\int_0^1 + \int_{-1}^0] d\cos\theta \, d\Gamma/d\cos\theta} \\ &= \frac{b}{2(a + c/3)} = \frac{3}{2} \frac{J_{6c} + 2J_{6s}}{J_{\rm tot}}. \end{aligned}$$

The coefficient $c/2(a + c/3)$ of the quadratic contribution is obtained by taking the second derivative of $\widetilde{J}(\theta)$. Accordingly, we define a convexity parameter by writing

$$C_F^\tau(q^2) = \frac{d^2\widetilde{J}(\theta)}{d(\cos\theta)^2} = \frac{c}{a + c/3} = \frac{6(J_{2c} + 2J_{2s})}{J_{\rm tot}}.$$

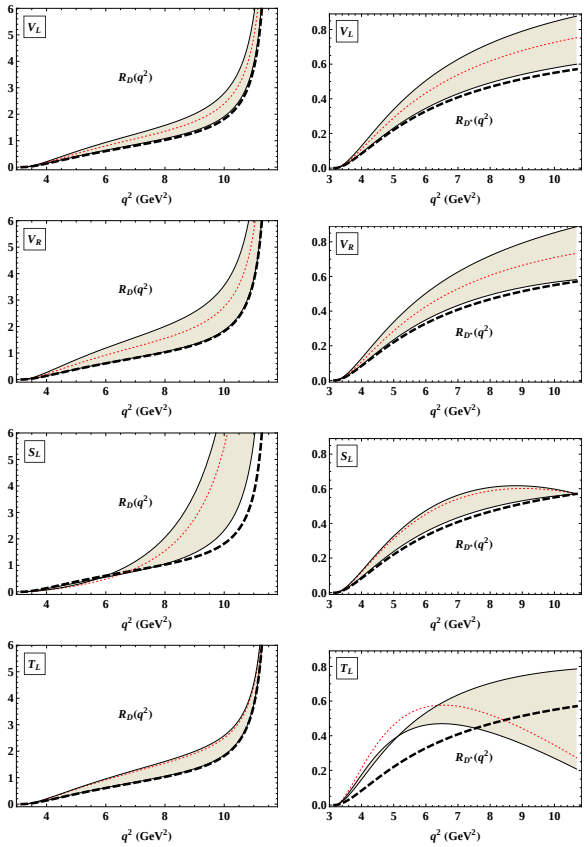


Figure 3: $R_D(q^2)$ (left) and $R_{D^*}(q^2)$ (right). The thick black dashed lines are the SM prediction; the gray bands include NP effects corresponding to the 2σ allowed regions in Fig. 1; the red dotted lines represent the best-fit values.

The q^2 dependence of $\mathcal{A}_{FB}$ is shown in Fig. 4. The coupling V_L does not effect $\mathcal{A}_{FB}$ in both decays. In the case of the $\bar{B}^0 \to D^*$ transition, the operators $\mathcal{O}_{V_R}$, $\mathcal{O}_{S_L}$, and $\mathcal{O}_{T_L}$ behave mostly similarly: they tend to decrease $\mathcal{A}_{FB}$ and shift the zero-crossing point to greater values than the SM one. However, the tensor operator can also increase $\mathcal{A}_{FB}$ in the high-q^2 region. In

the case of the $\bar{B}^0 \to D$ transition, the operator $\mathcal{O}_{V_R}$ does not affect $\mathcal{A}_{FB}$, the tensor operator $\mathcal{O}_{T_L}$ tends to lower $\mathcal{A}_{FB}$, and the scalar operator $\mathcal{O}_{S_L}$ thoroughly changes $\mathcal{A}_{FB}$: it can increase $\mathcal{A}_{FB}$ by up to 200% and implies a zero-crossing point, which is impossible in the SM. This unique effect of $\mathcal{O}_{S_L}$ would clearly distinguish it from the other NP operators.

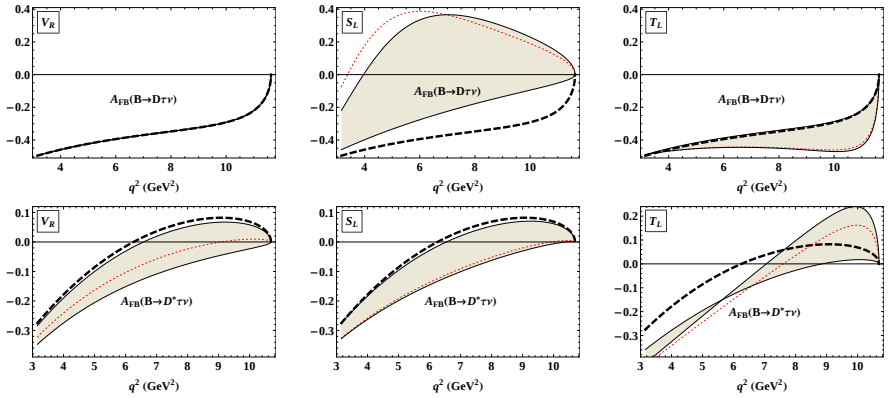


Figure 4: Forward-backward asymmetry $\mathcal{A}_{FB}$ for $\bar{B}^0 \to D\tau^-\bar{\nu}_\tau$ (upper) and $\bar{B}^0 \to D^*\tau^-\bar{\nu}_\tau$ (lower). Notations are the same as in Fig. 3.

In Fig. 5 we present the lepton-side convexity parameter $C_F^\tau(q^2)$. While $C_F^\tau(D)$ is only sensitive to $\mathcal{O}_{T_L}$, $C_F^\tau(D^*)$ is sensitive to $\mathcal{O}_{S_L}$, $\mathcal{O}_{V_R}$, and $\mathcal{O}_{T_L}$. Unlike $\mathcal{O}_{S_L}$, which can only increase $C_F^\tau(D^*)$, the operator $\mathcal{O}_{T_L}$ can only lower the parameter. It is worth mentioning that $C_F^\tau(D)$ and $C_F^\tau(D^*)$ are extremely sensitive to $\mathcal{O}_{T_L}$: it can change $C_F^\tau(D^{(*)})$ by a factor of 4 at $q^2 \approx 7$ GeV^2.

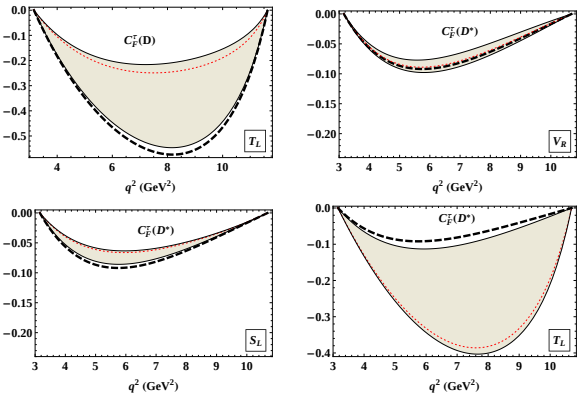


Figure 5: Lepton-side convexity parameter $C_F^\tau(q^2)$.

5.3 The $\cos\theta^*$ distribution and the hadron-side convexity parameter

By integrating the fourfold distribution over $\cos\theta$ and χ one obtains the hadron-side $\cos\theta^*$ distribution described by an untilted parabola (without a linear term). The normalized form of the $\cos\theta^*$ distribution reads $\widetilde{J}(\theta^*) = (a' + c'\cos^2\theta^*)/2(a' + c'/3)$, which can again be characterized by its convexity parameter given by

$$C_F^h(q^2) = \frac{d^2\widetilde{J}(\theta^*)}{d(\cos\theta^*)^2} = \frac{c'}{a' + c'/3} = \frac{3J_{1c} - J_{2c} - 3J_{1s} + J_{2s}}{J_{\rm tot}/3}.$$

The $\cos\theta^*$ distribution can be written as

$$\widetilde{J}(\theta^*) = 3/4 \cdot \left(2F_L(q^2)\cos^2\theta^* + F_T(q^2)\sin^2\theta^*\right),$$

where $F_L(q^2)$ and $F_T(q^2)$ are the polarization fractions of the D^* meson and are defined as

$$F_L(q^2) = J_L/(J_L + J_T), \qquad F_T(q^2) = J_T/(J_L + J_T), \qquad F_L(q^2) + F_T(q^2) = 1.$$

The hadron-side convexity parameter and the polarization fractions of the D^* are related by

$$C_F^h(q^2) = 3/2 \cdot \left(2F_L(q^2) - F_T(q^2)\right) = 3/2 \cdot \left(3F_L(q^2) - 1\right).$$

The effects of NP operators on the hadron-side convexity parameter $C_F^h(q^2)$ are shown in

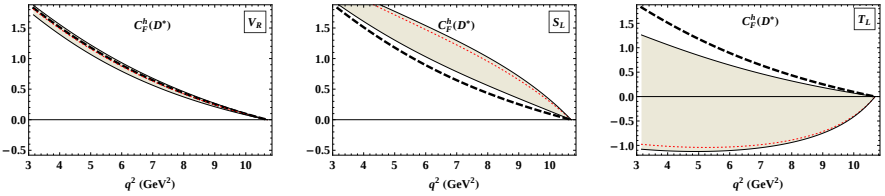


Figure 6: Hadron-side convexity parameter $C_F^h(q^2)$. Notations are the same as in Fig. 3.

Fig. 6. Each NP operator can change $C_F^h(q^2)$ in a unique way: the vector operator $\mathcal{O}_{V_R}$ almost does nothing to the parameter; the scalar operator $\mathcal{O}_{S_L}$ increases the parameter by about 50% nearly in the whole range of q^2; the tensor operator $\mathcal{O}_{T_L}$ lowers the parameter (by up to 200% at low q^2), and it also allows negative values of $C_F^h(q^2)$, which are impossible in the SM.

5.4 The χ distribution and the trigonometric moments

By integrating the fourfold distribution over $\cos\theta$ and $\cos\theta^*$, one obtains the χ distribution whose normalized form reads

$$\widetilde{J}^{(I)}(\chi) = \Big[1 + A_C^{(1)}(q^2)\cos 2\chi + A_T^{(1)}(q^2)\sin 2\chi\Big]/(2\pi),$$

where $A_C^{(1)}(q^2) = 4J_3/J_{\rm tot}$ and $A_T^{(1)}(q^2) = 4J_9/J_{\rm tot}$. Besides, one can also define other angular distributions in the angular variable χ as follows:

$$\begin{aligned} J^{(II)}(\chi) &= \Big[\int_0^1 - \int_{-1}^0\Big] d\cos\theta^* \int_{-1}^1 d\cos\theta \frac{d^4\Gamma}{dq^2 d\cos\theta d\chi d\cos\theta^*}, \\ J^{(III)}(\chi) &= \Big[\int_0^1 - \int_{-1}^0\Big] d\cos\theta^* \Big[\int_0^1 - \int_{-1}^0\Big] d\cos\theta \frac{d^4\Gamma}{dq^2 d\cos\theta d\chi d\cos\theta^*}. \end{aligned}$$

The normalized forms of these distributions read

$$\begin{aligned} \widetilde{J}^{(II)}(\chi) &= \frac{1}{4}\Big[A_C^{(2)}(q^2)\cos\chi + A_T^{(2)}(q^2)\sin\chi\Big], \\ \widetilde{J}^{(III)}(\chi) &= \frac{2}{3\pi}\Big[A_C^{(3)}(q^2)\cos\chi + A_T^{(3)}(q^2)\sin\chi\Big], \end{aligned}$$

where $A_C^{(2)}(q^2) = 3J_5/J_{\rm tot}$, $A_T^{(2)}(q^2) = 3J_7/J_{\rm tot}$, $A_C^{(3)}(q^2) = 3J_4/J_{\rm tot}$, $A_T^{(3)}(q^2) = 3J_8/J_{\rm tot}$.

Another method to project the coefficient functions J_i ($i = 3, 4, 5, 7, 8, 9$) out from the fourfold angular decay distribution is to take the appropriate trigonometric moments of the normalized decay distribution $\widetilde{J}(\theta^*, \theta, \chi)$ [4]. The trigonometric moments are defined by

$$W_i = \int d\cos\theta d\cos\theta^* d\chi M_i(\theta^*, \theta, \chi)\widetilde{J}(\theta^*, \theta, \chi) \equiv \langle M_i(\theta^*, \theta, \chi)\rangle\,,$$

where $M_i(\theta^*, \theta, \chi)$ defines the trigonometric moment that is being taken. One finds

$$\begin{aligned}
W_T(q^2) &\equiv \langle\cos 2\chi\rangle = 2\cdot(J_3/J_{\rm tot}) = (1/2)\cdot A_C^{(1)}(q^2),\\
W_{IT}(q^2) &\equiv \langle\sin 2\chi\rangle = 2\cdot(J_9/J_{\rm tot}) = (1/2)\cdot A_T^{(1)}(q^2),\\
W_A(q^2) &\equiv \langle\sin\theta\cos\theta^*\cos\chi\rangle = (3\pi/8)\cdot(J_5/J_{\rm tot}) = (\pi/8)\cdot A_C^{(2)}(q^2),\\
W_{IA}(q^2) &\equiv \langle\sin\theta\cos\theta^*\sin\chi\rangle = (3\pi/8)\cdot(J_7/J_{\rm tot}) = (\pi/8)\cdot A_T^{(2)}(q^2),\\
W_I(q^2) &\equiv \langle\cos\theta\cos\theta^*\cos\chi\rangle = (9\pi^2/128)\cdot(J_4/J_{\rm tot}) = (3\pi^2/128)\cdot A_C^{(3)}(q^2),\\
W_{II}(q^2) &\equiv \langle\cos\theta\cos\theta^*\sin\chi\rangle = (9\pi^2/128)\cdot(J_8/J_{\rm tot}) = (3\pi^2/128)\cdot A_T^{(3)}(q^2).
\end{aligned}$$

In Fig. 7 we show the q^2 dependence of the trigonometric moments $W_T(q^2)$, $W_I(q^2)$, $W_A(q^2)$,

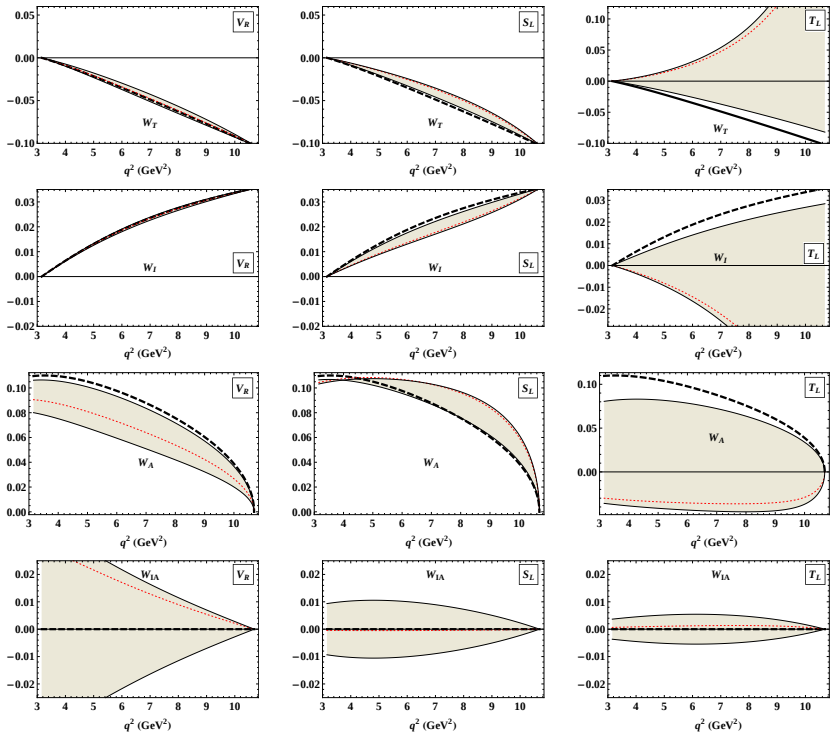


Figure 7: Trigonometric moments $W_T(q^2)$, $W_I(q^2)$, $W_A(q^2)$, and $W_{IA}(q^2)$. Notations are the same as in Fig. 3.

and $W_{IA}(q^2)$. The moments $W_T(q^2)$ and $W_I(q^2)$ are almost insensitive to $\mathcal{O}_{V_R}$ but highly sensitive to $\mathcal{O}_{T_L}$. The scalar and tensor operators are likely to raise $W_T(q^2)$ and to lower $W_I(q^2)$ in general. The moment $W_A(q^2)$ shows great sensitivity to $\mathcal{O}_{V_R}$, $\mathcal{O}_{S_L}$, and $\mathcal{O}_{T_L}$. Both $\mathcal{O}_{V_R}$ and $\mathcal{O}_{T_L}$ tend to decrease $W_A(q^2)$ while $\mathcal{O}_{S_L}$ tries to do the opposite. It is worth noting that all three moments $W_T(q^2)$, $W_I(q^2)$, and $W_A(q^2)$ are extremely sensitive to $\mathcal{O}_{T_L}$ and their sign can change in the presence of $\mathcal{O}_{T_L}$. Regarding the moment $W_{IA}(q^2)$, the three operators act in the same manner: they can change $W_{IA}(q^2)$ in both directions, and the sensitivity is maximal in the case of $\mathcal{O}_{V_R}$. The trigonometric moments $W_{II}(q^2)$ and $W_{IT}(q^2)$ are equal to

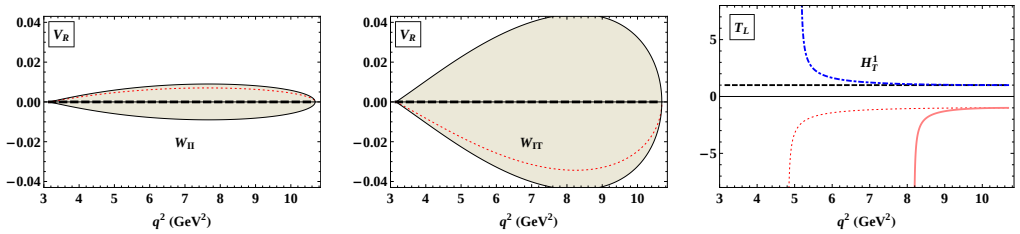


Figure 8: Trigonometric moments $W_{II}(q^2)$ (left) and $W_{IT}(q^2)$ (center), and the optimal angular observable $H_T^{(1)}(q^2)$ (right). The black dashed lines are the SM prediction. The red dotted lines represent the best-fit values. The blue dot-dashed line and the pink solid line in the right plot are the predictions for $T_L = 0.04 - 0.17i$ and $T_L = 0.18 + 0.23i$, respectively.

zero in the SM and obtain a nonzero contribution only from the right-chiral vector operator $\mathcal{O}_{V_R}$, as depicted in Fig. 8. Both moments are proportional to the imaginary part of V_R and the effect of $\mathcal{O}_{V_R}$ cancels in their ratio.

One can also consider certain combinations of angular observables where the form factor dependence drops out (at least in most NP scenarios) [16]. As a demonstration, we consider the optimized observable

$$H_T^{(1)} = \sqrt{2}J_4/\sqrt{-J_{2c}(2J_{2s} - J_3)},$$

which is equal to one not only in the SM but also in all NP scenarios except the tensor one, as shown in the right plot of Fig. 8. Therefore $H_T^{(1)}(q^2)$ plays a prominent role in confirming the appearance of the tensor operator $\mathcal{O}_{T_L}$ in the decay $\bar{B}^0 \to D^*\tau^-\bar{\nu}_\tau$.

6 Tau polarization as probe for NP

Recently, the Belle collaboration has reported on the first measurement of the longitudinal polarization of the tau lepton in the decay $\bar{B}^0 \to D^*\tau^-\bar{\nu}_\tau$ with the result $P_L^\tau = -0.38 \pm 0.51(\text{stat.})^{+0.21}_{-0.16}(\text{syst.})$ [2]. The errors are quite large but this pioneering measurement has opened a new window on the analysis of the dynamics of the semileptonic $B \to D^{(*)}$ transitions. The hope is that, with the Belle II super-B factory nearing completion, more precise values of the polarization can be achieved in the future, which would shed more light on the search for possible NP in these decays.

In a recent paper [6] we have studied the longitudinal (P_L), transverse (P_T), and normal (P_N) polarization components of the τ^- in $\bar{B}^0 \to D^{(*)}\tau^-\bar{\nu}_\tau$ and clarified their roles in the search for NP. In [6] one can find the q^2 dependence of the τ^- polarizations in the presence of NP

operators, which bears powerful information for discriminating between different NP scenarios. For example, it can be used to perform a bin-by-bin analysis to probe NP in different q^2 regions. One can also calculate the average polarizations over the whole q^2 region. The predictions for the mean polarizations are summarized in Table 2. One sees that the τ^- polarization

$\bar{B}^0 \to D$				
	$< P_L^D >$	$< P_T^D >$	$< P_N^D >$	$< \lvert\vec{P}^D\rvert >$
SM (CCQM)	0.33	0.84	0	0.91
S_L	$(0.36, 0.67)$	$(-0.68, 0.33)$	$(-0.76, 0.76)$	$(0.89, 0.96)$
T_L	$(0.13, 0.31)$	$(0.78, 0.83)$	$(-0.17, 0.17)$	$(0.79, 0.90)$
$\bar{B}^0 \to D^*$				
	$< P_L^{D^*} >$	$< P_T^{D^*} >$	$< P_N^{D^*} >$	$< \lvert\vec{P}^{D^*}\rvert >$
SM (CCQM)	-0.50	0.46	0	0.71
S_L	$(-0.40, -0.14)$	$(0.47, 0.62)$	$(-0.20, 0.20)$	$(0.69, 0.70)$
T_L	$(-0.36, 0.24)$	$(-0.61, 0.26)$	$(-0.17, 0.17)$	$(0.23, 0.69)$
V_R	-0.50	$(0.32, 0.43)$	0	$(0.48, 0.67)$

Table 2: q^2 averages of the polarization components and the total polarization. The two rows labeled by SM (CCQM) contain our predictions within the SM with form factors calculated in the CCQM. The predicted intervals for the observables in the presence of NP are given in correspondence with the 2σ allowed regions of the NP couplings depicted in Fig. 1.

components in $\bar{B}^0 \to D\tau^-\bar{\nu}_\tau$ are extremely sensitive to S_L. When S_L is present, $\langle P_L^D \rangle$ can be as large as 0.67, $\langle P_T^D \rangle$ can reach -0.68, and $\langle P_N^D \rangle$ can even reach ± 0.76. It is interesting to note that if one measures $\langle P_L^D \rangle$ and finds any excess over the SM value, it would be a clear sign of S_L. Meanwhile, the τ^- longitudinal and transverse polarization components in $\bar{B}^0 \to D^*\tau^-\bar{\nu}_\tau$ are more sensitive to T_L. The coupling T_L can enhance $\langle P_L^{D^*} \rangle$ from the SM value of -0.50 up to 0.24, or lower $\langle P_T^{D^*} \rangle$ from 0.46 down to -0.61. Notably, the average transverse polarization $\langle P_T^D \rangle$ is almost insensitive to T_L in comparison with S_L. When T_L is present, one finds $0.78 \leq \langle P_T^D \rangle \leq 0.83$, which is almost the same as the SM value $\langle P_T^D \rangle = 0.84$. In contrast, if S_L is present, one has $-0.68 \leq \langle P_T^D \rangle \leq 0.33$, which is much lower than the SM prediction. This unique property of $\langle P_T^D \rangle$ may play a very important role in probing the scalar coupling S_L. It is also interesting to note that the average total polarization $< \lvert\vec{P}^{D^*}\rvert >$ is almost insensitive to S_L.

7 Summary and discussion

We have provided a thorough analysis of possible NP in the decays $\bar{B}^0 \to D^{(*)}\tau^-\bar{\nu}_\tau$ using the form factors obtained from our covariant quark model. Starting with a general effective Hamiltonian including NP operators, we have derived the full angular distribution and defined a large set of physical observables. Assuming NP only affects leptons of the third generation and only one NP operator appears at a time, we have gained the allowed regions of NP couplings based on recent measurements at B factories, and studied their effects on the observables. It has turned out that the current experimental data of $R(D)$ and $R(D^*)$ prefer the operators $\mathcal{O}_{S_L}$ and $\mathcal{O}_{V_{L,R}}$, the operator $\mathcal{O}_{T_L}$ is less favored, and the operator $\mathcal{O}_{S_R}$ is disfavored at 2σ.

Our analysis has been done under the assumption of one-operator dominance. However, the large observable set has revealed unique behaviors of several observables and provided many correlations between them, which allows one to distinguish between NP operators. Our analysis can serve as a map for setting up various strategies to identify the origins of NP, one of which is as follows: first, one uses the null tests $W_{IT}(q^2) = 0$ and $H_T^{(1)}(q^2) - 1 = 0$ to probe the operators $\mathcal{O}_{V_R}$ and $\mathcal{O}_{T_L}$, respectively. Second, one measures the forward-backward asymmetry in $\bar{B}^0 \to D\tau^-\bar{\nu}_\tau$. If $\mathcal{A}_{FB}^D(q^2)$ has a zero-crossing point, then it is a clear sign of $\mathcal{O}_{S_L}$. The coupling V_L is more difficult to test because it is just a multiplier of the SM operator. However, if the tests above disconfirm $\mathcal{O}_{V_R}$, $\mathcal{O}_{T_L}$, and $\mathcal{O}_{S_L}$ at the same time, then the modification of V_L to $R(D)$ and $R(D^*)$ is a must. In the future when more precise data will be collected, one can adopt the strategies described here as a useful tool to discover NP in these decays if the deviation from the SM still remains.

Acknowledgments

This work was supported in part by the Heisenberg-Landau Grant and Mainz Institute for Theoretical Physics (MITP).

References

[1] J. Lees *et al.* (*BABAR* Collaboration), Phys. Rev. Lett. **109**, 101802 (2012).

[2] M. Huschle *et al.* (Belle Collaboration), Phys. Rev. **D92**, 072014 (2015);
Y. Sato *et al.* (Belle Collaboration), Phys. Rev. **D94**, 072007 (2016);
S. Hirose *et al.* (Belle Collaboration), arXiv:1612.00529.

[3] R. Aaij *et al.* (LHCb Collaboration), Phys. Rev. Lett. **115**, 111803 (2015).

[4] M. A. Ivanov, J. G. Körner, and C. T. Tran, Phys. Rev. **D92**, 114022 (2015).

[5] M. A. Ivanov, J. G. Körner and C. T. Tran, Phys. Rev. **D94**, 094028 (2016).

[6] M. A. Ivanov, J. G. Krner and C. T. Tran, Phys. Rev. D **95**, no. 3, 036021 (2017) [arXiv:1701.02937 [hep-ph]].

[7] H. Na *et al.* (HPQCD Collaboration), Phys. Rev. **D92**, 054510 (2015).

[8] S. Fajfer, J. F. Kamenik, and I. Nisandzic, Phys. Rev. **D85**, 094025 (2012).

[9] A. Crivellin, C. Greub and A. Kokulu, Phys. Rev. **D86**, 054014 (2012);
A. Celis, M. Jung, X. Q. Li and A. Pich, JHEP **1301**, 054 (2013).

[10] Y. Sakaki, M. Tanaka, A. Tayduganov and R. Watanabe, Phys. Rev. **D88**, 094012 (2013);
M. Bauer and M. Neubert, Phys. Rev. Lett. **116**, 141802 (2016);
S. Fajfer and N. Kosnik, Phys. Lett. **B755**, 270 (2016);
X. Q. Li, Y. D. Yang and X. Zhang, JHEP **1608**, 054 (2016).

[11] A. Datta, M. Duraisamy and D. Ghosh, Phys. Rev. **D86**, 034027 (2012);
D. Becirevic, N. Kosnik and A. Tayduganov, Phys. Lett. **B716**, 208 (2012);
M. Tanaka and R. Watanabe, Phys. Rev. **D87**, 034028 (2013);
P. Biancofiore, P. Colangelo and F. De Fazio, Phys. Rev. **D87**, 074010 (2013);
M. Duraisamy and A. Datta, JHEP **1309**, 059 (2013).

[12] M. Neubert, Heavy quark symmetry, Phys. Rept. **245**, 259 (1994).

[13] T. Branz *et al.*, Phys. Rev. **D81**, 034010 (2010);
M. A. Ivanov *et al.* Phys. Rev. **D85**, 034004 (2012);
M. A. Ivanov and C. T. Tran, Phys. Rev. **D92**, 074030 (2015).

[14] J. G. Körner and G. A. Schuler, Phys. Lett. **B231**, 306 (1989);
J. G. Körner and G. A. Schuler, Z. Phys. C **46**, 93 (1990).

[15] A. Faessler *et al.*, Eur. Phys. J. direct C **4**, 18 (2002).

[16] T. Feldmann, B. Müller and D. van Dyk, Phys. Rev. **D92**, 034013 (2015).

Implications from $B \to K^*\ell^+\ell^-$ observables using LHCb data.

Abinash Kumar Nayak, Rusa Mandal, Rahul Sinha

The Institute of Mathematical Sciences, Taramani, Chennai 600113, India

DOI: http://dx.doi.org/10.3204/DESY-PROC-2016-04/Sina

The decay $B \to K^*\ell^+\ell^-$ is regarded as one of the most important modes to search for physics beyond the standard model as the angular distribution enables the independent measurement of a plethora of observables. To disentangle new physics from the standard model effect an "exact" test of standard model is needed. This drive us to derive a relation including all short-distance and long-distance effects, factorizable and non-factorizable contributions, complete electromagnetic corrections to hadronic operators up to all orders, resonance contributions and the finite lepton masses in a complete model independent approach. The violation of this relation will provide a smoking gun signal of new physics. The model independent framework has also been implemented in the maximum q^2 limit to highlight strong evidence of right-handed currents, which are absent in the SM. The conclusions derived are free from hadronic corrections. Our approach differs from other approaches that probe new physics at low q^2 as it does not require estimates of hadronic parameters but relies instead on heavy quark symmetries that are reliable at the maximum q^2 kinematic endpoint.

The mode $B \to K^*\ell^+\ell^-$

The Standard Model(SM) is a gauge theory capable of explaining interactions between the observed particles. Most ingredients completed by 1974 and with the discovery of the Higgs, the SM is complete. Though this gauge theory has been remarkably successful in explaining a whole lot of physical phenomenons, it also fails to answer various others(e.g. the origin of its parameters, Naturalness problem, dark matter, dark energy etc.). Hence a lot of attempts have been made to extend this highly successful theory, which we call the Physics beyond SM or New Physics(NP). However, no conclusive NP signal has been seen till now. Which brings us to the question that how does one search for NP. It can be discovered either by direct production of new particles which are not accommodated in SM or by indirect searches at high luminosity facilities where NP can contribute virtually through loop processes.

A lot of effort has been put in observation of new particles through direct production. But if we were to follow the later approach, then we should focus on modes that are potentially sensitive to NP. One such mode is the mode $B \to K^*\ell^+\ell^-$. The underlying process is a Flavor Changing Neutral Current (FCNC) decay which happens through a penguin process. It has a large number of related observables. In addition, this mode can get contribution from variety of operators through the loop. Hence, this is very good candidate in probing NP. But this being a hadronic decay mode, we have to be careful in dealing with the hadronic uncertainties. In this

work we show that the hadronic uncertainties can be eliminated by carefully taking relation between observables. Then we use these relations to probe for NP.

Model independent framework

The decays $B \to K^*\ell^+\ell^-$ occurs at the quark level via a $b \to s\ell^+\ell^-$ flavor changing neutral current transition. The short-distance effective Hamiltonian for the inclusive process $b \to s\ell^+\ell^-$ is given in the SM by [1, 2, 3],

$$\mathcal{H}_{\rm eff} = -4\frac{G_F}{\sqrt{2}}\Big[V_{tb}V_{ts}^*\Big(C_1\mathcal{O}_1^c + C_2\mathcal{O}_2^c + \sum_{i=3}^{10} C_i\mathcal{O}_i\Big) + V_{ub}V_{us}^*\Big(C_1(\mathcal{O}_1^c - \mathcal{O}_1^u) + C_2(\mathcal{O}_2^c - \mathcal{O}_2^u)\Big)\Big]. \tag{1}$$

The local operators $\mathcal{O}_i$ are as given in Ref. [2], however, for completeness we present the relevant operators that are dominant:

$$\begin{aligned}
\mathcal{O}_7 &= \frac{e}{g^2}\big[\bar{s}\sigma_{\mu\nu}(m_bP_R + m_sP_L)b\big]F^{\mu\nu},\\
\mathcal{O}_9 &= \frac{e^2}{g^2}(\bar{s}\gamma_\mu P_L b)\,\bar{\ell}\gamma^\mu\ell,\\
\mathcal{O}_{10} &= \frac{e^2}{g^2}(\bar{s}\gamma_\mu P_L b)\,\bar{\ell}\gamma^\mu\gamma_5\ell,
\end{aligned}$$

where $g\,(e)$ is the strong(electromagnetic) coupling constant, $P_{L,R} = (1 \mp \gamma_5)/2$ are the left and right chiral projection operators and $m_b\,(m_s)$ are the running $b\,(s)$ quark mass in the $\overline{\rm MS}$ scheme. The Wilson coefficients C_i encode all the short-distance effects and are calculated in perturbation theory at a matching scale $\mu = M_W$ up to desired order in the strong coupling constant α_s before being evolved down to the scale $\mu = m_b \approx 4.8$GeV. All NP contributions to $B \to K^*\ell^+\ell^-$ contribute exclusively to C_i; this includes new Wilson coefficients corresponding to new operators that arise from NP.

The decay amplitude in terms of hadronic matrix elements must therefore include direct contributions proportional to C_7, C_9 and C_{10} multiplied by $B \to K^*$ form factors and contributions from non local hadronic matrix elements $\mathcal{H}_i$ such that [4, 5],

$$\begin{aligned}
A(B(p) \to K^*(k)\ell^+\ell^-) = \frac{G_F\alpha}{\sqrt{2}\pi}V_{tb}V_{ts}^*\Bigg[\Bigg\{&\widehat{C}_9\langle K^*|\bar{s}\gamma^\mu P_L b|\bar{B}\rangle\\
&- \frac{2\widehat{C}_7}{q^2}\langle K^*|\bar{s}i\sigma^{\mu\nu}q_\nu(m_bP_R + m_sP_L)b|\bar{B}\rangle\\
&- \frac{16\pi^2}{q^2}\sum_{i=\{1-6,8\}}\widehat{C}_i\mathcal{H}_i^\mu\Bigg\}\bar{\ell}\gamma_\mu\ell\\
&+ \widehat{C}_{10}\langle K^*|\bar{s}\gamma^\mu P_L b|\bar{B}\rangle\,\bar{\ell}\gamma_\mu\gamma_5\ell\Bigg],
\end{aligned} \tag{2}$$

where, $p = q + k$ with q being the dilepton invariant momentum and the non local hadron matrix element $\mathcal{H}_i^\mu$ is given by

$$\mathcal{H}_i^\mu = \langle K^*(k)|i\int d^4x\, e^{iq\cdot x} T\{j_{em}^\mu(x), \mathcal{O}_i(0)\}|\bar{B}(p)\rangle.$$

In Eq. (2), we have introduced *new notional theoretical parameters $\widehat{C}_7$, $\widehat{C}_9$ and $\widehat{C}_{10}$ to indicate the true values of Wilson coefficients, which are by definition not dependent on the order of the perturbative calculation to which they are evaluated.* Our definition is explicit and should not be confused with those defined earlier in literature. The amplitude expressed in Eq. (2) is *notionally complete and free from any approximations.* In this paper we do not attempt to estimate the hadronic matrix element involved in Eq. (2), instead we use Lorentz invariance to write out the most general form of the hadron matrix elements $\langle K^*|\bar{s}\gamma^\mu P_L b|\bar{B}(p)\rangle$ and $\langle K^*|\bar{s}i\sigma^{\mu\nu}q_\nu P_{R,L} b|\bar{B}(p)\rangle$ which may be defined as

$$\langle K^*(\epsilon^*,k))|\bar{s}\gamma^\mu P_L b|B(p)\rangle = \epsilon^*_\nu\Big(\mathcal{X}_0\, q^\mu q^\nu + \mathcal{X}_1\,(g^{\mu\nu} - \frac{q^\mu q^\nu}{q^2}) + \mathcal{X}_2\,(k^\mu - \frac{k.q}{q^2}q^\mu)q^\nu + i\mathcal{X}_3\,\epsilon^{\mu\nu\rho\sigma}\,k_\rho q_\sigma\Big), \tag{3}$$

$$\langle K^*(\epsilon^*,k))|i\bar{s}\sigma^{\mu\nu}q_\nu P_{R,L} b|B(p)\rangle = \epsilon^*_\nu\Big(\pm\,\mathcal{Y}_1\,(g^{\mu\nu} - \frac{q^\mu q^\nu}{q^2}) \pm \mathcal{Y}_2\,(k^\mu - \frac{k.q}{q^2}q^\mu)q^\nu + i\mathcal{Y}_3\,\epsilon^{\mu\nu\rho\sigma}\,k_\rho q_\sigma\Big). \tag{4}$$

We have written Eq. (3) such that the vector part of the current in $\langle K^*(\epsilon^*,k))|\bar{s}\gamma^\mu P_L b|B(p)\rangle$ is conserved and only the $\mathcal{X}_0$ term in the divergence of the axial part survives. Equation (4) is also written so as to ensure that $\langle K^*|i\bar{s}\sigma^{\mu\nu}q_\nu P_{R,L} b|B\rangle q_\mu = 0$. The relations between $\mathcal{X}_{0,1,2,3}$ and $\mathcal{Y}_{1,2,3}$ and the form factors conventionally defined for on-shell K^* are discussed in [6]. It should be noted that form factors $\mathcal{X}_{0,1,2,3}$ and $\mathcal{Y}_{1,2,3}$ are functions of q^2 and k^2, but we suppress the explicit dependence for simplicity of notation. The subsequent decay of the K^*, i.e., $K^*(k) \to K(k_1)\pi(k_2)$ can be easily taken into account [7, 2] resulting in the hadronic matrix element $\langle[K(k_1)\pi(k_2)]_{K^*}|\bar{s}\gamma^\mu P_L b|B(p)\rangle$ being written as

$$\begin{aligned}\langle[K(k_1)\pi(k_2)]_{K^*}|\bar{s}\gamma^\mu P_L b|B(p)\rangle = D_{K^*}(k^2)W_\nu\Big(&\mathcal{X}_0\, q^\mu q^\nu + \mathcal{X}_1(g^{\mu\nu} - \frac{q^\mu q^\nu}{q^2}) \\ &+ \mathcal{X}_2\,(k^\mu - \frac{k.q}{q^2}q^\mu)q^\nu + i\mathcal{X}_3\,\epsilon^{\mu\nu\rho\sigma}\,k_\rho q_\sigma\Big),\end{aligned} \tag{5}$$

$$\begin{aligned}\langle[K(k_1)\pi(k_2)]_{K^*}|i\bar{s}\sigma^{\mu\nu}q_\nu P_{R,L} b|B(p)\rangle = D_{K^*}(k^2)W_\nu\Big(&\pm\,\mathcal{Y}_1\,(g^{\mu\nu} - \frac{q^\mu q^\nu}{q^2}) \\ &\pm \mathcal{Y}_2\,(k^\mu - \frac{k.q}{q^2}q^\mu)q^\nu + i\mathcal{Y}_3\,\epsilon^{\mu\nu\rho\sigma}\,k_\rho q_\sigma\Big),\end{aligned} \tag{6}$$

where, the subscript K^* in $[K(k_1)\pi(k_2)]_{K^*}$ indicates that the final sate is produced by the decay of a K^*. $D_{K^*}(k^2)$ is the K^* propagator, so that

$$|D_{K^*}(k^2)|^2 = \frac{g^2_{K^*K\pi}}{(k^2 - m^2_{K^*})^2 + (m_{K^*}\Gamma_{K^*})^2}, \tag{7}$$

with $g_{K^*K\pi}$ being the $K^*K\pi$ coupling and the other parameters introduced are

$$W_\nu = K_\nu - \xi k_\nu,\ K = k_1 - k_2,\ k = k_1 + k_2,\ \xi = \frac{k_1^2 - k_2^2}{k^2}.$$

The most general expression for the hadronic matrix element $\mathcal{H}_i^\mu$ can also be written using Lorentz invariance. Since this hadronic matrix element arises from non local contributions at the quark level, it involves introducing "new" form factors $\mathcal{Z}_1^i$, $\mathcal{Z}_2^i$ and $\mathcal{Z}_3^i$ corresponding to nonfactorizable contribution from each $\mathcal{H}_i^\mu$ in analogy with those introduced in Eq. (3) as follows:

$$\begin{aligned}\mathcal{H}_i^\mu &= \langle K^*(\epsilon^*, k)|i\int d^4x\, e^{iq\cdot x} T\{j_{em}^\mu(x), \mathcal{O}_i(0)\}|\bar{B}(p)\rangle \\ &= \epsilon_\nu^*\Big(\mathcal{Z}_1^i\,(g^{\mu\nu} - \frac{q^\mu q^\nu}{q^2}) + \mathcal{Z}_2^i\,(k^\mu - \frac{k.q}{q^2}q^\mu)q^\nu + i\mathcal{Z}_3^i\,\epsilon^{\mu\nu\rho\sigma}\,k_\rho q_\sigma\Big). \end{aligned} \tag{8}$$

Our definition follows Ref. [8] of "nonfactorizable " and includes those corrections that are not contained in the definition of form factors introduced in Eqs. (3) and (4). Here the most general form of $\mathcal{H}_i^\mu$ is written to ensure the conservation of EM current i.e, $q_\mu \mathcal{H}_i^\mu = 0$.

The non local effects represented by $\mathcal{H}_i^\mu$ can be taken into account by absorbing the contributions into redefined $\widehat{C}_9$ and modifying the contribution from the electromagnetic dipole operator $\mathcal{O}_7$. The electromagnetic corrections to operators $\mathcal{O}_{1-6,8}$ can also contribute to $B \to K^*\gamma$ at $q^2 = 0$. Since only the Wilson coefficient $\widehat{C}_7$ contributes to $B \to K^*\gamma$, the charm loops at $q^2 = 0$ must contribute to $\widehat{C}_7$ in order for the Wilson coefficient to be process independent. It is easily seen that the effect of this is to modify the $\widehat{C}_7\langle K\pi|\bar{s}i\sigma^{\mu\nu}q_\nu(m_bP_R + m_sP_L)b|\bar{B}\rangle$ terms such that the form factors and Wilson coefficients mix in an essentially inseparable fashion. This holds true even for the leading logarithmic contributions [8, 9]. Both factorizable and nonfactorizable contributions arising from electromagnetic corrections to hadronic operators up to all orders can in principle be included in this approach. The remaining contributions can easily be absorbed into a redefined "effective" Wilson coefficient $\widehat{C}_9$ defined such that

$$\widehat{C}_9 \to \widetilde{C}_9^{(j)} = \widehat{C}_9 + \Delta C_9^{(\text{fac})}(q^2) + \Delta C_9^{(j),(\text{non-fac})}(q^2) \tag{9}$$

where, $j = 1, 2, 3$ and $\Delta C_9^{(\text{fac})}(q^2)$, $\Delta C_9^{(\text{non-fac})}(q^2)$ correspond to factorizable and soft gluon nonfactorizable contributions respectively. Note that the nonfactorizable contributions necessitates the introduction of new form factors $\mathcal{Z}_j$ and the explicit dependence on $\mathcal{Z}_j/\mathcal{X}_j$ is absorbed in defining

$$\Delta C_9^{(\text{fac})} + \Delta C_9^{(j),(\text{non-fac})} = -\frac{16\pi^2}{q^2}\sum_{i=\{1-6,8\}} \widehat{C}_i\,\frac{\mathcal{Z}_j^i}{\mathcal{X}_j}, \tag{10}$$

resulting in the j dependence of the term as indicated. We also mention that there is no nonfactorizable correction term in Eq. (8) analogous to $\mathcal{X}_0$ (in Eq. (3)) due EM current conservation as discussed above.

The corresponding corrections to $\widehat{C}_7$ are taken into by the replacement,

$$\frac{2(m_b+m_s)}{q^2}\widehat{C}_7\,\mathcal{Y}_j \to \widetilde{\mathcal{Y}}_j = \frac{2(m_b+m_s)}{q^2}\widehat{C}_7\,\mathcal{Y}_j + \cdots, \tag{11}$$

where the dots indicate other factorizable and nonfactorizable contributions and the factor $2(m_b + m_s)/q^2$ has been absorbed in the form factors $\widetilde{\mathcal{Y}}_j$. Note that the $\widetilde{\mathcal{Y}}_j$'s are in general complex because of the nonfactorizable contributions to the Wilson coefficient $\widehat{C}_7$, but on-shell quarks and resonances do not contribute to them. It should be noted that $\widetilde{C}_9^{(j)}$ includes contributions from both factorizable and nonfactorizable effects, whereas $\widehat{C}_{10}$ is unaffected by strong interaction effects coming from electromagnetic corrections to hadronic operators. The use of a 'widetilde' versus 'widehat' throughout the paper is also meant as a notation to indicate this fact. It should be noted that $\widehat{C}_{10}$ is real in the SM, whereas, $\widetilde{C}_9^{(j)}$ and $\widetilde{\mathcal{Y}}_j$ are in general complex within the SM. The amplitude in Eq. (2) can therefore be written as

$$\mathcal{A}_\lambda^{L,R} = C_{L,R}^\lambda \mathcal{F}_\lambda - \widetilde{\mathcal{G}}_\lambda = \big(\widetilde{C}_9^\lambda \mp \widehat{C}_{10}\big)\mathcal{F}_\lambda - \widetilde{\mathcal{G}}_\lambda = (\mp\widehat{C}_{10} - r_\lambda)\mathcal{F}_\lambda + i\varepsilon_\lambda, \tag{12}$$

r_λ and ε_λ are defined as,

$$r_\lambda = \frac{\mathrm{Re}(\widetilde{\mathcal{G}}_\lambda)}{\mathcal{F}_\lambda} - \mathrm{Re}(\widetilde{C}_9^\lambda), \quad \varepsilon_\lambda \equiv \mathrm{Im}(\widetilde{C}_9^\lambda)\mathcal{F}_\lambda - \mathrm{Im}(\widetilde{\mathcal{G}}_\lambda). \tag{13}$$

Observables and relations

With these amplitudes we can construct several observables. For us the relevant observables are the three helicity fractions and six asymmetries. The helicity fractions are defined as

$$F_L = \frac{|\mathcal{A}_0^L|^2 + |\mathcal{A}_0^R|^2}{\Gamma_f}\ , \tag{14a}$$

$$F_\parallel = \frac{|\mathcal{A}_\parallel^L|^2 + |\mathcal{A}_\parallel^R|^2}{\Gamma_f}\ , \tag{14b}$$

$$F_\perp = \frac{|\mathcal{A}_\perp^L|^2 + |\mathcal{A}_\perp^R|^2}{\Gamma_f}\ , \tag{14c}$$

where $\Gamma_f \equiv \sum_\lambda(|\mathcal{A}_\lambda^L|^2 + |\mathcal{A}_\lambda^R|^2)$ such that $F_L + F_\parallel + F_\perp = 1$. The rest six asymmetries are defined below.

$$A_{\mathrm{FB}} = \frac{3}{2}\frac{\mathrm{Re}(\mathcal{A}_\parallel^L \mathcal{A}_\perp^{L^*} - \mathcal{A}_\parallel^R \mathcal{A}_\perp^{R^*})}{\Gamma_f}, \tag{15}$$

$$A_4 = \frac{\sqrt{2}}{\pi}\frac{\mathrm{Re}(\mathcal{A}_0^L \mathcal{A}_\parallel^{L^*} + \mathcal{A}_0^R \mathcal{A}_\parallel^{R^*})}{\Gamma_f}, \tag{16}$$

$$A_5 = \frac{3}{2\sqrt{2}}\frac{\mathrm{Re}(\mathcal{A}_0^L \mathcal{A}_\perp^{L^*} - \mathcal{A}_0^R \mathcal{A}_\perp^{R^*})}{\Gamma_f}, \tag{17}$$

$$A_7 = \frac{3}{2\sqrt{2}}\frac{\mathrm{Im}(\mathcal{A}_0^L \mathcal{A}_\parallel^{L^*} - \mathcal{A}_0^R \mathcal{A}_\parallel^{R^*})}{\Gamma_f}, \tag{18}$$

$$A_8 = \frac{\sqrt{2}}{\pi}\frac{\mathrm{Im}(\mathcal{A}_0^L \mathcal{A}_\perp^{L^*} + \mathcal{A}_0^R \mathcal{A}_\perp^{R^*})}{\Gamma_f}, \tag{19}$$

$$A_9 = \frac{3}{2\pi}\frac{\mathrm{Im}(\mathcal{A}_\parallel^{L^*} \mathcal{A}_\perp^L + \mathcal{A}_\parallel^{R^*} \mathcal{A}_\perp^R)}{\Gamma_f}. \tag{20}$$

Using Eq. (12) and (13) we express the observables in terms of $\widehat{C}_{10}$, r_λ, $\mathcal{F}_\lambda$ and ε_λ as follows:

$$F_L\Gamma_f = 2\mathcal{F}_0^2\big(r_0^2+\widehat{C}_{10}^2\big)+2\varepsilon_0^2, \tag{21}$$
$$F_\parallel\Gamma_f = 2\mathcal{F}_\parallel^2\big(r_\parallel^2+\widehat{C}_{10}^2\big)+2\varepsilon_\parallel^2, \tag{22}$$
$$F_\perp\Gamma_f = 2\mathcal{F}_\perp^2\big(r_\perp^2+\widehat{C}_{10}^2\big)+2\varepsilon_\perp^2, \tag{23}$$
$$\sqrt{2}\pi A_4\Gamma_f = 4\mathcal{F}_0\mathcal{F}_\parallel\big(r_0 r_\parallel+\widehat{C}_{10}^2\big)+4\varepsilon_0\varepsilon_\parallel, \tag{24}$$
$$\sqrt{2}A_5\Gamma_f = 3\mathcal{F}_0\mathcal{F}_\perp\widehat{C}_{10}\big(r_0+r_\perp\big), \tag{25}$$
$$A_{\rm FB}\Gamma_f = 3\mathcal{F}_\parallel\mathcal{F}_\perp\widehat{C}_{10}\big(r_\parallel+r_\perp\big), \tag{26}$$
$$\sqrt{2}A_7\Gamma_f = 3\widehat{C}_{10}\big(\mathcal{F}_0\varepsilon_\parallel-\mathcal{F}_\parallel\varepsilon_0\big), \tag{27}$$
$$\pi A_8\Gamma_f = 2\sqrt{2}\big(\mathcal{F}_0 r_0\varepsilon_\perp-\mathcal{F}_\perp r_\perp\varepsilon_0\big), \tag{28}$$
$$\pi A_9\Gamma_f = 3\big(\mathcal{F}_\perp r_\perp\varepsilon_\parallel-\mathcal{F}_\parallel r_\parallel\varepsilon_\perp\big). \tag{29}$$

The ε_λ's can be solved using A_7, A_8 and A_9 from Eqs. (27)–(29) to give

$$\varepsilon_\perp = \frac{\sqrt{2}\pi\Gamma_f}{(r_0-r_\parallel)\mathcal{F}_\perp}\left[\frac{A_9\mathsf{P}_1}{3\sqrt{2}}+\frac{A_8\mathsf{P}_2}{4}-\frac{A_7\mathsf{P}_1\mathsf{P}_2 r_\perp}{3\pi\widehat{C}_{10}}\right], \tag{30}$$

$$\varepsilon_\parallel = \frac{\sqrt{2}\pi\Gamma_f}{(r_0-r_\parallel)\mathcal{F}_\perp}\left[\frac{A_9 r_0}{3\sqrt{2}r_\perp}+\frac{A_8\mathsf{P}_2 r_\parallel}{4\mathsf{P}_1 r_\perp}-\frac{A_7\mathsf{P}_2 r_\parallel}{3\pi\widehat{C}_{10}}\right], \tag{31}$$

$$\varepsilon_0 = \frac{\sqrt{2}\pi\Gamma_f}{(r_0-r_\parallel)\mathcal{F}_\perp}\left[\frac{A_9\mathsf{P}_1 r_0}{3\sqrt{2}\mathsf{P}_2 r_\perp}+\frac{A_8 r_\parallel}{4r_\perp}-\frac{A_7\mathsf{P}_1 r_0}{3\pi\widehat{C}_{10}}\right]. \tag{32}$$

Where,

$$\mathsf{P}_1=\frac{\mathcal{F}_\perp}{\mathcal{F}_\parallel},\quad \mathsf{P}_2=\frac{\mathcal{F}_\perp}{\mathcal{F}_0}. \tag{33}$$

As expected, we also get some relations between observables as there are only 6 amplitudes but several observables. Implying, all the observables are not independent. These relations are obtained by interplaying with the Eqs. (21)-(26). One such relation, with the imaginary contribution to the amplitudes, is given below

$$A_4 = \frac{2\sqrt{2}\varepsilon_\parallel\varepsilon_0}{\pi\Gamma_f}+\frac{8A_5A_{\rm FB}}{9\pi\Big(F_\perp-\frac{2\varepsilon_\perp^2}{\Gamma_f}\Big)} + \sqrt{2}\,\frac{\sqrt{\Big(F_L-\frac{2\varepsilon_0^2}{\Gamma_f}\Big)\Big(F_\perp-\frac{2\varepsilon_\perp^2}{\Gamma_f}\Big)-\frac{8}{9}A_5^2}\;\sqrt{\Big(F_\parallel-\frac{2\varepsilon_\parallel^2}{\Gamma_f}\Big)\Big(F_\perp-\frac{2\varepsilon_\perp^2}{\Gamma_f}\Big)-\frac{4}{9}A_{\rm FB}^2}}{\pi\Big(F_\perp-\frac{2\varepsilon_\perp^2}{\Gamma_f}\Big)}. \tag{34}$$

In real limit(i.e. $\varepsilon_\lambda\to 0$), the asymmetries $A_{7,8,9}\to 0$ from Eq.(27)-(29). Whereas the rest of the asymmetries are related to other observables through the following relations,

$$A_4 = \frac{8 A_5 A_{\rm FB}}{9\pi F_\perp} + \frac{\sqrt{4F_\parallel F_\perp - \frac{16}{9}A_{\rm FB}^2}\sqrt{4F_L F_\perp - \frac{32}{9}A_5^2}}{2\sqrt{2}\pi F_\perp}, \tag{35}$$

$$A_5 = \frac{\pi A_4 A_{\rm FB}}{2F_\parallel} \pm \frac{3\sqrt{4F_\parallel F_\perp - \frac{16}{9}A_{\rm FB}^2}\sqrt{2F_\parallel F_L - \pi^2 A_4^2}}{8F_\parallel}, \tag{36}$$

$$A_{\rm FB} = \frac{\pi A_4 A_5}{F_L} \pm \frac{3\sqrt{4F_L F_\perp - \frac{32}{9}A_5^2}\sqrt{2F_\parallel F_L - \pi^2 A_4^2}}{4\sqrt{2}F_L}. \tag{37}$$

The detailed derivations of the above relations are given in [6, 10]. We note that these relations do not depend on any hadronic parameters except the observables. Hence these relations should hold true unless some new operators, or New Physics operators to be precise, end up altering the whole angular distribution such that the above mentioned relations will no longer hold. So we emphasize that these relations can be used as a very clean and indirect probe for New Physics. However in the presence of right-handed currents and any extra vector current such as Z' which does not change the angular distributions, the relations will remain valid. At this point we'd also like to mention that the kind of New Physics contributing to this mode are not that arbitrary as there will be several constraints, on several kinds of New Physics, coming from several other hadronic as well as non-hadronic decay modes.

In Fig.1, we test the validity of Eq.(35)-(37). We get the values of the observable on LHS by putting experimentally observed observable values on the RHS in each q^2 bin. Then we plot this result against the experimentally observed values of the corresponding observables. The mean values and $\pm 1\sigma$ uncertainty bands for asymmetries $A_{\rm FB}$, A_4, A_5 and P_5' calculated using Eqs. (35)-(37), are shown in yellow, gray, green and brown bands, respectively. The error bars in red (dark) correspond to the LHCb measured [11] central values and errors for each observable for the respective q^2 bins. Sizable discrepancies are found for $A_{\rm FB}$ in $11.0 \leq q^2 \leq 12.5$ GeV^2 and $15 \leq q^2 \leq 17$ GeV^2 bins and for A_4 in the range $0.1 \leq q^2 \leq 0.98$ GeV^2.

Looking for New Physics

The rare decay $B \to K^* \ell^+ \ell^-$, which involves a $b \to s$ flavor changing loop induced quark transition at the quark level, provides an indirect but very sensitive probe of new physics (NP) beyond the standard model (SM). The angular distribution of the decay products provides a large number of observables [7] and thus can be used to reduce hadronic uncertainties making the mode a very special tool to probe for NP. We have already indicated some irregularities between the SM and the data in the previous discussion. While it implies the presence of NP, it says very little about the exact nature of the possible New Physics. In the following work we discover a specific kind of NP(i.e. Right-Handed Currents) at the kinematic endpoint of $B \to K^* \ell^+ \ell^-$. We emphasize that even with these RH-currents, which does not alter the angular distribution, the relations in Eq. (35)-(37) would still hold and some other kind of NP would be required to explain the discrepancies found in Fig.1.

Significant work has been done to probe NP in this mode. Most previous attempts have focused [12] on the low dilepton invariant mass squared region $q^2 = 1 - 6$ GeV^2. An alternative approach that probes the maximum q^2 limit has also been studied in literature [5, 13]. We show

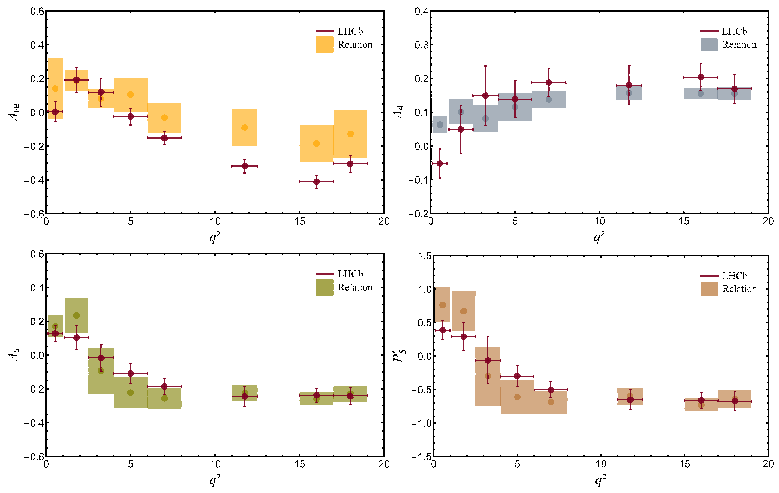


Figure 1: (color online) The mean values and $\pm 1\sigma$ uncertainty bands for asymmetries $A_{\rm FB}$, A_4, A_5 and P_5' calculated using Eqs. (35) – (37) are shown in yellow, gray, green and brown bands, respectively. The error bars in red (dark) correspond to the LHCb measured [11] central values and errors for each observable for the respective q^2 bins. The predictions for the asymmetries are obtained using the relations among observables which are independent of any hadronic parameters and depend on experimental measurements of the other observables remaining in the corresponding relations. Sizable discrepancies are shown for $A_{\rm FB}$ in $11.0 \leq q^2 \leq 12.5$ GeV^2 and $15 \leq q^2 \leq 17$ GeV^2 bins and for A_4 in the range $0.1 \leq q^2 \leq 0.98$ GeV^2. We note that the relations (Eqs. (35) – (37)) remain valid except in the presence of NP operators that result in modified angular distribution. Hence the presence of right-handed currents and any extra vector current such as Z' the relations will remain valid.

that this limit holds significant promise for clean probes of NP. A previous study suggested a possible signal of NP in the large q^2 region [10]. In this work we show that LHCb data implies a 5σ signal for the existence of NP. While the evidence for right handed currents is clear, other NP contributions are also possible. Our conclusions are derived in the maximum q^2 limit ($q^2_{\rm max}$) and are free from hadronic corrections. Our approach differs from other approaches that probe NP at low q^2 by not requiring estimates of hadronic parameters but relying instead on heavy quark symmetries that are completely reliable at the kinematic endpoint $q^2_{\rm max}$ [5, 14]. While the observables themselves remain unaltered from their SM values, their derivatives and second derivatives at the endpoint are sensitive to NP effects.

Right-Handed currents

As mentioned previously the Right-Handed currents do not alter the angular distributions. However, they introduce two new operators namely O_9' and O_{10}'. These operators O_9' and O_{10}', with respective couplings C_9' and C_{10}', modify the amplitudes in Eq. (12) as follows

$$\begin{aligned}\mathcal{A}_\perp^{L,R} &= \big((\widetilde{C}_9^{\perp} + C_9') \mp (C_{10} + C_{10}')\big)\mathcal{F}_\perp - \widetilde{\mathcal{G}}_\perp, \\ \mathcal{A}_{\parallel,0}^{L,R} &= \big((\widetilde{C}_9^{\parallel,0} - C_9') \mp (C_{10} - C_{10}')\big)\mathcal{F}_{\parallel,0} - \widetilde{\mathcal{G}}_{\parallel,0}\end{aligned} \tag{38}$$

We define two new variables

$$\xi = \frac{C'_{10}}{C_{10}} \quad \text{and} \quad \xi' = \frac{C'_9}{C_{10}}. \tag{39}$$

Ignoring the imaginary contributions for the time being, the observables in Eq.(21)-(26) can be rewritten as,

$$F_\perp = 2\zeta\,(1+\xi)^2(1+R_\perp^2) \tag{40}$$
$$F_\parallel \mathsf{P}_1^2 = 2\zeta\,(1-\xi)^2(1+R_\parallel^2) \tag{41}$$
$$F_L \mathsf{P}_2^2 = 2\zeta\,(1-\xi)^2(1+R_0^2) \tag{42}$$
$$A_{\rm FB}\mathsf{P}_1 = 3\zeta\,(1-\xi^2)\big(R_\parallel + R_\perp\big) \tag{43}$$
$$\sqrt{2}A_5\mathsf{P}_2 = 3\zeta\,(1-\xi^2)\big(R_0 + R_\perp\big) \tag{44}$$

where $\mathsf{P}_1 = \dfrac{\mathcal{F}_\perp}{\mathcal{F}_\parallel}$, $\mathsf{P}_2 = \dfrac{\mathcal{F}_\perp}{\mathcal{F}_0}$, $\zeta = \dfrac{\mathcal{F}_\perp^2 C_{10}^2}{\Gamma_f}$,

$$R_\perp = \frac{\frac{r_\perp}{C_{10}} - \xi'}{1+\xi},\ R_\parallel = \frac{\frac{r_\parallel}{C_{10}} + \xi'}{1-\xi},\ R_0 = \frac{\frac{r_0}{C_{10}} + \xi'}{1-\xi}. \tag{45}$$

We consider the observables F_L, $F_\parallel$, $F_\perp$, $A_{\rm FB}$ and A_5, with the constraint $F_L + F_\parallel + F_\perp = 1$. Using Eq. (40)–(44), we obtain expressions for $R_\perp$, $R_\parallel$, R_0 and P_2 in terms of the observables and P_1:

$$R_\perp = \pm\frac{3}{2}\frac{\left(\frac{1-\xi}{1+\xi}\right)F_\perp + \frac{1}{2}\mathsf{P}_1 Z_1}{\mathsf{P}_1 A_{\rm FB}} \tag{46}$$
$$R_\parallel = \pm\frac{3}{2}\frac{\left(\frac{1+\xi}{1-\xi}\right)\mathsf{P}_1 F_\parallel + \frac{1}{2}Z_1}{A_{\rm FB}} \tag{47}$$
$$R_0 = \pm\frac{3}{2\sqrt{2}}\frac{\left(\frac{1+\xi}{1-\xi}\right)\mathsf{P}_2 F_L + \frac{1}{2}Z_2}{A_5} \tag{48}$$
$$\mathsf{P}_2 = \frac{\left(\frac{1-\xi}{1+\xi}\right)2\mathsf{P}_1 A_{\rm FB} F_\perp}{\sqrt{2}A_5\left(\left(\frac{1-\xi}{1+\xi}\right)2F_\perp + Z_1\mathsf{P}_1\right) - Z_2\mathsf{P}_1 A_{\rm FB}} \tag{49}$$

where $Z_1 = (4F_\parallel F_\perp - \frac{16}{9}A_{\rm FB}^2)^{\frac{1}{2}}$ and $Z_2 = (4F_L F_\perp - \frac{32}{9}A_5^2)^{\frac{1}{2}}$. Since we have one extra parameter compared to observables, all of the above expressions depend on P_1. Fortunately in the large q^2 limit, the relations between form factors enable us to eliminate one parameter.

At the kinematic limit $q^2 = q^2_{\rm max} = (m_B - m_{K^*})^2$ the K^* meson is at rest and the two leptons travel back to back in the B meson rest frame. There is no preferred direction in the decay kinematics. Hence, the differential decay distribution in this kinematic limit must be independent of the angles θ_ℓ and ϕ, which can be integrated out. This imposes constraints on the amplitude $A_\lambda^{L,R}$ and hence the observables. The entire decay, including the decay $K^* \to K\pi$ takes place in a single plane, resulting in a vanishing contribution to the '$\perp$' helicity, or $F_\perp = 0$.

Since the K^* decays at rest, the distribution of $K\pi$ is isotropic and cannot depend on θ_K. It can easily be seen that this is only possible if $F_\parallel = 2F_L$ [14].

At $q^2 = q^2_{\rm max}$, $\Gamma_f \to 0$ as all the transversity amplitudes vanish in this limit. The constraints on the amplitudes described above result in unique values of the helicity fractions and the asymmetries at this kinematical endpoint. The values of the helicity fractions and asymmetries were derived in Ref. [14, 6] where it is explicitly shown that

$$\begin{aligned} F_L(q^2_{\rm max}) = \frac{1}{3}, \quad F_\parallel(q^2_{\rm max}) = \frac{2}{3}, \quad A_4(q^2_{\rm max}) = \frac{2}{3\pi}, \\ F_\perp(q^2_{\rm max}) = 0, \quad A_{\rm FB}(q^2_{\rm max}) = 0, \quad A_{5,7,8,9}(q^2_{\rm max}) = 0. \end{aligned} \tag{50}$$

At low recoil energy of K^* meson, only three independent form factors describe the whole $B \to K^*\ell^+\ell^-$ decay and there exist a relation among the form factors at leading order in $1/m_B$ expansion given by [5, 15],

$$\frac{\widetilde{\mathcal{G}}_\parallel}{\mathcal{F}_\parallel} = \frac{\widetilde{\mathcal{G}}_\perp}{\mathcal{F}_\perp} = \frac{\widetilde{\mathcal{G}}_0}{\mathcal{F}_0} = -\kappa \frac{2 m_b m_B C_7}{q^2}, \tag{51}$$

where $\kappa \approx 1$. The helicity independence of the ratios $\widetilde{\mathcal{G}}_\lambda/\mathcal{F}_\lambda$ at $q^2_{\rm max}$ is easy to understand, since both the B and K^* mesons are at rest, resulting in a complete overlap of the wave functions of these two mesons and the absence of any preferred direction in the $K\pi$ distribution. Hence at the maximum point in q^2, i.e. the kinematic endpoint $q^2_{\rm max}$, one gets from Eq.(13) $r_0 = r_\parallel = r_\perp \equiv r$. Therefore Eq. (45) implies that in the presence of RH currents one should expect $R_0 = R_\parallel \neq R_\perp$ at $q^2 = q^2_{\rm max}$ without any approximation. Interestingly, this relation is unaltered by non-factorizable and resonance contributions [14] at this kinematic endpoint.

To test the relation among R_λ's in light of LHCb data, first defining $\delta \equiv q^2_{\rm max} - q^2$, we expand the observables F_L, $F_\perp$, $A_{\rm FB}$ and A_5 around $q^2_{\rm max}$ as follows:

$$F_L = \frac{1}{3} + F_L^{(1)}\delta + F_L^{(2)}\delta^2 + F_L^{(3)}\delta^3, \tag{52}$$

$$F_\perp = F_\perp^{(1)}\delta + F_\perp^{(2)}\delta^2 + F_\perp^{(3)}\delta^3, \tag{53}$$

$$A_{\rm FB} = A_{\rm FB}^{(1)}\delta^{\frac{1}{2}} + A_{\rm FB}^{(2)}\delta^{\frac{3}{2}} + A_{\rm FB}^{(3)}\delta^{\frac{5}{2}}, \tag{54}$$

$$A_5 = A_5^{(1)}\delta^{\frac{1}{2}} + A_5^{(2)}\delta^{\frac{3}{2}} + A_5^{(3)}\delta^{\frac{5}{2}}. \tag{55}$$

where for each observable O, $O^{(n)}$ is the coefficient of the $n^{\rm th}$ term in the expansion. The polynomial fit to data is not based on Heavy Quark Effective Theory (HQET) or any other theoretical assumption. A parametric fit to data is performed, so as to obtain the limiting values of the coefficients to determine the slope and second derivative of the observables at $q^2_{\rm max}$. It should be noted that the polynomial parameterizations are inadequate to describe the q^2 dependent behavior of resonances. However, a very thorough discussion on the systematics of the resonance effects can be found in [16].

The relation in Eq. (51) between form factors is expected to be satisfied in the large q^2 region. Eq. (51) is naturally satisfied if it is valid at each order in the Taylor expansion of the form factors:

$$q^2 \frac{\widetilde{\mathcal{G}}_\lambda}{\mathcal{F}_\lambda} = q^2_{\rm max} \frac{\widetilde{\mathcal{G}}_\lambda^{(1)} + \delta\,(\widetilde{\mathcal{G}}_\lambda^{(2)} - \dfrac{\widetilde{\mathcal{G}}_\lambda^{(1)}}{q^2_{\rm max}}) + \mathcal{O}(\delta^2)}{\mathcal{F}_\lambda^{(1)} + \delta\,\mathcal{F}_\lambda^{(2)} + \mathcal{O}(\delta^2)}. \tag{56}$$

We require only that the relation be valid up to order δ. In order for Eq. (56) to have a constant value in the neighborhood of $q^2_{\rm max}$ up to $\mathcal{O}(\delta)$, we must have $\mathcal{F}^{(2)}_\lambda = c\,\mathcal{F}^{(1)}_\lambda$ and $(q^2_{\rm max}\,\widetilde{\mathcal{G}}^{(2)}_\lambda - \widetilde{\mathcal{G}}^{(1)}_\lambda) = c\,q^2_{\rm max}\,\widetilde{\mathcal{G}}^{(1)}_\lambda$ where c is any constant. As discussed earlier, $\mathsf{P}_2 = \sqrt{2}\mathsf{P}_1$ at $q^2_{\rm max}$, hence, we must have $\mathsf{P}^{(1)}_2 = \sqrt{2}\mathsf{P}^{(1)}_1$, where $\mathsf{P}^{(1)}_{1,2}$ are the coefficients of the leading $\mathcal{O}(\sqrt{\delta})$ term in the expansion. However, the above argument implies that at the next order, we must also have $\mathsf{P}^{(2)}_2 = \sqrt{2}\mathsf{P}^{(2)}_1$, since $\mathcal{F}^{(2)}_\lambda = c\,\mathcal{F}^{(1)}_\lambda$. This provides the needed input that together with Eq. (49) determines $\mathsf{P}^{(1)}_1$ purely in terms of observables.

The zeroth order coefficients of the observable expansions are assumed from the constraints arising from Lorentz invariance and decay kinematics derived in Ref. [14], whereas all the higher order coefficients are extracted by fitting the polynomials with 14 bin LHCb data as shown in Fig. 2.

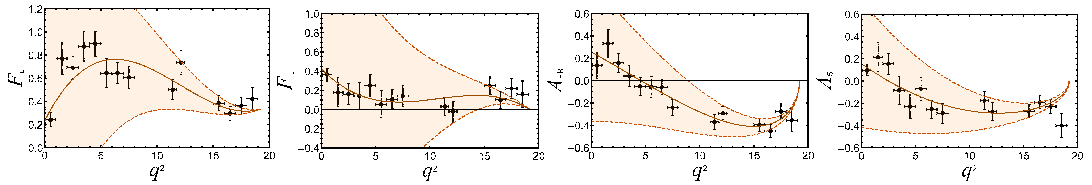


Figure 2: An analytic fit to 14-bin LHCb data using Taylor expansion at $q^2_{\rm max}$ for the observables F_L, $F_\perp$, $A_{\rm FB}$ and A_5 are shown as the brown curves. The $\pm1\sigma$ error bands are indicated by the light brown shaded regions, derived including correlation among all observables. The points with the black error bars are LHCb 14-bin measurements [11].

The limiting analytic expressions for R_λ at $q^2 = q^2_{\rm max}$ are

$$\begin{aligned} R_\perp(q^2_{\rm max}) &= \frac{8A^{(1)}_{\rm FB}(-2A^{(2)}_5 + A^{(2)}_{\rm FB}) + 9(3F^{(1)}_L + F^{(1)}_\perp)F^{(1)}_\perp}{8\,(2A^{(2)}_5 - A^{(2)}_{\rm FB})\,\sqrt{\frac{3}{2}F^{(1)}_\perp - A^{(1)\,2}_{\rm FB}}} \\ &= \frac{\omega_2 - \omega_1}{\omega_2\sqrt{\omega_1 - 1}}, \qquad (57) \\ R_\parallel(q^2_{\rm max}) &= \frac{3(3F^{(1)}_L + F^{(1)}_\perp)\,\sqrt{\frac{3}{2}F^{(1)}_\perp - A^{(1)\,2}_{\rm FB}}}{-8A^{(2)}_5 + 4A^{(1)}_{\rm FB} + 3A^{(1)}_{\rm FB}(3F^{(1)}_L + F^{(1)}_\perp)} \\ &= \frac{\sqrt{\omega_1 - 1}}{\omega_2 - 1} = R_0(q^2_{\rm max}) \qquad (58) \end{aligned}$$

where

$$\omega_1 = \frac{3}{2}\,\frac{F^{(1)}_\perp}{A^{(1)\,2}_{\rm FB}} \quad \text{and} \quad \omega_2 = \frac{4\,(2A^{(2)}_5 - A^{(2)}_{\rm FB})}{3\,A^{(1)}_{\rm FB}(3F^{(1)}_L + F^{(1)}_\perp)}. \qquad (59)$$

It should be noted that Eqs. (57)–(59) are derived only at $q^2_{\rm max}$. However, even at the endpoint, the expressions depend on polynomial coefficients: $F^{(1)}_L$ and $F^{(1)}_\perp$ as well as $A^{(2)}_{\rm FB}$ and $A^{(2)}_5$ which

are not related by HQET. Hence, in our approach, corrections beyond HQET are automatically incorporated through fits to data.

In the absence of RH currents or other NP that treats the "$\perp$" amplitude differently one would expect $R_\perp(q^2_{\rm max}) = R_\parallel(q^2_{\rm max}) = R_0(q^2_{\rm max})$. It is easily seen that the LHS of Eq. (43) is positive around $q^2_{\rm max}$ and since $\zeta > 0$, we must have $R_\perp = R_\parallel = R_0 > 0$. Since very large contributions from RH currents are not possible, as they would have been seen elsewhere, $R_\lambda(q^2_{\rm max}) > 0$ still holds and restricts ξ and ξ' to reasonably small values.

It can be seen that ω_1, ω_2 contain coefficients which are extracted completely from data and their estimates using LHCb measurements are: $\omega_1 = 1.10 \pm 0.30$ (1.03 ± 0.34) and $\omega_2 = -4.19 \pm 10.48$ (-4.04 ± 10.12), where the first values are determined using $A^{(1)}_{\rm FB}$ and the values in the round brackets use $2A^{(1)}_5$. The variables R_λ's can be estimated using data only and the allowed region is shown in gray bands in Fig. 3 left panel. A significant deviation is seen from a slope of 45° line (red line) which denotes $R_\perp = R_\parallel = R_0$ and thus hints toward the presence of RH currents without *using any estimate of hadronic contributions*. To quantify the RH couplings, we use Eq. (45) and the results are shown in the last two panels of Fig. 3. The middle panel uses the SM estimate of parameter r/C_{10} [15] and the SM prediction for C'_{10}/C_{10} and C'_9/C_{10} (the origin) is at more than 5σ confidence level. We have performed another analysis where the input r/C_{10} is considered as nuisance parameter and the result is shown in the right most panel of Fig. 3. It can be seen that the uncertainties in fitted parameters C'_{10}/C_{10} and C'_9/C_{10} have increased due to the variation of r/C_{10} and the SM prediction still remains on a 3σ level contour providing evidence of RH currents.

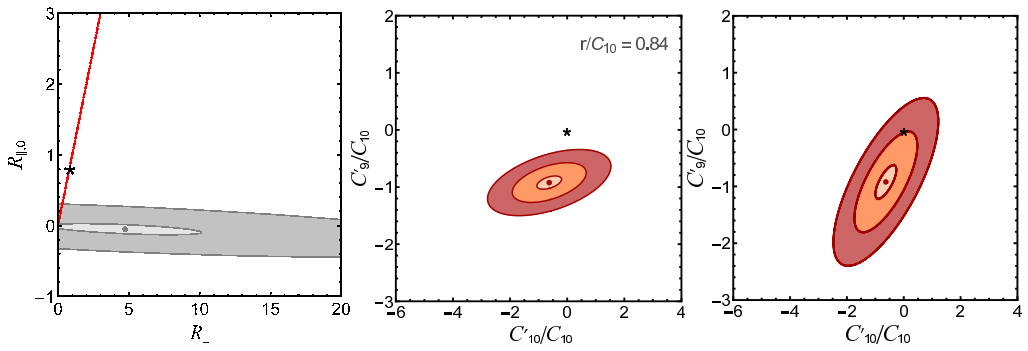


Figure 3: (left panel) Allowed regions in $R_\perp$ – $R_{\parallel,0}$ plane are shown in light and dark gray bands at 1σ and 5σ confidence level, respectively. The red straight line corresponds to the case $R_\perp = R_{\parallel,0}$ i.e. the absence of RH couplings. (middle panel) In C'_{10}/C_{10} – C'_9/C_{10} plane, the yellow, orange and red regions correspond to 1σ, 3σ and 5σ significance level, respectively, where SM input for r/C_{10} [15] is used. The best fit values of C'_{10}/C_{10} and C'_9/C_{10}, with $\pm 1\sigma$ errors are -0.63 ± 0.43 and -0.92 ± 0.10, respectively. (right panel) Same color code as the middle panel figure. The input r/C_{10} is varied as a nuisance parameter and hence the obtained uncertainties in C'_{10}/C_{10} and C'_9/C_{10} are increased. The SM predictions for all the three plots are indicated by the stars. Strong evidence of RH current is pronounced from the plots.

Conclusions

- The $B \to K^*\ell^+\ell^-$ mode is an excellent mode to study. It is sensitive to NP and indirect evidences have been found.
- Theoretical issues are well understood. However, the resonance effects are very important to be studied thoroughly.
- Non-local contributions are difficult to estimate but can be handled by eliminating them in terms of observables.
- More efforts should be put to estimate them. One should look for experimental hints to estimate how large they are.
- Observable relations, which are free from hadronic uncertainties, can be used as a probe for New Physics. Discrepancies are found with SM.
- A strong evidence of Right-Handed currents is also found.
- The possibility of some other kinds of NP are also suggested.

Acknowledgment

We acknowledge our coauthors T. E. Browder and Anirban Karan for the work done on Right-Handed currents.

References

[1] C. Bobeth, M. Misiak and J. Urban, Nucl. Phys. B **574**, 291 (2000), [arXiv:hep-ph/9910220].

[2] W. Altmannshofer, P. Ball, A. Bharucha *et al.*, JHEP **01**,(2009) 019, [arXiv:0811.1214].

[3] G. Buchalla, A. J. Buras, M. E. Lautenbacher, Rev. Mod. Phys. **68**, 1125-1144 (1996), [arXiv:hep-ph/9512380].

[4] A. Khodjamirian, Th.Mannel, A. A. Pivovarov and Y. -M. Wang, JHEP **09**, (2010) 089, [arXiv:1006.4945];

A. Khodjamirian, arXiv:1312.6480.

[5] B. Grinstein and Dan Prijol, Phys. Rev. D **70** 114005 (2004), [arXiv:hep-ph/0404250v3].

[6] R. Mandal, R. Sinha and D. Das, Phys. Rev. D **90**, no. 9, 096006 (2014)

[7] F. Kruger, L. M. Sehgal, N. Sinha and R. Sinha, Phys. Rev. **D 61**, 114028 (2000). [arXiv:hep-ph/9907386].

[8] M. Beneke, T. Feldmann and D. Seidel, Nucl. Phys. **B612**, 25 (2001), [arXiv:hep-ph/0106067].

[9] B. Grinstein, M. J. Savage and M. B. Wise, Nucl. Phys. B**319**, 271 (1989).

[10] R. Mandal and R. Sinha, Phys. Rev. D **95**, no. 1, 014026 (2017) doi:10.1103/PhysRevD.95.014026 [arXiv:1506.04535 [hep-ph]].

[11] R. Aaij *et al.* [LHCb Collaboration], arXiv:1606.04731 [hep-ex].

[12] W. Altmannshofer and D. M. Straub, Eur. Phys. J. C **75**, no. 8, 382 (2015); M. Ciuchini *et al.* JHEP **1606**, 116 (2016). S. Jäger and J. Martin Camalich, Phys. Rev. D **93** (2016) 1, 014028; S. Descotes-Genon, J. Matias and J. Virto, Phys. Rev. D **88**, 074002 (2013) [arXiv:1307.5683 [hep-ph]]. S. Descotes-Genon, L. Hofer, J. Matias and J. Virto, JHEP **1606**, 092 (2016) and references therein.

[13] C. Bobeth, G. Hiller and D. van Dyk, Phys. Rev. D **87** (2013) 3, 034016

[14] G. Hiller and Roman Ziwcky, JHEP **1403**,(2014) 042, [arxiv:1312.1923].

[15] C. Bobeth, G. Hiller and D. van Dyk, JHEP **1007**, 098 (2010).

[16] A. Karan, R. Mandal, A. K. Nayak, R. Sinha and T. E. Browder, arXiv:1603.04355 [hep-ph].

Probing New Physics through FCNC Transition

*Ishtiaq Ahmed**

National Centre for Physics, Quaid-i-Azam University Campus, Islamabad 45320, Pakistan

DOI: http://dx.doi.org/10.3204/DESY-PROC-2016-04/Ishtiaq

In this study, we analyze the implications of the non-universal Z' model to the lepton polarization asymmetries and the cp violation for the decay channel $B \to K^* \ell^+ \ell^-$ where $\ell = \mu^+ \mu^-$. To study the influence of the Z' on the mentioned observables we used the UTFit constraints for the parameters of Z'. We have found that these observables are sensitive to the coupling of the Z' boson with the fermions. Therefore, the accurant measurements of these observables could provide help to extract accurate values of Z' couplings.

1 Introduction

The study of rare B-meson decays which are induced by the flavor changing neutral currents (FCNC) is highly interesting research area in flavor physics because these transitions provide a fertile ground to check the SM and to probe new physics (NP) i.e. the physics beyond the SM. Among the many new physics models, the non universal Z' model looks an attractive extension of the SM (for a detailed review see Ref. [2]). As the behavior of the off diagonal couplings of the non-universal Z' boson with the fermions, the FCNC transitions can occur at tree level as well as this model is help out to resolve the puzzles in the data of rare B-meson decays such as anomaly in the $B_s - \bar{B}_s$ mixing phase [3, 4] and $\pi - K$ puzzle [5], etc.

Further to this, the investigation of non universal family coupling of Z' boson leading to FCNC transitions have also been studied by considering different observables such as branching ratio and forward backward asymmetry [6, 7]. In this context, the behavior of the other observables in the presence of Z' boson may play a crucial role to refine our knowledge about the family of non universal Z' model. With this motivation we have studied single lepton polarization asymmetries, polarized and unpolarized CP violation asymmetries within the SM and in the Z' model. In the context of CP asymmetry, it is important to emphasis here that the FCNC transitions are proportional to three CKM matrix elements, namely, $V_{tb}V_{ts}^*$, $V_{cb}V_{cs}^*$ and $V_{ub}V_{us}^*$ but due to the unitarity condition and neglecting $V_{ub}V_{us}^*$ in comparison of $V_{cb}V_{cs}^*$ and $V_{tb}V_{ts}^*$, the CP asymmetry is highly suppressed in the SM. Therefore, the measurement of CP violation asymmetries in FCNC processes could provide a key evidence for new physics.

The scheme of this report is as follows. The section 2 contains the basic formulation with Z' contribution, the matrix elements and the amplitude for $B \to K^* \ell^+ \ell^-$. In section 3, we give the analytical expressions of lepton polarization and cp violation. In sec 4 we present the

2 Theoretical formulation

The Effective Hamiltonian in the SM for the $b \to s\ell^+\ell^-$ transition is as follows

$$\mathcal{H}_{eff} = \frac{G_F}{\sqrt{2}} \sum_i V_{CKM} C_i(\mu) Q_i, \tag{1}$$

where G_F is the Fermi coupling constant, Q_i are the four-quark operators, V_{CKM} are the CKM matrix elements and $C_i(\mu)$ are the corresponding Wilson coefficients.

In the presence of Z', the FCNC transitions could occur at tree level and can be described by the following effective Hamiltonian

$$\mathcal{H}^{Z'}_{eff} = -\frac{4G_F}{\sqrt{2}} V_{tb}V^*_{ts}\Big[\Lambda_{sb}C^{Z'}_9 Q_9 + \Lambda_{sb}C^{Z'}_{10}Q_{10}\Big] + h.c., \tag{2}$$

where $\Lambda_{sb} = \frac{4\pi e^{-i\phi_{sb}}}{\alpha V^*_{ts}V_{tb}}$, $C^{Z'}_9 = \mathcal{R}e(B_{sb})S_{LL}; C^{Z'}_{10} = \mathcal{R}e(B_{sb})D_{LL}$ and $S_{LL} = \mathcal{S}^L_{\ell\ell} + \mathcal{S}^R_{\ell\ell}; D_{LL} = \mathcal{S}^L_{\ell\ell} - \mathcal{S}^R_{\ell\ell}$. B_{sb} is the Z' coupling with the b and s quarks and $\mathcal{S}^L_{\ell\ell}$, $\mathcal{S}^R_{\ell\ell}$ are the left and right handed coupling of Z' with the leptons. The required matrix elements for the channel $B \to K^*\ell^+\ell^-$ are as follows

$$\begin{aligned}
\langle K^*(k,\epsilon)|\bar{s}\gamma^\mu(1\pm\gamma^5)b|B(p)\rangle &= \mp iq_\mu \frac{2m_{K^*}}{s}\epsilon^*\cdot q\Big[A_3(s) - A_0(s)\Big] - \epsilon_{\mu\nu\lambda\sigma}p^\lambda q^\sigma \frac{2V(s)}{(m_B + m_{K^*})} \\
&\pm i\epsilon^*_\mu(m_B + m_{K^*})A_1(s) \mp i(p+k)_\mu \epsilon^*\cdot q \frac{A_2(s)}{(m_B + m_{K^*})}, \\
\langle K^*(k,\epsilon)|\bar{s}i\sigma_{\mu\nu}q^\nu(1\pm\gamma^5)b|B(p)\rangle &= 2\epsilon_{\mu\nu\lambda\sigma}p^\lambda q^\sigma F_1(s) \pm i\epsilon^*\cdot q\left\{q_\mu - \frac{(p+k)_\mu}{(m^2_B - m^2_{K^*})}\right\}F_3(s) \\
&\pm i\left\{\epsilon^*_\mu(m^2_B - m^2_{K^*}) - (p+k)_\mu\epsilon^*\cdot q\right\}F_2(s), \\
A_3(s) &= \frac{m_B + m_{K^*}}{2mK^*}A_1(s) - \frac{m_B - m_{K^*}}{2mK^*}A_2(s).
\end{aligned} \tag{3}$$

These seven independent form factors $V(s)$, $A_1(s)$, $A_2(s)$, $A_0(s)$, $F_1(s)$, $F_2(s)$ and $F_3(s)$ are calculated by different non perturbative schemes such as lattice QCD, Quark model (QM) [9] , perturbative QCD (PQCD) and light cone-QCD sum rules (LCSR) [13, 11], etc. By using Eqs. (1)-(3), the total amplitude for the process under consideration can be written in the following way.

$$\begin{aligned}
\mathcal{M}^{tot} = \frac{\alpha G_F}{4\sqrt{2}\pi}V^*_{tb}V_{ts}\Big[&\bar{l}\gamma^\mu(1-\gamma^5)l \times \big(-2\mathcal{A}\epsilon_{\mu\nu\lambda\sigma}\epsilon^*k^\lambda q^\sigma - i\mathcal{B}_1\epsilon^*_\mu + i\mathcal{B}_2\epsilon^*\cdot q(p+k)_\mu + \\
&+i\mathcal{B}_0\epsilon^*\cdot q q_\mu\big) + \bar{l}\gamma^\mu(1+\gamma^5)l \times \big(-2\mathcal{C}\epsilon_{\mu\nu\lambda\sigma}\epsilon^*k^\lambda q^\sigma - i\mathcal{D}_1\epsilon^*_\mu + i\mathcal{D}_2\epsilon^*\cdot q(p+k)_\mu + i\mathcal{D}_0\epsilon^*\cdot q q_\mu\big)\Big].
\end{aligned} \tag{4}$$

following form.

$$\begin{aligned}
\mathcal{A} &= 2C_{LL}\mathcal{H}_1 + 4m_b C_7^{eff}\frac{F_1(s)}{s}, \quad \mathcal{B}_1 = 2C_{LL}\mathcal{H}_3 + \frac{4m_b}{s}C_7^{eff}\mathcal{H}_4,\\
\mathcal{B}_2 &= 2C_{LL}\mathcal{H}_6 + 4\frac{m_b C_7^{eff}}{s}\mathcal{H}_5,\\
\mathcal{B}_0 &= \frac{2m_{k^*}}{s}\mathcal{H}_7 - \frac{4m_b}{s}C_7^{eff}F_3(s), \quad \mathcal{C} = \mathcal{A}(C_{LL}\to C_{LR}), \qquad \mathcal{D}_1 = \mathcal{B}_1(C_{LL}\to C_{LR}),\\
\mathcal{D}_2 &= \mathcal{B}_2(C_{LL}\to C_{LR}) \qquad \mathcal{D}_0 = \mathcal{B}_0(C_{LL}\to C_{LR}),\\
\mathcal{H}_1 &= \frac{V(s)}{(mB+m_{K^*})}, \quad \mathcal{H}_3 = (m_B+m_{K^*})A_1(s), \quad \mathcal{H}_4 = (m_B^2 - m_{K^*}^2)F_2(s),\\
\mathcal{H}_6 &= \frac{A_2(s)}{(mB+m_{K^*})}, \quad \mathcal{H}_5 = \left[F_2(s) + \frac{s}{(m_B^2-m_{K^*}^2)}F_3(s)\right], \quad \mathcal{H}_7 = (A_3 - A_0),\\
C_{LL} &= C_9^{tot} - C_{10}^{tot}, \quad C_{LR} = C_9^{tot} + C_{10}^{tot}, \quad C_9^{tot} = C_9^{eff} + \Lambda_{sb}C_9^{Z'},\\
C_{10}^{tot} &= C_{10} + \Lambda_{sb}C_{10}^{Z'}.
\end{aligned} \tag{5}$$

3 Formulas and analytical analysis of the physical observables

From the total amplitude in E. (4), we can write the decay rate of $B \to K^*\ell^+\ell^-$

$$\frac{d^2\Gamma(B\to K^* l^+ l^-)}{d\cos\theta ds} = \frac{1}{2m_B^3}\frac{2\beta\sqrt{\lambda}}{(8\pi)^3}|\mathcal{M}|^2, \tag{6}$$

where $\beta \equiv \sqrt{1-\frac{4m_l^2}{s}}$ and $\lambda \equiv m_B^4 + m_{k^*}^4 + s - 2m_B^2 m_{k^*}^2 - 2m_B^2 s - 2m_{k^*}^2 s$. By using the decay rate, we can find out the single lepton polarization asymmetries and the unpolarized and polarized cp violation asymmetries in $B \to K^*\ell^+\ell^-$ through the follwoing formulae

$$\begin{aligned}
P_i^{\pm} &= \frac{\frac{d\Gamma(\mathbf{S}^{\pm}=\mathbf{e}_i^{\pm})}{ds} - \frac{d\Gamma(\mathbf{S}^{\pm}=-\mathbf{e}_i^{\pm})}{ds}}{\frac{d\Gamma(\mathbf{S}^{\pm}=\mathbf{e}_i^{\pm})}{ds} + \frac{d\Gamma(\mathbf{S}^{\pm}=-\mathbf{e}_i^{\pm})}{ds}}, \quad \mathcal{A}_{CP}(\mathbf{S}^{\pm}=\mathbf{e}_i^{\pm}) = \frac{\frac{d\Gamma(\mathbf{S}^-)}{ds} - \frac{d\bar{\Gamma}(\mathbf{S}^+)}{ds}}{\frac{d\Gamma}{ds} - \frac{\bar{\Gamma}}{ds}},\\
\mathcal{A}_{CP}(\mathbf{S}^{\pm} &= \mathbf{e}_i^{\pm}) = \frac{1}{2}\left[\frac{\left(\frac{d\Gamma}{ds}\right) - \left(\frac{d\bar{\Gamma}}{ds}\right)}{\left(\frac{d\Gamma}{ds}\right) + \left(\frac{d\bar{\Gamma}}{ds}\right)} \pm \frac{\left(\frac{d\Gamma}{ds}\right)P_i - \left\{\left(\frac{d\Gamma}{ds}\right)P_i\right\}_{\Lambda_{sb}\to\Lambda_{sb}^*}}{\left(\frac{d\Gamma}{ds}\right) + \left(\frac{d\bar{\Gamma}}{ds}\right)}\right],\\
\frac{d\Gamma}{ds} &= \frac{d\Gamma(B\to K^*\ell^+\ell^-(\mathbf{S}^-))}{ds}, \quad \frac{d\bar{\Gamma}}{ds} = \frac{d\bar{\Gamma}(B\to K^*\ell^+(\mathbf{S}^+))\ell^-}{ds},
\end{aligned} \tag{7}$$

where i denotes the longitudinal (L),normal (N) and transverse (T) and $\mathbf{S}^{\pm}$ is the spin direction of $l^{\pm}$. The relation between the polarized and unpolarized invariant dilepton mass spectrum for the $B \to K^* l^+ l^-$ read as

Table 1: Numerical values of $\langle P_L \rangle$ in Z' model for scenario-I

		$\langle P_L \rangle$ at $D_{LL} = 0$				$\langle P_L \rangle$ at $S_{LL} = 0$			
ϕ_{sb} in Degree	Decay Channel	S_{LL} -6.7		S_{LL} 1.1		D_{LL} -9.3		D_{LL} -4.1	
		$B_{sb} = 0.87$	1.31	0.87	1.31	0.87	1.31	0.87	1.31
-65°	$B \to K^* \mu^+ \mu^-$	-0.785	-0.715	-0.774	-0.757	-0.597	-0.485	-0.731	-0.679
	$B \to K^* \tau^+ \tau^-$	-0.423	-0.347	-0.526	-0.519	-0.515	-0.476	-0.538	-0.532
-79°	$B \to K^* \mu^+ \mu^-$	-0.741	-0.651	-0.782	-0.772	-0.573	-0.442	-0.728	-0.669
	$B \to K^* \tau^+ \tau^-$	-0.443	-0.354	-0.517	-0.506	-0.454	-0.394	-0.509	-0.490

For the numerical analysis, we used the values of different input parameters and Wilson coefficients from [12, 13] while for Z' parameters we used the UTFit collaboration results [14].

To see the NP, we have plotted single lepton polarization asymmetries as a function of the momentum square s. (see Figs. 1-5 of ref. [1]). From these figures one can extract that the longitudinal and normal polarization asymmetries are sensitive to the Z' parameters at low s region for the case of muons while the transverse asymmetry is tiny, both, in the SM and in the Z' model. Some numerical values of the P_L are listed in Table 1 by using $\mathcal{S}_1$ scenario of Z' model (see ref. [1] for details).

To see the variation in the average values of single lepton polarization asymmetries $\langle P_i \rangle$, where $i = L, N$ or T, due to the influence of Z' boson effect see Figs. (6)-(11) of ref. [1] where we have plotted these asymmetries against the different coupling parameters of Z' models. From these graphs we have found that $\langle P_L \rangle$ sensitive to S_{LL} i.e. the NP contribution coming from Wilson coefficient C_9 while the values of $\langle P_N \rangle$ significantly effected by D_{LL} i.e. the NP contribution coming from Wilson coefficient C_{10}. Moreover, $\langle P_N \rangle$ value is influenced by the new weak phase ϕ_{sb} when tauons are the final state leptons.

Now we turn our attention to analysis of another interesting observable i.e. CP violation. As we have mentioned earlier in the introduction that for $b \to s\ell^+\ell^-$ transition the value of CP violation is negligible and any measurement of this observable is a clear sign of new physics. However, we have found that both the polarized and unpolarized CP violation asymmetries for $B \to K^* \mu^+ \mu^-$ are suppressed in the SM and in the Z' model. Similarly, CP violation when one of the final state tauon is transversely polarized is also found to be suppressed and therefore, we do not include these asymmetries in our numerical discussion. The other CP asymmetries $\mathcal{A}_{CP}$ and $\mathcal{A}^i_{CP}$ (where $i = L, N$) for $B \to K^* \tau^+ \tau^-$ are displayed in Figs. (12)-(15).From these figures, we have found that the values of direct unpolarized CP violation asymmetry $\mathcal{A}_{CP}$ is not significantly changed when we change the values of new weak phase ϕ_{sb} and D_{LL} but strongly depend on the value of S_{LL}. In contrast to the $\mathcal{A}_{CP}$ it is found that the $\mathcal{A}^L_{CP}$ is almost insensitive to the value of S_{LL} but sensitive to the values of D_{LL} . However, $\mathcal{A}^N_{CP}$ is sensitive for both S_{LL} and D_{LL}.

4 Conclusion

As the CP violation asymmetries are negligible in the SM and in this analysis it is found that $\mathcal{A}_{CP}$, $\mathcal{A}_{CP}^{L}$ and $\mathcal{A}_{CP}^{N}$ are considerably enhanced in the presence of Z' when tauons are the final state leptons. Similarly, the lepton polarization asymmetries are also significantly change their values from the SM values when we incorporate the effects of Z'. Therefore, the accurate measurements of these observables could be depict the precise values of the new weak phase ϕ_{sb} and coupling of Z' boson with the leptons and quarks.

5 Acknowledgments

The author would like to thank the organisers of *Quantum Field Theory at the Limits: from Strong Fields to Heavy Quarks* for their hospitality in Dubna.

References

[1] I. Ahmed, Phys. Rev. D **89**, no. 1, 014017 (2014). doi:10.1103/PhysRevD.89.014017

[2] P. Langacker and M. Plumacher, Phys. Rev. D **62** (2000) 013006 [hep-ph/0001204]; P. Langacker, arXiv:0801.1345 [hep-ph].

[3] V. Barger, L. Everett, J. Jiang, P. Langacker, T. Liu and C. Wagner, Phys. Rev. D 80 (2009) 055008 arXiv:0902.4507 [hep-ph]; JHEP 0912 (2009) 048 arXiv:0906.3745 [hep-ph].

[4] Q. Chang, X. Q. Li and Y. D. Yang, JHEP **1002** (2010) 082, arXiv:0907.4408 [hep-ph]

[5] V. Barger, C. W. Chiang, P. Langacker and H. S. Lee, Phys. Lett. B **598** (2004) 218; first ref in 48.

[6] C. W. Chiang, R. H. Li and C. D. Lu, Chin.Phys. C36 (2012) 14-24 arXiv:0911.2399.

[7] Q. Chang, Yin-Hao Gao arXiv:1101.1272v1 [hep-ph] 6 Jan 2011; Y. Li, J. Hua arXiv:1107.0630v2 [hep-ph] 6 Nov 2011.

[8] R. Aaij *et al.* [LHCb Collaboration], *Observation of $J/\psi p$ Resonances Consistent with Pentaquark States in $\Lambda_b^0 \to J/\psi K^- p$ Decays*, Phys. Rev. Lett. **115** (2015) 072001 [arXiv:1507.03414].

[9] D. Melikhov and B. Stech, Phys. Rev. D **62**, 014006 (2000).

[10] A. Ali, P. Ball, L. T. Handoko and G. Hiller, Phys. Rev. D **61**, 074024 (2000) [arXiv:hep-ph/9910221].

[11] C. Chen and C. Q. Geng, Nucl.Phys. B636 (2002) 338-364, hep-ph/0203003 [hep-ph].

[12] K. Nakamura et al. (Particle Data Group), *Review of particle Physics, J. Phys.* **G 37** (2010) 075021.

[13] A. Ali, P. Ball, L. T. Handoko and G. Hiller, Phys. Rev. D **61**, 074024 (2000) [arXiv:hep-ph/9910221].

[14] M. Bona et al., (UTfit collaboration), PMC Phys. a **3**, 6 (2009)[arXiv:0803.0659 [hep-ph]]; M. Bona et al., arXiv: 0906.0953 [hep-ph].

The study of b-s anomaly decays in covariant quark model

Aidos Issadykov[1,2], *Mikhail A. Ivanov*[1]

[1]Bogoliubov Laboratory of Theoretical Physics JINR, 141980 Dubna, Russia
[2]L.N.Gumilyov Eurasian National University, 010008 Astana, Republic of Kazakhstan

DOI: http://dx.doi.org/10.3204/DESY-PROC-2016-04/Aidos

The work is devoted to the study of b-s anomaly decays. We compute the relevant form factors in the framework of the covariant quark model with infrared confinement in the full kinematical momentum transfer region. The calculated form factors are used to evaluate branching fractions and polarization observables in the $B \to K\pi + \mu^+\mu^-$ decay caused by the presence of the intermediate scalar K_0^* and in the cascade decay $B \to \phi(\to K^+K^-)\ell^+\ell^-$. We compare the obtained results with available experimental data and the results from other theoretical approaches.

1 Introduction

The main aim of particle physics is to determine the fundamental principles that govern matter, energy, space and time. Standard Model (SM) in particle physics provides a thoroughly tested basis for describing the matter particles (quarks and leptons), together with bosons of strong and electroweak interactions (gluons,photons, W and Z bosons). However, historical data suggests that Standard model is not complete and that it is just a low-energy limit of a more fundamental theory. One has to admit very impressive progress achieved in the last decade in the electroweak and quantum chromodynamics perturbative calculations. This became possible due to the development of new techniques and computer codes for multi- loop and multi-leg calculations. Today the accuracy of theoretical calculations competes with that of experimental data and further progress is on the way in both the cases. Worth noting that Standard model has been extremely successful in explaining the results of experiments for particle physics. The outstanding success of SM in the description of almost all experimental data in particle physics is manifested in the electroweak pool for different observables. Nevertheless, in recent years observed discrepancies in B-meson rare decays with the predictions of SM. Flavour-changing neutral currents have been prominent tools in high-energy physics in the search for new degrees of freedom, due to their quantum sensitivity to energies much higher than the external particles involved and can be instrumental in order to determine where to look for new physics. During the last decade a lot of observables, including the branching ratios, CP and the angular asymmetry in inclusive and exclusive decay modes of B-meson were measured by B-factories and at LHC experiments. These data allow to explore the spiral structure in the interactions with the flavour-changing and a possible existence of new sources of CP violation.

The transition $b \to s\ell^+\ell^-$ mediated by Flavor-Changing Neutral Current (FCNC) is one of the key point in the SM which allows one to look for the possible manifestation of New

Physics. The physical processes induced by this transition are currently studied in great details at the LHC. The most popular and well–analyzed among them are the rare B-meson decays $B \to K^*(\to K\pi)\mu^+\mu^-$ and $B_s \to \phi(\to K^+K^-)\mu^+\mu^-$. The decay $\Lambda_b \to \Lambda(\to p\pi)\,\ell^+\ell^-$ can be considered to be a welcome complement to the above decay channels. The LHCb Collaboration [1] reported a measurement of form-factor independent angular observables in the decay $B \to K^*\mu^+\mu^-$. One observable was found to be in disagreement with the SM on the level of 3.7 σ. The improved measurements of the isospin asymmetries and branching fractions for $B \to K\mu^+\mu^-$ and $B \to K^*\mu^+\mu^-$ decays were reported in [2]. The isospin asymmetries were consistent with the SM, whereas some branching fractions were found to be slightly lower than the theoretical predictions. An angular analysis and a measurement of the differential branching fraction of the decay $B_s^0 \to \phi\mu^+\mu^-$ were presented in [3]. The results of the angular analysis are consistent with the SM. However, the differential branching fraction in one bin was found to be more than 3 σ below the SM predictions. The observed discrepancies (sometimes called *"$b \to s\ell\ell$"*) have generated a plenty of theoretical studies [4]-[15] involving the various scenarios of NP and analysis of the uncertainties from hadronic contributions.

2 The $b-s$ transition form factors in the covariant quark model

We define dimensionless form factors for scalar mesons by

$$\begin{aligned} < H_2(p_2)\,|\,\bar{s}\,O^\mu\,b\,|H_1(p_1) > &= F_+(q^2)\,P^\mu + F_-(q^2)\,q^\mu\,, \\ < H_2(p_2)\,|\,\bar{s}\,i\sigma^{\mu\nu}q_\nu(1+\gamma^5)\,b\,|\,H_1(p_1) > &= -\frac{1}{m_1+m_2}\,\Big(P_\mu\,q^2 - q_\mu\,Pq\Big)\,F_T(q^2)\,, \end{aligned} \quad (1)$$

and for vector mesons as:

$$\begin{aligned} &\langle\phi(p_2,\epsilon_2)\,|\,\bar{s}\,O^\mu\,b\,|\,B_s(p_1)\rangle = \\ &= N_c\,g_{B_s}\,g_\phi\int\frac{d^4k}{(2\pi)^4 i}\,\widetilde{\Phi}_{B_s}\Big(-(k+w_{13}p_1)^2\Big)\,\widetilde{\Phi}_\phi\Big(-(k+w_{23}p_2)^2\Big) \\ &\times\ \mathrm{tr}\Big[O^\mu\,S_b(k+p_1)\,\gamma^5\,S_s(k)\,\not\epsilon_2^\dagger\,S_s(k+p_2)\Big] \\ &= \frac{\epsilon_\nu^\dagger}{m_1+m_2}\Big(-g^{\mu\nu}\,P\cdot q\,A_0(q^2) + P^\mu\,P^\nu\,A_+(q^2) + q^\mu\,P^\nu\,A_-(q^2) \\ &\quad + i\,\varepsilon^{\mu\nu\alpha\beta}\,P_\alpha\,q_\beta\,V(q^2)\Big), \end{aligned} \quad (2)$$

$$\begin{aligned} &\langle\phi(p_2,\epsilon_2)\,|\,\bar{s}\,(\sigma^{\mu\nu}q_\nu(1+\gamma^5))\,b\,|\,B_s(p_1)\rangle = \\ &= N_c\,g_{B_s}\,g_\phi\int\frac{d^4k}{(2\pi)^4 i}\,\widetilde{\Phi}_{B_s}\Big(-(k+w_{13}p_1)^2\Big)\,\widetilde{\Phi}_\phi\Big(-(k+w_{23}p_2)^2\Big) \\ &\times\ \mathrm{tr}\Big[(\sigma^{\mu\nu}q_\nu(1+\gamma^5))\,S_b(k+p_1)\,\gamma^5\,S_s(k)\,\not\epsilon_2^\dagger\,S_s(k+p_2)\Big] \\ &= \epsilon_\nu^\dagger\Big(-(g^{\mu\nu}-q^\mu q^\nu/q^2)\,P\cdot q\,a_0(q^2) + (P^\mu\,P^\nu - q^\mu\,P^\nu\,P\cdot q/q^2)\,a_+(q^2) \\ &\quad + i\,\varepsilon^{\mu\nu\alpha\beta}\,P_\alpha\,q_\beta\,g(q^2)\Big). \end{aligned} \quad (3)$$

where $P = p_1 + p_2$ and $q = p_1 - p_2$, $\epsilon_2^\dagger \cdot p_2 = 0$, $p_1^2 = m_1^2 \equiv m_{B_s}^2$, $p_2^2 = m_2^2 \equiv m_\phi^2$ and the weak matrix $O^\mu = \gamma^\mu(1-\gamma^5)$. Since there are three quarks involved in these processes, we introduce the notation with two subscripts $w_{ij} = m_{q_j}/(m_{q_i} + m_{q_j})$ $(i,j = 1,2,3)$ so that $w_{ij} + w_{ji} = 1$. The form factors are calculated in the full kinematical region of momentum transfer squared.

The results of our numerical calculations are with high accuracy approximated by the parametrization

$$F(q^2) = \frac{F(0)}{1 - as + bs^2}\,, \qquad s = \frac{q^2}{m_1^2}\,, \tag{4}$$

the relative error is less than 1%. In our work we evaluate the b-s transition form factors assuming that mesons are ordinary two-quark states.

3 The $B \to K^*(\to K\pi)\mu^+\mu^-$ decay

Recently, it has been paid much attention to the rare flavor-changing neutral current decay $B \to K^*(\to K\pi)\mu^+\mu^-$. One of the reason was the first measurement of form-factor independent angular observables performed by LHCb-collaborationn [1, 16]. It has been claimed that there is a 3.7σ deviation from the Standard Model (SM) prediction for one of the angular observables. Much effort has been spent to explain this deviation by invoking the effects of new physics (NP) (see Refs. [17]-[23]). The main emphasis of the above mentioned papers was focusing on the search of the physical observables which have low sensitivity to the form factors. In addition to the NP effects, the uncertainties related to the presence of the intermediate scalar resonance K_0^* decaying also into $K\pi$ are intensively discussed in the literature Refs. [24]-[28]. In many papers, the Breit-Wigner form for the $K\pi$-mass spectra is used. However, this assumption can not be justified for the broad scalar resonances like the $K_0^*(800)$ meson. The improvement of the description was done in the paper [29] by invoking the chiral perturabation theory for $K\pi$-interaction. This issue was also generalized to $B_s \to K\pi\ell\bar{\nu}$ in Ref. [30]. As well-known, short-distance physics is under control in the description of the rare B-decays whereas the effects of long-distance physics described by the hadronic form factors lead to large uncertainties since it involves nonperturbative QCD.

Some remarks should be done before the calculations. The internal structure of the light scalar mesons is not yet well established, see for review [31] and [32]. Since they have large decay widths it is difficult to distinguish them from background. There are interpretations of these objects as four-quarks states and/or gluballs. Here, we describe the scalar mesons as two-quark states and evaluate the B-S form factors within our approach but when we use the calculated form factors in the matrix element of the cascade decay $B \to K_0^*(\to K\pi)\ell^+\ell^-$ we take into account the line shape of the K_0^* which reflect the broad width of this resonance. We will use the notation from PDG'14 [33] for the scalar mesons below 1 GeV.

We are going to explore the influence of the intermediate scalar K_0^* meson on the angular decay distribution of the cascade decay $B \to K\pi + \mu^+\mu^-$. Therefore, we give the maximum values of the form factors in Table 3 and branching ratios in Table 3 obtained for *size parameter* $\Lambda_S = 1.5$ GeV. The results for the e-mode are almost identical to those of the μ-mode and will not be shown separately. We compare the obtained results with those from other approaches. One can see that our values for branching ratios are less almost twice compare with those from other approaches.

Let us briefly discuss the impact of scalar resonance K_0^* on $B \to K^*(\to K\pi)\ell^+\ell^-$ decay. As well known, the narrow $K^*(892)$ vector resonance is described by a Breit-Wigner parametriza-

Table 1: The values of the form factors at $q^2 = 0$ in the covariant quark model ($\Lambda_S = 1.5$ GeV) and other approaches

$B - S$	$F(0)$	Our work [34]	[35]	[36]	[37]	[38]	[39]
$B_d^0 - a_0^+(980)$	$F_+(0)$	0.192	0.58	0.56			
	$F_T(0)$	0.182	0.78				
$B_s^0 - K_0^{*+}(800)$	$F_+(0)$	0.274	0.44	0.53			
	$F_T(0)$	0.292	0.60				
$B_s^0 - f_0(980)$	$F_+(0)$	0.254	0.45	0.44	0.19	0.35	0.12
	$F_T(0)$	0.285	0.60	0.58	0.23	0.40	-0.08
$B_d^0 - K_0^{*0}(800)$	$F_+(0)$	0.306	0.50	0.46			
	$F_T(0)$	0.306	0.67	0.58			
$B_d^0 - f_0(500)$	$F_+(0)$	0.210					
	$F_T(0)$	0.203					

Table 2: The branching fractions for the semileptonic and rare B-decays into light scalar mesons and lepton pairs

Decay modes	Branching fractions			
	Our work [34] ($\Lambda_S = 1.5$ GeV)	[40]	[37]	[38]
$B_d^0 \to a_0^+(980)\mu^-\bar{\nu}_\mu$	0.52×10^{-4}	$(2.74 \pm 0.40) \times 10^{-4}$		1.84×10^{-4}
$B_d^0 \to a_0^+(980)\tau^-\bar{\nu}_\tau$	0.11×10^{-4}	$(1.31 \pm 0.23) \times 10^{-4}$		1.01×10^{-4}
$B_s^0 \to K_0^{*+}(800)\mu^-\bar{\nu}_\mu$	1.23×10^{-4}	$(2.06 \pm 0.31) \times 10^{-4}$		1.42×10^{-4}
$B_s^0 \to K_0^{*+}(800)\tau^-\bar{\nu}_\tau$	0.25×10^{-4}	$(1.07 \pm 0.19) \times 10^{-4}$		0.88×10^{-4}
$B_d^0 \to K_0^{*0}(800)\mu^+\mu^-$	3.47×10^{-7}	$(7.31 \pm 1.21) \times 10^{-7}$		
$B_d^0 \to K_0^{*0}(800)\tau^+\tau^-$	0.61×10^{-7}	$(1.33 \pm 0.36) \times 10^{-7}$		
$B_s^0 \to f_0(980)\mu^+\mu^-$	2.45×10^{-7}	$(5.14 \pm 0.78) \times 10^{-7}$	0.95×10^{-7}	5.21×10^{-7}
$B_s^0 \to f_0(980)\tau^+\tau^-$	0.42×10^{-7}	$(0.74 \pm 0.17) \times 10^{-7}$	1.1×10^{-7}	0.38×10^{-7}
$B_d^0 \to K_0^{*0}(800)\bar{\nu}\nu$	2.53×10^{-6}	$(6.30 \pm 0.97) \times 10^{-6}$		
$B_s^0 \to f_0(980)\bar{\nu}\nu$	1.79×10^{-6}	$(4.39 \pm 0.63) \times 10^{-6}$	0.87×10^{-6}	

tion and the given cascade B-decay can be calculated by using the narrow width approximation. But it is not true in the case of the broad scalar $K_0^*(800)$ meson. There are several parametrizations of the $K-\pi$ line shapes in the literature, see, for instance, their discussion in Ref. [29]. We will use for the time being the parametrization accepted in Ref. [30] which integrated value in the K^*-resonance region is equal to

$$\int_{(m_{K^*}-\delta_m)^2}^{(m_{K^*}+\delta_m)^2} dm^2_{K\pi}|L_S(m^2_{K\pi})|^2 = 0.17, \quad \text{where} \quad \delta_m = 100\,\text{MeV}. \tag{5}$$

Then we scale the calculated value for the differential decay rate $d\Gamma(B\to K_0^*(800)\mu^+\mu^-)$ by this factor and compare with those for $B\to K(892)\mu^+\mu^-)$ decay. We display the behavior of the ratio

$$R(q^2) = \frac{2/3\, d\Gamma(B\to K^*(892)\mu^+\mu^-)}{2/3\, d\Gamma(B\to K^*(892)\mu^+\mu^-) + 0.17 d\Gamma(B\to K_0^*(800)\mu^+\mu^-)} \tag{6}$$

in Fig.1 which may be compared with the finding of Ref. [25]. The integrated ratio (numerator and denominator are integrated separately in the full kinematical region of q^2) gives the size of the S-wave pollution to the branching ratio of the $B\to K^*\ell^+\ell^-$ decay about 6%.

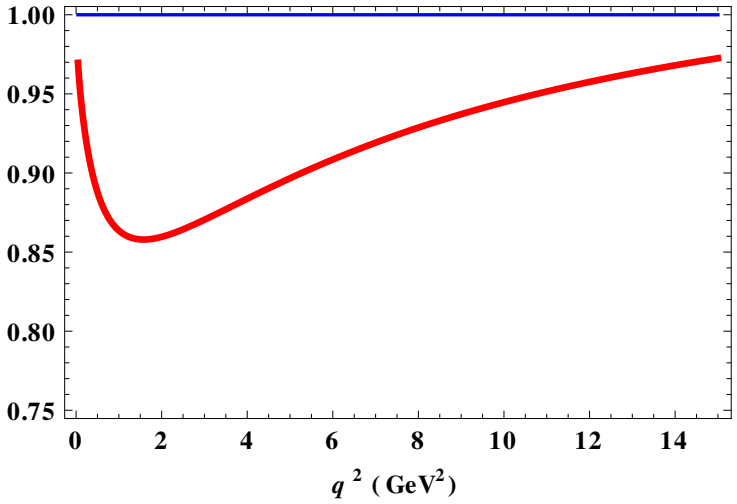


Figure 1: The ratio of the differential decay rate $d\Gamma(B\to K^*(892)(\to K^0\pi^+)\mu^+\mu^-))$ to the full differential decay rate $d\Gamma(B\to K^*(892)(\to K^+\pi^-)\mu^+\mu^-) + d\Gamma(B\to K_0^*(\to K^+\pi^-)\mu^+\mu^-)$.

4 The $B_s^0\to\phi(\to K^+K^-)\ell^+\ell^-$ decay

This decay channel was first discovered and studied by CDF collaboration [41, 42], later been studied by LHCB collaboration [22, 43]. Despite the fact that the angular distributions are in good agreement with the SM expectations, branching ratio of decay had a 3.1σ disagreement with the prediction of the SM [12, 22].

Table 3: The form factors at maximum recoil $q^2 = 0$.

	$V^c(0)$	$A_0^c(0)$	$A_1^c(0)$	$T_1^c(0)$	$T_3^c(0)$
Our work [45]	0.31 ± 0.03	0.28 ± 0.03	0.27 ± 0.03	0.27 ± 0.03	0.18 ± 0.02
Ref. [46]	0.32		0.29	0.28	
Ref. [47]	0.434 ± 0.035	0.474 ± 0.037	0.311 ± 0.029	0.349 ± 0.033	0.175 ± 0.018
Ref. [48]	0.406 ± 0.020	0.322 ± 0.016	0.320 ± 0.016	0.275 ± 0.014	0.133 ± 0.006
Ref. [49]	0.43	0.38	0.30	0.35	0.25
Ref. [50]	0.25 ± 0.05	0.30 ± 0.05	0.19 ± 0.04		
Ref. [51]	0.44	0.42	0.34	0.38	0.26
Ref. [52]	0.26 ± 0.07	0.31 ± 0.07	$0.18^{+0.06}_{-0.05}$	$0.23^{+0.06}_{-0.05}$	0.19 ± 0.05
Ref. [53]	0.329	0.279	0.232	0.276	0.170
Ref. [54]	0.339 ± 0.017		0.271 ± 0.014	0.299 ± 0.016	0.191 ± 0.010

The $B_s^0 \to \phi \ell^+ \ell^-$ decay is similar to the $B \to K^* \ell^+ \ell^-$ decay. The B_s meson production is suppressed compared to the B^0 meson by the relation $f_s/f_d \simeq 1/4$, but the narrow resonance ϕ provides a clean set of data with low background. The main difference between $B_s^0 \to \phi \ell^+ \ell^-$ and $B \to K^* \ell^+ \ell^-$ decays is that the final state do not contain information about the initial state of the meson, whether it was B_s or $\bar{B}_s$. Experimentally procurable angular observables in the $B_s^0 \to \phi \ell^+ \ell^-$ decay are CP-averaged $F_l, S_{3,4,7}$ and CP-asymmetries $A_{5,6,8,9}$[3, 44].

We display in Table 3 the form factors obtained in our model and compare them with those from other approaches.

The rare decay $b \to s \ell^+ \ell^-$ is described in terms of the effective Hamiltonian [55]:

$$\mathcal{H}_{\rm eff} = -\frac{4G_F}{\sqrt{2}} \lambda_t \sum_{i=1}^{10} C_i(\mu) \mathcal{O}_i(\mu), \tag{7}$$

where $C_i(\mu)$ and $\mathcal{O}_i(\mu)$ are the Wilson coefficients and local operators, respectively. $\lambda_t = |V_{tb} V_{ts}^*|$ is the product of CKM matrix elements. Note that we drop small corrections proportional to $\lambda_u = |V_{ub} V_{us}^*|$. By using the effective Hamiltonian defined by Eq. (7) one can write the matrix element of the exclusive transition $B_s \to \phi \ell^+ \ell^-$ as

$$\begin{aligned} \mathcal{M} &= \frac{G_F}{\sqrt{2}} \cdot \frac{\alpha \lambda_t}{\pi} \cdot \Big\{ C_9^{\rm eff} < \phi \,|\, \bar{s}\, \gamma^\mu\, P_L\, b \,|\, B_s > \big(\bar{\ell} \gamma_\mu \ell\big) \\ &- \frac{2 \bar{m}_b}{q^2}\, C_7^{\rm eff} < \phi \,|\, \bar{s}\, i \sigma^{\mu\nu} q_\nu\, P_R\, b \,|\, B_s > \big(\bar{\ell} \gamma_\mu \ell\big) \\ &+ C_{10} < \phi \,|\, \bar{s}\, \gamma^\mu P_L\, b \,|\, B_s > \big(\bar{\ell} \gamma_\mu \gamma_5 \ell\big) \Big\}, \end{aligned} \tag{8}$$

where $C_7^{\rm eff} = C_7 - C_5/3 - C_6$. One has to note that matrix element in Eq.(8) contains both a free quark decay amplitude coming from the operators $\mathcal{O}_7$, $\mathcal{O}_9$ and $\mathcal{O}_{10}$ (gluon magnetic penquin $\mathcal{O}_8$ does not contribute) and, in addition, certain long-distance effects from the matrix elements of four-quark operators $\mathcal{O}_i$ $(i = 1, \ldots, 6)$ which usually are absorbed into a redefinition of the short-distance Wilson-coefficients. The Wilson coefficient $C_9^{\rm eff}$ effectively takes into account, first, the contributions from the four-quark operators $\mathcal{O}_i$ $(i = 1, ..., 6)$ and, second, the nonperturbative effects coming from the $c\bar{c}$-resonance contributions which are as usual parametrized

by the Breit-Wigner ansatz [56]:

$$\begin{aligned} C_9^{\rm eff} &= C_9 + C_0 \left\{ h(\hat{m}_c, s) + \frac{3\pi}{\alpha^2}\,\kappa \sum_{V_i=\psi(1s),\psi(2s)} \frac{\Gamma(V_i \to l^+l^-)\, m_{V_i}}{{m_{V_i}}^2 - q^2 - i m_{V_i}\Gamma_{V_i}} \right\} \\ &- \frac{1}{2} h(1,s)\,(4C_3 + 4C_4 + 3C_5 + C_6) \\ &- \frac{1}{2} h(0,s)\,(C_3 + 3C_4) + \frac{2}{9}\,(3C_3 + C_4 + 3C_5 + C_6)\ , \end{aligned} \tag{9}$$

where $C_0 \equiv 3C_1 + C_2 + 3C_3 + C_4 + 3C_5 + C_6$. Here the charm-loop function is written as

$$\begin{aligned} h(\hat{m}_c, s) &= -\frac{8}{9}\ln\frac{\bar{m}_b}{\mu} - \frac{8}{9}\ln\hat{m}_c + \frac{8}{27} + \frac{4}{9}x \\ &- \frac{2}{9}(2+x)|1-x|^{1/2} \begin{cases} \left(\ln\left|\frac{\sqrt{1-x}+1}{\sqrt{1-x}-1}\right| - i\pi\right), & \text{for } x \equiv \frac{4\hat{m}_c^2}{s} < 1, \\ 2\arctan\frac{1}{\sqrt{x-1}}, & \text{for } x \equiv \frac{4\hat{m}_c^2}{s} > 1, \end{cases} \\ h(0,s) &= \frac{8}{27} - \frac{8}{9}\ln\frac{\bar{m}_b}{\mu} - \frac{4}{9}\ln s + \frac{4}{9}i\pi, \end{aligned}$$

where $\hat{m}_c = \bar{m}_c/m_1$, $s = q^2/m_1^2$ and $\kappa = 1/C_0$. In what follows we drop the charm resonance contributions by putting $\kappa = 0$. We will use the value of $\mu = \bar{m}_{b\,\rm pole}$ for the renormalization scale. Besides the charm-loop perturbative contribution, two loop contributions have been calculated in [57, 58]. They effectively modify the Wilson coefficients as

$$\begin{aligned} C_7^{\rm eff} &\to C_7^{\rm eff} - \frac{\alpha_S}{4\pi}\Big(C_1 F_1^{(7)} + C_2 F_2^{(7)}\Big)\,, \\ C_9^{\rm eff} &\to C_9^{\rm eff} - \frac{\alpha_S}{4\pi}\Big(C_1 F_1^{(9)} + C_2 F_2^{(9)}\Big) \end{aligned} \tag{10}$$

where the two-loop form factors $F_{1,2}^{(7,9)}$ are available in Ref. [58]. A global analysis of $b \to s\ell\ell$ anomalies has been performed in Ref. [4] with the NNLL corrections included. It was shown that they amount up to 15%. The discussion of the non-local $c\bar{c}$ contributions maybe also found in Ref. [11].

We are aiming to compare our results for the branching fractions and angular observables with the experimental data recently reported by the LHCb Collaboration [3] and the results of global analyses performed in Ref. [4]. A set of so-called optimized observables P_i have been constructed (see [18] and references therein) by taking appropriate ratios of the form factors in such a way to minimize the hadronic uncertainties. It seems however more difficult to give them a clean physical interpretation, as it was the case for A_{FB} and F_L.

The optimized observables have not been given explicitly in [3]. Their numerical values were obtained in [4] by converting the results for the CP averages $S_{3,4,7}$ into the optimized observables.

Finally, we present our results for the binned observables in Tables 4-7. Here, we take into account the NNLL corrections for the Wilson coefficients which have been calculated in [57, 58]. The NNLL corrections contribute up to 20% in the region of small transferred momentum squared $q^2 \le 6$ GeV^2 but their influence in the region of large q^2 is really negligible. Using

this optics one can address the 3.3σ deviation seen by [3] for branching fraction in the $1-6$ GeV range. In the covariant quark model this discrepancy is much reduced. The remaining deviation (1.4σ) shrinks is even further if the two-loop corrections for the Wilson coefficients are taken into account, down to 1.1σ. With such error reduction one cannot claim a discrepancy with the SM any longer.

Overall one observes a good description of the data by the covariant quark model and the agreement becomes even better if the two-loop corrections are taken into account. The biggest discrepancy of 2.5σ observed for F_L in the lowest bin $0.1 \leq q^2 \leq 2$ GeV is reduced to 1.7σ when these corrections are taken into account.

The remaining deviations do not exceed 2.0σ and only two of them are greater than 1.5σ if the two loops corrections are neglected (branching fraction and S_4, both for $15 \leq q^2 \leq 17$ GeV). When they are taken into account most measurements lie within one standard deviation, the only two exceeding 1.5σ are S_4 for $15 \leq q^2 \leq 17$ and the above mentioned measurement of F_L.

Table 4: Binned observables for $\mathcal{B}(B_s \to \phi\mu^+\mu^-)$.

$10^7\mathcal{B}(B_s \to \phi\mu^+\mu^-)$	2 loop	1 loop	[4]	Expt. [3]
$[0.1, 2]$	0.99 ± 0.2	0.86 ± 0.17	1.81 ± 0.36	1.11 ± 0.16
$[2, 5]$	0.90 ± 0.18	0.95 ± 0.19	1.88 ± 0.31	0.77 ± 0.14
$[5, 8]$	$--$	1.25 ± 0.25	2.25 ± 0.41	0.96 ± 0.15
$[11, 12.5]$	0.84 ± 0.17	0.88 ± 0.18	$--$	0.71 ± 0.12
$[15, 17]$	1.15 ± 0.23	1.19 ± 0.24	$--$	0.90 ± 0.13
$[17, 19]$	0.75 ± 0.15	0.77 ± 0.15	$--$	0.75 ± 0.13
$[1., 6.]$	1.56 ± 0.31	1.64 ± 0.33	$--$	1.29 ± 0.19
$[15, 19]$	1.89 ± 0.28	1.95 ± 0.29	2.20 ± 0.16	1.62 ± 0.20

Table 5: Binned observables for $F_L(B_s \to \phi\mu^+\mu^-)$.

$F_L(B_s \to \phi\mu^+\mu^-)$	2 loop	1 loop	[4]	Expt. [3]
$[0.1, 2]$	0.37 ± 0.07	0.46 ± 0.09	0.46 ± 0.09	0.20 ± 0.09
$[2, 5]$	0.72 ± 0.14	0.74 ± 0.15	0.79 ± 0.03	0.68 ± 0.15
$[5, 8]$	$--$	0.57 ± 0.11	0.65 ± 0.05	0.54 ± 0.10
$[11, 12.5]$	0.40 ± 0.08	0.40 ± 0.08	$--$	0.29 ± 0.11
$[15, 17]$	0.34 ± 0.07	0.34 ± 0.07	$--$	0.23 ± 0.09
$[17, 19]$	0.33 ± 0.06	0.33 ± 0.06	$--$	0.4 ± 0.14
$[1, 6]$	0.69 ± 0.14	0.71 ± 0.14	$--$	0.63 ± 0.09
$[15, 19]$	0.34 ± 0.07	0.34 ± 0.07	0.36 ± 0.02	0.29 ± 0.07

References

[1] LHCb Collab.(R.Aaij *et al.*), *Phys. Rev. Lett.* **111**, no. 19, 191801 (2013) [arXiv:1308.1707 [hep-ex]].

[2] R. Aaij *et al.* [LHCb Collaboration], JHEP **1406**, 133 (2014) [arXiv:1403.8044 [hep-ex]].

[3] R. Aaij *et al.* [LHCb Collaboration], JHEP **1509**, 179 (2015) [arXiv:1506.08777 [hep-ex]].

[4] S. Descotes-Genon, L. Hofer, J. Matias and J. Virto, arXiv:1510.04239 [hep-ph].

[5] S. Descotes-Genon, J. Matias, M. Ramon and J. Virto, JHEP **1301**, 048 (2013) [arXiv:1207.2753 [hep-ph]].

[6] S. Descotes-Genon, T. Hurth, J. Matias and J. Virto, JHEP **1305**, 137 (2013) [arXiv:1303.5794 [hep-ph]].

[7] S. Descotes-Genon, J. Matias and J. Virto, Phys. Rev. D **88**, 074002 (2013) [arXiv:1307.5683 [hep-ph]].

[8] W. Altmannshofer and D. M. Straub, Eur. Phys. J. C **73**, 2646 (2013) [arXiv:1308.1501 [hep-ph]].

[9] U. Egede, T. Hurth, J. Matias, M. Ramon and W. Reece, JHEP **1010**, 056 (2010) [arXiv:1005.0571 [hep-ph]].

Table 6: Binned observables for $S_3(B_s \to \phi\mu^+\mu^-)$.

$S_3(B_s \to \phi\mu^+\mu^-)$	2 loop	1 loop	[4]	Expt. [3]
$[0.1, 2]$	0.0031 ± 0.0006	0.0023 ± 0.0005	0.02 ± 0.02	-0.05 ± 0.13
$[2, 5]$	-0.035 ± 0.007	-0.039 ± 0.008	-0.01 ± 0.01	-0.06 ± 0.21
$[5, 8]$	$--$	-0.082 ± 0.016	-0.03 ± 0.02	-0.10 ± 0.25
$[11, 12.5]$	-0.15 ± 0.03	-0.15 ± 0.03	$--$	-0.19 ± 0.21
$[15, 17]$	-0.23 ± 0.05	-0.23 ± 0.05	$--$	-0.06 ± 0.18
$[17, 19]$	-0.29 ± 0.06	-0.29 ± 0.06	$--$	-0.07 ± 0.25
$[1, 6]$	-0.034 ± 0.007	-0.039 ± 0.008	$--$	-0.02 ± 0.13
$[15, 19]$	-0.25 ± 0.05	-0.25 ± 0.05	-0.22 ± 0.01	-0.09 ± 0.12

Table 7: Binned observables for $S_4(B_s \to \phi\mu^+\mu^-)$.

$S_4(B_s \to \phi\mu^+\mu^-)$	2 loop	1 loop	[4]	Expt. [3]
$[0.1, 2]$	-0.038 ± 0.008	-0.031 ± 0.006	-0.06 ± 0.03	-0.27 ± 0.23
$[2, 5]$	0.19 ± 0.04	0.21 ± 0.04	0.16 ± 0.03	0.47 ± 0.37
$[5, 8]$	$--$	0.28 ± 0.06	0.25 ± 0.02	0.10 ± 0.17
$[11, 12.5]$	0.30 ± 0.06	0.30 ± 0.06	$--$	0.47 ± 0.25
$[15, 17]$	0.31 ± 0.06	0.31 ± 0.06	$--$	0.03 ± 0.15
$[17, 19]$	0.32 ± 0.06	0.32 ± 0.06	$--$	0.39 ± 0.3
$[1, 6]$	0.17 ± 0.03	0.19 ± 0.04	$--$	0.19 ± 0.14
$[15, 19]$	0.31 ± 0.06	0.31 ± 0.06	0.31 ± 0.00	0.14 ± 0.11

Table 8: Binned observables for $S_7(B_s \to \phi\mu^+\mu^-)$.

$S_7(B_s \to \phi\mu^+\mu^-)$	2 loop	1 loop	[4]	Expt. [3]
$[0.1, 2]$	0.0065 ± 0.0013	0	0.03 ± 0.01	0.04 ± 0.12
$[2, 5]$	0.0065 ± 0.0013	0	0.02 ± 0.01	-0.03 ± 0.21
$[5, 8]$	$--$	0	0.01 ± 0.00	0.04 ± 0.18
$[11, 12.5]$	0.0021 ± 0.0004	0	$--$	0.00 ± 0.16
$[15, 17]$	0.00087 ± 0.0002	0	$--$	0.12 ± 0.15
$[17, 19]$	0.00034 ± 0.00007	0	$--$	0.20 ± 0.26
$[1, 6]$	0.0065 ± 0.0013	0	$--$	-0.03 ± 0.14
$[15, 19]$	0.00066 ± 0.00013	0	0.00 ± 0.03	0.13 ± 0.11

[10] M. Beneke, T. Feldmann and D. Seidel, Nucl. Phys. B **612**, 25 (2001) [hep-ph/0106067].

[11] M. Beylich, G. Buchalla and T. Feldmann, Eur. Phys. J. C **71** (2011) 1635 [arXiv:1101.5118 [hep-ph]].

[12] J. Lyon and R. Zwicky, arXiv:1406.0566 [hep-ph].

[13] A. Bharucha, D. M. Straub and R. Zwicky, arXiv:1503.05534 [hep-ph].

[14] A. Khodjamirian, T. Mannel, A. A. Pivovarov and Y.-M. Wang, JHEP **1009**, 089 (2010) [arXiv:1006.4945 [hep-ph]].

[15] X. W. Kang, B. Kubis, C. Hanhart and U. G. Meiner, Phys. Rev. D **89**, 053015 (2014) [arXiv:1312.1193 [hep-ph]].

[16] LHCb Collab.(R.Aaij *et al.*), *JHEP* **1308**, 131 (2013) [arXiv:1304.6325, arXiv:1304.6325 [hep-ex]].

[17] T. Hurth and F. Mahmoudi, *JHEP* **1404**, 097 (2014) [arXiv:1312.5267 [hep-ph]].

[18] S. Descotes-Genon, T. Hurth, J. Matias and J. Virto, *JHEP* **1305**, 137 (2013) [arXiv:1303.5794 [hep-ph]].

[19] A. Datta, M. Duraisamy and D. Ghosh, *Phys. Rev. D* **89**, no. 7, 071501 (2014) [arXiv:1310.1937 [hep-ph]].

[20] C. Bobeth, G. Hiller and D. van Dyk, *Phys. Rev. D* **87**, 034016 (2013) [arXiv:1212.2321 [hep-ph]].

[21] W. Altmannshofer and D. M. Straub, *Eur. Phys. J. C* **73**, no. 12, 2646 (2013) [arXiv:1308.1501 [hep-ph]].

[22] W. Altmannshofer and D. M. Straub, "State of new physics in $b \to s$ transitions", arXiv:1411.3161 [hep-ph].

[23] R. Mandal, R. Sinha and D. Das, *Phys. Rev. D* **90**, no. 9, 096006 (2014) [arXiv:1409.3088 [hep-ph]].

[24] C. D. Lu and W. Wang, *Phys. Rev. D* **85**, 034014 (2012) [arXiv:1111.1513 [hep-ph]].

[25] D. Becirevic and A. Tayduganov, *Nucl. Phys. B* **868**, 368 (2013) [arXiv:1207.4004 [hep-ph]].

[26] J. Matias, *Phys. Rev. D* **86**, 094024 (2012) [arXiv:1209.1525 [hep-ph]].

[27] T. Blake, U. Egede and A. Shires, *JHEP* **1303**, 027 (2013) [arXiv:1210.5279 [hep-ph]].

[28] D. Das, G. Hiller, M. Jung and A. Shires, *JHEP* **1409**, 109 (2014) [arXiv:1406.6681 [hep-ph]].

[29] M. Döring, U. G. Meissner and W. Wang, *JHEP* **1310**, 011 (2013) [arXiv:1307.0947 [hep-ph]].

[30] U. G. Meissner and W. Wang, *JHEP* **1401**, 107 (2014) [arXiv:1311.5420 [hep-ph]].

[31] C. Amsler, S. Eidelman, T. Gutsche, C. Hanhart, S. Spanier and N. A. Tornqvist, "Note on Scalar Mesons below 2 GeV," see PDG'14.

[32] C. Amsler and N. A. Tornqvist, *Phys. Rept.* **389**, 61 (2004).

[33] Particle Data Group Collab.(K. A. Olive *et al.*), *Chin. Phys. C* **38**, 090001 (2014).

[34] A. Issadykov, M. A. Ivanov and S. K. Sakhiyev, *Phys. Rev. D* **91**, no. 7, 074007 (2015) [arXiv:1502.05280 [hep-ph]].

[35] Z. G. Wang, "$B - S$ transition form-factors with the light-cone QCD sum rules," arXiv:1409.6449 [hep-ph].

[36] Y. J. Sun, Z. H. Li and T. Huang, *Phys. Rev. D* **83**, 025024 (2011) [arXiv:1011.3901 [hep-ph]].

[37] P. Colangelo, F. De Fazio, P. Santorelli and E. Scrimieri, *Phys. Rev. D* **53**, 3672 (1996) [*Erratum-ibid. D* **57**, 3186 (1998)] [hep-ph/9510403].

[38] R. H. Li, C. D. Lu, W. Wang and X. X. Wang, *Phys. Rev. D* **79**, 014013 (2009) [arXiv:0811.2648 [hep-ph]].

[39] N. Ghahramany and R. Khosravi, *Phys. Rev. D* **80**, 016009 (2009).

[40] Z. G. Wang, "Semi-leptonic $B \to S$ decays in the standard model and in the universal extra dimension model," arXiv:1411.7961 [hep-ph].

[41] T. Aaltonen *et al.* [CDF Collaboration], Phys. Rev. Lett. **107**, 201802 (2011) [arXiv:1107.3753 [hep-ex]].

[42] T. Aaltonen *et al.* [CDF Collaboration], Phys. Rev. Lett. **106**, 161801 (2011) [arXiv:1101.1028 [hep-ex]].

[43] R. Aaij *et al.* [LHCb Collaboration], JHEP **1307**, 084 (2013) [arXiv:1305.2168 [hep-ex]].

[44] C. Bobeth, G. Hiller and G. Piranishvili, JHEP **0807**, 106 (2008) [arXiv:0805.2525 [hep-ph]].

[45] S. Dubnika, A. Z. Dubnikov, A. Issadykov, M. A. Ivanov, A. Liptaj and S. K. Sakhiyev, Phys. Rev. D **93**, no. 9, 094022 (2016) [arXiv:1602.07864 [hep-ph]].

[46] M. A. Ivanov, J. G. Körner, S. G. Kovalenko, P. Santorelli and G. G. Saidullaeva, *Phys. Rev. D* **85**, 034004 (2012) [arXiv:1112.3536 [hep-ph]].

[47] P. Ball and R. Zwicky, Phys. Rev. D **71**, 014029 (2005) [hep-ph/0412079].

[48] R. N. Faustov and V. O. Galkin, Eur. Phys. J. C **73**, no. 10, 2593 (2013) [arXiv:1309.2160 [hep-ph]].

[49] U. O. Yilmaz, Eur. Phys. J. C **58** (2008) 555 [arXiv:0806.0269 [hep-ph]].

[50] A. Ali, G. Kramer, Y. Li, C. D. Lu, Y. L. Shen, W. Wang and Y. M. Wang, Phys. Rev. D **76** (2007) 074018 [hep-ph/0703162 [HEP-PH]].

[51] D. Melikhov and B. Stech, Phys. Rev. D **62** (2000) 014006 [hep-ph/0001113].

[52] R. H. Li, C. D. Lu and W. Wang, Phys. Rev. D **79** (2009) 034014 [arXiv:0901.0307 [hep-ph]].

[53] C. D. Lu, W. Wang and Z. T. Wei, Phys. Rev. D **76** (2007) 014013 [hep-ph/0701265 [HEP-PH]].

[54] Y. L. Wu, M. Zhong and Y. B. Zuo, Int. J. Mod. Phys. A **21** (2006) 6125 [hep-ph/0604007].

[55] G. Buchalla, A. J. Buras and M. E. Lautenbacher, Rev. Mod. Phys. **68**, 1125 (1996) [hep-ph/9512380].

[56] A. Ali, T. Mannel, T. Morozumi: Phys. Lett. B **273** 505 (1991).

[57] H. H. Asatryan, H. M. Asatrian, C. Greub and M. Walker, Phys. Rev. D **65**, 074004 (2002) [hep-ph/0109140].

[58] C. Greub, V. Pilipp and C. Schupbach, JHEP **0812**, 040 (2008) [arXiv:0810.4077 [hep-ph]].

LKF Transformations in QCD and Quark Propagator

M. Jamil Aslam[1]*and L.X. Gutiérrez-Guerrero[2]

[1] Department of Physics, Quaid-i-Azam University, Islamabad, 45320, Pakistan.
[2] CONACyT-Mesoamerican Centre for Theoretical Physics, Universidad Autónoma de Chiapas, Carretera Zapata Km. 4, Real del Bosque (Terán), Tuxtla Gutiérrez 29040, Chiapas, México.

DOI: http://dx.doi.org/10.3204/DESY-PROC-2016-04/Aslam

In this article, we present the derivation of Landau-Khalatnikov-Fradkin (LKF) transformation for the quark propagator in an arbitrary $SU(N)$ gauge theory. Working in the system of covariant gauges, we derive transformation law by making perturbative expansions till $\mathcal{O}(g_s^6)$ and, for some terms, till $\mathcal{O}(g_s^8)$. The corresponding transformation for the abelian case of quantum electrodynamics is trivially recovered by setting the color factors $C_F = 1$ and $C_A = 0$. Finally, we study the implications of this QCD transformation for the quark-antiquark condensate, multiplicative renormalizability of mass less quark propagator and its relation with the quark-gluon vertex at one loop order.

1 Introduction

In gauge field theories, Green functions transform in a specific manner under a variation of gauge. In quantum electrodynamics (QED) these transformations carry the name of Landau-Khalatnikov-Fradkin transformations (LKFT), derived by these authors in 1965 using canonical formulation [1]. Later, these were also derived through functional method by Johnson and Zumino [2]. Just like the Ward-Fradkin-Green-Takahashi identities (WFGTI) identities, the LKFT are also non perturbative in nature [3]. WGTI relate the behviour of different Green functions under the local gauge transformations, whereas, the LKFT take care of the behaviour of single Green function under the variation of covariant gauge parameter. It can be shown that if a given WFGTI holds in one gauge, then if the Green functions involved are transformed to another gauge under LKFT, the WFGTI in that other gauge will be satisfied automatically. The utility of LFKT, as compared to WFGTI is less appreciated, because of the fact that they are written in coordinate space and this adds complexity in the calculation.

Both the WFGTI and the LKFT are satisfied at every order of approximation in QED. The only gauge theory whose non perturbative understanding is relevant to fundamental interactions within the standard model is quantum chromodynamics (QCD). In line with the WFGTI, the gauge identities which relate Green functions in QCD are called Slavnov-Tayolr identities (STI), [4] and they play a key role in the proof of gauge-invariant renormalizability of QCD.

gauge theory bearing in mind that the mathematical structure of QCD is not too different from any other $SU(N)$ theory.

Our study is organised as follows: In Sec. 2, we give the derivation the local gauge transformation relation for the quark propagator in the coordinate space by making expansion till $\mathcal{O}(g_s^6)$ and for some terms till $\mathcal{O}(g_s^8)$. Sec. 3 details the role of the quark-gluon vertex in ensuring the multiplicative renormalizability of the quark propagator and also provides the conclusions.

2 Quark Propagator Under Local $SU(N)$ Gauge Transformations

Local $SU(N)$ gauge transformation for the quark field is defined as :

$$\psi_i(x) \;\rightarrow\; \psi_i'(x)=\mathrm{e}^{i[g_s\varphi_a(x)T_a]}\;\psi_i(x)\,, \tag{1}$$

where $\varphi_a(x)$ is an arbitrary free scalar field operator carrying color quantum number a ($a = 1, 2, \cdots, N^2-1$), g_s is the strong coupling constant and $T_a = \lambda_a/2$, λ_a being the well-known Gell-Mann matrices for $N = 3$. The quark Green function (propagator in coordinate space) is defined as :

$$iS_{ij}^F(x,x') \equiv iS_{ij}^F = \langle \mathrm{T}\{\psi_i(x)\bar{\psi}_j(x')\}\rangle\,, \tag{2}$$

where the angle brackets stand for the vacuum expectation value. Under $SU(N)$ local gauge transformation of Eq. (1), we have

$$iS_{ij}^F(x,x')\rightarrow\langle \mathrm{T}\{\mathrm{e}^{i[g_s\varphi_a(x)T_a]}\psi_i(x)\bar{\psi}_j(x')\mathrm{e}^{-i[g_s\varphi_b(x')T_b]}\rangle. \tag{3}$$

Since there are two fermion and two scalar fields, the only surviving contractions yield :

$$iS_{ij}^F(x,x')\rightarrow iS_{ij}^{0F}(x,x')\langle \mathrm{T}\{\mathrm{e}^{i[g_s\varphi_a(x)T_a]}\,\mathrm{e}^{-i[g_s\varphi_b(x')T_b]}\rangle, \tag{4}$$

where $S_{ij}^{0F}(x,x')$ stands for the Green function for quarks in the Landau gauge. In QCD, the color factor C_A enters only at $\mathcal{O}(g_s^4)$ in the quark propagator expansion which is inherent to its non-commutative nature. In the abelian approximation of QCD, i.e., $C_A = 0$, the final result resembles that of QED with C_F sitting as an overall multiplication factor:

$$iS_{ij}^F(x,x') = iS_{ij}^{0F}(x,x')\;\mathrm{e}^{\,g_s^2\,C_F\,\left[i\Delta_F(x-x')-i\Delta_F(0)\right]}. \tag{5}$$

Let us calculate the term involving the exponentials :

$$\begin{aligned}
&\langle 0|\mathrm{T}\{\mathrm{e}^{i[g_s\varphi_a(x)T_a]}\,\mathrm{e}^{-i[g_s\varphi_b(x')T_b]}\}|0\rangle \\
=\;&\langle 0|\mathrm{T}\Bigg\{\left[1+ig_s\varphi_a(x)T_a+\frac{(ig_s)^2}{2!}(\varphi_a(x)T_a)^2+\frac{(ig_s)^3}{3!}(\varphi_a(x)T_a)^3+\frac{(ig_s)^4}{4!}(\varphi_a(x)T_a)^4+\cdots\right] \\
&\times\left[1-ig_s\varphi_b(x')T_b+\frac{(-ig_s)^2}{2!}(\varphi_b(x')T_b)^2+\frac{(-ig_s)^3}{3!}(\varphi_b(x')T_b)^3+\frac{(-ig_s)^4}{4!}(\varphi_b(x')T_b)^4+\cdots\right]\Bigg\}|0\rangle\,.
\end{aligned} \tag{6}$$

By employing the following notation for the Green functions associated with the scalar

We can now simplify the $\mathcal{O}(g_s^4)$ terms in expression (6) that leads to :

$$\begin{aligned} iS_{ij}^F(x,x') &= iS_{ij}^{0F}(x,x')\Big[\mathrm{e}^{g_s^2\,C_F\left[i\Delta_F(x-x')-i\Delta_F(0)\right]} \\ &- \frac{g_s^4\,C_A\,C_F}{24}\left\{(i\Delta_F(x-x')-i\Delta_F(0))\,(3i\Delta_F(x-x')-i\Delta_F(0))\right\}+\mathcal{O}(g_s^6)\Big]. \quad (8) \end{aligned}$$

Note that at $\mathcal{O}(g_s^4)$, we have a factors of C_A in the quark propagator that leads to self interaction of gluons. Note that the quark gluon vertex will contribute factors of $C_F - C_A/2$ for the abelian diagram and C_A for the non-abelian diagram including 3-point self gluon interactions. The ghost and gluon loop will also contribute a factor of C_A. By employing the same method, the quark propagator till $\mathcal{O}(g_s^8)$ for certain terms could be written as

$$\begin{aligned} iS_{ij}^F(x,x') &= iS_{ij}^{0F}(x,x')\Big[\mathrm{e}^{g_s^2\,C_F\left[i\Delta_F(x-x')-i\Delta_F(0)\right]} \\ &-\frac{g_s^4\,C_A\,C_F}{(2!)(3!2!1!)}\left\{[i\Delta_F(x-x')-i\Delta_F(0)]\,[3i\Delta_F(x-x')-i\Delta_F(0)]\right\}\mathrm{e}^{g_s^2\,C_F\left[i\Delta_F(x-x')-i\Delta_F(0)\right]} \\ &+\frac{g_s^6\,C_F C_A^2}{(1!)(4!3!2!1!)}\,[i\Delta_F(x-x')-i\Delta_F(0)]\times \\ &\left[8(i\Delta_F(x-x'))^2-7(i\Delta_F(x-x'))(i\Delta_F(0))+(i\Delta_F(0))^2\right]+\mathcal{O}(g_s^8)\Big]. \quad (9) \end{aligned}$$

One can note some key points regarding this transformation: Subsitituting $C_F = 1$, $g_s = e$, $C_A = 0$, one can get back the LKFT for the electron propagator in QED [1]. In the color factor in the fundamental representation, i.e., C_F^n, we find a closed expression in perturbative series. However, a closed expression for the perturbative series in C_A^n (color factor in adjoint representation), was not achieved as it has several sources. Finally in the definition the chiral quark condensate

$$\langle\bar{\psi}\psi\rangle_\xi = -\mathrm{Tr}\left[S^F(x,x')\right]_{x'=x} = -\mathrm{Tr}\left[S^{0F}(x,x')\right]_{x'=x} = \langle\bar{\psi}\psi\rangle_0 \quad (10)$$

making use of and the final expression for the quark propagator in an arbitrary covariant gauge, Eq. (9), we can see that the chiral quark condensate is manifestly a gauge invariant quantity in any $SU(N)$ theory.

3 Quark-Gluon Vertex and LKF Transformations

We know form our knowledge of QED that the structure of the quark gluon vertex dictates multiplicative renormalizability (discussed in length in section 2 of reference [5]) of the charged fermion and hence ensures LKFT for the 2-point function are satisfied. One can note that the quark propagator beyond $\mathcal{O}(g_s^2)$ involves gluon self interactions and hence introduces a color factor C_A in the adjoint representation. Just to give an example, the one-loop calculation of the transverse quark-gluon vertex, defined by $(k-p)_\mu\Gamma^\mu(k,p)$=0, where k and p are the incoming and outgoing fermion momenta, respectively, for $k^2 >> p^2$, gives:

$$\Gamma_\mu^{T(a)}(k,p) = \left(C_F - \frac{1}{2}C_A\right)\frac{\alpha_s\xi}{8\pi k^2}\log\left(\frac{p^2}{k^2}\right)T_\mu(k,p)\,,$$
$$\Gamma_\mu^{T(n)}(k,p) = C_A\,\frac{\alpha_s(3\xi-1)}{64\pi k^2}\log\left(\frac{p^2}{k^2}\right)T_\mu(k,p)\,, \qquad (11)$$

where the subscripts a and n correspond to the abelian and non-abelian diagram, respectively and the vector $T^\mu(k,p)$ is defined as $T_\mu(k,p) = k^2\gamma_\mu - k_\mu k\cdot p$. In the wave function renormalization, the gauge parameter dependent piece of the quark gluon vertex would result in the following type of $\mathcal{O}(g_s^4)$ terms :

$$F(p^2/\mu^2;\xi) = 1 + \alpha_s\, f_0\, C_F \ln\left(\frac{p^2}{\mu^2}\right)$$
$$+\alpha_s^2\left[\frac{f_0^2 C_F^2}{2}\ln^2\left(\frac{p^2}{\mu^2}\right) + C_F\,(f_1^a C_F + f_1^b C_A)\ln\left(\frac{p^2}{\mu^2}\right)\right].$$

Note that to this order, the C_A terms would also be contributed by the gluon and ghost loop correction to the gluon propagator in the quark gap equation.

Recall that the gap equation for QCD is

$$S(p;\xi)^{-1} = [S^0(p;\xi)]^{-1} + g^2 C_F\int\frac{d^4k}{(2\pi)^4}D_{\mu\nu}(p-k;\xi)\gamma_\mu S(k;\xi)\Gamma_\nu(k,p)\,,$$

where $D_{\mu\nu}(q;\xi)$ is the gluon propagator:

$$D_{\mu\nu}(q;\xi) = \left[\delta_{\mu\nu} - \frac{q_\mu q_\nu}{q^2}\right]\frac{1}{q^2[1+\Pi(q^2)]} + \xi\frac{q_\mu q_\nu}{q^4}\,.$$

Vertex	Structure	a_2, a_3, a_6, a_8	MR	ν
Bare	γ_μ	–	No	
BC	$\Gamma^{BC}_\mu = \sum_{i=1}^{4} \lambda_i L_\mu$	–	No	
CP	$\Gamma^{CP}_\mu = \Gamma^{BC}_\mu + \tau_6 T^6_\mu$	$a_6 = \frac{1}{2}$	Yes	$C_F\alpha\xi/(4\pi)$
B	$\Gamma^{B}_\mu = \Gamma^{BC}_\mu + \sum_{i=2,3,6,8} \tau_i T^i_\mu$	$a_6 = -\frac{1}{2}, a_2 + 2(a_3 + a_8) = -2$	Yes	Numerical
QC	$\Gamma^{QC}_\mu = \Gamma^{BC}_\mu + \sum_{i=2,3,6,8} \tau_i T^i_\mu$	$a_2 = a_6 = 0, a_3 = 1/2, a_8 = -1$	Yes	Numerical
Our	$\Gamma_\mu \;\; = \Gamma^{BC}_\mu + \sum_{i=2,3,6,8} \tau_i T^i_\mu$	$a_6 = +\frac{1}{2}, a_2 + 2(a_3 + a_8) = 0$	Yes	$C_F\alpha\xi/(4\pi)$

Table 1: Different vertex *ansätze* as regards the LKFT for the massless quark propagator are compared. The first three columns define the vertex considered (see details in Ref. [5]). The fourth column shows whether the quark propagator is Multiplicatively Renormalizable (MR) or not. The last column states the exact exponent of the quark propagator to determine if the vertex complies with the exact prediction of the LKFT for the leading log series, namely $\nu = C_F\alpha\xi/(4\pi)$.

We take the liberty to work with the quenched theory, i.e., $\Pi(q^2) = 0$ in order to see the role of LKFT for different choices of quark-gluon vertex $\Gamma_\nu(k, p)$.

In Table (1), we provide an explicit comparison of different vertex *ansätze* as tested against the constraints of LKFT. Obviously, the bare and the Ball-Chiu vertices do not support an MR solution but the *ansätze* given in [6, 7] do exhibit an MR solution due to the condition given by Eq. (39) of ref. [5]. However, they fail to produce exact analytical value of $\nu = C_F\alpha\xi/(4\pi)$ and hence deny the predictions of the LKFT for the leading logs. The proposal given in ref. [5], does satisfy all these features.

To conclude: The generalized LKFT for the quark propagator in an $SU(N)$ gauge field theory are derived where perturbative expansion under the local gauge(c.f. Eq. (4)) to $\mathcal{O}(g_s^6)$ and, for some terms, to $\mathcal{O}(g_s^8)$ is made. A close perturbative series is obtained for $C_F^n C_A^0$ and $C_F^{n-1} C_A$ but not in the color factor for the adjoint representation C_A. We have seen that due to the explicit presence of the overall factor of $(i\Delta_F(x - x') - i\Delta_F(0))$, the gauge invariance of the chiral quark condensate is guaranteed just as in QED [8].

Using the most common truncations employed by the scientific community to represent the quark-gluon vertex we have deduced that only CP vertex and the vertex proposed in our work in ref. [5] are the ones which comply with all the requirements of LKFT and MR. The bare and BC vertices do not even yield an MR quark propagator.

Acknowledgments: J. A. would like to thank the organisers of *Quantum Field Theory at the Limits: from Strong Fields to Heavy Quarks* for providing local hospitality and partial grant towards air fare.

References

[1] L. D. Landau, I. M. Khalatnikov, Zh. Éksp. Teor. Fiz. **29**, 89 (1956), Sov. Phys. JETP **2**, 69 (1956); E. S. Fradkin, Zh. Éksp. Teor. Fiz. **29**, 258 (1955), Sov. Phys. JETP **2**, 361 (1956).

[2] K. Johnson, B. Zumino, Phys. Rev. Lett. **3**, 351 (1959); B. Zumino, J. Math. Phys. **1**, 1 (1960).

[3] J. C. Ward, Phys. Rev. **78**, 182 (1950); E. S. Fradkin, Zh. Éksp. Teor. Fiz. **29**, 258 (1955) [Sov. Phys.

[5] M. J. Aslam, A. Bashir and L. X. Gutierrez-Guerrero, Phys. Rev. D **93**, no. 7, 076001 (2016)

[6] A. Bashir, R. Bermudez, Phys. Rev. C **85**, 045205 (2012).

[7] S-x. Qin, L. Chang, Y-x. Liu, C. D. Roberts, S.M. Schmidt, Phy. Lett. B **722**, 384 (2013).

[8] A. Bashir, A. Raya, Few Body Syst. **41**, 185 (2007).

Critical behaviour of (2+1)-dimensional QED: $1/N$-corrections

Anatoly V. Kotikov[1], *Sofian Teber*[2,3]

[1]Bogoliubov Laboratory of Theoretical Physics, Joint Institute for Nuclear Research, 141980 Dubna, Russia
[2]Sorbonne Universités, UPMC Univ Paris 06, UMR 7589, LPTHE, F-75005, Paris, France
[3]CNRS, UMR 7589, LPTHE, F-75005, Paris, France

DOI: http://dx.doi.org/10.3204/DESY-PROC-2016-04/Kotikov

We present recently obtained results for dynamical chiral symmetry breaking studied within (2+1)-dimensional QED with N four-component fermions. The leading and next-to-leading orders of the $1/N$ expansion are computed exactly in an arbitrary non-local gauge.

1 Introduction

In these Proceedings we present the results of our recent papers [1, 2], where the critical behavior of Quantum Electrodynamics in $2+1$ dimensions (QED_3) has been studied. QED_3 is described by the Lagrangian:

$$L = \overline{\Psi}(i\hat{\partial} - e\hat{A})\Psi - \frac{1}{4}F_{\mu\nu}^2\,, \tag{1}$$

where Ψ is taken to be a four component complex spinor. In the presence of N fermion flavours, the model has a $U(2N)$ symmetry. A (parity-invariant) fermion mass term, $m\overline{\Psi}\Psi$, breaks this symmetry to $U(N) \times U(N)$. In the massless case, loop expansions are plagued by infrared divergences. The latter soften upon analysing the model in a $1/N$ expansion [3, 4]. Since the theory is super-renormalizable, the mass scale is then given by the dimensionful coupling constant: $a = Ne^2/8$, which is kept fixed as $N \to \infty$. Early studies of this model [5, 6] suggested that the physics is rapidly damped at momentum scales $p \gg a$ and that a fermion mass term breaking the flavour symmetry is dynamically generated at scales which are orders of magnitude smaller than the intrinsic scale a. Since then, dynamical chiral symmetry breaking ($\mathrm{D}\chi\mathrm{SB}$) in QED_3 and the dependence of the dynamical fermion mass on N have been the subject of extensive studies, see, *e.g.*, [1]-[20].

One of the central issue is related to the value of the critical fermion number, N_c, which is such that $\mathrm{D}\chi\mathrm{SB}$ takes place only for $N < N_c$. An accurate determination of N_c is of crucial importance to understand the phase structure of QED_3 with far reaching implications from particle physics to planar condensed matter physics systems having relativistic-like low-energy excitations [21, 22]. It turns out that the values that can be found in the literature vary from $N_c \to \infty$ [5, 7, 8, 9] corresponding to $\mathrm{D}\chi\mathrm{SB}$ for all values of N, all the way to $N_c \to 0$ in the case where no sign of $\mathrm{D}\chi\mathrm{SB}$ is found [10, 11].

Of importance to us in the following, is the approach of Appelquist et al. [6] who found that

$N_c = 32/\pi^2 \approx 3.24$ by solving the Schwinger-Dyson (SD) gap equation using a leading order (LO) $1/N$-expansion. Lattice simulations in agreement with a finite non-zero value of N_c can be found in [15]. Soon after the analysis of [6], Nash approximately included next-to-leading order (NLO) corrections and performed a partial resummation of the wave-function renormalization constant at the level of the gap equation; he found [16]: $N_c \approx 3.28$.

Recently in [1], the NLO corrections could be computed exactly in the Landau gauge yielding $N_c \approx 3.29$, a value which is suprisingly close to the one of Nash in Ref. [16]. More recently, in [2], the results of [1] were generalized to an arbitrary non-local gauge [23]. Moreover, it was shown in [2] that a resummation of the wave-function renormalization yields a strong suppression of the gauge dependence of the critical fermion flavour number, $N_c(\xi)$ where ξ is the gauge fixing parameter, which is such that DχSB takes place for $N < N_c(\xi)$. Neglecting the gauge-dependent terms yields $N_c = 2.8469$, that coincides with results in [18]. In the general case, it is found that: $N_c(1) = 3.0084$ in the Feynman gauge, $N_c(0) = 3.0844$ in the Landau gauge and $N_c(2/3) = 3.0377$ in the $\xi = 2/3$ gauge where the leading order fermion wave function is finite. These results suggest that DχSB should take place for integer values $N \leq 3$. Using a very different method, Herbut obtained [19] a close value: $N_c \approx 2.89$.

The purpose of the present work is to *demonstrate the basic steps of the papers [1, 2]* leading to the exact results for DχSB in an arbitrary non-local gauge [23]. Such an achievement represents an essential improvement with respect to Nash's approximate NLO results which were carried out in the Feynman gauge. In this respect, there is presently a strong ongoing interest in the study of the gauge dependence of DχSB in several models, see [24, 20]. The choice of the Landau gauge in [1] was motivated by recent results on QED$_3$ [20] showing the gauge invariance of N_c in this gauge when using the Ball-Chiu vertex [25]. Actually, after resumming the wave-function renormalization constant, we find that the LO term in the gap equation becomes gauge-invariant, in agreement with Nash, but also that NLO terms become only weakly gauge-variant. As will be shown in the following, this leads to a very stable value of N_c upon varying the gauge-fixing parameter.

2 Schwinger-Dyson equations

With the conventions of Ref. [1], the inverse fermion propagator is defined as: $S^{-1}(p) = [1 + A(p)]\ (i\hat{p} + \Sigma(p))$ where $A(p)$ is the fermion wave function and $\Sigma(p)$ is the dynamically generated parity-conserving mass which is taken to be the same for all the fermions. The SD equation for the fermion propagator may be decomposed into scalar and vector components as follows:

$$\tilde{\Sigma}(p) = \frac{2a}{N}\,\mathrm{Tr}\int \frac{d^3k}{(2\pi)^3}\,\frac{\gamma^\mu D_{\mu\nu}(p-k)\Sigma(k)\Gamma^\nu(p,k)}{[1+A(k)]\,(k^2+\Sigma^2(k))}\,, \tag{2a}$$

$$A(p)p^2 = -\frac{2a}{N}\,\mathrm{Tr}\int \frac{d^3k}{(2\pi)^3}\,\frac{D_{\mu\nu}(p-k)\hat{p}\gamma^\mu\hat{k}\Gamma^\nu(p,k)}{[1+A(k)]\,(k^2+\Sigma^2(k))}\,, \tag{2b}$$

where $\tilde{\Sigma}(p) = \Sigma(p)[1 + A(p)]$, $D_{\mu\nu}(p)$ is the photon propagator in the non-local ξ-gauge:

$$D_{\mu\nu}(p) = \frac{P^\xi_{\mu\nu}(p)}{p^2\,[1+\Pi(p)]}, \quad P^\xi_{\mu\nu}(p) = g_{\mu\nu} - (1-\xi)\frac{p_\mu p_\nu}{p^2}\,, \tag{3}$$

$\Pi(p)$ is the polarization operator and $\Gamma^\nu(p,k)$ is the vertex function. In the following, Eqs. (2) will be studied for an arbitrary value of the gauge-fixing parameter ξ. All calculations will be

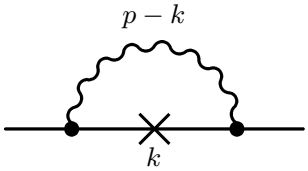


Figure 1: LO diagram to the dynamically generated mass $\Sigma(p)$. The crossed line denotes mass insertion.

performed with the help of the standard rules of perturbation theory for massless Feynman diagrams as in [26], see also the recent short review [27]. For the most complicated diagrams, the Gegenbauer polynomial technique will be used following [28].

3 Gap equation at leading order

The LO approximations in the $1/N$ expansion are given by: $A(p) = 0$, $\Pi(p) = a/|p|$ and $\Gamma^\nu(p,k) = \gamma^\nu$, where the fermion mass has been neglected in the calculation of $\Pi(p)$. A single diagram contributes to the gap equation (2a) at LO, see Fig. 1, and the latter reads:

$$\Sigma(p) = \frac{8(2+\xi)a}{N} \int \frac{d^3k}{(2\pi)^3} \frac{\Sigma(k)}{(k^2+\Sigma^2(k))\left[(p-k)^2 + a\,|p-k|\right]}\,. \tag{4}$$

Following [6], we consider the limit of large a and linearize Eq. (4) which yields:

$$\Sigma(p) = \frac{8(2+\xi)}{N} \int \frac{d^3k}{(2\pi)^3} \frac{\Sigma(k)}{k^2\,|p-k|}\,. \tag{5}$$

The mass function may then be parametrized as [6]:

$$\Sigma(k) = B\,(k^2)^{-\alpha}\,, \tag{6}$$

where B is arbitrary and the index α has to be self-consistently determined. Using this ansatz, Eq. (5) reads:

$$\Sigma^{(\mathrm{LO})}(p) = \frac{4(2+\xi)B}{N}\,\frac{(p^2)^{-\alpha}}{(4\pi)^{3/2}}\,\frac{2\beta}{\pi^{1/2}}\,, \tag{7}$$

from which the LO gap equation is obtained:

$$1 = \frac{(2+\xi)\beta}{L}, \quad \text{where} \quad \beta = \frac{1}{\alpha\,(1/2-\alpha)} \quad \text{and} \quad L \equiv \pi^2 N\,. \tag{8}$$

Solving this gap equation, yields:

$$\alpha_\pm = \frac{1}{4}\left(1 \pm \sqrt{1 - \frac{16(2+\xi)}{L}}\right)\,, \tag{9}$$

which reproduces the solution given by Appelquist et al. [6]. The gauge-dependent critical number of fermions: $N_c \equiv N_c(\xi) = 16(2+\xi)/\pi^2$, is such that $\Sigma(p) = 0$ for $N > N_c$ and

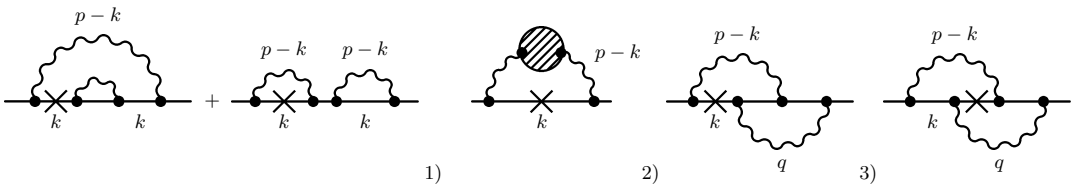


Figure 2: NLO diagrams to the dynamically generated mass $\Sigma(p)$. The shaded blob contains the sum of diagrams shown in Fig.3

$\Sigma(0) \simeq \exp\left[-2\pi/(N_c/N-1)^{1/2}\right]$, for $N < N_c$. Thus, DχSB occurs when α becomes complex, that is for $N < N_c$.

The gauge-dependent fermion wave function may be computed in a similar way. At LO, Eq. (2b) simplifies as:

$$A(p)p^2 = -\frac{2a}{N}\mathrm{Tr}\int\frac{d^Dk}{(2\pi)^D}\frac{P^\xi_{\mu\nu}(p-k)\hat{p}\gamma^\mu\hat{k}\gamma^\nu}{k^2|p-k|}\,, \tag{10}$$

where the integral has been dimensionally regularized with $D = 3 - 2\varepsilon$. Taking the trace and computing the integral on the r.h.s. yields:

$$A(p) = \frac{\overline{\mu}^{2\varepsilon}}{p^{2\varepsilon}}\,C_1(\xi) + \mathrm{O}(\varepsilon)\,,\quad C_1(\xi) = +\frac{2}{3\pi^2 N}\left((2-3\xi)\left[\frac{1}{\varepsilon} - 2\ln 2\right] + \frac{14}{3} - 6\xi\right)\,. \tag{11}$$

where the $\overline{MS}$ parameter $\overline{\mu}$ has the standard form $\overline{\mu}^2 = 4\pi e^{-\gamma_E}\mu^2$ with the Euler constant γ_E. We note that in the $\xi = 2/3$-gauge, the value of $A(p)$ is finite and $C_1(\xi = 2/3) = +4/(9\pi^2 N)$. ¿From Eq. (11), the LO wave-function renormalization constant may be extracted: $\lambda_A = \mu(d/d\mu)A(p) = 4(2-3\xi)/(3\pi^2 N)$ a result which coincides with the one of [38].

4 Next-to-leading order

We now consider the NLO contributions and parametrize them as:

$$\Sigma^{(\mathrm{NLO})}(p) = \left(\frac{8}{N}\right)^2 B\,\frac{(p^2)^{-\alpha}}{(4\pi)^3}\,\left(\Sigma_A + \Sigma_1 + 2\,\Sigma_2 + \Sigma_3\right)\,, \tag{12}$$

where each contribution to the linearized gap equation is represented graphically in Fig. 2. Adding these contributions to the LO result, Eq. (7), the gap equation has the following general form:

$$1 = \frac{(2+\xi)\beta}{L} + \frac{\overline{\Sigma}_A(\xi) + \overline{\Sigma}_1(\xi) + 2\,\overline{\Sigma}_2(\xi) + \overline{\Sigma}_3(\xi)}{L^2}\,, \tag{13}$$

where $\overline{\Sigma}_i = \pi\Sigma_i$, $(i = 1, 2, 3.A)$.

The contribution Σ_A, see Fig. 2 A), originates from the LO value of $A(p)$ and is singular. Using dimensional regularization, and for an arbitrary parameter ξ, it reads:

$$\overline{\Sigma}_A(\xi) = 4\,\frac{\overline{\mu}^{2\varepsilon}}{p^{2\varepsilon}}\,\beta\left[\left(\frac{4}{3}(1-\xi) - \xi^2\right)\left[\frac{1}{\varepsilon} + \Psi_1 - \frac{\beta}{4}\right] + \left(\frac{16}{9} - \frac{4}{9}\xi - 2\xi^2\right)\right]\,, \tag{14}$$

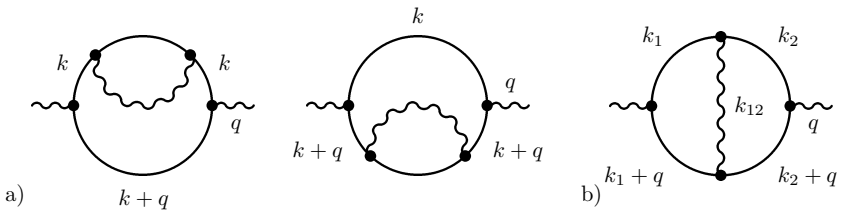


Figure 3: Diagrams contributing to the shaded blob shown in Fig.2

where

$$\Psi_1 = \Psi(\alpha) + \Psi(1/2-\alpha) - 2\Psi(1) + \frac{3}{1/2-\alpha} - 2\ln 2\,, \tag{15}$$

and Ψ is the digamma function.

The contribution of diagram 1) in Fig. 2 is finite and reads:

$$\overline{\Sigma}_1(\xi) = -2(2+\xi)\,\beta\,\hat{\Pi}, \qquad \hat{\Pi} = \frac{92}{9} - \pi^2\,, \tag{16}$$

where the gauge dependence comes from the fact that we work in a non-local gauge and $\hat{\Pi}$ arises from the two-loop polarization operator in dimension $D = 3$ [40, 39, 29, 30].

The contribution of diagram 2) in Fig. 2 is again singular. Dimensionally regularizing it yields:

$$\begin{aligned}
\overline{\Sigma}_2(\xi) &= -2\,\frac{\overline{\mu}^{2\varepsilon}}{p^{2\varepsilon}}\,\beta\left[\frac{(2+\xi)(2-3\xi)}{3}\left(\frac{1}{\varepsilon} + \Psi_1 - \frac{\beta}{4}\right) + \frac{\beta}{4}\left(\frac{14}{3}(1-\xi) + \xi^2\right)\right. \\
&\quad \left. + \frac{28}{9} + \frac{8}{9}\,\xi - 4\xi^2\right] + (1-\xi)\,\hat{\Sigma}_2\,, \\
\hat{\Sigma}_2(\alpha) &= (4\alpha-1)\beta\Big[\Psi'(\alpha) - \Psi'(1/2-\alpha)\Big] + \frac{\pi}{2\alpha}\,\tilde{I}_1(\alpha) + \frac{\pi}{2(1/2-\alpha)}\tilde{I}_1(\alpha+1)\,,
\end{aligned} \tag{17}$$

where Ψ' is the trigamma function and $\tilde{I}_1(\alpha)$ is a dimensionless integral that was defined in [1].

The singularities in $\overline{\Sigma}_A(\xi)$ and $\overline{\Sigma}_2(\xi)$ cancel each other and their sum is therefore finite. Defining: $\overline{\Sigma}_{2A}(\xi) = \overline{\Sigma}_A(\xi) + 2\overline{\Sigma}_2(\xi)$, the latter reads:

$$\overline{\Sigma}_{2A}(\xi) = 2(1-\xi)\hat{\Sigma}_2(\alpha) - \left(\frac{14}{3}(1-\xi) + \xi^2\right)\beta^2 - 8\beta\left(\frac{2}{3}(1+\xi) - \xi^2\right). \tag{18}$$

Finally, the contribution of diagram 3) in Fig. 2 is finite and reads:

$$\begin{aligned}
\overline{\Sigma}_3(\xi) &= \hat{\Sigma}_3(\alpha,\xi) + \Big(3 + 4\xi - 2\xi^2\Big)\beta^2, \;\; \hat{\Sigma}_3(\alpha,\xi) = \frac{1}{4}\big(1 + 8\xi + \xi^2 + 2\alpha(1-\xi^2)\big)\pi\tilde{I}_2(\alpha) \\
&\quad + \frac{1}{2}\big(1 + 4\xi - \alpha(1-\xi^2)\big)\pi\tilde{I}_2(1+\alpha) + \frac{1}{4}\big(-7 - 16\xi + 3\xi^2\big)\pi\tilde{I}_3(\alpha)\,,
\end{aligned} \tag{19}$$

where the dimensionless integrals $\tilde{I}_2(\alpha)$ and $\tilde{I}_3(\alpha)$ were defined in [1].

4.1 Gap equation

Combining all of the above results, the gap equation (13) may be written in an explicit form as:

$$1 = \frac{(2+\xi)\beta}{L} + \frac{1}{L^2}\left[8S(\alpha,\xi) - 2(2+\xi)\hat{\Pi}\beta + \left(-\frac{5}{3} + \frac{26}{3}\xi - 3\xi^2\right)\beta^2 - 8\beta\left(\frac{2}{3}(1-\xi) - \xi^2\right)\right], \quad (20)$$

where $S(\alpha,\xi) = \Big(\hat{\Sigma}_3(\alpha,\xi) + 2(1-\xi)\hat{\Sigma}_2(\alpha)\Big)/8$.

At this point, we consider Eq. (20) directly at the critical point $\alpha = 1/4$, *i.e.*, at $\beta = 16$. This yields:

$$L_c^2 - 16(2+\xi)L_c - 8\Big[S(\xi) - 4(2+\xi)\hat{\Pi} - 16\left(4 - 50\xi/3 + 5\xi^2\right)\Big] = 0\,, \quad (21)$$

where $S(\xi) = S(\alpha = 1/4, \xi) = (\hat{\Sigma}_3(\xi) + 2(1-\xi)\hat{\Sigma}_2)/8$ with $\hat{\Sigma}_2 = \hat{\Sigma}_2(\alpha = 1/4)$ and $\hat{\Sigma}_3(\xi) = \hat{\Sigma}_3(\alpha = 1/4, \xi)$. Solving Eq. (21), we have two standard solutions:

$$L_{c,\pm} = 8(2+\xi) \pm \sqrt{d_1(\xi)}\,, \quad d_1(\xi) = 8\left[S(\xi) - 8\left(4 - \frac{112}{3}\xi + 9\xi^2 + \frac{2+\xi}{2}\hat{\Pi}\right)\right]. \quad (22)$$

In order to provide a numerical estimate for N_c, we have used the series representations (see Ref. [1]) to evaluate the integrals: $\pi\tilde{I}_1(\alpha = 1/4) \equiv R_1$ and $\pi\tilde{I}_2(\alpha = 1/4 + i\delta) \equiv R_2 - iP_2\delta + O(\delta^2)$ where $\delta \to 0$ regulates an artificial singularity in $\pi\tilde{I}_3(\alpha = 1/4) = R_2 + P_2/4$. With 10000 iterations for each series, the following numerical estimates are obtained [1]: $R_1 = 163.7428$, $R_2 = 209.175$, $P_2 = 1260.720$, from which the complicated part of the self-energies can be evaluated:

$$\hat{\Sigma}_2 = 4R_1, \quad \hat{\Sigma}_3(\xi) = (\xi^2 - 1)R_2 - (7 + 16\xi - 3\xi^2)\,P_2/16\,. \quad (23)$$

Combining these values with the one of $\hat{\Pi}$, yields:

$$N_c(\xi = 0) = 3.29, \quad N_c(\xi = 2/3) = 3.09\,, \quad (24)$$

where "$-$" solutions are unphysical and there is no solution in the Feynman gauge. The range of ξ-values for which there is a solution corresponds to $\xi_- \le \xi \le \xi_+$, where $\xi_+ = 0.88$ and $\xi_- = -2.36$.

4.2 Extraction of the most "important" terms at NLO

Following Ref. [16], we would like to resum the LO term together with part of the NLO corrections containing terms $\sim \beta^2$. In order to do so, we will now rewrite the gap equation (20) in a form which is suitable for resummation. This amounts to extract the terms $\sim \beta$ and $\sim \beta^2$ from the complicated parts of the fermion self-energy, Eqs. (17) and (19). All calculations done this yields:

$$\hat{\Sigma}_2(\alpha) = \beta\big(3\beta - 8\big) + \tilde{\Sigma}_2(\alpha)\,, \quad \tilde{\Sigma}_2 = \tilde{\Sigma}_2(\alpha = 1/4) = 4\tilde{R}_1, \quad \tilde{R}_1 = 3.7428\,, \quad (25)$$

where the rest, $\tilde{\Sigma}_2 = \tilde{\Sigma}_2(\alpha = 1/4)$, was determined by imposing Eq. (23). Similarly:

$$\overline{\Sigma}_3(\xi) = -4\xi(4+\xi)\beta + \tilde{\Sigma}_3(\alpha,\xi)\,, \quad \tilde{\Sigma}_3(\xi) = \big(\xi^2 - 1\big)\tilde{R}_2 - \big(7 + 16\xi - 3\xi^2\big)\,\frac{\tilde{P}_2}{16}\,, \quad (26)$$

where $\tilde{R}_2 = 1.175$, $\tilde{P}_2 = -19.28$ and the form $\tilde{\Sigma}_3(\xi) = \tilde{\Sigma}_3(\alpha = 1/4, \xi)$, is imposed by Eq. (23). With the help of the results (25) and (26), the gap equation (20) may be written as:

$$1 = \frac{(2+\xi)\beta}{L} + \frac{1}{L^2}\left[8\tilde{S}(\alpha,\xi) - 2(2+\xi)\hat{\Pi}\beta + \left(\frac{2}{3} - \xi\right)(2+\xi)\,\beta^2 + 4\beta\left(\xi^2 - \frac{4}{3}\xi - \frac{16}{3}\right)\right], \quad (27)$$

where $\tilde{S}(\alpha,\xi) = \Big(\tilde{\Sigma}_3(\alpha,\xi) + 2(1-\xi)\tilde{\Sigma}_2(\alpha)\Big)/8$. At this point Eqs. (20) and (27) are strictly equivalent to each other and yield the same values for $N_c(\xi)$.

4.3 Resummation

Eq. (27) is the convenient starting point to perform a resummation of the wave function renormalization constant. Up to second order, the expansion of the latter reads [40]:

$$\lambda_A = \frac{\lambda^{(1)}}{L} + \frac{\lambda^{(2)}}{L^2} + \cdots, \quad \lambda^{(1)} = 4\left(\frac{2}{3} - \xi\right), \quad \lambda^{(2)} = -8\left(\frac{8}{27} + \left(\frac{2}{3} - \xi\right)\hat{\Pi}\right). \quad (28)$$

As can be seen from Eq. (27), the NLO term $\sim \beta^2$ is proportional to the LO wave function renormalization constant. This term, together with the LO term in the gap equation, can be thought of the first and zeroth order terms, respectively, of an expansion in λ_A. Following Nash, it is possible to resum the full expansion of λ_A at the level of the gap equation (see Ref. [2]) leading to:

$$1 = \frac{8\beta}{3L} + \frac{\beta}{4L^2}\left(\lambda^{(2)} - 4\lambda^{(1)}\left(\frac{14}{3} + \xi\right)\right) + \frac{\Delta(\alpha,\xi)}{L^2}, \quad (29)$$

where $\Delta(\alpha,\xi) = 8\tilde{S}(\alpha,\xi) - 4\beta\,(\xi^2 + 4\xi + 8/3) + 2\beta\,(2+\xi)\,\hat{\Pi}$. Interestingly, the LO term in Eq. (29) is now gauge independent. With the help of Eq. (28), Eq. (29) can now be explicited as:

$$1 = \frac{8\beta}{3L} + \frac{1}{L^2}\left[8\tilde{S}(\alpha,\xi) - \frac{16}{3}\,\beta\,\left(\frac{40}{9} + \hat{\Pi}\right)\right], \quad (30)$$

which displays a strong suppression of the gauge dependence even at NLO as ξ-dependent terms do exist but they enter the gap equation only through the rest, $\tilde{S}$, which is very small numerically.

We now consider Eq. (30) at the critical point, $\alpha = 1/4$ ($\beta = 16$), which yields:

$$L_c^2 - \frac{128}{3}L_c - \left[8\tilde{S}(\xi) - \frac{256}{3}\,\left(\frac{40}{9} + \hat{\Pi}\right)\right] = 0\,. \quad (31)$$

Solving Eq. (31), we have two standard solutions:

$$L_{c,\pm} = \frac{64}{3} \pm \sqrt{d_2(\xi)}\,, \quad d_2(\xi) = \left(\frac{64}{3}\right)^2 + \left[8\tilde{S}(\xi) - \frac{256}{3}\,\left(\frac{40}{9} + \hat{\Pi}\right)\right]. \quad (32)$$

In order to provide a numerical estimate for N_c, we have used the values of $\tilde{R}_1$, $\tilde{R}_2$ and $\tilde{P}_2$. Combining these values with: $\tilde{S}(\xi = 0) = \tilde{R}_1 - \tilde{R}_2/8 - 7\tilde{P}_2/128$, $\tilde{S}(\xi = 1) = -5\tilde{P}_2/32$ and $\tilde{S}(\xi = 2/3) = \tilde{R}_1/3 - 5\tilde{R}_2/72 - 49\tilde{P}_2/384$, together with the value of $\hat{\Pi}$, yields, for $L_c(\xi)$ and $N_c(\xi)$ ("$-$" solutions being unphysical):

$$N_c(0) = 3.08,\ N_c(2/3) = 3.04,\ N_c(1) = 3.01\,. \quad (33)$$

Actually, solutions exist for a broad range of values of ξ: $\tilde{\xi}_- \leq \xi \leq \tilde{\xi}_+$, where $\tilde{\xi}_+ = 4.042$ and $\tilde{\xi}_- = -8.412$; this is consistent with the weak ξ-dependence of the gap equation. Moreover, following [31], we think that the "right(est)" gauge choice is one close to $\xi = 2/3$ where the LO fermion wave function is finite. Indeed, as can be seen by comparing Eqs. (24) and (33), upon resumming the theory, the value of $N_c(\xi)$ increases (decreases) for small (large) values of ξ. For $\xi = 2/3$, the value of N_c is very stable, decreasing only by 1-2% during resummation. Finally, if we neglect the rest, *i.e.*, $\tilde{S}(\xi) = 0$ in Eq. (31), the gap equation becomes ξ-independent and we have: $\overline{L}_c = 28.0981$ and therefore: $\overline{N}_c = 2.85$, a value that coincides with the one in [18].

5 Conclusion

We have presented the studies [1, 2] of DχSB in QED$_3$ where $1/N^2$ corrections to the SD equation were included exactly and the full ξ-dependence of the gap equation was taken into account. Following Nash, the wave function renormalization constant has been resummed at the level of the gap equation leading to a very weak gauge-variance of the critical fermion number N_c. The value obtained for the latter, Eq. (33), suggests that DχSB takes place for integer values $N \leq 3$ in QED$_3$.

As noticed in [30, 33], the large-N limit of the photon propagator in QED$_3$ has precisely the same momentum dependence as the one in the so-called reduced QED [31, 32]. One difference is that the gauge fixing parameter in reduced QED is twice less than the one in QED$_3$. Such a difference can be taken into account with the help of our present results for QED$_3$ together with the multi-loop results obtained in [29, 30, 33]. The case of reduced QED, and its relation with dynamical gap generation in graphene which is the subject of active ongoing research, see, *e.g.*, the reviews [34, 35], was considered in our paper [36].

6 Acknowledgments

One of us (A.V.K.) was supported by RFBR grant 16-02-00790-a. He thanks the Organizing Committee of Helmholtz - DIAS International Summer School "Quantum Field Theory at the Limits: from Strong Fields to Heavy Quarks " for their invitation.

References

[1] A. V. Kotikov, V. I. Shilin and S. Teber, Phys. Rev. D **94**, 056009 (2016).

[2] A. V. Kotikov and S. Teber, Phys. Rev. D **94** 114011 (2016).

[3] T. Appelquist and R. Pisarski, Phys. Rev. D **23** 2305 (1981).

[4] R. Jackiw and S. Templeton, Phys. Rev. D **23** 2291 (1981); T. Appelquist and U. Heinz, Phys. Rev. D **24** 2169 (1981).

[5] R. Pisarski, Phys. Rev. D **29** 2423 (1984).

[6] T. Appelquist, D. Nash and L. C. R. Wijewardhana, Phys. Rev. Lett. **60** 2575 (1988).

[7] M. R. Pennington and D. Walsh, Phys. Lett. **253B** 246 (1991); D. C. Curtis, M. R. Pennington and D. Walsh, Phys. Lett. **295B** 313 (1992).

[8] R. Pisarski, Phys. Rev. D **44** 1866 (1991).

[9] V. Azcoiti and X. Q. Luo, Nucl. Phys. Proc. Suppl. **30** 741 (1993); V. Azcoiti, V. Laliena and X. Q. Luo, Nucl. Phys. Proc. Suppl. **47** 565 (1996).

[10] D. Atkinson, P. W. Johnson and P. Maris, Phys. Rev. D **42** 602 (1990).

[11] N. Karthik and R. Narayanan, Phys. Rev. D **93** 045020 (2016); N. Karthik and R. Narayanan, arXiv:1606.04109 [hep-th].

[12] T. Appelquist, A. Cohen and M. Schmaltz, Phys. Rev. D **60** 045003 (1999).

[13] S. Giombi, I. R. Klebanov and G. Tarnopolsky, J. Phys. **A49** 135403 (2016).

[14] L. Di Pietro, Z. Komargodski, I. Shamir and E. Stamou, Phys. Rev. Lett. **116** 131601 (2016).

[15] E. Dagotto, A. Kocic and J. B. Kogut, Phys. Rev. Lett. **62** 1083 (1989); Nucl. Phys. **B334** 279 (1990); S. J. Hands, J. B. Kogut, L. Scorzato and C. G. Strouthos, Phys. Rev. B **70** 104501 (2004); C. Strouthos and J. B. Kogut, PoS LAT **2007**, 278 (2007).

[16] D. Nash, Phys. Rev. Lett. **62** 3024 (1989).

[17] A. V. Kotikov, JETP Lett. **58** 734 (1993); Phys. Atom. Nucl. **75** 890 (2012).

[18] V. P. Gusynin and P. K. Pyatkovskiy, arXiv:1607.08582 [hep-ph].

[19] I. F. Herbut, Phys. Rev. D **94**, 025036 (2016)

[20] A. Bashir, A. Raya, S. Sanchez-Madrigal and C. D. Roberts, Few Body Syst. **46** 229 (2009).

[21] J. B. Marston and I. Affleck, Phys. Rev. B **16** 11538 (1989); L. B. Ioffe and A. I. Larkin, Phys. Rev. B **13** 8988 (1989).

[22] G. W. Semenoff, Phys. Rev. Lett. **53** 2449 (1984); P. R. Wallace, Phys. Rev. **71** 622 (1947).

[23] E. H. Simmons, Phys. Rev. D **42** 2933 (1990); T. Kugo and M. G. Mitchard, Phys. Lett. **B282** 162 (1992).

[24] A. Ahmad, J. J. Cobos-Martinez, Y. Concha-Sanchez and A. Raya, Phys. Rev. D **93**, 094035 (2016)

[25] J. S. Ball and T. W. Chiu, Phys. Rev. D **22** 2542 (1980).

[26] D. I. Kazakov, Phys. Lett. **133B** 406 (1983); "Analytical Methods For Multiloop Calculations: Two Lectures On The Method Of Uniqueness" - 1984. Preprint JINR E2-84-410, Dubna.

[27] S. Teber and A. V. Kotikov, arXiv:1602.01962 [hep-th], Theor.Math.Phys. (2017), in press.

[28] A. V. Kotikov, Phys. Lett. B **375** 240 (1996).

[29] S. Teber, Phys. Rev. D **86** 025005 (2012).

[30] A. V. Kotikov and S. Teber, Phys. Rev. D **87** 087701 (2013).

[31] E. V. Gorbar, V. P. Gusynin and V. P. Miransky, Phys. Rev. D **64** 105028 (2001).

[32] E. C. Marino, Nucl. Phys. **B408** 551 (1993); N. Dorey and N. E. Mavromatos, Nucl. Phys. B **386** 614 (1992); A. Kovner and B. Rosenstein, Phys. Rev. D **42** 4748 (1990).

[33] A. V. Kotikov and S. Teber, Phys. Rev. D **89** 065038 (2014); S. Teber, Phys. Rev. D **89** 067702 (2014).

[34] V. N. Kotov, B. Uchoa, V. M. Pereira, F. Guinea and A. H. Castro Neto, Rev. Mod. Rev. **84** 1067 (2012).

[35] V. A. Miransky and I. A. Shovkovy, Phys. Rept. **576** 1 (2015); V. P. Gusynin, Prob. Atomic Sci. Technol. **2013N3**, 29 (2013).

[36] A. V. Kotikov and S. Teber, Phys. Rev. D **94** 114010 (2016).

[37] V. P. Gusynin, A. H. Hams and M. Reenders, Phys. Rev. D **53** 2227 (1996).

[38] J. A. Gracey, Nucl. Phys. B **414** 614 (1994); C. S. Fischer, R. Alkofer, T. Dahm and P. Maris, Phys. Rev. D **70** 073007 (2004).

[39] V. P. Gusynin, A. H. Hams and M. Reenders, Phys. Rev. D **63** 045025 (2001).

[40] J.A. Gracey, Phys. Lett. B **317** 415 (1993).

QCD Vacuum as Domain Wall Network

Sergei N. Nedelko[1], *Vladimir E. Voronin*[1]

[1]Bogoliubov Laboratory of Theoretical Physics, JINR, 141980 Dubna, Russia

DOI: http://dx.doi.org/10.3204/DESY-PROC-2016-04/Voronin

Domain model of confinement, chiral symmetry breaking and hadronization is based on description of QCD vacuum gluon configurations as an ensemble of almost everywhere homogeneous Abelian (anti-)self-dual fields. The ensemble can be explicitly constructed as domain wall network. We shortly overview this approach and within this framework discuss the effects of QCD vacuum polarization by strong electromagnetic fields. It is stressed that such polarization effects can play the role of trigger for deconfinement.

1 Domain wall network

The following effective Lagrangian for gluon field and its motivation were discussed in [1]:

$$\mathcal{L}_{\rm eff} = -\frac{1}{4\Lambda^2}\left(D^{ab}_\nu F^b_{\rho\mu} D^{ac}_\nu F^c_{\rho\mu} + D^{ab}_\mu F^b_{\mu\nu} D^{ac}_\rho F^c_{\rho\nu}\right) - U_{\rm eff}$$
$$U_{\rm eff} = \frac{\Lambda^4}{12}{\rm Tr}\left(C_1 \breve{f}^2 + \frac{4}{3}C_2\breve{f}^4 - \frac{16}{9}C_3\breve{f}^6\right). \quad (1)$$

Here Λ is a scale of QCD related to gluon condensate, $\breve{f} = \breve{F}/\Lambda^2$, and

$$D^{ab}_\mu = \delta^{ab}\partial_\mu - i\breve{A}^{ab}_\mu = \partial_\mu - iA^c_\mu (T^c)^{ab},$$
$$F^a_{\mu\nu} = \partial_\mu A^a_\nu - \partial_\nu A^a_\mu - if^{abc}A^b_\mu A^c_\nu, \quad \breve{F}_{\mu\nu} = F^a_{\mu\nu}T^a, \quad T^a_{bc} = -if^{abc}$$
$${\rm Tr}\left(\breve{F}^2\right) = \breve{F}^{ab}_{\mu\nu}\breve{F}^{ba}_{\nu\mu} = -3F^a_{\mu\nu}F^a_{\mu\nu} \le 0, \quad C_1 > 0,\ C_2 > 0,\ C_3 > 0.$$

The minima of the effective potential are achieved for covariantly constant Abelian (anti-)self-dual fields

$$\breve{A}_\mu = -\frac{1}{2}\breve{n}_k F_{\mu\nu}x_\nu,\ \tilde{F}_{\mu\nu} = \pm F_{\mu\nu}, \quad F_{\mu\nu}F_{\mu\nu} = b^2_{\rm vac}\Lambda^4$$

where the matrix $\breve{n}_k$ belongs to the Cartan subalgebra of $su(3)$

$$\breve{n}_k = T^3\ \cos(\xi_k) + T^8\ \sin(\xi_k), \quad \xi_k = \frac{2k+1}{6}\pi,\ k = 0, 1, \ldots, 5.$$

The minima are connected by discrete parity and Weyl transformations, which indicates that the system is prone to existence of solitons in real space-time and kink configurations in Euclidean space. Group-theoretical analysis of symmetry breaking and domain wall formation was done in [2].

Let us consider the simplest kink configuration – kink interpolating between self-dual and anti-self-dual Abelian vacua. If the angle ω between chromoelectric and chromomagnetic fields is allowed to deviate from the constant vacuum value and all other parameters are fixed to the vacuum values, then the Lagrangian reads

$$\mathcal{L}_{\text{eff}} = -\frac{1}{2}\Lambda^2 b_{\text{vac}}^2 \partial_\mu\omega\partial_\mu\omega - b_{\text{vac}}^4\Lambda^4\left(C_2 + 3C_3 b_{\text{vac}}^2\right)\sin^2\omega.$$

The corresponding equation of motion is sine-Gordon equation

$$\partial^2\omega = m_\omega^2 \sin 2\omega, \quad m_\omega^2 = b_{\text{vac}}^2\Lambda^2\left(C_2 + 3C_3 b_{\text{vac}}^2\right),$$

which have the following kink solution:

$$\omega(x_\nu) = 2\ \text{arctg}\left(\exp(\mu x_\nu)\right).$$

The angle ω interpolates between 0 and π. x_μ stays for one of the four Euclidean coordinates. The kink describes a planar domain wall between the regions with almost homogeneous Abelian self-dual and anti-self-dual gluon fields. Chromomagnetic and chromoelectric fields are orthogonal to each other on the wall. Far away from the wall the field is self-dual or anti-self-dual, and absolute value of the topological charge density is equal to the value of the gluon condensate. The topological charge density vanishes on the wall.

We may now construct kink superposition with the standard methods. Let us denote the general kink configuration as

$$\zeta(\mu_i, \eta_\nu^i x_\nu - q^i) = \frac{2}{\pi}\arctan\exp(\mu_i(\eta_\nu^i x_\nu - q^i)),$$

where μ_i is the inverse width of the kink, η_ν^i is a normal vector to the plane of the wall. The general kink network is then given by

$$\omega = \pi\sum_{j=1}^{\infty}\prod_{i=1}^{k}\zeta(\mu_{ij}, \eta_\nu^{ij}x_\nu - q^{ij}). \tag{2}$$

Now we consider more general kink-like solution: three parameters b_{vac}, ω and ξ deviate from their vacuum values near the center of the kink (Fig. 1). One may see that the value of scalar condensate $F_{\mu\nu}F_{\mu\nu} = b_{\text{vac}}^2\Lambda^4$ decreases in the center of the kink which may increase size of stable chromomagnetic flux tube.

2 Chromomagnetic trap

Calculation of one-loop quark contribution to the QCD effective potential demonstrated that strong electromagnetic fields can play the role of a trigger for deconfinement [3]. The catalyzing role of strong magnetic fields was also observed in Lattice QCD simulations [4, 5, 6]. During heavy ion collisions, the electric $\mathbf{E}_{\text{el}}$ and magnetic $\mathbf{H}_{\text{el}}$ fields are almost orthogonal to each other [7, 8]: $\mathbf{E}_{\text{el}}\mathbf{H}_{\text{el}} \approx 0$. For this configuration of the external electromagnetic field, the one-loop quark contribution to the QCD effective potential for the homogeneous Abelian gluon fields is minimal for the chromoelectric and chromomagnetic fields directed along the electric and magnetic fields respectively [3, 9]. The orthogonal chromo-fields are not confining: color charged

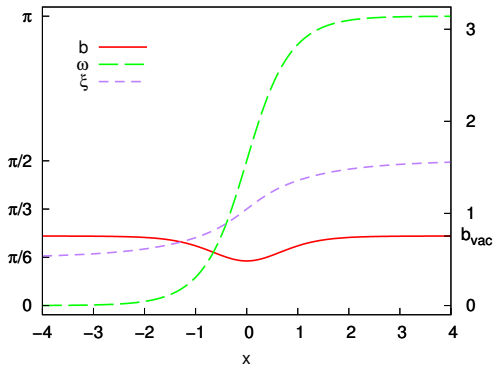


Figure 1: Kink connecting distinct vacua. Angle ω varies from 0 to π, angle ξ varies from $\pi/6$ to $\pi/2$. Global minima of effective potential (1) are degenerate in the value of field strength $b = b_{\rm vac}$, so its magnitude is the same for all vacua. Dimensionless variable $x \equiv \Lambda x$ is used.

quasiparticles can move along the chromomagnetic field. Deconfined quarks as well as gluons can move preferably along the direction of the magnetic field even after the electromagnetic field turns off. This means that a defect in domain wall network may be formed during heavy ion collision (see Fig. 2).

Let us consider eigenvalue problem for vector field

$$\left[-\check{D}^2\delta_{\mu\nu} + 2i\check{n}B_{\mu\nu}\right] Q_\nu = \lambda^2 Q_\mu \tag{3}$$

with the boundary conditions

$$\check{n}Q_\mu(x) = 0,\ x \in \partial\mathcal{T}, \quad \partial\mathcal{T} = \left\{x_1^2 + x_2^2 = R^2,\ (x_3, x_4) \in \mathrm{R}^2\right\}.$$

The corresponding eigenvalues are

$$\lambda^2_{alk\nu} = p_4^2 + p_3^2 + \mu^2_{alk} + 2s_\nu\kappa_a v, \quad k = 0, 1, \ldots, \infty, \quad l \in Z,$$
$$s_1 = 1,\ s_2 = -1,\ s_3 = s_4 = 0,\ \kappa_a = \pm 1.$$

In the finite trap the lowest eigenvalue is

$$\lambda^2_{a00\nu} = p_4^2 + p_3^2 + \mu^2_{a00} - 2v,\ s_\nu\kappa_a = -1.$$

Few lowest eigenvalues μ^2_{akl} as functions of $\sqrt{H}R$ are shown in Fig. 2. One concludes that if the dimensionless size $\sqrt{H}R$ of the trap is sufficiently small

$$\sqrt{H}R < \sqrt{H}R_{\rm c} \approx 1.91, \tag{4}$$

then there are no unstable tachyonic modes in the spectrum of color charged vector fields.

To estimate the critical size one may use the mean phenomenological value of the gluon condensate (gauge coupling constant g is included into the field strength tensor)

$$\langle F^a_{\mu\nu}F^{a\mu\nu}\rangle = 2H^2 \approx 0.5\mathrm{GeV}^4.$$

Equation (4) leads to the critical radius

$$R_{\rm c} \approx 0.51 \text{ fm } (2R_{\rm c} \approx 1 \text{ fm}).$$

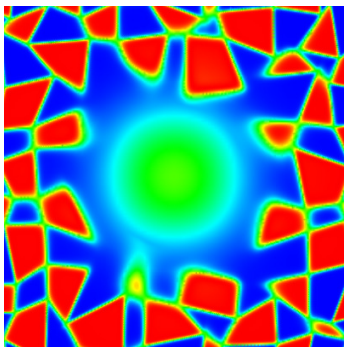


Figure 2: Example of two-dimensional slice of the cylindrical thick domain wall junction. Self-dual and anti-self-dual fields are indicated by blue and red colors respectively. The topological charge densityvanishes inside the junction (green color).

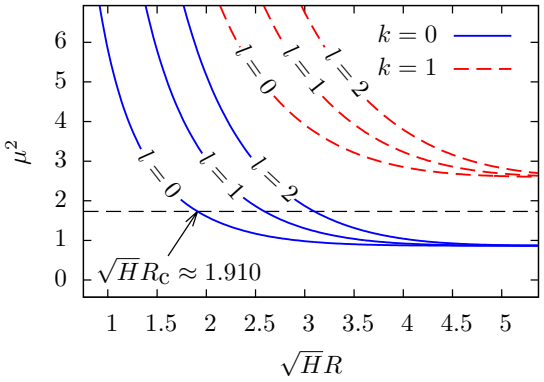


Figure 3: The lowest eigenvalues corresponding to positive color orientation $\kappa^a = 1$ as functions of $\sqrt{H}R$. The critical radius R_c corresponds to $\mu^2_{a00} = 2v = \sqrt{3}$. For large $\sqrt{H}R$ eigenvalues approach correct Landau levels, the degeneracy in l is restored.

However, as it follows from Fig. 1, scalar condensate become smaller at the domain wall and may increase the value of critical radius.

In Minkowski space-time the eigenvalue problem turns to the wave equation:

$$\left[-\check{D}^2\delta_{\mu\nu} + 2i\check{n}B_{\mu\nu}\right] Q_\nu = 0.$$

Solution for this equation can be found as a linear combination of eigenmodes (3) with $\lambda = 0$.

$$p_0^2 = p_3^2 + \mu^2_{alk} + 2s_\nu\kappa_a v, \tag{5}$$
$$p_0 = \pm\omega_{alk\nu}(p_3),\ \omega_{alk\nu} = \sqrt{p_3^2 + \mu^2_{alk\nu} + 2s_\nu,\kappa_a v}.$$

Equation (5) can be treated as the dispersion relation between energy p_0 and momentum p_3 for the quasiparticles. Unlike the chromomagnetic field, the (anti-)self-dual fields characteristic for the bulk of domain network configuration lead to purely discrete spectrum of eigenmodes in Euclidean space and do not possess any quasiparticle treatment in terms of dispersion relation between energy and momentum for elementary color charged excitations.

3 Discussion

Even though a single chromomagnetic trap has critical size, overall volume of deconfinement transition in hadronic matter is not restricted by L_c. Numerous traps may be formed, for instance, due to the influence of strong electromagnetic fields in the whole region of relativistic heavy ion collision [3]. The traps may merge into a large chromomagnetic lump developing the flux tube structure inside the lump. Equivalently, one may also think about formation of the flux tubes inside the traps with overcritical size emerging under conditions of high energy or/and baryon number density, strong electromagnetic fields.

In the absence of any external impact one expects that the fraction of the deconfinement phase is statistically negligible as it occupies an essentially three-dimensional sub-manifold in the four-dimensional space R^4. The influence of external conditions like the high energy density, high baryon density and strong electromagnetic fields can trigger the growth of the relative fraction of the deconfined phase. Under certain conditions high energy density accumulated by colorless collective excitations can be converted into the thermodynamics of color charged quasiparticles. The growth of the deconfinement phase fraction may be described in terms of creation of either numerous stable chromomagnetic traps or/and the trap with overcritical size, populated by the polarized chromomagnetic tubes [10].

In the confinement regime (color charge quasiparticles are completely suppressed) one may expect

$$q(x) = \langle |g^2 \tilde{F}(x) F(x)| \rangle_{\mathcal{B}} = \langle g^2 F(x) F(x) \rangle_{\mathcal{B}} = B^2_{\rm vac},$$

while the deconfinement regime (color charged quasiparticles are fully activated) occurs if

$$q(x) \ll \langle g^2 F(x) F(x) \rangle_{\mathcal{B}} = B^2_{\rm vac}.$$

The scalar gluon condensate may stay practically unchanged during the phase transformation. The regime of dilute plasma can not be reached unless the scalar gluon condensate density vanishes, which would require complete rearrangement of the quantum effective action. However, as soon as the color charged quasiparticles are activated the structure of the effective action itself in principle becomes dependent on their temperature and density, and it cannot be excluded that the scalar condensate vanishes at certain critical values of the temperature and density.

In summary, the domain wall network representation of QCD vacuum is suggestive of a two-stage deconfinement transition. At the first stage topological charge density vanishes, but the scalar condensate stays almost unchanged, color charged quasiparticles are activated at this stage while the colorless collective excitations can decay into the color charged ones. The system is far from being a dilute gas. At the second stage the scalar gluon condensate vanishes, and the system turns into dilute quark-gluon plasma.

References

[1] B. V. Galilo and S. N. Nedelko, Phys. Part. Nucl. Lett. **8**, 67 (2011) [arXiv:1006.0248 [hep-ph]].

[2] D. P. George, A. Ram, J. E. Thompson and R. R. Volkas, Phys. Rev. D **87**, 105009 (2013) [arXiv:1203.1048 [hep-th]].

[3] B. V. Galilo and S. N. Nedelko, Phys. Rev. D84 (2011) 094017.

[4] C. Bonati, M. D'Elia, M. Mariti, M. Mesiti, F. Negro, A. Rucci and F. Sanfilippo, Phys. Rev. D **94**, no. 9, 094007 (2016) [arXiv:1607.08160 [hep-lat]].

[5] G. S. Bali, F. Bruckmann, G. Endrodi and A. Schafer, Phys. Rev. Lett. **112**, 042301 (2014) [arXiv:1311.2559 [hep-lat]].

[6] G. S. Bali, F. Bruckmann, G. Endrődi, S. D. Katz and A. Schäfer, JHEP **1408**, 177 (2014) [arXiv:1406.0269 [hep-lat]].

[7] V. Voronyuk, V. D. Toneev, W. Cassing, E. L. Bratkovskaya, V. P. Konchakovski and S. A. Voloshin, Phys. Rev. C **83**, 054911 (2011) [arXiv:1103.4239 [nucl-th]].

[8] V. Skokov, A. Y. Illarionov and V. Toneev, Int. J. Mod. Phys. A **24** (2009) 5925 [arXiv:0907.1396 [nucl-th]].

[9] S. Ozaki, Phys. Rev. D **89**, no. 5, 054022 (2014) [arXiv:1311.3137 [hep-ph]].

[10] J. Ambjorn and P. Olesen, Nucl. Phys. B **170**, 265 (1980).

List of Authors

M. Jamil Aslam, 239

Abdur Rehman, 239
Adeva, Bernardo, 177
Ahmed, Ishtiaq, 239
Ahmed, Ishtiaq, 353
Ali, Ahmed, 239
Ali, Ahmed, 208

Bellantuono, L., 79
Blaschke, D. B., 1
Bydžovský, P., 286

Colangelo, P., 79

Ebert, D., 297, 307

Faustov, R. N., 297, 307
Fazio, F. De, 79
Fedotov, Alexander, 68

Galkin, V. O., 297, 307
Grozin, Andrey, 121
Gutiérrez-Guerrero, L.X., 371
Gutsche, T., 286
Gutsche, Thomas, 256

Issadykov, Aidos, 358
Ivanov, M. A., 326
Ivanov, Mikhail A., 358

Jamil Aslam, M., 371
Juchnowski, L., 1

Kämpfer, Burkhard, 58
Körner, J. G., 326
Kamiński, R., 286
Karbstein, Felix, 44
Karpishkov, Anton, 266
Kochelev, Nikolai, 246
Kotikov, Anatoly V., 377
Krasnikov, S. N. Gninenko and N. V., 167

Leonardo, Nuno T., 187
Lipatov, A. V., 276
Lykasov, G. I., 276
Lyubovitskij, V. E., 286
Lyubovitskij, Valery E., 256

Mandal, Rusa, 339

Nagy, M., 286
Nayak, Abinash Kumar, 339
Nedelko, Sergei N., 387
Nefedov, Maxim, 266
Nicotri, F. Giannuzzi and S., 79

Panferov, A., 1
Parkhomenko, Alexander, 150

Saleev, Vladimir, 266
Santorelli, Pietro, 317
Schmidt, Ivan, 256
Seipt, Daniel, 24
Shipilova, Alexandra, 266
Sinha, Rahul, 339
Smolyansky, S. A., 1
Stepanenko, Yu. Yu., 276
Surovtsev, Yu. S., 286

Takabe, A Hosaka and H., 58
Takizawa, Makoto, 198
Teber, Sofian, 377
Titov, Alexander I., 58
Tran, C. T., 326

Voronin, Vladimir E., 387

Zwicky, Roman, 93

Participants

AHMED, Ali (DESY, Hamburg)
AHMED, Ishtiaq (NCP, Islamabad)
ASLAM, Muhammad Jamil (Quaid-i-Azam Univ., Islamabad)
AVAKYAN, Elena (SSTU, GOMEL)
AVAKYAN, Sergey (SSTU, GOMEL)
AZNABAYEV, Damir (JINR, Dubna)

BARINOVA, Sofija (SSU, Saratov)
BASTIAN, Niels-Uwe (Univ. of Wroclaw, Wroclaw)
BEDNYAKOV, Alexander (JIRN, Dubna)
BEKBAYEV, Askhat (KazNU, Almaty)
BHATT, Palak (Sardar Patel Univ.)
BILANISHVILI, Shalva (TSU, Tbilisi)
BLASCHKE, David (JINR Dubna, Uni Wroclaw, MEPhI Moscow)
BER, Philipp (Univ. of Siegen)
BYSTRITSKIY, Yury (JINR, Dubna)

CHATURVEDI, Raghav (NIT, Surat)
CZAKON, Michal (RWTH, Aachen)

DAS, Chitta Ranjan (BLTP, JINR, Dubna)
DEKA, Mridupawan (BLTP, JINR, Dubna)
DEVLANI, Nayneshkumar (PTU, Baroda)
DUC THONG, Le (NCST,Hanoi)

GARCIA-NAVARRO, Jose Enrique (IFIC, Valencia)
GIES, Holger (HI, Jena)
GRATREX, James (Univ. of Edinburgh, Edinburgh)

ILGENFRITZ, Ernst-Michael (JINR, Dubna)
ISSADYKOV, Aidos (JINR, Dubna)
ISSIMOV, Nurdaulet (KazNU, Almaty)
IVANOV, Mikhail A. (JINR, Dubna)

JANSEITOV, Daniyar (ENU, Astana)
JUCHNOWSKI, ukasz (Univ. of Wroclaw, Wroclaw)

KALIKIN, Mikhail (DYSU, Yaroslavl)
KARABANOV, Ilya (DYSU, Yaroslavl)
KARPISHKOV, Anton (NRU, Samara)
KHER, Virendrasinh (PTU, Baroda)
KHVOROSTUKHIN, Andey (JINR, Dubna)
KLOPOT, Yaroslav (JINR, Dubna)
KOBZAK, Sergei (MEPhI, Moscow)
KOLOMIYTSEV, Georgy (MEPhI, Moscow)
KOLOMOYETS, Natalia (DNU,Dnepropetrovsk)
KORCHAGIN, Nikolai (IMP, Nanchang)
KRYLOV, Konstantin (MEPhi, Moscow)
KRYUKOV, Ivan (MEPhi, Moscow)

KUZNIETSOV, Philip (IERT NAS, Kharkov)

LIEBING, Simon (ITP, Freiberg)
LUKASHEVICH, Svetlana (GSU, Gomel)
LYUKASOV, Gennady I. (JINR, Dubna)
MARFATIA, Zalak (NIT, Surat)

MASLOV, Konstantin (MEPhI, Moscow)
MIRONOV, Arseniy (MEPhI, Moscow)

NAGY, Miroslav (IP, Bratislava)
NAZAROVA, Elizaveta (SINP MSU)
NEFEDOV, Maxim (SSAU, Samara)
NOVIKOVA, Valentina (JINR, Dubna)
NURBAKOVA, Guliya (KazNU, Almaty)

PANDIAT, Saumia (JINR, Dubna)
PARKHOMENKO, Alexander (DYSU, Yaroslavl)
PATEL, Smruti (SPU, Gujarat)
PIROGOV, Stanislav (NRSSU, Saratov)
PIROZHENKO, Irina (JINR, Dubna)

RATHAUD, Dharmesh (NIT, Surat)
REHMAN, Abdur (NCP, Islamabad)
RUIJTER, Marcel (HIJ, Jena)
RUSNAK, Alexander (MIPT(MSU), Moscow)
RUSOV, Aleksey (Univ. of Siegen, Siegen)
RUSOV, Alexander (DYSU, Yaroslavl)

SHEKHANOV, Svyatoslav (MEPhI, Moscow)
SHIPILOVA, Aleksandra (NRU, Samara)
SCHMELZER, Jurn (Rostock Univ., JINR, Dubna)
SINGH, Captain Rituraj (BITS, Pilani)
SINHA, Rahul (IMSC, Chennai)
SONI, Nakul (MSUB, Vadodara)
SPERLING, Anton (JINR, Dubna)
SUNDQVIST, Chantal (HIJ, Jena)

TRAN, Chien-Thang (JINR, Dubna)
TULSKY, Vasily (MEPhi, Moscow)
TUYLEMISOV, Zhomart (KazNU, Almaty)

VALIOLDA, Dinara (KazNU, Almaty)
VORONIN, Vladimir (JINR, Dubna)

ZHANG, Pengming (IMP, Nanchang)
ZHAUGASHEVA, Saule (KazNU, Almaty)
ZHEMCHUGOV, Evgenii (ITEP, Moscow)
ZHURAVLEV, Vyacheslav (JINR, Dubna)
ZWICKY, Roman (Univ. of Edinburgh, Edinburgh)